University of Glasgow

Onah, Ifeanyi Sunday (2024) *Riemann problems in the retinal circulation.* PhD thesis.

https://theses.gla.ac.uk/84507/

Copyright and moral rights for this work are retained by the author

A copy can be downloaded for personal non-commercial research or study, without prior permission or charge

This work cannot be reproduced or quoted extensively from without first obtaining permission in writing from the author

The content must not be changed in any way or sold commercially in any format or medium without the formal permission of the author

When referring to this work, full bibliographic details including the author, title, awarding institution and date of the thesis must be given

Enlighten: Theses
https://theses.gla.ac.uk/
research-enlighten@glasgow.ac.uk

Riemann problems in the retinal circulation

Ifeanyi Sunday Onah

Submitted in fulfilment of the requirements for the
Degree of Doctor of Philosophy

School of Mathematics and Statistics
College of Science and Engineering
University of Glasgow

December, 2023

Abstract

Retinal haemorrhage (abnormal bleeding of the blood vessels in the retina) is often observed following traumatic brain injury. The retinal blood vessels, known as the retinal circulation, are supplied by the central retinal artery (CRA) and the central retinal vein (CRV), which pass along the optic nerve after passing through a region of ceresbrospinal fluid (CSF) in the nerve sheath. In this thesis we develop a theoretical model for blood flow in the retinal blood vessels which forms the foundation of a predictive model of retinal haemorrhage.

We first consider a case where sudden change in CSF pressure (*i.e.* following brain injury) drives a large amplitude pressure perturbation (shock waves), treating the blood vessel as a single compliant tube with uniform material properties. We develop a Riemann problem to consider the response to an instantaneous discontinuity in flow and/or tube cross-sectional area across an interface, and examine the flow propagation. We identify the four classical flow structures that emerge from the discontinuity.

We extend our Riemann problem to consider an abrupt change in material properties coincident with the initial discontinuity, as a model for the central retinal vessels crossing between regions (*e.g.* between the optic nerve and the retina). Our Riemann problem exhibits the four classical solutions each with an additional stationary wave across the point of discontinuity. However, these classical solutions are not sufficient to cover the entire parameter space, and we demonstrate the existence of transcritical states resulting from a rarefaction wave resonating with the stationary wave, producing additional shock waves. These new resonant solutions were enough to close the gaps in our parameter space left by the classical solutions.

Finally we investigate the propagation of these large-amplitude pressure waves through a symmetric junction (mimicking blood flow through the retinal vessel networks). Our Riemann problem exhibits analogs of the four classical wave structures (again with a discontinuity across the stationary wave at the junction) as well as analogs of the transcritical (resonant) states identified in flow through a single vessel with a discontinuity in material properties. Furthermore, we find that the onset of resonance is delayed when the daughter vessels are chosen to be less stiff than the parent vessel and can be eliminated entirely if the reduction in stiffness is sufficiently large.

Contents

Abstract **i**

Acknowledgements **xx**

Declaration and Publications **xxi**

1 Introduction **1**
1.1 The eye . . . 1
1.1.1 Structure of the retina . . . 3
1.1.2 Structure of the optic nerve . . . 3
1.2 Retinal haemorrhage . . . 4
1.2.1 The pressure rise hypothesis . . . 4
1.2.2 Vitreoretinal traction . . . 5
1.3 Modelling blood flow circulation . . . 5
1.3.1 Linear and non-linear wave theory . . . 6
1.3.2 Modelling of flexible walls . . . 11
1.3.3 Inviscid approaches . . . 11
1.3.4 Viscous effects . . . 12
1.3.5 Three-dimensional flow through networks . . . 12
1.3.6 Reduction to 1D equations in a single blood vessel . . . 12
1.3.7 1D models for blood vessels coupled at junctions . . . 13
1.3.8 Large amplitude pressure waves - shock capture . . . 14
1.3.9 Models specific to the retinal circulation . . . 15
1.4 Modeling retinal haemorrhage . . . 15
1.5 Physiological parameters . . . 16
1.6 Outline of the thesis . . . 18

2 A blood vessel with uniform material properties **21**
2.1 Governing equations . . . 21
2.2 Non dimensionalization . . . 22

2.3 Long wavelength approximation . . . 23
2.4 Riemann problem in an elastic tube . . . 26
2.5 Nonlinear shock waves . . . 28
2.5.1 Left shock . . . 30
2.5.2 Right shock . . . 31
2.6 Nonlinear rarefaction waves . . . 32
2.6.1 Left rarefaction . . . 32
2.6.2 Right rarefaction . . . 34
2.7 Composite wave profiles . . . 34
2.8 Newton's method . . . 37
2.8.1 Left rarefaction, Right shock (LRRS) . . . 37
2.8.2 Left shock, Right rarefaction (LSRR) . . . 37
2.8.3 Left rarefaction, Right rarefaction (LRRR) . . . 37
2.8.4 Left shock, Right shock (LSRS) . . . 38
2.9 Numerical approach . . . 38
2.9.1 Algorithm of Brook et al. (1999). . . . 38
2.9.2 Right shock . . . 40
2.9.3 Right rarefaction . . . 40
2.9.4 Left shock . . . 40
2.9.5 Left rarefaction . . . 40
2.9.6 Algorithm . . . 41
2.10 Numerical simulations of both models . . . 41
2.10.1 Left rarefaction, right shock (LRRS) . . . 42
2.10.2 Left shock, right rarefaction (LSRR) . . . 42
2.10.3 Left rarefaction, right rarefaction (LRRR) . . . 44
2.10.4 Left shock, right shock (LSRS) . . . 44
2.11 Bifurcation diagrams varying one parameter . . . 45
2.11.1 Case 1 . . . 45
2.11.2 Case 2 . . . 46
2.11.3 Case 3 . . . 49
2.11.4 Case 4 . . . 51
2.12 Overview of the parameter space . . . 53
2.12.1 Overview using Newton's method . . . 53
2.12.2 Overview using method of Brook et al. . . . 54
2.12.3 Overview in terms of initial conditions in region 1 . . . 55
2.12.4 Parameter space plot for different values of the exponent m . . . 55
2.13 General tube law . . . 59
2.13.1 Nonlinear shock wave . . . 60
2.13.2 Nonlinear Rarefaction wave . . . 61
2.13.3 Newton's method and numerical simulation . . . 61
2.13.4 Baseline cases . . . 62
2.13.5 Overview of parameter space . . . 64
2.14 Summary and conclusion . . . 67

3 A blood vessel with discontinuous material properties 69
3.1 Model setup . . . 69
3.1.1 Dimensional parameters, variables and equations . . . 70
3.1.2 Non dimensionalization and final governing equations . . . 70
3.2 Riemann problem . . . 72
3.2.1 Compartment 1 . . . 72
3.2.2 Compartment 2 . . . 73
3.2.3 Boundary conditions between compartments . . . 73
3.3 Nonlinear flow structure . . . 74
3.3.1 Left Rarefaction . . . 74
3.3.2 Right Rarefaction . . . 75
3.3.3 Left shock . . . 76
3.3.4 Right shock . . . 76
3.3.5 Boundary conditions . . . 77
3.4 Numerical method . . . 77
3.5 Simple connection across the discontinuity: no resonance . . . 77
3.5.1 Left rarefaction, right shock . . . 78
3.5.2 Left shock, right rarefaction . . . 79
3.5.3 Left shock, right shock . . . 80
3.5.4 Left rarefaction, right rarefaction . . . 80
3.6 Small amplitude waves . . . 82
3.7 Other possible flow states: resonance . . . 85
3.7.1 Governing equations for configuration C . . . 86
3.7.2 Governing equations for configuration D . . . 89
3.8 Typical results: Traces through the parameter space . . . 91
3.8.1 Case 1 . . . 91
3.8.2 Case 2 . . . 95
3.8.3 Case 3 . . . 98
3.8.4 Case 4 . . . 100
3.8.5 Case 5 . . . 102
3.8.6 Cases 6, 7 and 8 . . . 107
3.8.7 Case 9 . . . 107
3.8.8 Case 10 . . . 107
3.8.9 Case 11 . . . 107
3.9 Overview of the parameter space . . . 112
3.10 General tube law . . . 115
3.10.1 Compartment 1 . . . 115
3.10.2 Compartment 2 . . . 116
3.10.3 Boundary conditions between compartments . . . 116
3.10.4 Nonlinear flow structure . . . 116
3.10.5 Left rarefaction . . . 116
3.10.6 Right rarefaction . . . 117
3.10.7 Left shock . . . 117
3.10.8 Right shock . . . 118
3.10.9 Boundary conditions . . . 118

3.11 Numerical method . . . 118
3.11.1 Left rarefaction, right shock (LRRS) . . . 119
3.11.2 Left shock, right rarefaction . . . 120
3.12 Other possible flow states: resonance . . . 120
3.12.1 Governing equations for configuration C using the general tube law . . . 121
3.12.2 Governing equations for configuration D using the general tube law . . . 122
3.13 Traces through the parameter space . . . 123
3.13.1 Case 12 . . . 123
3.13.2 Case 13 . . . 123
3.13.3 Overview of parameter space . . . 125
3.14 Summary and conclusion . . . 129

4 A blood vessel with a symmetric junction 130
4.1 Model setup . . . 130
4.1.1 Non dimensionalization and final governing equations . . . 131
4.1.2 Boundary conditions between vessels . . . 132
4.2 Nonlinear flow structure . . . 132
4.2.1 Riemann invariants . . . 133
4.2.2 Parent rarefaction . . . 133
4.2.3 Daughter rarefaction . . . 134
4.2.4 Parent shock . . . 135
4.2.5 Daughter shock . . . 135
4.2.6 Boundary conditions . . . 136
4.3 Numerical method . . . 136
4.4 Simple connection across the junction: no resonance . . . 136
4.4.1 Parent rarefaction, daughter shock . . . 136
4.4.2 Parent shock, daughter rarefaction . . . 137
4.4.3 Parent shock, daughter shock . . . 137
4.4.4 Parent rarefaction, daughter rarefaction . . . 138
4.5 Small amplitude waves . . . 140
4.6 Resonance . . . 143
4.6.1 Riemann solution of configuration C^+ . . . 143
4.6.2 Riemann solution for configuration D^+ . . . 146
4.7 Results of the Riemann problem with no change in material or environmental properties 148
4.7.1 Variation of cross-sectional area in daughter vessel . . . 148
4.7.2 Variation of cross-sectional area in parent vessel . . . 156
4.8 Overview of parameter space . . . 159
4.8.1 Variation of cross-sectional area in daughter vessel with jump in stiffness . . . 161
4.8.2 Variation of cross-sectional area in parent vessel with jump in stiffness . . . 167
4.9 Overview of the parameter space with a jump in stiffness . . . 168
4.10 General tube law . . . 172
4.10.1 Riemann problem . . . 173
4.10.2 Riemann invariants . . . 173
4.10.3 Boundary conditions between vessels . . . 174
4.10.4 Nonlinear flow structure . . . 174

4.10.5 Parent rarefaction . . . 174
4.10.6 Daughter rarefaction . . . 174
4.10.7 Parent shock . . . 175
4.10.8 Daughter shock . . . 175
4.10.9 Boundary conditions . . . 176
4.10.10 Numerical method . . . 176
4.11 Resonance . . . 176
4.11.1 Riemann solution of configuration C^+ using general tube law . . . 176
4.11.2 Riemann solution for configuration D^+ . . . 177
4.12 Overview of parameter space with no jump in material properties using general tube law 178
4.13 Overview of parameter space with splitting of mass and jump in material properties using general tube law . . . 180
4.14 Summary . . . 183

5 Summary and Conclusion **184**
5.1 Future work . . . 185

Appendices **186**
A MATLAB codes . . . 186
A.1 MATLAB code for Chapter 2 . . . 186
A.2 MATLAB code for Chapter 3 . . . 191
A.3 MATLAB code for Chapter 4 . . . 206

Bibliography **222**

List of Tables

1.1 Measured data of some generations in the human arterial network according to Takahashi et al. [90] . . . 16
1.2 Estimated data of some generations in the human arterial network . . . 17
1.3 Measured data of some generations in the human venous network according to Takahashi et al. [90] . . . 17
1.4 Estimated data of some generations in the human venous network . . . 17

3.1 Summary of dimensional parameters in both compartments . . . 70
3.2 Summary of dimensional variables in both compartments . . . 70
3.3 Summary of dimensionless parameters . . . 71
3.4 Summary of cases considered. . . . 92

List of Figures

1.1 Physiology of the human eye [11]. . . . 2
1.2 Healthy and haemorrhaged retina. . . . 4
1.3 Illustration of the wave profiles and corresponding characteristics generated with an instantenous removal of the dam. Figure 2.4(a,b) is a left moving rarefaction and right moving rarefaction wave. . . . 8
1.4 Anatomy of the superior-inferior axis of the human eye through the optic nerve to the retina [103]. The path of the central retinal artery and vein are clearly marked, entering the nerve about 1cm from the eye and entering the retina through the center of the optic nerve. . . . 19
1.5 Set-up of the different components of the thesis. . . . 20

2.1 Comparison of dimensionless tube laws showing the different values of m and n. . . . 26
2.2 Set-up of the mathematical model. . . . 27
2.3 Plot of the $x - t$ plane showing regions 1 (upstream), region 2 (downstream) and region 3 which spans the origin connecting the two regions. . . . 27
2.4 Illustration of the wave profiles in cross-sectional area and corresponding characteristics generated with a discontinuous initial condition. Figure 2.4(a,b) is a left moving shock and right moving rarefaction wave. . . . 31
2.5 Illustration of the wave profiles in cross-sectional area and corresponding characteristics generated with a discontinuous initial condition. Figure 2.5(a,b) is a left rarefaction wave and right moving shock wave. . . . 32
2.6 Illustrations of the wave profiles in cross-sectional area and corresponding characteristics generated with a discontinuous initial condition. Figure 2.6(a,b) is a left moving rarefaction and right moving shock wave, Figure 2.6(c,d) is a left moving shock and right moving rarefaction wave, Figure 2.6(e,f) is a left and right moving shock wave and Figure 2.6(g,h) is a left and right moving rarefaction waves, respectively. . . . 36

2.7 LRRS. Figure 2.7(a) shows the cross-sectional area, flow speed and wave speed wave profiles, respectively for LRRS shock wave (where blue line denotes rarefaction, red line denotes shock and black line denotes uniform region), while Figure 2.7(b) displays a typical characteristics diagram showing regions 1, 2 and 3, respectively for a LRRS waves. For $\mathcal{A}_1 = 1.6$, $\mathcal{A}_2 = 1.2$, $\mathcal{U}_1 = 0$, $\mathcal{U}_2 = 0.5$ and $t = 0.012$. 43
2.8 LSRR. Figure 2.8(a) shows the cross-sectional area, flow speed and wave speed wave profiles, respectively for LSRR wave, while Figure 2.8(b) displays a typical characteristics diagram showing regions 1, 2 and 3, respectively for a LSRR waves. For $\mathcal{A}_1 = 1$, $\mathcal{A}_2 = 1.1$, $\mathcal{U}_1 = 0$, $\mathcal{U}_2 = 0.03$ and $t = 0.04$. 43
2.9 LRRR. Figure 2.9(a) shows the cross-sectional area, flow speed and wave speed wave profiles, respectively for LRRR wave, while Figure 2.9(b) displays a typical characteristics diagram showing regions 1, 2 and 3, respectively for a LRRR waves. For $\mathcal{A}_1 = 1.1$, $\mathcal{A}_2 = 1.1$, $\mathcal{U}_1 = 0$, $\mathcal{U}_2 = 0.3$ and $t = 0.03$. 44
2.10 LSRS wave. Figure 2.10(a) shows the cross-sectional area, flow speed and wave speed wave profiles, respectively for LSRS wave, while Figure 2.10(b) displays a typical characteristics diagram showing regions 1, 2 and 3, respectively for a LSRS waves. For $\mathcal{A}_1 = 1$, $\mathcal{A}_2 = 1.1$, $\mathcal{U}_1 = 0$, $\mathcal{U}_2 = 0.99$ and $t = 0.008$. 45
2.11 Bifurcation plot and characteristics profile plot of unique solutions $\mathcal{U}_2 = 0$ with corresponding values of $\mathcal{A}_3$, $\mathcal{A}_2$, respectively. Figure 2.11(a) displays the cross-sectional area, flow speed and wave speed of the unique solutions with different points of $\mathcal{A}_2$ marked as (i) and (ii) such that (i) denotes $\mathcal{A}_2 = 0.5$ and (ii) denotes $\mathcal{A}_2 = 1.24$, respectively, while Figure 2.11(b) shows the corresponding characteristics values of these different values of $\mathcal{A}_2$ for (i) and (ii) with $\mathcal{U}_2 = 0$. 47
2.12 Bifurcation plot and characteristics profile plot of multiple solutions at $\mathcal{U}_2 = 0.6$ with corresponding values of $\mathcal{A}_3$, $\mathcal{A}_2$, respectively. Figure 2.12(a) displays the the cross-sectional area, flow speed and wave speed of the multiple solutions with different points of $\mathcal{A}_2$ marked as (i) to (xii) such that (i) denotes $\mathcal{A}_2 = 0.3$, (ii) denotes $\mathcal{A}_2 = 0.615$, (iii) denotes $\mathcal{A}_2 = 0.615$, (iv) denotes $\mathcal{A}_2 = 0.8592$, (v) denotes $\mathcal{A}_2 = 0.8592$, (vi) denotes $\mathcal{A}_2 = 0.8592$, (vii) denotes $\mathcal{A}_2 = 1.091$, $(viii)$ denotes $\mathcal{A}_2 = 1.091$, (ix) denotes $\mathcal{A}_2 = 1.091$, (x) denotes $\mathcal{A}_2 = 1.14$, (xi) denotes $\mathcal{A}_2 = 1.142$ and (xii) denotes $\mathcal{A}_2 = 1.368$, while Figure 2.12(b) shows the corresponding characteristics values of these different values of $\mathcal{A}_2$ from (i) to (xii) with $\mathcal{U}_2 = 0.6$. 48
2.13 Bifurcation plot of physical solutions at $\mathcal{U}_2 = 0.6$, $\mathcal{A}_1 = 1$, $\mathcal{U}_1 = 0$ with corresponding values of $\mathcal{A}_3$, $\mathcal{U}_3$, $\mathcal{C}_3$ $\mathcal{A}_2$, respectively. 49
2.14 Bifurcation plot and characteristics profile plot of multiple solutions at $\mathcal{U}_2 = 1$ with corresponding values of $\mathcal{A}_3$, $\mathcal{A}_2$, respectively. Figure 2.14(a) displays the the cross-sectional area, flow speed and wave speed of the multiple solutions with different points of $\mathcal{A}_2$ marked as (i) to (ix) such that (i) denotes $\mathcal{A}_2 = 0.34$, (ii) denotes $\mathcal{A}_2 = 0.77$, (iii) denotes $\mathcal{A}_2 = 0.77$, (iv) denotes $\mathcal{A}_2 = 1.07$, (v) denotes $\mathcal{A}_2 = 1.07$, (vi) denotes $\mathcal{A}_2 = 1.07$, (vii) denotes $\mathcal{A}_2 = 1.203$, $(viii)$ denotes $\mathcal{A}_2 = 1.208$, (ix) denotes $\mathcal{A}_2 = 1.38$, while Figure 2.14(b) shows the corresponding characteristics values of these different values of $\mathcal{A}_2$ from (i) to (ix) with $\mathcal{U}_2 = 1.0$. 50
2.15 Bifurcation plot of physical solutions at $\mathcal{U}_2 = 1.0$, $\mathcal{A}_1 = 1$, $\mathcal{U}_1 = 0$ with corresponding values of $\mathcal{A}_3$, $\mathcal{U}_3$, $\mathcal{C}_3$ $\mathcal{A}_2$, respectively. 51

2.16 Bifurcation plot and characteristics profile plot of multiple solutions at $\mathcal{U}_2 = -0.6$ with corresponding values of $\mathcal{A}_3$, $\mathcal{A}_2$, respectively. Figure 2.16(a) displays the the cross-sectional area, flow speed and wave speed of the multiple solutions with different points of $\mathcal{A}_2$ marked as (i) to (vi) such that (i) denotes $\mathcal{A}_2 = 0.5$, (ii) denotes $\mathcal{A}_2 = 0.86$, (iii) denotes $\mathcal{A}_2 = 0.86$, (iv) denotes $\mathcal{A}_2 = 1.06$, (v) denotes $\mathcal{A}_2 = 1.06$, and (vi) denotes $\mathcal{A}_2 = 1.269$, while Figure 2.16(b) shows the corresponding characteristics values of these different values of $\mathcal{A}_2$ from (i) to (vi) with $\mathcal{U}_2 = -0.6$. 52

2.17 Bifurcation plot of physical solutions at $\mathcal{U}_2 = -0.6$ with corresponding values of $\mathcal{A}_3$, $\mathcal{U}_3$, $\mathcal{C}_3$ $\mathcal{A}_2$, respectively. 53

2.18 Overview of parameter space showing regions of no solution, one solution, two solutions and three solutions. Figure 2.18(a) illustrates parameter space plot for both physical and unphysical solutions for $\mathcal{A}_2 \leq 1$ and $\mathcal{U}_2 > 0.5$ we have regions of no solutions marked with green triangles and red open circles with two solutions which are not physical, dotted lines of green and cyan showed regions of one solution, red circle and red dot showed two solutions with the dot been the physical solution while blue dot and red squares showed three solutions with only the blue dot been the physical solution. Figure 2.18(b) shows parameter space plot for only physical solutions and little patch with no solution (tube collapse). For $\mathcal{A}_2 \leq 1$ and $\mathcal{U}_2 > 0.5$ we have regions of no solutions marked with black triangles. Dotted lines of green, cyan, red and blue denote the physical solutions. 54

2.19 Showing parameter space plot comparison between our Newton method and the algorithm of Brook et al. [44] for $\mathcal{A}_1 = 1$, $\mathcal{U}_1 = 0$, $-2 \leq \mathcal{U}_2 \leq 2$ and $0 \leq \mathcal{A}_2 \leq 2$. Figure 2.19(a) shows the paramrter space plot from our Newton method while, Figure 2.19(b) shows parameter space plot from the algorithm by Brook et al. [44]. 55

2.20 Parameter space plot of our Newton method with different initial conditions. Figure 2.20(a) shows parameter space plot of our Newton method for $\mathcal{U}_1 = 0.5$, $\mathcal{A}_1 = 0.5$, Figure 2.20(b) shows parameter space plot of our Newton method for $\mathcal{U}_1 = 0.5$, $\mathcal{A}_1 = 1$, Figure 2.20(c) shows parameter space plot of our Newton method for $\mathcal{U}_1 = 0.5$, $\mathcal{A}_1 = 1.5$, Figure 2.20(d) shows parameter space plot of our Newton method for $\mathcal{U}_1 = 0$, $\mathcal{A}_1 = 0.5$, Figure 2.20(e) shows parameter space plot of our Newton method for $\mathcal{U}_1 = 0$, $\mathcal{A}_1 = 1.0$, Figure 2.20(f) shows parameter space plot of our Newton method for $\mathcal{U}_1 = 0$, $\mathcal{A}_1 = 1.5$, Figure 2.20(g) shows parameter space plot of our Newton method for $\mathcal{U}_1 = -0.5$, $\mathcal{A}_1 = 0.5$, Figure 2.20(h) shows parameter space plot of our Newton method for $\mathcal{U}_1 = -0.5$, $\mathcal{A}_1 = 1.0$, and Figure 2.20(i) shows parameter space plot of our Newton method for $\mathcal{U}_1 = -0.5$, $\mathcal{A}_1 = 1.5$, respectively. Here green dotted line denotes LRRS, blue dotted line denotes LRRR, red doted line denotes LSRS and cyan dotted lines denotes LSRR. The white space denote regions of no solution 56

2.21 Diagram of characteristic and spatial profiles of supercritical flow in region 2 for $\mathcal{A}_2 = 0.6$, $\mathcal{U}_2 = 0.6$. Figure 2.21(a) shows the characteristic profile where the blue line shows the outer edge of the rarefaction in region 1 and the blue dotted line showing the outer edge of rarefaction in region 2. Figure 2.21(b) shows the spatial profiles of cross-sectional area, flow speed and wavespeed of the supercritical flow in region 2. 57

2.22 Showing the parameter space plots with physical solutions for different values of m. Figure 2.22(a) shows the parameter space plot for our Newton's method for $m = 10.0$, Figure 2.22(b) shows the parameter space plot for our Newton's method for $m = 5.0$, Figure 2.22(c) shows the parameter space plot for our Newton's method for $m = 0.1$, while Figure 2.22(d) shows the parameter space plot for our Newton's method for $m = 0.05$. . 58
2.23 A LRRS. Figure 2.23(a) shows the cross-sectional area, flow speed and wave speed wave profiles, respectively for LRRS shock wave of a general tube law, while Figure 2.23(b) displays a typical characteristics diagram showing regions 1, 2 and 3, respectively for a LRRS waves from a general tube law. 62
2.24 A LSRR. Figure 2.24(a) shows the cross-sectional area, flow speed and wave speed wave profiles, respectively for LSRR wave of a general tube law, while Figure 2.24(b) displays a typical characteristics diagram showing regions 1, 2 and 3, respectively for a LSRR waves. 63
2.25 Bifurcation plot of unique solutions at $\mathcal{U}_2 = 0$ with corresponding values of $\mathcal{A}_3$, $\mathcal{U}_3$, $\mathcal{C}_3$, $\mathcal{A}_2$. Figure 2.25(a) displays the the cross-sectional area, flow speed and wave speed of the unique solutions with general tube law and Figure 2.25(b) displays the the cross-sectional area, flow speed and wave speed of the unique solutions with expanding tube law. . . . 64
2.26 Bifurcation plot of unique solutions at $\mathcal{U}_2 = 0.6$ with corresponding values of $\mathcal{A}_3$, $\mathcal{U}_3$, $\mathcal{C}_3$, $\mathcal{A}_2$. Figure 2.26(a) displays the the cross-sectional area, flow speed and wave speed of the unique solutions with general tube law and Figure 2.26(b) displays the the cross-sectional area, flow speed and wave speed of the unique solutions with expanding tube law. . . . 65
2.27 Bifurcation plot of unique solutions at $\mathcal{U}_2 = 1$ with corresponding values of $\mathcal{A}_3$, $\mathcal{U}_3$, $\mathcal{C}_3$, $\mathcal{A}_2$. Figure 2.27(a) displays the the cross-sectional area, flow speed and wave speed of the unique solutions with general tube law and Figure 2.27(b) displays the the cross-sectional area, flow speed and wave speed of the unique solutions with expanding tube law. . . . 65
2.28 Bifurcation plot of unique solutions at $\mathcal{U}_2 = -0.6$ with corresponding values of $\mathcal{A}_3$, $\mathcal{U}_3$, $\mathcal{C}_3$, $\mathcal{A}_2$. Figure 2.28(a) displays the the cross-sectional area, flow speed and wave speed of the unique solutions with general tube law and Figure 2.28(b) displays the the cross-sectional area, flow speed and wave speed of the unique solutions with expanding tube law. . . . 66
2.29 Overview of parameter space for vessel with uniform material properties using the expanding and general tube law showing only physical solutions and regions of no solution. Figure 2.29(a) is for general tube law showing all four classical solutions while Figure 2.29(b) is for expanding tube law showing all four classical solutions and a white space denoting region of no solution. 67

3.1 Illustrations of the possible wave profiles generated due to discontinuity in elastic stiffness across $x = 0$. 78
3.2 Left rarefaction, right shock with discontinuity at $x = 0$. Figure 3.2(a) displays profile of cross-sectional area, Figure 3.2(b), displays profile of flow speed, Figure 3.2(c) displays profile of the wave speed and Figure 3.2(d) Left rarefaction, right shock showing continuity of flux at $x = 0$. We choose $\mathcal{A}_1 = 1.6$, $\mathcal{A}_2 = 1.2$, $\mathcal{U}_1 = 0$, $\mathcal{U}_2 = 0.5$, $k = 1.1$ and using Newton's method we compute $\mathcal{A}_3^L = 1.436$, $\mathcal{A}_3^R = 1.422$ and $\mathcal{U}_3^L = 2.775$, $\mathcal{U}_3^R = 2.801$ at $t = 0.012$. 79

3.3 Left shock, right rarefaction with discontinuity at $x = 0$. Figure 3.3(a) displays profile of cross-sectional area; Figure 3.3(b) displays profile of flow speed and Figure 3.3(c) displays profile of the wave speed. We choose $\mathcal{A}_1 = 1.0$, $\mathcal{A}_2 = 1.4$, $\mathcal{U}_1 = 0$, $\mathcal{U}_2 = 0.1$, $k_2 = 1.1$ and using Newton's method we compute $\mathcal{A}_3^L = 1.257$, $\mathcal{A}_3^R = 1.247$ and $\mathcal{U}_3^L = -1.458$, $\mathcal{U}_3^R = -1.471$ at $t = 0.012$. 80
3.4 Left shock, right shock with discontinuity at $x = 0$. Figure 3.4(a) displays profile of cross-sectional area; Figure 3.4(b) displays profile of flow speed and Figure 3.4(c) displays profile of the wave speed. We choose $\mathcal{A}_1 = 1.0$, $\mathcal{A}_2 = 1.1$, $\mathcal{U}_1 = 0$, $\mathcal{U}_2 = -0.1$, $k = 1.1$ and using Newton's method we compute $\mathcal{A}_3^L = 1.070$, $\mathcal{A}_3^R = 1.065$ and $\mathcal{U}_3^L = -0.258$, $\mathcal{U}_3^R = -0.257$ at $t = 0.03$. 81
3.5 Left rarefaction, right rarefaction with discontinuity at $x = 0$. Figure 3.5(a) displays profile of cross-sectional area; Figure 3.5(b) displays profile of flow speed and Figure 3.5(c) displays profile of the wave speed. We choose $\mathcal{A}_1 = 1.1$, $\mathcal{A}_2 = 1.1$, $\mathcal{U}_1 = 0$, $\mathcal{U}_2 = 0.3$, $k = 1.1$ and using Newton's method we compute $\mathcal{A}_3^L = 1.095$, $\mathcal{A}_3^R = 1.037$ and $\mathcal{U}_3^L = 0.024$, $\mathcal{U}_3^R = 0.025$ at $t = 0.13$. 82
3.6 Bifurcation diagram showing comparison with linear and nonlinear case of our wave profile. 85
3.7 Sketch of possible resonance cases: Left rarefaction crossing the contact discontinuity into compartment 2. Figure 3.7(a) shows configuration B, Figure 3.7(b) shows configuration C with a left transcritical rarefaction, Figure 3.7(c) shows Configuration C with a right transcritical rarefaction, Figure 3.7(d) shows configuration D with left transcritical rarefaction. 87
3.8 Sketch of the Riemann problem for configuration C according to [89], where the green line represent the edge of the left rarefaction in region 1, while the blue line is the outer edge rarefaction in region 3 88
3.9 Sketch of the Riemann problem for configuration D following Han et al. [89] 90
3.10 **Case 1**: Bifurcation plot and characteristics profile plot of physical solutions at $\mathcal{U}_1 = 0$ and $\mathcal{U}_2 = 0$ with corresponding values of $\mathcal{A}_2$, $\mathcal{A}_3^L$, and $\mathcal{A}_3^R$, respectively. Figure 3.10(a) displays the the cross-sectional area, and flow speed of the physical solutions with different points of $\mathcal{A}_2$ marked as (i) to (iv) such that (i) denotes $\mathcal{A}_2 = 0.23$, (ii) denotes $\mathcal{A}_2 = 0.33$, (iii) denotes $\mathcal{A}_2 = 0.62$ and (iv) denotes $\mathcal{A}_2 = 1.38$. Figure 3.10(b) shows the corresponding characteristics values of these different values of $\mathcal{A}_2$ from (i) to (iv) with $\mathcal{U}_1 = 0$ and $\mathcal{U}_2 = 0$. 94
3.11 Illustration of configuration C and D. Figure 3.11(a) shows the range of the intermediate stiffness k_s lying between 1 and 1.1 while Figure 3.11(b) shows the shock speeds $\dot{s}_{res}$, $\dot{s}_R$, respectively of configuration D. 95
3.12 Configuration C showing supercritical and subcritical region around $x = 0$. Figure 3.12(a) shows that the speed index of $\mathcal{U}_3^L$, $\mathcal{C}_3^L$ (blue dotted line) is 1 hence, critical and that the speed index of $\mathcal{U}_{12}$, $\mathcal{C}_{12}$ (red dotted line) is greater than 1, hence supercritical. Figure 3.12 shows that the speed index of $\mathcal{U}_{21}$, $\mathcal{C}_{21}$ (green dotted line) and $\mathcal{U}_3^R$, $\mathcal{C}_3^R$ (cyan dotted line) are both less than 1, hence subcritical. 95
3.13 Comparison of bifurcation diagram of tube with discontinuous material properties and tube with uniform material properties for $\mathcal{U}_1 = 0$ and $\mathcal{U}_2 = 0$. Figure 3.13(a) shows the bifurcation diagram of tube with discontinuous material properties. While Figure 3.13(b) shows the bifurcation diagram of tube with uniform material properties. 96

3.14 **Case 2**: Bifurcation plot and characteristics profile plot of physical solutions at $\mathcal{U}_1 = -0.5$ and $\mathcal{U}_2 = 0$ with corresponding values of $\mathcal{A}_2$, $\mathcal{A}_3^L$, and $\mathcal{A}_3^R$, respectively. Figure 3.14(a) displays the the cross-sectional area, and flow speed of the multiple solutions with different points of $\mathcal{A}_2$ marked as (i) to (v) such that (i) denotes $\mathcal{A}_2 = 0.3$, (ii) denotes $\mathcal{A}_2 = 0.64$, (iii) denotes $\mathcal{A}_2 = 0.75$, (iv) denotes $\mathcal{A}_2 = 0.998$ and (v) denotes $\mathcal{A}_2 = 1.38$. Figure 3.14(b) shows the corresponding characteristics values of these different values of $\mathcal{A}_2$ from (i) to (v) with $\mathcal{U}_1 = -0.5$ and $\mathcal{U}_2 = 0$. 97

3.15 Comparison of bifurcation diagram of two blood vessels with varying material properties and single blood vessel with uniform material properties for $\mathcal{U}_1 = -0.5$ and $\mathcal{U}_2 = 0$. Figure 3.15(a) shows the bifurcation diagram of tube with discontinuous material properties. While Figure 3.15(b) shows the bifurcation diagram of tube with uniform material properties. 98

3.16 **Case 3**: Bifurcation plot and characteristics profile plot of physical solutions at $\mathcal{U}_1 = 0.5$ and $\mathcal{U}_2 = 0$ with corresponding values of $\mathcal{A}_2$, $\mathcal{A}_3^L$, and $\mathcal{A}_3^R$, respectively. Figure 3.16(a) displays the the cross-sectional area, and flow speed of the multiple solutions with different points of $\mathcal{A}_2$ marked as (i) to (v) such that (i) denotes $\mathcal{A}_2 = 0.1$, (ii) denotes $\mathcal{A}_2 = 0.213$, (iii) denotes $\mathcal{A}_2 = 0.5$, (iv) denotes $\mathcal{A}_2 = 0.99$ and (v) denotes $\mathcal{A}_2 = 1.4$. Figure 3.16(b) shows the corresponding characteristics values of these different values of $\mathcal{A}_2$ from (i) to (v) with $\mathcal{U}_1 = 0.5$ and $\mathcal{U}_2 = 0$. 99

3.17 **Case 4**: Bifurcation plot and characteristics profile plot of physical solutions at $\mathcal{U}_1 = 0$ and $\mathcal{U}_2 = -0.6$ with corresponding values of $\mathcal{A}_2$, $\mathcal{A}_3^L$, and $\mathcal{A}_3^R$, respectively. Figure 3.17(a) displays the the cross-sectional area, and flow speed of the multiple solutions with different points of $\mathcal{A}_2$ marked as (i) to (v) such that (i) denotes $\mathcal{A}_2 = 0.05$, (ii) denotes $\mathcal{A}_2 = 0.09$, (iii) denotes $\mathcal{A}_2 = 0.5$, (iv) denotes $\mathcal{A}_2 = 0.99$ and (v) denotes $\mathcal{A}_2 = 1.4$. Figure 3.17(b) shows the corresponding characteristics values of these different values of $\mathcal{A}_2$ from (i) to (v) with $\mathcal{U}_1 = 0$ and $\mathcal{U}_2 = -0.6$. 101

3.18 **Case 5**: Bifurcation plot and characteristics profile plot of multiple solutions at $\mathcal{U}_1 = 0$ and $\mathcal{U}_2 = 0.6$ with corresponding values of $\mathcal{A}_2$, $\mathcal{A}_3^L$, and $\mathcal{A}_3^R$, respectively. Figure 3.18(a) displays the the cross-sectional area, and flow speed of the multiple solutions with different points of $\mathcal{A}_2$ marked as (i) to (vi) such that (i) denotes $\mathcal{A}_2 = 0.026$, (ii) denotes $\mathcal{A}_2 = 0.5$, but different values of $\mathcal{A}_3^L$ and $\mathcal{A}_3^R$, (iii) denotes $\mathcal{A}_2 = 0.82$, (iv) denotes $\mathcal{A}_2 = 0.91$, (v) denotes $\mathcal{A}_2 = 0.94$ and (vi) denotes $\mathcal{A}_2 = 1.3$ with different values of $\mathcal{A}_3^L$ and $\mathcal{A}_3^R$, respectively. Figure 3.18(b) shows the corresponding characteristics values of these different values of $\mathcal{A}_2$ from (i) to (vi) with $\mathcal{U}_1 = 0$ and $\mathcal{U}_2 = 0.6$. 104

3.19 Comparison of bifurcation diagram of tube with discontinuous material properties and tube with uniform material properties. Figure 3.19(a) shows the bifurcation diagram of tube with discontinuous material properties for $\mathcal{U}_1 = 0$ and $\mathcal{U}_2 = 0.6$. While Figure 3.19(b) shows the bifurcation diagram of tube with uniform material properties for $\mathcal{U}_1 = 0$ and $\mathcal{U}_2 = 0.6$. 105

3.20 Comparison of flow profiles of tube with discontinuous material properties and tube with uniform material properties. Figure 3.20(a) shows the flow profile of tube with discontinuous material properties for $\mathcal{U}_1 = 0$, $\mathcal{A}_1 = 1$, $\mathcal{A}_2 = 0.4$ and $\mathcal{U}_2 = 0.6$. While Figure 3.20(b) shows the flow profiles of tube with uniform material properties for the same values. 105

3.21 Comparison of flow profiles of tube with discontinuous material properties and tube with uniform material properties. Figure 3.21(a) shows the flow profile of tube with discontinuous material properties for $\mathcal{U}_1 = 0$, $\mathcal{A}_1 = 1$, $\mathcal{A}_2 = 0.75$ and $\mathcal{U}_2 = 0.6$. While Figure 3.21(b) shows the flow profiles of tube with uniform material properties for the same values. 106
3.22 Illustration of the resonant and right shock solutions of configuration D resonant solution with a right shock. Figure 3.22(a) illustrates the two shocks on the right while Figure 3.22(b) shows the two shocks on the right and also the accompanying Lax entropy conditions. 106
3.23 **Case 6, 7, and 8**: Bifurcation plot of physical solutions cases 6 to 8. Figure 3.23(a) displays the bifurcation plot for case 6 with $\mathcal{U}_1 = \mathcal{U}_2 = 0$, $\mathcal{A}_2 = 1.0$ while varying $\mathcal{A}_1$ and $k = 1.1$. Figure 3.23(b) displays the bifurcation plot for case 7 with $\mathcal{U}_1 = -0.6$, $\mathcal{U}_2 = 0$, $\mathcal{A}_2 = 1.0$ while varying $\mathcal{A}_1$ and $k = 1.1$, and Figure 3.23(c) displays the bifurcation plot for case 8 with $\mathcal{U}_1 = 0.6$, $\mathcal{U}_2 = 0$, $\mathcal{A}_2 = 1.0$ while varying $\mathcal{A}_1$ and $k = 1.1$. 108
3.24 **Case 9**: Bifurcation plot and characteristics profile plot of physical solutions at $\mathcal{U}_1 = 0$ and $\mathcal{U}_2 = 0$, $k = 0.9$ with corresponding values of $\mathcal{A}_1$, $\mathcal{A}_3^L$, and $\mathcal{A}_3^R$, respectively. Figure 3.24(a) displays the the cross-sectional area, and flow speed of the physical solutions with different points of $\mathcal{A}_1$ marked as (i) to (iv) such that (i) denotes $\mathcal{A}_1 = 0.15$, (ii) denotes $\mathcal{A}_1 = 0.38$, (iii) denotes $\mathcal{A}_1 = 0.9$ and (iv) denotes $\mathcal{A}_1 = 1.5$. Figure 3.24(b) shows the corresponding characteristics values of these different values of $\mathcal{A}_1$ from (i) to (iv) with $\mathcal{U}_1 = 0$, $k = 0.9$ and $\mathcal{U}_2 = 0$. 109
3.25 **Case 10**: Bifurcation plot and characteristics profile plot of physical solutions at $\mathcal{U}_1 = -0.6$ and $\mathcal{U}_2 = 0$, $k = 0.9$ with corresponding values of $\mathcal{A}_1$, $\mathcal{A}_3^L$, and $\mathcal{A}_3^R$, respectively. Figure 3.25(a) displays the the cross-sectional area, and flow speed of the physical solutions with different points of $\mathcal{A}_1$ marked as (i) to (v) such that (i) denotes $\mathcal{A}_1 = 0.4$, (ii) denotes $\mathcal{A}_1 = 0.8$, (iii) denotes $\mathcal{A}_1 = 0.92$, (iv) denotes $\mathcal{A}_1 = 1.03$ and (v) denotes $\mathcal{A}_1 = 1.5$. Figure 3.25(b) shows the corresponding characteristics values of these different values of $\mathcal{A}_1$ from (i) to (v) with $\mathcal{U}_1 = -0.6$, $k = 0$. and $\mathcal{U}_2 = 0$. 110
3.26 **Case 11**: Bifurcation plot and characteristics profile plot of physical solutions at $\mathcal{U}_1 = 0.6$ and $\mathcal{U}_2 = 0$, $k = 0.9$ with corresponding values of $\mathcal{A}_1$, $\mathcal{A}_3^L$, and $\mathcal{A}_3^R$, respectively. Figure 3.26(a) displays the the cross-sectional area, and flow speed of the physical solutions with different points of $\mathcal{A}_1$ marked as (i) to (v) such that (i) denotes $\mathcal{A}_1 = 0.03$, (ii) denotes $\mathcal{A}_1 = 0.096$, (iii) denotes $\mathcal{A}_1 = 0.5$, (iv) denotes $\mathcal{A}_1 = 0.95$ and (v) denotes $\mathcal{A}_1 = 1.6$. Figure 3.26(b) shows the corresponding characteristics values of these different values of $\mathcal{A}_1$ from (i) to (v) with $\mathcal{U}_1 = 0.6$, $k = 0.5$ and $\mathcal{U}_2 = 0$. 111
3.27 Overview of the parameter space spanned by $\mathcal{U}_2$ $(-1.0 \leq \mathcal{U}_2 \leq 1.0)$ and $\mathcal{A}_2$ $(0 \leq \mathcal{A}_2 \leq 2.0)$ with $\mathcal{U}_1 = 0$, $\mathcal{A}_1 = 1$, $k = 1.1$ and $\bar{A}_2 = 1$. 113
3.28 Overview of the parameter space spanned by $\mathcal{U}_2$ $(-1.0 \leq \mathcal{U}_2 \leq 1.0)$ and $\mathcal{A}_2$ $(0 \leq \mathcal{A}_2 \leq 2.0)$ with $\mathcal{U}_1 = 0$, $\mathcal{A}_1 = 1$, $k = 0.9$ and $\bar{A}_2 = 1$. 113
3.29 Overview of the parameter space spanned by $\mathcal{U}_1$ $(-1.0 \leq \mathcal{U}_1 \leq 1.0)$ and $\mathcal{A}_1$ $(0 \leq \mathcal{A}_1 \leq 2.0)$ with $\mathcal{U}_2 = 0$, $\mathcal{A}_2 = 1$, $k = 1.1$ and $\bar{A}_2 = 1$. 114
3.30 Overview of the parameter space spanned by $\mathcal{U}_1$ $(-1.0 \leq \mathcal{U}_1 \leq 1.0)$ and $\mathcal{A}_1$ $(0 \leq \mathcal{A}_1 \leq 2.0)$ with $\mathcal{U}_2 = 0$, $\mathcal{A}_2 = 1$, $k = 0.9$ and $\bar{A}_2 = 1$. 114

3.31 Left rarefaction, right shock with discontinuity at $x = 0$. Figure 3.31(a) displays profile of cross-sectional area, Figure 3.31(b), displays profile of flow speed and Figure 3.31(c) displays profile of the wave speed. We choose $\mathcal{A}_1 = 1.0, \mathcal{A}_2 = 0.8, \mathcal{U}_1 = 0, \mathcal{U}_2 = 0, k_2 = 1.1$ and using Newton's method we compute $\mathcal{A}_3^L = 1.309$, $\mathcal{A}_3^R = 1.297$ and $\mathcal{U}_3^L = -1.989$, $\mathcal{U}_3^R = -2.007$ at $t = 0.06$. 119
3.32 Left shock, right rarefaction with discontinuity at $x = 0$. Figure 3.32(a) displays profile of cross-sectional area; Figure 3.32(b) displays profile of flow speed and Figure 3.32(c) displays profile of the wave speed. We choose $\mathcal{A}_1 = 1.0, \mathcal{A}_2 = 1.5, \mathcal{U}_1 = 0, \mathcal{U}_2 = 0.6, k_2 = 1.1$ and using Newton's method we compute $\mathcal{A}_3^L = 1.309$, $\mathcal{A}_3^R = 1.297$ and $\mathcal{U}_3^L = 0.989$, $\mathcal{U}_3^R = -2.007$ at $t = 0.02$. 120
3.33 **Case 12**:Bifurcation diagram for case where $\mathcal{U}_1 = 0$, $\mathcal{U}_2 = 0$, $\mathcal{A}_1 = 1$ and $k = 1.1$ with corresponding values of $\mathcal{A}_2$. $\mathcal{A}_3^L$, $\mathcal{A}_3^R$, $\mathcal{U}_3^L$ and $\mathcal{U}_3^R$, respectively. 124
3.34 Comparison of the bifurcation diagram for case where $\mathcal{U}_1 = 0$, $\mathcal{U}_2 = 0$, $\mathcal{A}_1 = 1$ and $k = 1.1$ with corresponding values of $\mathcal{A}_2$. $\mathcal{A}_3^L$, $\mathcal{A}_3^R$ for general tube and expanding tube law. Figure 3.34(a) illustrates use of general tube law while, Figure 3.34(b) illustrates use of expanding tube law. 124
3.35 **Case 13**: Bifurcation diagram for case where $\mathcal{U}_1 = 0, \mathcal{U}_2 = 0.6, \mathcal{A}_1 = 1$ and $k = 1.1$ with corresponding values of $\mathcal{A}_2$, $\mathcal{A}_3^L$, $\mathcal{A}_3^R$, $\mathcal{U}_3^L$ and $\mathcal{U}_3^R$, respectively. 125
3.36 Comparison between using general tube law and expanding tube law for case where $\mathcal{U}_1 = 0$, $\mathcal{U}_2 = 0.6$, $\mathcal{A}_1 = 1$ and $k = 1.1$ with corresponding values of $\mathcal{A}_2$, $\mathcal{A}_3^L$, $\mathcal{A}_3^R$, respectively. Figure 3.36(a) shows general tube law while, Figure 3.36(b) shows the expanding tube law. 125
3.37 Comparison between using general tube law and expanding tube law for case where $\mathcal{U}_1 = 0$, $\mathcal{U}_2 = 0.6$, $\mathcal{A}_1 = 1$ and $k = 0.9$ with corresponding values of $\mathcal{A}_2$, $\mathcal{A}_3^L$, $\mathcal{A}_3^R$, respectively. Figure 3.37(a) shows general tube law while, Figure 3.37(b) shows the expanding tube law. 126
3.38 Overview of parameter space for vessel with discontinuous material properties using the general and expanding tube law showing regions of classical and resonant solutions with $\mathcal{A}_1 = 1$, $\mathcal{U}_1 = 0$, $-1 \leq \mathcal{U}_2 \leq 1$, $0 \leq \mathcal{A}_2 \leq 2$ and $k = 1.1$. Figure 3.38(a) illustrates parameter space for general tube law while figure 3.38(b) illustrates parameter space for expanding tube law. 127
3.39 Overview of parameter space for vessel with discontinuous material properties using the general and expanding tube law showing regions of classical solutions only with $\mathcal{A}_1 = 1$, $\mathcal{U}_1 = 0$, $-1 \leq \mathcal{U}_2 \leq 1$, $0 \leq \mathcal{A}_2 \leq 2$ and $k = 0.9$. Figure 3.39(a) illustrates parameter space for general tube law while figure 3.39(b) illustrates parameter space for expanding tube law. 127
3.40 Overview of parameter space for vessel with discontinuous material properties using the general and expanding tube law showing regions of classical solutions only with $\mathcal{A}_2 = 1$, $\mathcal{U}_2 = 0$, $-1 \leq \mathcal{U}_1 \leq 1$, $0 \leq \mathcal{A}_1 \leq 2$ and $k = 1.1$. Figure 3.40(a) illustrates parameter space for general tube law while figure 3.40(b) illustrates parameter space for expanding tube law. 128

3.41 Overview of parameter space for vessel with discontinuous material properties using the general and expanding tube law showing regions of classical and resonant solutions with $\mathcal{A}_2 = 1$, $\mathcal{U}_2 = 0$, $-1 \leq \mathcal{U}_1 \leq 1$, $0 \leq \mathcal{A}_1 \leq 2$ and $k = 0.9$. Figure 3.41(a) illustrates parameter space for general tube law while figure 3.41(b) illustrates parameter space for expanding tube law. 128

4.1 Set-up of the mathematical model. 132
4.2 Parent rarefaction, daughter shock with discontinuity at $x = 0$. Figure 4.2(a) displays profile of cross-sectional area, Figure 4.2(b), displays profile of flow speed, Figure 4.2(c) displays profile of the wave speed and Figure 4.2(d) Parent rarefaction, daughter shock showing continuity of flux at $x = 0$. We choose $\mathcal{A}_p = 1.6$, $\mathcal{A}_d = 1.2$, $\mathcal{U}_p = 0$, $\mathcal{U}_d = 0.5$, $k = 1.0$ and using Newton's method we compute $\mathcal{A}_3^P = 1.322$, $\mathcal{A}_3^D = 1.366$, $\mathcal{U}_3^P = 4.079$ and $\mathcal{U}_3^D = 1.973$ at $t = 0.005$. 137
4.3 Parent shock, daughter rarefaction with discontinuity at $x = 0$. Figure 4.3(a) displays profile of cross-sectional area; Figure 4.3(b) displays profile of flow speed and Figure 4.3(c) displays profile of the wave speed. We choose $\mathcal{A}_p = 1.0$, $\mathcal{A}_d = 1.45$, $\mathcal{U}_p = 0$, $\mathcal{U}_d = 0.35$, $k = 1.0$ and using Newton's method we compute $\mathcal{A}_3^P = 1.319$, $\mathcal{A}_3^D = 1.333$, $\mathcal{U}_3^P = -2.107$ and $\mathcal{U}_3^D = -1.043$ at $t = 0.006$. 138
4.4 Parent shock, daughter shock with discontinuity at $x = 0$. Figure 4.4(a) displays profile of cross-sectional area; Figure 4.4(b) displays profile of flow speed and Figure 4.4(c) displays profile of the wave speed. We choose $\mathcal{A}_p = 1.0$, $\mathcal{A}_d = 0.9$, $\mathcal{U}_p = 0$, $\mathcal{U}_d = -0.5$, $\bar{A}_d = 1$ and $k = 1.0$ using Newton's method we compute $\mathcal{A}_3^P = 1.044$, $\mathcal{A}_3^D = 1.044$, $\mathcal{U}_3^P = -0.151$ and $\mathcal{U}_3^D = -0.075$ at $t = 0.009$. 139
4.5 Parent rarefaction, daughter rarefaction with discontinuity at $x = 0$. Figure 4.5(a) displays profile of cross-sectional area; Figure 4.5(b) displays profile of flow speed and Figure 4.5(c) displays profile of the wave speed. We choose $\mathcal{A}_p = 1.1$, $\mathcal{A}_d = 1.05$, $\mathcal{U}_p = 0$, $\mathcal{U}_d = 0.5$, $k = 1.0$ and using Newton's method we compute $\mathcal{A}_3^P = 1.040$, $\mathcal{A}_3^D = 0.933$, $\mathcal{U}_3^P = 0.250$, $\mathcal{U}_3^D = 0.140$ at $t = 0.01$. 139
4.6 Bifurcation diagram showing comparison with Numerical and analytical solution of our wave. The numerical solution is denoted by the green and cyan lines representing PRDS and PSDR solutions, respectively. While the black thick line represent the analytical solution of our model. 143
4.7 Sketch of the Riemann problem for configuration C^+ 144
4.8 Sketch of the Riemann problem for configuration D^+ 147
4.9 **Case 1**: Bifurcation diagram for case where $\mathcal{U}_p = 0$, $\mathcal{U}_d = 0$, and $\mathcal{A}_p = 1$ with corresponding values of $\mathcal{A}_d$. $\mathcal{A}_3^P$, $\mathcal{A}_3^D$, $\mathcal{U}_3^P - \mathcal{C}_3^P$ and $\mathcal{U}_3^D + \mathcal{C}_3^D$, respectively. 149
4.10 Illustration of wave profiles and characteristics curves for PRDS for $\mathcal{U}_p = 0$, $\mathcal{U}_d = 0$, $\mathcal{A}_p = 1$ and $\mathcal{A}_d = 0.6$. Figure 4.10(a) shows the wave profile while Figure 4.10(b) illustrates the characteristic lines. 150
4.11 Illustration of the range of splitting factor r_s across the configuration C solution for $\mathcal{U}_p = 0$, $\mathcal{U}_d = 0$, and $\mathcal{A}_p = 1$ and the two shock waves in the daughter vessels for configuration D solution. 150
4.12 Wave profiles of the configuration D solution with a daughter shock for $\mathcal{U}_p = 0$, $\mathcal{U}_d = 0$, and $\mathcal{A}_p = 1$. Figure 4.12(a) shows the configuration D solution for $\mathcal{A}_d = 0.3$, while Figure 4.12(b) shows the configuration D solution for $\mathcal{A}_d = 0.05$. 151

4.13 **Case 2**: Bifurcation diagram for case where $\mathcal{U}_p = -0.5$, $\mathcal{U}_d = 0$, and $\mathcal{A}_p = 1$ with corresponding values of $\mathcal{A}_d$, $\mathcal{A}_3^P$, $\mathcal{A}_3^D$, $\mathcal{U}_3^P - \mathcal{C}_3^P$ and $\mathcal{U}_3^D + \mathcal{C}_3^D$, respectively. 151
4.14 **Case 3**: Bifurcation diagram for case where $\mathcal{U}_p = 0.5$, $\mathcal{U}_d = 0$, and $\mathcal{A}_p = 1$ with corresponding values of $\mathcal{A}_d$, $\mathcal{A}_3^P$, $\mathcal{A}_3^D$, $\mathcal{U}_3^P - \mathcal{C}_3^P$ and $\mathcal{U}_3^D + \mathcal{C}_3^D$, respectively. 152
4.15 **Case 4**: Bifurcation diagram for case where $\mathcal{U}_p = 0$, $\mathcal{U}_d = -0.6$, and $\mathcal{A}_p = 1$ with corresponding values of $\mathcal{A}_d$, $\mathcal{A}_3^P$, $\mathcal{A}_3^D$, $\mathcal{U}_3^P - \mathcal{C}_3^P$ and $\mathcal{U}_3^D + \mathcal{C}_3^D$, respectively. 153
4.16 **Case 5**: Bifurcation diagram for case where $\mathcal{U}_p = 0$, $\mathcal{U}_d = 0.6$, and $\mathcal{A}_p = 1$ with corresponding values of $\mathcal{A}_d$, $\mathcal{A}_3^P$, $\mathcal{A}_3^D$, $\mathcal{U}_3^P - \mathcal{C}_3^P$ and $\mathcal{U}_3^D + \mathcal{C}_3^D$, respectively. 154
4.17 Illustration of the splitting mass factor and the configuration D^+ solution (tPRSDR). Figure 4.17(a) is the range of the splitting of mass factor, while Figure 4.17(b) illustrates the resonant shock and the outer edge of the rarefaction in the daughter vessel. 154
4.18 Illustration of the splitting mass factor and the configuration D^+ solution (tPRSDR). Figure 4.18(a) illustrates the wave profile for configuration D^+ solution (tPRSDR) for $\mathcal{U}_p = 0$, $\mathcal{U}_d = 0.6$, $\mathcal{A}_p = 1$ and $\mathcal{A}_2 = 0.8$, while Figure 4.18(b) illustrates the wave profile for configuration D^+ solution (tPRSDR) for $\mathcal{U}_p = 0$, $\mathcal{U}_d = 0.6$, $\mathcal{A}_p = 1$ and $\mathcal{A}_2 = 0.533$. . 155
4.19 Illustration of the PRDR solutions at both sides of the resonance solution for $\mathcal{U}_p = 0$, $\mathcal{U}_d = 0.6$, $\mathcal{A}_p = 1$. Figure 4.19(a) is the PRDR characteristics profile for $\mathcal{A}_d = 0.52$, while Figure 4.19(b) is the PRDR characteristics profile for $\mathcal{A}_d = 0.993$. 155
4.20 **Case 6**: Bifurcation diagram for case where $\mathcal{U}_p = 0$, $\mathcal{U}_d = 0$, and $\mathcal{A}_d = 1$ with corresponding values of $\mathcal{A}_p$, $\mathcal{A}_3^P$, $\mathcal{A}_3^D$, $\mathcal{U}_3^P - \mathcal{C}_3^P$ and $\mathcal{U}_3^D + \mathcal{C}_3^D$, respectively. 156
4.21 **Case 7, 8, and 9**: Bifurcation plot of physical solutions cases 7 to 9. Figure 4.21(a) displays the bifurcation plot for case 7 with $\mathcal{U}_p = -0.6$, $\mathcal{U}_d = 0$, $\mathcal{A}_d = 1.0$ while varying $\mathcal{A}_p$. Figure 4.21(b) displays the bifurcation plot for case 8 with $\mathcal{U}_p = 0.6, \mathcal{U}_d = 0$, $\mathcal{A}_d = 1.0$ while varying $\mathcal{A}_p$, and Figure 4.21(c) displays the bifurcation plot for case 9 with $\mathcal{U}_p = 0$, $\mathcal{U}_d = -0.6$, $\mathcal{A}_d = 1.0$ while varying $\mathcal{A}_p$. 157
4.22 **Case 10**: Bifurcation diagram for case where $\mathcal{U}_p = 0$, $\mathcal{U}_d = 0.6$, $\mathcal{A}_d = 1$ and $k = 1$ with corresponding values of $\mathcal{A}_p$, $\mathcal{A}_3^P$, $\mathcal{A}_3^D$, $\mathcal{U}_3^P - \mathcal{C}_3^P$ and $\mathcal{U}_3^D + \mathcal{C}_3^D$, respectively. 158
4.23 Illustration of the profile for PRDR solution and intermediate splitting factor r_s. Figure 4.23(a) shows the profile of PRDR solution close to the transcritical point (*i.e.* $\mathcal{A}_p \approx 1.182$) while Figure 4.23(b) shows the range of the intermediate splitting factor r_s. . . . 158
4.24 Overview of the parameter space spanned by $\mathcal{U}_d$ ($-1.0 \leq \mathcal{U}_d \leq 1.0$) and $\mathcal{A}_d$ ($0 \leq \mathcal{A}_d \leq 2.0$) with $\mathcal{U}_p = 0$, $\mathcal{A}_p = 1$, $k = 1$ and $\bar{A}_d = 1$. 160
4.25 Overview of the parameter space spanned by $\mathcal{U}_p$ ($-1.0 \leq \mathcal{U}_p \leq 1.0$) and $\mathcal{A}_p$ ($0 \leq \mathcal{A}_p \leq 2.0$) with $\mathcal{U}_d = 0$, $\mathcal{A}_d = 1$, $k = 1$ and $\bar{A}_d = 1$. 160
4.26 Characteristics profile for a supercritical daughter rarefaction 161
4.27 **Case 11**: Bifurcation diagram for case where $\mathcal{U}_p = 0$, $\mathcal{U}_d = 0$, $\mathcal{A}_p = 1$ and $k = 1.1$ with corresponding values of $\mathcal{A}_d$, $\mathcal{A}_3^P$, $\mathcal{A}_3^D$, $\mathcal{U}_3^P - \mathcal{C}_3^P$ and $\mathcal{U}_3^D + \mathcal{C}_3^D$, respectively. 162
4.28 **Case 11a**: Bifurcation diagram for case where $\mathcal{U}_p = 0$, $\mathcal{U}_d = 0$, $\mathcal{A}_p = 1$ and $k = 0.9$ with corresponding values of $\mathcal{A}_d$, $\mathcal{A}_3^P$, $\mathcal{A}_3^D$, $\mathcal{U}_3^P - \mathcal{C}_3^P$ and $\mathcal{U}_3^D + \mathcal{C}_3^D$, respectively. 163
4.29 **Case 11b**: Bifurcation diagram for case where $\mathcal{U}_p = 0$, $\mathcal{U}_d = 0$, $\mathcal{A}_p = 1$ and $k = 0.8$ with corresponding values of $\mathcal{A}_d$, $\mathcal{A}_3^P$, $\mathcal{A}_3^D$, $\mathcal{U}_3^P - \mathcal{C}_3^P$ and $\mathcal{U}_3^D + \mathcal{C}_3^D$, respectively. 163

4.30 Illustration of the transcritical rarefaction and daughter shock and the different intermediate parameters. Figure 4.30(a) shows that the resonance of the parent rarefaction with the stationary wave while Figure 4.30(b) shows the two parameters that changes from parent to daughter vessel denoted as r_s and k_s. It also shows the range from parent to daughter vessel denoted as s. 164
4.31 Figure 4.31(a) illustrates the two shocks in the daughter vessel, while Figure 4.31(b) shows the bifurcation diagram for various values of k. 164
4.32 **Case 12**: Bifurcation diagram for case where $\mathcal{U}_p = 0$, $\mathcal{U}_d = -0.6$, $\mathcal{A}_p = 1$ and various values of k with corresponding values of $\mathcal{A}_d$, $\mathcal{A}_3^P$, $\mathcal{A}_3^D$, $\mathcal{U}_3^P - \mathcal{C}_3^P$ and $\mathcal{U}_3^D + \mathcal{C}_3^D$, respectively. 165
4.33 **Case 13a**: Bifurcation diagram for case where $\mathcal{U}_p = 0$, $\mathcal{U}_d = 0.6$, $\mathcal{A}_p = 1$ and $k = 1.1$ with corresponding values of $\mathcal{A}_d$, $\mathcal{A}_3^P$, $\mathcal{A}_3^D$, $\mathcal{U}_3^P - \mathcal{C}_3^P$ and $\mathcal{U}_3^D + \mathcal{C}_3^D$, respectively. 166
4.34 **Case 13b**: Bifurcation diagram for case where $\mathcal{U}_p = 0$, $\mathcal{U}_d = 0.6$, $\mathcal{A}_p = 1$ and $k = 0.9$ with corresponding values of $\mathcal{A}_d$, $\mathcal{A}_3^P$, $\mathcal{A}_3^D$, $\mathcal{U}_3^P - \mathcal{C}_3^P$ and $\mathcal{U}_3^D + \mathcal{C}_3^D$, respectively. 167
4.35 **Case 13c**: Bifurcation diagram for case where $\mathcal{U}_p = 0$, $\mathcal{U}_d = 0.6$, $\mathcal{A}_p = 1$ and $k = 0.8$ with corresponding values of $\mathcal{A}_d$, $\mathcal{A}_3^P$, $\mathcal{A}_3^D$, $\mathcal{U}_3^P - \mathcal{C}_3^P$ and $\mathcal{U}_3^D + \mathcal{C}_3^D$, respectively. 167
4.36 Bifurcation diagram for case where $\mathcal{U}_p = 0$, $\mathcal{U}_d = 0$, $\mathcal{A}_d = 1$ for decreasing values of k with corresponding values of $\mathcal{A}_p$, $\mathcal{A}_3^P$, $\mathcal{A}_3^D$, $\mathcal{U}_3^P - \mathcal{C}_3^P$ and $\mathcal{U}_3^D + \mathcal{C}_3^D$, respectively. 168
4.37 Overview of the parameter space spanned by $\mathcal{U}_d$ ($-1.0 \leq \mathcal{U}_d \leq 1.0$) and $\mathcal{A}_d$ ($0 \leq \mathcal{A}_d \leq 2.0$) with $\mathcal{U}_p = 0$, $\mathcal{A}_p = 1$, $k = 1.1$ and $\bar{A}_d = 1$. 169
4.38 Overview of the parameter space spanned by $\mathcal{U}_d$ ($-1.0 \leq \mathcal{U}_d \leq 1.0$) and $\mathcal{A}_d$ ($0 \leq \mathcal{A}_d \leq 2.0$) with $\mathcal{U}_p = 0$, $\mathcal{A}_p = 1$, $k = 0.9$ and $\bar{A}_d = 1$. 170
4.39 Overview of the parameter space spanned by $\mathcal{U}_d$ ($-1.0 \leq \mathcal{U}_d \leq 1.0$) and $\mathcal{A}_d$ ($0 \leq \mathcal{A}_d \leq 2.0$) with $\mathcal{U}_p = 0$, $\mathcal{A}_p = 1$, $k = 0.8$ and $\bar{A}_d = 1$. 170
4.40 Overview of the parameter space spanned by $\mathcal{U}_p$ ($-1.0 \leq \mathcal{U}_p \leq 1.0$) and $\mathcal{A}_p$ ($0 \leq \mathcal{A}_p \leq 2.0$) with $\mathcal{U}_d = 0$, $\mathcal{A}_d = 1$, $k = 1.1$ and $\bar{A}_d = 1$. 171
4.41 Overview of the parameter space spanned by $\mathcal{U}_p$ ($-1.0 \leq \mathcal{U}_p \leq 1.0$) and $\mathcal{A}_p$ ($0 \leq \mathcal{A}_p \leq 2.0$) with $\mathcal{U}_d = 0$, $\mathcal{A}_d = 1$, $k = 0.9$ and $\bar{A}_d = 1$. 171
4.42 Parameter space plot of our Newton method with different initial conditions. Figure 4.42(a) for $\mathcal{U}_p = 0.5$, $\mathcal{A}_p = 1.0$, $k = 0.8$, Figure 4.42(b) for $\mathcal{U}_p = 0$, $\mathcal{A}_p = 1$, $k = 0.8$, Figure 4.42(c) for $\mathcal{U}_p = 0.5$, $\mathcal{A}_p = 1.5$, $k = 0.8$, Figure 4.42(d) for $\mathcal{U}_p = 0$, $\mathcal{A}_p = 1.5$, $k = 0.8$, respectively. 172
4.43 Overview of parameter space for vessel with splitting of mass across a junction using the general and expanding tube law showing regions of classical and resonant solutions with $\mathcal{A}_p = 1$, $\mathcal{U}_p = 0$, $-1 \leq \mathcal{U}_d \leq 1$, $0 \leq \mathcal{A}_d \leq 2$ and $k = 1$. Figure 4.43(a) illustrates parameter space for general tube law while Figure 4.43(b) illustrates parameter space for expanding tube law. 179
4.44 Overview of parameter space for vessel with splitting of mass across a junction using the general and expanding tube law showing regions of classical and resonant solutions with $\mathcal{A}_d = 1$, $\mathcal{U}_d = 0$, $-1 \leq \mathcal{U}_p \leq 1$, $0 \leq \mathcal{A}_p \leq 2$ and $k = 1$. Figure 4.44(a) illustrates parameter space for general tube law while Figure 4.44(b) illustrates parameter space for expanding tube law. 179

4.45 Overview of parameter space for vessel with splitting of mass across a junction using the general and expanding tube law showing regions of classical and resonant solutions with $\mathcal{A}_p = 1$, $\mathcal{U}_p = 0$, $-1 \leq \mathcal{U}_d \leq 1$, $0 \leq \mathcal{A}_d \leq 2$ and $k = 1.1$. Figure 4.45(a) illustrates parameter space for general tube law while Figure 4.45(b) illustrates parameter space for expanding tube law. 180
4.46 Overview of parameter space for vessel with splitting of mass across a junction using the general and expanding tube law showing regions of classical and resonant solutions with $\mathcal{A}_p = 1$, $\mathcal{U}_p = 0$, $-1 \leq \mathcal{U}_d \leq 1$, $0 \leq \mathcal{A}_d \leq 2$ and $k = 0.9$. Figure 4.46(a) illustrates parameter space for general tube law while Figure 4.46(b) illustrates parameter space for expanding tube law. 181
4.47 Overview of parameter space for vessel with splitting of mass and jump in stiffness across a junction using the general and expanding tube law showing regions of classical and resonant solutions with $\mathcal{A}_d = 1$, $\mathcal{U}_d = 0$, $-1 \leq \mathcal{U}_p \leq 1$, $0 \leq \mathcal{A}_p \leq 2$ and $k = 1.1$. Figure 4.47(a) illustrates parameter space for general tube law while Figure 4.47(b) illustrates parameter space for expanding tube law. 181
4.48 Overview of parameter space for vessel with splitting of mass and jump in stiffness across a junction using the general and expanding tube law showing regions of classical and resonant solutions with $\mathcal{A}_d = 1$, $\mathcal{U}_d = 0$, $-1 \leq \mathcal{U}_p \leq 1$, $0 \leq \mathcal{A}_p \leq 2$ and $k = 0.9$. Figure 4.48(a) illustrates parameter space for general tube law while Figure 4.48(b) illustrates parameter space for expanding tube law. 182

Acknowledgements

The end of my PhD studies has officially come. It has been a beautiful, yet challenging road to travel. I could not have come this far without the support I have received from several people.

First my sincere appreciation goes to my main supervisor, Prof. Peter Stewart, for whom I owe so much gratitude, high respect and thanks for making this journey a beautiful one. Peter, you are the explicit definition of a mentor, one who motivated me so much and kept my hope alive, who has generously shared his wealth of knowledge with me, devoted his time to continuously polish my work to the desired standard required. For these and so much more, I thank you very much.

Also, my appreciation goes to my second supervisor, Dr. David MacTaggart for quality discussions, guidance, providing needed conducive environment for many informative discussions we have had and for the knowledge you have passed on to me.

I would not be writing this if not for the support I received from my family who, although not without sacrifice have encouraged me to pursue my studies here in Glasgow. To my late mum who was my number one support stone, you firmly believed in my chosen career and has always been an inspiration to me. Your prayers and continuous advice has brought me this far, even though it is unfortunate you are not here to witness this milestone. I will eternally remain grateful mum. To my wife and daughter who were always with me through the period of sleepless nights, listening to my many complaints and providing the needed support. I lack words to describe my true feelings, I am saying a big thank you to my babes, you guys are the best. My deepest thanks goes to my father, my two brothers, my elder sister, my mother inlaw and many extended relations who kept wishing me well. Thank you for your constant support, encouragements, prayers and for the unconditional love. I truly could not have asked for a more supportive family.

I sincerely appreciate Petroleum Technology Development Fund (PTDF) who provided the funding to support my study and life abroad and making all the work in this thesis possible.

I also appreciate the School of Mathematics and Statistics in University of Glasgow for providing a positive research atmosphere where researchers can communicate freely and cooperate closely.

To all my friends here in Glasgow, the Nigerian Society, University of Glasgow and the Nsukka cultural group here in Glasgow, I say a big thank you. Also to my friends and colleagues in Nigeria and in the diaspora, Prof. Godwin Mbah (Nigeria), Dr PraiseGod Madueme (South Africa), Dr Obiora Collins (Nigeria), Dr. Aroh (United States of America) who are constantly inquiring of my welfare and encouraging this journey, I love you all.

Declaration and Publications

I, Ifeanyi Sunday Onah declare that this thesis titled 'Retinal Problems in the Retinal Circulation' was carried out by myself except where explicit reference is made to the contribution of others and has not been submitted for any other degree at the University of Glasgow or any other institution.

The work in Chapter 3 is in preparation for submission in this form

1. Ifeanyi S. Onah, David MacTaggart and Peter S. Stewart. Elastic jump propagation across a blood vessel with an abrupt discontinuity in elastic stiffness. *In preparation.*

The work in Chapter 4 has been published in this form

2. Spelman, T. A., Onah, I. S., MacTaggart, D., & Stewart, P. S. (2024). Elastic jump propagation across a blood vessel junction. *Royal Society Open Science, 11(7), 232000.*

CHAPTER 1

Introduction

1.1 The eye

The **eye** is an important, complex (and the most used) organ of the human body which gathers incoming light into electrical signals which are transmitted to the brain [1]. The eyeball is enclosed by a bony protective structure called the orbit, shaped like a four-sided pyramid, and is surrounded by the sinuses on its three sides. The globe of the eye consists of three components enclosing the transparent refractive media in the center (the vitreous): the outermost component is a dense fibrous layer comprising the transparent cornea and sclera, the middle component is vascular comprising the choroid, the ciliary body and the iris, and the innermost component comprises the retina and the optic nerve. The structure is illustrated in Figure 1.1.

The **vitreous** is a clear, jelly-like substance composed mainly of water and collagen. The vitreous body normally maintains adhesion to the retina, optic disk, major retinal blood vessels and the macula (a pigmented region in the center of the retina responsible for high-resolution color vision). The main role of the vitreous is to maintain the round shape of the eye, offer support to the structures within the eye and also help maintain the transparency of the media. The size, shape and pressure of the vitreous also ensures that it remains attached to the retina. It is important to note that with the normal process of aging, the vitreous may begin to shrink due to a decrease in viscosity or thickness. This process is called vitreous degeneration. As the fluid changes from a thick gel-like substance to a thinner liquid consistency, the vitreous humor separates from the retina. This can lead to vitreous floaters, or small disruptions in the visual field such as spots, web-like lines, or rings [2, 3].

The **cornea** is a unique tissue in the eye that is composed of fibres enclosed in a thick, watery jelly called *glycosaminoglycan*. The cornea is responsible for much of eye focussing (up to twice that of the lens). Its focusing power comes from the collagen fiber layers which are ordered to help maintain transparency, and resistance to injury from any direction, while the jelly gives flexibility [4].

The **sclera** is the white part of the eye that acts as protection around the eyeball. It is a strong tissue that extends from the cornea at the front to the optic nerve at the back. Unlike the cornea, which contains arranged collagen fibres, the sclera is made up of tough collagen fibers which crisscross

in random directions giving the sclera strength. It is also covered by conjunctiva, which are clear mucus membranes that lubricate the eye and the muscles attached to the sclera to help move the eyeball [5].

The **choroid** is a dense network of blood vessels between the retina and the sclera. It is separated from the retina by two membranes (the membrane of Bruch and the retina pigment epithelium RPE). The choroid is extremely vascular, with its capillaries arranged in a single layer on the inner surface to nourish the outer retinal layers and maintain the temperature and volume of the eye. Most blood supply to the eye comes through the choroid and it accounts for about 85% of blood flow in the eye [6–8].

The **ciliary body** is an inner eye structure, located between the anterior part of the choroid and the posterior part of the iris. It is made up of three structures: the ciliary muscle, ciliary processes, and ciliary epithelium. The ciliary muscle controls the shape of the lens, the ciliary processes help in the production of aqueous humor, while the ciliary epithelium insulates the ciliary body from aqueous humour and the vitreous. The ciliary body is attached to the lens by the collection of tiny fibrous cords known as the zonular fibers. This attachment is crucial in focusing the eye by changing the shape of the lens, a process known as accommodation. In order to provide these function the ciliary body requires rich vascularization and innervation [9].

The **iris** is the coloured structure of the eye that surrounds the pupil located at the front of the lens behind the cornea. The colour of the iris is unique to each individual and it contains two sheaths of muscles that helps in controlling the expansion and contraction of the pupil and determines the amount of light that reaches the retina. The amount of pigment contained in the iris determines eye colour. When there is very little pigment, the eye appears blue. With increased pigment, the shade becomes deep brown to black [10].

In this study, we are interested in the inner layer of the eye, most especially the retina and optic nerve and these will be discussed in detail in the next section.

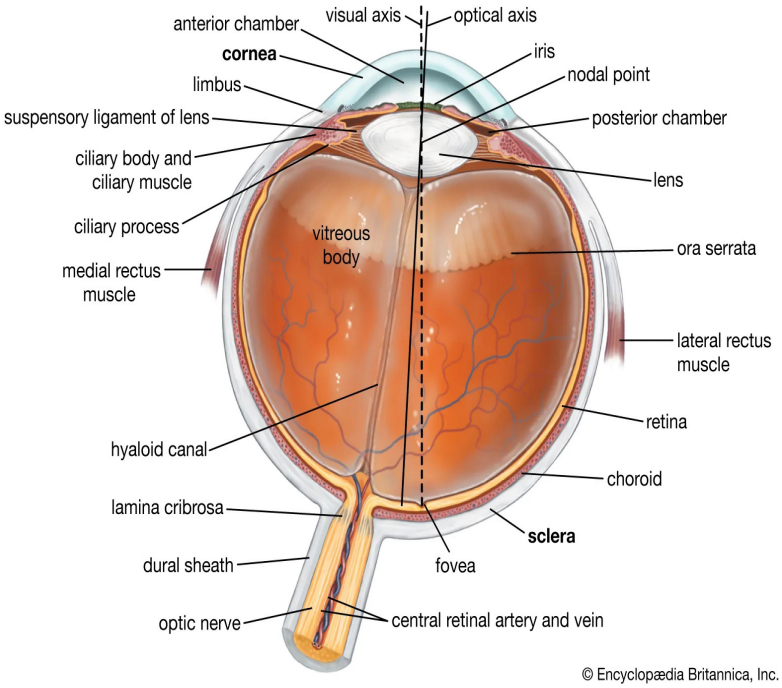

Figure 1.1: Physiology of the human eye [11].

1.1.1 Structure of the retina

The **retina** is a thin layer of tissue located in the posterior portion of the eyeball near the optic nerve. The retina develops ontogenetically as an outgrowth of the brain and it is composed of two main layered structures: the neural retina (or neuroretina, neurosensory retina) which contains the photoreceptor and neuronal cells. The retina receives light that has been focused by the lens and then casts this into neural signals, which are then sent onto the brain for visual recognition. The retina processes light through a layer of light-sensitive photoreceptor cells responsible for detecting color and light-intensity. Due to the retina's vital role in vision, damage to it can cause permanent blindness. Conditions such as retinal detachment, where the retina is abnormally detached from its usual position, can prevent the retina from receiving or processing light. Development of the retina is a long and complex process that begins during the fourth week of embryogenesis and continues into the first year of life. This long and complex embryonic development makes the retina vulnerable to genetic and environmental insults that can negatively affect retinal development. Retinal tissue develops to become the most metabolically expensive tissue in the human body, consuming oxygen more rapidly than any other tissue. The retina is fed oxygen from a unique dual blood supply that divides the retina into outer and inner layers for more efficient oxygenation [12, 13]. One supply is the choriod (mentioned above) and the other is the retinal circulation which is the focus of this thesis.

We mentioned earlier that the retina contains specialised neurons called *photoreceptors* which helps to convert light into electrical signals that stimulate physiological processes. There are two kinds of these receptors in the retina, known as cones and rods. The cones are activated when bright light shines on the eye and their function is to help the eye to see color. There are three types of cones; blue, red and green cones and each of them is sensitive to various wavelengths of light, which allows the eye to see multiple colours. The eye has approximately 6 million cones located in the fovea at the center of the retina which helps to sharpen images. On the other hand, the rods are located in the outer region of the retina and are more sensitive to dimly-lit environments. So, they assist the eye in night vision and seeing black and white. They are much more numerous than cones (these are over a 100 million rods in the eye).

This project focuses on how blood is supplied to the eye. The main source of blood to the inner layers of the retina of the human eye is the retinal circulation, which is fed by the central retinal artery which enters the eye through the center of the optic nerve Figure 1.2. The retinal vessels enter the eye through the optic disc and then branch out through the retina, forming superior and inferior branches lining in the inner surface of the vitreous [14].

1.1.2 Structure of the optic nerve

The **optic nerve** consists mostly of a bundle of nerve fibers that transmit impulses from the retina to the occipital lobe of the brain. The blind spot of the eye (with no light sensitive cells) is the region of the retina at the optic nerve head where the nerve fibres coalesce into a dense cable (also called the optic disc). The optic nerve is protected by a sheath containing a thin layer of cerebrospinal fluid (CSF) which is directly connected to the CSF surrounding the brain. Indeed CSF pressure is a measure of brain (intracranial) pressure [15]. The central retinal artery plays a vital role in the supply of blood to the anterior part of the optic nerve and also the rest of the orbital and the canalicular part of the nerve [16, 17]. However, these vessels do not follow the course of the nerve entirely, but instead turn and pass through the nerve sheath into the extra-neural space about a centimetre back from the eye.

Hence, these central retinal blood vessels are externally exposed to the CSF pressure as they cross the nerve sheath. This point of coupling between the eye and the brain is key to the mechanism of retinal haemorrhage explored in the thesis.

1.2 Retinal haemorrhage

Retinal haemorrhage (RH) is the abnormal bleeding of the blood vessels in the retina [18]. RH occurs when there is an unintentional leakage of blood, either into the retina itself (intraretinal), between the retina and the RPE (subretinal), or between the retina and the vitreous (subhyaloid or preretinal) (see Figure 1.2) [19].

RH is closely linked with early child abuse and inflicted head injuries with particular emphasis to "shaken baby/shaking-impact syndrome", and most common in young children. Shaken baby syndrome is described as the act of holding a baby and shaking the baby in order to stop it from crying, especially in babies who are 6 months old or younger [20]. This inflicts trauma in infants leading to subdural haemorrhages (SDH), neck injuries, bone fracture and retinal haemorrhages.

RH are also caused by other factors other than those mentioned above, which includes vehicle accidents, birth trauma and sudden intracranial hypertension. It is therefore very important to be able to explain the onset of retinal haemorrhage and its correlation to traumatic brain injury, as this will help in legal cases to determine whether it is a deliberate injury, especially in infants who may not be able to speak on their own [21, 22].

There have been various studies on the mechanisms leading to RH and we now review two of these mechanisms.

Healthy retina Haemorrhaged retina

Figure 1.2: Healthy and haemorrhaged retina.

1.2.1 The pressure rise hypothesis

One of the foremost clinical hypothesis to explain RH in abused children was described by Gilkes and Mann [23]. They described RH as a result of rise in intracranial pressure and subsequently intraocular venous pressure due to injury in the brain. The intracranial pressure builds up in the CSF around the optic nerve sheath and is then transmitted to the central retinal vessels as they cross the nerve sheath. This in turn triggers a rise in vascular pressure which then propagates into the eyes; this pressure wave spreads leading to bursting of one or more retinal veins (as these are weaker than arteries) and causing a retinal haemorrhage. This hypothesis was supported by Binenbaum et al. [24, 25] in their work studying patterns of RH associated with increased intracranial pressure in children, where they

further showed that nontraumatic RH is rare in children and that the most dominant cause of RH is due to abusive head trauma. The idea of RH been caused by increased intracranial pressure and/or obstruction of the retinal vasculature was supported by Duhaime et al. [26]. Gabaeff (2011) [27, 28] studied the connection between subdural hematoma, retinal haemorrhage and shaken baby syndrome and observed that RH can be caused by an increase in intracranial pressure, but noted that this may not necessarily result directly from shaking a baby but rather from infection or hypoxic brain injury. The study also highlights that human shaking may not be enough to trigger RH in a healthy child, but children with perinatal subdural hematoma or pre-existing SDH can re-bleed from minimal force applied to the head. This was further corroborated by other authors [29–31]. Furthermore, Gabaeff (2016) [32] strengthened his argument by exploring an extensive list of child abuses, showing that RH occurs when there is a reasonable degree of increased intracranial pressure in the brain.

1.2.2 Vitreoretinal traction

Anoother clinical hypothesis for RH is known as vitreoretinal traction, which is thought to occur when a child is subjected to repetitive acceleration and deceleration due to back and forth movement of the skull. As forces transmits between the lens, vitreous and retina, it could lead to significant traction on the retinal surface and thereby resulting to the rupture of the blood vessels near the surface, particularly around the posterior pole [16, 33, 34]. Greenwald et al. [33] first proposed this hypothesis as the major cause of RH calling it "traumatic retinoschisis" after a study of five children who had features related to inflicted trauma. There was evidence of damage in the inner layers of the retina amongst all the five children. This hypothesis was supported by Massicotte et al. [35] and Green et al. [36] in their separate studies. Massicotte et al. [35] also used the term "traumatic retinoschisis" in describing a haemorrhage between the internal limiting membrane (which separates the retina and the vitreous) and the vitreous. This was further supported by Forbes who stated that "vein occlusions are uncommon in shaken baby syndrome", thereby questioning the hypothesis that retinal haemorrhage is linked with increase in intracranial pressure [37]. Also, optical coherence tomography imaging suggests a strong attachment between the vitreous and the retina at the tip of the perimacular region, which would explain why vitreous could damage the surface of the retina as it is displaced.

However, there are a number of objections to this hypothesis: the eye rotates naturally (*e.g.* during sarcadic eye movements) and is not routinely damaged by rotation of the head [34]. In fact, surgeons intentionally apply rotational forces during strabismus surgery which is termed as the 'spring back balance test' and this does not cause haemorrhage [38]. Furthermore, Emerson et al. [39] studied 41 cases of RH, showing bleeding to be more common around the mid periphery of the retina rather than at the vitreous surface contradicting a mechanism that originates the trauma at the vitreoretinal boundary.

In this work, we construct model for the pressure rise hypothesis [23] to determine if it can lead to RH.

1.3 Modelling blood flow circulation

Any predictive model for retinal haemorrhage following brain injury must capture both the blood flow and wave propagation induced by the trauma. In this section we summarise models for wave propagation fluid system (Section 1.3.1), models for the elastic deformation of flexible walled-blood vessels (Section 1.3.2), simple inviscid models coupling blood flow to flexible vessel walls (Section 1.3.3), extension

of these models to include viscous effects (Section 1.3.4), full unsteady three-dimensional blood flow models through flexible networks (Section 1.3.5), and their reduction to one-dimensional equations (Section 1.3.6), extensions of these one-dimensional models in large cardiovascular networks (Section 1.3.7), application of these one-dimensional equations to large amplitude disturbances including shock waves (Section 1.3.8) and applications of these models specific to the retinal circulation (Section 1.3.9).

1.3.1 Linear and non-linear wave theory

A wave is a signal that is transferred from one part of a medium to another with a recognizable velocity of propagation [42]. In mathematical terms, wave-bearing systems are described by hyperbolic partial differential equations. When these equations are linearised they can typically be reduced to the canonical wave equation and described in terms of a dispersive relation.

To give a general overview of linear and nonlinear wave theory in fluid systems, we consider a prototypical system known as the shallow water equations [43]. We show how we can compute a dispersion relation for small perturbations (the linear case) and then show how we can compute large amplitude waves such as shocks and rarefactions. In particular we formulate a classical Riemann problem which we show below forms a building block for a numerical method for capturing nonlinear waves.

The shallow water equations over a flat impermeable surface are given as [43]

$$\frac{\partial h}{\partial t} + \frac{\partial}{\partial x}(hu) = 0, \tag{1.1}$$

$$\frac{\partial}{\partial t}(hu) + \frac{\partial}{\partial x}(hu^2 + \frac{1}{2}gh^2) = 0, \tag{1.2}$$

where t is time, x is the distance along the lower surface, $h = h(x,t)$ is water depth, $u = u(x,t)$ is the flow velocity and g is the (constant) acceleration due to gravity. We show below that the corresponding nonlinear wave speed is defined as

$$c = \sqrt{gh}. \tag{1.3}$$

We now linearise these shallow water equations in order to establish the dispersion relation for the system. We consider small amplitude perturbations to the uniform state ($h = \bar{h}$) with constant flow ($u = \bar{u}$) in order derive the linearised shallow water equations, we linearise the variables according to

$$h = \bar{h} + \epsilon\hat{h}, \quad u = \bar{u} + \epsilon\hat{u}, \tag{1.4}$$

where $\epsilon \ll 1$ is a dimensionless perturbation amplitude. So, considering only terms of $O(\epsilon)$ we have from equations (1.1) and (1.2)

$$\frac{\partial \hat{h}}{\partial t} + \bar{h}\frac{\partial \hat{u}}{\partial x} + \bar{u}\frac{\partial \hat{h}}{\partial x} = 0, \tag{1.5}$$

$$\frac{\partial \hat{u}}{\partial t} + g\frac{\partial \hat{h}}{\partial x} + \bar{u}\frac{\partial \hat{u}}{\partial x} = 0. \tag{1.6}$$

We further differentiate (1.5) with respect to t and substitute into (1.6) to derive

$$\frac{\partial^2 \hat{h}}{\partial t^2} = (g\bar{h} + \bar{u}^2)\frac{\partial^2 \hat{h}}{\partial x^2} + 2\bar{u}\bar{h}\frac{\partial^2 \hat{h}}{\partial x^2}. \tag{1.7}$$

In what follows, we assume a zero baseline flow ($\bar{u} = 0$) *i.e.* the flow induced by the perturbation is much larger than the baseline flow and so the baseline flow can be effectively ignored.

For $\bar{u} = 0$ from equation (1.3) we have that (1.7) becomes

$$\frac{\partial^2 \hat{h}}{\partial t^2} = \hat{c}^2 \frac{\partial^2 \hat{h}}{\partial x^2}, \quad \hat{c} = \sqrt{g\bar{h}} \tag{1.8}$$

the linearised wave equation [42] where $\hat{c}$ is the linearised wavespeed. We consider a plane wave solution of the form

$$h(x,t) = Ae^{i(kx-\omega t)}, \tag{1.9}$$

where A is the amplitude, k is the wave number, and ω is the frequency of the wave. Substituting into the linearised wave equation, we obtain the dispersion relation

$$\omega^2 = \hat{c}^2 k^2 = g\bar{h}k^2, \tag{1.10}$$

so that the phase speed $\hat{c} = \omega/k$ consistent with (1.8).

For large amplitude perturbations we consider nonlinear wave theory, particularly focusing on the propagation of shock and rarefaction waves. One of the foundational concepts in the mathematical theory of nonlinear waves is the theory of hyperbolic conservation laws. These laws arise in various physical phenomena where the quantity of interest (such as mass, momentum, or energy) is conserved locally but can change due to fluxes across boundaries. Examples include the Euler equations in fluid dynamics, the Burgers' equation in nonlinear acoustics, and the traffic flow equations in traffic dynamics [45]. We now demonstrate how we can quantify propagation of shock and rarefaction waves using the method of characteristics in the shallow water equations.

We write (1.1) and (1.2) in terms of $c = \sqrt{gh}$ to have

$$\frac{\partial u}{\partial t} + u\frac{\partial u}{\partial x} + 2c\frac{\partial c}{\partial x} = 0, \tag{1.11}$$

$$\frac{2c}{g}\frac{\partial c}{\partial t} + u\left(\frac{2c}{g}\frac{\partial c}{\partial x}\right) + \frac{c^2}{g}\frac{\partial u}{\partial x} = 0. \tag{1.12}$$

Multiplying (1.12) by g/c and adding to (1.11), we can write the shallow water equation in Riemann invariant form as

$$\left(\frac{\partial}{\partial t} + (u \pm c)\frac{\partial}{\partial x}\right)(u \pm 2c) = 0. \tag{1.13}$$

This implies that the Riemann invariant of the flow are given by

$$R_\pm = u \pm 2c, \tag{1.14}$$

which are constant along the characteristics $C_\pm$, defined according to

$$\frac{dx}{dt} = u \pm c. \tag{1.15}$$

Consider now the initial state in which the fluid is of two different (uniform) depths separated by a barrier. We calculate the different flow profiles after instantaneously removing the barrier, this is an

example of a Riemann problem. We denote the region to the left of the barrier as region 1 with initial length h_1 and denote the region to the right of the barrier as region 2 with initial length h_2, such that $h_1 > h_2$. It emerges (See Whitham (2011) [42]) that for instantaneous removal of the barrier, we will have a left propagating rarefaction wave and a right propagating shock wave; see Figure 1.3 for the wave profile (Figure 1.3a) and the corresponding characteristics profile in the x, t plane (Figure 1.3b). As the flow evolves we denote the region between the rarefaction and shock as region 3.

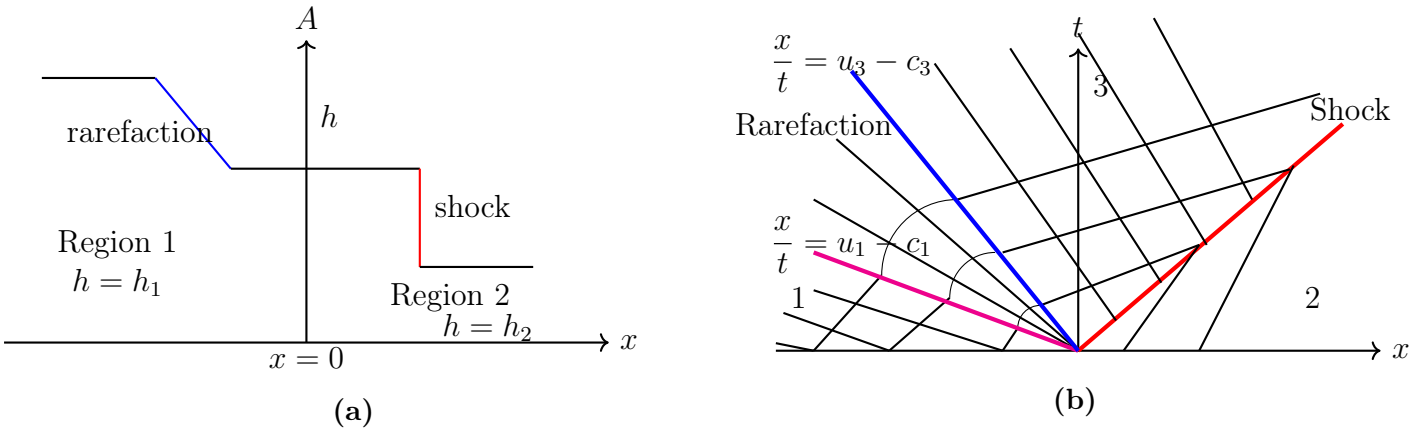

Figure 1.3: Illustration of the wave profiles and corresponding characteristics generated with an instantenous removal of the dam. Figure 2.4(a,b) is a left moving rarefaction and right moving rarefaction wave.

We first consider a rarefaction wave, also known as an expansion wave. These are regions of smooth, gradual change in the state variables of the solution. Rarefactions arise when the characteristic speeds of the system decrease, causing the wave to spread out as it propagates. Rarefaction waves are common in various physical systems, such as gas dynamics, where they represent the spreading out of a disturbance.

So, in region $x < 0$, $t = 0$, the fluid is at rest, so we consider positive characteristics entering the rarefaction region (denoted with subscript r) from region 1 such that $u_r = 0$, $c_r = c_1$ and $h_r = h_1$ along $x = -c_1 t$. This means that the information carried on these positive characteristics (1.15) becomes

$$R_+ = u_r + 2c_r = 2c_1 = C \quad \text{on} \quad \frac{dx}{dt} = u_r + c_r, \tag{1.16}$$

where C is a constant. Since the Riemann invariant takes the same value for all positive characteristics, we deduce that $R_+ = C$ everywhere.

Conversely, for the Riemann invariant along the negative characteristics, we have

$$R_- = u_r - 2c_r = D \quad \text{on} \quad \frac{dx}{dt} = u_r - c_r, \tag{1.17}$$

where D is a constant. Note that this definition only holds on negative characteristics and D can change from characteristic to characteristic.

Adding (1.16) to (1.17) gives $u_r = (C + D)/2$ which is a constant on negative characteristics. Also subtracting (1.17) from (1.16) gives h_r is constant on negative characteristics, which then implies c_r is constant on negative characteristics. Therefore, integrating (1.17) with respect to time along negative

characteristics (since u_r and c_r are constants) and simplifying, we have

$$u_r = c_r + \frac{x}{t}. \tag{1.18}$$

Hence, negative characteristics are straight lines consistent with a rarefaction fan.

Substituting (1.18) into (1.16) and simplifying, we have the wave speed given as

$$c_r = \frac{1}{3}\left(2c_1 - \frac{x}{t}\right). \tag{1.19}$$

Also, substituting (1.19) into (1.18) and simplifying, we have the fluid speed given as

$$u_r = \frac{2}{3}\left(c_1 + \frac{x}{t}\right). \tag{1.20}$$

From (1.19) we have the shape of the free surface in the rarefaction fan given as

$$h_r = \frac{1}{9g}\left(2\sqrt{gh_1} - \frac{x}{t}\right)^2. \tag{1.21}$$

Now, to the right of the barrier we compute a right propagating shock wave. Shock waves are discontinuities in the solution of a hyperbolic system that represent abrupt changes in the variables. They typically occur when the characteristic speeds of the system vary discontinuously, leading to a rapid transition from one state to another. These shock waves are characterized by steep gradients and so are difficult to capture numerically. We now discuss shock propagation in the shallow water equations, where conservation of mass and momentum equations *i.e.* (1.1) and (1.2), can be expressed in general form as

$$\frac{\partial}{\partial t}(E_i) + \frac{\partial}{\partial x}(F_i) = 0, \quad (i = 1, 2), \tag{1.22}$$

where $E_1 = h$, $F_1 = hu$, corresponding to conservation of mass (1.1) and $E_2 = hu$, $F_2 = hu^2 + \frac{1}{2}gh^2$ corresponding to conservation of momentum (1.2).

We move to the frame of shock wave and assume the shock front is located at $x = s(t)$ and write (1.16) in frame of the moving shock using the transformation

$$\zeta = x - \int \dot{s}(t')dt', \tag{1.23}$$

where $\dot{s}$ is the corresponding shock speed. If we assume that the depth of the vessel and pressure profile are uniform either side of the shock front, we can write (1.22) in the form

$$\dot{s} = \frac{F_i(s^+, t) - F_i(s^-, t)}{E_i(s^+, t) - E_i(s^-, t)}, \qquad (i = 1, 2), \tag{1.24}$$

where $s^+(s^-)$ denotes the ζ location to the right (left) of the shock. So, from (1.24), we have the shock

speed given as

$$\dot{s} = \frac{h(s^+,t)u(s^+,t) - h(s^-,t)u(s^-,t)}{h(s^+,t) - h(s^-,t)}, \tag{1.25}$$

$$\dot{s} = \frac{h(s^+,t)u^2(s^+,t) + \frac{1}{2}gh^2(s^+,t) - (h(s^-,t)u^2(s^-,t) + \frac{1}{2}gh^2(s^-,t)}{h(s^+,t)u(s^+,t) - h(s^-,t)u(s^-,t)}. \tag{1.26}$$

The shock speed can be eliminated from (1.25) and (1.26) to obtain a single jump condition between h and u across the shock front.

We have between region 1 and 2 and intermediate uniform region where we let $h = h_3$, $u = u_3$ and $c = c_3$. So, from Figure 1.3 for $x > 0$, $t > 0$, we compute a right moving shock, such that from (1.25) we have

$$\dot{s} = \frac{u_3 h_3}{h_3 - h_2}, \tag{1.27}$$

Also, from (1.26) we have

$$\dot{s} = \frac{u_3^2 h_3 + \frac{1}{2}gh_2 + \frac{1}{2}gh_3}{u_3 h_3}. \tag{1.28}$$

Equating (1.27) and (1.28), we have the shock speed given as

$$u_3^2 = \frac{g(h_3 + h_2)(h_3 - h_2)^2}{2h_2 h_3}. \tag{1.29}$$

To determine the flow in the intermediate region (where $u = u_3$, $h = h_3$ and $c = c_3$), then from (1.20) we have

$$\frac{x}{t} = \frac{3}{2}u_3 - c_1. \tag{1.30}$$

Substituting (1.30) into (1.21), we have the fluid speed in the intermediate region as

$$u_3 = 2\sqrt{g}(\sqrt{h_1} - \sqrt{h_3}). \tag{1.31}$$

Finally, equating (1.29) and (1.31) and simplifying we have the water depth h_3 in the undisturbed region given by

$$(h_2 + h_3)(h_2 - h_3)^2 = 8h_2 h_3(h_1 + h_3 - 2\sqrt{h_1 h_3}). \tag{1.32}$$

Now, for the shock to be a physical solution, we must check against the Lax entropy condition, where we need

$$(u_2 + c_2) < \dot{s} < (u_3 + c_3). \tag{1.33}$$

Entropy is a measure of the disorder or randomness in a system. The entropy condition states that the entropy of a system must increase across a shock wave. So, the entropy condition ensures that the shock wave moves in the direction of increasing entropy, corresponding to the direction of greater disorder or randomness. This condition ensures that shocks propagate in a physically meaningful way and prevents the formation of non-physical solutions [42].

1.3.2 Modelling of flexible walls

An elastic wall can deform when subject to fluid loading in a process known as fluid-structure interaction. In principle the vessel wall can be regarded as an elastic sheet (in $2D$) or an elastic annulus (in $3D$). In both cases one can write down conservation laws which govern the elastic response, solving for the displacement profiles across the wall thickness [46]. However, one often desires an asymptotic approximation where we exploit the aspect ratio to reduce to a lower order system. For example, for a $2D$ sheet one can derive the Euler Bernoulli beam equation which links the net pressure drop across the wall to the normal displacement [47]. This approach can include effect such as elastic springs, wall mass, bending resistance, viscous damping and longitudinal tension. Such an approach generalises to cylindrical walls also including azimuthal components of bending resistance (and possibly tension) [48–50]. In this thesis, similar to much of the literature on modelling blood vessels, we assume the response is dominated by the elastic spring component. However, again following experimental observations we assume that these springs are a nonlinear function of the vessel cross-sectional area in a so-called "tube law".

In the remaining sections below, we review general blood flow models in the human body (not necessarily in the eye).

1.3.3 Inviscid approaches

The human circulatory system is composed of a bifurcating network of arteries and veins (coupled through capillaries) which conduct blood to and from the heart. There has been a wide range of theoretical models to describe blood flow in different parts of the body coupling the fluid mechanics to models for the elastic walls. One of the earliest models was developed by Lighthill [45], further summarised in Pedley's book [51]. They considered propagation of pressure waves in a straight, initially uniform, elastic tube. The fluid in the tube was assumed inviscid, homogeneous and incompressible and this led to a closed $1D$ model for the flow. The resultant conservation of mass and momentum equations are analogous to those used in all the chapters of this thesis. In most of the analysis they lineareized the model (similar to the linearised shallow water equation, Section 1.3.1) ending up with a linear wave equation in the fluid pressure.

To accommodate branching in arterial networks, Pedley [51] extended the $1D$ linear theory for inviscid flow to describe flow at junctions. As a result the inviscid flow in each constituent vessel is described through a characteristic impedance [45, 51], and the division of mass across each junction is characterised by a reflection coefficient; this simple description facilitates coupling into small networks *i.e.* one can combine impedances and reflection coefficients to describe small networks of vessels [52].

This linearised analysis is typically sufficient to capture the dynamics because the flow remains strongly subcritical, where the maximal Mach number (the ratio of the maximal flow speed to the wavespeed) has been estimated as $0.2 - 0.25$ in dogs, with humans believed to be similar [51]. In different studies of the human cardiovascular system that is made of network of arteries and veins with physiological parameter values. They have adopted similar approaches as described earlier (*e.g.* [53,54]). In what follows we extend this network model to include large amplitude perturbations (*i.e.* shocks and rarefactions) approach.

1.3.4 Viscous effects

We now consider cases where there is an additional inclusion of viscous effects in the flow. This inclusion makes things more complicated. For example in an idealised setting driving viscous flow by an oscillating pressure gradient (Womersley 1955 [55]) it is seen that an exact solution of the equations of viscous fluid motion results in a phase shift between pressure and velocity. In general, it is harder to combine viscous effects into the inviscid approaches described above as the system can no longer be solved using impedances and reflection coefficients. Instead the governing equations must be solved numerically, significantly increasing the computational cost.

1.3.5 Three-dimensional flow through networks

To study full unsteady three-dimensional flow in a single vessel, numerical solutions are required as the hyperbolic governing equations facilitate wave propagation. So, the three-dimensional fluid-structure interaction models require a careful numerical algorithm to resolve the wave propagation (*e.g.* [63–65]).

Such fluid-structure interaction approaches can be extended to consider three-dimensional flows through single blood vessel junctions (*e.g.* [66]) but extensions to model large portions of the cardiovascular system in this way are computationally demanding, particularly for networks composed of multiple generations (*e.g.* [67]).

1.3.6 Reduction to 1D equations in a single blood vessel

A more computationally tractable approach for solving the unsteady three-dimensional flow through a large vessel network is to apply cross-sectional averaging of the three-dimensional governing equations and use a closure condition to derive a spatially one-dimensional representation of the flow in each vessel. These $1D$ equations are similar to invsicid systems above, but also include viscous terms so they must be solved numerically.

For example, Alastruey et al. [56] considered one-dimensional blood flow simulations with corresponding effects on pulse wave propagation. They lumped the zero-dimensional models of the microcirculation in the time domain with both the nonlinear and one-dimensional equations of blood flow in arteries to develop a time-domain algorithm that accommodates periodic and transient phenomena. Their analysis of the one-dimensional system allowed them to identify the effects of the parameters on arterial pulse waveforms. Previously the hydrodynamic effect of vessels beyond one-dimensional model arteries has been simulated using lumped parameter or zero-dimensional models governed by ordinary differential equations that relate pressure to the flow at the outflow of each one-dimensional terminal vessel [57–62].

The reduced equations can also present a significant numerical challenge to resolve the wave propagation, and are typically solved numerically using bespoke finite volume schemes (*e.g.* [68, 69]). Finite-volume schemes are widely used for solving hyperbolic conservation laws because they naturally conserve mass, momentum, and energy within each control volume. The scheme discretises the spatial domain into a set of control volumes or cells, where the conservation equations are integrated over each volume. These volumes are then coupled by imposing carefully chosen fluxes between neighbouring cells. One way to compute these fluxes is through analysis of the Riemann problem in each finite volume.

These $1D$ hyperbolic models with viscous terms have also been used to investigate additional effects such as vessel tapering (*e.g.* [70]), wall viscoelasticity (*e.g.* [71]) and blood rheology (*e.g.* [72, 73]).

1.3.7 1D models for blood vessels coupled at junctions

These lower-order models for individual vessels can be extended to networks by coupling spatially one-dimensional flow within each vessels, through boundary conditions imposed at single points which mimic the junction. These models impose conservation of (total or static) pressure and mass, either by directly imposing continuity across the junction using extrapolation along characteristics to inform the matching (*e.g.* [68, 69, 74, 75]) or by introducing a separate junction compartment (*e.g.* [76–78]).

There have been numerous studies of large arterial networks. For example, Vignon and Taylor [79] developed a 'coupled multidomain method' to solve the one-dimensional nonlinear equations of blood flow in elastic vessels where they demonstrated the importance of selecting appropriate boundary conditions in analysing wave propagation in transient and periodic states.

Sherwin et al. [81] investigated a one-dimensional model of blood flow in human arteries using both a discontinuous Galerkin and a Taylor–Galerkin formulation. They first resolved the problem associated boundary conditions at the terminal ends of a compliant artery or system of arteries, as identified by Vignon and Taylor, [79] using the characteristic equations for the hyperbolic system. They also used these two schemes to investigate the effect of local narrowing (or stent) inclusion and vessel stiffness on the wave propagation along the artery. They also investigated a network of 55 arteries with different bifurcation points, and showed there there are superimposition of waves resulting from wave reflections at the bifurcation points which leads to build up of pressure in the vessel. Marchandise and Flaud [80] extended the model for haemodynamics in arteries and used it for the flow in collapsible tubes such as veins, where they proposed an accurate one-dimensional Runge-Kutta discontinuous Galerkin method coupled with lumped parameter models for the boundary conditions. Their method was able to capture shocks. Also, they presented some benchmark problems and proved that their method produces stable and highly accurate solutions.

Olufsen et al. [82] carried out a similar study but restricted to only the arterial circulation where they attempted to assess the pressure drop over both large and small vessels. They showed that their model can predict effects of rarefaction waves by altering the geometry of the arterial microvascular network. They further postulated that hypertension in the large proximal arteries may be as a result of rarefaction in smaller arteries. Finally, they showed agreement with Sherwin et al. [81] in that stiffening of the large arteries results in a pressure increase as is evident with observations of isolated systolic hypertension, consistent with ageing.

There are also a number of studies considering just the systemic veins, with particular emphasis on the venous circulation reported by Fullana and Zaleski [77]. They investigated how their system responds to a transient entry flow, where they showed that there is output of two different frequencies related to lengths of the associated vein. They also identified wave reflections at major points where they veins meet showing qualitative agreement with flow in arteries. Muller and Toro [75] used a different approach in studying the systemic vein. They validated the models by Olufsen et al. [82] and Sherwin et al. [81] by comparing with physiological values. They showed that the same conclusion made earlier for an arterial system can also be used for the veins.

Qureshi et al. [83] extended the work of Olufsen et al. [82] to develop a multiscale mathematical and computational model of the pulmonary circulation to analyse both arterial and venous flows. Their model can be used in merging dynamic predictions in networks containing both arterial and venous trees. Furthermore, their model addresses the issue of pulmonary hypertension as earlier identified by Sherwin et al. [81]. Noe et al. [84] extended this work to address the problem of inference in a multiscale computational model of pulmonary arterial and venous blood circulation.

These models mentioned above are all $1D$ flow equations including the convective inertia term in the momentum equation (*i.e.* the uu_x term in the shallow water equations ((1.1) and (1.2)). However, the influence of this term is typically not strong enough to to allow the flow generate shocks and so the flow remains subcritical everywhere.

1.3.8 Large amplitude pressure waves - shock capture

In some cases the hyperbolic flow equations described above can exhibit wave steepening (*e.g.* when the Reynolds number is large enough) and thus the numerical schemes must be specifically developed to allow the propagation of shock waves.

The seminal work on shock capture in blood vessels was conducted by Brook *et al.* [44], who developed a numerical scheme which exploits a local Riemann problem in each finite volume. This Riemann problem is analogous to the Riemann problem considered for the shallow water equations (Section 1.3.1). The Riemann problem was subsequently studied in detail using sophisticated constitutive laws for the vessel wall mechanics for both arteries [85] and veins [86].

To extend this approach to circulatory networks the Riemann problem first needs to be adapted for use across a junction, known as the junction Riemann problem [87, 88]. In this case the junction boundary conditions are embedded at the point of discontinuity in initial conditions of the Riemann problem, similar to an abrupt discontinuity in vessel stiffness [85, 89]. The analysis is analogous to these classical Riemann problems while the flow remains subcritical, but extension to transcritical and supercritical flows is not straightforward [87]. Subsequent analysis has posed iterative methods to deal with the supercritical regime [88], but what is currently missing is an understanding of how the flow can become transcritical, as may occur in physiological situations such as when a vein becomes highly collapsed [87].

Contarino et al. [87] designed a new implicit solver for the Junction-Generalized Riemann Problem (J-GRP), based on their recently proposed implicit method for solving the Generalized Riemann Problem (GRP) for systems of hyperbolic balance laws. They only considered solutions of the classical problem (J-CRP) for the one-dimensional blood flow equations assuming subcritical flow. They did not consider other solutions like resonance, transcritical and supercritical flows. They note:

> *Here we present the solution of the J-CRP for the one-dimensional blood flow equations assuming subcritical flow. To the authors' knowledge, the complete solution of the J-CRP considering all possible wave-patterns is not available. This implies that we cannot handle supercritical and transcritical flows at junctions, which might be present in physiological situations due to vein collapse with discontinuous parameters in the human body [87].*

We will address this challenge in this thesis, showing how subcritical and transcritical flow are connected.

Murillo and Garcia-Navarro [88] proposed a methodology for the solution of the Junction Riemann Problem for $1D$ hyperbolic balance laws in networks of elastic vessels. They investigated subsonic and supersonic waves, and the transmission of backward waves from downstream vessels through the junction. They isolated particular examples of sub-supercritical flows, but no attempt was made to explore connections between these wave solutions.

In the analysis below we extend the junction Riemann problem to include transcritical flow, which we show spans a wide range of the parameter space.

1.3.9 Models specific to the retinal circulation

Takahashi et al. [90] formulated a mathematical model of the haemodynamic behaviour in the microvasculature network of the human retina, where they assumed that the branching of the vascular network is dichotomous symmetric. This enabled a systematic prediction of the pressure hierarchy through the generations of arteries into the veins. Also, Ganesan et al. [91] developed a more realistic image-based network model of a murine retinal vasculature to describe that the distribution of the blood haematocrit in the retinal network; they demonstrated that this distribution is extremely nonuniform, exhibiting lower values at the pre-equator region and higher values at the equator region of the retina.

Guidoboni et al. [92] developed a lumped parameter (ODE) model to simulate blood flow in the central retinal vessels and retinal microvasculature. They divided the vasculature into five main compartments namely the central retinal artery, retinal arterioles, capillaries, retinal venules and the central retinal vein. Results from their model suggests that the capacity of intraocular pressure (IOP) to influence changes in the retinal hemodynamics depends on the levels of blood pressure and autoregulation of the individual. Their model did not consider the three-dimensional spatial arrangements of the retinal vasculature and also did not take into account IOP alterations for patients who suffer metabolic dysfunction. This extension was considered by Arciero et al. [93] who considered a vascular wall mechanics model to predict the relative importance of regulatory mechanisms in achieving retinal autoregulation. Their model predicts that with an increase in IOP there is a corresponding decrease in the autoregulation towards lower perfusion pressures which is consistent with the observation that glaucoma is associated with a decrease of perfusion pressure.

Stewart et al. [94] developed a theoretical model for the onset of retinal venous pulsation in the central retinal vein as a result of pressure changes resulting from intraocular pressure (IOP) and intracranial pressure (ICP). In their model, they considered the vein as a flexible-walled channel divided into four compartments, with each compartment representing the different external environments along the vein. This enabled them to predict the shape of the vessel wall as blood traverses through the compartments, showing how the system sponteneously exhibit a self-excited oscillation for some parameters (*i.e.* retinal vein pulsation). Their model was able to predict a threshold in IOP for a fixed ICP to triger vigorous oscillation *i.e.* retinal venous pulsation.

Earlier studies have investigated the trigger of large amplitude pressure wave propagation. For example, where we have incompetent or sever aortic stenosis resulting in generating large amplitude pressure that increases the volume of blood ejected by the heart into the aorta. This can cause extremely high systolic and increased pressure pulse (sometimes known as 'pistol shock' pulse) [95,96]. Also, some studies have employed different ways of computing shocks and rarefactions like the nonlinear analysis of flow pulses and shock waves in arteries by Anliker et al. (1971) [97].

1.4 Modeling retinal haemorrhage

Several possible mechanisms of RH have been outlined in Section 1.2. We acknowledge that there are disparities between clinical practitioners, and so we pursue mathematical modeling in an attempt to elucidate an unambiguous mechanism of RH. Here we review some modelling studies in this direction.

Bonshek et al. [98] formulated mathematical model of the infant skull to estimate the rise in intracranial pressure (ICP) following an injury. They also modelled the resulting flow of CSF along the optic nerve subarachnoid space (ONSAS) with the aim of investigating how pressure disturbance prop-

agates towards the back of the eye. They modeled the skull of an infant as a set of hinged plates and the ONSAS as a collapsible fluid-filled channel. Their model predicts that the propagating disturbance steepens into a shock at its leading edge and the reflection of the disturbance at the sclera leads to significantly increased cerebrospinal (CSF) pressure. This result gives a possible explanation for bleeding in the ONSAS close to the back of the eye resulting from head injuries in infants.

A model for the subsequent transmission of this CSF pressure rise into the retinal circulation was formulated by Spelman and Stewart [16]. They considered the central retinal vessels as long collapsible tubes with different regions (similar to the models of retinal venous pulse discussed above) with each region experiencing a different external pressure environment. Their study examined how a sudden change in CSF pressure in the nerve sheath (by an injury in the brain) drives large amplitude (shock) waves along the central retinal vessels towards the eye. They showed that the length of the vessel within the optic nerve was key to the outcome: larger lengths protected the eye from damage by reducing the pressure wave amplitude, driving spreading over a larger length scale.

1.5 Physiological parameters

It is also essential to estimate the parameters of the retinal circulation to understand how they influence our model. In the model considered in this thesis, we assume an inviscid flow where the vessel has constant baseline cross-sectional area, while also assuming that the baseline flux is negligible. However, it remains to characterise the geometry of the network for the first few generations of the superior-temporal quadrant of the human retinal circulation for both the arteries and veins (*i.e.* starting from the third generation from the actual retinal artery and vein). Following the approach of Takahashi et al. [90] we present measured data of some generations of the superior-temporal quadrant of the human retinal circulation such that Tables 1.1 is for arteries while Table 1.3 is for veins alongside the corresponding pressure drop. We further estimated other data of the arterial and venous network as shown in Tables 1.2 for arteries and 1.4 for veins.

We observe that the lengths and cross-sectional areas of vessels reduce systematically as we progress along the vascular tree. In particular, this change in cross-sectional area results in an abrupt discontinuity across junctions. As used by Takahashi et al. [90] the radius of different generations of arteries or veins can be estimated from Murray's law [90]; for a symmetric bifurcation from generation j to $j+1$,

Artery Generation	Radius μm	Length μm	Flow rate m^3/s	Baseline cross-sectional area μm^2	Pressure $mmHg$	Pressure drop $mmHg$	Viscosity cP
1	54.00	726.9	1.88×10^{-4}	9.2×10^3	38.9	1.1	3.7
2	42.35	549.6	9.41×10^{-5}	5.7×10^3	37.8	1.1	3.6
3	33.20	415.5	4.71×10^{-5}	3.5×10^3	36.7	0.9	3.4
4	26.05	314.1	2.35×10^{-5}	2.1×10^3	35.8	0.9	3.2
5	20.40	237.5	1.18×10^{-5}	1.3×10^3	34.9	0.9	2.9
6	16.00	179.5	5.88×10^{-6}	8.1×10^2	34.0	0.7	2.7
7	12.55	135.7	2.94×10^{-6}	5.0×10^2	33.3	0.6	2.4

Table 1.1: Measured data of some generations in the human arterial network according to Takahashi et al. [90]

Artery Generation	Stiffness Pa	Flow speed (baseline) m/s	Reynolds No (baseline)	Flow speed (perturbation) m/s	Reynolds No (perturbation)
1	2382.68	0.022	0.337	1.591	24.32
2	4765.10	0.017	0.210	1.591	19.65
3	9531.51	0.014	0.144	1.591	16.31
4	19061.41	0.011	0.094	1.591	13.60
5	38137.30	0.009	0.067	1.591	11.75
6	76252.04	0.007	0.044	1.591	9.90
7	152805.38	0.006	0.033	1.591	8.74

Table 1.2: Estimated data of some generations in the human arterial network

Vein Generation	Radius μm	Length μm	Flow rate m^3/s	Baseline cross-sectional area μm^2	Pressure $mmHg$	Pressure drop $mmHg$	Viscosity cP
1	73.50	1036.2	1.88×10^{-4}	1.7×10^4	17.9	0.5	4.2
2	57.65	783.4	9.41×10^{-5}	1.0×10^4	18.4	0.5	4.0
3	45.2	592.3	4.71×10^{-5}	6.4×10^3	18.9	0.5	3.9
4	35.45	447.8	2.35×10^{-5}	4.0×10^3	19.4	0.5	3.7
5	27.80	338.5	1.18×10^{-5}	2.4×10^3	19.9	0.4	3.5
6	21.80	255.9	5.88×10^{-6}	1.5×10^3	20.3	0.4	3.2
7	17.10	193.5	2.94×10^{-6}	9.2×10^2	20.7	0.4	3.0

Table 1.3: Measured data of some generations in the human venous network according to Takahashi et al. [90]

Vein Generation	Stiffness Pa	Flow speed (baseline) m/s	Reynolds No (baseline)	Flow speed (perturbation) m/s	Reynolds No (perturbation)
1	37.09	0.011	0.202	1.591	29.43
2	74.18	0.008	0.124	1.591	24.08
3	148.33	0.007	0.085	1.591	19.36
4	296.72	0.006	0.060	1.591	16.01
5	593.26	0.005	0.042	1.591	13.27
6	1187.14	0.004	0.029	1.591	11.38
7	2373.77	0.003	0.018	1.591	9.52

Table 1.4: Estimated data of some generations in the human venous network

so that

$$r_j^3 = 2r_{j+1}^3, \tag{1.34}$$

where r_j is the radius of each generation. While the length of the vessel can be estimated from the ratio of length and radius given as [100]

$$L_j = 7.4 r_j^{1.15}. \tag{1.35}$$

The flow rate through each generation of vessels estimated by Takahashi et al. [90] is also summarised in Tables 1.1 and 1.3, showing decrease in flow rate as we progress down generations. However, in the analysis in this thesis we assume this baseline flow is negligible in comparison to the flow induced by the perturbation.

The stiffness of each generation of vessels can be computed through [16]

$$k^* = \frac{E^*}{12(1-\nu^2)} \left(\frac{h^*}{r_0^*} \right)^3, \tag{1.36}$$

where the Young's modulus of the tissue is given as E^*, the Poisson ratio is denoted as ν, the wall thickness is denoted as h^* and the inner lumen radius denoted as r_0^* [101]. For the retinal blood vessels the tissue is approximately incompressible ($\nu = 0.49$) and the Young's modulus can be inferred from experimental measurements of the pulse wave velocity within the human retinal vessels, such that $E^* = 0.3MPa$ in the artery and $E^* = 0.6MPa$ in the vein [102]. The vessel wall thickness is estimated as $39.7\mu m$ for arteries and $10.7\mu m$ for veins. The corresponding estimates of the vessel stiffness and Reynolds number for each generation are listed in Table 1.2 for the arteries and Table 1.4 for the veins.

The corresponding Reynolds number of the flow in the blood vessels is estimated as

$$\mathcal{R} = \frac{\rho^* u_0^* A_0^{*1/2}}{\mu^*}, \tag{1.37}$$

(see derivation in Section 2.2) where ρ^* is density, u_0^* is a typical velocity set by a typical pressure perturbation to the system, A_0^* is the baseline cross-sectional area and μ^* is the blood viscosity. Given different values of μ^* (listed in Tables 1.1 and 1.3) for each generation and for $\rho^* = 1050\ kg/m^3$, we use the cross-sectional area quoted in the Tables 1.1 and 1.3 for arteries and veins, respectively. We estimate the velocity scale for the perturbed flow as $u_0^* = (\Delta p^*/\rho^*)$ where Δp^* is the pressure drop associated with the perturbation. Assuming a pressure of $\Delta p^* = 20mmHg$ driven by an injury or traumatic event, we compute u_0^* and the corresponding values of the Reynolds number are listed in Tables 1.2 and 1.4, respectively. We also computed a velocity scale at baseline (based on flow rate) where the Reynolds number is substantially lower. We note that the Reynolds numbers associated with the perturbations are very large consistent with the inviscid approach taken in the thesis.

1.6 Outline of the thesis

This thesis is motivated by the intention to create a full computational model of the retinal circulation. The flow equations are hyperbolic and so the appropriate method is to use a finite volume scheme to discretize the domain and then solve the governing equations [104]. As part of this finite volume scheme we intend to follow the approach of Brook et al. [44] and apply a Riemann problem within each finite volume to construct fluxes connecting each volume. To completely solve our system there are at least

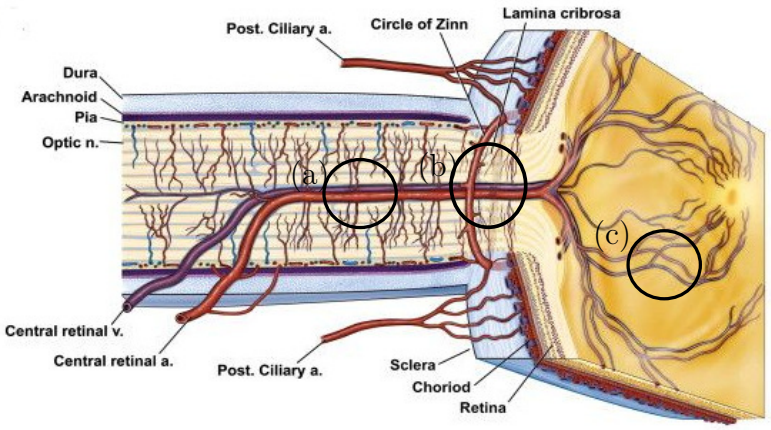

Figure 1.4: Anatomy of the superior-inferior axis of the human eye through the optic nerve to the retina [103]. The path of the central retinal artery and vein are clearly marked, entering the nerve about 1cm from the eye and entering the retina through the center of the optic nerve.

three different Riemann problems to be considered.

In Chapter 2 of this thesis we consider blood flow in the central retinal vessels, which pass along the centre of the optic nerve (see region (a) in Figure 1.4) and construct the classical Riemann problem where the finite volume spans a narrow region in a single blood vessel with uniform material properties (see Figure 1.5a); we introduce a new numerical scheme to explore the entire parameter space.

In Chapter 3 we consider blood flow in the central retinal vessels, through the optic nerve into the retina via the optic disc (see region (b) in Figure 1.4) and construct a Riemann problem where the finite volume spans a region with two different elastic stiffnesses (see Figure 1.5b). This chapter extends existing analysis to explore the entire parameter space showing how the solutions isolated by others (*e.g.* Han et al. [89], Toro and Siviglia [105]) fit together.

Finally, in Chapter 4 we consider blood flow in the central retinal vessels, as they branch into the retinal circulation (see region (c) in Figure 1.4) following similar geometry described by Hayreh and others [15–17, 102]. We construct a Riemann problem where the finite volume spans a symmetric junction with a jump in stiffness between the parent and daughter vessels (see Figure 1.5c). This junction Riemann problem is similar to Contarino et al. [87], but in our case we extend the existing analysis to include transcritical flow, demonstrating how resonance can produce additional shock waves in the system.

We conclude this thesis in Chapter 5 with a brief conclusion summarising the main outcomes of the thesis.

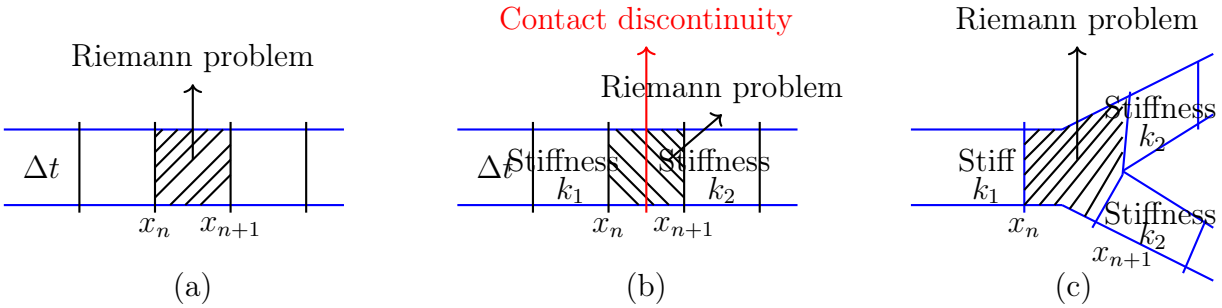

Figure 1.5: Set-up of the different components of the thesis.

CHAPTER 2

A blood vessel with uniform material properties

In this chapter we consider a simple model for blood flow through a single compliant vessel (which could be an artery, vein or capillary) with uniform baseline cross-sectional area (*i.e.* no tapering) and uniform material properties. The model was previously derived by Lighthill [45] and summarised in the monograph of Pedley [51] and has since been used in a wide number of studies of flow in the cardiovascular system (for example [16, 81, 102, 105]). In particular, we consider a Riemann problem when a discontinuity is imposed in the initial profiles of flow and vessel cross-sectional area and examine the subsequent evolution of the system.

2.1 Governing equations

We consider a long blood vessel of length L^* with uniform baseline cross-sectional area A_0^*. The vessel is described using cylindrical polar coordinates (r^*, θ, x^*) where r^* represents the radial coordinate, θ represents the azimuthal coordinate and x^* is measured along the axis of the vessel with corresponding unit vectors $\hat{\mathbf{r}}$, $\hat{\boldsymbol{\theta}}$ and $\hat{\mathbf{x}}$, respectively. Time is denoted as t^*.

The flow of blood is assumed to be homogeneous and Newtonian, so we denote the (constant) viscosity and density of the blood as μ^* and ρ^*, respectively.

We assume that the deformation of the vessel walls can be described by the radius $r^* = R^*(\theta, x^*, t^*)$ and we denote the corresponding vessel cross-sectional area as $A^*(x^*, t^*)$.

We describe the elasticity of the vessel in a simple manner through an elastic stiffness parameter k^*, which is assumed uniform along the tube. Note that in subsequent chapters we consider a step-wise change in this property as an example of discontinuity in the system. Finally, we apply a uniform external pressure p_e^* to the vessel and assume a reference pressure p_0^*, which we fix below.

From the Navier-Stokes equations for an incompressible fluid with velocity $\boldsymbol{u}^*$ and pressure p^* [106], we have conservation of mass (the continuity equation) in dimensional form given as

$$\nabla^* \cdot \boldsymbol{u}^* = 0, \tag{2.1}$$

and the momentum equation in dimensional form given as

$$\rho^* \left[\frac{\partial \boldsymbol{u}^*}{\partial t^*} + \boldsymbol{u}^* \cdot \nabla^* \mathbf{u}^* \right] = -\nabla^* p^* + \mu^* \nabla^{*2} \boldsymbol{u}^*, \tag{2.2}$$

where ∇^* represents the gradient operator in cylindrical polar coordinates.

On the flexible wall we impose the dimensional kinematic condition in the form

$$u_r^* = \frac{\partial R^*}{\partial t^*} + \frac{u_\theta^*}{R^*} \frac{\partial R^*}{\partial \theta} + u_x^* \frac{\partial R^*}{\partial x^*}, \quad (r^* = R^*), \tag{2.3}$$

and the no slip condition

$$\boldsymbol{u}^* \cdot \hat{\mathbf{t}} = 0, \quad (r^* = R^*), \tag{2.4}$$

where $\hat{\mathbf{t}}$ is a unit tangent vector to the wall.

We henceforth assume that the flow is axisymmetric, such that all variables are independent of θ and the azimuthal component of the fluid velocity is zero ($u_\theta^* = 0$). Hence we have that $A^* = \pi R^{*2}$ as the cross-section must always be circular.

To close the system we follow previous studies and apply an empirical tube law to represent the wall elasticity, which is given as

$$p^* = p_e^* + k^* f\left(A^*/A_0^*\right), \quad (r^* = R^*). \tag{2.5}$$

The tube law provides a relationship between the fluid pressure just inside the tube wall (p^*) and the external pressure around the tube (p_e^*) and the vessel cross-sectional area A^*. This law is proportional to the stiffness of the tube (k^*) multiplied by a dimensionless function that describes the expansion and compression of the tube relative to the baseline value $f(A^*/{A_0}^*)$. Note that this law immediately simplifies the wall mechanics to be axisymmetric, which is consistent with our earlier assumption.

2.2 Non dimensionalization

To reduce the number of parameters in the system, we define non-dimensional variables (written without asterisks) by scaling lengths on the square root of the baseline cross-sectional area $A_0^{*1/2}$, pressure (stresses) on the vessel stiffness k^*, velocities on an inertial scale constructed by balancing the elastic pressure gradient with the flow inertia $u_0^* = (k^*/\rho^*)^{1/2}$. So that

$$A^* = A_0^* A, \quad u^* = u_0^* u, \quad x^* = A_0^{*1/2} x, \quad t^* = \frac{A_0^{*1/2}}{u_0^*} t. \tag{2.6}$$

Furthermore, we rescale the pressure according to

$$p^* = k^* p + p_0^*. \tag{2.7}$$

The dimensionless variables and parameters are denoted with the same symbol as that of their dimensional counterpart without asterisks. The resulting non-dimensional parameters are

$$p_e = \frac{p_e^* - p_0^*}{k^*}, \quad L = \frac{L^*}{A_0^{*1/2}}, \quad \mathcal{R} = \frac{\rho^* u_0^* A_0^{*1/2}}{\mu^*}, \tag{2.8}$$

where p_e is the dimensionless external pressure, L is the dimensionless vessel length and $\mathcal{R}$ is the Reynolds number.

Denoting the dimensionless flow velocity as $\mathbf{u} = u_r\hat{\mathbf{r}} + u_x\hat{\mathbf{x}}$ and dimensionless blood pressure as p, the non-dimensional fluid equations take the form

$$\nabla \cdot \boldsymbol{u} = 0, \tag{2.9}$$

$$\frac{\partial \boldsymbol{u}}{\partial t} + \boldsymbol{u} \cdot \nabla \boldsymbol{u} = -\nabla p + \mathcal{R}^{-1}\nabla^2 \boldsymbol{u}. \tag{2.10}$$

The dimensionless tube law and boundary conditions take the form

$$p = p_e + f(A), \qquad (r = R) \tag{2.11}$$

$$u_r = \frac{\partial R}{\partial t} + u_x \frac{\partial R}{\partial x}, \quad (r = R) \tag{2.12}$$

$$\boldsymbol{u} \cdot \hat{\mathbf{t}} = 0, \qquad (r = R). \tag{2.13}$$

2.3 Long wavelength approximation

Assuming the vessel is typically long and thin, we choose a small parameter $\beta = 1/L \ll 1$ [16] and rescale the variables and parameters as

$$x = \beta^{-1}\tilde{x}, \quad r = \tilde{r}, \quad t = \beta^{-1}\tilde{t}, \quad u_r = \beta\tilde{u}_r, \quad u_x = \tilde{u}_x, \quad p = \tilde{p}, \quad A = \tilde{A}, \quad \mathcal{R} = \tilde{\mathcal{R}}. \tag{2.14}$$

Neglecting terms of $O(\beta^2)$, the continuity and momentum equations can be written in component form as

$$\frac{1}{\tilde{r}}\frac{\partial}{\partial \tilde{r}}(\tilde{r}\tilde{u}_r) + \frac{\partial \tilde{u}_x}{\partial \tilde{x}} = 0, \tag{2.15}$$

$$\frac{\partial \tilde{p}}{\partial \tilde{r}} = 0, \tag{2.16}$$

$$\frac{\partial \tilde{u}_x}{\partial \tilde{t}} + \tilde{u}_r\frac{\partial \tilde{u}_x}{\partial \tilde{r}} + \tilde{u}_x\frac{\partial \tilde{u}_x}{\partial \tilde{x}} = -\frac{\partial \tilde{p}}{\partial \tilde{x}} + \frac{1}{\tilde{\mathcal{R}}}\frac{1}{\tilde{r}}\frac{\partial}{\partial \tilde{r}}\left(\tilde{r}\frac{\partial \tilde{u}_x}{\partial \tilde{r}}\right), \tag{2.17}$$

subject to (dimensionless) long wavelength kinematic and no slip conditions

$$\tilde{u}_r = \frac{\partial \tilde{R}}{\partial \tilde{t}} + \tilde{u}_r\frac{\partial \tilde{R}}{\partial \tilde{r}} + \tilde{u}_x\frac{\partial \tilde{R}}{\partial \tilde{x}}, \quad (\tilde{r} = \tilde{R}), \tag{2.18}$$

$$\tilde{u}_x = 0, \qquad (\tilde{r} = \tilde{R}), \tag{2.19}$$

$$\tilde{p} = \tilde{p}_e + f(\tilde{A}). \tag{2.20}$$

We note that the blood pressure is independent of $\tilde{r}$ through (2.16) and so the long-wavelength tube law (2.20) determines the pressure across the entire cross-section.

For simplicity we remove the tildes in our equations and following method of Spelman and Stewart [16], we then integrate equations (2.15) and (2.17) across the vessel cross-section such that the

conservation of mass equation (2.15) becomes

$$2\pi[ru_r]_0^R + 2\pi\int_0^R \frac{\partial u_x}{\partial x} r dr = 0. \tag{2.21}$$

Evaluating the first term using the kinematic condition (2.18), manipulating the second term we have

$$2\pi R\frac{\partial R}{\partial t} + 2\pi\frac{\partial}{\partial x}\int_0^R u_x r dr = 0. \tag{2.22}$$

The axial flux along the vessel takes the form

$$q = 2\pi\int_0^R u_x r dr. \tag{2.23}$$

We substitute (2.23) into (2.22) and express the first term in (2.22) in terms of vessel cross-sectional area $A(=\pi R^2)$, so that (2.15) reduces to

$$\frac{\partial A}{\partial t} + \frac{\partial q}{\partial x} = 0. \tag{2.24}$$

Similarly, the conservation of momentum equation (2.17) becomes

$$2\pi\int_0^R \frac{\partial u_x}{\partial t} r dr + 2\pi\int_0^R \left(u_r\frac{\partial u_x}{\partial r} + u_x\frac{\partial u_x}{\partial x}\right) r dr = -2\pi\int_0^R \frac{\partial p}{\partial x} r dr - \frac{2\pi}{\mathcal{R}}\left[r\frac{\partial u_x}{\partial r}\right]. \tag{2.25}$$

Manipulating the convective inertia terms using the conservation of mass equation and cancelling boundary terms using the kinematic condition (2.18) we have

$$2\pi\frac{\partial}{\partial t}\int_0^R u_x r dr + 2\pi\frac{\partial}{\partial x}\left(\int_0^R u_x^2 r dr\right) = -2\pi\int_0^R \frac{\partial p}{\partial x} r dr + \frac{2\pi}{\mathcal{R}} R\frac{\partial u_x}{\partial r}\bigg|_{r=R}. \tag{2.26}$$

We rewrite the unsteady inertia terms in terms of the axial flux in (2.23) to have

$$\frac{\partial q}{\partial t} + 2\pi\frac{\partial}{\partial x}\left(\int_0^R u_x^2 r dr\right) = -2\pi\int_0^R \frac{\partial p}{\partial x} r dr + \frac{2\pi}{\mathcal{R}} R\frac{\partial u_x}{\partial r}\bigg|_{r=R}. \tag{2.27}$$

Here we note that p is independent of r from (2.16), so we integrate the first term of the RHS such that equation (2.17) becomes

$$\frac{\partial q}{\partial t} + 2\pi\frac{\partial}{\partial x}\left(\int_0^R u_x^2 r dr\right) = -A\frac{\partial p}{\partial x} + \frac{2\pi}{\mathcal{R}} R\frac{\partial u_x}{\partial r}\bigg|_{r=R}. \tag{2.28}$$

To close this system we assume the fluid is approximately inviscid ($\mathcal{R}\to\infty$) such that the flow has a simple plug flow profile *i.e.* $u_x = u(x,t)$ over the timescales considered, so the viscous term is neglected and then (2.24) and (2.28) can be written as one-dimensional conservation of mass and momentum equations for an incompressible fluid with the corresponding tube law [44], Also, with this choice of flow

profile (2.23) implies $q = uA$, we can rewrite the system (2.24) and (2.28) in terms of A, u in the form

$$\frac{\partial A}{\partial t} + \frac{\partial}{\partial x}(uA) = 0, \tag{2.29}$$

$$\frac{\partial}{\partial t}(Au) + \frac{\partial}{\partial x}(u^2 A) + A\frac{\partial p}{\partial x} = 0, \tag{2.30}$$

$$p - p_e = f(A). \tag{2.31}$$

We recognise that the neglect of viscocity is a rather restrictive assumption and means that we must also neglect the no-slip condition on the tube walls. However, we argue that viscous effects are usually too slow to strongly influence the rapid changes in blood flow induced by traumatic injury (see argument in [16]). Our inviscid model constitutes one of the simplest available approaches for modelling this system (based on models discussed in Pedley's book [51]). However, we intend that this analysis will be modified to include viscous effects at a later date. With no viscous pressure gradient the blood pressure will be constant when the tube is undeformed (*i.e.* $A = 1$) and this pressure is the baseline pressure p_0^* identified above.

The tube law is generally written as a power law function of A [107]. Following Brook et. al. [44] we set (in our notation)

$$p - p_e = A^m - A^{-n}, \tag{2.32}$$

where both m and n are non-negative exponents describing the resistance to expansion and collapse. For instance Han et al. [89] considered the case where $m = 1/2$ and $n = 0$, as a model for arteries (see dashed line in Figure 2.1). Conversely, Brook et al [44] used $m = 10$, $n = 3/2$ as a model for the giraffe jugular vein (see blue line in Figure 2.1). We denote this as the general tube law (see Section 2.13), which includes resistance to both expansion and collapse as the internal pressure increases or decreases.

To facilitate analytical solution of our system, in Chapters 2, 3 and 4 we first use a simplified (expanding) tube law with $n = 0$ and $m = 10$, (denoted as the red line in Figure 2.1) even though it does not (strongly) resist collapse and allows us to have zero cross-sectional area for a finite pressure $p = p_e - 1$. There is also the collapsing tube law where $m = 0$ and $n = 3/2$, (denoted as the green line in Figure 2.1) which does not resist expansion which was not considered in this study.

For the purpose of the early sections of this chapter, we assume a simplified (expanding) tube law of the form

$$p - p_e = A^m - 1 \quad (n = 0). \tag{2.33}$$

Note that the simplified tube law (2.33) allows us to solve the Riemann problem almost entirely analytically. The more general tube law which resists collapse is studied in Section 2.13.

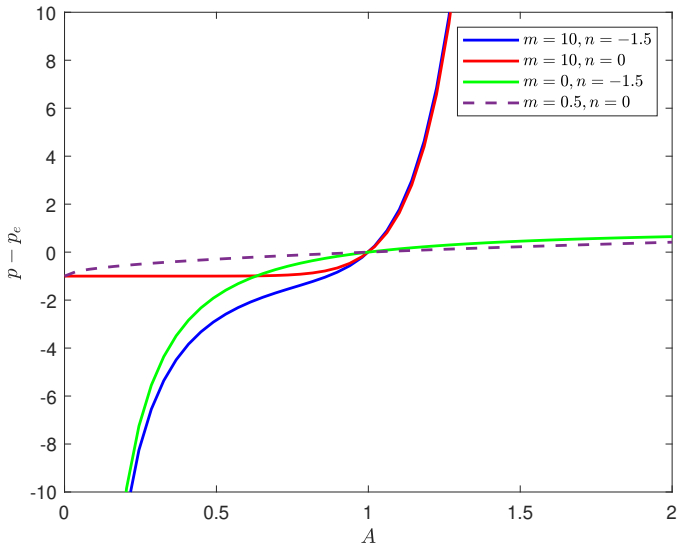

Figure 2.1: Comparison of dimensionless tube laws showing the different values of m and n.

2.4 Riemann problem in an elastic tube

We consider the analogue of the dam break problem from the study of the shallow water equations [108], where we impose an instantaneous discontinuity in flow and/or tube cross-sectional area across an interface and predict how the system responds. The problem is described in Figure 2.2, where the vessel is initially divided into two regions across $x = 0$, denoted as regions 1 and 2, respectively and the corresponding Riemann problem in the $x - t$ plane is shown in Figure 2.3. We view this system as an idealised model to understand the fundamental Riemann problem in a single blood vessel which we will later generalise to apply more particularly to the retinal circulation (considering discontinuity in stiffness and a vessel junction in subsequent chapters). We impose a discontinuity in initial conditions at $x = 0$ such that the initial flow velocities in region 1 and region 2 are constants (given as $\mathcal{U}_1$ and $\mathcal{U}_2$), respectively and the initial cross-sectional areas are also constants (given as $\mathcal{A}_1$ and $\mathcal{A}_2$), respectively.

We introduce the dimensionless nonlinear wave speed $c(x, t)$ [44], defined as

$$c^2(x,t) = A\frac{dp}{dA} = mA^m, \tag{2.34}$$

for our choice of tube law [109] (note that c is non-dimensionalised by u_0^*, as with other velocities). The baseline wavespeed (when the vessel is undeformed $A = 1$) is therefore

$$c_0^2 = m. \tag{2.35}$$

Under this definition of wavespeed, the system (2.29) and (2.30) can be written independently of pressure

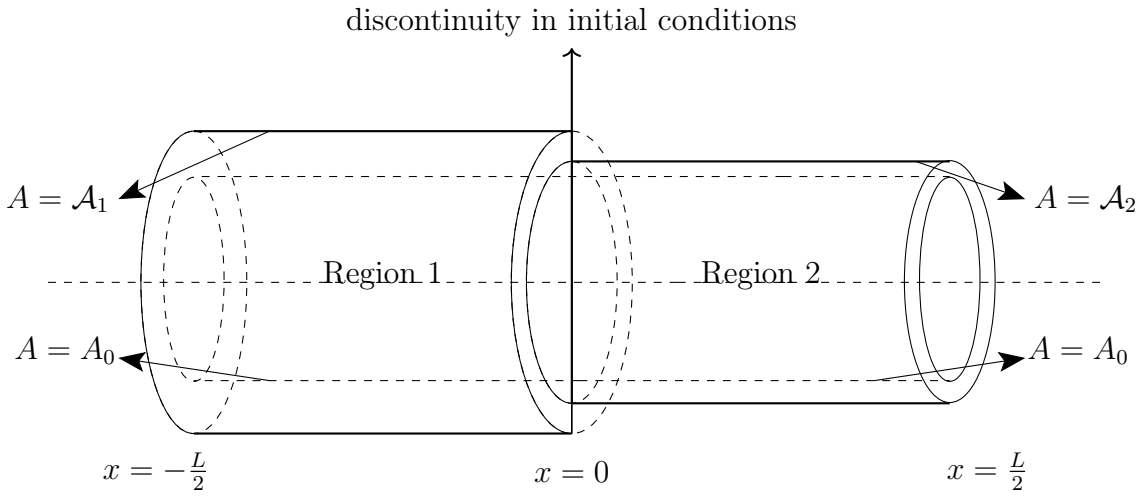

Figure 2.2: Set-up of the mathematical model.

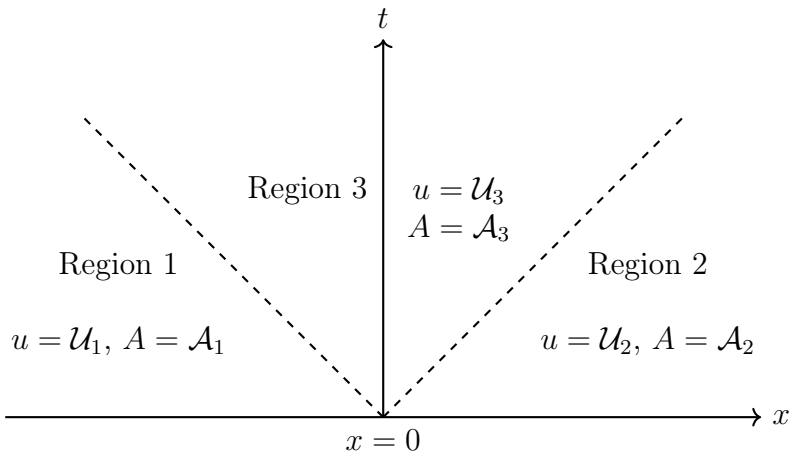

Figure 2.3: Plot of the $x - t$ plane showing regions 1 (upstream), region 2 (downstream) and region 3 which spans the origin connecting the two regions.

in the form

$$\frac{\partial A}{\partial t} + A\frac{\partial u}{\partial x} + u\frac{\partial A}{\partial x} = 0, \tag{2.36}$$

$$\frac{\partial u}{\partial t} + u\frac{\partial u}{\partial x} + \frac{c^2}{A}\frac{\partial A}{\partial x} = 0, \tag{2.37}$$

subject to initial conditions

$$\begin{aligned} A(x,0) &= \mathcal{A}_1, \quad u(x,0) = \mathcal{U}_1, \quad (x < 0), \\ A(x,0) &= \mathcal{A}_2, \quad u(x,0) = \mathcal{U}_2, \quad (x > 0). \end{aligned}$$

Multiplying (2.36) by $\pm c/A$ and adding to (2.37), we can write as the single conservation equation

$$\left(\frac{\partial u}{\partial t} \pm \frac{c}{A}\frac{\partial A}{\partial t}\right) + \left(u\frac{\partial u}{\partial x} \pm c\frac{\partial u}{\partial x}\right) + \left(\frac{c^2}{A}\frac{\partial A}{\partial x} \pm \frac{uc}{A}\frac{\partial A}{\partial x}\right) = 0, \tag{2.38}$$

which can be written in the Riemann invariant form as [51, 83]

$$\left(\frac{\partial}{\partial t} + (u \pm c)\frac{\partial}{\partial x}\right)\left[u \pm \int_{A_0}^{A} \frac{c}{A^*} dA^*\right] = 0. \tag{2.39}$$

This implies that the Riemann invariants of the flow are given by

$$R_{\pm} = u \pm \int_{A_0}^{A} \frac{c}{A^*} dA^*, \tag{2.40}$$

which are constant along characteristics $C_{\pm}$, defined according to

$$\frac{dx}{dt} = u \pm c. \tag{2.41}$$

Substituting the particular expression for c (2.34) and evaluating, we derive an explicit equation involving A and u alone in the form

$$\left(\frac{\partial}{\partial t} + (u \pm \sqrt{m}A^{\frac{m}{2}})\frac{\partial}{\partial x}\right)\left[u \pm \frac{2}{\sqrt{m}}(A^{\frac{m}{2}} - 1)\right] = 0, \tag{2.42}$$

where $R_{\pm} = u \pm \frac{2}{\sqrt{m}}(A^{\frac{m}{2}} - 1)$ are the Riemann invariants of the flow, which remain unchanged along the characteristic curves

$$\frac{dx}{dt} = u \pm \sqrt{m}A^{\frac{m}{2}}. \tag{2.43}$$

It emerges that the initial discontinuity breaks up into waves (propagating left and right). In the fully nonlinear model these can each be either a shock or a rarefaction (Section 2.7, see discussion by Brook et. al. (1999) [44]). The corresponding characteristics are sketched in the $x - t$ plane in Figure 2.3, where the discontinuity is applied at $x = 0$. For any configuration of shocks and rarefactions, the system exhibits a region between the two propagating waves which has uniform cross-sectional area and flow speed. We label this intermediate region as region 3 (this is often known as the star region in dam break problems) and denote the (uniform) cross-sectional area as $\mathcal{A}_3$ and the corresponding (uniform) flow velocity as $\mathcal{U}_3$. We now discuss how the region 3 flow profile is computed, considering both shock waves (Section 2.5) and rarefaction waves (Section 2.6).

2.5 Nonlinear shock waves

We now focus on large amplitude perturbations and consider a shock formed in response to the discontinuity in initial conditions (sometimes known as an elastic jump in this collapsible tubes literature [110–112]). To ensure conservation of mass and momentum across the shock front, we write (2.30)

in conservative form as

$$\frac{\partial}{\partial t}(Au) + \frac{\partial}{\partial x}\left(Au^2 + \frac{m}{m+1}A^{m+1}\right) = 0. \tag{2.44}$$

Hence, both (2.29) and (2.44), can be expressed in the general form of

$$\frac{\partial}{\partial t}(E_i) + \frac{\partial}{\partial x}(F_i) = 0, \qquad (i = 1, 2), \tag{2.45}$$

where $E_1 = A$, $F_1 = Au$, correspond to conservation of mass (2.29), and $E_2 = Au$, $F_2 = Au^2 + \frac{m}{m+1}A^{m+1}$ follow from conservation of momentum (2.44).

We assume the shock front is located at $x = s(t)$ and write (2.45) in frame of the moving shock using the transformation

$$\zeta = x - \int_0^t \dot{s}(t')dt', \tag{2.46}$$

where $\dot{s}(t)$ is the corresponding shock speed. Assuming the flow, cross-sectional area and pressure profiles are uniform either side of the shock front, we can write (2.45) in the form

$$\frac{\partial}{\partial t}(E_i) - \dot{s}\frac{\partial}{\partial \zeta}(E_i) + \frac{\partial}{\partial \zeta}(F_i) = 0. \tag{2.47}$$

Assuming the flow is propagating steadily in this moving frame and integrate (2.47) with respect to ζ and apply boundary conditions on either side of the shock to derive

$$\dot{s} = \frac{F_i(s^+, t) - F_i(s^-, t)}{E_i(s^+, t) - E_i(s^-, t)}, \qquad (i = 1, 2), \tag{2.48}$$

where $s^+(s^-)$ denotes the ζ location to the right (left) of the shock. So, from (2.45), we have the shock speed given as

$$\dot{s} = \frac{A(s^+, t)u(s^+, t) - A(s^-, t)u(s^-, t)}{A(s^+, t) - A(s^-, t)}, \tag{2.49}$$

$$\dot{s} = \frac{A(s^+, t)u^2(s^+, t) + \frac{m}{m+1}A^{m+1}(s^+, t) - A(s^-, t)u^2(s^-, t) - \frac{m}{m+1}A^{m+1}(s^-, t)}{A(s^+, t)u(s^+, t) - A(s^-, t)u(s^-, t)}. \tag{2.50}$$

The shock speed can be eliminated from (2.49) and (2.50) to obtain a single jump condition between A and u across the shock front, as given in equations (2.53) and (2.58) below for a left and right propagating shock.

2.5.1 Left shock

Here we consider a shock wave moving to the left separating regions 1 and 3. In this case we now consider equations (2.49) and (2.50), and obtain

$$\dot{s}_L = \frac{\mathcal{A}_3\mathcal{U}_3 - \mathcal{A}_1\mathcal{U}_1}{\mathcal{A}_3 - \mathcal{A}_1}, \tag{2.51}$$

$$\dot{s}_L = \frac{\mathcal{A}_3\mathcal{U}_3^2 - \mathcal{A}_1\mathcal{U}_1^2 + \frac{m}{m+1}\left(\mathcal{A}_3^{m+1} - \mathcal{A}_1^{m+1}\right)}{\mathcal{A}_3\mathcal{U}_3 - \mathcal{A}_1\mathcal{U}_1}, \tag{2.52}$$

where $\dot{s}_L$ denotes the speed of the shock in region 1. Equating (2.51) and (2.52), and simplifying, we have the nonlinear constraint

$$\mathcal{A}_1\mathcal{A}_3(\mathcal{U}_3 - \mathcal{U}_1)^2 = \frac{m}{m+1}\left(\mathcal{A}_3^{m+1} - \mathcal{A}_1^{m+1}\right)(\mathcal{A}_3 - \mathcal{A}_1), \tag{2.53}$$

linking $\mathcal{U}_3$ and $\mathcal{A}_3$ to the far-field conditions. Equation (2.53) is rearranged to get $\mathcal{U}_3$ as a function of other variables, resulting in two possibilities

$$\mathcal{U}_3 = \mathcal{U}_1 \pm \sqrt{\frac{m\left(\mathcal{A}_3^{m+1} - \mathcal{A}_1^{m+1}\right)(\mathcal{A}_3 - \mathcal{A}_1)}{\mathcal{A}_1\mathcal{A}_3(m+1)}}. \tag{2.54}$$

When calculating the solution to the Riemann problem we must consider both possibilities. This difference facilitates multiple solutions with the same structure at the same point in the parameter space.

Note that the shock speed is just the average of the characteristic speeds immediately to the left and right of the shock. So, for uniqueness it is required that the shock speed satisfies the Lax entropy condition [113]. This means that nearby characteristics should always run into the shock rather than emanating from the shocks. We refer to shocks which satisfy the Lax entropy conditions as physical solutions.

So, or a left shock to have physical solutions we need

$$(\mathcal{U}_3 - \mathcal{C}_3) < \dot{s}_L < (\mathcal{U}_1 - \mathcal{C}_1). \tag{2.55}$$

So that the shock front in region 1 must lie between the negative characteristics in region 1 and that of region 3, *i.e.*, the gradient of the negative characteristics in region 1 must be less than the gradient of the shock trajectory in the $x-t$ plane while the gradient of the negative characteristics in region 3 must be greater than the gradient of the shock trajectory in the $x-t$ plane as shown in Figure 2.4(b).

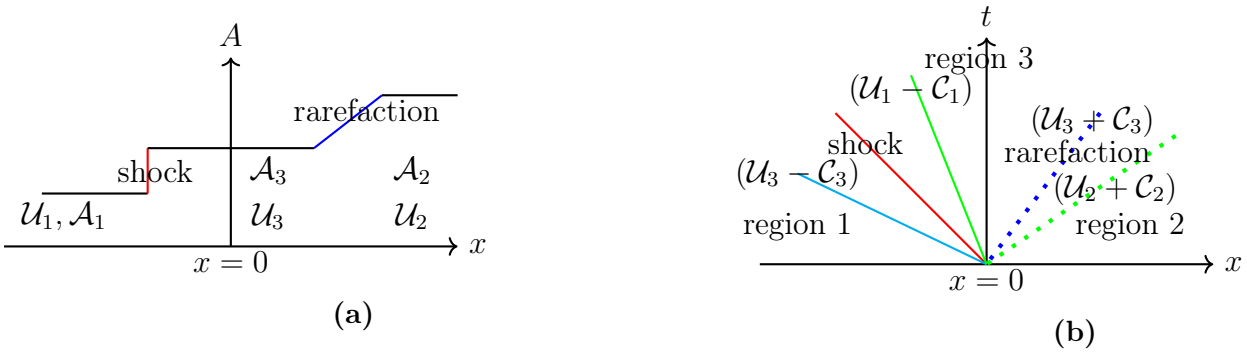

Figure 2.4: Illustration of the wave profiles in cross-sectional area and corresponding characteristics generated with a discontinuous initial condition. Figure 2.4(a,b) is a left moving shock and right moving rarefaction wave.

2.5.2 Right shock

Alternatively, we consider a case where the wave is a shock moving to the right separating regions 2 and 3. So applying conditions (2.49) and (2.50), we have

$$\dot{s}_R = \frac{\mathcal{A}_2\mathcal{U}_2 - \mathcal{A}_3\mathcal{U}_3}{\mathcal{A}_2 - \mathcal{A}_3}, \tag{2.56}$$

$$\dot{s}_R = \frac{\mathcal{A}_2\mathcal{U}_2^2 - \mathcal{A}_3\mathcal{U}_3^2 + \frac{m}{m+1}\left(\mathcal{A}_2^{m+1} - \mathcal{A}_3^{m+1}\right)}{\mathcal{A}_2\mathcal{U}_2 - \mathcal{A}_3\mathcal{U}_3}. \tag{2.57}$$

Once again, equating (2.56) and (2.57) and solving, we have the nonlinear constraint

$$\mathcal{A}_2\mathcal{A}_3(\mathcal{U}_3 - \mathcal{U}_2)^2 = \frac{m}{m+1}\left(\mathcal{A}_2^{m+1} - \mathcal{A}_3^{m+1}\right)(\mathcal{A}_2 - \mathcal{A}_3), \tag{2.58}$$

again linking $\mathcal{U}_3$ and $\mathcal{A}_3$ to the initial conditions on the right. Again, (2.58) is rearranged to get $\mathcal{U}_3$ as a function of other variables, resulting in two possibilities

$$\mathcal{U}_3 = \mathcal{U}_2 \pm \sqrt{\frac{m\left(\mathcal{A}_2^{m+1} - \mathcal{A}_3^{m+1}\right)(\mathcal{A}_2 - \mathcal{A}_3)}{\mathcal{A}_2\mathcal{A}_3(m+1)}}, \tag{2.59}$$

which must both be accounted for.

Note that for these shocks to be physical we must also check against the Lax entropy conditions [113], where we need

$$(\mathcal{U}_2 + \mathcal{C}_2) < \dot{s}_R < (\mathcal{U}_3 + \mathcal{C}_3), \tag{2.60}$$

where $\mathcal{C}_i = \sqrt{m}\mathcal{A}_i^{m/2}$, $(i = 1, 2, 3)$. This means that the gradient of the shock trajectory in the $x - t$ plane in region 2 must be less than the gradient of the positive characteristics in region 2 and greater than the gradient of the positive characteristics in region 3. These conditions are further illustrated in Figure 2.5 below.

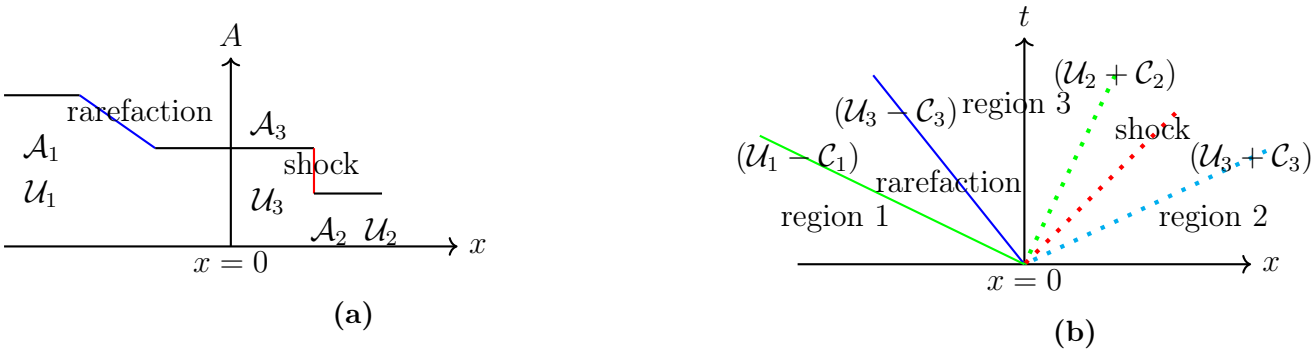

Figure 2.5: Illustration of the wave profiles in cross-sectional area and corresponding characteristics generated with a discontinuous initial condition. Figure 2.5(a,b) is a left rarefaction wave and right moving shock wave.

2.6 Nonlinear rarefaction waves

The system can also admit nonlinear rarefaction waves which are adjacent to either region 1 or region 2 and are connected to the uniform flow in region 3. We denote the rarefaction profile with the subscript r, with cross-sectional area $A_r(x,t)$, flow velocity $u_r(x,t)$ and wavespeed $c_r(x,t)$, respectively. In this vessel with uniform material properties, there are two possibilities: the rarefaction forms at the right edge of region 1 (where $A_r = \mathcal{A}_1$, $u_r = \mathcal{U}_1$, $c_r = \mathcal{C}_1 = \sqrt{m\mathcal{A}_1^m}$ on the interface between the rarefaction and region 1 ($x = (\mathcal{U}_1 - \mathcal{C}_1)t$), or on the left edge of region 2 (where $A_r = \mathcal{A}_2$, $u_r = \mathcal{U}_2$, $c_r = \mathcal{C}_2 = \sqrt{m\mathcal{A}_2^m}$ on the interface between the rarefaction and region 2 ($x = (\mathcal{U}_2 + \mathcal{C}_2)t$). We have the Riemann invariants and corresponding characteristics from (2.42) given as

$$R_\pm = u \pm \frac{2}{\sqrt{m}}(A^{m/2} - 1), \quad \text{along} \qquad \frac{dx}{dt} = u \pm \sqrt{m}A^{m/2}. \tag{2.61}$$

We apply these Riemann invariants and characteristics to explicitly construct the left and right rarefaction waves.

2.6.1 Left rarefaction

For positive characteristics entering the rarefaction region from region 1, we have $u_r = \mathcal{U}_1$, $c_r = \mathcal{C}_1$ and $A_r = \mathcal{A}_1$ along $x = (\mathcal{U}_1 - \mathcal{C}_1)t$. This implies that the information carried on these positive characteristics (2.61) becomes

$$R_+ = u_r + \frac{2}{\sqrt{m}}(A_r^{\frac{m}{2}} - 1) = \mathcal{U}_1 + \frac{2}{\sqrt{m}}(\mathcal{A}_1^{\frac{m}{2}} - 1) = C_1 \quad \text{on} \quad \frac{dx}{dt} = u_r + c_r, \tag{2.62}$$

where C_1 is a constant. Since the Riemann invariant takes the same value for all positive characteristics, we deduce that $R_+ = C_1$ everywhere.

Conversely, for the Riemann invariant along the negative characteristics, we have

$$R_- = u_r - \frac{2}{\sqrt{m}}(A_r^{\frac{m}{2}} - 1) = C_2 \quad \text{on} \quad \frac{dx}{dt} = u_r - c_r, \tag{2.63}$$

where C_2 is a constant. Note that this definition only holds on negative characteristics and C_2 can change from characteristic to characteristic.

Adding (2.62) to (2.63) gives $u_r = (C_1 + C_2)/2$ which is a constant on negative characteristics. Also subtracting (2.63) from (2.62) gives A_r =constant on negative characteristics, which then implies c_r =constant on negative characteristics. Therefore, integrating (2.63) with respect to time along negative characteristics (since u_r and c_r are constants) and simplifying, we have

$$u_r = c_r + \frac{x}{t}. \tag{2.64}$$

Hence, negative characteristics are straight lines consistent with a rarefaction fan.

Substituting (2.62) into (2.64) and simplifying, we have

$$A_r = \left(\frac{\sqrt{m}\mathcal{U}_1}{(m+2)} + \frac{2\mathcal{C}_1}{\sqrt{m}(m+2)} - \frac{\sqrt{m}x}{(m+2)t} \right)^{\frac{2}{m}}, \tag{2.65}$$

where $c_r = \sqrt{m}A_r^{\frac{m}{2}}$. Substituting (2.65) into (2.63), we have

$$u_r = \frac{m\mathcal{U}_1}{m+2} + \frac{2\mathcal{C}_1}{m+2} + \frac{2x}{(m+2)t}. \tag{2.66}$$

From (2.66), if we let $A_r = \mathcal{A}_3$, $u_r = \mathcal{U}_3$, $c_r = \mathcal{C}_3$ at the edge of the rarefaction in contact with region 3, we find that this edge lies along

$$x = (\mathcal{U}_3 - \mathcal{C}_3)\, t, \tag{2.67}$$

as expected.

Substituting (2.67) into (2.65), we have

$$\mathcal{U}_3 = \mathcal{U}_1 + \frac{2}{\sqrt{m}} \left(\mathcal{A}_1^{m/2} - \mathcal{A}_3^{m/2} \right) = \mathcal{U}_1 + \frac{2}{m}(\mathcal{C}_1 - \mathcal{C}_3), \tag{2.68}$$

which relates $\mathcal{U}_3$ and $\mathcal{A}_3$ to the initial conditions on the left.

In this case, since we have uniform material properties across the two regions the left rarefaction is not necessarily restricted to region 1. However, we must impose a number of physicality conditions for the rarefaction solution to be sensible (analogous to the Lax conditions for the shocks).

$$(\mathcal{U}_3 - \mathcal{C}_3) > (\mathcal{U}_1 - \mathcal{C}_1). \tag{2.69}$$

In this case we need the outer edge of the left rarefaction to be to the right of the edge of region 1 in the $x - t$ plane so that $(\mathcal{U}_3 - \mathcal{C}_3) > (\mathcal{U}_1 - \mathcal{C}_1)$. Furthermore, we require that the right most edge of the rarefaction fan remain to the left of the right moving wave between regions 2 and 3. This is illustrated pictorially in Figure 2.5(b).

2.6.2 Right rarefaction

Conversely, for negative characteristics entering a right rarefaction from region 2, we have $u_r = \mathcal{U}_2$, $c_r = \mathcal{C}_2$ and $A_r = \mathcal{A}_2$ along $x = (\mathcal{U}_2 + \mathcal{C}_2)t$. Here (2.61) becomes

$$R_- = u_r - \frac{2}{\sqrt{m}}(A_r^{\frac{m}{2}} - 1) = \mathcal{U}_2 - \frac{2}{\sqrt{m}}(\mathcal{A}_2^{\frac{m}{2}} - 1) = D_1 \quad \text{on} \quad \frac{dx}{dt} = u_r - c_r, \tag{2.70}$$

so, applying the same logic as before, R_- is constant everywhere. In contrast, for the Riemann invariant along the positive characteristics, we have

$$R_+ = u_r + \frac{2}{\sqrt{m}}(A_r^{\frac{m}{2}} - 1) = D_2 \quad \text{constant on} \quad \frac{dx}{dt} = u_r + c_r. \tag{2.71}$$

Using an identical argument to Section 2.6.1 we derive

$$A_r = \left(-\frac{\sqrt{m}\mathcal{U}_2}{(m+2)} + \frac{2\mathcal{C}_2}{\sqrt{m}(m+2)} + \frac{\sqrt{m}x}{(m+2)t}\right)^{\frac{2}{m}}, \tag{2.72}$$

$$u_r = \frac{1}{m+2}\left(m\mathcal{U}_2 - 2\mathcal{C}_2 + \frac{2x}{t}\right), \tag{2.73}$$

$$c_r = \frac{1}{m+2}\left(-m\mathcal{U}_2 + 2\mathcal{C}_2 + \frac{mx}{t}\right). \tag{2.74}$$

The edge of the rarefaction adjacent to region 3 is then given by

$$x = (\mathcal{U}_3 + \mathcal{C}_3)\, t. \tag{2.75}$$

Along this edge of the rarefaction, substituting (2.75) into (2.72), we have

$$\mathcal{U}_3 = \mathcal{U}_2 + \frac{2}{\sqrt{m}}\left(\mathcal{A}_3^{m/2} - \mathcal{A}_2^{m/2}\right) = \mathcal{U}_2 + \frac{2}{m}(\mathcal{C}_3 - \mathcal{C}_2), \tag{2.76}$$

which relates $\mathcal{U}_3$ and $\mathcal{A}_3$ to the far-field conditions on the right.

We note that for a uniform tube the right rarefaction must not necessarily remain on the right hand side of the vessel, although it must remain to the right of the left-moving wave separating regions 1 and 2 and to the left of the boundary with region 2, so that

$$(\mathcal{U}_3 + \mathcal{C}_3) < (\mathcal{U}_2 + \mathcal{C}_2), \tag{2.77}$$

illustrated in Figure 2.4(b).

2.7 Composite wave profiles

We now describe the composite structure of the waves generated in response to a discontinuity in initial conditions. The four possibilities (discussed by [44]) are sketched in Figure 2.6 with sketches of the cross-sectional area along the tube in panels (a), (c), (e) and (g) where we represent the inner edge of the rarefaction with a blue line and a shock with a red line. This notation will be consistent through the

thesis. We also plot the corresponding characteristics of each profile in panels (b), (d), (f) and (h) in Figure 2.6 which will enable us determine what constitutes physical solutions of our Riemann problem. Figure 2.6(a,b) is a sketch that illustrates a rarefaction wave moving to to the left and a shock wave moving to the right (LRRS) together with its corresponding characteristics. In this case the rarefaction fan is contained between the green and blue solid lines (in accordance with (2.69)), while the shock line lies to the left of the positive characteristics in region 3 and to the right of the positive characteristics in region 2, consistent with the Lax conditions (2.60).

Figure 2.6(c,d) shows a shock wave moving to the left and a rarefaction wave traveling to the right (LSRR), together with its corresponding characteristics. Here the shock line lies to the right of the negative characteristics in region 3 and to the left of the negative characteristics in region 1 which is consistent with the Lax entropy condition in (2.55) while for the right rarefaction, the rarefaction fan is contained between the blue and green dashed lines consistent with (2.77).

Figure 2.6(e,f) illustrates a case where the waves travelling to both the left and right of the discontinuity are shock waves (LSRS) together with its corresponding characteristics. In this case the left shock line lies to the right of the negative characteristics in region 3 and to the left of the negative characteristics in region 1 in consistency with (2.55), while the right shock line lies to the left of the positive characteristics in region 3 and to right of the positive characteristics in region 2 consistent with (2.60).

Finally Figure 2.6(g,h) illustrates a case where the waves travelling to both the left and right of the initial discontinuity are rarefaction waves (LRRR), together with its corresponding characteristics. Here, for the left rarefaction, the rarefaction fan lies between the solid blue and green lines, while for the right rarefaction, the rarefaction fan is contained between the blue and green dashed lines consistent with equations (2.69) and (2.77), respectively.

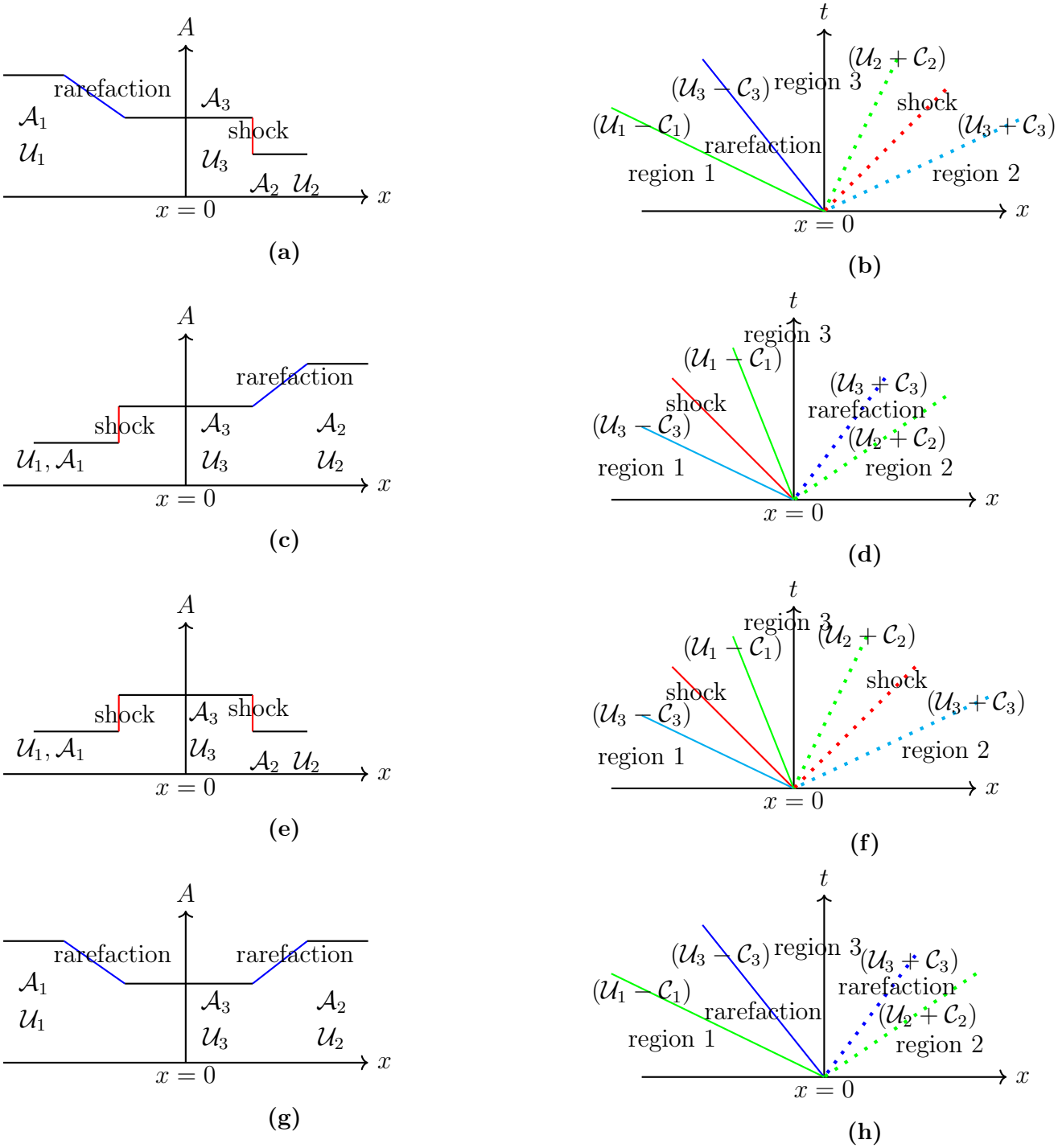

Figure 2.6: Illustrations of the wave profiles in cross-sectional area and corresponding characteristics generated with a discontinuous initial condition. Figure 2.6(a,b) is a left moving rarefaction and right moving shock wave, Figure 2.6(c,d) is a left moving shock and right moving rarefaction wave, Figure 2.6(e,f) is a left and right moving shock wave and Figure 2.6(g,h) is a left and right moving rarefaction waves, respectively.

2.8 Newton's method

We use Newton's method implemented in MATLAB to solve for the different cases sketched in Figure 2.4. We consider in turn: left rarefaction, right shock denoted as LRRS (see Section 2.8.1); left shock, right rarefaction denoted as LSRR (see Section 2.8.2); left rarefaction, right rarefaction denoted as LRRR (see Section 2.8.3) and left shock, right shock denoted as LSRS (see Section 2.8.4). We take care to include all cases resulting from the square root in equations (2.54) and (2.59). This implies that the LSRR and LRRS each have two possibilities, while LSRS has four possibilities, facilitating multiple branches of solutions across our parameter space.

2.8.1 Left rarefaction, Right shock (LRRS)

We consider the case where the wave formed to the left of the initial discontinuity is a rarefaction, described by (2.68), and that formed to the right is a shock, described by (2.59) as sketched in Figure 2.6(a,b). To obtain a single nonlinear equation for $\mathcal{A}_3$ in this case we substitute (2.68) into (2.59) to obtain

$$\mathcal{A}_2\mathcal{A}_3\left((\mathcal{U}_1-\mathcal{U}_2)+\frac{2}{\sqrt{m}}\left(\mathcal{A}_1^{m/2}-\mathcal{A}_3^{m/2}\right)\right)^2=\frac{m}{m+1}\left(\mathcal{A}_2^{m+1}-\mathcal{A}_3^{m+1}\right)(\mathcal{A}_2-\mathcal{A}_3), \tag{2.78}$$

which relates $\mathcal{A}_3$ (the uniform cross-sectional area across region 3) as a function of the far-field conditions $\mathcal{A}_1$, $\mathcal{A}_2$, $\mathcal{U}_1$, $\mathcal{U}_2$. Given $\mathcal{A}_3$, the value of $\mathcal{U}_3$ can be computed from either (2.68) or (2.59). Note that equation (2.59) when simplified has a square root in the solution implying that there is possibility of two sets of solutions coming from $\pm$. For consistency this solution must satisfy the physicality condition (2.69) on the left rarefaction and Lax conditions (2.60) on the right shock.

2.8.2 Left shock, Right rarefaction (LSRR)

We next consider a case where we have a shock wave to the left of the initial discontinuity, described by (2.76), and a rarefaction to the right, described by (2.53) as sketched in Figure 2.6(c,d). To obtain a single nonlinear equation for $\mathcal{A}_3$ we substitute (2.76) into (2.53) to obtain the nonlinear equation

$$\mathcal{A}_1\mathcal{A}_3\left((\mathcal{U}_2-\mathcal{U}_1)+\frac{2}{\sqrt{m}}\left(\mathcal{A}_3^{m/2}-\mathcal{A}_2^{m/2}\right)\right)^2=\frac{m}{m+1}(\mathcal{A}_3^{m+1}-\mathcal{A}_1^{m+1})(\mathcal{A}_3-\mathcal{A}_1), \tag{2.79}$$

which again relates $\mathcal{A}_3$ as a function of the far-field conditions $\mathcal{A}_1$, $\mathcal{A}_2$, $\mathcal{U}_1$, $\mathcal{U}_2$. Given $\mathcal{A}_3$, the value of $\mathcal{U}_3$ can be computed from either (2.54) or (2.76). Note that equation (2.54) involves $\pm$ resulting from the square root, giving two possible solutions. For consistency this solution must satisfy the Lax condition (2.55) on the left shock and the physicality condition (2.77) on the right rarefaction.

2.8.3 Left rarefaction, Right rarefaction (LRRR)

We next consider the case where we have that the waves generated to the left and right of the initial discontinuity are both rarefactions as sketched in Figure 2.6(g,h). To solve this we eliminate $\mathcal{U}_3$ from

equations (2.68) and (2.76) and simplify to obtain the explicit expression

$$\mathcal{A}_3 = \left(\frac{\sqrt{m}}{4}(\mathcal{U}_1 - \mathcal{U}_2) + \frac{1}{2}(\mathcal{A}_1^{m/2} + \mathcal{A}_2^{m/2}) \right)^{2/m}. \tag{2.80}$$

Again relates $\mathcal{A}_3$ as a function of the initial conditions $\mathcal{A}_1$, $\mathcal{A}_2$, $\mathcal{U}_1$, $\mathcal{U}_2$. The corresponding value of $\mathcal{U}_3$ can be computed from (2.68) or (2.76). For consistency this solution must satisfy the physicality conditions (2.69) and (2.77) on the left and right rarefaction waves.

2.8.4 Left shock, Right shock (LSRS)

Finally, we consider the case where both waves generated to the left and right of the discontinuity are shock waves as sketched in Figure 2.6(e,f). This is solved by eliminating $\mathcal{U}_3$ between equations (2.53) and (2.58), which we simplify to obtain the nonlinear equation

$$\mathcal{A}_1\mathcal{A}_2\mathcal{A}_3(m+1)(\mathcal{U}_2^2 - \mathcal{U}_1^2) = m\left(\left(\mathcal{A}_3^{m+1} - \mathcal{A}_1^{m+1}\right)(\mathcal{A}_3 - \mathcal{A}_1) - \left(\mathcal{A}_2^{m+1} - \mathcal{A}_3^{m+1}\right)(\mathcal{A}_2 - \mathcal{A}_3) \right). \tag{2.81}$$

This again relates $\mathcal{A}_3$ as a function of the initial conditions $\mathcal{A}_1$, $\mathcal{A}_2$, $\mathcal{U}_1$, $\mathcal{U}_2$. Given $\mathcal{A}_3$, the value of $\mathcal{U}_3$ can be computed from (2.54) or (2.59). Note that equations (2.54) and (2.59) both involve $\pm$ when simplified and so give four possible solutions. For consistency this solution must satisfy the Lax conditions (2.55) and (2.60) on the left and right moving shocks.

2.9 Numerical approach

We solve each of the four cases by numerically solving (2.78)-(2.81) for $\mathcal{A}_3$ for a variety of initial conditions. For a given point in the parameter space our approach is to solve for all four possibilities ((2.78), (2.79), (2.80) and (2.81)) and post-process to determine which solutions are self-consistent with corresponding physicality conditions. To initiate the Newton method requires an initial guess for $\mathcal{A}_3$. The solver is not too particular to the choice of initial condition, but we try a variety of values of $\mathcal{A}_3$ until we find a self-consistent solution for one of the cases. Once a solution has been identified we then follow this branch until the solver no longer converges or the physicality conditions are violated, at which point we start again. We benchmark these solutions against an alternative method which uses an iterative approach to isolate the wave structure. This approach is detailed in Section 2.9.1 below.

2.9.1 Algorithm of Brook et al. (1999).

In this section we revisit the numerical algorithm developed by Brook et al. [44] for solving the Riemann problem in a flexible-walled vessel. Note that this solver forms part of their sophisticated numerical method for computing shock fronts in collapsible tube flows in the giraffe jugular vein. The aim here is to compare their algorithm with our approach. We first present their semi-analytical solution to the tube problem, where the flow states to the left and right of the initial discontinuity are described as $\mathcal{V}_1 = (\mathcal{A}_1, \mathcal{P}_1, \mathcal{U}_1, \mathcal{C}_1)$ and $\mathcal{V}_2 = (\mathcal{A}_2, \mathcal{P}_2, \mathcal{U}_2, \mathcal{C}_2)$, respectively, where $\mathcal{P}_j$ and $\mathcal{C}_j$ are the corresponding pressures and wavespeeds in the far-field ($j = 1, 2$). Note that $\mathcal{P}_1$ and $\mathcal{P}_2$ are derived from our tube law (2.33). Also, $\mathcal{C}_1$ and $\mathcal{C}_2$ are computed from the definition of wavespeed given in equation (2.34). The method uses the equations of conservation of mass (2.29) and momentum (2.30) in the tube to calculate

the unknown state in region 3, denoted as $\mathcal{V}_3 = (\mathcal{A}_3, \mathcal{P}_3, \mathcal{U}_3, \mathcal{C}_3)$, where $\mathcal{P}_3$ and $\mathcal{C}_3$ are computed in the analogous manner to region 1 and 2. This algorithm proceeds by iterating to identify $\mathcal{P}_3$.

We denote the moving wave front as $x = s(t)$, which can be either a shock or a rarefaction. Transforming to the frame of reference moving with this wave front (parameterized by ζ), we rescale according to

$$x = \int \dot{s} dt + \zeta. \tag{2.82}$$

In this frame the conservation of mass equation (2.29) can be expressed as

$$A_t - \dot{s} A_\zeta + (uA)_\zeta = 0. \tag{2.83}$$

For a steadily propagating wave (in the moving frame) we can integrate once and write (2.83) as

$$A(u - \dot{s}) \quad = \quad Q,$$

where Q is an unknown constant, the flux through the wave front.

Considering a shock/rarefaction propagating to the right, regions 2 and 3 can be connected through the mass balance in the form

$$\mathcal{A}_2(\mathcal{U}_2 - \dot{s}) = \mathcal{A}_3(\mathcal{U}_3 - \dot{s}). \tag{2.84}$$

Rearranging, it follows that

$$\mathcal{W}_2 \left(\frac{1}{\mathcal{A}_2} - \frac{1}{\mathcal{A}_3} \right) + (\mathcal{U}_2 - \mathcal{U}_3) \quad = \quad 0, \tag{2.85}$$

where $\mathcal{W}_2 = \mathcal{A}_2(\dot{s} - \mathcal{U}_2)$ denotes the mass flux moving through the wave front. Applying a similar argument to the conservation of momentum equation (2.30), regions 2 and 3 can be connected in the form

$$\dot{s}(\mathcal{A}_3\mathcal{U}_3 - \mathcal{A}_2\mathcal{U}_2) + \mathcal{A}_2\mathcal{U}_2^2 - \mathcal{A}_3\mathcal{U}_3^2 \quad = \quad \mathcal{P}_3 - \mathcal{P}_2. \tag{2.86}$$

Eliminating $\dot{s}$ in (2.86) in combination with (2.84) and simplifying it follows that

$$\mathcal{W}_2(\mathcal{U}_3 - \mathcal{U}_2) = \mathcal{P}_3 - \mathcal{P}_2. \tag{2.87}$$

Similarly, considering a wave propagating to the left (connecting regions 1 and 3) it follows from conservation of mass that

$$-\mathcal{W}_1 \left(\frac{1}{\mathcal{A}_1} - \frac{1}{\mathcal{A}_3} \right) + (\mathcal{U}_1 - \mathcal{U}_3) = 0, \tag{2.88}$$

where $\mathcal{W}_1 = \mathcal{A}_1(\dot{s} + \mathcal{U}_1)$ is the mass flux moving with the shock front. Similarly, from conservation of momentum we deduce that

$$-\mathcal{W}_1(\mathcal{U}_3 - \mathcal{U}_1) = \mathcal{P}_3 - \mathcal{P}_2. \tag{2.89}$$

Hence, assembling the left and right propagating waves (2.87) and (2.89), it follows that

$$\mathcal{U}_3 - \mathcal{U}_2 = \frac{\mathcal{P}_3 - \mathcal{P}_2}{\mathcal{W}_2}, \tag{2.90}$$

$$\mathcal{U}_1 - \mathcal{U}_3 = \frac{\mathcal{P}_3 - \mathcal{P}_1}{\mathcal{W}_1}. \tag{2.91}$$

Manipulating to eliminate $\mathcal{U}_3$, we obtain a solution for $\mathcal{P}_3$ in terms of $\mathcal{W}_1$ and $\mathcal{W}_2$ in the form

$$\mathcal{P}_3 = \frac{1}{\mathcal{W}_1 + \mathcal{W}_2}\left(\mathcal{W}_2\mathcal{P}_1 + \mathcal{W}_1\mathcal{P}_2 - \mathcal{W}_1\mathcal{W}_2(\mathcal{U}_2 - \mathcal{U}_1)\right), \tag{2.92}$$

which gives an explicit prediction of the pressure in region 3, from which we then compute $\mathcal{A}_3$ through inverting the tube law and then deduce $\mathcal{U}_3$ from (2.90) and (2.91), respectively.

To complete the algorithm it remains to compute $\mathcal{W}_1$ and $\mathcal{W}_2$ from equations (2.90) and (2.91), respectively for either a shock or a rarefaction. A more complete derivation of this algorithm was given by Brook et al. [44].

2.9.2 Right shock

If the wave moving to the right of the discontinuity is a shock, it implies that $\mathcal{P}_3 > \mathcal{P}_2$ and $\mathcal{A}_3 > \mathcal{A}_2$. Hence, we can eliminate $(\mathcal{U}_3 - \mathcal{U}_2)$ from (2.85) and (2.87), to obtain

$$\mathcal{W}_2 = \left(\mathcal{A}_2\mathcal{A}_3\frac{(\mathcal{P}_3 - \mathcal{P}_2)}{(\mathcal{A}_3 - \mathcal{A}_2)}\right)^{\frac{1}{2}}. \tag{2.93}$$

2.9.3 Right rarefaction

Alternatively, if the wave travelling to the right is a rarefaction then $\mathcal{P}_3 < \mathcal{P}_2$ and $\mathcal{A}_3 < \mathcal{A}_2$. We know that the negative characteristics connect region 2 to region 3, and so continuity of the Riemann invariant implies (2.70). Eliminating $(\mathcal{U}_2 - \mathcal{U}_3)$ from (2.76) and (2.87) we have

$$\mathcal{W}_2 \;=\; \frac{2\mathcal{A}_2\mathcal{A}_3}{\sqrt{m}}\frac{(\mathcal{A}_3^{\frac{m}{2}} - \mathcal{A}_2^{\frac{m}{2}})}{\mathcal{A}_3 - \mathcal{A}_2}. \tag{2.94}$$

2.9.4 Left shock

When the wave moving to the left of the initial discontinuity is a shock, it implies that $\mathcal{P}_3 > \mathcal{P}_1$ and $\mathcal{A}_3 > \mathcal{A}_1$. Eliminating $(\mathcal{U}_3 - \mathcal{U}_1)$ from (2.88) and (2.89), we derive

$$\mathcal{W}_1 = \left(\mathcal{A}_1\mathcal{A}_3\frac{(\mathcal{P}_3 - \mathcal{P}_1)}{(\mathcal{A}_3 - \mathcal{A}_1)}\right)^{\frac{1}{2}}. \tag{2.95}$$

2.9.5 Left rarefaction

If the wave travelling to the left of the tube is a rarefaction then $\mathcal{P}_3 < \mathcal{P}_1$ and $\mathcal{A}_3 < \mathcal{A}_1$. Applying continuity of the positive Riemann invariant between regions 1 and 2 we obtain (2.68). Combining with

(2.89) we derive

$$\mathcal{W}_1 = \frac{2\mathcal{A}_1\mathcal{A}_3}{\sqrt{m}}\frac{(\mathcal{A}_3^{\frac{m}{2}} - \mathcal{A}_1^{\frac{m}{2}})}{\mathcal{A}_3 - \mathcal{A}_1}. \tag{2.96}$$

2.9.6 Algorithm

The algorithm starts by assuming that waves propagating to both the left and right are shock waves. Choosing an initial guess for $\mathcal{P}_3$ gives an estimate of $\mathcal{W}_1$ and $\mathcal{W}_2$ for both shock waves, calculated from (2.93) and (2.95), respectively. At each stage in the algorithm the procedure is as follows:

If $\mathcal{P}_3 > \mathcal{P}_2$ then the right propagating wave is a shock, then $\mathcal{W}_2$ is given by equation (2.93).

If $\mathcal{P}_3 < \mathcal{P}_2$ then the right propagating wave is a rarefaction, then $\mathcal{W}_2$ is given by equation (2.94).

If $\mathcal{P}_3 > \mathcal{P}_1$ then the left propagating wave is a shock, then $\mathcal{W}_1$ is used as in equation (2.95).

If $\mathcal{P}_3 < \mathcal{P}_1$ then the left propagating wave is a rarefaction, then $\mathcal{W}_1$ is used as in equation (2.96).

These new values of $\mathcal{W}_1$ and $\mathcal{W}_2$ are then substituted into (2.92) to give a new prediction for $\mathcal{P}_3$ which is used to find $\mathcal{W}_1$ and $\mathcal{W}_2$. The new value of $\mathcal{W}_1$ and $\mathcal{W}_2$ is then substituted again into (2.92) to get a new value of $\mathcal{P}_3$. This process is repeated until the relative change in $\mathcal{P}_3$ is less than a threshold denoted $T1$. Once $\mathcal{P}_3$ is determined, $\mathcal{A}_3$ is then calculated by inverting the tube law (2.31). Also $\mathcal{U}_3$ can be obtained from (2.90) or (2.91), computing from the left or the right. However, we find that these two values of $\mathcal{U}_3$ are not exactly the same for a rarefaction wave, where the assumption that the wave is a propagating discontinuity across a single point breaks down. Instead the rarefaction is spatially distributed with a spatial variation in the velocity profile.

2.10 Numerical simulations of both models

In this section, we first present typical waves profile generated from our Newton's method pseudo-code for the four different cases sketched in Figures 2.4. At each point we also compute the corresponding profiles generated using the algorithm of Brook et al. [44].

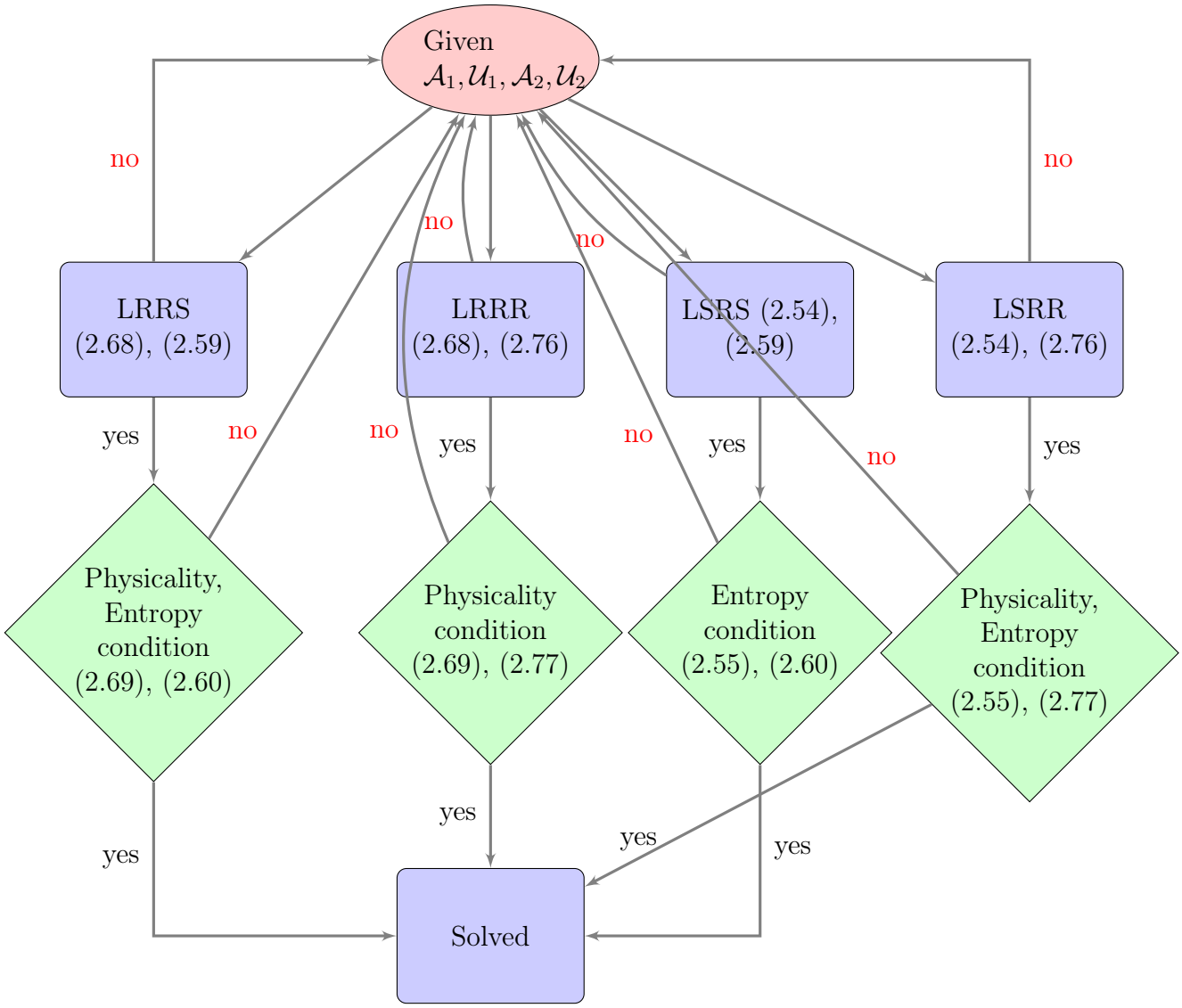

2.10.1 Left rarefaction, right shock (LRRS)

We consider boundary conditions $\mathcal{A}_1 = 1.6$, $\mathcal{A}_2 = 1.2$, $\mathcal{U}_1 = 0$, $\mathcal{U}_2 = 0.5$ which we identify as a LRRS by solving (2.78) using Newton's method. We compute $\mathcal{A}_3 = 1.449$ and $\mathcal{U}_3 = 2.492$. Typical profiles of the cross-sectional area, flow speed and wave speed are shown in Figure 2.7(a), while the corresponding characteristics are shown in Figure 2.7(b). Brook et al.'s [44] algorithm also identified this point to be a LRRS where $\mathcal{A}_3 = 1.448$ and $\mathcal{U}_3 = 2.593$, respectively.

2.10.2 Left shock, right rarefaction (LSRR)

We consider boundary conditions $\mathcal{A}_1 = 1$, $\mathcal{A}_2 = 1.1$, $\mathcal{U}_1 = 0$, $\mathcal{U}_2 = 0.03$, which we identify as a LSRR by solving (2.79) using Newton's method. We compute $\mathcal{A}_3 = 1.050$ and $\mathcal{U}_3 = -0.193$. Typical profiles of the cross-sectional area, flow speed and wave speed are shown in Figure 2.8(a), while the corresponding characteristics are shown in Figure 2.8(b). Alternatively, using the algorithm of Brook et al. [44] with same boundary conditions we also find a LSRR with $\mathcal{A}_3 = 1.055$ and $\mathcal{U}_3 = -0.193$, respectively.

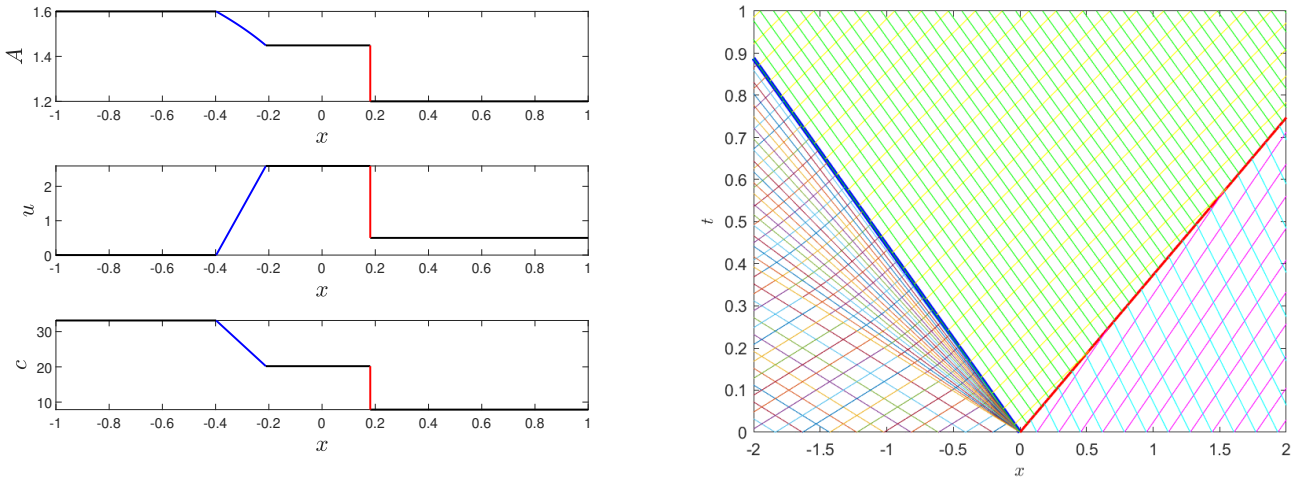

(a) **(b)**

Figure 2.7: LRRS. Figure 2.7(a) shows the cross-sectional area, flow speed and wave speed wave profiles, respectively for LRRS shock wave (where blue line denotes rarefaction, red line denotes shock and black line denotes uniform region), while Figure 2.7(b) displays a typical characteristics diagram showing regions 1, 2 and 3, respectively for a LRRS waves. For $\mathcal{A}_1 = 1.6$, $\mathcal{A}_2 = 1.2$, $\mathcal{U}_1 = 0$, $\mathcal{U}_2 = 0.5$ and $t = 0.012$.

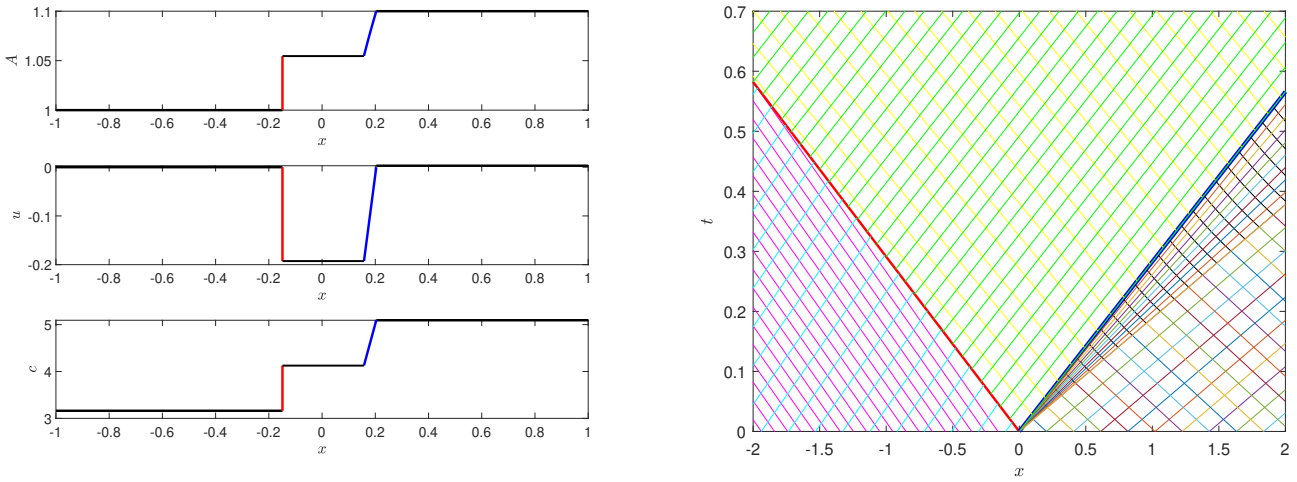

(a) **(b)**

Figure 2.8: LSRR. Figure 2.8(a) shows the cross-sectional area, flow speed and wave speed wave profiles, respectively for LSRR wave, while Figure 2.8(b) displays a typical characteristics diagram showing regions 1, 2 and 3, respectively for a LSRR waves. For $\mathcal{A}_1 = 1$, $\mathcal{A}_2 = 1.1$, $\mathcal{U}_1 = 0$, $\mathcal{U}_2 = 0.03$ and $t = 0.04$.

2.10.3 Left rarefaction, right rarefaction (LRRR)

We consider boundary conditions $\mathcal{A}_1 = 1.1$, $\mathcal{A}_2 = 1.1$, $\mathcal{U}_1 = 0$, $\mathcal{U}_2 = 0.3$ which we identify as a LRRR by solving (2.80) using Newton's method. We compute $\mathcal{A}_3 = 1.060$ and $\mathcal{U}_3 = 0.150$. Typical profiles of the cross-sectional area, flow speed and wave speed are shown in Figure 2.9(a), while the corresponding characteristics as shown in Figure 2.9(b). Brook et al.'s [44] algorithm also identified this point to be a LRRR, where $\mathcal{A}_3 = 1.072$ and $\mathcal{U}_3 = 0.142$, respectively.

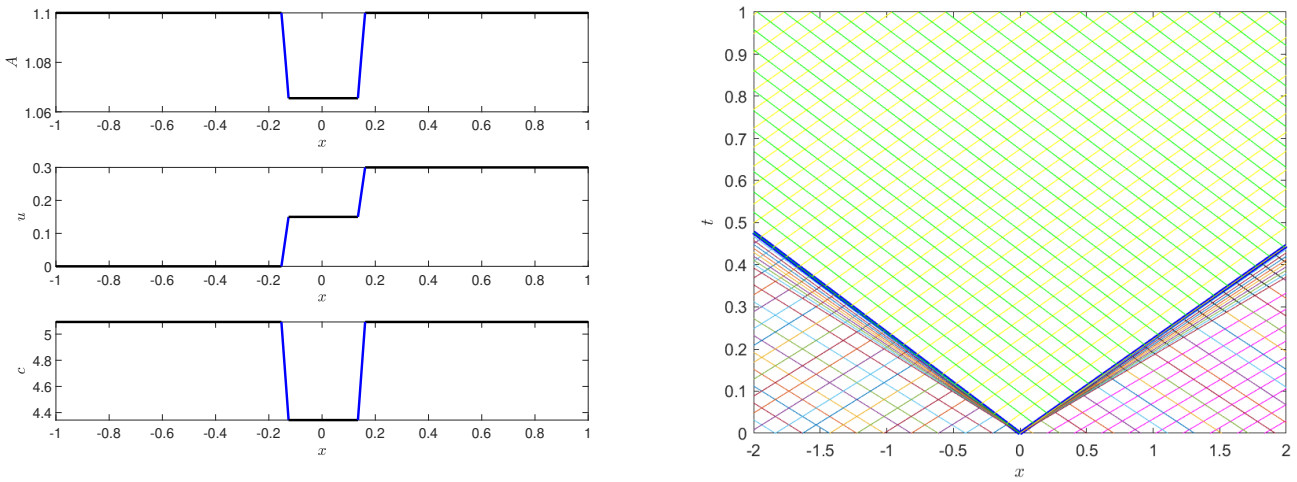

(a) **(b)**

Figure 2.9: LRRR. Figure 2.9(a) shows the cross-sectional area, flow speed and wave speed wave profiles, respectively for LRRR wave, while Figure 2.9(b) displays a typical characteristics diagram showing regions 1, 2 and 3, respectively for a LRRR waves. For $\mathcal{A}_1 = 1.1$, $\mathcal{A}_2 = 1.1$, $\mathcal{U}_1 = 0$, $\mathcal{U}_2 = 0.3$ and $t = 0.03$.

2.10.4 Left shock, right shock (LSRS)

We consider boundary conditions $\mathcal{A}_1 = 1$, $\mathcal{A}_2 = 1.1$, $\mathcal{U}_1 = 0$, $\mathcal{U}_2 = 0.99$ which we identify as a LSRS by solving (2.81) using Newton's method. We compute $\mathcal{A}_3 = 1.241$ and $\mathcal{U}_3 = -4.393$. Typical profiles of the cross-sectional area, flow speed and wave speed are shown in Figure 2.10(a), while the corresponding characteristics as shown in Figure 2.10(b). Brook et al.'s [44] algorithm where we also identified this point as a LSRS with $\mathcal{A}_3 = 1.168$ and $\mathcal{U}_3 = -4.372$, respectively.

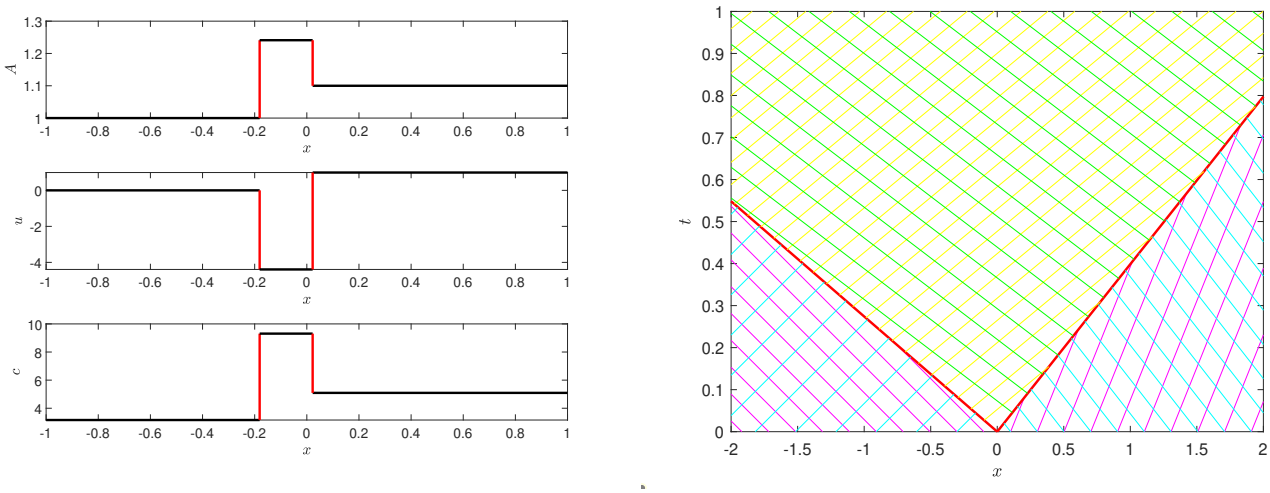

(a) **(b)**

Figure 2.10: LSRS wave. Figure 2.10(a) shows the cross-sectional area, flow speed and wave speed wave profiles, respectively for LSRS wave, while Figure 2.10(b) displays a typical characteristics diagram showing regions 1, 2 and 3, respectively for a LSRS waves. For $\mathcal{A}_1 = 1$, $\mathcal{A}_2 = 1.1$, $\mathcal{U}_1 = 0$, $\mathcal{U}_2 = 0.99$ and $t = 0.008$.

2.11 Bifurcation diagrams varying one parameter

In this section we summarise the overall behaviour of the system by constructing bifurcation diagrams by varying the initial area to the right of the discontinuity, $\mathcal{A}_2$, for all other boundary conditions held fixed. We consider four representative cases: case 1 considers where there is no flow out of region 2 (*i.e.* $\mathcal{U}_2 = 0$), cases 2 and 3 consider flow out of region 2 (*i.e.* $\mathcal{U}_2 > 0$) and case 4 considers flow coming into region 2 ($\mathcal{U}_2 < 0$), for no flow in/out of region 1 ($\mathcal{U}_1 = 0$). In each of the bifurcation diagrams blue dotted lines represent points where we have a LRRR, red dotted lines represent points where we have a LSRS, green dotted lines represent points where we have a LRRS, while cyan dotted lines represent points where we have a LSRR.

2.11.1 Case 1

In Figure 2.11 we summarize the overall behaviour of the system when where there is initially no flow out of region 2 (*i.e.* $\mathcal{U}_2 = 0$) and $\mathcal{A}_1 = 1$, $\mathcal{U}_1 = 0$. Figure 2.11(a) shows bifurcation diagram traced as a function of the cross-sectional area at the end of compartment 2 $\mathcal{A}_2$, plotting the cross-sectional area in region 3, $\mathcal{A}_3$, the flow velocity in region 3, $\mathcal{U}_3$, and the wavespeed in region 3, $\mathcal{C}_3$. In this case the system exhibits two configurations: for $\mathcal{A}_2 < 1 (= \mathcal{A}_1)$ the system exhibits LRRS, while for $\mathcal{A}_2 > 1 (= \mathcal{A}_1)$ the system exhibits LSRR. We illustrate the corresponding characteristics for these two different flow structures in figure 2.11(b) at the points labelled (i) and (ii) in Figure 2.11(a). At point (i), where $\mathcal{A}_2 = 0.5$, we compute $\mathcal{A}_3 = 0.9243$, $\mathcal{U}_3 = 0.5920$ and $\mathcal{C}_3 = 2.1332$ in which case the Lax entropy condition holds for the right shock ($(\mathcal{U}_2 + \mathcal{C}_2) < \dot{s}_2 < (\mathcal{U}_3 + \mathcal{C}_3)$, where $\dot{s}_2 = (\mathcal{A}_2\mathcal{U}_2 - \mathcal{A}_3\mathcal{U}_3)/(\mathcal{A}_2 - \mathcal{A}_3) = 0.5826$). Similarly, for point (ii), where $\mathcal{A}_2 = 1.24$, we compute

$\mathcal{A}_3 = 1.1433$, $\mathcal{U}_3 = -0.6028$, $\mathcal{C}_3 = 6.177$ in which case the Lax entropy condition holds for the left shock $((\mathcal{U}_3 - \mathcal{C}_3) < \dot{s}_1 < (\mathcal{U}_1 - \mathcal{C}_1)$, where $\dot{s}_1 = (\mathcal{A}_3\mathcal{U}_3 - \mathcal{A}_1\mathcal{U}_1)/(\mathcal{A}_3 - \mathcal{A}_1) = -4.8095)$. Hence in this case the flow always exhibits a shock and a rarefaction pair, with the order switching through $\mathcal{A}_2 = \mathcal{A}_1 = 1$ (since there is no outflow from the left or the right). This is similar to the classical dam break problem in shallow water theory with water on both sides of the dam [114]. However, the flow becomes more complicated for $\mathcal{U}_2 \neq \mathcal{U}_1$.

2.11.2 Case 2

In Figure 2.12 we consider where there is flow out of region 2 (*i.e.* $\mathcal{U}_2 = 0.6$) for $\mathcal{A}_1 = 1$, $\mathcal{U}_1 = 0$ In this case we firstly retain all the converged solutions of the Newton,s method (not applying physicality conditions for rarefactions or shocks (2.69), (2.77), (2.55) and (2.60)) tracing a bifurcation diagram as a function of $\mathcal{A}_2$. This system exhibits all four flow profiles (LRRS, LRRR, LSRS and LSRR) along different parts of the bifurcation diagram. For low $\mathcal{A}_2$ the system exhibits LRRS, while for large $\mathcal{A}_2$ the system exhibits LSRR in agreement with case 1 (Figure 2.11). We plot characteristics at two representative points $\mathcal{A}_2 = 0.3$ (point (i), Figure 2.12 b), and $\mathcal{A}_2 = 1.368$ (point (xii), Figure 2.12 b), showing qualitative agreement with case 1. As $\mathcal{A}_2$ increases from low values, the system exhibits a bifurcation into two branches at $\mathcal{A}_2 \approx 0.612$. Beyond this value the system exhibits both a continuation of LRRS and a new branch of LRRR, with typical characteristics shown at points (ii) and (iii) of Figure 2.12(b). The new branch of LRRS is unphysical because the Lax condition for a right moving shock fails (see Figure 2.4a) while the LRRR branch is physical. The LRRR branch persists as $\mathcal{A}_2$ increases and eventually connects to the LSRR branch at a second bifurcation point at $\mathcal{A}_2 \approx 1.142$. Hence, the path from LRRS, LRRR to LSRR represents the physical solutions in this case. However for $0.612 \leq \mathcal{A}_2 \leq 1.142$ the system exhibits other solutions in addition to the unphysical LRRS. In particular, the LRRS branch bifurcates at $\mathcal{A}_2 \approx 0.715$ into two branches of LSRS as shown in Figure 2.12(a) and the corresponding characteristics shown in panels (iv), (v), (vii) and $(viii)$ of Figure 2.12(b) where the Lax entropy condition fails for both the left and right moving shocks. Then the two branches of LSRS merge at $\mathcal{A}_2 \approx 1.138$ into an unphysical LSRR, which then joins to the physical branch at $\mathcal{A}_2 \approx 1.427$.

Hence, this system with $\mathcal{U}_2 > 0$ now exhibits a much more complicated flow structure with multiple solutions for a range of $\mathcal{A}_2$. However, the same bifurcation diagram is plotted in Figure 2.13 applying the physicality conditions (2.69) and (2.77) for rarefactions and (2.55) and (2.60) for shocks. In this case we observe a transition from LRRS for low $\mathcal{A}_2$ into LRRR as $\mathcal{A}_2$ increases, followed by a second transition to LSRR as $\mathcal{A}_2$ increases further. Hence in this case, only one branch of solutions is ever stable for all values of $\mathcal{A}_2$. Note the initial condition on the left is always subcritical (*i.e.* magnitude of flow speed is less than the wave speed), but the initial condition on the right is supercritical (*i.e.* magnitude of flow speed is greater than the wave speed) $(\mathcal{U}_2 > \mathcal{C}_2)$ for $\mathcal{A}_2 < 0.717$ marked on Figure 2.12(a) with a yellow dashed line. Note that this transition does not influence the overall behaviour in this case.

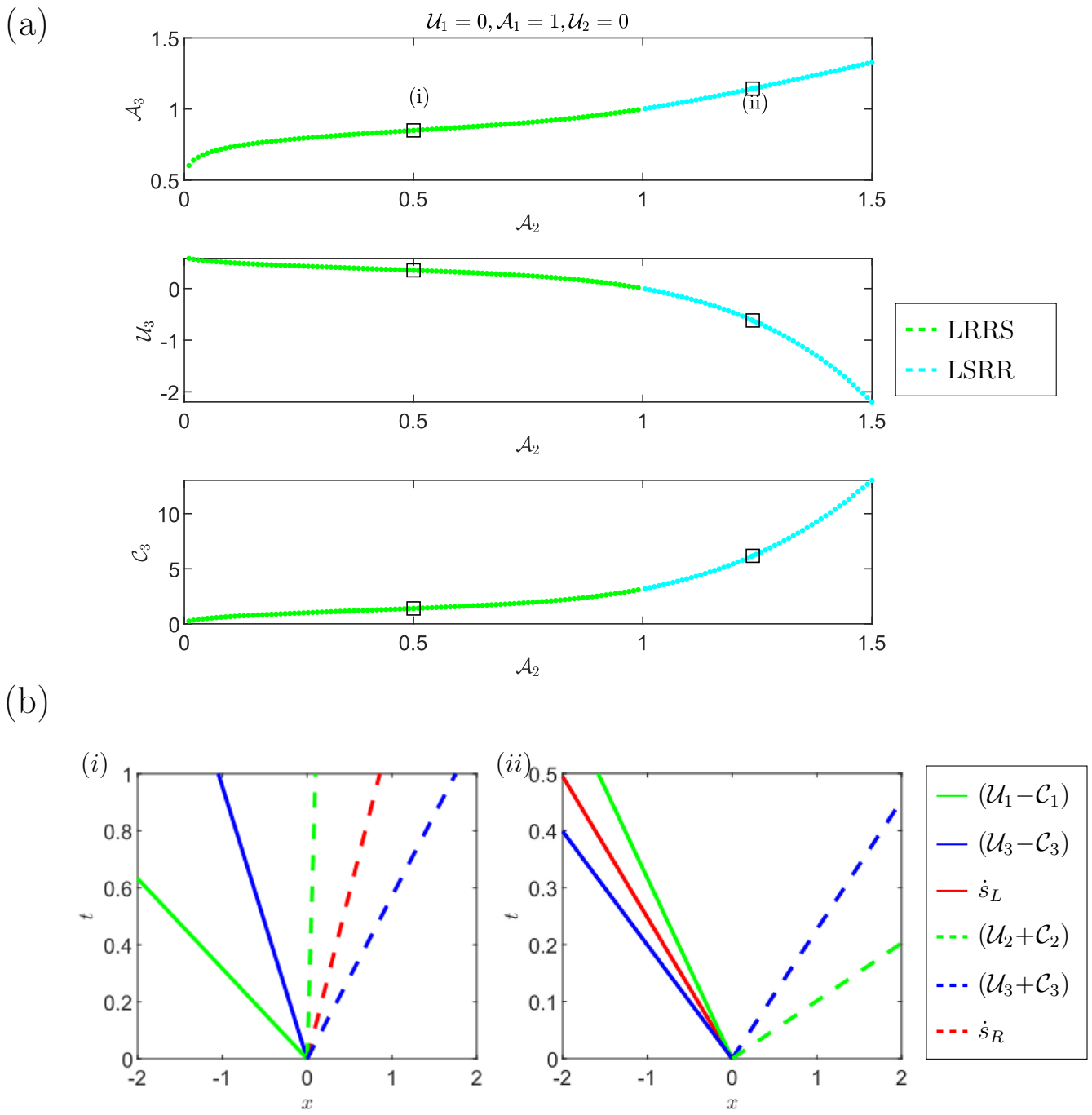

Figure 2.11: Bifurcation plot and characteristics profile plot of unique solutions $\mathcal{U}_2 = 0$ with corresponding values of $\mathcal{A}_3$, $\mathcal{A}_2$, respectively. Figure 2.11(a) displays the cross-sectional area, flow speed and wave speed of the unique solutions with different points of $\mathcal{A}_2$ marked as (i) and (ii) such that (i) denotes $\mathcal{A}_2 = 0.5$ and (ii) denotes $\mathcal{A}_2 = 1.24$, respectively, while Figure 2.11(b) shows the corresponding characteristics values of these different values of $\mathcal{A}_2$ for (i) and (ii) with $\mathcal{U}_2 = 0$.

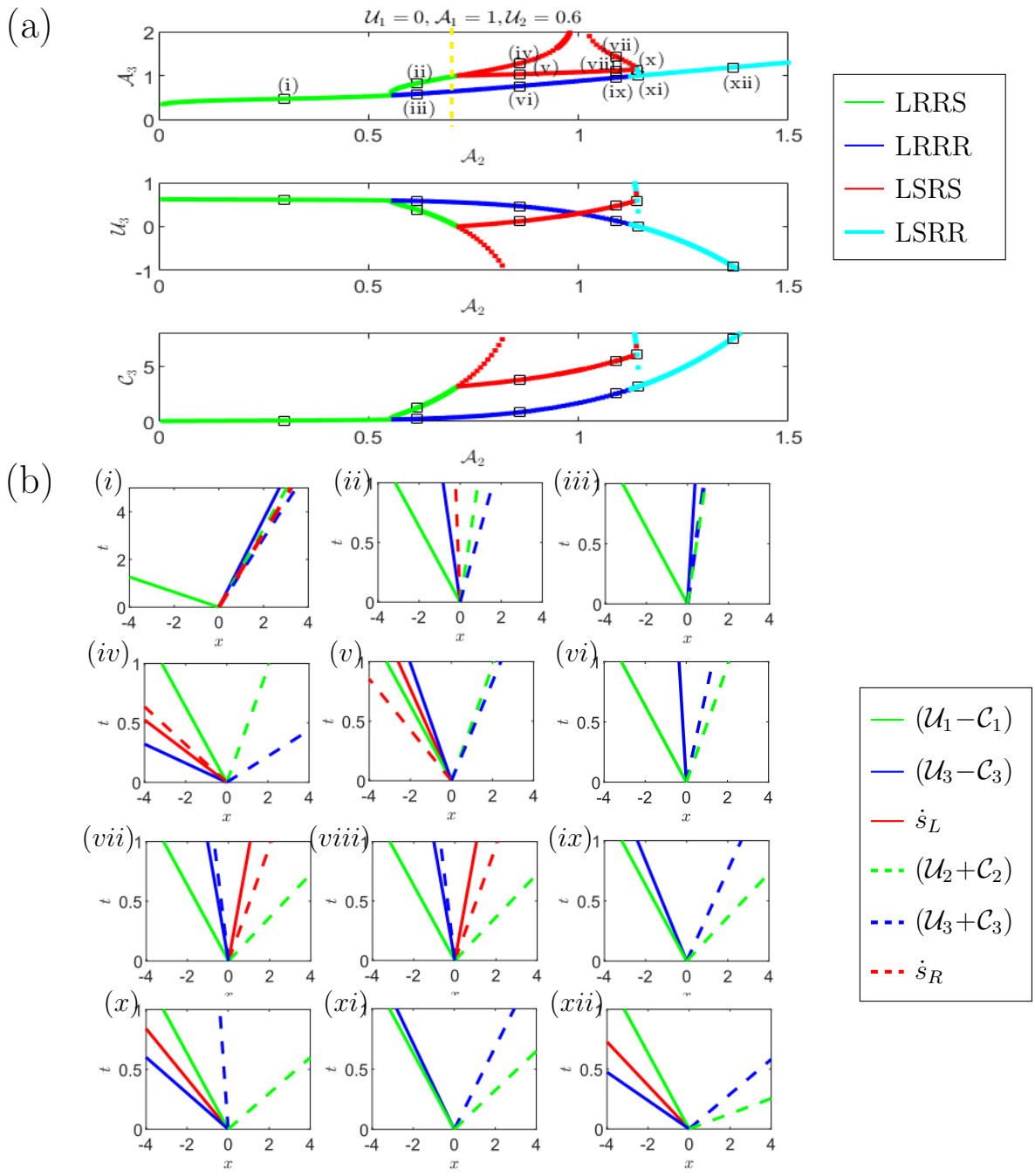

Figure 2.12: Bifurcation plot and characteristics profile plot of multiple solutions at $\mathcal{U}_2 = 0.6$ with corresponding values of $\mathcal{A}_3$, $\mathcal{A}_2$, respectively. Figure 2.12(a) displays the the cross-sectional area, flow speed and wave speed of the multiple solutions with different points of $\mathcal{A}_2$ marked as (i) to (xii) such that (i) denotes $\mathcal{A}_2 = 0.3$, (ii) denotes $\mathcal{A}_2 = 0.615$, (iii) denotes $\mathcal{A}_2 = 0.615$, (iv) denotes $\mathcal{A}_2 = 0.8592$, (v) denotes $\mathcal{A}_2 = 0.8592$, (vi) denotes $\mathcal{A}_2 = 0.8592$, (vii) denotes $\mathcal{A}_2 = 1.091$, $(viii)$ denotes $\mathcal{A}_2 = 1.091$, (ix) denotes $\mathcal{A}_2 = 1.091$, (x) denotes $\mathcal{A}_2 = 1.14$, (xi) denotes $\mathcal{A}_2 = 1.142$ and (xii) denotes $\mathcal{A}_2 = 1.368$, while Figure 2.12(b) shows the corresponding characteristics values of these different values of $\mathcal{A}_2$ from (i) to (xii) with $\mathcal{U}_2 = 0.6$.

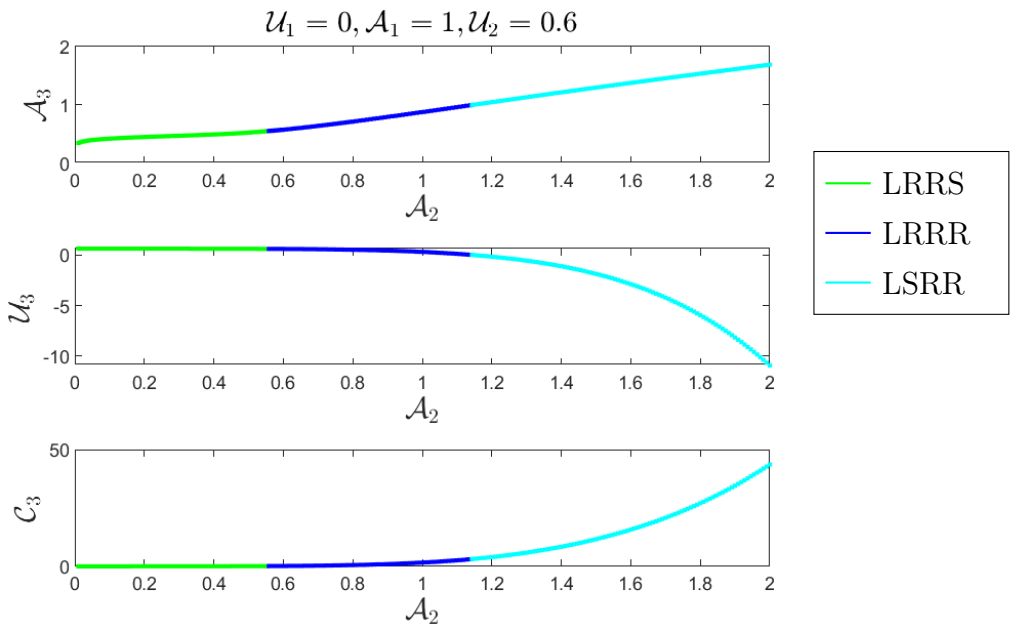

Figure 2.13: Bifurcation plot of physical solutions at $\mathcal{U}_2 = 0.6$, $\mathcal{A}_1 = 1$, $\mathcal{U}_1 = 0$ with corresponding values of $\mathcal{A}_3$, $\mathcal{U}_3$, $\mathcal{C}_3$ $\mathcal{A}_2$, respectively.

2.11.3 Case 3

In Figure 2.14 we extend the analysis of Figures 2.12 and 2.13 to consider a larger outflow from region 2 (*i.e.* $\mathcal{U}_2 = 1$) for $\mathcal{A}_1 = 1$, $\mathcal{U}_1 = 0$. This case is remarkably different to case 2. As before we begin by plotting all solutions of the Newton's method, before restricting attention to just physical solutions. The system again exhibits LRRS for low $\mathcal{A}_2$ and LSRR for large $\mathcal{A}_2$. However, this LRRS state is unphysical because it fails the Lax entropy condition for a right moving shock (see Figure 2.14(b), point (i)). Furthermore, the LRRS state now only connects to the two unphysical LSRS branches but does not connect to LRRR. In this case the LRRR state (a physical branch) emerges from $\mathcal{A}_3 = 0$ for $\mathcal{A}_2 \approx 0.898$. Note this state is only possible because of the choice of our tube law which does not strongly resist vessel collapse *i.e.* $n = 0$. This physical branch of solutions connects to the physical branch of LSRR at $\mathcal{A}_2 \approx 1.207$. The same bifurcation diagram is plotted in Figure 2.15, applying the physicality conditions for rarefaction and shocks. Now, for larger values of $\mathcal{U}_2$ the system only exhibits a physical solution for $\mathcal{A}_2$ greater than a threshold. This results in a region of the parameter space with no physical solution (see Section 2.12).

As before, the left hand state is always subcritical, but the right hand initial state becomes supercritical for $\mathcal{A}_2 < 0.794$ when $\mathcal{U}_2 > \mathcal{C}_2$, (marked with a yellow dashed line on Figure 2.14). Hence, the loss of a physical solution due to complete vessel collapse occurs within the supercritical region.

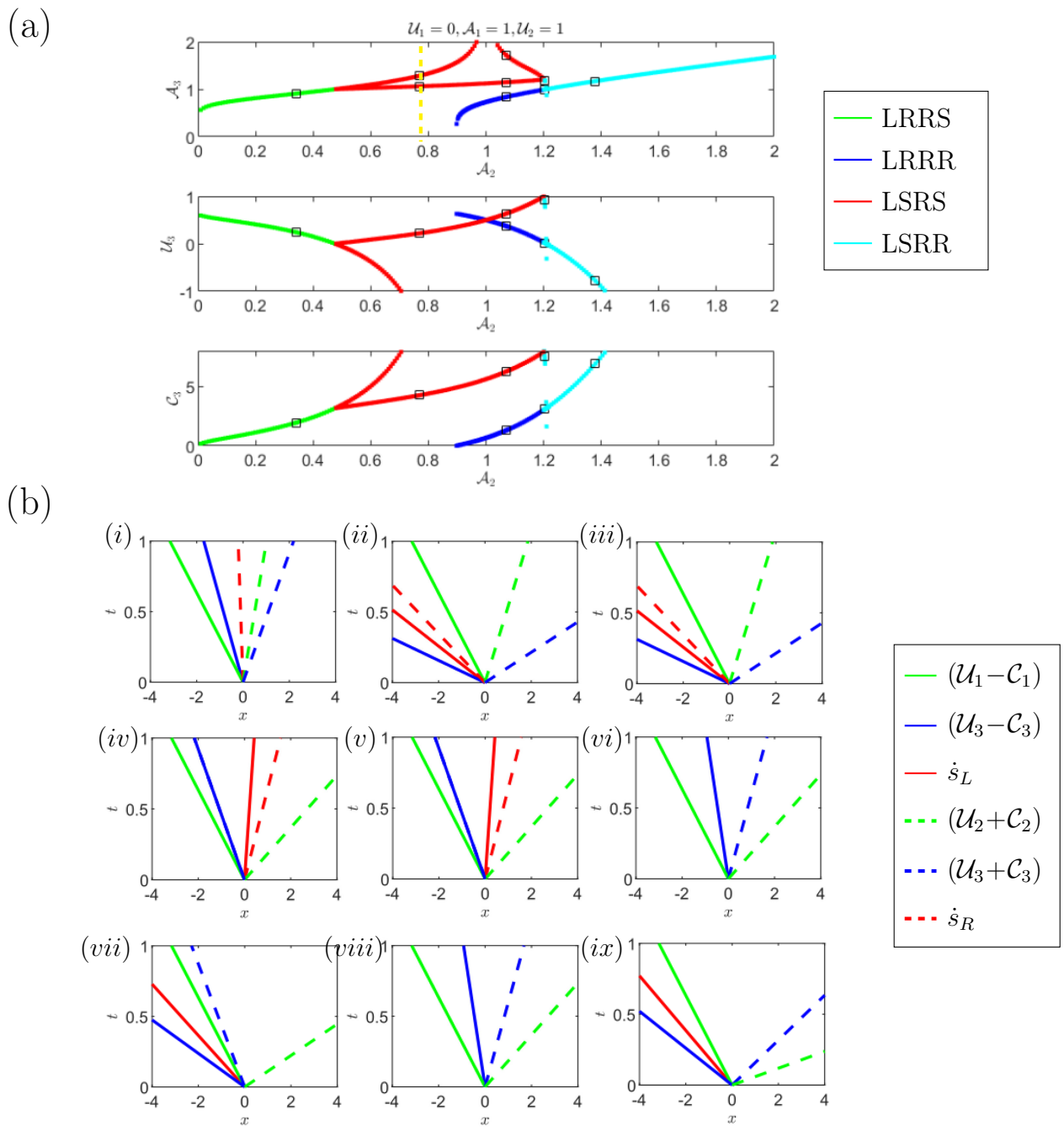

Figure 2.14: Bifurcation plot and characteristics profile plot of multiple solutions at $\mathcal{U}_2 = 1$ with corresponding values of $\mathcal{A}_3$, $\mathcal{A}_2$, respectively. Figure 2.14(a) displays the the cross-sectional area, flow speed and wave speed of the multiple solutions with different points of $\mathcal{A}_2$ marked as (i) to (ix) such that (i) denotes $\mathcal{A}_2 = 0.34$, (ii) denotes $\mathcal{A}_2 = 0.77$, (iii) denotes $\mathcal{A}_2 = 0.77$, (iv) denotes $\mathcal{A}_2 = 1.07$, (v) denotes $\mathcal{A}_2 = 1.07$, (vi) denotes $\mathcal{A}_2 = 1.07$, (vii) denotes $\mathcal{A}_2 = 1.203$, $(viii)$ denotes $\mathcal{A}_2 = 1.208$, (ix) denotes $\mathcal{A}_2 = 1.38$, while Figure 2.14(b) shows the corresponding characteristics values of these different values of $\mathcal{A}_2$ from (i) to (ix) with $\mathcal{U}_2 = 1.0$.

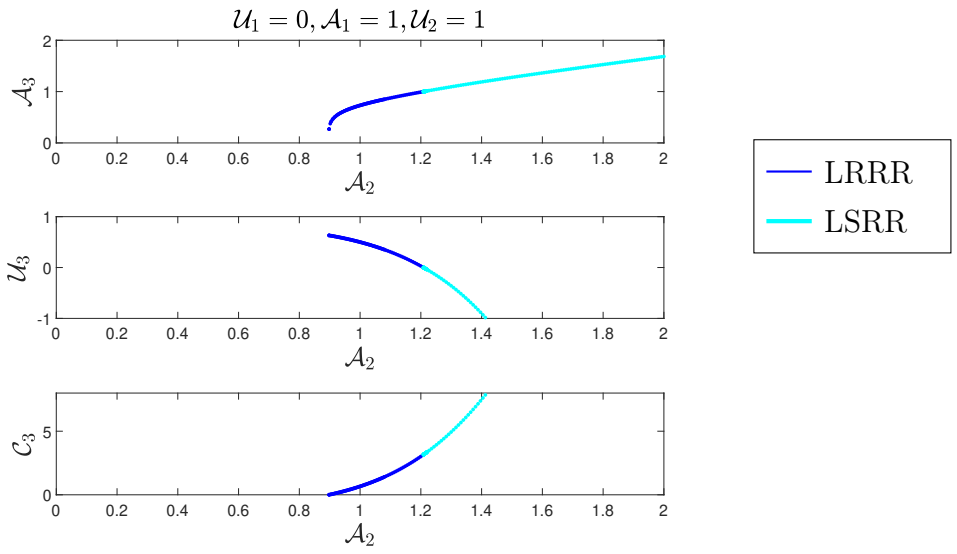

Figure 2.15: Bifurcation plot of physical solutions at $\mathcal{U}_2 = 1.0$, $\mathcal{A}_1 = 1$, $\mathcal{U}_1 = 0$ with corresponding values of $\mathcal{A}_3$, $\mathcal{U}_3$, $\mathcal{C}_3$ $\mathcal{A}_2$, respectively.

2.11.4 Case 4

In Figure 2.16 we consider a case with flow coming into region 2 (*i.e.* $\mathcal{U}_2 = -0.6$) for $\mathcal{A}_1 = 1$ and $\mathcal{U}_1 = 0$. As before, we plot a bifurcation diagram parametized by $\mathcal{A}_2$ in terms of $\mathcal{A}_3$, $\mathcal{U}_3$ and $\mathcal{C}_3$ focusing first on all solutions to the Newton's method. Similar to cases 1 to 3 for low $\mathcal{A}_2$ the system exhibits LRRS, while for large $\mathcal{A}_2$ the system exhibits LSRR. We again plot characteristics at representative points in Figure 2.16(b), where points (i) and (vi) exhibit qualitative agreement with case 1. As $\mathcal{A}_2$ increases from low values, the system exhibits LRRS which bifurcates into two branches of of LRRS at $\mathcal{A}_2 \approx 0.713$ with characteristics illustrated at points (ii) and (iii) of Figure 2.16(a). The upper branch of LSRS is unphysical as the right shock fails the entropy condition (see points (ii) and (iv) in Figure 2.16b). Conversely, the lower branch of LSRS exhibits a physical solution, with typical characteristics shown for points (iii) and (v) shown in Figure 2.16(b). The physical and unphysical branch of LSRS merge at $\mathcal{A}_2 \approx 1.137$ and join with the physical branch of LSRR. Hence, the path from LRRS, lower branch of LSRS to LSRR represents the physical solution in this case. Therefore, for negative values of $\mathcal{U}_2$ the system exhibits multiple solutions for a range of $\mathcal{A}_2$ but does not exhibit LRRR. However, the characteristic plots and Lax conditions indicate that only the lower branch of LSRS is ever stable. Figure 2.17 plots the same bifurcation diagram while applying the physicality conditions for rarefactions and shocks, confirming that only one branch of solution is physical for all values of $\mathcal{A}_2$.

(a)

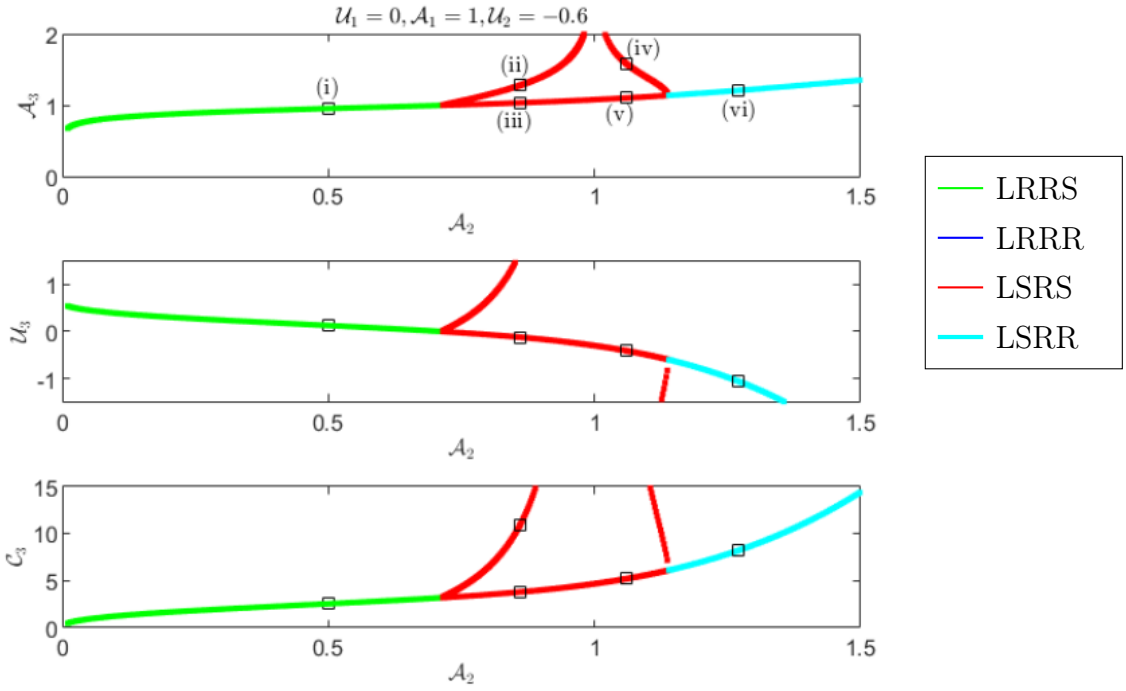

(b)

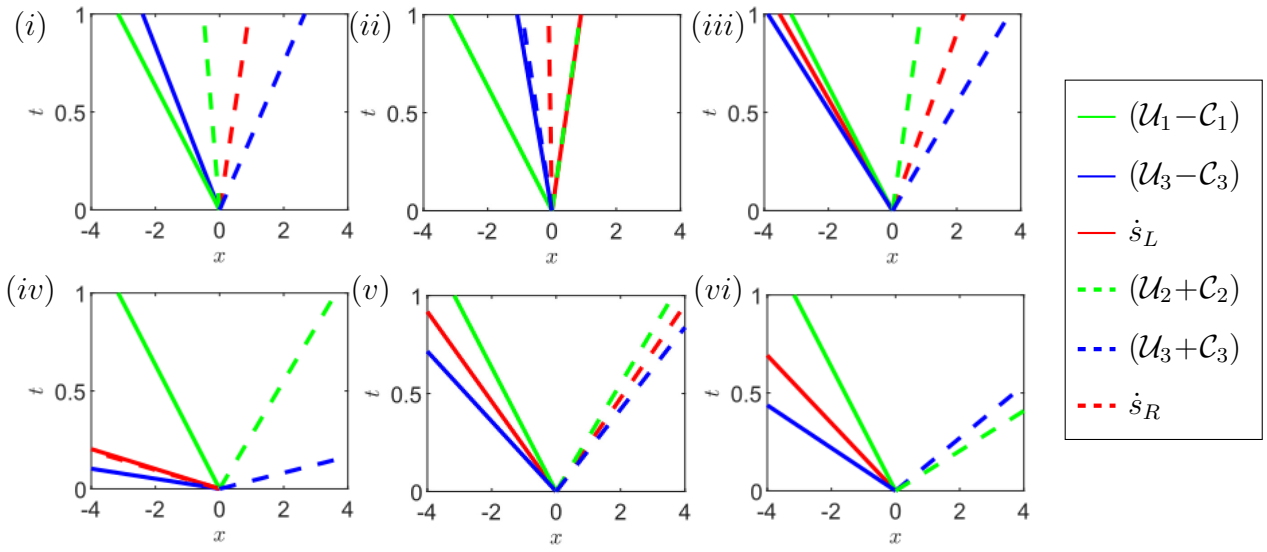

Figure 2.16: Bifurcation plot and characteristics profile plot of multiple solutions at $\mathcal{U}_2 = -0.6$ with corresponding values of $\mathcal{A}_3$, $\mathcal{A}_2$, respectively. Figure 2.16(a) displays the the cross-sectional area, flow speed and wave speed of the multiple solutions with different points of $\mathcal{A}_2$ marked as (i) to (vi) such that (i) denotes $\mathcal{A}_2 = 0.5$, (ii) denotes $\mathcal{A}_2 = 0.86$, (iii) denotes $\mathcal{A}_2 = 0.86$, (iv) denotes $\mathcal{A}_2 = 1.06$, (v) denotes $\mathcal{A}_2 = 1.06$, and (vi) denotes $\mathcal{A}_2 = 1.269$, while Figure 2.16(b) shows the corresponding characteristics values of these different values of $\mathcal{A}_2$ from (i) to (vi) with $\mathcal{U}_2 = -0.6$.

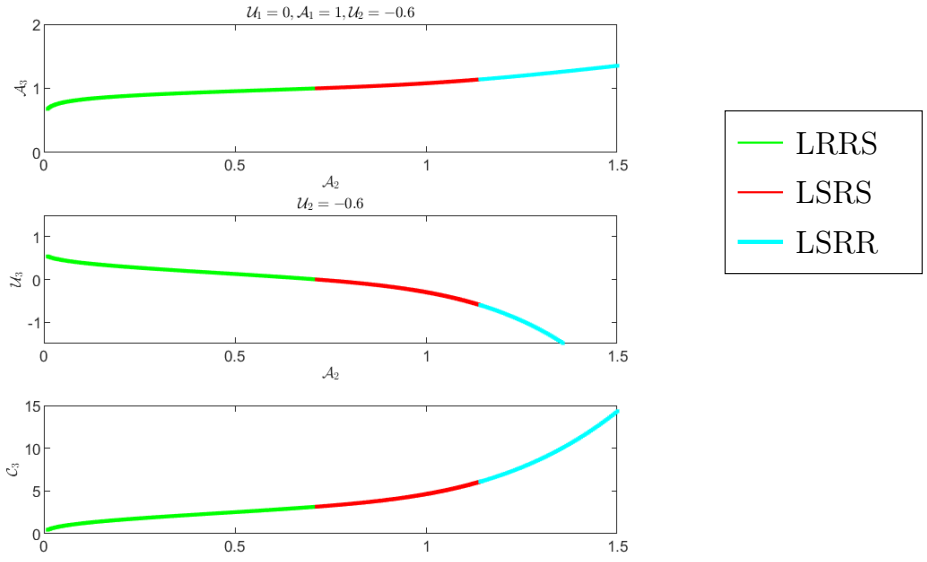

Figure 2.17: Bifurcation plot of physical solutions at $\mathcal{U}_2 = -0.6$ with corresponding values of $\mathcal{A}_3$, $\mathcal{U}_3$, $\mathcal{C}_3$ $\mathcal{A}_2$, respectively.

2.12 Overview of the parameter space

2.12.1 Overview using Newton's method

We now summarise the overall behaviour of the system by highlighting the different types of solutions that can occur in the parameter space spanned by $\mathcal{U}_2$ and $\mathcal{A}_2$ for fixed $\mathcal{A}_1$ and $\mathcal{U}_1$. We use the same colour scheme as before (blue denoting LRRR, red denoting LSRS, green denoting LRRS and cyan denoting LSRR). Figure 2.18(a) displays the parameter space plot computed using our Newton's method approach showing regions of unique solution, multiple solutions (although only one is ever physical), and no solution as the tube is fully collapsed in region 3. Filled circles in the parameter space denote a unique solution, open circles denote two solutions (one being physical and the other non physical), while squares denotes three solutions (one being a physical solution) while the triangle denotes where there exists no physical solution. For low value of $\mathcal{A}_2$ the parameter space shows a region of LRRS, while for large values of $\mathcal{A}_2$ the parameter space shows a region of LSRR, which agrees with the cases discussed above. It is also seen that for $0.5 \lesssim \mathcal{A}_2 \lesssim 1.2$ (for the range of $\mathcal{U}_2$ considered), the parameter space plot exhibits a region of multiple solutions. Here negative $\mathcal{U}_2$ exhibits multiple solutions in the LSRS region (in agreement with case 4). However, for positive $\mathcal{U}_2$, we have regions of multiple solution in both LSRS and LRRS, as well as a region of no solution, which is also in agreement with cases 2 and 3. Hence, for sufficient large positive or negative values of $\mathcal{U}_2$, our system can exhibit multiple solutions for a range of values of $\mathcal{A}_2$. But there is at most only one physical solution. We note that our choice of initial conditions spans both sub and supercritical states. Figure 2.18(b) summarises only the physical solutions of our parameter space plot in dividing the region with no solution.

We note that the region with no solution emerges only because of our simplified choice of tube law, where the vessel can exhibit zero cross-sectional area for finite pressure. Note that this region spans both sub and super-critical initial conditions.

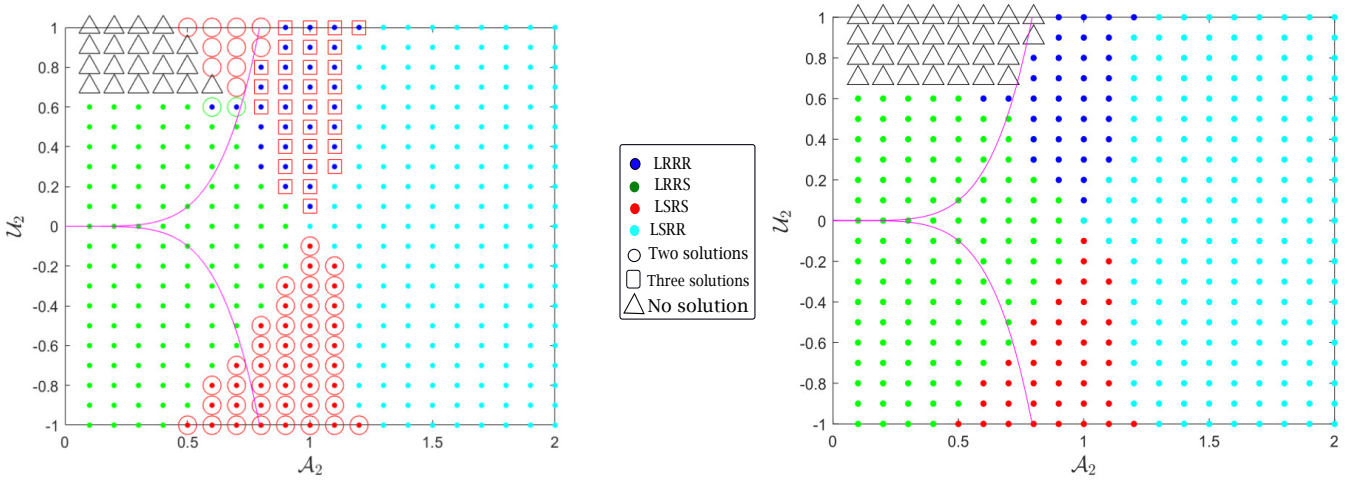

Figure 2.18: Overview of parameter space showing regions of no solution, one solution, two solutions and three solutions. Figure 2.18(a) illustrates parameter space plot for both physical and unphysical solutions for $\mathcal{A}_2 \leq 1$ and $\mathcal{U}_2 > 0.5$ we have regions of no solutions marked with green triangles and red open circles with two solutions which are not physical, dotted lines of green and cyan showed regions of one solution, red circle and red dot showed two solutions with the dot been the physical solution while blue dot and red squares showed three solutions with only the blue dot been the physical solution. Figure 2.18(b) shows parameter space plot for only physical solutions and little patch with no solution (tube collapse). For $\mathcal{A}_2 \leq 1$ and $\mathcal{U}_2 > 0.5$ we have regions of no solutions marked with black triangles. Dotted lines of green, cyan, red and blue denote the physical solutions.

2.12.2 Overview using method of Brook et al.

In this section we now produce a similar overview of the parameter space using the algorithm constructed by Brook et al. [44], as shown in Figure 2.19(b) and compare it with the physical solutions from our Newton's method as shown in Figure 2.19(a). This algorithm does not find unphysical solutions, so there is a maximum of one solution at every point in the parameter space. However, we identify regions where the algorithm does not converge at all with a filled black circle. We note that the physical solutions identified by Brook's method are very similar to those identified with our Newton's method approach. We also note that the regions where the algorithm does not converge are close to (but not overlapping with) the regions where our method found no physical solution as the tube has entirely collapsed in region 3. We note that the region of no solution found using this method is larger than with our method, and also that this region includes both sub and super-critical initial conditions.

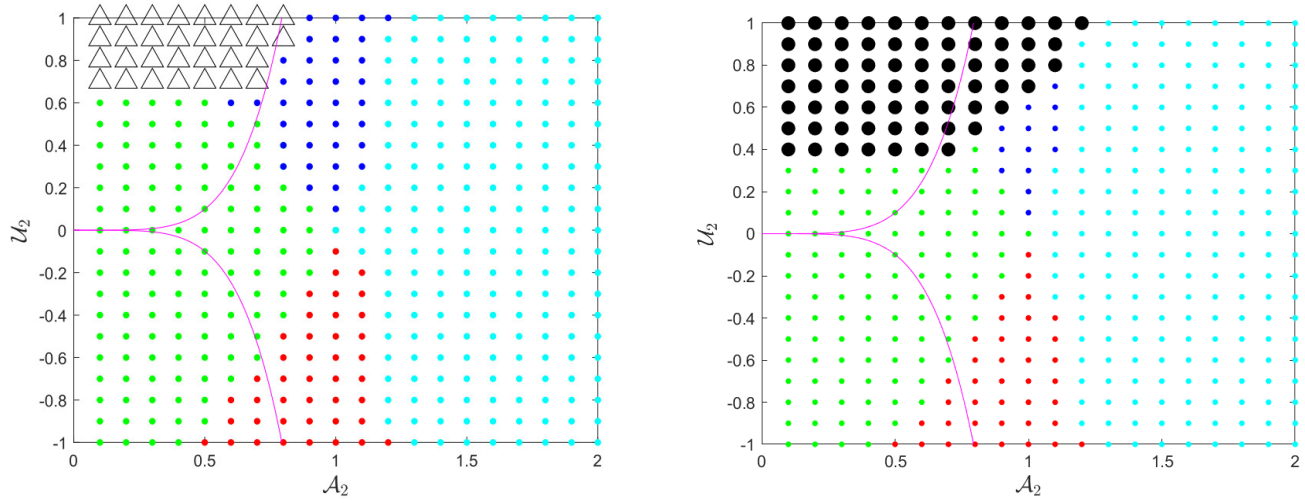

Figure 2.19: Showing parameter space plot comparison between our Newton method and the algorithm of Brook et al. [44] for $\mathcal{A}_1 = 1$, $\mathcal{U}_1 = 0$, $-2 \leq \mathcal{U}_2 \leq 2$ and $0 \leq \mathcal{A}_2 \leq 2$. Figure 2.19(a) shows the paramrter space plot from our Newton method while, Figure 2.19(b) shows parameter space plot from the algorithm by Brook et al. [44].

2.12.3 Overview in terms of initial conditions in region 1

In Figure 2.20, we explore the behaviour of our system across the parameter space spanned by $\mathcal{A}_2$ and $\mathcal{U}_2$ as we also vary the initial conditions in region 1. First, in Figures 2.20(a,d,g) we fix the cross-sectional area and flow speed in region 1 as $\mathcal{A}_1 = 0.5$ and reduce the value of $\mathcal{U}_1$ from 0.5 to -0.5, respectively. It is seen that as value of $\mathcal{U}_1$ decreases we have an enlarged region with no solution with the LSRR dominating the parameter space. The LRRS solution also reduces as $\mathcal{U}_1$ decreases. It is also pertinent to note that for very low $\mathcal{A}_1$ for a given $\mathcal{U}_1$ (example Figure 2.20(a) for $\mathcal{A}_1 = 0.5, \mathcal{U}_1 = 0.5$) the far-field flow in region 1 is supercritical *i.e.* $\mathcal{U}_1 > \mathcal{C}_1$. In this case any left rarefaction must be entirely in $x > 0$. A slightly different example of a physical solution with a supercritical rarefaction in region 2 is shown in Figure 2.21, plotting the characteristics and spatial profiles for $\mathcal{A}_2 = 0.6$ (so that $\mathcal{C}_2 = 0.24$) and $\mathcal{U}_2 = 0.6$. We see that even though it is within the supercritical regime, the right rarefaction is confined to $x > 0$, but the resulting flow in region 3 is also supercritical and so the edge of the rarefaction adjacent to region 1 is moved into $x > 0$.

Similar trends are also evident in all the plots in the first two columns of Figure 2.20, where the region with no solution enlarges as $\mathcal{U}_1$ decreases but is absent in the third column where we don't see any case of supercriticality or vessel collapse.

2.12.4 Parameter space plot for different values of the exponent m

In Figure 2.22 we explore dependency of parameter space on the exponent m, plotting the $\mathcal{A}_2$, $\mathcal{U}_2$ parameter space for fixed $\mathcal{A}_1$ and $\mathcal{U}_1$, considering a reduction in the exponent from $m = 10$ (Figure 2.22a), to $m = 5$ (Figure 2.22b), to $m = 1$ (Figure 2.22) to $m = 1/2$ (Figure 2.22d). Across the range

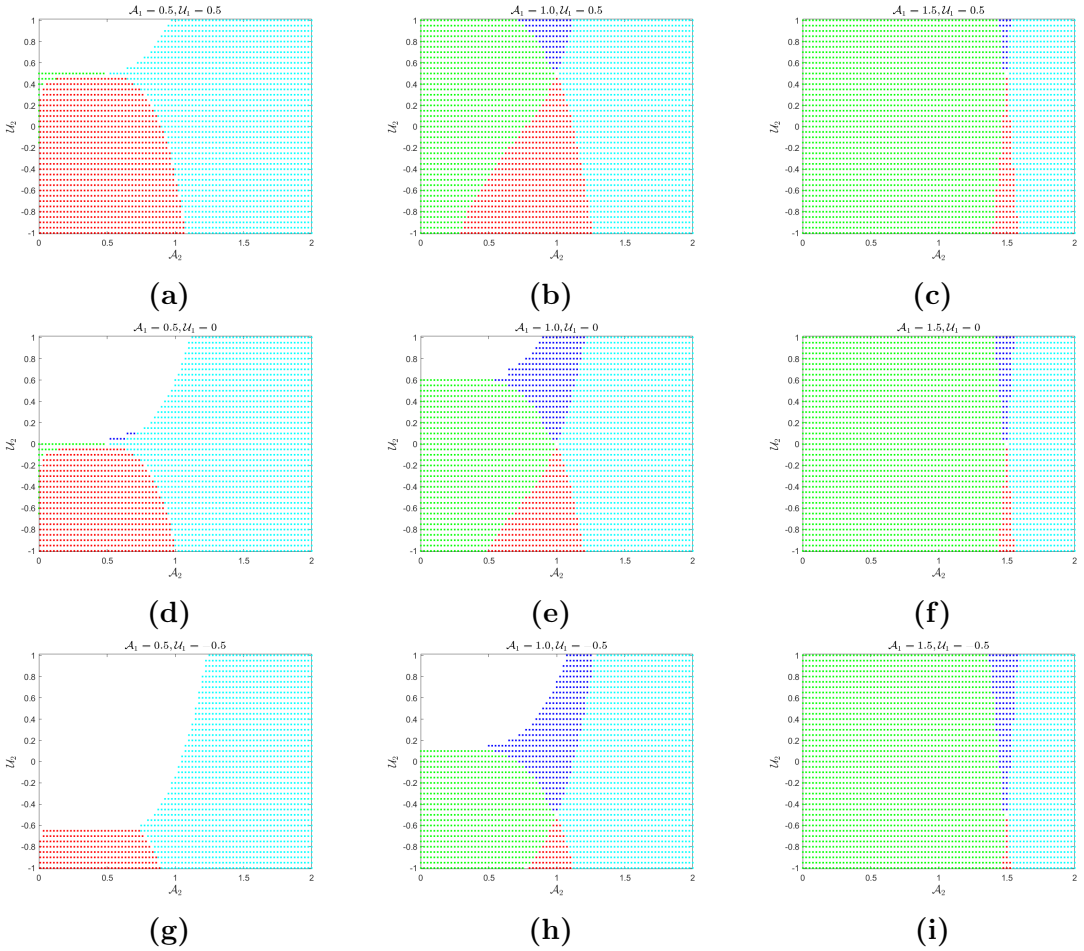

Figure 2.20: Parameter space plot of our Newton method with different initial conditions. Figure 2.20(a) shows parameter space plot of our Newton method for $\mathcal{U}_1 = 0.5$, $\mathcal{A}_1 = 0.5$, Figure 2.20(b) shows parameter space plot of our Newton method for $\mathcal{U}_1 = 0.5$, $\mathcal{A}_1 = 1$, Figure 2.20(c) shows parameter space plot of our Newton method for $\mathcal{U}_1 = 0.5$, $\mathcal{A}_1 = 1.5$, Figure 2.20(d) shows parameter space plot of our Newton method for $\mathcal{U}_1 = 0$, $\mathcal{A}_1 = 0.5$, Figure 2.20(e) shows parameter space plot of our Newton method for $\mathcal{U}_1 = 0$, $\mathcal{A}_1 = 1.0$, Figure 2.20(f) shows parameter space plot of our Newton method for $\mathcal{U}_1 = 0$, $\mathcal{A}_1 = 1.5$, Figure 2.20(g) shows parameter space plot of our Newton method for $\mathcal{U}_1 = -0.5$, $\mathcal{A}_1 = 0.5$, Figure 2.20(h) shows parameter space plot of our Newton method for $\mathcal{U}_1 = -0.5$, $\mathcal{A}_1 = 1.0$, and Figure 2.20(i) shows parameter space plot of our Newton method for $\mathcal{U}_1 = -0.5$, $\mathcal{A}_1 = 1.5$, respectively. Here green dotted line denotes LRRS, blue dotted line denotes LRRR, red doted line denotes LSRS and cyan dotted lines denotes LSRR. The white space denote regions of no solution

of parameters the response is qualitatively similar, although as m decreases the region with no solution is pushed to increasingly larger $\mathcal{U}_2$ and the wedge of LRRR and LSRS becomes gradually expanded.

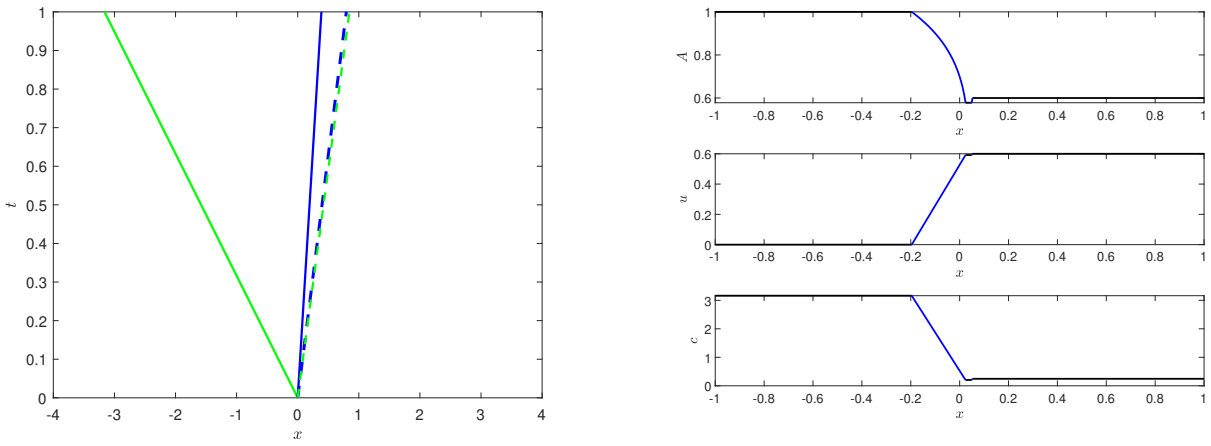

(a) **(b)**

Figure 2.21: Diagram of characteristic and spatial profiles of supercritical flow in region 2 for $\mathcal{A}_2 = 0.6$, $\mathcal{U}_2 = 0.6$. Figure 2.21(a) shows the characteristic profile where the blue line shows the outer edge of the rarefaction in region 1 and the blue dotted line showing the outer edge of rarefaction in region 2. Figure 2.21(b) shows the spatial profiles of cross-sectional area, flow speed and wavespeed of the supercritical flow in region 2.

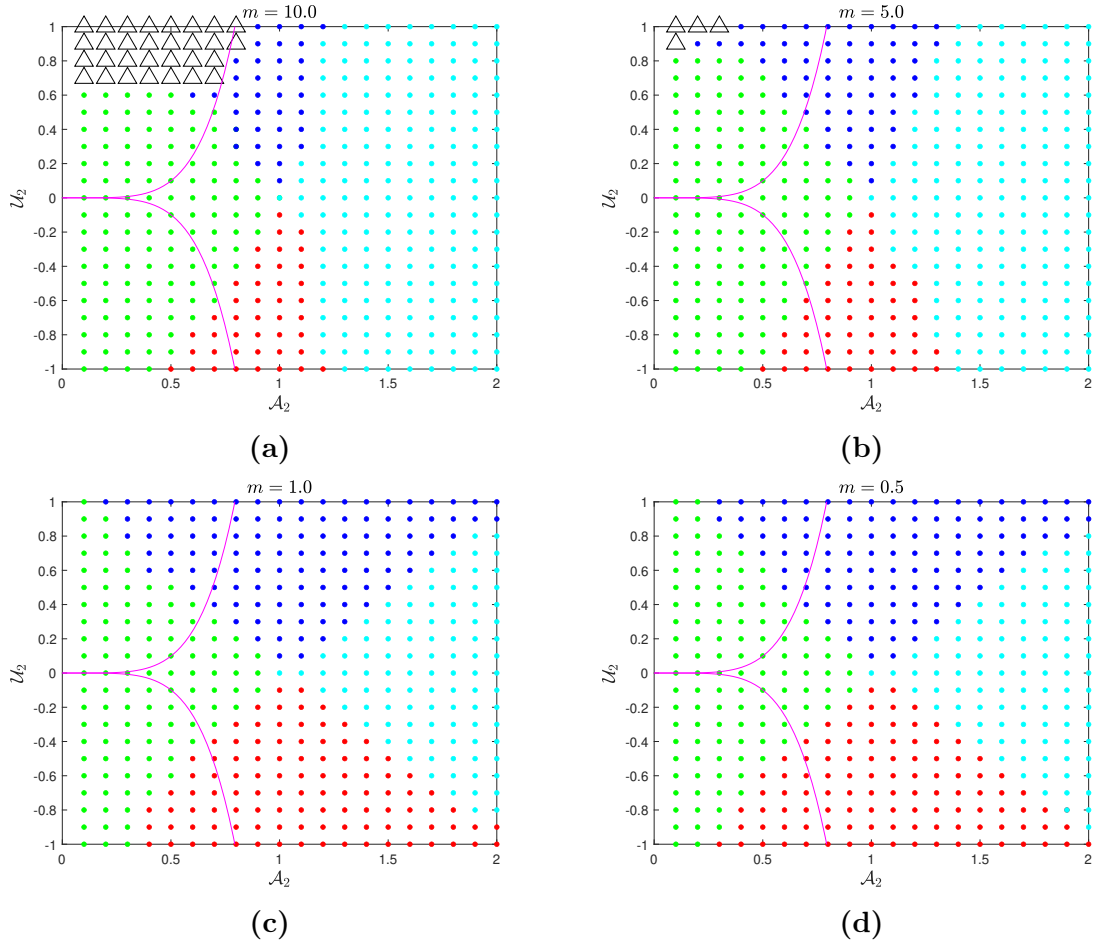

Figure 2.22: Showing the parameter space plots with physical solutions for different values of m. Figure 2.22(a) shows the parameter space plot for our Newton's method for $m = 10.0$, Figure 2.22(b) shows the parameter space plot for our Newton's method for $m = 5.0$, Figure 2.22(c) shows the parameter space plot for our Newton's method for $m = 0.1$, while Figure 2.22(d) shows the parameter space plot for our Newton's method for $m = 0.05$.

2.13 General tube law

In this section we extend our Riemann problem where we consider blood vessel with uniform material properties using the general tube law which resist both expansion and collapse. The model setup and assumptions are the same as Section 2.1, so we follow analogous procedure to derive the conservation of mass and momentum equations as

$$\frac{\partial A}{\partial t} + \frac{\partial (Au)}{\partial x} = 0, \tag{2.97}$$

$$\frac{\partial}{\partial t}(Au) + \frac{\partial}{\partial x}(Au^2) + A\frac{\partial p}{\partial x} = 0, \tag{2.98}$$

with the corresponding dimensionless nonlinear general tube law given as

$$p - p_e = \left(A^m - A^{-n}\right), \tag{2.99}$$

for m and n been any constant. We now have the nonlinear wave speed given as

$$c^2(x,t) = \left(mA^m + nA^{-n}\right). \tag{2.100}$$

From equations (2.97) and (2.98), we write both independent of p in the form

$$\frac{\partial A}{\partial t} + A\frac{\partial u}{\partial x} + u\frac{\partial A}{\partial x} = 0, \tag{2.101}$$

$$\frac{\partial u}{\partial t} + u\frac{\partial u}{\partial x} + \frac{c^2}{A}\frac{\partial A}{\partial x} = 0. \tag{2.102}$$

subject to

$$\begin{aligned} A(x,0) &= \mathcal{A}_1, \quad u(x,0) = \mathcal{U}_1, \quad (x<0), \\ A(x,0) &= \mathcal{A}_2, \quad u(x,0) = \mathcal{U}_2, \quad (x>0). \end{aligned}$$

Following similar approach from Section 2.4 we have (2.101) and (2.102) written in the Riemann invariant form as

$$\left(\frac{\partial}{\partial t} + (u \pm (\sqrt{mA^m + nA^{-n}})\frac{\partial}{\partial x}\right)\left[u \pm \int_1^A \sqrt{mA'^{(m-2)} + nA'^{-(n+2)}}dA'\right] = 0, \tag{2.103}$$

where $c = \sqrt{mA^m + nA^{-n}}$. This implies that the Riemann invariants of the flow are given by

$$R = u \pm \int_1^A \sqrt{mA'^{(m-2)} + nA'^{-(n+2)}}dA', \tag{2.104}$$

which are constant along characteristics $C_\pm$, defined according to

$$\frac{dx}{dt} = u \pm \sqrt{mA^m + nA^{-n}}. \tag{2.105}$$

The resulting nonlinear wave following discontinuity in initial conditions also produces two waves which

are either a shock or a rarefaction wave, which we now discuss in turn.

2.13.1 Nonlinear shock wave

In respect to large amplitude perturbations, we show here that a shock can be formed in a tube in response to discontinuity in initial conditions. So, we adopt a similar approach as in Section 2.5 and write equation (2.98) in conservation form as

$$\frac{\partial}{\partial t}(Au) + \frac{\partial}{\partial x}\left(Au^2 + \frac{m}{m+1}A^{m+1} - \frac{n}{(n-1)}A^{-(n-1)}\right) = 0. \tag{2.106}$$

We proceed to invoke similar method as used in Section 2.5 to find the left shock and right shock solutions.

Left shock

Here we consider a shock wave moving to the left separating regions 1 and 3. In similar manner as with the expanding tube law discussed above, we consider equations (2.49) and (2.50), and obtain

$$\dot{s} = \frac{\mathcal{A}_3\mathcal{U}_3 - \mathcal{A}_1\mathcal{U}_1}{\mathcal{A}_3 - \mathcal{A}_1}, \tag{2.107}$$

$$\dot{s} = \frac{\mathcal{A}_3\mathcal{U}_3^2 + \frac{m}{m+1}\mathcal{A}_3^{m+1} - \frac{n}{(n-1)}\mathcal{A}_3^{-(n-1)} - \mathcal{A}_1\mathcal{U}_1^2 + \frac{n}{(n-1)}\mathcal{A}_1^{-(n-1)} - \frac{m}{m+1}\mathcal{A}_1^{m+1}}{\mathcal{A}_3\mathcal{U}_3 - \mathcal{A}_1\mathcal{U}_1}. \tag{2.108}$$

Equating (2.107) and (2.108), and simplifying, we have

$$\mathcal{U}_3 = \mathcal{U}_1 \pm \sqrt{\frac{\left(\frac{m}{m+1}\left(\mathcal{A}_3^{m+1} - \mathcal{A}_1^{m+1}\right) + \frac{n}{n+1}\left(\mathcal{A}_1^{-(n-1)} - \mathcal{A}_3^{-(n-1)}\right)\right)(\mathcal{A}_3 - \mathcal{A}_1)}{\mathcal{A}_1\mathcal{A}_3}}, \tag{2.109}$$

linking $\mathcal{U}_3$ and $\mathcal{A}_3$ to the initial conditions.

Also, for physical shocks we must consider the Lax entropy conditions [113] as in equation (2.55).

Right shock

For a shock moving to the right separating regions 2 and 3, we follow same approach as in Section 2.5.2 to have the nonlinear constraint

$$\mathcal{U}_3 = \mathcal{U}_2 \pm \sqrt{\frac{\left(\frac{m}{m+1}\left(\mathcal{A}_2^{m+1} - \mathcal{A}_3^{m+1}\right) + \frac{n}{n+1}\left(\mathcal{A}_3^{-(n-1)} - \mathcal{A}_2^{-(n-1)}\right)\right)(\mathcal{A}_2 - \mathcal{A}_3)}{\mathcal{A}_2\mathcal{A}_3}}, \tag{2.110}$$

again linking $\mathcal{U}_3$ and $\mathcal{A}_3$ to the initial conditions.

Note again that for physical shocks on the right hand side we must impose Lax conditions (2.60).

2.13.2 Nonlinear Rarefaction wave

Following similar method as in Section 2.6 we simultaneously apply the Riemann invariants and characteristics to construct a left- and right- travelling rarefaction waves, in order to determine the flow properties at the edge of the rarefaction adjacent to region 3.

Left rarefaction

We follow similar method as in Section 2.6.1 such that at the edge of the rarefaction in contact with region 3, we have that $u_r = \mathcal{U}_3$, $A_r = \mathcal{A}_3$ and $c_r = \mathcal{C}_3$ such that

$$x_r = \left(\mathcal{U}_1 + \int_1^{\mathcal{A}_1} \sqrt{mA^{*(m-2)} + nA^{*-(n+2)}}dA^* - \sqrt{m\mathcal{A}_3^m + n\mathcal{A}_3^{-n}} - \int_1^{\mathcal{A}_3} \sqrt{mA^{*(m-2)} + nA^{*-(n+2)}}dA^*\right) t. \tag{2.111}$$

Simplifying, we have that at the edge of the rarefaction region adjacent to region 3

$$\mathcal{U}_3 = \mathcal{U}_1 + \int_1^{\mathcal{A}_1} \sqrt{mA^{*(m-2)} + nA^{*-(n+2)}}dA^* - \int_1^{\mathcal{A}_3} \sqrt{mA^{*(m-2)} + nA^{*-(n+2)}}dA^*. \tag{2.112}$$

From above, we can use Simpson's rule to evaluate our integral and solve for $\mathcal{U}_3$ for a given $\mathcal{A}_3$.

Right rarefaction

For negative characteristics entering the rarefaction region (R) we use the same method as in Section 2.6.2 such that at the edge of the rarefaction in contact with region 3, we have that $u_r = \mathcal{U}_3$, $A_r = \mathcal{A}_3$ and $c_r = \mathcal{C}_3$ such that

$$x_r = \left(\mathcal{U}_2 + \int_1^{\mathcal{A}_3} \sqrt{mA^{*(m-2)} + nA^{*-(n+2)}}dA^* + \sqrt{m\mathcal{A}_3^m + n\mathcal{A}_3^{-n}} - \int_1^{\mathcal{A}_2} \sqrt{mA^{*(m-2)} + nA^{*-(n+2)}}dA^*\right) t. \tag{2.113}$$

Simplifying, we have that at the edge of the rarefaction region adjacent to region 3

$$\mathcal{U}_3 = \mathcal{U}_2 + \int_1^{\mathcal{A}_3} \sqrt{mA^{*(m-2)} + nA^{*-(n+2)}}dA^* - \int_1^{\mathcal{A}_2} \sqrt{mA^{*(m-2)} + nA^{*-(n+2)}}dA^*. \tag{2.114}$$

From above, we again use Simpson's rule to numerically integrate part of (2.114) to solve for $\mathcal{U}_3$ for a given $\mathcal{A}_3$.

2.13.3 Newton's method and numerical simulation

We also have four possible wave profiles similar to the case considered formerly, so we use the Newton method to solve the four different cases which are LRRS, LSRR, LSRS and LRRR. We only present two representative profiles of the cross-sectional area, flow speed and wave speed, respectively with its corresponding characteristics profile (Figure 2.23 and 2.24).

Left rarefaction, right shock (LRRS)

We consider the same boundary conditions with the expanding tube law such that $\mathcal{A}_1 = 1.6$, $\mathcal{A}_2 = 0.8$, $\mathcal{U}_1 = 0$, $\mathcal{U}_2 = 0.5$. Typical profiles of the cross-sectional area, flow speed and wave speed are shown in Figure 2.23(a) while the corresponding characteristics are shown in Figure 2.23(b). The profiles are qualitatively similar to Figure 2.7.

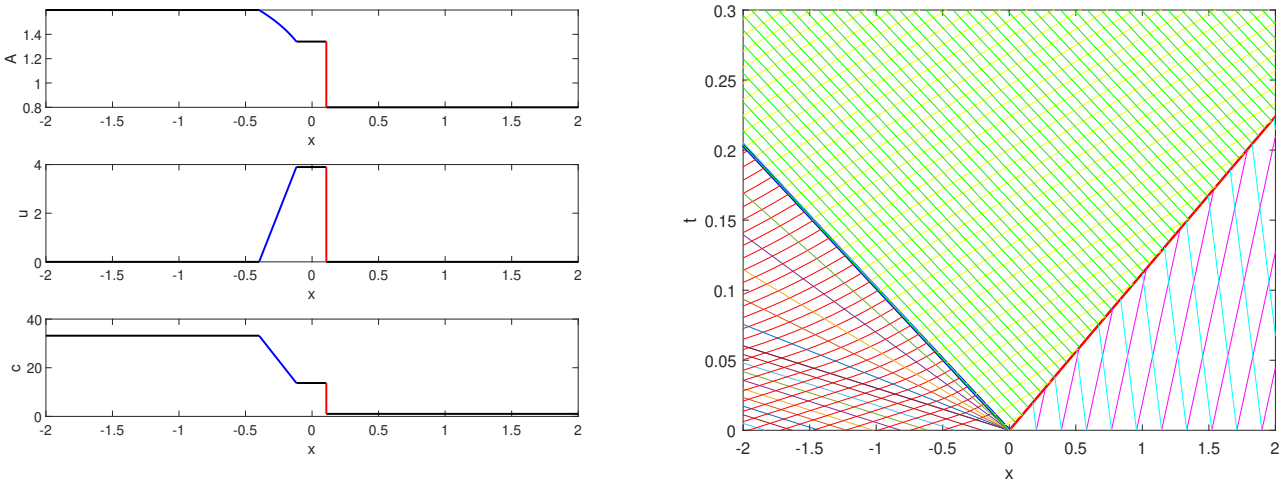

(a) **(b)**

Figure 2.23: A LRRS. Figure 2.23(a) shows the cross-sectional area, flow speed and wave speed wave profiles, respectively for LRRS shock wave of a general tube law, while Figure 2.23(b) displays a typical characteristics diagram showing regions 1, 2 and 3, respectively for a LRRS waves from a general tube law.

Left shock, right rarefaction (LSRR)

We consider boundary conditions $\mathcal{A}_1 = 1$, $\mathcal{A}_2 = 1.1$, $\mathcal{U}_1 = 0$, $\mathcal{U}_2 = 0.2$. Typical profiles of the cross-sectional area, flow speed and wave speed are shown in Figure 2.24(a) while the corresponding characteristics as shown in Figure 2.24(b). The profiles in this case are qualitatively similar to Figure 2.8.

2.13.4 Baseline cases

In this section, similar to the expanding tube law, we summarise the system by constructing bifurcation diagrams in terms of the initial area to the right of the discontinuity, $\mathcal{A}_2$ for all other boundary conditions held fixed. We consider some representative cases and compare them with the cases shown earlier using the expanding tube law. We consider four cases while continuing the numbering scheme from the cases in the expanding tube law initiated in Section 2.11: case 5 considers where there is no flow out of region 2 (*i.e.* $\mathcal{U}_2 = 0$), cases 6 and 7 consider flow out of region 2 (*i.e.* $\mathcal{U}_2 > 0$) and cases 8 considers flow coming into region 2 ($\mathcal{U}_2 < 0$), respectively all for no flow in/out of region 1 ($\mathcal{U}_1 = 0$). Here, we only

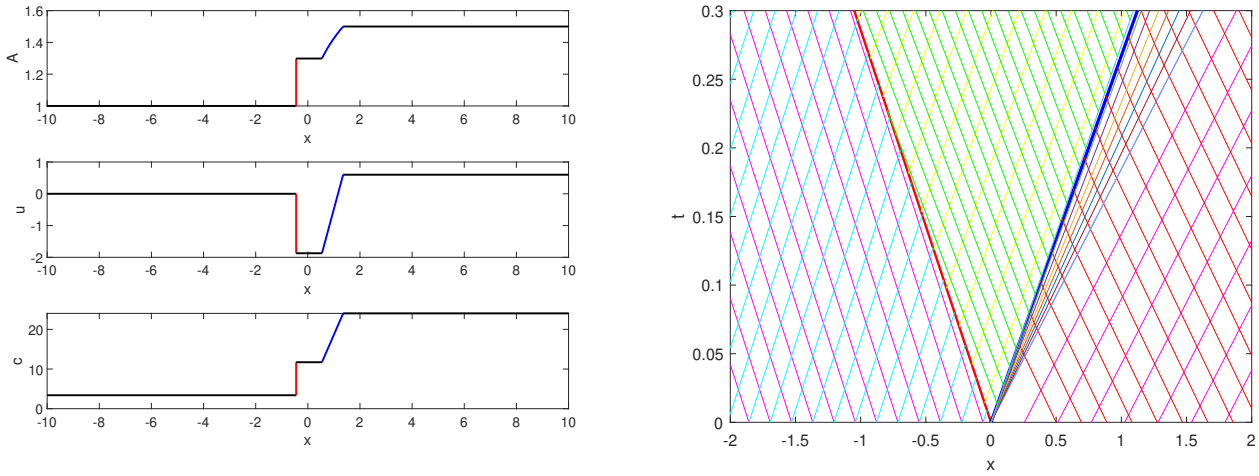

(a) **(b)**

Figure 2.24: A LSRR. Figure 2.24(a) shows the cross-sectional area, flow speed and wave speed wave profiles, respectively for LSRR wave of a general tube law, while Figure 2.24(b) displays a typical characteristics diagram showing regions 1, 2 and 3, respectively for a LSRR waves.

consider physical solutions of our system by imposing the Lax entropy conditions. The colour scheme is the same with the expanding tube law.

Case 5

Here, similar to case 1 we present the bifurcation diagram for a case where there is initially no flow out of region 2 (*i.e.* $\mathcal{U}_2 = 0$) and $\mathcal{A}_1 = 1$, $\mathcal{U}_1 = 0$. Figure 2.25(a) shows the bifurcation diagram as a function of $\mathcal{A}_2$. Similar to case 1, the system exhibits two configurations ie LRRS and LSRR. Figure 2.25 compares the system using the general tube law and the expanding tube law. Figure 2.25(a) shows that using the general tube law for no flow out of region 2 shows qualitative and qauntitative similarity with using the expanding tube law as shown in Figure 2.25(b). Both solutions shows that for $\mathcal{A}_2 < 1$ the system exhibits a LRRS, and for $\mathcal{A}_2 > 1$ the system exhibits a LSRR. Here, for the full tube law both $\mathcal{A}_2$ and $\mathcal{A}_3$ approach zero simultaneously, while for the expanding tube law the tube can have zero area in region 2 with finite area in region 3.

Case 6 and 7

In both cases we present the corresponding bifurcation diagram of a general tube law in $\mathcal{A}_2$ where there is flow out of region 2 (*i.e.* $\mathcal{U}_2 = 0.6$ and $\mathcal{U}_2 = 1.0$) for $\mathcal{A}_1 = 1, \mathcal{U}_1 = 0$. Figure 2.26 shows the comparison between the general tube law and the expanding tube law for $\mathcal{U}_2 = 0.6$. In both cases the system exhibit three out of the four profiles (LRRS, LRRR and LSRR).The only difference is that for the general tube law, we have that LRRS expands to a larger region thereby compressing the LRRR solution to a smaller region (see Figure 2.26a) compared to the expanding tube law (Figure 2.26b).

Figure 2.27 shows increased flow out of region 2 (*i.e.* $\mathcal{U}_2 = 1.0$) for both the general tube and the expanding tube laws. As before they both exhibit three classical wave profiles, LRRS, LRRR and LSRR

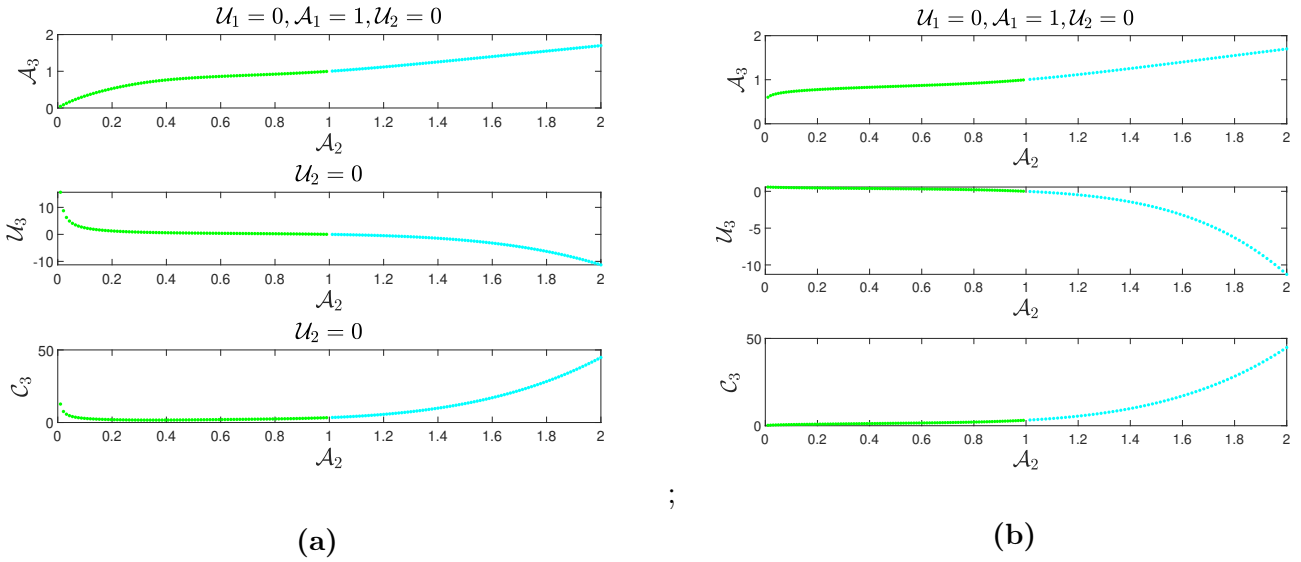

;

(a) **(b)**

Figure 2.25: Bifurcation plot of unique solutions at $\mathcal{U}_2 = 0$ with corresponding values of $\mathcal{A}_3$, $\mathcal{U}_3$, $\mathcal{C}_3$, $\mathcal{A}_2$. Figure 2.25(a) displays the the cross-sectional area, flow speed and wave speed of the unique solutions with general tube law and Figure 2.25(b) displays the the cross-sectional area, flow speed and wave speed of the unique solutions with expanding tube law.

as $\mathcal{A}_2$ increases from 0. From Figure 2.27(a), where we used the general tube law, we have that the three solutions fill the parameter range. Conversely for the expanding tube law (Figure 2.27b) the LRRR is tending to zero area for $\mathcal{A}_2 < 1$ and so we have a range of parameters with no physical solution.

Case 8

In this case we present bifurcation diagram in $\mathcal{A}_2$ for flow coming into region 2 (*i.e.* $\mathcal{U}_2 = -0.6$) for $\mathcal{A}_1 = 1$ and $\mathcal{U}_1 = 0$. The system exhibits LRRS, LSRS and LSRR as shown in Figure 2.28.

For low $\mathcal{A}_2$ the system exhibits LRRS, while for large $\mathcal{A}_2$ the system exhibits LSRR similar to cases 1 to 3. The LSRS lies between the LRRS and LSRR. For the general tube law (Figure 2.28a) we see that the LSRS solution occupies a smaller region compared to the expanding tube law (Figure 2.28b).

2.13.5 Overview of parameter space

We summarise the behaviour of the entire system as before by plotting the parameter space which shows the different solutions generated along the bifurcation diagram given different values of our variables. Here, we present a parameter space plot spanned by $\mathcal{U}_2$ and $\mathcal{A}_2$ for fixed $\mathcal{U}_1 = 0$ and $\mathcal{A}_1 = 1$ as in Section 2.12 of Chapter 2. As usual we use same colour scheme, where green dots denote LRRS, red dots denote LSRS, blue dots denote LRRR, cyan dots denote LSRR while open green circle denote no solution. Figure 2.29 illustrates the parameter space of our system for general tube law (see Figure 2.29a) and expanding tube law (see Figure 2.29b). We see that both figures share both qualitative and quantitative similarity, the only difference is that with the general tube law, the region with no solution is absent as the general tube law allows the tube to resist collapse and prevent contact. This shows that

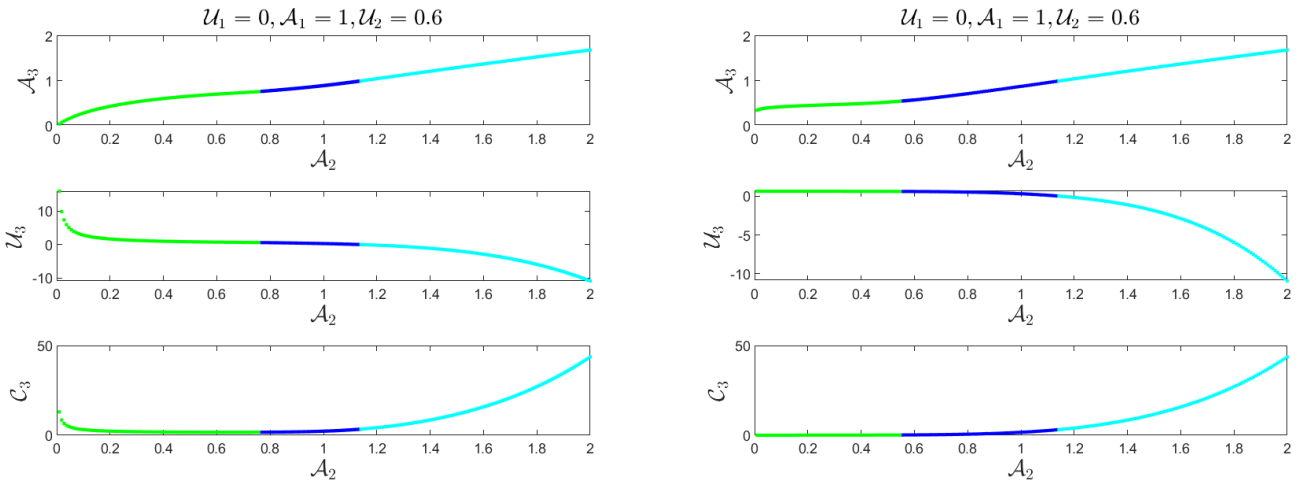

;

(a) **(b)**

Figure 2.26: Bifurcation plot of unique solutions at $\mathcal{U}_2 = 0.6$ with corresponding values of $\mathcal{A}_3$, $\mathcal{U}_3$, $\mathcal{C}_3$, $\mathcal{A}_2$. Figure 2.26(a) displays the the cross-sectional area, flow speed and wave speed of the unique solutions with general tube law and Figure 2.26(b) displays the the cross-sectional area, flow speed and wave speed of the unique solutions with expanding tube law.

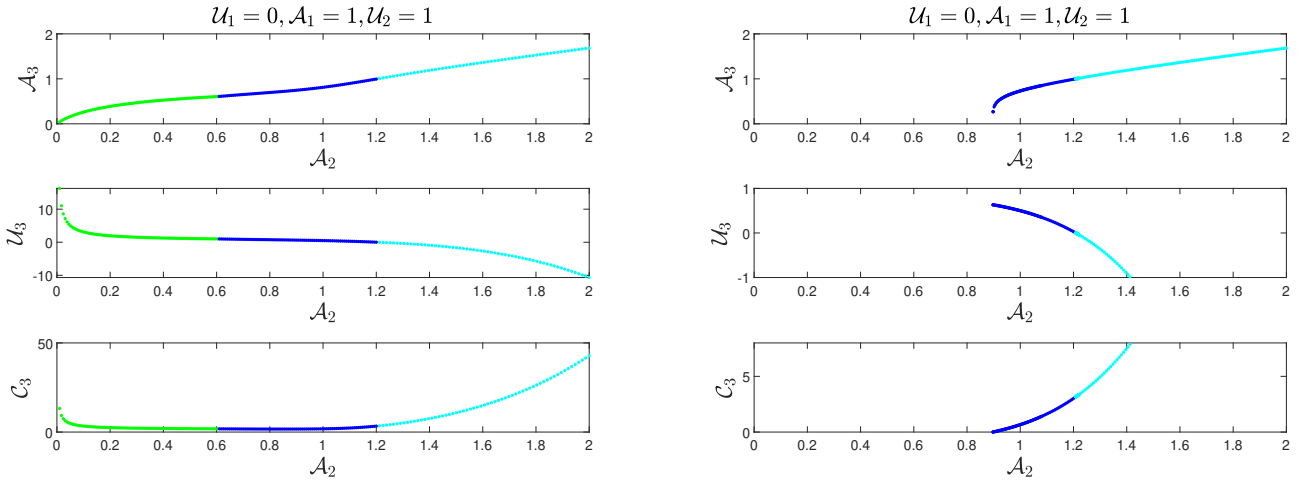

;

(a) **(b)**

Figure 2.27: Bifurcation plot of unique solutions at $\mathcal{U}_2 = 1$ with corresponding values of $\mathcal{A}_3$, $\mathcal{U}_3$, $\mathcal{C}_3$, $\mathcal{A}_2$. Figure 2.27(a) displays the the cross-sectional area, flow speed and wave speed of the unique solutions with general tube law and Figure 2.27(b) displays the the cross-sectional area, flow speed and wave speed of the unique solutions with expanding tube law.

the using the general tube law eliminates some of the unusual solutions seen with the expanding tube

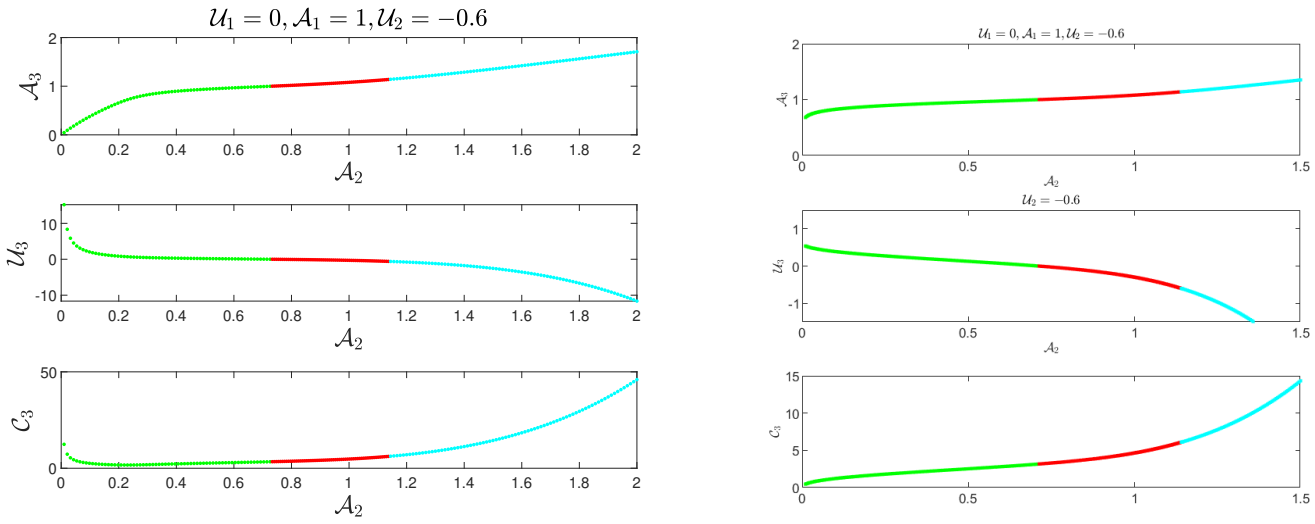

;

(a) **(b)**

Figure 2.28: Bifurcation plot of unique solutions at $\mathcal{U}_2 = -0.6$ with corresponding values of $\mathcal{A}_3$, $\mathcal{U}_3$, $\mathcal{C}_3$, $\mathcal{A}_2$. Figure 2.28(a) displays the the cross-sectional area, flow speed and wave speed of the unique solutions with general tube law and Figure 2.28(b) displays the the cross-sectional area, flow speed and wave speed of the unique solutions with expanding tube law.

law.

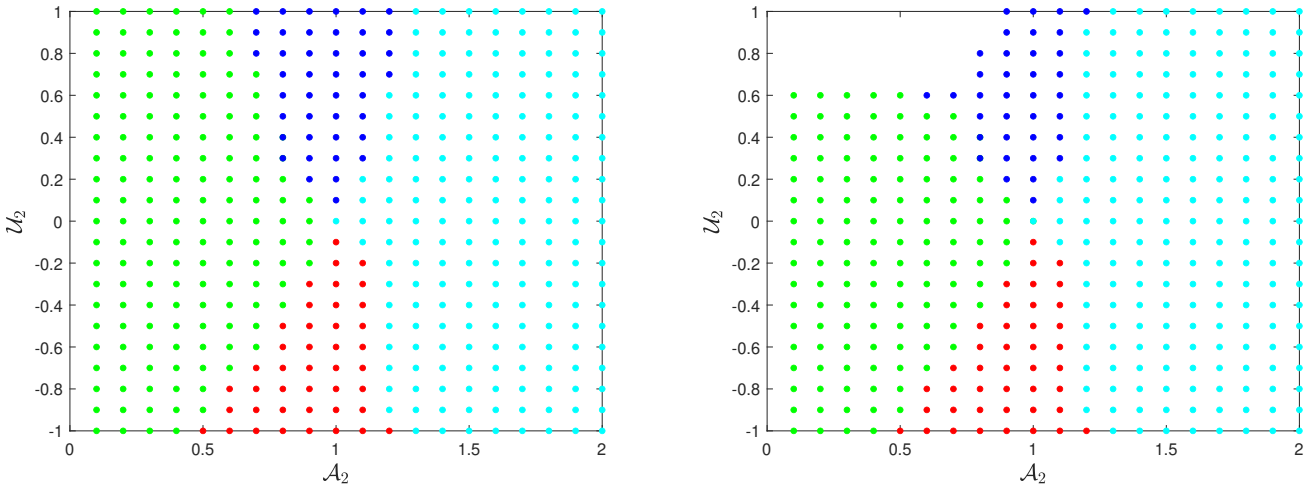

Figure 2.29: Overview of parameter space for vessel with uniform material properties using the expanding and general tube law showing only physical solutions and regions of no solution. Figure 2.29(a) is for general tube law showing all four classical solutions while Figure 2.29(b) is for expanding tube law showing all four classical solutions and a white space denoting region of no solution.

2.14 Summary and conclusion

In this chapter we have constructed solutions to the Riemann problem in a single collapsible tube with uniform material properties, as a simple mathematical model for blood flow in the central retinal vessels along the optic nerve (Note, that the boundary conditions used in this study are not physiologically relevant). We considered the response to an instantaneous discontinuity in flow and tube cross-sectional area across an interface, examining the subsequent wave propagation. We identified four possible flow structures that can emerge in response to the discontinuity, similar to Brook et al. [44] but using a new approach based on Newton's method to solve the nonlinear system of equations. We compared this with the algorithm of Brook et al. [44], showing that the flow profiles generated by the two methods are qualitatively similar for the cases considered (Figure 2.18).

Furthermore, we described the system using bifurcation diagrams constructed as a function of the cross-sectional area of the tube for downstream while fixing other parameters (Figure 2.11). The bifurcation diagrams (from our Newton's method) showed existence of multiple solutions and no solutions for sufficiently large flow in or out of the tube at the downstream end (Figure 2.12). However, we further showed that at most only one solution is ever physical for the cases tested.

We then merged these bifurcation diagrams into an overview of the parameter space, highlighting the regions with multiple solutions and showing that the region with no solution are confined to large $\mathcal{U}_2$ and low $\mathcal{A}_2$ (Figure 2.18). We examined the same parameter space using the algorithm of Brook et al. [44], showing that their method exhibited large regions where it did not converge for sufficiently large $\mathcal{U}_2$, close to the regions where our method exhibited multiple or no solutions.

Furthermore, we illustrate the parameter space plot for different values of the exponent m. We saw that with reduction in value of m, the behaviour of the different cases are qualitatively similar, with

the only difference been that there was reduction in the regions of no solution as m decreases.

Finally, we extended our system using the general tube law which also resists collapse. The four classical solutions now span the entire parameter space.

Our work in this chapter is significant as our numerical method was able to identify one physical solution (*i.e.* unique solution) with any given initial or far-field conditions updating the result from Sheng et al. [115] where their solutions lose uniqueness having up to three solutions for each initial condition which is due to flow becoming supercritical. Also, our Newton's method showed existence of more solutions when compared with the algorithm by Brook et al. [44] where across the parameter space, they had regions where their solutions embed a two cycle as the iterations proceed and so their is no converged solution. But in our method we again showed existence of only one solution, except the case where the tube become fully collapsed in the case when we used the expanding tube law. Finally, we extended our results to the general tube law (for veins) where we showed that only one solution remained physical as states with zero cross-sectional area are not admitted, neither as initial condition, nor as the evolving solution of the Riemann problem similar to the work of Spiller et al. [86]. We advanced the study to explore the entire parameter space using this general tube law and showed uniqueness of solution in the entire parameter space.

We now proceed to examine how this behaviour changes when the vessel has a discontinuity in material properties coincident with the discontinuity applied to the initial condition.

CHAPTER 3

A blood vessel with discontinuous material properties

In Chapter 2 of the thesis we considered the Riemann problem associated with blood flow in a long blood vessel with uniform material properties. We now extend this work to consider blood flow in a vessel with an abrupt change in material properties, coincident with the point of initial discontinuity in the Riemann problem. Such a set-up is reminiscent of the human eye, where blood flows along the central retinal vessels within the optic nerve and crosses through the lamina cribosa into the retina itself. Across this junction the central retinal artery and vein experience a jump in external environment, where each vessel is effectively less stiff as it is no longer tightly adhered by the optic nerve fibres. We seek to understand how this abrupt discontinuity in material properties can influence the resulting flow.

3.1 Model setup

In this chapter, similar to Chapter 2, we consider blood flow along a blood vessel. This vessel is divided into two long compartments, each of length L^*, arranged in series, with baseline cross-sectional areas $\bar{A}_1^*$ and $\bar{A}_2^*$, respectively, not necessarily equal. We label these as compartments 1 and 2, respectively. This vessel is further described using cylindrical polar coordinates (r^*, θ, x^*). Note that in this chapter the term compartment will be used to describe the two pieces of the tube with different material properties, while the term region will be used to describe the different pieces of the Riemann problem (as in Chapter 2). These compartments are joined together at a single point which we denote as $x^* = 0$, so the inlet is at $x^* = -L^*$ and outlet is at $x^* = L^*$.

As in Chapter 2, flow along the vessels is assumed to be homogeneous and inviscid. Also the density of the blood is again assumed constant and equal in both compartments, denoted ρ^*. However, the tube walls are assumed to be of different elastic stiffness between compartments, denoted as k_1^* and k_2^* respectively.

We assume the vessel walls have radii of $r^* = R_j^*(\theta, x^*, t^*)$ $(j = 1, 2)$ respectively, where t^* is time. Lastly, we denote the (uniform) baseline external pressure applied to the two compartments as p_{e1}^* and p_{e2}^*, respectively. We assume that each compartment exhibits a steady baseline pressure distribution $\bar{p_j}^*$ $(j = 1, 2)$. Note that the regions can differ in baseline cross sectional area $(\bar{A}_1^*, \bar{A}_2^*)$, external pressure

Parameter	**Compartment** 1	**Compartment** 2
Baseline cross-sectional area	$\bar{A}_1^*$	$\bar{A}_2^*$
Wall stiffness	k_1^*	k_2^*
Blood density	ρ^*	ρ^*
External pressure	p_{e1}^*	p_{e2}^*

Table 3.1: Summary of dimensional parameters in both compartments

Variable	**Compartment** 1	**Compartment** 2
Vessel cross-sectional area	$A_1^*(x,t)$	$A_2^*(x,t)$
Flow velocity	$\boldsymbol{u}_1^*(x,t)$	$\boldsymbol{u}_2^*(x,t)$
Fluid pressure	$p_1^*(x,t)$	$p_2^*(x,t)$
Vessel radius	$R_1^*(x,t)$	$R_2^*(x,t)$

Table 3.2: Summary of dimensional variables in both compartments

(p_{e1}^*, p_{e2}^*), and wall stiffness (k_1^*, k_2^*). The response of the flow to these step changes in material and environmental properties are investigated below.

3.1.1 Dimensional parameters, variables and equations

The model equations are identical to those presented in Section 2.1 of Chapter 2 with the only exception that the tube law for each region takes the modified form

$$p_j^* = p_{ej}^* + k_j^* f\left(A_j^*/\bar{A}_j^*\right), \quad (j = 1, 2), \tag{3.1}$$

where we use the same functional form for each compartment.

3.1.2 Non dimensionalization and final governing equations

We non-dimensionalize the governing equations with respect to the properties of compartment 1. In particular we non-dimensionalize all lengths on the square root of the baseline cross sectional area in compartment 1, $(\bar{A}_1^*)^{\frac{1}{2}}$, velocities on $\boldsymbol{u}^* = \left(\frac{k_1^*}{\rho^*}\right)^{\frac{1}{2}}$, time on $T^* = \left(\frac{\rho^* \bar{A}_1^*}{k_1^*}\right)^{\frac{1}{2}}$ and pressures on the stiffness in compartment 1 according to $p_j^* = k_1^* p_j + \bar{p}_{10}^*$, where $\bar{p}_{10}^*$ is the baseline pressure at the outlet to compartment 2 (at $x = L^*$). The dimensionless variables and parameters are denoted with the same symbol as that of their dimensional counterpart without the asterisks. The dimensionless tube laws in each compartment take the form

$$p_1 = \bar{p}_{e1} + f(A_1), \tag{3.2}$$

$$p_2 = \bar{p}_{e2} + k f\left(A_2/\bar{A}_2\right), \tag{3.3}$$

Description	parameters
Baseline cross-sectional area in compartment 2	$\bar{A}_2 = \frac{A_2^*}{A_1^*}$
Baseline pressure in compartment 2	$\bar{p}_2 = \frac{p_2^* - p_0^*}{k_1^*}$
External pressure in compartment 1	$\bar{p}_{e1} = \frac{p_{e1}^* - p_0^*}{k_1^*}$
External pressure in compartment 2	$\bar{p}_{e2} = \frac{p_{e2}^* - p_0^*}{k_1^*}$
Wall stiffness	$k = \frac{k_2^*}{k_1^*}$
Length of compartment 1	$L_1 = \frac{L_1^*}{\sqrt{A_1^*}}$
Length of compartment 2	$L_2 = \frac{L_2^*}{\sqrt{A_1^*}}$

Table 3.3: Summary of dimensionless parameters

where the other dimensionless parameters take the form

$$k = \frac{k_2^*}{k_1^*}, \quad \bar{p}_{e1} = \frac{p_{e1}^* - \bar{p}_{10}^*}{k_1^*}, \quad \bar{p}_{e2} = \frac{p_{e2}^* - \bar{p}_{10}^*}{k_1^*}. \tag{3.4}$$

The corresponding dimensionless compartment lengths and baseline cross-sectional areas take the form

$$L_1 = \frac{L_1^*}{\sqrt{\bar{A}_1^*}}, \quad L_2 = \frac{L_2^*}{\sqrt{\bar{A}_1^*}}, \quad \bar{A}_2 = \frac{\bar{A}_2^*}{\bar{A}_1^*}. \tag{3.5}$$

The non-dimensional fluid equations in each compartment take the form ($j = 1, 2$)

$$\nabla \cdot \boldsymbol{u}_j = 0, \tag{3.6}$$

$$\frac{\partial \boldsymbol{u}_j}{\partial t} + \boldsymbol{u}_j \cdot \nabla \boldsymbol{u}_j = -\nabla p_j, \tag{3.7}$$

where $\boldsymbol{u}_j = u_{rj}\mathbf{r} + u_{\theta j}\boldsymbol{\theta} + u_{xj}\boldsymbol{x}$ is the fluid velocity vector and p_j is the fluid pressure in compartment j. In tandem, the dimensionless kinematic condition takes the form

$$u_{rj} = \frac{\partial R_j}{\partial t} + \frac{u_{\theta j}}{R_j}\frac{\partial R_j}{\partial \theta} + u_{xj}\frac{\partial R_j}{\partial x}, \quad (r_j = R_j). \tag{3.8}$$

The list of dimensionless parameters is given in Table 3.3. Henceforth we assume the flow is axis-symmetric, so $u_{\theta j} = 0$ and all variables are independent of θ. Hence, we can express the model in terms of the cross-sectional area of the circular profile $A_j = \pi R_j^2$ ($j = 1, 2$). Also, similar to Chapter 2, we assume long-wavelength plug flow in both compartments such that the flow is uni-directional with $\boldsymbol{u}_{xj}(x, r, t) = u_{xj}(x, t)\hat{\boldsymbol{x}}$. Following an identical method to Chapter 2, we derive nonlinear governing equations in the form

$$\frac{\partial A_j}{\partial t} + \frac{\partial}{\partial x}(A_j u_j) = 0, \tag{3.9}$$

$$\frac{\partial}{\partial t}(A_j u_j) + \frac{\partial}{\partial x}(A_j u_j^2) + A_j \frac{\partial p_j}{\partial x} = 0, \quad (j = 1, 2). \tag{3.10}$$

These equations are subject to dimensionless tube laws in each compartment

$$p_1 = \bar{p}_{e1} + f(A_1), \tag{3.11}$$

$$p_2 = \bar{p}_{e2} + k f(A_2/\bar{A}_2). \tag{3.12}$$

In this first section of this chapter we use a simple tube law similar to that of Chapter 2, such that

$$f(s) = s^m - 1, \tag{3.13}$$

and $m > 0$ is an exponent [44]. A more general tube law, where the tube can strongly resist collapse, will be considered in Section 3.10.

We proceed to discuss the solution to this problem compartment by compartment for easy illustration of our problem.

3.2 Riemann problem

We now consider a Riemann problem, where we impose a spatially uniform initial profile in both compartment 1 and compartment 2, but not necessarily continuous across $x = 0$. At $x = -L$ (inlet to compartment 1) we impose $A_1 = \mathcal{A}_1$, $u_1 = \mathcal{U}_1$, such that through (3.11) the fluid pressure becomes

$$p_1 = \bar{p}_{e1} + (\mathcal{A}_1^m - 1)\,. \tag{3.14}$$

Conversely at $x = L$ (outlet to compartment 2) we impose $A_2 = \mathcal{A}_2$, $u_2 = \mathcal{U}_2$. Also, from (3.12) we have

$$p_2 = \bar{p}_{e2} + k\left(\left(\frac{\mathcal{A}_2}{\bar{A}_2}\right)^m - 1\right). \tag{3.15}$$

3.2.1 Compartment 1

In compartment 1 (upstream) equations (3.9) and (3.10) can be rewritten in the form

$$\left(\frac{\partial u_1}{\partial t} \pm \frac{c_1}{A_1}\frac{\partial A_1}{\partial t}\right) + \left(u_1\frac{\partial u_1}{\partial x} \pm c_1\frac{\partial u_1}{\partial x}\right) + \left(\frac{c_1^2}{A_1}\frac{\partial A_1}{\partial x} \pm \frac{u_1 c_1}{A_1}\frac{\partial A_1}{\partial x}\right) = 0, \tag{3.16}$$

where the nonlinear wavespeed is

$$c_1^2 = m A_1^m. \tag{3.17}$$

Following a similar method to Chapter 2, the system can be further be written as

$$\left(\frac{\partial}{\partial t} + (u_1 \pm c_1)\frac{\partial}{\partial x}\right)\left[u_1 \pm \int_1^{A_1} \frac{c_1}{A^*} dA^*\right] = 0. \tag{3.18}$$

Substituting (3.17) into (3.18) and simplifying, we have

$$\left(\frac{\partial}{\partial t} + (u_1 \pm c_1)\frac{\partial}{\partial x}\right)\left[u_1 \pm \frac{2}{\sqrt{m}}(A_1^{m/2} - 1)\right] = 0. \tag{3.19}$$

This implies that from (3.19), the Riemann invariants for compartment 1 are given as

$$R_1 = u_1 \pm \frac{2}{\sqrt{m}}(A_1^{m/2} - 1), \quad \text{constant on} \quad \frac{dx}{dt} = u_1 \pm \sqrt{m}A_1^{m/2} = u_1 \pm c_1. \tag{3.20}$$

Throughout this chapter we focus primarily on subcritical flow i.e. $|\mathcal{U}_1| < \mathcal{C}_1$ but as we vary the parameters we also cross over into the supercritical regime for some cases.

3.2.2 Compartment 2

Similarly, in compartment 2 equations (3.9) and (3.10), can be written in the form

$$\left(\frac{\partial u_2}{\partial t} \pm \frac{c_2}{A_2}\frac{\partial A_2}{\partial t}\right) + \left(u_2\frac{\partial u_2}{\partial x} \pm c_2\frac{\partial u_2}{\partial x}\right) + \left(\frac{c_2^2}{A_2}\frac{\partial A_2}{\partial x} \pm \frac{u_2 c_2}{A_2}\frac{\partial A_2}{\partial x}\right) = 0, \tag{3.21}$$

with nonlinear wavespeed

$$c_2^2 \;=\; km\left(\frac{A_2}{\bar{A}_2}\right)^m. \tag{3.22}$$

Again, the system can be further written as

$$\left(\frac{\partial}{\partial t} + (u_2 \pm c_2)\frac{\partial}{\partial x}\right)\left[u_2 \pm \int_{\bar{A}_2}^{A_2}\frac{c_2}{A^*}dA^*\right] = 0. \tag{3.23}$$

Substituting (3.22) into (3.23) and simplifying, we have

$$\left(\frac{\partial}{\partial t} + \left(u_2 \pm \sqrt{km}\left(\frac{A_2}{\bar{A}_2}\right)^{m/2}\right)\frac{\partial}{\partial x}\right)\left[u_2 \pm \frac{2\sqrt{k}}{\sqrt{m}}\left(\left(\frac{A_2}{\bar{A}_2}\right)^{m/2} - 1\right)\right] = 0. \tag{3.24}$$

This implies that from (3.24), the Riemann invariants are given as

$$R_2 = u_2 \pm \frac{2\sqrt{k}}{\sqrt{m}}\left(\left(\frac{A_2}{\bar{A}_2}\right)^{m/2} - 1\right), \quad \text{constant on} \quad \frac{dx}{dt} = u_2 \pm \sqrt{km}\left(\frac{A_2}{\bar{A}_2}\right)^{m/2} = u_2 \pm c_2. \tag{3.25}$$

3.2.3 Boundary conditions between compartments

As the material property (stiffness) is discontinuous between the two compartments we cannot impose continuity of all variables across the junction (as in Chapter 2). Instead we impose continuity of fluid flux and continuity of total pressure across the discontinuous point ($x = 0$) (see discussion in Sherwin

et. al. [81]), such that we have

$$A_1 u_1 = A_2 u_2, \quad (x = 0), \tag{3.26}$$

$$\bar{p}_{e1} + ((A_1)^m - 1) + \frac{1}{2}u_1^2 = \bar{p}_{e2} + k\left(\left(\frac{A_2}{\bar{A}_2}\right)^m - 1\right) + \frac{1}{2}u_2^2, \quad (x = 0). \tag{3.27}$$

3.3 Nonlinear flow structure

Far from the point of disturbance the flow will behave in a similar manner to the Riemann problem in a tube with uniform properties (see Chapter 2) *i.e.* the flow will remain in its initial state far from $x = 0$ such that $A_1 \to \mathcal{A}_1, u_1 \to \mathcal{U}_1, c_1 \to \mathcal{C}_1$ for $x \leq (\mathcal{U}_1 - \mathcal{C}_1)t$ and $A_2 \to \mathcal{A}_2, u_2 \to \mathcal{U}_2, c_2 \to \mathcal{C}_2$ for $x \geq (\mathcal{U}_2 + \mathcal{C}_2)t$. Adjacent to the ambient region the flow will either exhibit a rarefaction wave or a shock wave (as discussed in Chapter 2). In the intermediate region between the shock(s)/rarefaction(s) the flow will generally be uniform [114]. However, the presence of the discontinuity in material/environmental properties creates additional difficulties. Firstly, we cannot assume continuity of all variables across $x = 0$. Instead there is a stationary wave across the part of discontinuity (see discussion in Spiller et al. [86]) and we must specify boundary conditions (3.26), and (3.27). In region 3 we denote properties of the flow to the left (right) of the discontinuity with superscript L(R) such that $A_1 = \mathcal{A}_3^L$, $u_1 = \mathcal{U}_3^L$ for $x < 0$ and $A_2 = \mathcal{A}_3^R$, $u_2 = \mathcal{U}_3^R$ for $x > 0$. Note that this structure will change in particular (resonant) cases discussed in Section 3.8 below.

3.3.1 Left Rarefaction

We now consider a left-moving rarefaction in compartment 1. We apply a method analogous to Chapter 2 (see Section 2.6.1) in deriving profiles for cross-sectional area, flow velocity and wave speed, such that we have

$$A_r^L(x,t) = \left(\frac{\sqrt{m}}{(m+2)}\left(\left(\mathcal{U}_1 - \frac{x}{t}\right) + \frac{2\mathcal{C}_1}{m}\right)\right)^{2/m}, \quad \text{where} \quad \mathcal{C}_1 = \sqrt{m}\mathcal{A}_1^{m/2}, \tag{3.28}$$

$$u_r^L(x,t) = \frac{m\mathcal{U}_1}{m+2} + \frac{2\mathcal{C}_1}{m+2} + \frac{2x}{(m+2)t}, \tag{3.29}$$

$$c_r^L(x,t) = \frac{m}{m+2}\left(\left(\mathcal{U}_1 - \frac{x}{t}\right) + \frac{2\mathcal{C}_1}{m}\right). \tag{3.30}$$

From (3.29), if we let $A_r^L = \mathcal{A}_3^L$, $u_r^L = \mathcal{U}_3^L$ and $c_r^L = \mathcal{C}_3^L$ on the edge of the rarefaction adjacent to region 3 (denoted as $x = x_r^L$) such that

$$x = \left(\mathcal{U}_3^L - \mathcal{C}_3^L\right)t. \tag{3.31}$$

Substituting (3.31) into (3.28), we have at the edge of the rarefaction region adjacent to region 3

$$\mathcal{U}_3^L = \mathcal{U}_1 + \frac{2}{\sqrt{m}}\left(\mathcal{A}_1^{m/2} - (\mathcal{A}_3^L)^{m/2}\right), \tag{3.32}$$

a nonlinear constraint which relates $\mathcal{U}_3^L$ and $\mathcal{A}_3^L$ to the initial conditions in region 1.

We note that for the left rarefaction to remain on the left hand side of the domain and be a physical solution, we need

$$\mathcal{A}_1 > \mathcal{A}_3^L, \quad (\mathcal{U}_3^L - \mathcal{C}_3^L) \leq 0 \quad \text{and} \quad (\mathcal{U}_3^L - \mathcal{C}_3^L) > (\mathcal{U}_1 - \mathcal{C}_1). \tag{3.33}$$

Note that this left rarefaction cannot become supercritical, as this would mean that the wave had expanded into a compartment with different material and/or environmental properties. The transcritical case ($\mathcal{U}_3^L = \mathcal{C}_3^L$) is explored in Section 3.7 below.

These physicality conditions can be manipulated into an alternative form. Just inside the left rarefaction we let $x = (\mathcal{U}_1 - \mathcal{C}_1)t + \zeta$ for $\zeta > 0$, where we have

$$A_r^L = \left(\frac{\sqrt{m}\mathcal{U}_1}{(m+2)} + \frac{2\mathcal{C}_1}{\sqrt{m}(m+2)} - \frac{\sqrt{m}\left((\mathcal{U}_1 - \mathcal{C}_1)t + \zeta\right)}{(m+2)t} \right)^{2/m}. \tag{3.34}$$

For $\mathcal{C}_1 = \sqrt{m}\mathcal{A}_1^{m/2}$, equation (3.34) becomes

$$A_r^L = \left(\mathcal{A}_1^{m/2} - \frac{\sqrt{m}\zeta}{t(m+2)} \right)^{2/m} < \mathcal{A}_1. \tag{3.35}$$

Hence, we have the physicality condition $\mathcal{A}_r^L < \mathcal{A}_1$, and rarefaction is associated with a decrease in cross-sectional area.

3.3.2 Right Rarefaction

Similarly we compute the profile of a right rarefaction in compartment 2 by considering the Riemann invariant and characteristics (3.20): applying a similar method to Section 2.6.2 of Chapter 2, the profiles in compartment 2 are given as

$$A_r^R(x,t) = \bar{A}_2 \left(\frac{\sqrt{m}}{\sqrt{k}(m+2)} \left(\left(\frac{x}{t} - \mathcal{U}_2 \right) + \frac{2\mathcal{C}_2}{m} \right) \right)^{2/m}, \quad \text{where} \quad \mathcal{C}_2 = \sqrt{km} \left(\frac{\mathcal{A}_2}{\bar{A}_2} \right)^{m/2}, \tag{3.36}$$

$$u_r^R(x,t) = \frac{m\mathcal{U}_2}{m+2} - \frac{2\mathcal{C}_2}{m+2} + \frac{2x}{(m+2)t}, \tag{3.37}$$

$$c_r^R(x,t) = \frac{m}{m+2} \left(\left(\frac{x}{t} - \mathcal{U}_2 \right) + \frac{2\mathcal{C}_2}{m} \right). \tag{3.38}$$

From (3.37), if we let $A_r^R = \mathcal{A}_3^R$, $u_r^R = \mathcal{U}_3^R$ and $c_r^R = \mathcal{C}_3^R$ on the edge of the rarefaction adjacent to region 3 (denoted as $x = x_r^R$) we have

$$x = \left(\mathcal{U}_3^R + \mathcal{C}_3^R \right) t. \tag{3.39}$$

Substituting (3.39) into (3.36), we have at the edge of the rarefaction region adjacent to region 3

$$\mathcal{U}_3^R = \mathcal{U}_2 + 2\sqrt{\frac{k}{m\bar{A}_2{}^m}} \left(\left(\mathcal{A}_3^R \right)^{m/2} - \mathcal{A}_2^{m/2} \right), \tag{3.40}$$

a nonlinear constraint which relates $\mathcal{U}_3^R$ and $\mathcal{A}_3^R$ to the initial conditions in region 2.

We note that for the right rarefaction to remain on the right hand side of the domain and be a physical solution, we need

$$\mathcal{A}_2 > \mathcal{A}_3^R, \quad (\mathcal{U}_3^R + \mathcal{C}_3^R) > 0 \quad \text{and} \quad (\mathcal{U}_3^R + \mathcal{C}_3^R) < (\mathcal{U}_2 + \mathcal{C}_2). \tag{3.41}$$

Again the right rarefaction cannot encroach into compartment 1.

3.3.3 Left shock

We now consider a left moving shock wave in compartment 1. To ensure conservation of mass and momentum across the shock, we write (3.9) and (3.10) in the form

$$\frac{\partial A_1}{\partial t} + \frac{\partial}{\partial x}(A_1 u_1) = 0, \tag{3.42}$$

$$\frac{\partial}{\partial t}(A_1 u_1) + \frac{\partial}{\partial x}\left(A_1 u_1^2 + \frac{m}{m+1} A_1^{m+1}\right) = 0. \tag{3.43}$$

Applying the method discussed in Chapter 2, for a left moving shock at $x = s_L$ in compartment 1 we have

$$\dot{s}_L = \frac{\mathcal{A}_3^L \mathcal{U}_3^L - \mathcal{A}_1 \mathcal{U}_1}{\mathcal{A}_3^L - \mathcal{A}_1} = \frac{\mathcal{A}_3^L (\mathcal{U}_3^L)^2 + \frac{m}{m+1} \mathcal{A}_3^{L^{m+1}} - \mathcal{A}_1 \mathcal{U}_1^2 - \frac{m}{m+1} \mathcal{A}_1^{m+1}}{\mathcal{A}_3^L \mathcal{U}_3^L - \mathcal{A}_1 \mathcal{U}_1}, \tag{3.44}$$

from which we determine the cross-sectional area to the left of the discontinuity as

$$\mathcal{A}_1 \mathcal{A}_3^L (\mathcal{U}_3^L - \mathcal{U}_1)^2 = \frac{m}{m+1} \left((\mathcal{A}_3^L)^{m+1} - \mathcal{A}_1^{m+1}\right) (\mathcal{A}_3^L - \mathcal{A}_1), \tag{3.45}$$

a nonlinear constraint which relates $\mathcal{U}_3^L$ and $\mathcal{A}_3^L$ to the initial conditions.

Note that for the shock to be a physical solution we must also check against the Lax entropy conditions [116]. For a left shock this means that we need

$$(\mathcal{U}_3^L - \mathcal{C}_3^L) < \dot{s}_L < (\mathcal{U}_1 - \mathcal{C}_1). \tag{3.46}$$

3.3.4 Right shock

Similarly, for a right moving shock wave in compartment 2 we have

$$\dot{s}_R = \frac{\mathcal{A}_2 \mathcal{U}_2 - \mathcal{A}_3^R \mathcal{U}_3^R}{\mathcal{A}_2 - \mathcal{A}_3^R} = \frac{\mathcal{A}_2 (\mathcal{U}_2)^2 + \frac{km}{\bar{A}_2^m (m+1)} \mathcal{A}_2^{m+1} - \mathcal{A}_3^R (\mathcal{U}_3^R)^2 - \frac{km}{\bar{A}_2^m (m+1)} (\mathcal{A}_3^R)^{m+1}}{\mathcal{A}_2 \mathcal{U}_2 - \mathcal{A}_3^R \mathcal{U}_3^R}. \tag{3.47}$$

As before, we compute the two expressions for the shock speed to determine the cross sectional area at the right of the discontinuity relative to the shock as

$$\mathcal{A}_2 \mathcal{A}_3^R (\mathcal{U}_3^R - \mathcal{U}_2)^2 = \frac{km}{(m+1)\bar{A}_2{}^m} \left(\mathcal{A}_2^{m+1} - (\mathcal{A}_3^R)^{m+1}\right) (\mathcal{A}_2 - \mathcal{A}_3^R), \tag{3.48}$$

a nonlinear constraint which relates $\mathcal{U}_3^R$ and $\mathcal{A}_3^R$ to the initial conditions.

Again for physicality of the right shock, we must also check against the Lax entropy conditions [116]. For a right shock this means that we need

$$(\mathcal{U}_2 + \mathcal{C}_2) < \dot{s}_R < (\mathcal{U}_3^R + \mathcal{C}_3^R). \tag{3.49}$$

3.3.5 Boundary conditions

Having determined the flow structure, we can now rewrite the the boundary conditions (3.26) and (3.27) at $x = 0$ in terms of the variables of the Riemann problem in the form

$$\mathcal{U}_3^L \mathcal{A}_3^L = \mathcal{U}_3^R \mathcal{A}_3^R, \tag{3.50}$$

$$\bar{p}_{e1} + \left((\mathcal{A}_3^L)^m - 1\right) + \frac{1}{2}(\mathcal{U}_3^L)^2 = \bar{p}_{e2} + k\left(\left(\frac{\mathcal{A}_3^R}{\bar{A}_2}\right)^m - 1\right) + \frac{1}{2}(\mathcal{U}_3^R)^2. \tag{3.51}$$

3.4 Numerical method

The analysis that follows applies to discontinuities in the material and environmental properties between compartments 1 and 2 which we collect in the vector $\mathbf{r}_j (j = 1, 2)$, comparing the vessel stiffness, the baseline cross-sectional area and the external pressure, so that $\mathbf{r}_1 = (1, 1, \bar{p}_{e1})$ and $\mathbf{r}_2 = (k, \bar{A}_2, \bar{p}_{e2})$.

Similar to Chapter 2, we expect the solution admits modified versions of the four classical solutions which are sketched in Figure 3.1. Here we apply Newton's method similar to Section 2.8 of Chapter 2 to solve for these four possible wave structures: for each wave structure (see Figure 3.1) we determine the values of $\mathcal{A}_3^L$ and $\mathcal{A}_3^R$ as a function of the initial conditions. In particular: for a left rarefaction, right shock (LRRS), (see Figure 3.1a), we use equations (3.32) and (3.48); for a left shock, right rarefaction (LSRR), (see Figure 3.1b), we use equations (3.45) and (3.40); for left shock right shock (LSRS), (see Figure 3.1c), we use (3.45) and (3.48); for a left rarefaction, right rarefaction (LRRR) (see Figure 3.1d), we use equations (3.32) and (3.40). For each of these cases, we assume continuity of fluid flux (3.50) and continuity of total pressure (3.51) across the point of discontinuity to ensure enough information to determine all the variables. We again check that the computed solution profile satisfies the physicality conditions for a rarefaction (3.33), (3.41) and that for a shock (3.46), (3.49). Note that in all wave structures we prescribe $L = 1$, such that $-1 \leq x \leq 1$ although this does not influence the behaviour of the solution in any way.

In general we treat $\mathcal{A}_1$ and $\mathcal{U}_1$ (and $\mathcal{A}_2$ and $\mathcal{U}_2$) as independent quantities. However, in the special case where the initial condition mimicks a propagating shock wave originating from the far left of the domain (*e.g.* like in Spelman & Stewart 2020 [16]) we must choose $\mathcal{U}_1$ as a function of $\mathcal{A}_1$ to ensure that the fluid on the right of this (hypothetical) shock would be undisturbed before arriving at the boundary.

3.5 Simple connection across the discontinuity: no resonance

In this section, we present analysis of the four baseline cases where the system exhibits one type of discontinuity in material properties *i.e.* discontinuity in elastic stiffness at $x = 0$ by setting $k = 1.1$. This is analogous to our earlier predictions in a tube with uniform elastic properties (see Section 2.7) where the system does not exhibit any kind of discontinuity in material properties. With this discontinuity at $x = 0$, we cannot impose continuity of all variables across $x = 0$ as in Section 2.7, rather we impose

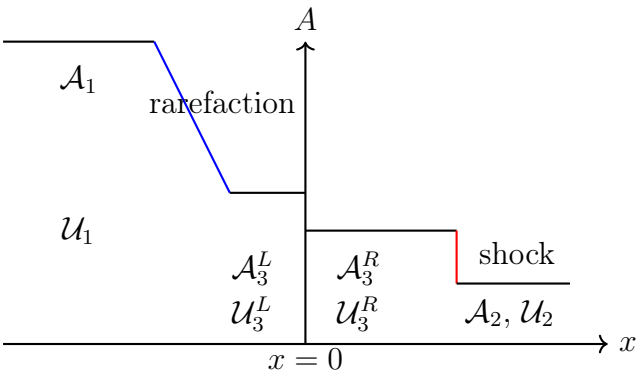

(a) Sketch of left rarefaction and right shock.

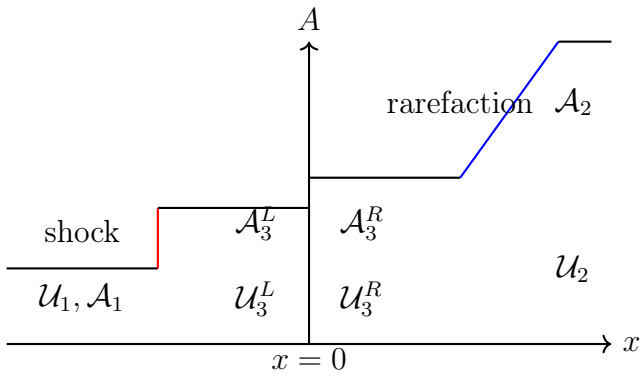

(b) Sketch of left shock and right rarefaction.

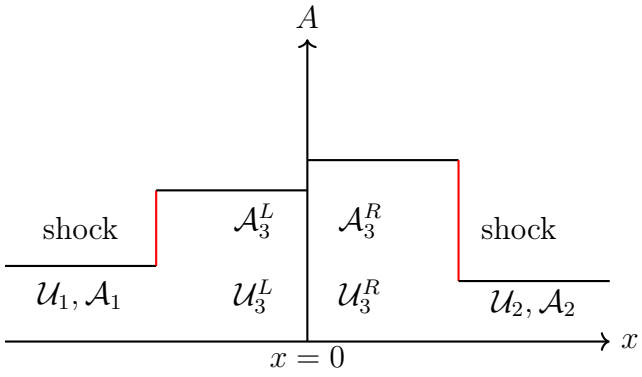

(c) Sketch of left shock and right shock.

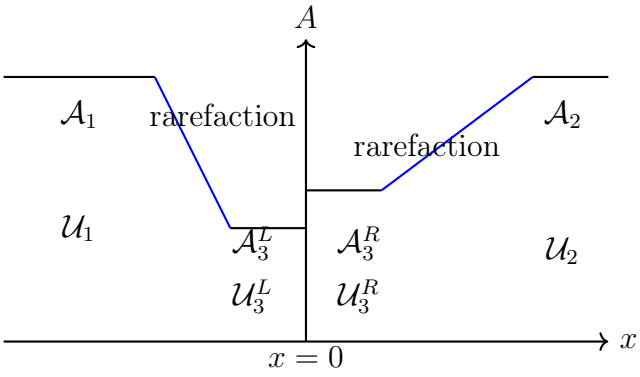

(d) Sketch of left rarefaction and right rarefaction.

Figure 3.1: Illustrations of the possible wave profiles generated due to discontinuity in elastic stiffness across $x = 0$.

continuity of flux and total pressure at $x = 0$. We consider in turn: left rarefaction and right shock, denoted as LRRS (see Section 3.5.1, compared to Section 2.8.1); left shock and right rarefaction, denoted as LSRR (see Section 3.5.2, compared to Section 2.8.2); left shock and right shock denoted as LSRS (see Section 3.5.3, compared to Section 2.8.3); left rarefaction and right rarefaction denoted as LRRR (see Section 3.5.4, compared to Section 2.8.4). We use the same colour scheme as used in Chapter 2 (Section 2.11). Also, throughout we will be applying the physicality conditions for rarefactions (3.33), (3.41) and shocks (3.46), (3.49) in all our solutions thereby avoiding any non-physical solutions. Note that in later sections we elucidate new resonant cases not present in a tube with uniform properties which occur when a rarefaction becomes transcritical. We now consider each case in turn where we choose for each case $\bar{p}_{e1} = \bar{p}_{e2} = 0$, $\bar{A}_2 = 1$.

3.5.1 Left rarefaction, right shock

We consider a left rarefaction wave in compartment 1 and a right shock wave in compartment 2 (LRRS), applying equations (3.32) and (3.48) imposing continuous flux and continuous total pressure across the junction between compartments as in equations (3.50) and (3.51). We present an example of such

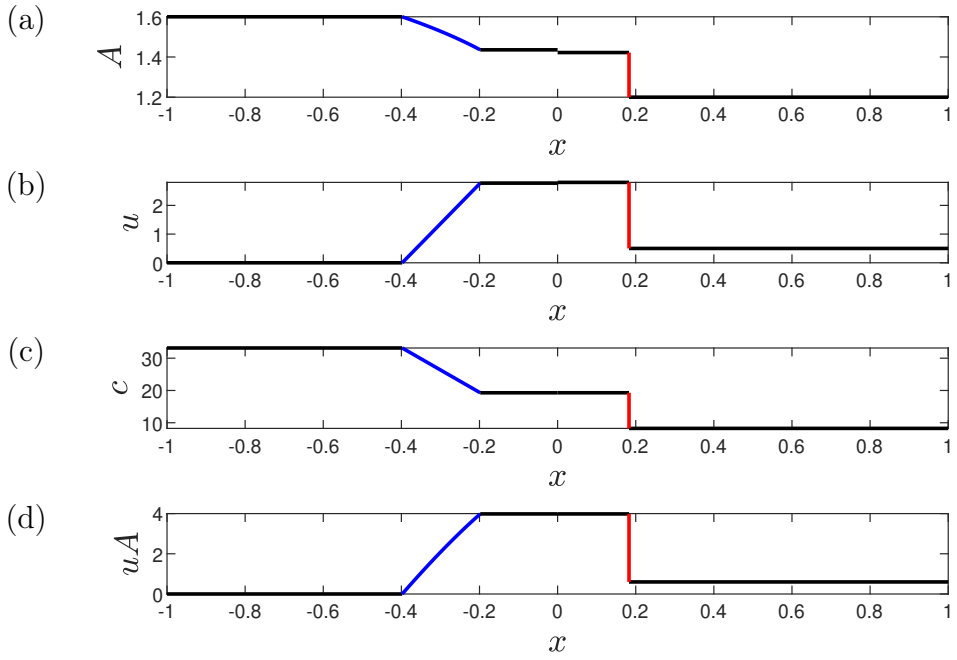

Figure 3.2: Left rarefaction, right shock with discontinuity at $x = 0$. Figure 3.2(a) displays profile of cross-sectional area, Figure 3.2(b), displays profile of flow speed, Figure 3.2(c) displays profile of the wave speed and Figure 3.2(d) Left rarefaction, right shock showing continuity of flux at $x = 0$. We choose $\mathcal{A}_1 = 1.6$, $\mathcal{A}_2 = 1.2$, $\mathcal{U}_1 = 0$, $\mathcal{U}_2 = 0.5$, $k = 1.1$ and using Newton's method we compute $\mathcal{A}_3^L = 1.436$, $\mathcal{A}_3^R = 1.422$ and $\mathcal{U}_3^L = 2.775$, $\mathcal{U}_3^R = 2.801$ at $t = 0.012$.

behaviour for $\mathcal{A}_1 = 1.6$, $\mathcal{A}_2 = 1.2$, $\mathcal{U}_1 = 0$, $\mathcal{U}_2 = 0.5$, $\bar{p}_{e1} = \bar{p}_{e2} = 0$, $k = 1.1$, where using Newton's method we compute $\mathcal{A}_3^L = 1.436$, $\mathcal{A}_3^R = 1.422$ and $\mathcal{U}_3^L = 2.775$, $\mathcal{U}_3^R = 2.801$ with typical profiles shown in Figure 3.2. As expected, we have a left moving rarefaction in compartment 1 and a right moving shock in compartment 2 separated by a contact discontinuity (stationary wave) at $x = 0$ which results in an expansion of the tube cross-sectional area and a reduction in flow speed from compartment 1 to compartment 2. Figure 3.2(d) demonstrates continuity of flux as the profile crosses between the compartments.

3.5.2 Left shock, right rarefaction

We consider a left shock wave in region 1 and a right rarefaction wave in region 2 (LSRR), applying equations (3.45) and (3.40) and assume continuous flux and continuous total pressure as in equations (3.50) and (3.51). We present an example of such behaviour for $\mathcal{A}_1 = 1$, $\mathcal{A}_2 = 1.4$, $\mathcal{U}_1 = 0$, $\mathcal{U}_2 = 0.1$, $\bar{p}_{e1} = \bar{p}_{e2} = 0$, $k = 1.1$ where using Newton's method we compute $\mathcal{A}_3^L = 1.257$, $\mathcal{A}_3^R = 1.247$ and $\mathcal{U}_3^L = -1.458$, $\mathcal{U}_3^R = -1.471$; a typical profile is shown in Figure 3.3 where, as expected, we have a left moving shock in compartment 1 and a right moving rarefaction in compartment 2 which is separated by a contact discontinuity at $x = 0$, resulting in a slight compression in the tube cross-sectional area

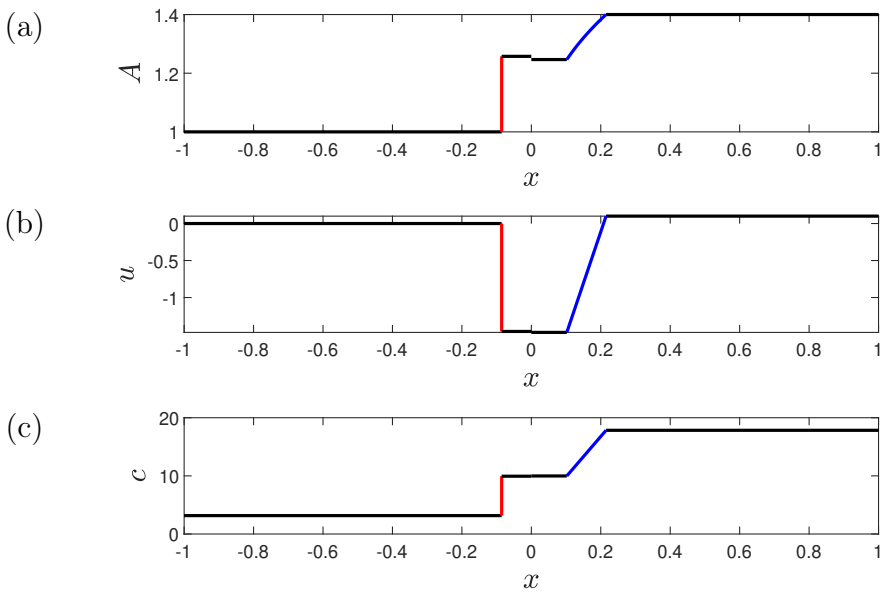

Figure 3.3: Left shock, right rarefaction with discontinuity at $x = 0$. Figure 3.3(a) displays profile of cross-sectional area; Figure 3.3(b) displays profile of flow speed and Figure 3.3(c) displays profile of the wave speed. We choose $\mathcal{A}_1 = 1.0$, $\mathcal{A}_2 = 1.4$, $\mathcal{U}_1 = 0$, $\mathcal{U}_2 = 0.1$, $k_2 = 1.1$ and using Newton's method we compute $\mathcal{A}_3^L = 1.257$, $\mathcal{A}_3^R = 1.247$ and $\mathcal{U}_3^L = -1.458$, $\mathcal{U}_3^R = -1.471$ at $t = 0.012$.

from compartment 1 to compartment 2.

3.5.3 Left shock, right shock

We consider a left shock wave in compartment 1 and a right shock wave in compartment 2 (LSRS), solving equations (3.45) and (3.48) assuming continuous flux and continuous total pressure across $x = 0$, as in equations (3.50) and (3.51). We present an example of such behaviour for $\mathcal{A}_1 = 1$, $\mathcal{A}_2 = 1.1$, $\mathcal{U}_1 = 0$, $\mathcal{U}_2 = -0.1$, $\bar{p}_{e1} = \bar{p}_{e2} = 0$, $k = 1.1$ where using Newton's method we compute $\mathcal{A}_3^L = 1.070$, $\mathcal{A}_3^R = 1.065$ and $\mathcal{U}_3^L = -0.258$, $\mathcal{U}_3^R = -0.257$ with typical profiles shown in Figure 3.4, where, as expected, we have a left and right moving shock in compartment 1 and 2, respectively and a contact discontinuity at $x = 0$. The discontinuity at $x = 0$ induces compression in cross-sectional area and corresponding expansion in the wave speed from compartment 1 to compartment 2.

3.5.4 Left rarefaction, right rarefaction

We consider a left rarefaction wave in compartment 1 and a right rarefaction wave in compartment 2 (LRRR), solving equations (3.32) and (3.40) and applying continuous flux and continuous total pressure as in equations (3.50) and (3.51). We show an example such behaviour for $\mathcal{A}_1 = 1.1$, $\mathcal{A}_2 = 1.1$, $\mathcal{U}_1 = 0$, $\mathcal{U}_2 = 0.3$, $\bar{p}_{e1} = \bar{p}_{e2} = 0$, $k = 1.1$ where using Newton's method we compute $\mathcal{A}_3^L = 1.095$, $\mathcal{A}_3^R = 1.037$ and $\mathcal{U}_3^L = 0.024$, $\mathcal{U}_3^R = 0.025$. Typical profiles are shown in Figure 3.5, where we have a left and

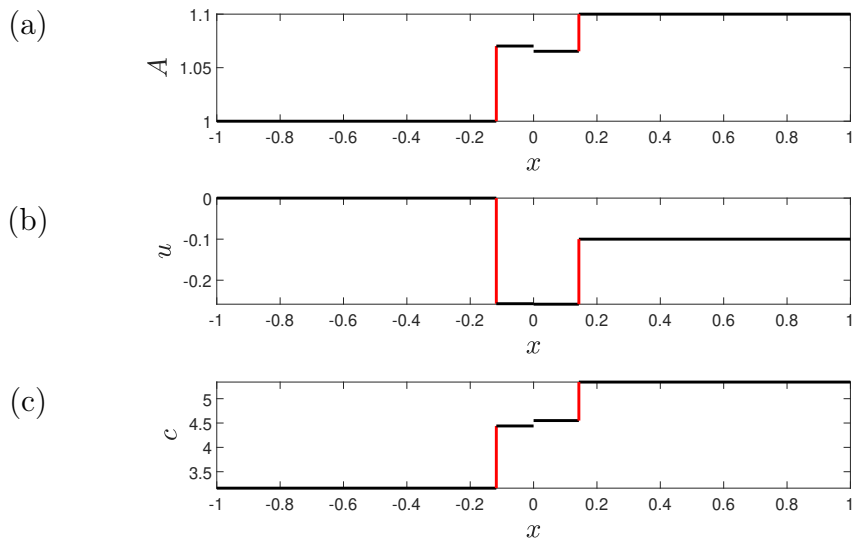

Figure 3.4: Left shock, right shock with discontinuity at $x = 0$. Figure 3.4(a) displays profile of cross-sectional area; Figure 3.4(b) displays profile of flow speed and Figure 3.4(c) displays profile of the wave speed. We choose $\mathcal{A}_1 = 1.0$, $\mathcal{A}_2 = 1.1$, $\mathcal{U}_1 = 0$, $\mathcal{U}_2 = -0.1$, $k = 1.1$ and using Newton's method we compute $\mathcal{A}_3^L = 1.070$, $\mathcal{A}_3^R = 1.065$ and $\mathcal{U}_3^L = -0.258$, $\mathcal{U}_3^R = -0.257$ at $t = 0.03$.

right moving rarefaction in compartment 1 and compartment 2, respectively separated by a contact discontinuity (stationary wave) at $x = 0$ resulting in an expansion in the cross-sectional area of the tube, flow speed and the wave-speed from compartment 1 to compartment 2.

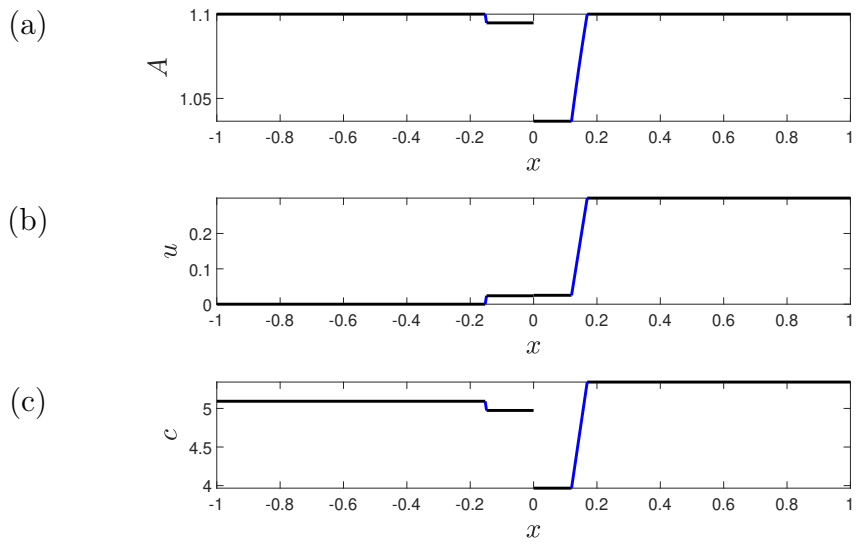

Figure 3.5: Left rarefaction, right rarefaction with discontinuity at $x = 0$. Figure 3.5(a) displays profile of cross-sectional area; Figure 3.5(b) displays profile of flow speed and Figure 3.5(c) displays profile of the wave speed. We choose $\mathcal{A}_1 = 1.1$, $\mathcal{A}_2 = 1.1$, $\mathcal{U}_1 = 0$, $\mathcal{U}_2 = 0.3$, $k = 1.1$ and using Newton's method we compute $\mathcal{A}_3^L = 1.095$, $\mathcal{A}_3^R = 1.037$ and $\mathcal{U}_3^L = 0.024$, $\mathcal{U}_3^R = 0.025$ at $t = 0.13$.

3.6 Small amplitude waves

In this section, we present linearised form of our Riemann problem and compare with the numerical solution of the nonlinear problem to verify the agreement between the two cases. This is done by comparing the amplitude of reflected wave in compartments 1 and 2, respectively.

We start by considering small amplitude perturbations to derive a linearised form of the Riemann problem. In this case it is necessary to set $\bar{A}_2 = 1$, $\bar{p}_{e1} = \bar{p}_{e2} = 0$ for consistency. We consider equations (3.9) and (3.10) and linearise the variables according to

$$A_1 = 1 + \epsilon\hat{A}_1, \quad A_2 = 1 + \epsilon\hat{A}_2, \quad u_1 = \bar{u} + \epsilon\hat{u}_1, \quad u_2 = \bar{u} + \epsilon\hat{u}_2, \quad p_1 = \epsilon\hat{p}_1, \quad p_2 = \epsilon\hat{p}_2, \tag{3.52}$$

where $\epsilon \ll 1$ is a dimensionless perturbation amplitude and $\bar{u}$ is some constant velocity which we choose depending on boundary conditions. Furthermore, we express the Riemann problem boundary conditions as

$$\mathcal{A}_1 = 1 + \epsilon\hat{\mathcal{A}}_1, \quad \mathcal{A}_2 = 1 + \epsilon\hat{\mathcal{A}}_2, \quad \mathcal{U}_1 = \bar{u} + \epsilon\hat{\mathcal{U}}_1, \quad \mathcal{U}_2 = \bar{u} + \epsilon\hat{\mathcal{U}}_2. \tag{3.53}$$

Note, however that in this linearised problem $\hat{\mathcal{A}}_1$ and $\hat{\mathcal{U}}_1$ are coupled together by the governing equations, as are $\hat{\mathcal{A}}_2$ and $\hat{\mathcal{U}}_2$ (*i.e.* they cannot be chosen independently).

We consider only terms of $O(\epsilon)$, where we have for compartment 1

$$\frac{\partial \hat{A}_1}{\partial t} + \bar{u}\frac{\partial \hat{A}_1}{\partial x} + \frac{\partial \hat{u}_1}{\partial x} = 0, \tag{3.54}$$

$$\frac{\partial \hat{u}_1}{\partial t} + \bar{u}\frac{\partial \hat{u}_1}{\partial x} = -\frac{\partial \hat{p}_1}{\partial x}, \tag{3.55}$$

$$\hat{p}_1 = \hat{A}_1 f_1'(1). \tag{3.56}$$

We further differentiate (3.54) with respect to t, and substitute (3.55) to have

$$\frac{\partial^2 \hat{A}_1}{\partial t^2} = \frac{\partial^2}{\partial x^2}(\bar{u}^2 \hat{A}_1 + 2\bar{u}\hat{u}_1) + \frac{\partial^2 \hat{p}_1}{\partial x^2}. \tag{3.57}$$

Similarly, for compartment 2, we have

$$\frac{\partial \hat{A}_2}{\partial t} + \bar{u}\frac{\partial \hat{A}_2}{\partial x} + \frac{\partial \hat{u}_2}{\partial x} = 0, \tag{3.58}$$

$$\frac{\partial \hat{u}_2}{\partial t} + \bar{u}\frac{\partial \hat{u}_2}{\partial x} = -\frac{\partial \hat{p}_2}{\partial x}, \tag{3.59}$$

$$\hat{p}_2 = k\hat{A}_2 f_2'(\bar{A}_2). \tag{3.60}$$

Again, further differentiating (3.58) with respect to t, and substituting (3.59) we have

$$\frac{\partial^2 \hat{A}_2}{\partial t^2} = \frac{\partial^2}{\partial x^2}(\bar{u}^2 \hat{A}_2 + 2\bar{u}\hat{u}_2) + \frac{\partial^2 \hat{p}_2}{\partial x^2}. \tag{3.61}$$

We write both $\hat{p}_1$ and $\hat{p}_2$ in terms of $\hat{A}_1$ and $\hat{A}_2$, respectively, such that we have

$$\frac{\partial^2 \hat{A}_1}{\partial t^2} = \frac{\partial^2}{\partial x^2}(\bar{u}^2 \hat{A}_1 + 2\bar{u}\hat{u}_1) + f_1'(1)\frac{\partial^2 \hat{A}_1}{\partial x^2}. \tag{3.62}$$

$$\frac{\partial^2 \hat{A}_2}{\partial t^2} = \frac{\partial^2}{\partial x^2}(\bar{u}^2 \hat{A}_2 + 2\bar{u}\hat{u}_2) + kf_2'(\bar{A}_2)\frac{\partial^2 \hat{A}_2}{\partial x^2}. \tag{3.63}$$

For $\bar{u} = 0$ in both (3.62) and (3.63) we have

$$\frac{\partial^2 \hat{A}_1}{\partial t^2} = f_1'(1)\frac{\partial^2 \hat{A}_1}{\partial x^2} = c_1^2\frac{\partial^2 \hat{A}_1}{\partial x^2}, \tag{3.64}$$

$$\frac{\partial^2 \hat{A}_2}{\partial t^2} = kf_2'(\bar{A}_2)\frac{\partial^2 \hat{A}_2}{\partial x^2} = c_2^2\frac{\partial^2 \hat{A}_2}{\partial x^2}, \tag{3.65}$$

where $c_1 = \sqrt{f_1'(1)}$ and $c_2 = \sqrt{kf_2'(\bar{A}_2)}$ are the linearised wavespeeds in compartments 1 and 2.

We now proceed to solve (3.64) and (3.65), by looking for a travelling wave solution of the form $z = x \pm c_j t$ such that for a cross-sectional area profile of amplitude $\hat{\mathcal{A}}_j$ For compartment 1, the profiles

of the incoming wave in compartment 1 take the form

$$\hat{A}_1 = \hat{\mathcal{A}}_1 g_1(t - x/c_1), \tag{3.66}$$
$$\hat{p}_1 = \hat{\mathcal{A}}_1 f_1'(1) g_1(t - x/c_1), \tag{3.67}$$
$$\hat{u}_1 = \hat{\mathcal{A}}_1 \frac{f_1'(1)}{c_1} g_1(t - x/c_1), \tag{3.68}$$

where $g_1(t - x/c_1)$ is the form of the wave determined by the initial conditions and (3.66)-(3.68).

For the reflected wave in compartment 1, we have the amplitude given as $\hat{\mathcal{A}}_1^L$ such that the profiles are given as

$$\hat{A}_3 = \hat{\mathcal{A}}_1^L g_2(t + x/c_1), \tag{3.69}$$
$$\hat{p}_3 = \hat{\mathcal{A}}_1^L f_1'(1) g_2(t + x/c_1), \tag{3.70}$$
$$\hat{u}_3 = -\hat{\mathcal{A}}_1^L \frac{f_1'(1)}{c_1} g_2(t + x/c_1), \tag{3.71}$$

where $g_2(t + x/c_1)$ is the form of the wave in compartment 1 also determined by the initial conditions and (3.72)-(3.74) is the reflected wave in compartment 1. Note that once the wave has reflected the total wave in compartment 1 is the superposition of the incident wave $\hat{\mathcal{A}}_1$ and reflected wave $\hat{\mathcal{A}}_1^L$ which we denote as $\hat{\mathcal{A}}_3^L$ as an analogue to our solution in region 3 of the Riemann problem.

For compartment 2, we have from (3.65)

$$\hat{A}_2 = \hat{\mathcal{A}}_2 g_3(t - x/c_2), \tag{3.72}$$
$$\hat{p}_2 = \hat{\mathcal{A}}_2 k f_2'(\bar{A}_2) g_3(t - x/c_2), \tag{3.73}$$
$$\hat{u}_2 = \hat{\mathcal{A}}_2 \frac{k f_2'(\bar{A}_2)}{c_2} g_3(t - x/c_2), \tag{3.74}$$

where $g_3(t - x/c_2)$ is the form of the wave in compartment 2 also determined by the initial conditions.

We match the waves across the discontinuous point $x = 0$ by first linearizing the continuity of flux (3.26) and continuity of total pressure (3.27) and with $\bar{u} = 0$, to have

$$\hat{u}_1 = \hat{u}_2, \quad (x = 0), \tag{3.75}$$
$$\hat{p}_1 = \hat{p}_2, \quad (x = 0). \tag{3.76}$$

To match at $x = 0$, we substitute (3.68) into (3.75) and (3.67) into (3.76) to have

$$\hat{\mathcal{A}}_1 \sqrt{f_1'(1)} g_1(t) - \hat{\mathcal{A}}_1^L \sqrt{f_1'(1)} g_2(t) = \hat{\mathcal{A}}_3^R \sqrt{k f_2'(\bar{A}_2)} g_3(t), \tag{3.77}$$
$$\hat{\mathcal{A}}_1 f_1'(1) g_1(t) + \hat{\mathcal{A}}_1^L f_1'(1) g_2(t) = \hat{\mathcal{A}}_3^R k f_2'(\bar{A}_2) g_3(t). \tag{3.78}$$

For consistency we require $g_1(t) = g_2(t) = g_3(t)$ and solving (3.77) and (3.78) simultaneously we

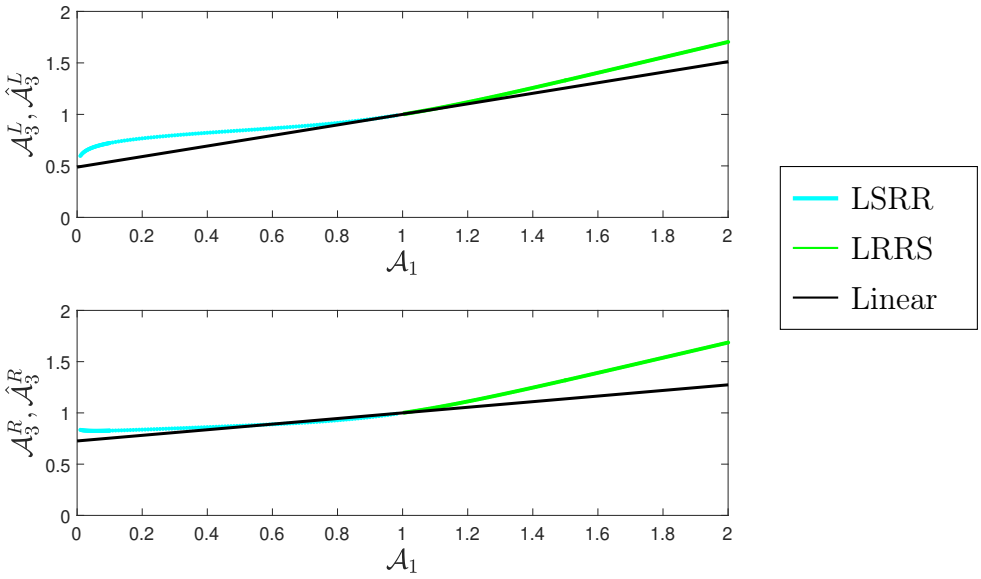

Figure 3.6: Bifurcation diagram showing comparison with linear and nonlinear case of our wave profile.

have

$$\hat{\mathcal{A}}_3^L = \frac{2\bar{\mathcal{A}}_1 k f_2'(\bar{A}_2)}{k f_2'(\bar{A}_2) + \sqrt{k f_2'(\bar{A}_2)}\sqrt{f_1'(1)}}, \tag{3.79}$$

$$\hat{\mathcal{A}}_3^R = \frac{2\bar{\mathcal{A}}_1 f_1'(1)}{k f_2'(\bar{A}_2) + \sqrt{k f_2'(\bar{A}_2)}\sqrt{f_1'(1)}}. \tag{3.80}$$

In Figure 3.6 we present a comparison between the linear and our nonlinear theory described through the amplitude of reflected wave in compartments 1 and 2. The numerical solution of the nonlinear system was presented along a slice of the parameter space, tracing a bifurcation diagram using $\mathcal{A}_1$ as a bifurcation parameter. Here, we fix $\mathcal{A}_2 = 1$, $\mathcal{U}_1 = 0$, $\mathcal{U}_2 = 0$, $k = 1.1$ while varying $\mathcal{A}_1$. As before, the green and cyan lines denotes the LRRS and LSRR solutions from the nonlinear case, while the black lines denote the wave amplitude in compartments 1 and 2, respectively, from the linearised model. In both cases the linear curves are tangential to the nonlinear curves at the baseline cross-sectional area. This calculation validates our numerical results for the nonlinear Riemann problem.

3.7 Other possible flow states: resonance

So far we have considered the classical wave profiles which are possible for flow in a blood vessel in a response to discontinuity in initial conditions, a direct analog with the cases considered in Chapter 2. In what follows below we observe that these four cases are insufficient to span the parameter space, and there are a number of extra (resonant) cases which arise as a result of the discontunity in material properties as first discussed by Han et. al. [89]. We now consider these resonant cases. It emerges that

a rarefaction wave can expand to fill an entire compartment and become transcritical, resonating with the stationary wave at $x = 0$. For subcritical initial conditions this resonance falls into three broad categories, denoted B, C and D by Han et al. [89] (note that configuration A denotes the classical cases). Each of these is sketched in Figure 3.7, assuming it is a left rarefaction which becomes transcritical. Resonance of a right rarefaction is analogous, and so is not discussed in detail, but a configuration C resonance on the right is evident in some of the examples below.

In configuration B of Han et al. [89], the left rarefaction resonates with the stationary wave and produces an additional rarefaction to the right of the stationary wave. This new produced rarefaction is pinned to the stationary wave at $x = 0$ (see Figure 3.7a). However, it emerges that case B does not appear in any of the examples considered below, and so will not be pursued further.

In configuration C of Han et al. [89] a rarefaction resonates with the stationary wave and produces a transcritical rarefaction alongside three successive waves around the point of discontinuity an infinitesimal distance $\epsilon \ll 1$ apart, alongside a classical wave (shock or rarefaction) on the other side. For a transcritical left rarefaction these waves are successively a supercritical stationary wave at $(x = -\epsilon)$, a zero speed shock $(x = 0)$ and a subcritical stationary wave at $(x = \epsilon)$ (Figure 3.7b). Conversely, when a right rarefaction resonates with the stationary wave and produces a right transcritical rarefaction, the three successive waves are reversed *i.e.* a supercritical stationary wave $(x = \epsilon)$, a zero speed shock $(x = 0)$ and a subcritical stationary wave $(x = -\epsilon)$ (see Figure 3.8). The two cases of configuration C (*i.e.* transcritical left rarefaction or transcritical right rarefaction) plays major role in completing the gaps created as a result of resonance and we will explore these solutions in detail below.

Furthermore, we also consider configuration D of Han et al. [109], where a rarefaction resonates with the stationary wave, resulting in an additional propagating shock wave which moves away from the stationary wave (see Figure 3.9). In particular, we mainly focus on a transcritical left rarefaction which generates a new right-moving shock in addition to the original right propagating wave. Configuration D also plays a vital role in filling the gap left by the claasical cases..

In what follows, we present the Riemann solutions for configurations C and D, and subsequently show how these solutions fill the gaps in our bifurcation diagram not covered by the classical cases.

3.7.1 Governing equations for configuration C

Configuration C, as shown in Figure 3.8, arises when either a left or right rarefaction becomes transcritical and resonates with the stationary wave. Here, we consider a resonating left rarefaction, but did not consider a resonating right rarefaction as the solution is analogous to left resonating rarafaction.

Following instances from Han et. al. [89], around the point discontinuity we must have three successive waves each separated by a small distance $\epsilon \ll 1$; from left to right we have a supercritical stationary wave, a zero speed shock, and a subcritical stationary wave, as shown in Figure 3.8. Note that a stationary wave is considered to be subcritical (supercritical) if the flow on both sides of that wave is subcritical (supercritical). Between these waves we assume the vector of vessel material and environmental properties $\mathbf{r}_s = (k_s, \bar{A}_s, \bar{p}_{es})$ takes an intermediate value between the left values $\mathbf{r}_1 = (1, 1, \bar{p}_{e1})$ and right values $\mathbf{r}_2 = (k, \bar{A}_2, \bar{p}_{e2})$. This intermediate value is chosen across the transition zone such that it spans between the two outer regions. In particular we assume a linear interpolation such that $\mathbf{r}_s = \mathbf{r}_1 + s(\mathbf{r}_2 - \mathbf{r}_1)$, where $0 \leq s \leq 1$, so that $s = 0$ corresponds to compartment 1 and $s = 1$ corresponds to compartment 2. Note that s needs to be determined as part of the solutions.

Following equations (3.28), (3.29) and (3.30) we have profiles for cross-sectional area, flow speed and wave speed across the transcritical rarefaction given as

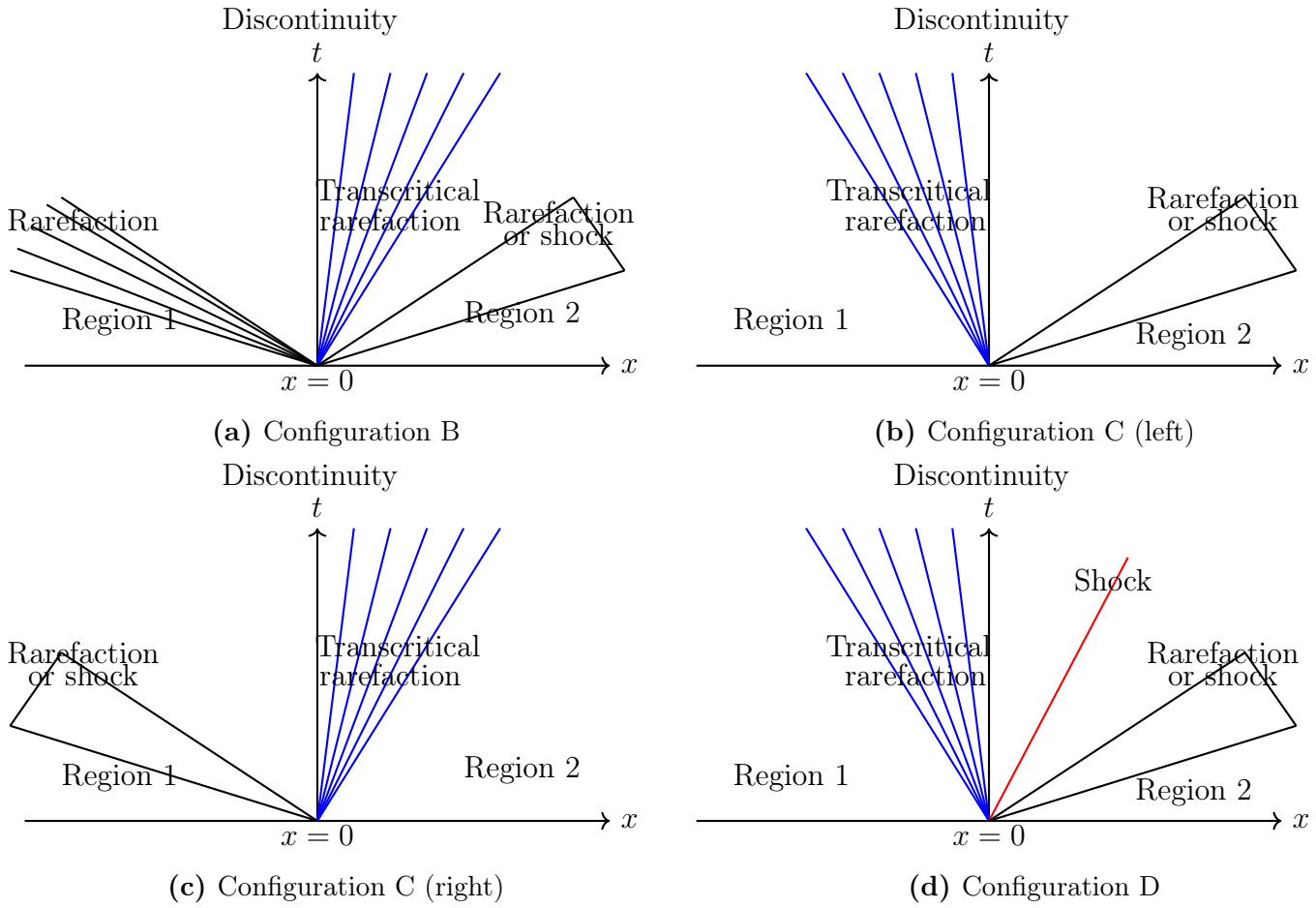

(a) Configuration B

(b) Configuration C (left)

(c) Configuration C (right)

(d) Configuration D

Figure 3.7: Sketch of possible resonance cases: Left rarefaction crossing the contact discontinuity into compartment 2. Figure 3.7(a) shows configuration B, Figure 3.7(b) shows configuration C with a left transcritical rarefaction, Figure 3.7(c) shows Configuration C with a right transcritical rarefaction, Figure 3.7(d) shows configuration D with left transcritical rarefaction.

$$A_r^L(x,t) = \left(\frac{\sqrt{m}\mathcal{U}_1}{(m+2)} + \frac{2\mathcal{C}_1}{\sqrt{m}(m+2)} - \frac{\sqrt{m}x}{(m+2)t}\right)^{2/m}, \tag{3.81}$$

$$u_r^L(x,t) = \frac{m\mathcal{U}_1}{m+2} + \frac{2\mathcal{C}_1}{m+2} + \frac{2x}{(m+2)t}, \tag{3.82}$$

$$c_r^L(x,t) = \frac{m\mathcal{U}_1}{m+2} + \frac{2\mathcal{C}_1}{m+2} - \frac{mx}{(m+2)t}, \tag{3.83}$$

which span all the way to $x = -\epsilon$.

At the left edge of the supercritical stationary wave (i.e. $x = -\epsilon$), we denote $A_r^L = \mathcal{A}_3^L$, $u_r^L = \mathcal{U}_3^L$

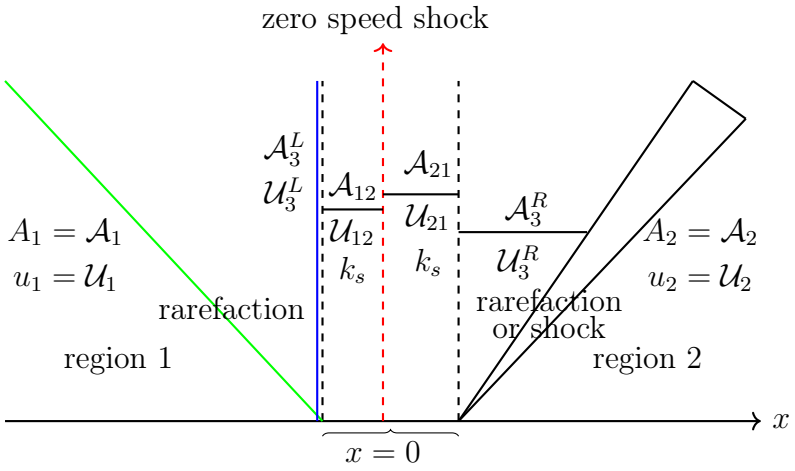

Figure 3.8: Sketch of the Riemann problem for configuration C according to [89], where the green line represent the edge of the left rarefaction in region 1, while the blue line is the outer edge rarefaction in region 3

.

and $c_r^L = \mathcal{C}_3^L$, such that the profiles (3.81)-(3.83) becomes

$$\mathcal{A}_3^L = \left(\frac{\sqrt{m}\mathcal{U}_1}{(m+2)} + \frac{2\mathcal{C}_1}{\sqrt{m}(m+2)}\right)^{2/m} + \mathcal{O}(\epsilon), \tag{3.84}$$

$$\mathcal{U}_3^L = \mathcal{C}_3^L = \frac{m\mathcal{U}_1}{m+2} + \frac{2\mathcal{C}_1}{m+2} + +\mathcal{O}(\epsilon). \tag{3.85}$$

Furthermore, we denote the profiles of cross-sectional area, velocity and wavespeed on the right side of the supercritical stationary wave ($x > -\epsilon$) as $A_1 = \mathcal{A}_{12}$, $u_1 = \mathcal{U}_{12}$ and $c_1 = \mathcal{C}_{12}$, respectively. So, across the supercritical stationary wave we impose continuity of flux and total pressure (*i.e.* conditions (3.26) and (3.27)) to have

$$\mathcal{A}_3^L\mathcal{U}_3^L = \mathcal{A}_{12}\mathcal{U}_{12}, \tag{3.86}$$

$$\bar{p}_{e1} + \frac{1}{2}(\mathcal{U}_3^L)^2 + ((\mathcal{A}_3^L)^m - 1) = \bar{p}_{es} + \frac{1}{2}(\mathcal{U}_{12})^2 + k_s\left(\left(\frac{\mathcal{A}_{12}}{\bar{A}_s}\right)^m - 1\right), \tag{3.87}$$

where we note that the parameter s which sets the material and environmental properties in the intermediate region, is still to be determined.

To the right of the zero speed shock we denote the (uniform) profiles of cross-sectional area, velocity and wavespeed as $\mathcal{A}_{21}$, $\mathcal{U}_{21}$ and $\mathcal{C}_{21}$, respectively. Across the zero speed shock we invoke conservation of mass and momentum to have the shock front as

$$\dot{s_{res}} = \frac{\mathcal{A}_{21}\mathcal{U}_{21} - \mathcal{A}_{12}\mathcal{U}_{12}}{\mathcal{A}_{21} - \mathcal{A}_{12}}, \tag{3.88}$$

$$\dot{s_{res}} = \frac{\mathcal{A}_{21}(\mathcal{U}_{21})^2 - \mathcal{A}_{12}(\mathcal{U}_{12})^2 + \frac{k_s m}{m+1}\left(((\mathcal{A}_{21})^{m+1}) - (\mathcal{A}_{12})^{m+1}\right)}{\mathcal{A}_{21}\mathcal{U}_{21} - \mathcal{A}_{12}\mathcal{U}_{12}}, \tag{3.89}$$

where $\dot{s}_{res}$ is shock speed to the right of the stationary wave resulting from resonance of the left rarefaction.

Equating equations (3.88) and (3.89) and simplifying, we have

$$\mathcal{U}_{21} = \mathcal{U}_{12} \pm \sqrt{\frac{k_s m \left((\mathcal{A}_{21})^{m+1} - (\mathcal{A}_{12})^{m+1}\right)(\mathcal{A}_{21} - \mathcal{A}_{12})}{\mathcal{A}_{21}\mathcal{A}_{12}(m+1)}}, \tag{3.90}$$

a nonlinear equation connecting $\mathcal{A}_{21}$ to $\mathcal{U}_{21}$, involving the material and environmental properties of the intermediate region.

To the right of the subcritical stationary wave we denote the (uniform) profile as $A_2 = \mathcal{A}_3^R$, $u_2 = \mathcal{U}_3^R$ and $c_2 = \mathcal{C}_3^R$ analogous to the previous cases. Across the subcritical stationary wave, we further impose continuity of flux and total pressure (*i.e.* conditions (3.26) and (3.27)) to have

$$\mathcal{A}_3^R \mathcal{U}_3^R = \mathcal{A}_{21}\mathcal{U}_{21}, \tag{3.91}$$

$$\bar{p}_{es} + \frac{1}{2}(\mathcal{U}_{21})^2 + k_s\left(\left(\frac{\mathcal{A}_{21}}{\bar{A}_s}\right)^m - 1\right) = \bar{p}_{e2} + \frac{1}{2}(\mathcal{U}_3^R)^2 + k\left(\left(\frac{\mathcal{A}_3^R}{\bar{A}_2}\right)^m - 1\right). \tag{3.92}$$

It then follows that the (uniform) flow to the right of the stationary waves (*i.e.* $x > \epsilon$) is connected to the far-field in region 2 by either a shock or a rarefaction.

For a shock at the edge of region 2, we employ equation (3.48) to write $\mathcal{U}_3^R$ as a function of $\mathcal{A}_3^R$, and apply the necessary physicality conditions. For configuration C with a right shock to be a physical solution, we apply physicality conditions as

$$\begin{aligned} (\mathcal{U}_3^L - \mathcal{C}_3^L) > (\mathcal{U}_1 - \mathcal{C}_1), \qquad & (\mathcal{U}_{12} - \mathcal{C}_{12}) > (\mathcal{U}_3^L - \mathcal{C}_3^L), \\ (\mathcal{U}_2 + \mathcal{C}_2) < \dot{s} < (\mathcal{U}_3^R + \mathcal{C}_3^R), \qquad & 0 \le s \le 1. \end{aligned} \tag{3.93}$$

Conversely, for a rarefaction adjoining region 2 we employ equation (3.40) to write $\mathcal{U}_3^R$ as a function of $\mathcal{A}_3^R$ and apply physicality conditions.

$$\begin{aligned} (\mathcal{U}_3^L - \mathcal{C}_3^L) > (\mathcal{U}_1 - \mathcal{C}_1), \qquad & (\mathcal{U}_{12} - \mathcal{C}_{12}) > (\mathcal{U}_3^L - \mathcal{C}_3^L), \\ (\mathcal{U}_3^R + \mathcal{C}_3^R) < (\mathcal{U}_2 + \mathcal{C}_2), \qquad & 0 \le s \le 1. \end{aligned} \tag{3.94}$$

3.7.2 Governing equations for configuration D

Configuration D is sketched in Figure 3.9 and arises when the left rarefaction resonates with the stationary wave and generates a new wave on the right side of the stationary wave, while the transcritical left rarefaction remains in contact with the stationary wave. In our results below we only ever see a new shock produced to the right of the discontinuity, so we only consider the Riemann solution when a propagating shock is produced. Han et. al. [89] also discussed the case with a new rarefaction generated to the right, but this is omitted here as it does not produce meaningful solutions for any of the parameter considered here.

In this case the transcritical left rarefaction profile, as in configuration C, is given by equations (3.81), (3.82) and (3.83), respectively. Also at the edge of the transcritical left rarefaction, similar to

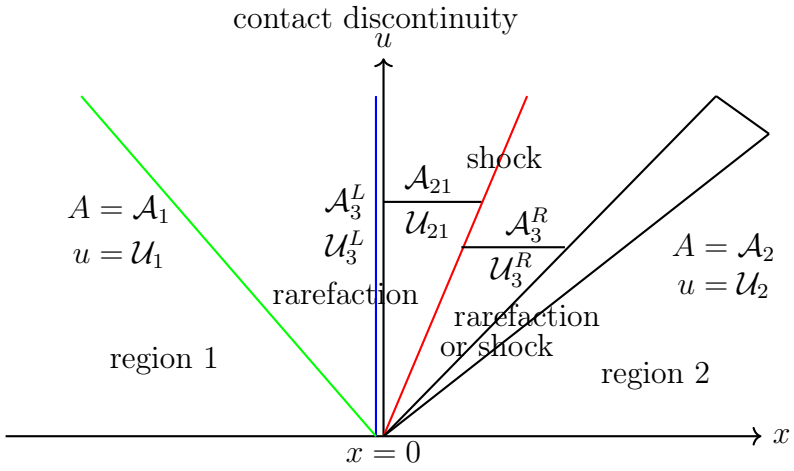

Figure 3.9: Sketch of the Riemann problem for configuration D following Han et al. [89]

configuration C, we let $A_r^L = \mathcal{A}_3^L$, $u_r^L = \mathcal{U}_3^L$ and $c_r^L = \mathcal{C}_3^L$ such that we have

$$\mathcal{A}_3^L = \left(\frac{\sqrt{m}\mathcal{U}_1}{(m+2)} + \frac{2\mathcal{C}_1}{\sqrt{m}(m+2)}\right)^{2/m}, \tag{3.95}$$

$$\mathcal{U}_3^L = \mathcal{C}_3^L = \frac{m\mathcal{U}_1}{m+2} + \frac{2\mathcal{C}_1}{m+2}. \tag{3.96}$$

Denoting the profiles of cross-sectional area, velocity and wavespeed in the region between the stationary wave and the new shock (generated by the resonance) as $A_2 = \mathcal{A}_{21}$, $u_2 = \mathcal{U}_{21}$ and $c_2 = \mathcal{C}_{21}$, we impose the continuity of flux and continuity of total pressure across the contact discontinuity at $x = 0$ to have

$$\mathcal{A}_3^L\mathcal{U}_3^L = \mathcal{A}_{21}\mathcal{U}_{21}, \tag{3.97}$$

$$\bar{p}_{e1} + \frac{1}{2}(\mathcal{U}_3^L)^2 + \left((\mathcal{A}_3^L)^m - 1\right) = \bar{p}_{e2} + \frac{1}{2}(\mathcal{U}_{21})^2 + k\left(\left(\frac{\mathcal{A}_{21}}{\bar{A}_2}\right)^m - 1\right). \tag{3.98}$$

Across the newly generated shock, we invoke conservation of mass and momentum across the front at $x = s_{res}$ in the form

$$\dot{s}_{res} = \frac{\mathcal{A}_3^R\mathcal{U}_3^R - \mathcal{A}_{21}\mathcal{U}_{21}}{\mathcal{A}_{22} - \mathcal{A}_{21}}, \tag{3.99}$$

$$\dot{s}_{res} = \frac{\mathcal{A}_3^R(\mathcal{U}_3^R)^2 - \mathcal{A}_{21}(\mathcal{U}_{21})^2 + \frac{km}{\bar{A}_2^m(m+1)}\left((\mathcal{A}_3^R)^{m+1} - (\mathcal{A}_{21})^{m+1}\right)}{\mathcal{A}_3^R\mathcal{U}_3^R - \mathcal{A}_{21}\mathcal{U}_{21}}. \tag{3.100}$$

Equating equations (3.99) and (3.100) and simplifying, we have

$$\mathcal{U}_3^R = \mathcal{U}_{21} \pm \sqrt{\frac{km\left((\mathcal{A}_3^R)^{m+1} - (\mathcal{A}_{21})^{m+1}\right)(\mathcal{A}_3^R - \mathcal{A}_{21})}{\mathcal{A}_3^R\mathcal{A}_{21}(m+1)\bar{A}_2^m}}, \tag{3.101}$$

a nonlinear equation connecting $\mathcal{A}_{21}$ to $\mathcal{U}_{21}$.

As in configuration C the second right-moving wave can be either a shock or rarefaction, where we have either (3.48) for a right shock or (3.40) for a right rarefaction.

Note, for configuration D to be a physical solution, we impose the following physicality/Lax conditions if the far right wave is a shock

$$\begin{aligned} (\mathcal{U}_1 - \mathcal{C}_1) < 0, \quad \mathcal{A}_1 > \mathcal{A}_3^L, \qquad & (\mathcal{U}_{21} - \mathcal{C}_{21}) > 0, \\ (\mathcal{U}_3^R - \mathcal{C}_3^R) < \dot{s}_{res} < (\mathcal{U}_{21} - \mathcal{C}_{21}), \qquad & (\mathcal{U}_2 + \mathcal{C}_2) < \dot{s}_R < (\mathcal{U}_3^R + \mathcal{C}_3^R), \end{aligned} \tag{3.102}$$

while if the far right wave is a rarefaction we impose

$$\begin{aligned} (\mathcal{U}_1 - \mathcal{C}_1) < 0, \quad \mathcal{A}_1 > \mathcal{A}_3^L, \qquad & (\mathcal{U}_{21} - \mathcal{C}_{21}) > 0, \\ (\mathcal{U}_3^R - \mathcal{C}_3^R) < \dot{s}_{res} < (\mathcal{U}_{21} - \mathcal{C}_{21}), \qquad & (\mathcal{U}_3^R + \mathcal{C}_3^R) < (\mathcal{U}_2 + \mathcal{C}_2), \end{aligned} \tag{3.103}$$

Note, that the new shock produced in compartment 2 as a resulting of the left rarefaction resonating with the stationary wave must satisfy Lax entropy condition for a shock on the left (despite being on the right hand of the vessel), since the shock was produced from the resonance of a left rarefaction.

3.8 Typical results: Traces through the parameter space

In this section, we summarise the behaviour of our nonlinear system by constructing bifurcation diagrams by plotting properties of the system across region 3 (*e.g.* $\mathcal{A}_3^L, \mathcal{A}_3^R, \mathcal{U}_3^L, \mathcal{U}_3^R$) as a function of one of the far-field parameters. We first vary the initial cross-sectional area far to the right of the discontinuity, $\mathcal{A}_2$, for a tube with discontinuous elastic stiffness, with all other components held fixed (cases 1 to 5). This is followed by varying the cross-sectional area far to the left of the discontinuity, $\mathcal{A}_1$, again for a tube with discontinuous stiffness but with all other components held fixed (cases 6 to 11). We consider both a stiffer compartment 2 ($k = 1.1$ cases 6 to 8 while varying the cross-sectional area in the far right $\mathcal{A}_2$ and that of the far left $\mathcal{A}_1$) and less stiff compartment 2 ($k = 0.9$, cases 9 to 11 while only varying the cross-sectional area to the far left $\mathcal{A}_1$). We consider eleven representative cases as summarised in Table 3.4. We also compare some of these cases with similar cases for a vessel with uniform material properties (Chapter 2).

In each of these cases, the colour scheme remains the same as has been used in vessels with uniform material properties. Also, throughout this section we only plot physical solutions using the physicality conditions for rarefactions and shocks, (3.33), (3.41) and (3.46), (3.49), respectively.

3.8.1 Case 1

In Figure 3.10 we present a bifurcation diagram of region 3 properties as a function of $\mathcal{A}_2$ and corresponding characteristics profiles for a case where compartment 2 is stiffer than compartment 1 ($k = 1.1$) and there is no flow out of both regions 1 and 2 (*i.e.* $\mathcal{U}_1 = \mathcal{U}_2 = 0$) for $\mathcal{A}_1 = 1$, $\bar{A}_2 = 1$ $\bar{p}_{e1} = \bar{p}_{e2} = 0$. Close to $\mathcal{A}_2 = 1$ the behaviour is similar to Figure 2.11, where for $\mathcal{A}_2 < 1$ the system exhibits a LRRS (see characteristics in panel (iii)), while for $\mathcal{A}_2 > 1$ the system exhibits a LSRR (see charateristics in panel (iv)). However, unlike the uniform tube the LRRS branch exhibits a turning point as the left rarefaction becomes transcritical at $\mathcal{A}_2 \approx 0.359$ producing a second (unphysical) branch of LRRS beneath where the left rarefaction moves into compartment 2; this is not possible due to the discontinuity in

Cases	$\mathcal{U}_1$	$\mathcal{U}_2$	$\mathcal{A}_1$	$\mathcal{A}_2$	k
1	0	0	1	vary	1.1
2	-0.5	0	1	vary	1.1
3	0.5	0	1	vary	1.1
4	0	-0.6	1	vary	1.1
5	0	0.6	1	vary	1.1
6	0	0	vary	1	1.1
7	-0.6	0	vary	1	1.1
8	0.6	0	vary	1	1.1
9	0	0	vary	1	0.9
10	-0.6	0	vary	1	0.9
11	0.6	0	vary	1	0.9

Table 3.4: Summary of cases considered.

material properties and hence the solution is not physical. As $\mathcal{A}_2$ decreases below ≈ 0.359 the physical branch of LRRS transitions a configuration C resonance with a transcritical left rarefaction and a right shock (see characteristics in panel (ii)) which further transitions into a class D resonance solution with a transcritical left rarefaction for $\mathcal{A}_2 \approx 0.310$ with two right shocks in compartment 2 (see characteristics in panel (i)).

Across the small range of configuration C resonance evident in Figure 3.10 ($0.310 \leq \mathcal{A}_2 \leq 0.359$) we plot other properties of the system not present in the other cases. In particular, Figure 3.11(a) plots the value of the parameter k_s, showing that it takes the value $k_s = 1$ adjacent to LRRS (so the region between the stationary waves exhibits the properties of compartment 1), ramping almost linearly to $k_s = 1.1$ as the system intersects the configuration D resonance (where the region between the stationary waves shares the properties of compartment 2). Furthermore, the flowspeed and the wavespeed of the transcritical left rarefaction ($\mathcal{U}_3^L$, $\mathcal{C}_3^L$) is equal and this agrees with our ascertion that the flow is critical at the edge of the left transcritical rarefaction (see Figure 3.12a). Also, the flowspeed around the left stationary wave $x = -\epsilon$ is always greater than or equal to the corresponding wavespeed, consistent with our assertion that this stationary wave must be supercritical (see Figure 3.12a) where the speed index is greater than or equal to 1. Similarly, the flowspeed around the right stationary wave ($x = \epsilon$) is less or equal to the corresponding wavespeed, which again is consistent with our assertion that the right stationary wave must be subcritical (see Figure 3.12b) where the wavespeed is less than 1. Finally, we also have that the resonance solution of configuration D persists for all $\mathcal{A}_2$ and this is consequent on the fact that the two shocks on the right are yet to coalesce at a point (see Figure 3.11b). Hence, even with no inflow into compartment 1 and no outflow out from compartment 2, we still have a significantly more complicated flow structure with a change in stiffness between compartments. Solutions of Configuration C and D in subsequent bifurcation diagrams follow similar logic, so we will not be exploring each of them in the same level of detail as this case.

In Figure 3.13, we compare to the corresponding case with uniform material properties. We find that both exhibit the same flows close to $\mathcal{A}_2 = 1$, but for uniform material properties the LRRS solution remains unique and persists for all $\mathcal{A}_2 < 1$ (see Figure 3.13b). Conversely, for a tube with discontinuous stiffness the LRRS in Figure 3.13(a) does not persist for all $\mathcal{A}_2$ but transitions into a class C and class

D resonant solutions, respectively. Hence for $\mathcal{A}_2 > 1$ solutions for both the tube with uniform material properties and that with discontinuity in stiffness are both qualitatively and quantitatively similar.

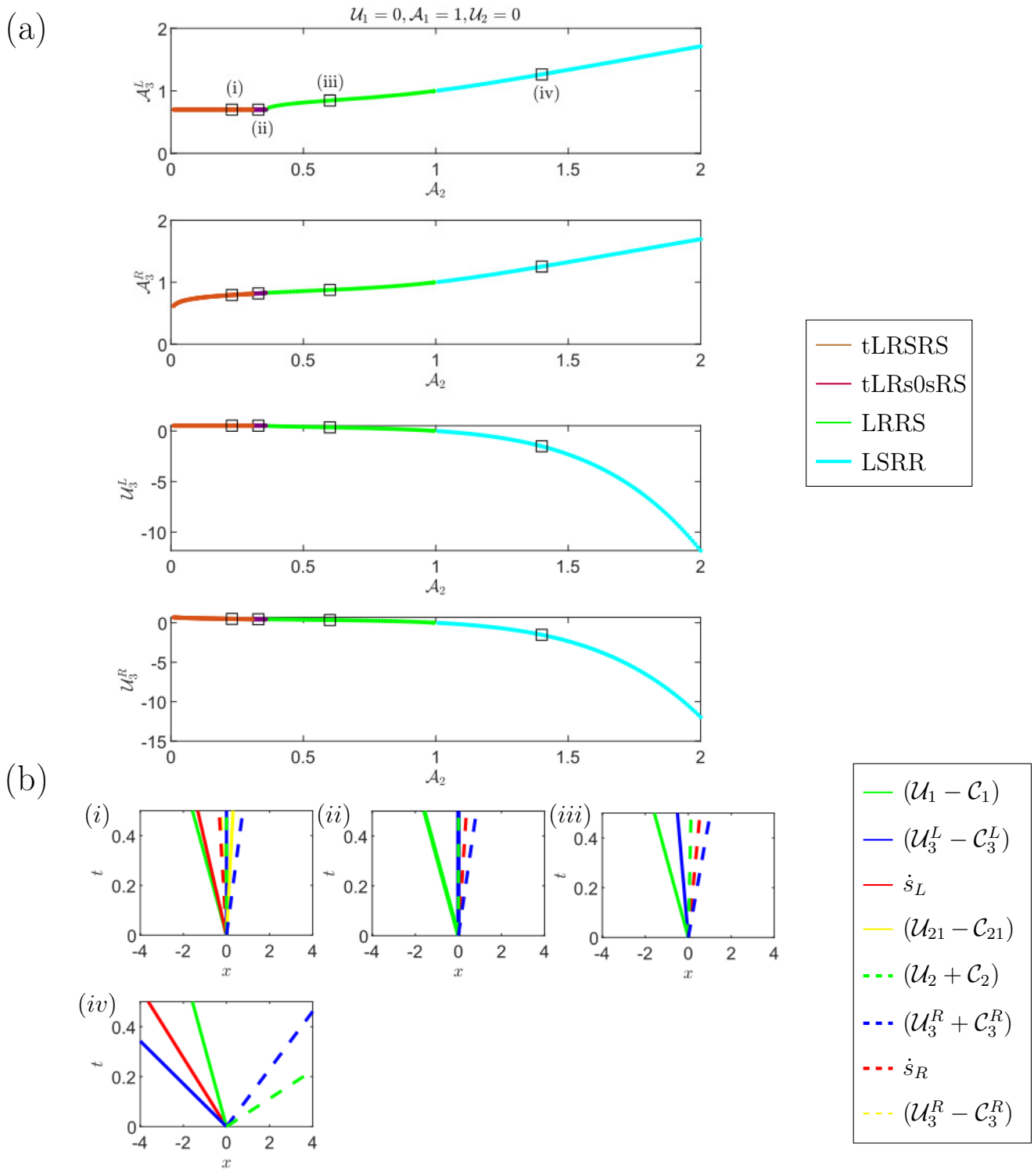

Figure 3.10: Case 1: Bifurcation plot and characteristics profile plot of physical solutions at $\mathcal{U}_1 = 0$ and $\mathcal{U}_2 = 0$ with corresponding values of $\mathcal{A}_2$, $\mathcal{A}_3^L$, and $\mathcal{A}_3^R$, respectively. Figure 3.10(a) displays the the cross-sectional area, and flow speed of the physical solutions with different points of $\mathcal{A}_2$ marked as (i) to (iv) such that (i) denotes $\mathcal{A}_2 = 0.23$, (ii) denotes $\mathcal{A}_2 = 0.33$, (iii) denotes $\mathcal{A}_2 = 0.62$ and (iv) denotes $\mathcal{A}_2 = 1.38$. Figure 3.10(b) shows the corresponding characteristics values of these different values of $\mathcal{A}_2$ from (i) to (iv) with $\mathcal{U}_1 = 0$ and $\mathcal{U}_2 = 0$.

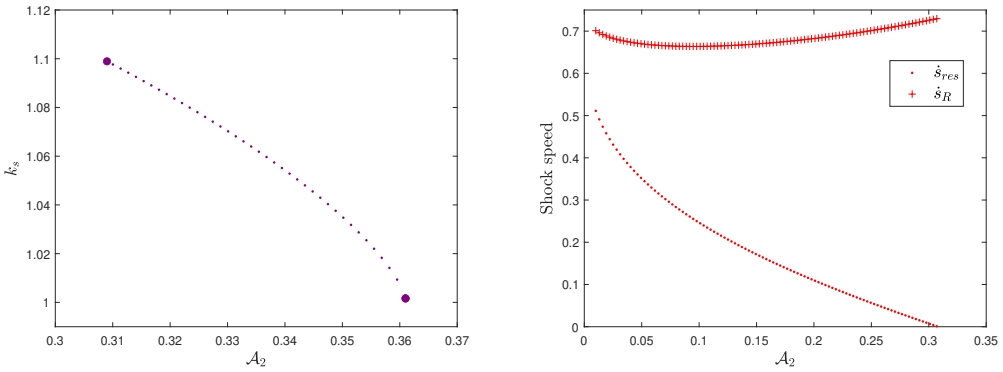

(a) **(b)**

Figure 3.11: Illustration of configuration C and D. Figure 3.11(a) shows the range of the intermediate stiffness k_s lying between 1 and 1.1 while Figure 3.11(b) shows the shock speeds $\dot{s}_{res}$, $\dot{s}_R$, respectively of configuration D.

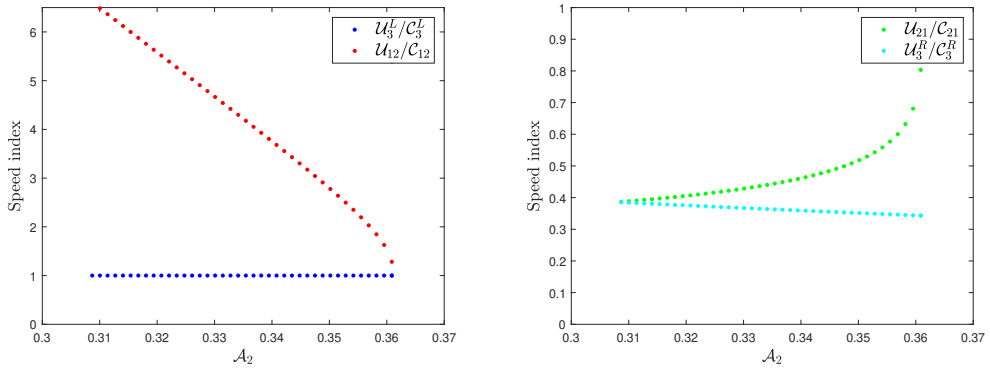

(a) **(b)**

Figure 3.12: Configuration C showing supercritical and subcritical region around $x = 0$. Figure 3.12(a) shows that the speed index of $\mathcal{U}_3^L$, $\mathcal{C}_3^L$ (blue dotted line) is 1 hence, critical and that the speed index of $\mathcal{U}_{12}$, $\mathcal{C}_{12}$ (red dotted line) is greater than 1, hence supercritical. Figure 3.12 shows that the speed index of $\mathcal{U}_{21}$, $\mathcal{C}_{21}$ (green dotted line) and $\mathcal{U}_3^R$, $\mathcal{C}_3^R$ (cyan dotted line) are both less than 1, hence subcritical.

3.8.2 Case 2

In Figure 3.14 we consider a bifurcation diagram where there is suction flow out of region 1 and no flow out of region 2 ($\mathcal{U}_1 = -0.5$, $\mathcal{U}_2 = 0$) for $\mathcal{A}_1 = 1$, $\bar{p}_{e1} = \bar{p}_{e2} = 0$, $k = 1.1$ and $\bar{A}_2 = 1$. Across the range of $\mathcal{A}_2$ the system exhibits three out of the four classical profiles LRRS, LRRR and LSRR and two resonance profiles, as shown in Figure 3.14.

For large $\mathcal{A}_2$ the system exhibits a physical branch of LSRR (see characteristics in panel (v)). As $\mathcal{A}_2$ decreases the system transitions to LRRR when $\mathcal{A}_3^L = \mathcal{A}_3^R = 1$ (Figure 3.14a), with typical characteristics shown in panel (iv). As $\mathcal{A}_2$ decreases further the system transitions to a physical branch

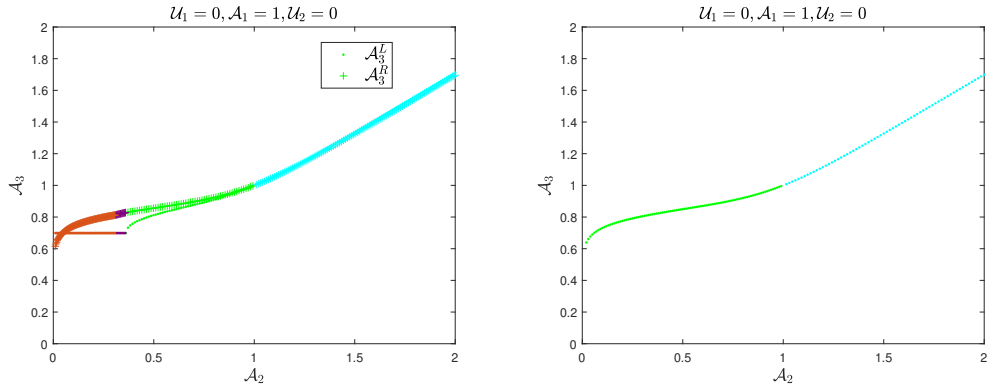

(a) **(b)**

Figure 3.13: Comparison of bifurcation diagram of tube with discontinuous material properties and tube with uniform material properties for $\mathcal{U}_1 = 0$ and $\mathcal{U}_2 = 0$. Figure 3.13(a) shows the bifurcation diagram of tube with discontinuous material properties. While Figure 3.13(b) shows the bifurcation diagram of tube with uniform material properties.

of LRRS at $\mathcal{A}_3^L = \mathcal{A}_3^R \approx 0.815$ ($\mathcal{U}_3^L \approx 0.815$, $\mathcal{U}_3^R \approx 0.815$), with typical characteristics shown in panel (iii). However, as $\mathcal{A}_2$ becomes lower than ≈ 0.727, the LRRS exhibits a turning point with a second (unphysical) branch of LRRS formed beneath with the left rarefaction having crossed into compartment 2, contradicting our assumptions. So as $\mathcal{A}_2$ decreases below ≈ 0.727 the physical branch of LRRS transitions into the class C resonant state with a right shock (see panel (ii)) which further transitions to the class D resonant state with a right shock (see panel (i)), similar to case 1 above (Section 3.8.1).

In Figure 3.15, we compare to the corresponding case with uniform material properties (where the setups only differ through the value of vessel stiffness in compartment 2). We found that both exhibit similar flows, but for uniform material properties the LRRS, LRRR and LSRR solutions remain unique and persist for all $\mathcal{A}_2$. The solutions are qualitatively and quantitatively similar for large $\mathcal{A}_2$, but for lower $\mathcal{A}_2$ the LRRS for a uniform tube (Figure 3.15 b) persists to $\mathcal{A}_2 = 0$ while the LRRS for a tube with discontinuous stiffness (Figure 3.15 a) transistions into two resonant solutions (tLRs0sRS) and (tLRSRS) resulting from the transcritical left rarefaction.

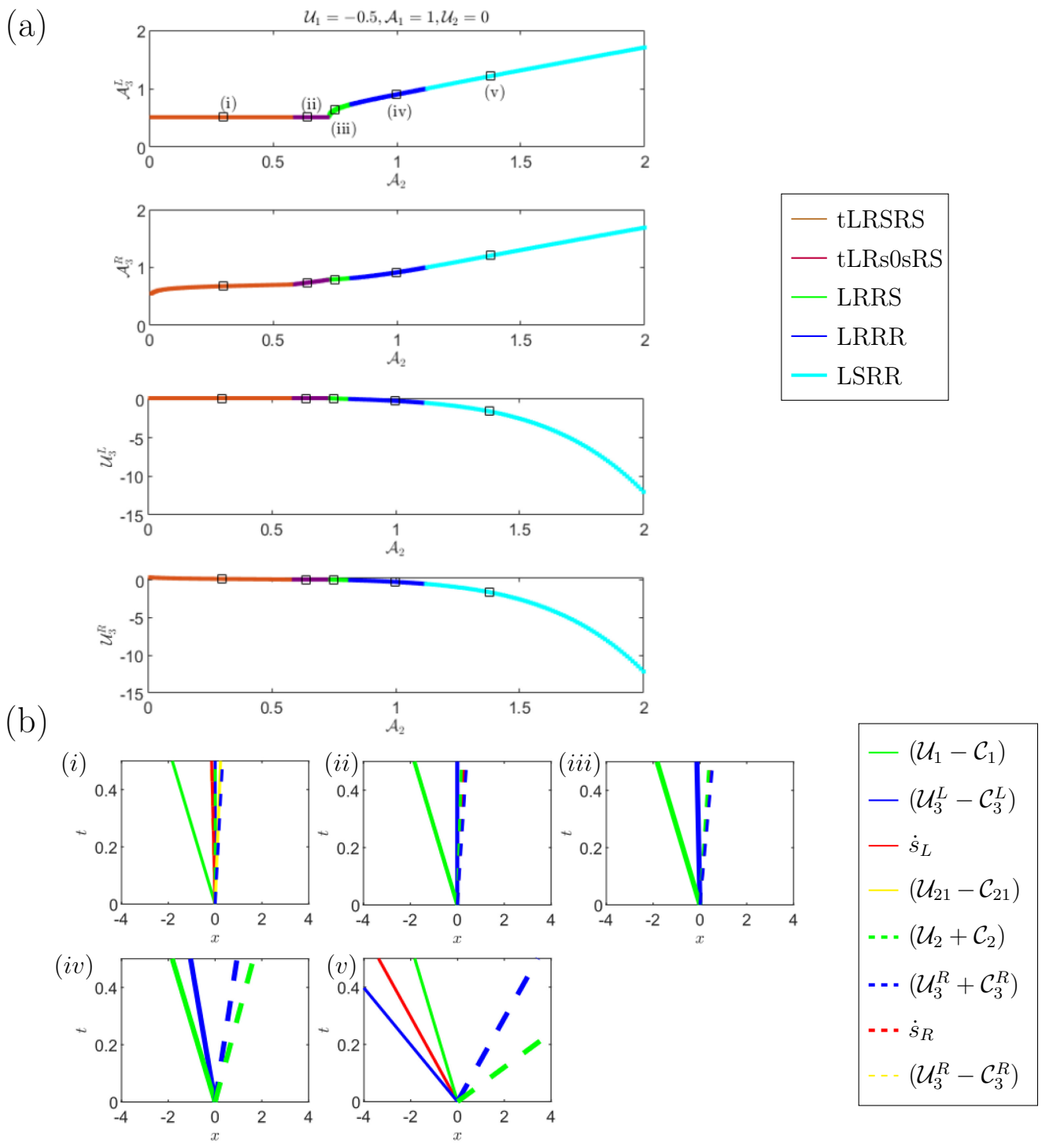

Figure 3.14: Case 2: Bifurcation plot and characteristics profile plot of physical solutions at $\mathcal{U}_1 = -0.5$ and $\mathcal{U}_2 = 0$ with corresponding values of $\mathcal{A}_2$, $\mathcal{A}_3^L$, and $\mathcal{A}_3^R$, respectively. Figure 3.14(a) displays the the cross-sectional area, and flow speed of the multiple solutions with different points of $\mathcal{A}_2$ marked as (i) to (v) such that (i) denotes $\mathcal{A}_2 = 0.3$, (ii) denotes $\mathcal{A}_2 = 0.64$, (iii) denotes $\mathcal{A}_2 = 0.75$, (iv) denotes $\mathcal{A}_2 = 0.998$ and (v) denotes $\mathcal{A}_2 = 1.38$. Figure 3.14(b) shows the corresponding characteristics values of these different values of $\mathcal{A}_2$ from (i) to (v) with $\mathcal{U}_1 = -0.5$ and $\mathcal{U}_2 = 0$.

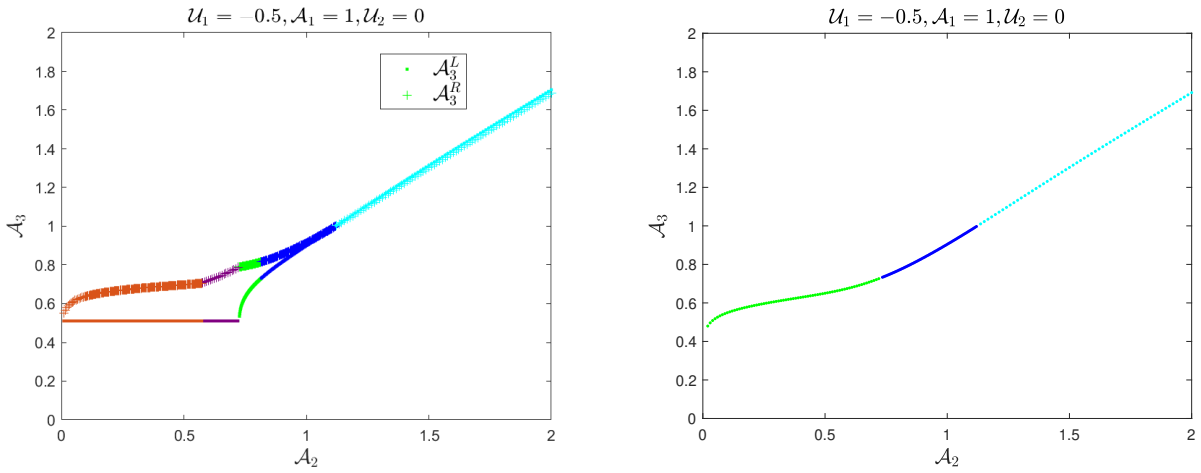

Figure 3.15: Comparison of bifurcation diagram of two blood vessels with varying material properties and single blood vessel with uniform material properties for $\mathcal{U}_1 = -0.5$ and $\mathcal{U}_2 = 0$. Figure 3.15(a) shows the bifurcation diagram of tube with discontinuous material properties. While Figure 3.15(b) shows the bifurcation diagram of tube with uniform material properties.

3.8.3 Case 3

In Figure 3.16 we present the bifurcation diagram in $\mathcal{A}_2$ and corresponding characteristics profiles for a case where compartment 2 is stiffer than compartment 1 ($k = 1.1$) and there is inflow into region 1 and no flow in or out of region 2 (*i.e.* $\mathcal{U}_1 = 0.5, \mathcal{U}_2 = 0$) for $\mathcal{A}_1 = 1$, $\bar{A}_2 = 1$ $\bar{p}_{e1} = \bar{p}_{e2} = 0$. Here, like in cases 1 and 2, the system exhibits three out of the four classical solutions. For large $\mathcal{A}_2$ the system exhibits LSRR which the transitions to LSRS as $\mathcal{A}_2$ decreases (see characteristics in panels (v) and (iv)). As $\mathcal{A}_2$ decreases further the LSRS transitions to a physical branch of LRRS. For $\mathcal{A}_2 \approx 0.291$ the left rarefaction becomes transcritical and the bifurcation diagram exhibits a turning point and connects to a second branch of LSRR beneath where the inner edge of the left rarefaction has moved into compartment 2, which in turn makes the solution unphysical. Now for $\mathcal{A}_2 \lesssim 0.219$ the system again transitions into a class C resonant solution (see characteristics in panel (ii)) and again transitions to class D resonant solution for further decrease in $\mathcal{A}_2$. Hence, the system again exhibits a unique (physical) solution for all values of $\mathcal{A}_2$.

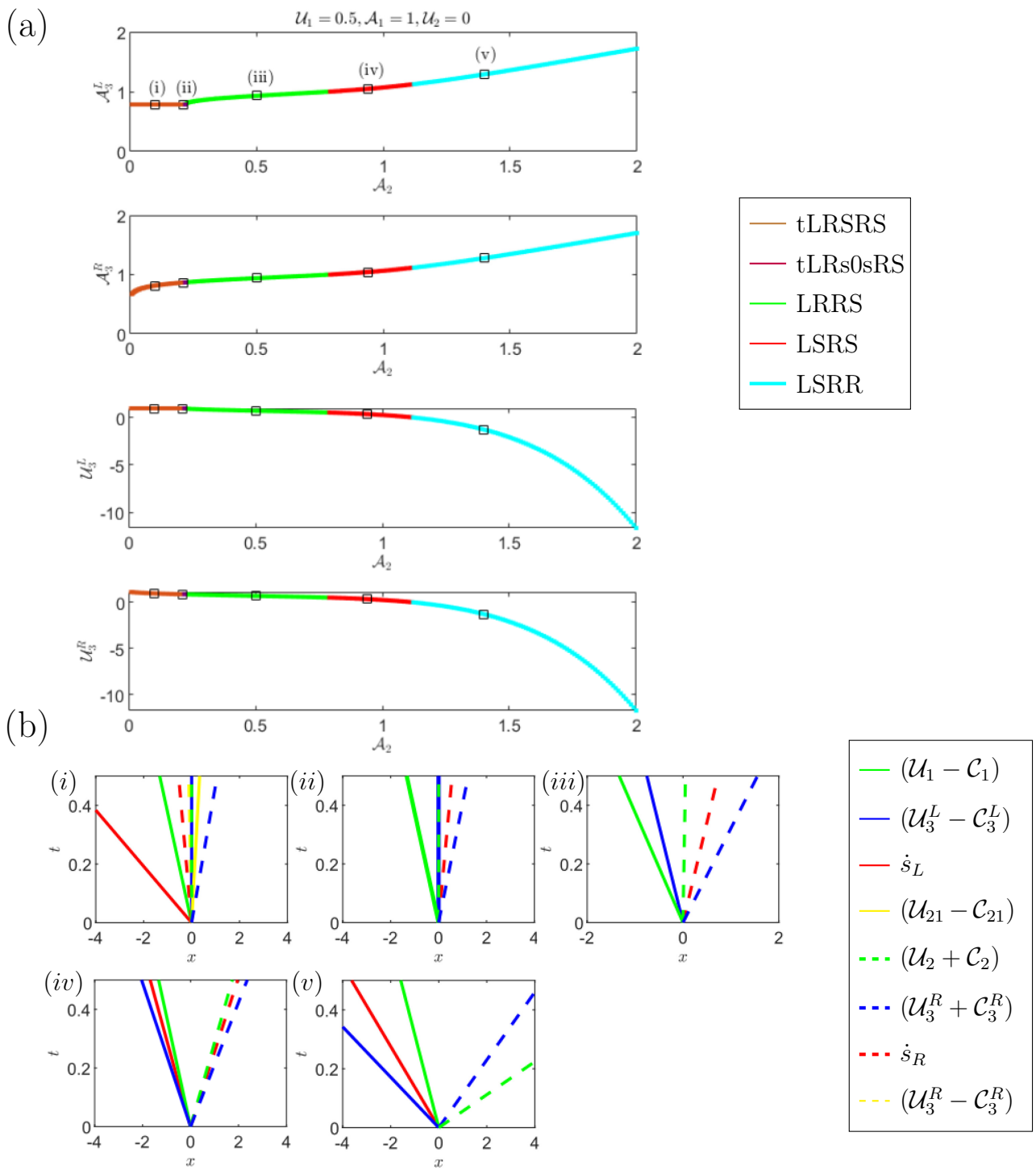

Figure 3.16: Case 3: Bifurcation plot and characteristics profile plot of physical solutions at $\mathcal{U}_1 = 0.5$ and $\mathcal{U}_2 = 0$ with corresponding values of $\mathcal{A}_2$, $\mathcal{A}_3^L$, and $\mathcal{A}_3^R$, respectively. Figure 3.16(a) displays the the cross-sectional area, and flow speed of the multiple solutions with different points of $\mathcal{A}_2$ marked as (i) to (v) such that (i) denotes $\mathcal{A}_2 = 0.1$, (ii) denotes $\mathcal{A}_2 = 0.213$, (iii) denotes $\mathcal{A}_2 = 0.5$, (iv) denotes $\mathcal{A}_2 = 0.99$ and (v) denotes $\mathcal{A}_2 = 1.4$. Figure 3.16(b) shows the corresponding characteristics values of these different values of $\mathcal{A}_2$ from (i) to (v) with $\mathcal{U}_1 = 0.5$ and $\mathcal{U}_2 = 0$.

3.8.4 Case 4

In Figure 3.17 we now consider inflow into compartment 2 (which is $\mathcal{U}_2 = -0.6$) and compartment 2 stiffer than compartment 1 (*i.e.* $k = 1.1$) for $\mathcal{A}_1 = 1$, $\mathcal{U}_1 = 0$ with $\bar{A}_2 = 1$, $\bar{p}_{e1} = \bar{p}_{e2} = 0$ and vary the value of $\mathcal{A}_2$ to construct a bifurcation diagram. Four points on the bifurcation diagram, labelled (i) to (iv) are summarised in Figure 3.17(a) while characteristics are shown in Figures 3.17(b). Similar to Figure 3.16, for large values of $\mathcal{A}_2$ the system exhibits a physical branch of LSRR (see characteristics in panel (v)). Now as $\mathcal{A}_2$ decreases, the LSRR solution transitions into a physical branch of LSRS (see characteristics in panel (iv)). As $\mathcal{A}_2$ further deceases the system transitions into a physical branch of LRRS (see characteristics in panel (iii)). For further decrease in $\mathcal{A}_2$, the LRRS curve exhibits a turning point at $\mathcal{A}_2 \approx 0.101$ which then connects to a second (unphysical) branch of LRRS beneath where again the edge of the left rarefaction has moved into compartment 2. As before, this turning point coincides with the rarefaction becoming transcritical. As $\mathcal{A}_2$ further decreases below the turning point the system again exhibits a class C resonance (tLRs0sRS) solution which further transitions to a class D resonant solution which then persists as $\mathcal{A}_2$ approaches zero.

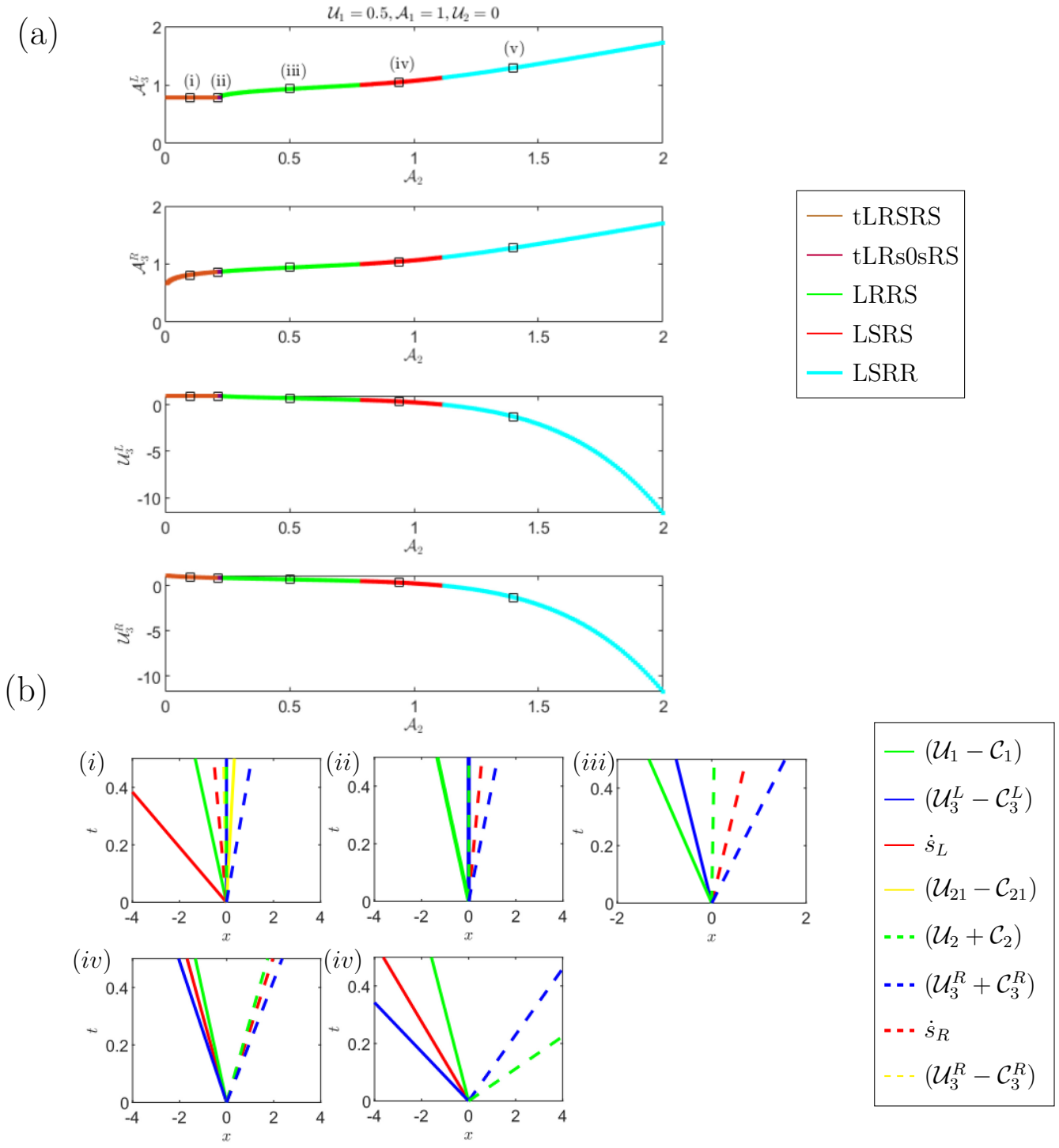

Figure 3.17: Case 4: Bifurcation plot and characteristics profile plot of physical solutions at $\mathcal{U}_1 = 0$ and $\mathcal{U}_2 = -0.6$ with corresponding values of $\mathcal{A}_2$, $\mathcal{A}_3^L$, and $\mathcal{A}_3^R$, respectively. Figure 3.17(a) displays the the cross-sectional area, and flow speed of the multiple solutions with different points of $\mathcal{A}_2$ marked as (i) to (v) such that (i) denotes $\mathcal{A}_2 = 0.05$, (ii) denotes $\mathcal{A}_2 = 0.09$, (iii) denotes $\mathcal{A}_2 = 0.5$, (iv) denotes $\mathcal{A}_2 = 0.99$ and (v) denotes $\mathcal{A}_2 = 1.4$. Figure 3.17(b) shows the corresponding characteristics values of these different values of $\mathcal{A}_2$ from (i) to (v) with $\mathcal{U}_1 = 0$ and $\mathcal{U}_2 = -0.6$.

3.8.5 Case 5

In Figure 3.18 we extend case 4 to consider greater outflow from compartment 2 ($\mathcal{U}_2 = 0.6$), keeping all other conditions identical, again constructing a bifurcation diagram in $\mathcal{A}_2$. This system exhibits three flow structures out of the four classical solutions and three resonant structures. For very low $\mathcal{A}_2$, we have a physical branch of LRRS which then exhibits a new turning point at $\mathcal{A}_2 \approx 0.0312$. As before, this turning point is the left rarefaction crossing the discontinuity such that the lower branch of LRRS again is unphysical (see characteristics in panel (i)). Conversely, for large $\mathcal{A}_2$ we have a physical branch of LSRR which persists as $\mathcal{A}_2$ decreases (see characteristics in panel (iv)). This solution transitions to LRRR when $\mathcal{A}_3^L = \mathcal{A}_3^R = 1$. For lower $\mathcal{A}_2$ then LRRR solution exhibits a turning point, where again the left rarefaction becomes transcritical for $\mathcal{A}_2 \approx 0.911$. Hence, the classical solutions create a gap between the edge of LRRS and LRRR in a region of parameter space ($0.0312 \leq \mathcal{A}_2 \leq 0.911$) where the solution is more complicated. This gap is now filled with a succession of three resonant solutions. For $\mathcal{A}_2 > 0.0312$ the LRRS transitions an example of the configuration D resonant solution with two right propagating shocks in compartment 2 (tLRSRS) (see characteristics in panel (ii)). As $\mathcal{A}_2$ increases further the tLRSRS solution transitions into another example of the configuration D resonant solution where the shock adjacent to region 2 is replaced by a subcritical rarefaction (tLRSRR) (see characteristics in panel (iii)) and to completely close the gap created from the classical solution, the tLRSRR transistions into an example of the configuration C resonant solution with a right rarefaction tLRs0sRR (see characteristics in panel (iv)) which now merges with the edge of LRRR at $\mathcal{A}_2 \approx 0.911$. Hence, for every value of $\mathcal{A}_2$, the system again exhibits a unique solution.

In Figure 3.19 we compare the bifurcation diagram for a vessel with discontinuous material properties (Figure 3.19a) to that obtained for a vessel with uniform material properties (Figure 3.19b). The two systems exhibits LRRS and LSRR at low $\mathcal{A}_2$ and large $\mathcal{A}_2$, respectively. The LSRR of both systems transitions to LRRR states at almost same point, but for the case of tube with uniform material properties the LRRR transitions smoothly into the LRRS solution while for tube with discontinuous material properties the LRRR does not persist for all $\mathcal{A}_2$ but exhibits a turning point and loss of existence of solution creating a gap between LRRR and LRRS which is completed with three resonant solutions. Hence, change in stiffness in one compartment triggers a complicated solution qualitatively different from the case where stiffness is assumed uniform.

Furthermore, in this case we compare the flow profiles of the tube with discontinuous material properties to that of a tube with uniform material properties in Figure 3.20 and 3.21. From Figure 3.20 we have that for low values of $\mathcal{A}_2$ ($\mathcal{A}_2 = 0.5$) and $\mathcal{U}_2 = 0.6$ that the tube with discontinuous material property shows the left rarefaction resonates with the stationary wave and produces a shock to the right of the stationary wave (see Figure 3.20a) while for the tube with uniform material property the left rarefaction crosses into region 2 (see Figure 3.20b). Also, in Figure 3.21(a) we have that for large $\mathcal{A}_2$ ($\mathcal{A}_2 = 0.8$) the left rarefaction from LRRR resonates with the stationary wave and again producing a shock to the right of the stationary wave but in Figure 3.21(b) the left rarefaction again crosses into region 2. This is the crux of this chapter, showing how a discontinuity in material properties can lead to additional flow examples where a new propagating shock generated by a rarefaction becomes transcritical.

An intriguing feature of the bifurcation diagram shown in Figure 3.18 is that the configuration D resonant solution with a right shock (*e.g.* characteristics in panel (ii)) merges smoothly with a classical LRRS state without the configuration C solution in between. We also see that even though the configuration D resonant solution transitions to a subcritical solution, the resonant shock and the right

shock did not become close enough to merge (see Figure 3.22a) but they remained far apart similar to Figure 3.11(b) where the configuration D resonant solution with a right shock persisted for all $\mathcal{A}_2$. We probed further to know why this is possible, we saw that even though the two shocks did not meet, it transitioned into a classical solution because one of the shocks failed the Lax condition (see Figure 3.22b) where the resonant shock failed the Lax condition as $(\mathcal{U}_{21} - \mathcal{C}_{21})$ is supposed to be greater that $\dot{s}_{res}$ but at the point which the solution became classical again $(\mathcal{U}_{21} - \mathcal{C}_{21}) = \dot{s}_{res}$. So, the failure of the Lax condition suppressed the resonant behaviour.

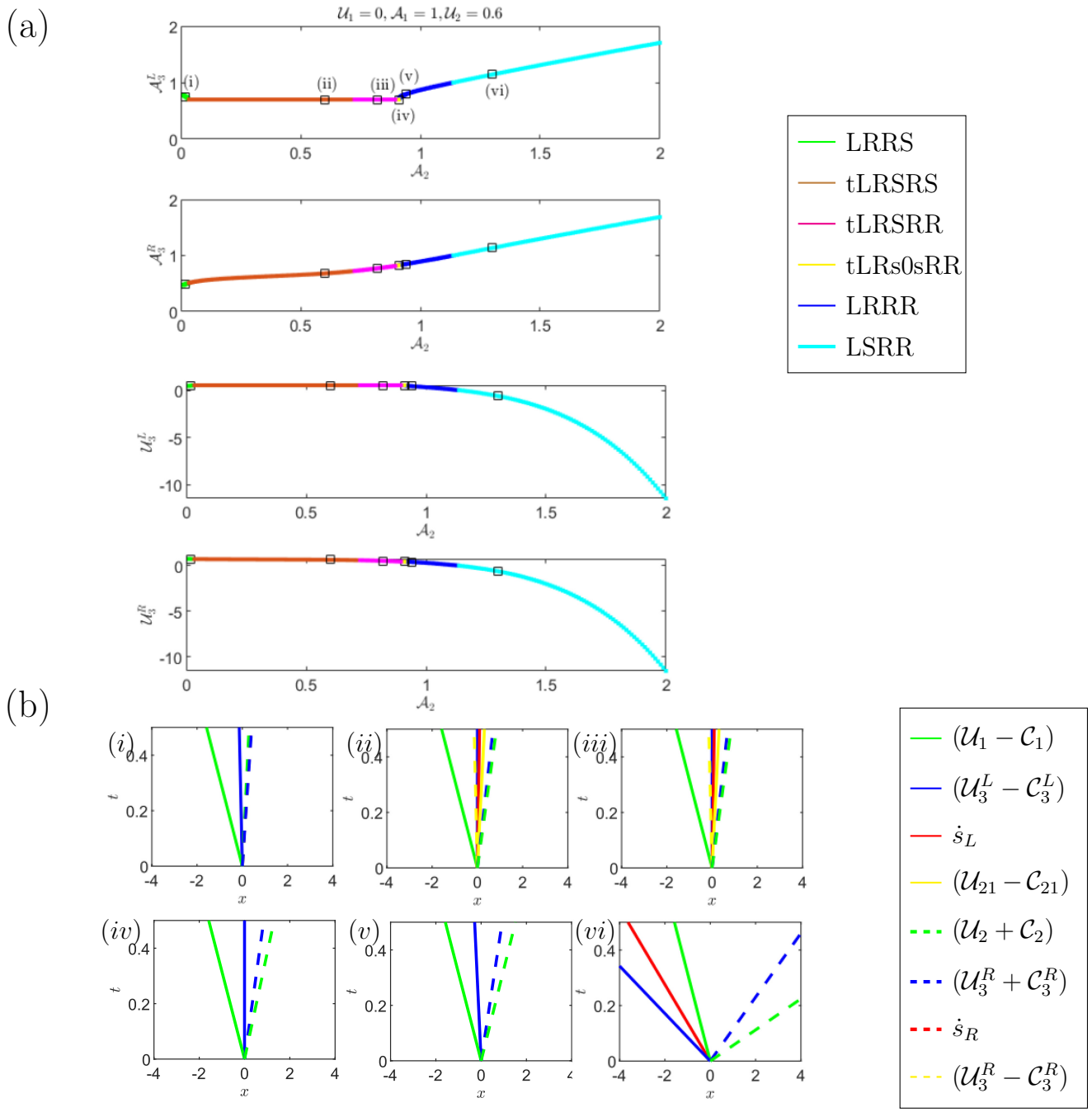

Figure 3.18: Case 5: Bifurcation plot and characteristics profile plot of multiple solutions at $\mathcal{U}_1 = 0$ and $\mathcal{U}_2 = 0.6$ with corresponding values of $\mathcal{A}_2$, $\mathcal{A}_3^L$, and $\mathcal{A}_3^R$, respectively. Figure 3.18(a) displays the the cross-sectional area, and flow speed of the multiple solutions with different points of $\mathcal{A}_2$ marked as (i) to (vi) such that (i) denotes $\mathcal{A}_2 = 0.026$, (ii) denotes $\mathcal{A}_2 = 0.5$, but different values of $\mathcal{A}_3^L$ and $\mathcal{A}_3^R$, (iii) denotes $\mathcal{A}_2 = 0.82$, (iv) denotes $\mathcal{A}_2 = 0.91$, (v) denotes $\mathcal{A}_2 = 0.94$ and (vi) denotes $\mathcal{A}_2 = 1.3$ with different values of $\mathcal{A}_3^L$ and $\mathcal{A}_3^R$, respectively. Figure 3.18(b) shows the corresponding characteristics values of these different values of $\mathcal{A}_2$ from (i) to (vi) with $\mathcal{U}_1 = 0$ and $\mathcal{U}_2 = 0.6$.

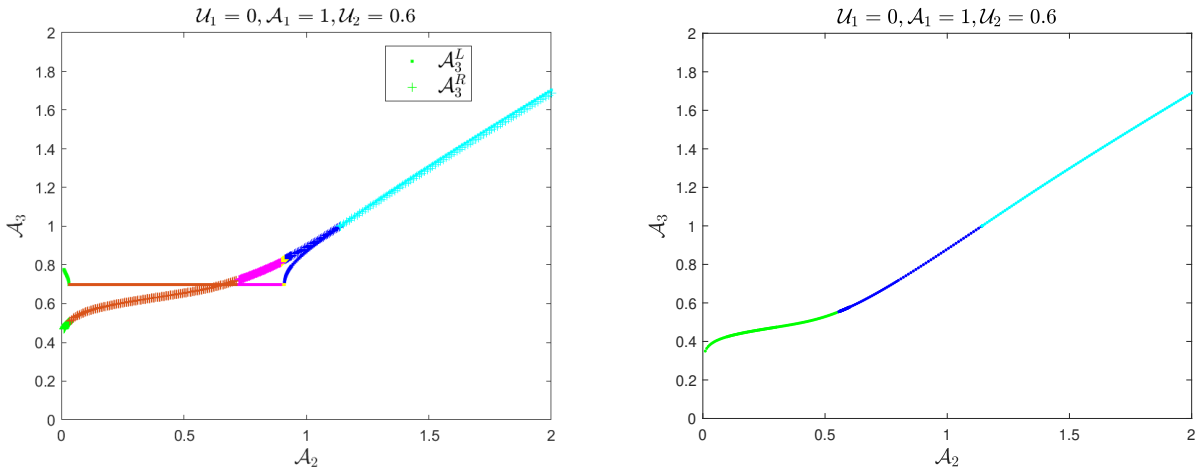

(a) **(b)**

Figure 3.19: Comparison of bifurcation diagram of tube with discontinuous material properties and tube with uniform material properties. Figure 3.19(a) shows the bifurcation diagram of tube with discontinuous material properties for $\mathcal{U}_1 = 0$ and $\mathcal{U}_2 = 0.6$. While Figure 3.19(b) shows the bifurcation diagram of tube with uniform material properties for $\mathcal{U}_1 = 0$ and $\mathcal{U}_2 = 0.6$.

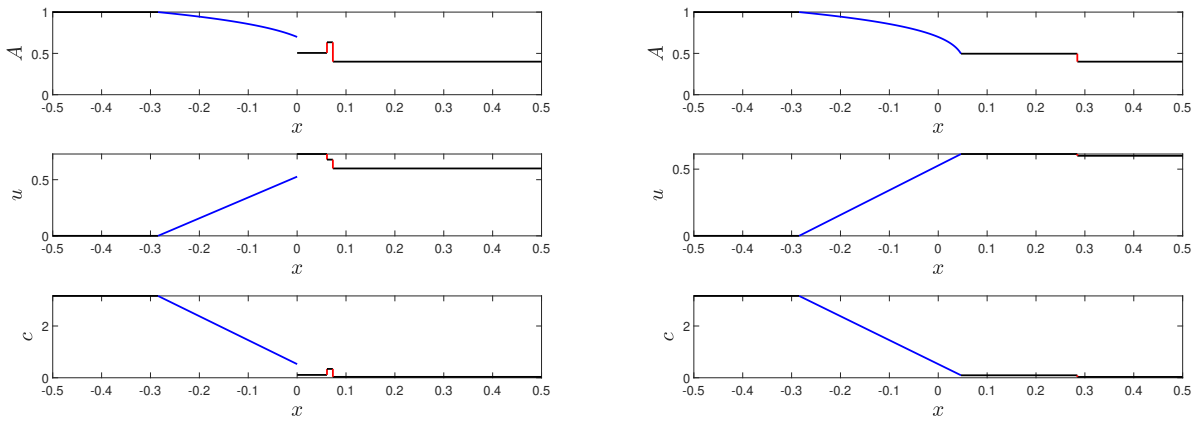

(a) **(b)**

Figure 3.20: Comparison of flow profiles of tube with discontinuous material properties and tube with uniform material properties. Figure 3.20(a) shows the flow profile of tube with discontinuous material properties for $\mathcal{U}_1 = 0$, $\mathcal{A}_1 = 1$, $\mathcal{A}_2 = 0.4$ and $\mathcal{U}_2 = 0.6$. While Figure 3.20(b) shows the flow profiles of tube with uniform material properties for the same values.

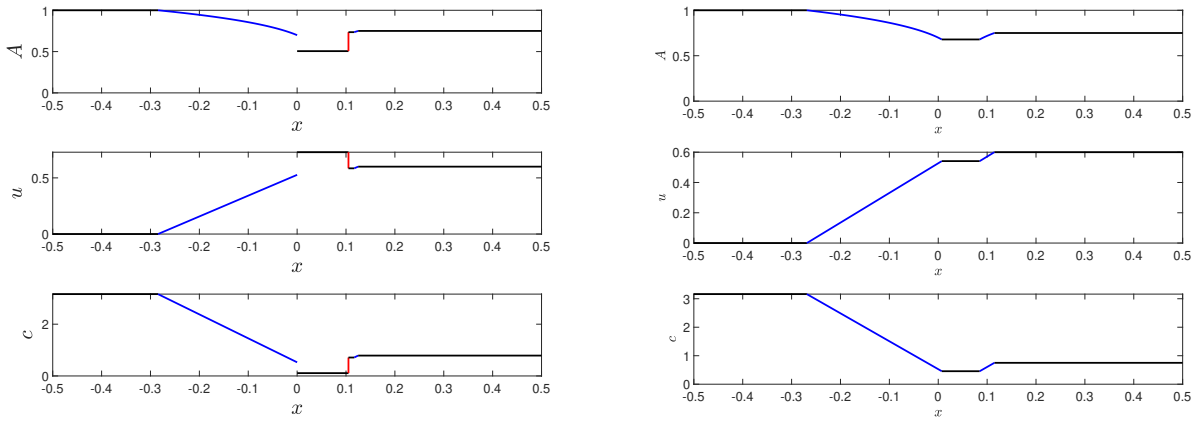

(a) **(b)**

Figure 3.21: Comparison of flow profiles of tube with discontinuous material properties and tube with uniform material properties. Figure 3.21(a) shows the flow profile of tube with discontinuous material properties for $\mathcal{U}_1 = 0$, $\mathcal{A}_1 = 1$, $\mathcal{A}_2 = 0.75$ and $\mathcal{U}_2 = 0.6$. While Figure 3.21(b) shows the flow profiles of tube with uniform material properties for the same values.

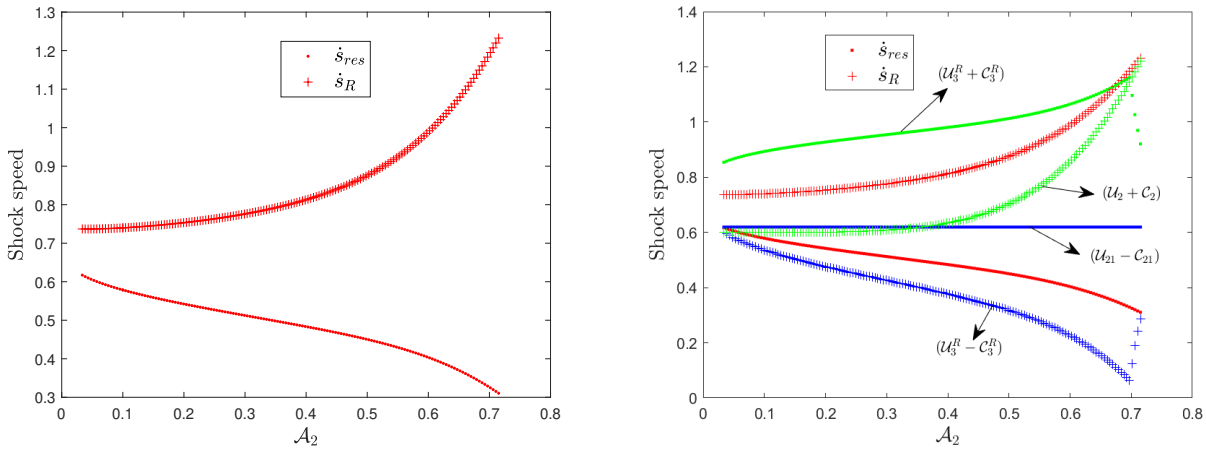

(a) **(b)**

Figure 3.22: Illustration of the resonant and right shock solutions of configuration D resonant solution with a right shock. Figure 3.22(a) illustrates the two shocks on the right while Figure 3.22(b) shows the two shocks on the right and also the accompanying Lax entropy conditions.

In the remaining cases presented below, we will no longer be comparing our solutions with that of the system with uniform material properties, but simply show solutions generated as we vary boundary conditions across the parameter space.

3.8.6 Cases 6, 7 and 8

In Figure 3.23 we consider three different cases where compartment 2 is stiffer than compartment 1 ($k = 1.1$) setting $\mathcal{A}_2 = 1$, $\mathcal{U}_2 = 0$ and construct a bifurcation diagram by varying the cross-sectional area in compartment 1 for $\mathcal{U}_1 = 0$ (Figure 3.23a), $\mathcal{U}_1 = -0.6$ (Figure 3.23b), and $\mathcal{U}_1 = 0.6$ (Figure 3.23c), respectively. In each of these three cases the classical solutions are sufficient to span the parameter space: in all cases the behaviour is LSRR for low $\mathcal{A}_1$ and LRRS for large $\mathcal{A}_1$ (Figure 3.23a, b, c), while for $\mathcal{U}_1 < 0$ the system exhibits a region of LRRR close to $\mathcal{A}_1 = 1$ (Figure 3.23b) and for $\mathcal{U}_1 < 0$ the system a region of LSRS close to $\mathcal{A}_1 = 1$ (Figure 3.23c).

3.8.7 Case 9

In Figure 3.24 we consider a case where compartment 2 is less stiff than compartment 1 ($k = 0.9$) with $\mathcal{U}_1 = 0$, $\mathcal{U}_2 = 0$ and $\mathcal{A}_2 = 1$ constructing bifurcation diagrams by varying the cross-sectional area in compartment 1 $\mathcal{A}_1$. First we consider $k = 0.9$, $\mathcal{U}_1 = 0$, $\mathcal{U}_2 = 0$, $\mathcal{A}_2 = 1$ and in construct a bifurcation diagram by varying the value of $\mathcal{A}_1$. For $\mathcal{A}_1 > 1$ the system exhibits a physical branch of LRRS (see characteristics in panel (iv), which transitions into a LSRR solution as $\mathcal{A}_1$ decreases below 1 (see characteristics in panel (iii)). As the value of $\mathcal{A}_1$ decreases further the LSRR exhibits a turning point at $\mathcal{A}_1 \approx 0.375$ and connects to a second (unphysical) branch beneath, where the inner edge of the right rarefaction has moved into compartment 1. Immediately after the turning point of LSRR as $\mathcal{A}_1$ further decreases, the system exhibits an example of configuration C resonant solution with a transcritical right rarefaction and a left shock (tRRs0sLS), which then transitions into a class D resonance solution with the right rarefaction resonating and a left shock (tRRSLS) (see characteristics in panel (i) and (ii)) which then persists as $\mathcal{A}_1$ approaches zero.

3.8.8 Case 10

In Figure 3.25 we extend case 9 to consider flow drawn out of compartment 1 ($\mathcal{U}_1 = -0.6$) while varying $\mathcal{A}_1$. For large values of $\mathcal{A}_1$ the system exhibits a physical branch of LRRS (see characteristics in panel (v)). As $\mathcal{A}_1$ decreases the LRRS transitions into the LRRR solution (see characteristics in panel (iv)) which then exhibits a turning point at $\mathcal{A}_1 \approx 0.931$ and then connects to a lower (unphysical) branch of LRRR where the right rarefaction has moved into compartment 1. After the turning point, further decrease in $\mathcal{A}_1$ leads to the system exhibiting class C resonance with a transcritical right rarefaction and a left rarefaction (tRRs0sLR) (see characteristics in panel (iii)). As $\mathcal{A}_1$ decreases further this transitions again into two successive configuration D solutions, firstly configuration D with a left rarefaction (tRRSLR) (see characteristics in panel (ii)) and then for lower $\mathcal{A}_1$ a configuration D solution with a right shock (tRRSLS) (see characteristics in panel (i)).

3.8.9 Case 11

Finally, we modify case 9 to include flow into compartment 1 while varying the value of $\mathcal{A}_1$ ($\mathcal{U}_1 = 0.6$). For large value of $\mathcal{A}_1$ the system exhibits a LRRS solution (see characteristics in panel (v)) which transitions into a LSRS solution as $\mathcal{A}_1$ decreases (see characteristics in panel (iv)). As $\mathcal{A}_1$ further deceases the system exhibits a physical branch of LSRR (see characteristics in panel (iii)), which exhibits a turning point at $\mathcal{A}_1 \approx 0.095$ and connects to a second (unphysical) branch beneath, where the inner

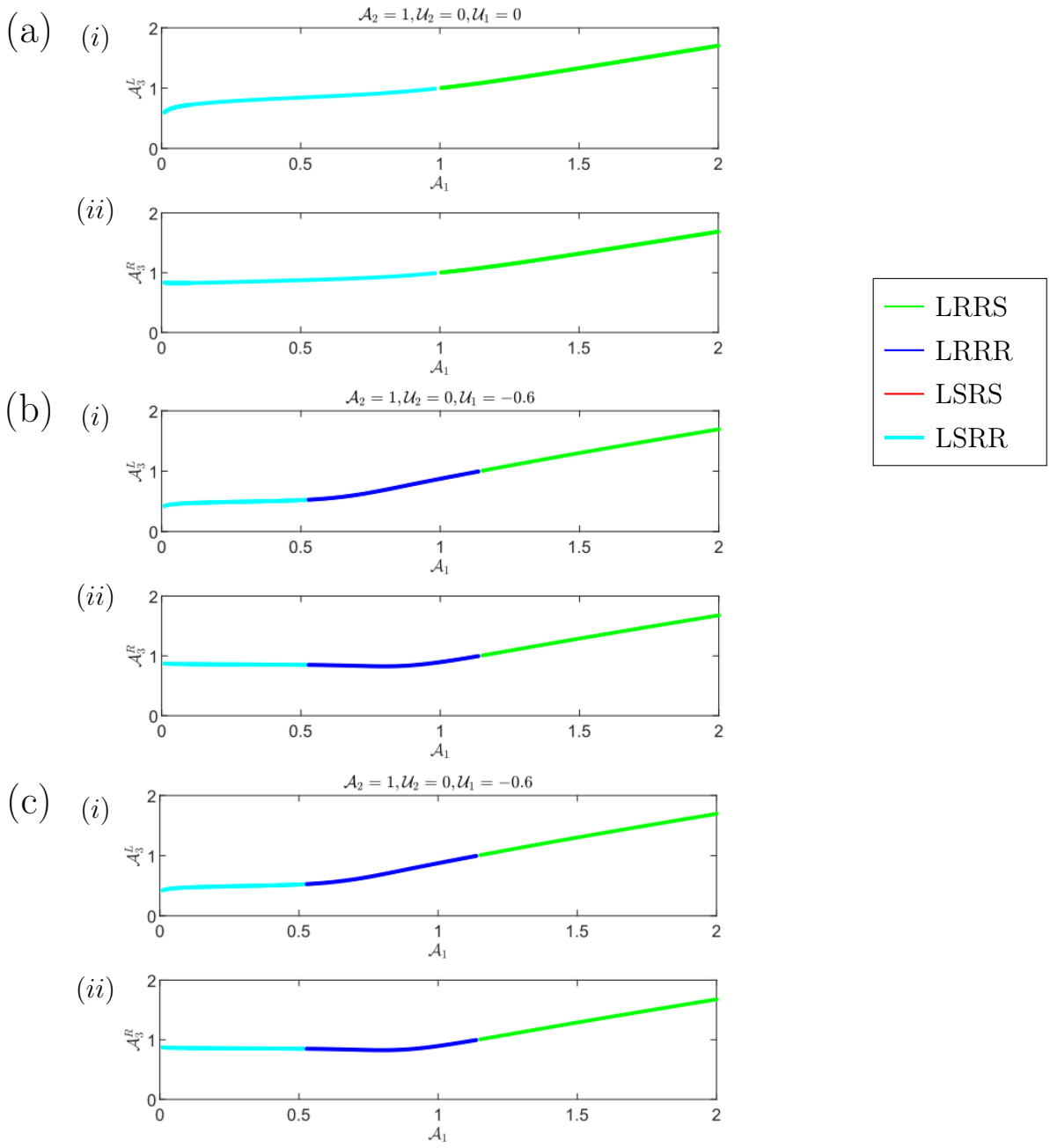

Figure 3.23: Case 6, 7, and 8: Bifurcation plot of physical solutions cases 6 to 8. Figure 3.23(a) displays the bifurcation plot for case 6 with $\mathcal{U}_1 = \mathcal{U}_2 = 0$, $\mathcal{A}_2 = 1.0$ while varying $\mathcal{A}_1$ and $k = 1.1$. Figure 3.23(b) displays the bifurcation plot for case 7 with $\mathcal{U}_1 = -0.6$, $\mathcal{U}_2 = 0$, $\mathcal{A}_2 = 1.0$ while varying $\mathcal{A}_1$ and $k = 1.1$, and Figure 3.23(c) displays the bifurcation plot for case 8 with $\mathcal{U}_1 = 0.6$, $\mathcal{U}_2 = 0$, $\mathcal{A}_2 = 1.0$ while varying $\mathcal{A}_1$ and $k = 1.1$.

edge of the right rarefaction has moved into compartment 1. Immediately after the turning point of LSRR as $\mathcal{A}_1$ further decreases, the system exhibits an example of configuration C resonance with a

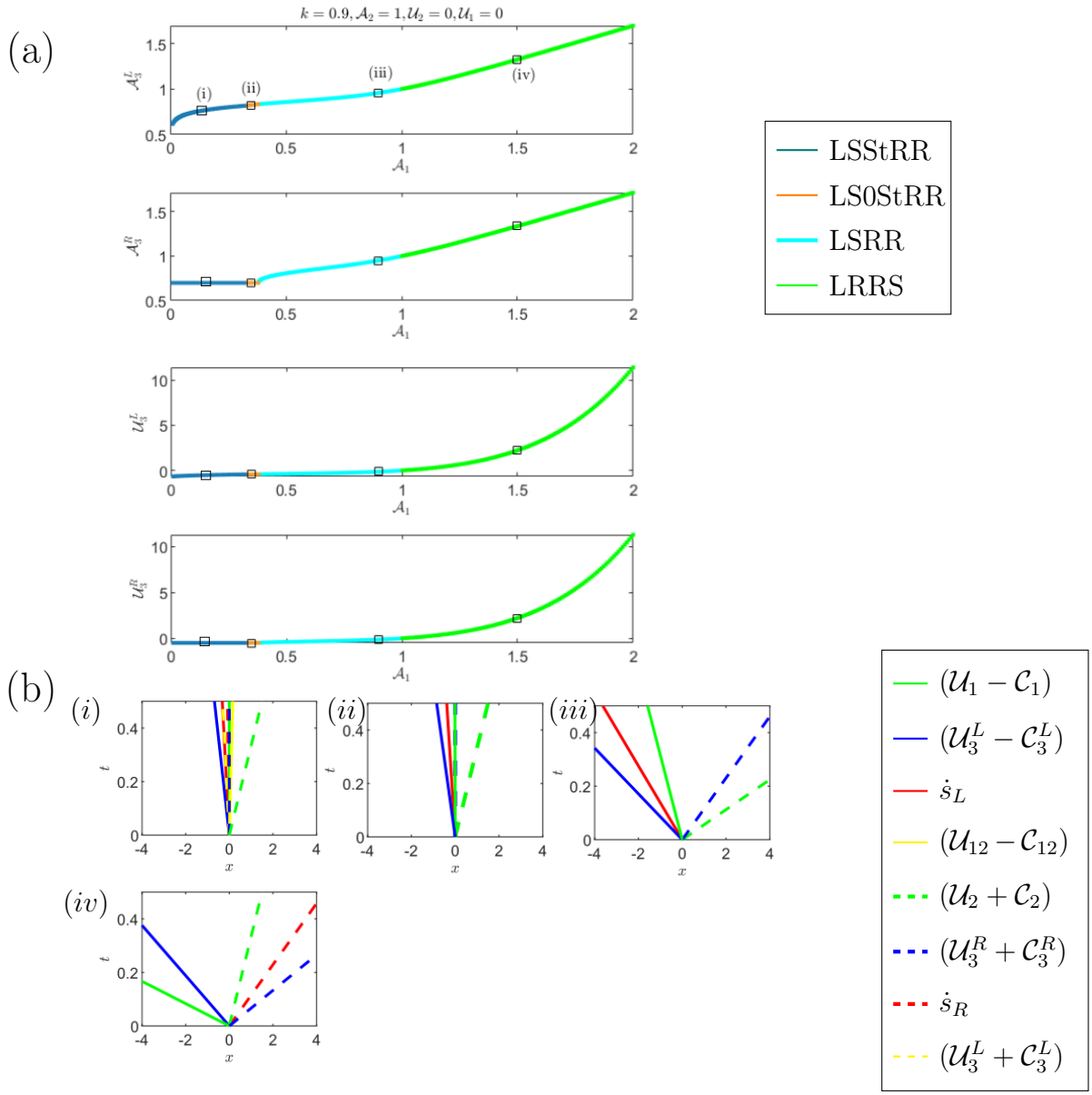

Figure 3.24: Case 9: Bifurcation plot and characteristics profile plot of physical solutions at $\mathcal{U}_1 = 0$ and $\mathcal{U}_2 = 0$, $k = 0.9$ with corresponding values of $\mathcal{A}_1$, $\mathcal{A}_3^L$, and $\mathcal{A}_3^R$, respectively. Figure 3.24(a) displays the the cross-sectional area, and flow speed of the physical solutions with different points of $\mathcal{A}_1$ marked as (i) to (iv) such that (i) denotes $\mathcal{A}_1 = 0.15$, (ii) denotes $\mathcal{A}_1 = 0.38$, (iii) denotes $\mathcal{A}_1 = 0.9$ and (iv) denotes $\mathcal{A}_1 = 1.5$. Figure 3.24(b) shows the corresponding characteristics values of these different values of $\mathcal{A}_1$ from (i) to (iv) with $\mathcal{U}_1 = 0$, $k = 0.9$ and $\mathcal{U}_2 = 0$.

transcritical right rarefaction and a left shock (tRRs0sLS) (see characteristics in panel (ii)) which again transitions into a class D resonance solution with a transcritical right rarefaction (tRRSLS) which persists as $\mathcal{A}_1$ approaches zero (see characteristics in panel (i)).

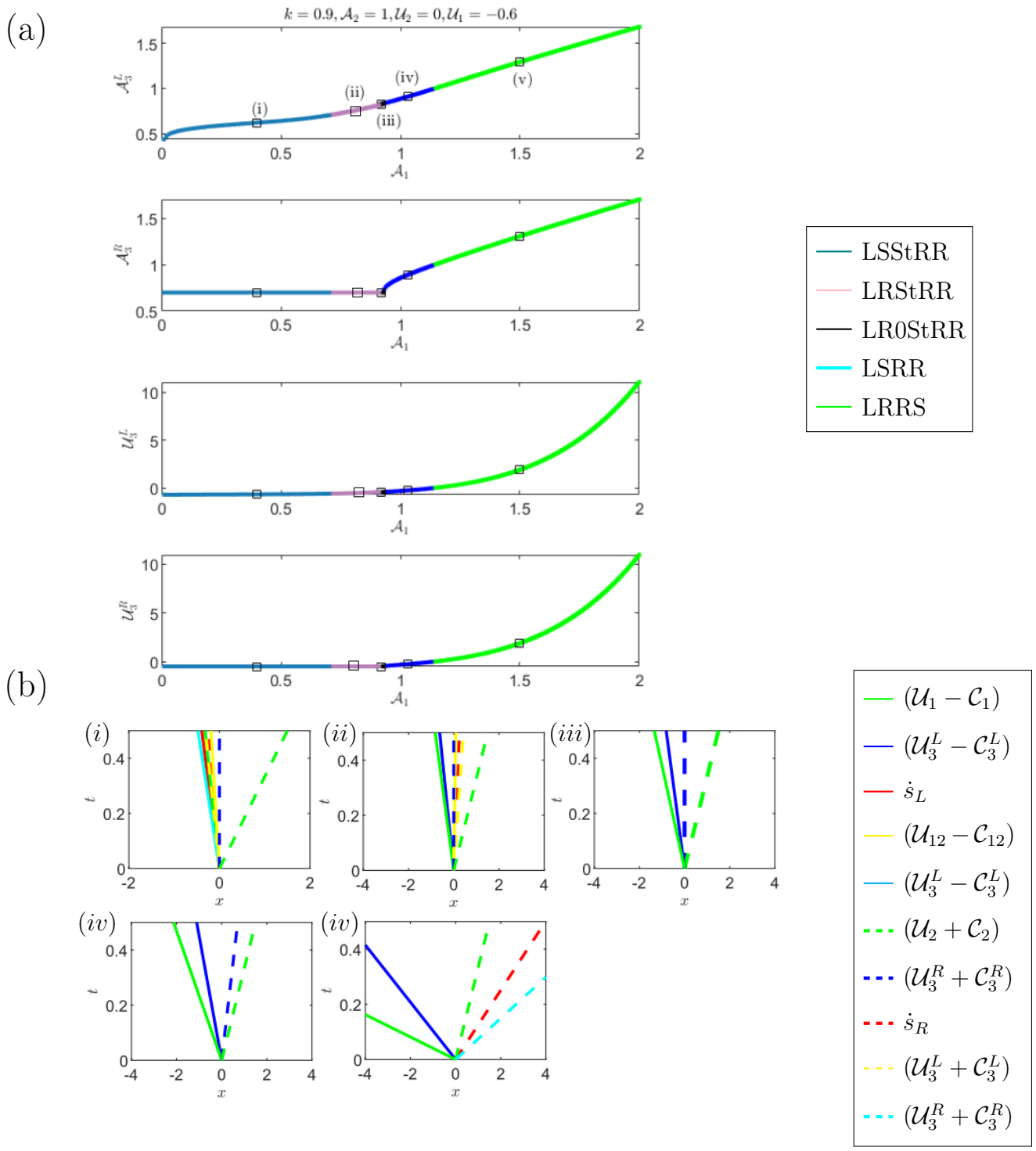

Figure 3.25: Case 10: Bifurcation plot and characteristics profile plot of physical solutions at $\mathcal{U}_1 = -0.6$ and $\mathcal{U}_2 = 0$, $k = 0.9$ with corresponding values of $\mathcal{A}_1$, $\mathcal{A}_3^L$, and $\mathcal{A}_3^R$, respectively. Figure 3.25(a) displays the the cross-sectional area, and flow speed of the physical solutions with different points of $\mathcal{A}_1$ marked as (i) to (v) such that (i) denotes $\mathcal{A}_1 = 0.4$, (ii) denotes $\mathcal{A}_1 = 0.8$, (iii) denotes $\mathcal{A}_1 = 0.92$, (iv) denotes $\mathcal{A}_1 = 1.03$ and (v) denotes $\mathcal{A}_1 = 1.5$. Figure 3.25(b) shows the corresponding characteristics values of these different values of $\mathcal{A}_1$ from (i) to (v) with $\mathcal{U}_1 = -0.6$, $k = 0.$ and $\mathcal{U}_2 = 0$.

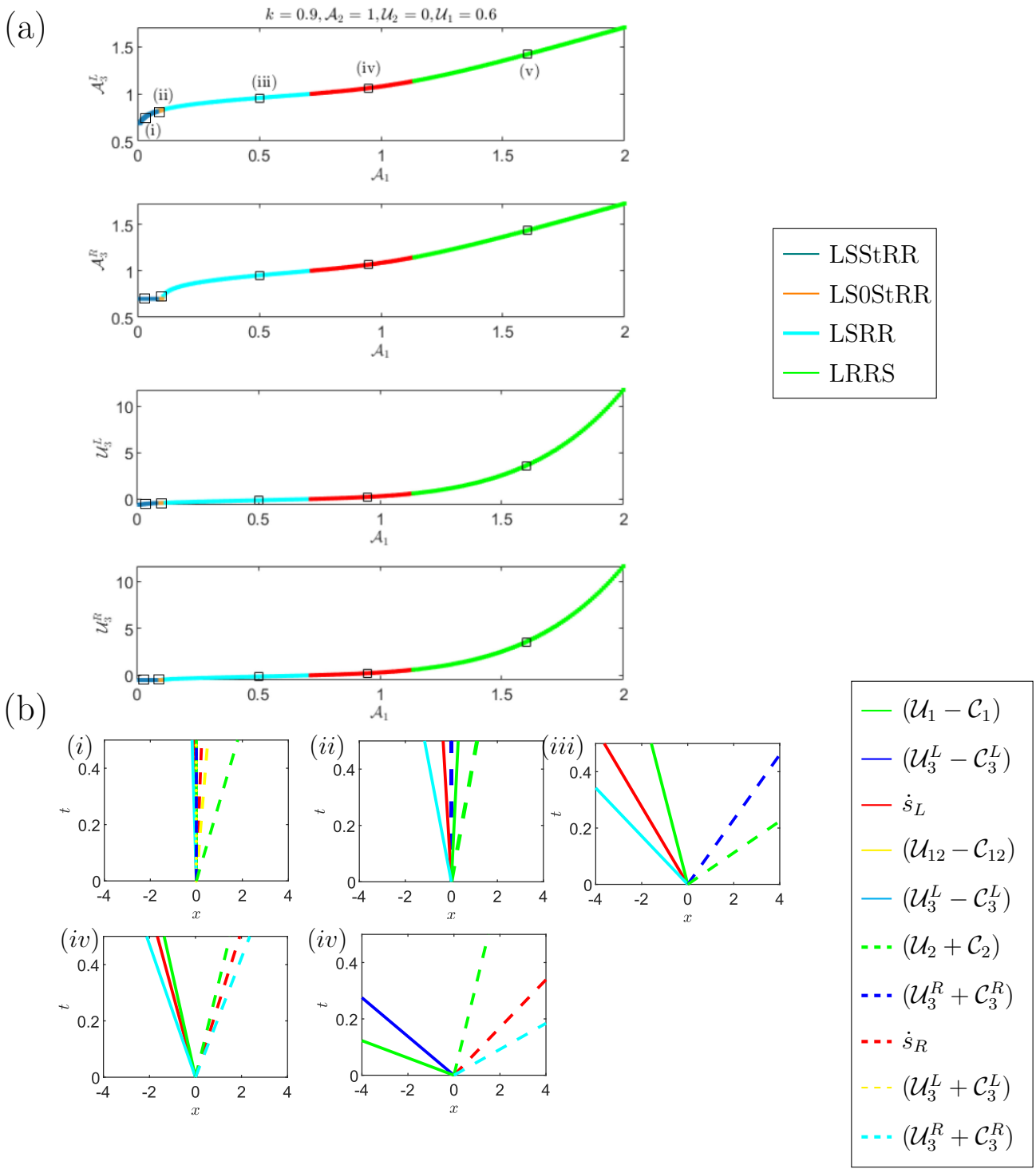

Figure 3.26: Case 11: Bifurcation plot and characteristics profile plot of physical solutions at $\mathcal{U}_1 = 0.6$ and $\mathcal{U}_2 = 0$, $k = 0.9$ with corresponding values of $\mathcal{A}_1$, $\mathcal{A}_3^L$, and $\mathcal{A}_3^R$, respectively. Figure 3.26(a) displays the the cross-sectional area, and flow speed of the physical solutions with different points of $\mathcal{A}_1$ marked as (i) to (v) such that (i) denotes $\mathcal{A}_1 = 0.03$, (ii) denotes $\mathcal{A}_1 = 0.096$, (iii) denotes $\mathcal{A}_1 = 0.5$, (iv) denotes $\mathcal{A}_1 = 0.95$ and (v) denotes $\mathcal{A}_1 = 1.6$. Figure 3.26(b) shows the corresponding characteristics values of these different values of $\mathcal{A}_1$ from (i) to (v) with $\mathcal{U}_1 = 0.6$, $k = 0.5$ and $\mathcal{U}_2 = 0$.

3.9 Overview of the parameter space

We now summarise the overall behaviour of the system by producing a parameter space plot that highlights the different solutions that can occur across the parameter space. As before the green, blue, red and cyan filled circles represent the classical solutions *i.e.* LRRS, LRRR, LSRS and LSRR, respectively. Similarly, the resonant solutions are also denoted as filled circles: yellow circles represent configuration C resonant solution with a left transcritical rarefaction and a right rarefaction (tLR0SRR), purple circles denote a configuration C resonant solution with a left transcritical rarefaction and a right shock (tLR0SRS), magenta circles denote a configuration D resonant solutions with a left transcritical rarefaction and a right rarefaction (tLRSRR), and orange circles denote a configuration D resonant solution with a left transcritical rarefaction and a right shock (tLRSRS). On the otherhand, black circles represent a configuration C resonant solution with a right transcritical rarefaction and a left rarefaction (LR0StRR), amber circles represent a configuration C resonant solution with a right transcritical rarefaction and a left shock (LS0StRR), lilac circles represent a configuration D resonant solution with a right transcritical rarefaction and a left rarefaction (LRStRR) and teal circles represent a configuration D resonant solution with a right transcritical rarefaction and a left shock (LSStRR).

Figure 3.27 illustrates a parameter space for compartment 2 stiffer than compartment 1 encompassing cases 1, 4 and 5 plotting the solutions as a function of $\mathcal{A}_2$ and $\mathcal{U}_2$ for $\mathcal{U}_1 = 0$ and $\mathcal{A}_1 = 1$. The classical solutions fill the domain in a similar way to Figure 2.18(a) with the exception of a large tongue of resonant solutions (the magenta, yellow, purple and orange filled circles). This tongue is confined to low values of $\mathcal{A}_2$ for negative $\mathcal{U}_2$ but approaches a range around the baseline (*i.e.* $\bar{A}_2$) as $\mathcal{U}_2$ increases. Hence, the system is increasingly likely to become resonant as flow is drawn out of the system at the downstream end.

In Figure 3.28 we have the parameter space spanned by $\mathcal{U}_2$ and $\mathcal{A}_2$ while fixing $\mathcal{U}_1 = 0$ and $\mathcal{A}_1 = 1$ but in this case compartment 2 is now less stiff than compartment 1 ($k = 0.9$), but otherwise identical to the setup in Figure 3.27. In this case the partition of space across the classical solutions is qualitatively similar to Figure 3.27 but these are now sufficient to entirely span the space without any resonant solutions. This feature will be discussed further below.

Figure 3.29 illustrates the parameter space spanned by $\mathcal{U}_1$ and $\mathcal{A}_1$ while fixing $\mathcal{U}_2 = 0$ and $\mathcal{A}_2 = 1$ where compartment 2 is more stiff than compartment 1 (*i.e.* $k = 1.1$), similar to Figure 3.28 the partition of the classical solution sufficiently spans the entire parameter space: the four tongues are now almost a complete mirror image of Figure 3.28 with the four quadrants oriented in the opposite direction. Again this feature is discussed below.

Finally, Figure 3.30 shows a parameter space plot spanned by $\mathcal{U}_1$ and $\mathcal{A}_1$ (while we fix $\mathcal{U}_2 = 0$, $\mathcal{A}_2 = 1$) for compartment 2 less stiff than compartment 1 encompassing cases 9, 10 and 11. Similar to Figure 3.27 the classical solutions fill the domain (but in mirror image compared to Figure 3.27) with a large tongue of resonant solutions. The tongue is confined to low values of $\mathcal{A}_1$ for positive $\mathcal{U}_1$ but approaches a range around the baseline value ($\bar{A}_1 = 1$) as $\mathcal{U}_1$ decreases.

So, perhaps the most interesting observation from this section is that only some of the parameter sweeps exhibit resonance: for these choices resonance occurs when we vary the properties of the stiffer compartment.

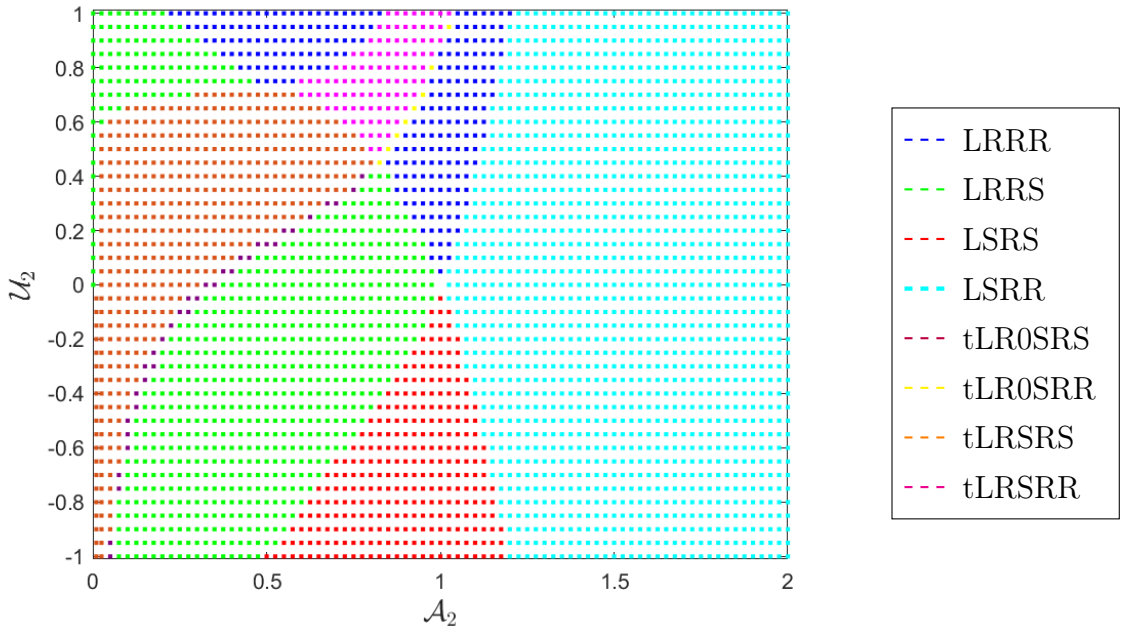

Figure 3.27: Overview of the parameter space spanned by $\mathcal{U}_2$ ($-1.0 \leq \mathcal{U}_2 \leq 1.0$) and $\mathcal{A}_2$ ($0 \leq \mathcal{A}_2 \leq 2.0$) with $\mathcal{U}_1 = 0$, $\mathcal{A}_1 = 1$, $k = 1.1$ and $\bar{A}_2 = 1$.

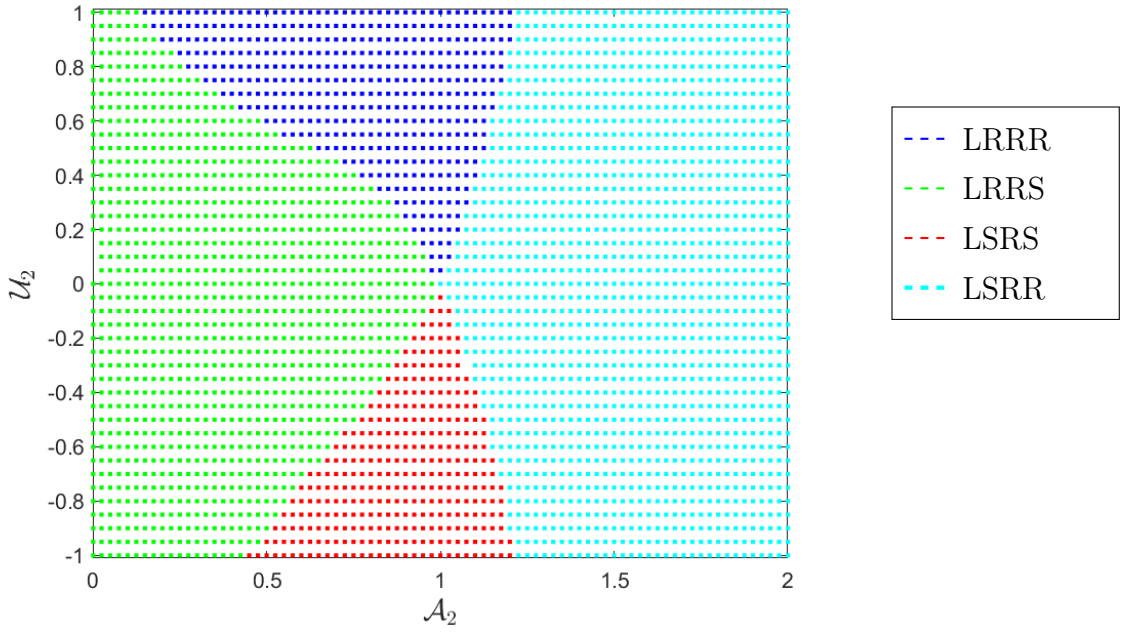

Figure 3.28: Overview of the parameter space spanned by $\mathcal{U}_2$ ($-1.0 \leq \mathcal{U}_2 \leq 1.0$) and $\mathcal{A}_2$ ($0 \leq \mathcal{A}_2 \leq 2.0$) with $\mathcal{U}_1 = 0$, $\mathcal{A}_1 = 1$, $k = 0.9$ and $\bar{A}_2 = 1$.

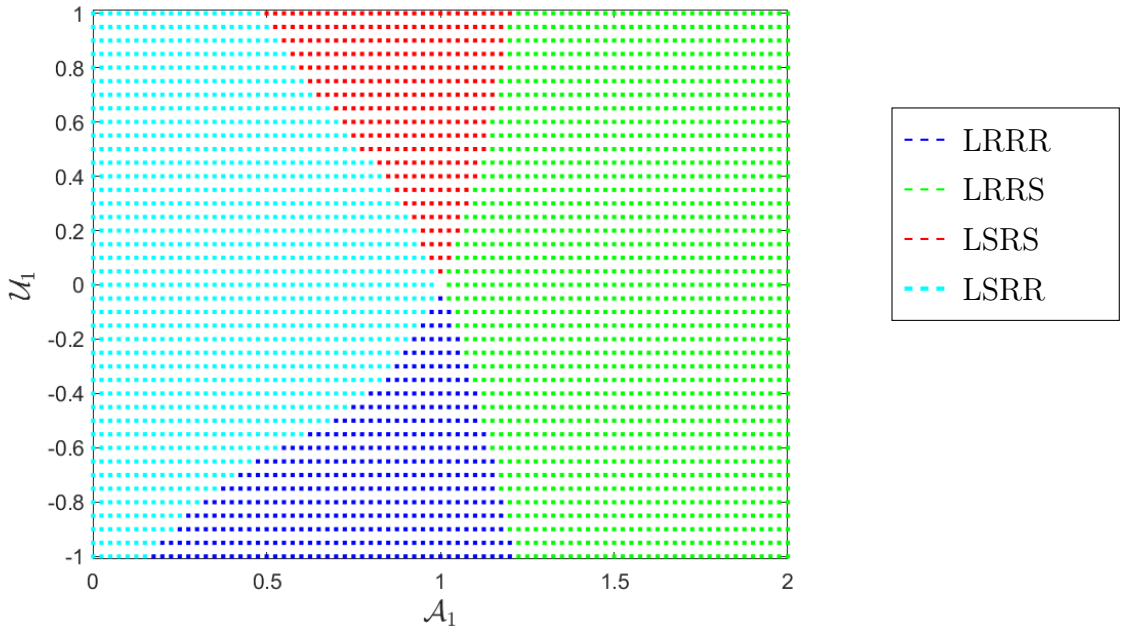

Figure 3.29: Overview of the parameter space spanned by $\mathcal{U}_1$ ($-1.0 \leq \mathcal{U}_1 \leq 1.0$) and $\mathcal{A}_1$ ($0 \leq \mathcal{A}_1 \leq 2.0$) with $\mathcal{U}_2 = 0$, $\mathcal{A}_2 = 1$, $k = 1.1$ and $\bar{A}_2 = 1$.

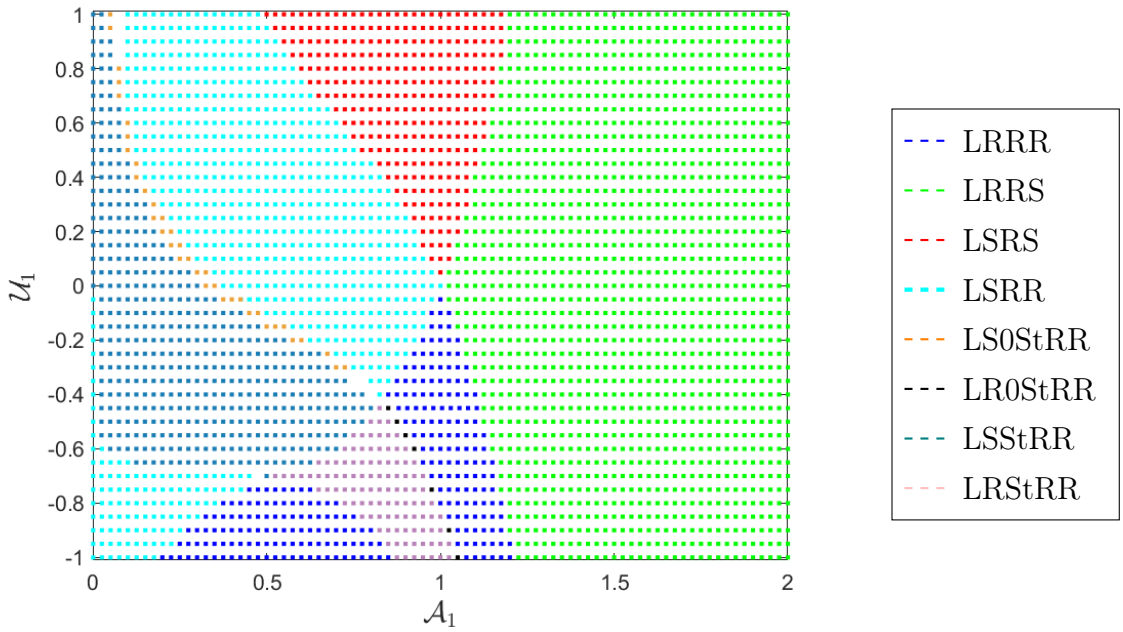

Figure 3.30: Overview of the parameter space spanned by $\mathcal{U}_1$ ($-1.0 \leq \mathcal{U}_1 \leq 1.0$) and $\mathcal{A}_1$ ($0 \leq \mathcal{A}_1 \leq 2.0$) with $\mathcal{U}_2 = 0$, $\mathcal{A}_2 = 1$, $k = 0.9$ and $\bar{A}_2 = 1$.

3.10 General tube law

In this section we close our simple model for blood flow in a single complaint vessel with a sudden change in material properties at the point of initial discontinuity in the Riemann problem using the general tube law. This section will follow same structure as in the case of expanding tube law with the only difference been that some integrals may not be possible to compute analytically, so numerical integration is used. Following similar method of Section 3.1, 3.1.1, Section 3.1.2 we have the dimensionless conservation of mass and momentum equations as

$$\frac{\partial A_j}{\partial t} + \frac{\partial}{\partial x}(A_j u_j) = 0, \tag{3.104}$$

$$\frac{\partial}{\partial t}(A_j u_j) + \frac{\partial}{\partial x}(A_j u_j^2) + A_j \frac{\partial p_j}{\partial x} = 0, \quad (j = 1, 2). \tag{3.105}$$

These equations are subject to dimensionless tube laws in each compartment

$$p_1 = \bar{p}_{e1} + f(A_1), \tag{3.106}$$

$$p_2 = \bar{p}_{e2} + kf(A_2/\bar{A}_2), \tag{3.107}$$

where f denotes the general tube laws for both compartment 1 and 2 such that

$$f(s) = (s^m - s^{-n}) \tag{3.108}$$

and $m, n \geq 0$ is an exponent [44]. We proceed to discuss the solution to this problem compartment by compartment for easy illustration of our problem.

As in Section 3.2 we now consider a Riemann problem, where we impose a uniform initial condition in both compartment 1 and compartment 2, but not necessarily continuous across $x = 0$. At $x = -L$ (inlet to compartment 1) we impose $A_1 = \mathcal{A}_1$, $u_1 = \mathcal{U}_1$, such that through (3.106) the fluid pressure becomes

$$p_1 = \bar{p}_{e1} + \mathcal{A}_1^m - \mathcal{A}_1^{-n}. \tag{3.109}$$

Conversely at $x = L$ (outlet to compartment 2) we impose $A_2 = \mathcal{A}_2$, $u_2 = \mathcal{U}_2$. Also, from (3.107) we have

$$p_2 = \bar{p}_{e2} + k\left(\left(\frac{\mathcal{A}_2}{\bar{A}_2}\right)^m - \left(\frac{\mathcal{A}_2}{\bar{A}_2}\right)^{-n}\right). \tag{3.110}$$

3.10.1 Compartment 1

Here, following same method as in Section 3.2.1 we have the Riemann invariants for compartment 1 given as

$$R_1 = u_1 \pm \int_1^{A_1} \sqrt{mA^{*(m-2)} + nA^{*-(n+2)}}\, dA^*, \tag{3.111}$$

which are constant along characteristics $C_\pm$, defined according to

$$\frac{dx}{dt} = u_1 \pm \sqrt{mA_1^m + nA_1^{-n}}. \tag{3.112}$$

3.10.2 Compartment 2

Also, we follow same method as in Section 3.2.2 to compute the Riemann invariants for compartment 2 as

$$R_2 = u_2 \pm \int_{\bar{A}_2}^{A_2} \sqrt{k\left(mA^{*(m-2)} + nA^{*-(n+2)}\right)}dA^*, \quad \text{constant on} \tag{3.113}$$

$$\frac{dx}{dt} = u_2 \pm \sqrt{k\left(m\left(\frac{A_2}{\bar{A}_2}\right)^m + n\left(\frac{A_2}{\bar{A}_2}\right)^{-n}\right)} = u_2 \pm c_2. \tag{3.114}$$

3.10.3 Boundary conditions between compartments

With discontinuity in material properties similar to Section 3.2.3 we impose continuity of fluid flux and continuity of total pressure across the discontinuous point ($x = 0$), such that we have

$$A_1 u_1 = A_2 u_2, \quad (x = 0), \tag{3.115}$$

$$\bar{p}_{e1} + (A_1^m - A_1^{-n}) + \frac{1}{2}u_1^2 = \bar{p}_{e2} + k\left(\left(\frac{A_2}{\bar{A}_2}\right)^m - \left(\frac{A_2}{\bar{A}_2}\right)^{-n}\right) + \frac{1}{2}u_2^2, \quad (x = 0). \tag{3.116}$$

3.10.4 Nonlinear flow structure

As in Section 3.3 the flow will exhibit either shock or rarefaction adjacent to the ambient region and exhibit uniform state at the intermediate region. Again due to discontinuity in material properties we specify boundary conditions as in (3.115), (3.116) and consider the different flow possibilities in turn.

3.10.5 Left rarefaction

Following similar method as in Section 3.3.1 we have that at the edge of the rarefaction in contact with region 3, we have that $u_r^L = \mathcal{U}_3^L$, $A_r^L = \mathcal{A}_3^L$ and $c_r^L = \mathcal{C}_3^L$ such that

$$x_r = \Bigg(\mathcal{U}_1 + \int_1^{\mathcal{A}_1} \sqrt{mA^{*(m-2)} + nA^{*-(n+2)}}dA^* - \sqrt{m(\mathcal{A}_3^L)^m + n(\mathcal{A}_3^L)^{-n}} - \int_1^{\mathcal{A}_3^L} \sqrt{mA^{*(m-2)} + nA^{*-(n+2)}}dA^*\Bigg)t. \tag{3.117}$$

Simplifying, we have that at the edge of the rarefaction region adjacent to region 3

$$\mathcal{U}_3^L = \mathcal{U}_1 + \int_1^{\mathcal{A}_1} \sqrt{mA^{*(m-2)} + nA^{*-(n+2)}}dA^* - \int_1^{\mathcal{A}_3^L} \sqrt{mA^{*(m-2)} + nA^{*-(n+2)}}dA^* \tag{3.118}$$

From above, we can apply numerical integration solve for $\mathcal{U}_3^L$ for given $\mathcal{A}_3^L$.

For physical solution of the left rarefaction, we need

$$(\mathcal{U}_3^L - \mathcal{C}_3^L) < 0 \quad \text{and} \quad (\mathcal{U}_3^L - \mathcal{C}_3^L) > (\mathcal{U}_1 - \mathcal{C}_1) \tag{3.119}$$

3.10.6 Right rarefaction

Again we follow same method as in Section 3.3.2 such that at the edge of the rarefaction in contact with region 3, we have that $u_r^R = \mathcal{U}_3^R$, $A_r^R = \mathcal{A}_3^R$ and $c_r^R = \mathcal{C}_3^R$ and

$$x_r = \left(\mathcal{U}_2 + \int_{\bar{A}_2}^{\mathcal{A}_3^R} \sqrt{k(mA^{*(m-2)} + nA^{*-(n+2)})}dA^* + \sqrt{k(m(\mathcal{A}_3^R)^m + n(\mathcal{A}_3^R)^{-n})} \right. \tag{3.120}$$

$$\left. - \int_{\bar{A}_2}^{\mathcal{A}_2} \sqrt{k(mA^{*(m-2)} + nA^{*-(n+2)})}dA^* \right)t. \tag{3.121}$$

Simplifying, we have that at the edge of the rarefaction region adjacent to region 3

$$\mathcal{U}_3^R = \mathcal{U}_2 + \int_{\bar{A}_2}^{\mathcal{A}_3^R} \sqrt{k(mA^{*(m-2)} + nA^{*-(n+2)})}dA^* - \int_{\bar{A}_2}^{\mathcal{A}_2} \sqrt{k(mA^{*(m-2)} + nA^{*-(n+2)})}dA^* \tag{3.122}$$

From above, we can apply Simpson's numerical integration method to solve for $\mathcal{U}_3^R$ for given $\mathcal{A}_3^R$.

Also, for the right rarefaction to be a physical solution, we need

$$(\mathcal{U}_3^R + \mathcal{C}_3^R) > 0, \quad \text{and} \quad (\mathcal{U}_3^R + \mathcal{C}_3^R) < (\mathcal{U}_2 + \mathcal{C}_2). \tag{3.123}$$

3.10.7 Left shock

We now consider a left moving shock wave in compartment 1. To ensure conservation of mass and momentum across the shock, we write (3.104) and (3.105) in the form

$$\frac{\partial A_1}{\partial t} + \frac{\partial}{\partial x}(A_1 u_1) = 0, \tag{3.124}$$

$$\frac{\partial}{\partial t}(A_1 u_1) + \frac{\partial}{\partial x}\left(A_1 u_1^2 + \frac{m}{m+1}A_1^{m+1} - \frac{n}{n-1}A^{-(n-1)}\right) = 0. \tag{3.125}$$

Following similar method as in Section 3.3.3, for a left moving shock in compartment 1 we have

$$\dot{s}_L = \frac{\mathcal{A}_3^L\mathcal{U}_3^L - \mathcal{A}_1\mathcal{U}_1}{\mathcal{A}_3^L - \mathcal{A}_1}, \tag{3.126}$$

$$\dot{s}_L = \frac{\mathcal{A}_3^L(\mathcal{U}_3^L)^2 + \frac{m}{m+1}\mathcal{A}_3^{L^{m+1}} - \frac{n}{n-1}(\mathcal{A}_3^L)^{-(n-1)} - \mathcal{A}_1\mathcal{U}_1^2 - \frac{m}{m+1}\mathcal{A}_1^{m+1} + \frac{n}{n-1}\mathcal{A}_1^{-(n-1)}}{\mathcal{A}_3^L\mathcal{U}_3^L - \mathcal{A}_1\mathcal{U}_1}. \tag{3.127}$$

We now equate (3.126) and (3.127) and simplify to compute the velocity immediately to the left of the discontinuity as

$$\mathcal{U}_3^L = \mathcal{U}_1 + \sqrt{\frac{\left(\frac{m}{m+1}\left((\mathcal{A}_3^L)^{m+1} - \mathcal{A}_1^{m+1}\right) + \frac{n}{n-1}\left(\mathcal{A}_1^{-(n-1)} - (\mathcal{A}_3^L)^{-(n-1)}\right)\right)(\mathcal{A}_3^L - \mathcal{A}_1)}{\mathcal{A}_1\mathcal{A}_3^L}}, \tag{3.128}$$

a nonlinear constraint which relates $\mathcal{U}_3^L$ and $\mathcal{A}_3^L$ to the initial conditions.

Note that for the shock to be a physical solution we must also check against the Lax entropy

conditions [116]. For a left shock this means that we need

$$(\mathcal{U}_3^L - \mathcal{C}_3^L) < \dot{s}_L < (\mathcal{U}_1 - \mathcal{C}_1). \tag{3.129}$$

3.10.8 Right shock

We now consider a right moving shock wave in compartment 2. To ensure conservation of mass and momentum across the shock, we again write (3.104) and (3.105) in the form

$$\frac{\partial A_2}{\partial t} + \frac{\partial}{\partial x}(A_2 u_2) = 0, \tag{3.130}$$

$$\frac{\partial}{\partial t}(A_2 u_2) + \frac{\partial}{\partial x}\left(A_2 u_2^2 + \frac{\bar{A}_2 km}{m+1}\left(\frac{A_2}{\bar{A}_2}\right)^{m+1} - \frac{\bar{A}_2 kn}{n-1}\left(\frac{A_2}{\bar{A}_2}\right)^{-(n-1)}\right) = 0. \tag{3.131}$$

As before, we compute the two expressions for the shock speed to determine the cross sectional area at the right of the barrier relative to shock as

$$\mathcal{A}_2\mathcal{A}_3^R(\mathcal{U}_3^R - \mathcal{U}_2)^2 = \left(\frac{km}{(m+1)\bar{A}_2{}^m}\left(\mathcal{A}_2^{m+1} - (\mathcal{A}_3^R)^{m+1}\right) + \frac{kn}{(n-1)\bar{A}_2{}^n}\left((\mathcal{A}_3^R)^{-(n-1)} - \mathcal{A}_2^{-(n-1)}\right)\right)(\mathcal{A}_2 - \mathcal{A}_3^R). \tag{3.132}$$

From (3.132), we also determine the velocity at the discontinuity relative to the shock as

$$\mathcal{U}_3^R = \mathcal{U}_2 + \sqrt{\frac{\left(\frac{km}{(m+1)\bar{A}_2{}^m}\left(\mathcal{A}_2^{m+1} - (\mathcal{A}_3^R)^{m+1}\right) + \frac{kn}{(n-1)\bar{A}_2{}^n}\left((\mathcal{A}_3^R)^{-(n-1)} - \mathcal{A}_2^{-(n-1)}\right)\right)(\mathcal{A}_2 - \mathcal{A}_3^R)}{\mathcal{A}_2\mathcal{A}_3^R}}, \tag{3.133}$$

a nonlinear constraint which relates $\mathcal{U}_3^R$ and $\mathcal{A}_3^R$ to the initial conditions.

Again for physicality of the right shock, we must also check against the Lax entropy conditions [116]. For a right shock this means that we need

$$(\mathcal{U}_2 + \mathcal{C}_2) < \dot{s}_R < (\mathcal{U}_3^R + \mathcal{C}_3^R). \tag{3.134}$$

3.10.9 Boundary conditions

Having determined the flow structure, we can now rewrite the the continuity conditions (3.115) and (3.116) at $x = 0$ as

$$\mathcal{U}_3^L\mathcal{A}_3^L = \mathcal{U}_3^R\mathcal{A}_3^R, \tag{3.135}$$

$$\bar{p}_{e1} + \left((\mathcal{A}_3^L)^m - (\mathcal{A}_3^L)^{-n}\right) + \frac{1}{2}(\mathcal{U}_3^L)^2 = \bar{p}_{e2} + k\left(\left(\frac{\mathcal{A}_3^R}{\bar{A}_2}\right)^m - \left(\frac{\mathcal{A}_3^R}{\bar{A}_2}\right)^{-n}\right) + \frac{1}{2}(\mathcal{U}_3^R)^2. \tag{3.136}$$

3.11 Numerical method

Here we apply Newton iteration method similar to Section 3.4 to solve for the four possible wave structures: for each wave structure we determine the values of $\mathcal{A}_3^L$ and $\mathcal{A}_3^R$ as a function of the initial

conditions. Here we present just two representative cases (LRRS and LSRR) while assuming continuity of fluid flux (3.135) and continuity of total pressure (3.136) across the discontinuity to ensure enough information to determine all the variables.

3.11.1 Left rarefaction, right shock (LRRS)

We consider a left rarefaction wave in compartment 1 and a right shock wave in compartment 2 (LRRS) and by imposing continuous flux and continuous total pressure across the junction between compartments as in equations (3.135) and (3.136).

We present an example of such behaviour for $\mathcal{A}_1 = 1.0$, $\mathcal{A}_2 = 0.8$, $\mathcal{U}_1 = 0$, $\mathcal{U}_2 = 0$, $\bar{p}_{e1} = \bar{p}_{e2} = 0$, $k_2 = 1.1$, $m = 10$ and $n = 1.5$ where using Newton's method we compute $\mathcal{A}_3^L = 1.309$, $\mathcal{A}_3^R = 1.297$ and $\mathcal{U}_3^L = -1.989$, $\mathcal{U}_3^R = -2.007$ with typical profiles shown in Figure 3.31. As expected, we have a left moving rarefaction in compartment 1 and a right moving shock in compartment 2 separated by a contact discontinuity (stationary wave) at $x = 0$ which results in reduction of the tube cross-sectional area, flow speed and wave speed from compartment 1 to compartment 2.

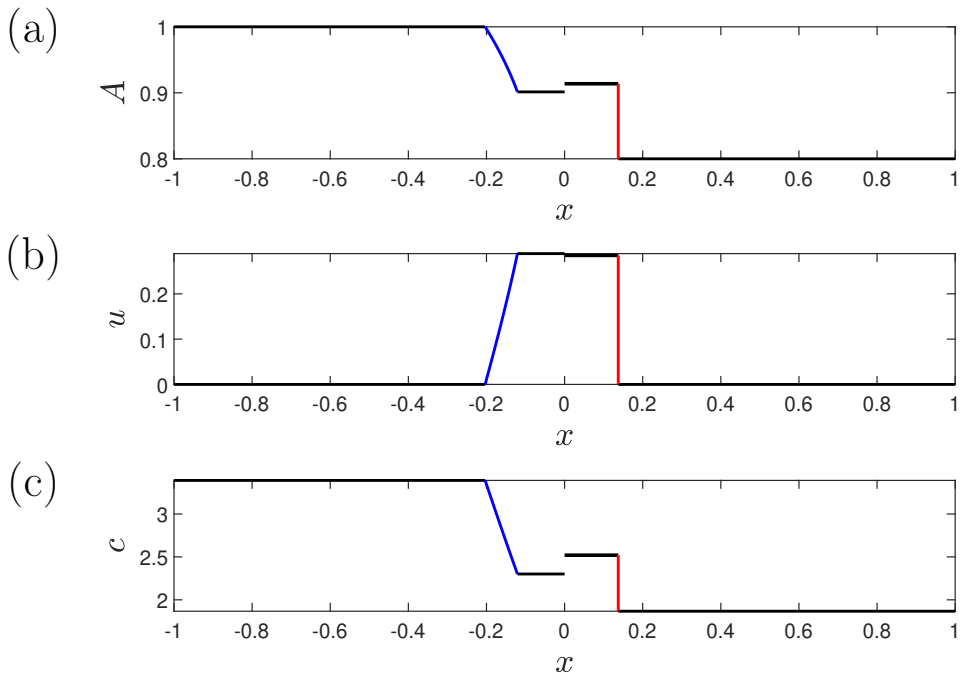

Figure 3.31: Left rarefaction, right shock with discontinuity at $x = 0$. Figure 3.31(a) displays profile of cross-sectional area, Figure 3.31(b), displays profile of flow speed and Figure 3.31(c) displays profile of the wave speed. We choose $\mathcal{A}_1 = 1.0$, $\mathcal{A}_2 = 0.8$, $\mathcal{U}_1 = 0$, $\mathcal{U}_2 = 0$, $k_2 = 1.1$ and using Newton's method we compute $\mathcal{A}_3^L = 1.309$, $\mathcal{A}_3^R = 1.297$ and $\mathcal{U}_3^L = -1.989$, $\mathcal{U}_3^R = -2.007$ at $t = 0.06$.

3.11.2 Left shock, right rarefaction

We consider a left shock wave in compartment 1 and a right rarefaction wave in compartment 2 (LSRR), we assume continuous flux and continuous total pressure as in equations (3.135) and (3.136).

We present an example of such behaviour for $\mathcal{A}_1 = 1.0$, $\mathcal{A}_2 = 1.5$, $\mathcal{U}_1 = 0$, $\mathcal{U}_2 = 0.6$, $\bar{p}_{e1} = \bar{p}_{e2} = 0$, $k_2 = 1.1$ where using Newton's method we compute $\mathcal{A}_3^L = 1.309$, $\mathcal{A}_3^R = 1.297$ and $\mathcal{U}_3^L = 1.989$, $\mathcal{U}_3^R = -2.007$; a typical profile is shown in Figure 3.32 where, as expected, we have a left moving shock in compartment 1 and a right moving rarefaction in compartment 2 which is separated by a contact discontinuity at $x = 0$, resulting in an expansion of the tube cross-sectional area, flow speed and wave speed from compartment 1 to compartment 2.

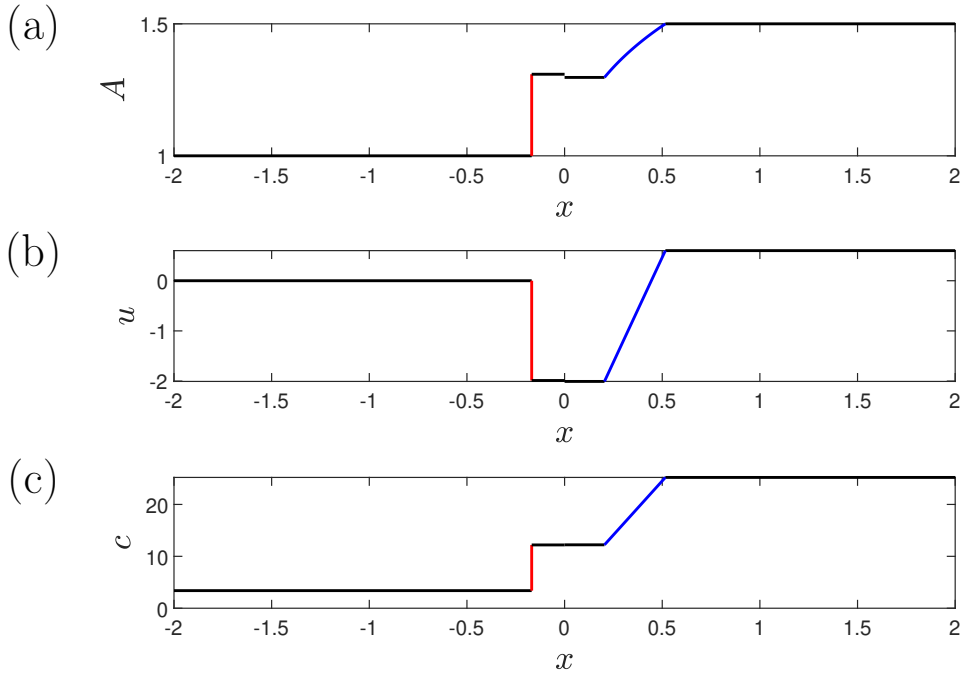

Figure 3.32: Left shock, right rarefaction with discontinuity at $x = 0$. Figure 3.32(a) displays profile of cross-sectional area; Figure 3.32(b) displays profile of flow speed and Figure 3.32(c) displays profile of the wave speed. We choose $\mathcal{A}_1 = 1.0$, $\mathcal{A}_2 = 1.5$, $\mathcal{U}_1 = 0$, $\mathcal{U}_2 = 0.6$, $k_2 = 1.1$ and using Newton's method we compute $\mathcal{A}_3^L = 1.309$, $\mathcal{A}_3^R = 1.297$ and $\mathcal{U}_3^L = 0.989$, $\mathcal{U}_3^R = -2.007$ at $t = 0.02$.

3.12 Other possible flow states: resonance

In this section we generalize the configuration C and configuration D resonant solutions (Section 3.7) to use the general tube law.

3.12.1 Governing equations for configuration C using the general tube law

In this section, we explore Riemann problem for configuration C using the general tube law. The setup is similar to what we have previously in Section 3.7.1, such that the left rarefaction resonates with the stationary wave and produces three successive waves where each is separated by a small distance $\epsilon \ll 1$. Such that from left to right we have a supercritical stationary wave, a zero speed shock, and a subcritical stationary wave. The transcritical rarefaction spans all the way from $x = (\mathcal{U}_1 - \mathcal{C}_1)$ to $x = -\epsilon$. Following similar method as in Section 3.7.1 at the outer edge of the supercritical stationary wave adjacent to the transcritical left rarefaction we denote $A_r^L = \mathcal{A}_3^L$, $u_r^L = \mathcal{U}_3^L$ and $c_r^L = \mathcal{C}_3^L$, such that the profiles inner limit as $\epsilon \to 0$ becomes

$$\mathcal{U}_3^L = \mathcal{C}_3^L = \sqrt{k\,(m(\mathcal{A}_3^L)^m + n(\mathcal{A}_3^L)^{-n})}. \tag{3.137}$$

Also, similar to Section 3.7.1, across the supercritical stationary wave ($x > -\epsilon$) we denote $A_1 = \mathcal{A}_{12}$, $u_1 = \mathcal{U}_{12}$ and $c_1 = \mathcal{C}_{12}$ and impose continuity of flux and total pressure, to have

$$\mathcal{A}_3^L \mathcal{U}_3^L = \mathcal{A}_{12}\mathcal{U}_{12}, \tag{3.138}$$

$$\bar{p}_{e1} + \frac{1}{2}(\mathcal{U}_3^L)^2 + ((\mathcal{A}_3^L)^m - (\mathcal{A}_3^L)^{-n}) = \bar{p}_{es} + \frac{1}{2}(\mathcal{U}_{12})^2 + k_s\left(\left(\frac{\mathcal{A}_{12}}{\bar{A}_s}\right)^m - \left(\frac{\mathcal{A}_{12}}{\bar{A}_s}\right)^{-n}\right). \tag{3.139}$$

Following a similar method as before, to the right of the zero speed shock we denote the (uniform) profiles of cross-sectional area, velocity and wavespeed as $\mathcal{A}_{21}$, $\mathcal{U}_{21}$ and $\mathcal{C}_{21}$ and imposing a zero speed shock at $x = 0$ gives the flow velocity as

$$\mathcal{U}_{21} = \mathcal{U}_{12} + \sqrt{\frac{\left(\frac{k_s m}{(m+1)\bar{A_s}^m}\left(\mathcal{A}_{21}^{m+1} - (\mathcal{A}_{12})^{m+1}\right) + \frac{k_s n}{(n-1)\bar{A_s}^n}\left((\mathcal{A}_{12})^{-(n-1)} - \mathcal{A}_{21}^{-(n-1)}\right)\right)(\mathcal{A}_{21} - \mathcal{A}_{12})}{\mathcal{A}_{21}\mathcal{A}_{12}}}, \tag{3.140}$$

a nonlinear equation connecting $\mathcal{A}_{21}$ to $\mathcal{U}_{21}$.

To the right of the subcritical stationary wave (*i.e.* $x = \epsilon$) we denote the (uniform) profile $A_2 = \mathcal{A}_3^R$, $u_2 = \mathcal{U}_3^R$, $c_2 = \mathcal{C}_3^R$ and impose continuity of flux and total pressure (*i.e.* conditions (3.135) and (3.136)) to have

$$\mathcal{A}_{21}\mathcal{U}_{21} = \mathcal{A}_3^R \mathcal{U}_3^R, \tag{3.141}$$

$$\bar{p}_{es} + \frac{1}{2}(\mathcal{U}_{21})^2 + k_s\left(\left(\frac{\mathcal{A}_{21}}{\bar{A}_s}\right)^m - \left(\frac{\mathcal{A}_{21}}{\bar{A}_s}\right)^{-n}\right) = \bar{p}_{e2} + \frac{1}{2}(\mathcal{U}_3^R)^2 + k\left(\left(\frac{\mathcal{A}_3^R}{\bar{A}_2}\right)^m - \left(\frac{\mathcal{A}_3^R}{\bar{A}_2}\right)^{-n}\right) \tag{3.142}$$

It then follows that the (uniform) flow to the right of the subcritical stationary wave (*i.e.* $x > \epsilon$) is then connected to the the far-field in region 2 with two flow possibilities *i.e.* either a shock or a rarefaction.

For a shock in the daughter vessel, we have

$$\mathcal{U}_3^R = \mathcal{U}_2 + \sqrt{\frac{\left(\frac{km}{(m+1)\bar{A}_2^m}\left(\mathcal{A}_2^{m+1} - (\mathcal{A}_3^R)^{m+1}\right) + \frac{kn}{(n-1)\bar{A}_2^n}\left((\mathcal{A}_3^R)^{-(n-1)} - \mathcal{A}_2^{-(n-1)}\right)\right)(\mathcal{A}_2 - \mathcal{A}_3^R)}{\mathcal{A}_2\mathcal{A}_3^R}}, \tag{3.143}$$

a nonlinear equation connecting $\mathcal{A}_3^R$ to $\mathcal{U}_3^R$. Note we also apply the physicality conditions (3.93).

Conversely, for a rarefaction in the daughter vessel adjacent to the far-field of region 2, following similar method as in Section 3.7.1, we have at the edge of the daughter region

$$\mathcal{U}_3^R = \mathcal{U}_2 - \int_1^{\mathcal{A}_2} \sqrt{k(mA^{*(m-2)} + nA^{*-(n+2)})}dA^* + \int_1^{\mathcal{A}_3^R} \sqrt{k(mA^{*(m-2)} + nA^{*-(n+2)})}dA^* \tag{3.144}$$

Again, we use Simpson's rule to evaluate our integrals to solve for $\mathcal{U}_3^R$ for a given $\mathcal{A}_3^R$, and also apply physicality conditions (3.94).

3.12.2 Governing equations for configuration D using the general tube law

In this section, we follow similar method as in Section 3.7.2 where left rarefaction resonates with the stationary wave and generates a new wave (shock) on the right side of the stationary wave, while the transcritical left rarefaction remains in contact with the stationary wave. Similar to Section 3.12.1 we let $A_r^L = \mathcal{A}_3^L$, $u_r^L = \mathcal{U}_3^L$ and $c_r^L = \mathcal{C}_3^L$ at the edge of the transcritical left rarefaction such that the flow speed which is also equal to the wave speed is given as

$$\mathcal{U}_3^L \;=\; \mathcal{C}_3^L = \sqrt{k\left(m(\mathcal{A}_3^L)^m + n(\mathcal{A}_3^L)^{-n}\right)}, \tag{3.145}$$

and the cross-sectional area is to be determined by Newtons's method.

We now denote the profiles of cross-sectional area, velocity and wavespeed in the region between the stationary wave and the new shock (generated by the resonance) by $\mathcal{A}_{21}$, $\mathcal{U}_{21}$ and $\mathcal{C}_{21}$, respectively. Then following a similar method in Section 3.7.2 we impose continuity of flux and total pressure across the contact discontinuity to have

$$\mathcal{A}_3^L\mathcal{U}_3^L \;=\; \mathcal{A}_{21}\mathcal{U}_{21}, \tag{3.146}$$

$$\bar{p}_{e1} + \frac{1}{2}(\mathcal{U}_3^L)^2 + \left((\mathcal{A}_3^L)^m - (\mathcal{A}_3^L)^{-n}\right) \;=\; \bar{p}_{e2} + \frac{1}{2}(\mathcal{U}_{21})^2 + k\left(\left(\frac{\mathcal{A}_{21}}{\bar{A}_2}\right)^m - \left(\frac{\mathcal{A}_{21}}{\bar{A}_2}\right)^{-n}\right). \tag{3.147}$$

Across the resonant shock wave produced in the compartment 2, we invoke conservation of mass and momentum across the front at $x = s_{res}(t)$ and follow same method as in Section 3.7.2 and compute the velocity of the resonant shock as

$$\mathcal{U}_3^R = \mathcal{U}_{21} + \sqrt{\frac{\left(\frac{km}{(m+1)\bar{A}_2^m}\left((\mathcal{A}_3^R)^{m+1} - (\mathcal{A}_{21})^{m+1}\right) + \frac{kn}{(n-1)\bar{A}_2^n}\left((\mathcal{A}_{21})^{-(n-1)} - (\mathcal{A}_3^R)^{-(n-1)}\right)\right)(\mathcal{A}_3^R - \mathcal{A}_{21})}{\mathcal{A}_3^R\mathcal{A}_{21}}}, \tag{3.148}$$

a nonlinear equation connecting $\mathcal{A}_3^R$ to $\mathcal{U}_3^R$.

The second wave in the daughter vessels can be either a shock or rarefaction, and we then apply a similar approach as in configuration C of Section 3.12.1 and use (3.143) for a shock wave in region 2 or (3.144) for a rarefaction wave in region 2. Note, we also impose the physicality conditions for shock and rarefaction.

3.13 Traces through the parameter space

In this section we summarise the overall behaviour of our nonlinear system by constructing bifurcation diagrams as a function of the far-field parameters. We first vary the initial cross-sectional area far to the right of the stationary wave, $\mathcal{A}_2$, using the general tube law for a tube with discontinuous material properties with all other components held fixed. Furthermore, we consider variation in the cross-sectional area far to the left of the stationary wave, $\mathcal{A}_1$ while again holding other components fixed. For each of these cases, we first consider a case where compartment 2 is stiffer than compartment 1 (*i.e.* $k = 1.1$) followed by where compartment 2 is less stiff compared to compartment 1 (*i.e.* $k = 0.9$). We consider few representative cases and compare them with the cases where we used expanding tube law.

3.13.1 Case 12

Figure 3.33 illustrates bifurcation diagram where compartment 2 is stiffer than compartment 1 for tube with discontinuous material property using the general tube law. Here we vary the cross-sectional area in the far right of the discontinuity, $\mathcal{A}_2$ and consider $\mathcal{U}_1 = \mathcal{U}_2 = 0$, $\mathcal{A}_1 = 1$ and $k = 1.1$.

We have that for large $\mathcal{A}_2$ the system exhibits LSRR solution which transitions to LRRS solution for $\mathcal{A}_2 \leq 1$ similar to Figure 3.10. The LRRS solution persists and exhibits a turning point as the left rarefaction becomes transcritical at $\mathcal{A}_2 \approx 0.175$. Also, for very low $\mathcal{A}_2$ we have another LRRS solution which again exhibits a turning point at $\mathcal{A}_2 \approx 0.050$ forming a gap across $0.05 \leq \mathcal{A}_2 \leq 0.175$. This gap in the classical solutions is filled by two resonant solutions, from the right of the loop we have configuration C solution with a right shock which transitions to a configuration D solution with a right shock and then meets up with the transcritical LRRS at low $\mathcal{A}_2$. Figure 3.34 compares the result of the general tube law and the expanding tube law and it is seen that for the general tube law, the resonance region occupies a small region and also does not persist for all $\mathcal{A}_2$ but transitions back into a classical solution (see Figure 3.34a) but for the expanding tube law the resonant solution occupies a much larger region and persists for as $\mathcal{A}_2 \to 0$ (see Figure 3.34b).

3.13.2 Case 13

In Figure 3.35 we consider $\mathcal{U}_2 = 0.6$, $\mathcal{U}_1 = 0$, $\mathcal{A}_1 = 1$ and vary $\mathcal{A}_2$ to construct a bifurcation diagram where compartment 2 is stiffer than compartment 1 (*i.e.* $k = 1.1$) for a tube with discontinuous material properties using the general tube law.

Figure 3.35 show that for large $\mathcal{A}_2$ the system is similar to figure 3.18, exhibiting a LSRR solution which transitions to LRRR as $\mathcal{A}_2$ decreases and further transitions to LRRS solution as $\mathcal{A}_2$ decreases further. The LRRS solution persists and exhibits a turning point as the left rarefaction becomes transcritical at $\mathcal{A}_2 \approx 0.197$. Also, for very low $\mathcal{A}_2$ we have another LRRS solution which again exhibits a turning point at $\mathcal{A}_2 \approx 0.054$ forming a gap for $0.054 \leq \mathcal{A}_2 \leq 0.197$. This gap is filled by two resonant solutions, similar to case 12, from the right of the gap we have configuration C solution with a right shock which transitions to a configuration D solution with a right shock.

Figure 3.36 compares case 13 to the equivalent with the expanding tube law Figure 3.18. We again note that although the behaviour for large $\mathcal{A}_2$ is very similar the resonant solutions are pushed to much more collapsed profiles for the general tube law (Figure 3.36a) compared to the expanding tube law (Figure 3.36b). In Figure 3.37 we look at the analogous case where compartment 1 is stiffer than compartment 2 (*i.e.* $k = 0.9$). Both the general tube law (Figure 3.37a) and the expanding tube law

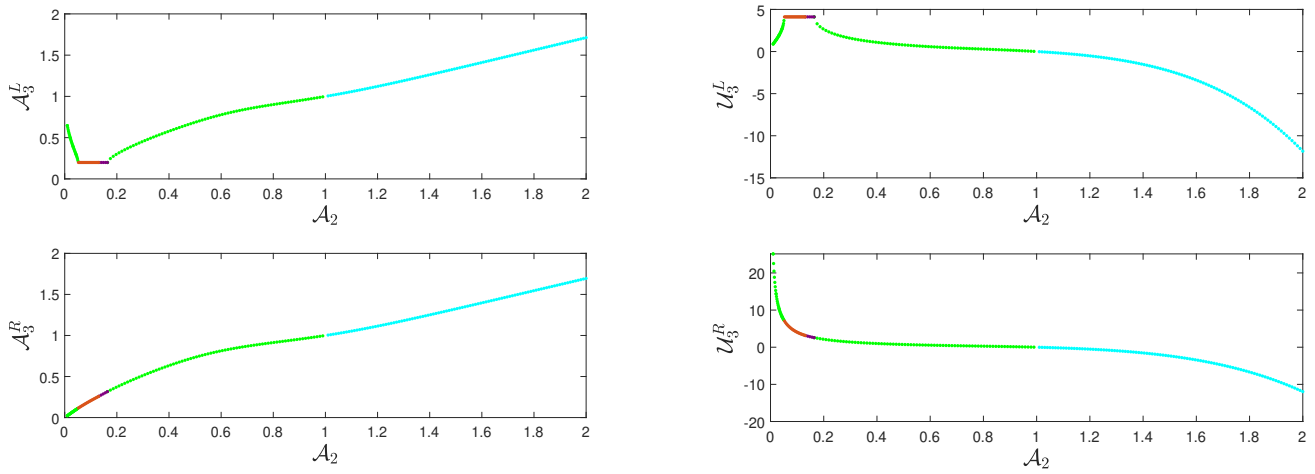

(a) **(b)**

Figure 3.33: Case 12:Bifurcation diagram for case where $\mathcal{U}_1 = 0$, $\mathcal{U}_2 = 0$, $\mathcal{A}_1 = 1$ and $k = 1.1$ with corresponding values of $\mathcal{A}_2$. $\mathcal{A}_3^L$, $\mathcal{A}_3^R$, $\mathcal{U}_3^L$ and $\mathcal{U}_3^R$, respectively.

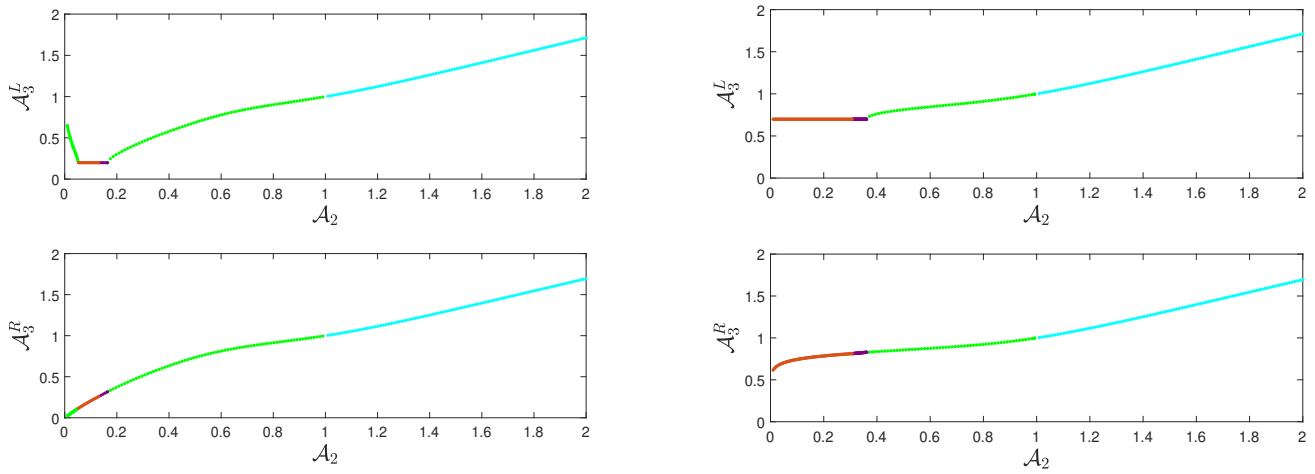

(a) **(b)**

Figure 3.34: Comparison of the bifurcation diagram for case where $\mathcal{U}_1 = 0$, $\mathcal{U}_2 = 0$, $\mathcal{A}_1 = 1$ and $k = 1.1$ with corresponding values of $\mathcal{A}_2$. $\mathcal{A}_3^L$, $\mathcal{A}_3^R$ for general tube and expanding tube law. Figure 3.34(a) illustrates use of general tube law while, Figure 3.34(b) illustrates use of expanding tube law.

(Figure 3.37b) show no resonant solution and the bifurcation diagrams are qualitatively similar. The only difference is that for general tube law, the LRRR solution is restricted to a smaller region.

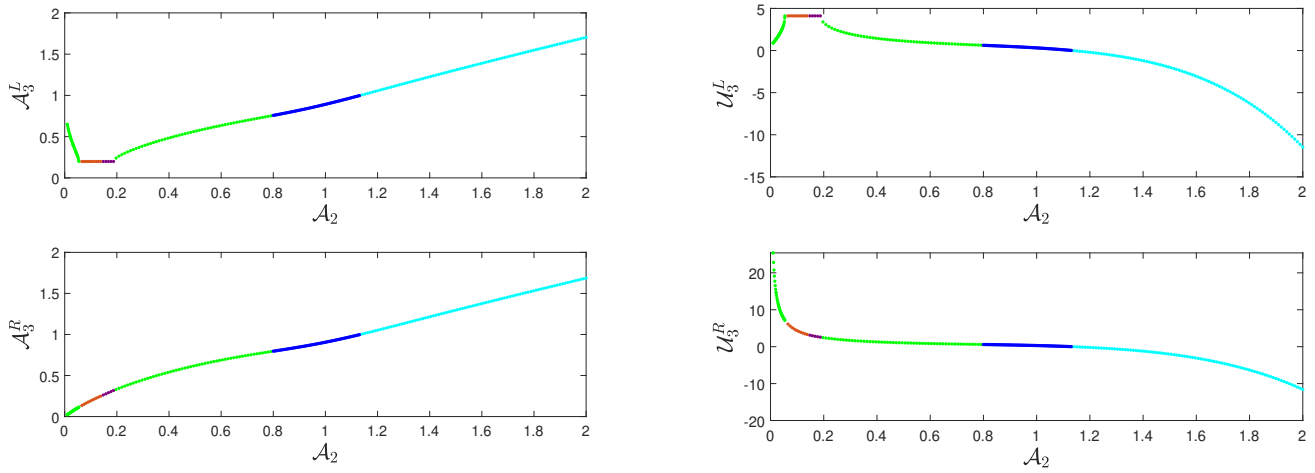

(a) **(b)**

Figure 3.35: Case 13: Bifurcation diagram for case where $\mathcal{U}_1 = 0, \mathcal{U}_2 = 0.6$, $\mathcal{A}_1 = 1$ and $k = 1.1$ with corresponding values of $\mathcal{A}_2$, $\mathcal{A}_3^L$, $\mathcal{A}_3^R$, $\mathcal{U}_3^L$ and $\mathcal{U}_3^R$, respectively.

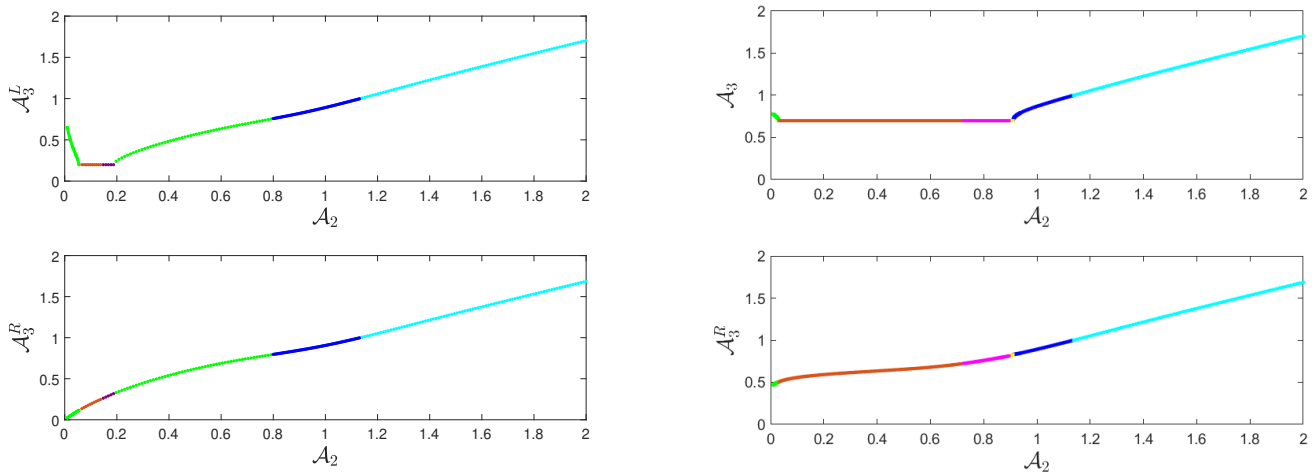

(a) **(b)**

Figure 3.36: Comparison between using general tube law and expanding tube law for case where $\mathcal{U}_1 = 0, \mathcal{U}_2 = 0.6$, $\mathcal{A}_1 = 1$ and $k = 1.1$ with corresponding values of $\mathcal{A}_2$, $\mathcal{A}_3^L$, $\mathcal{A}_3^R$, respectively. Figure 3.36(a) shows general tube law while, Figure 3.36(b) shows the expanding tube law.

3.13.3 Overview of parameter space

In this section, we summarise the overall behaviour of system by producing parameter space plots Here we retain the colour scheme as in Section 3.9.

Figure 3.38 illustrates parameter space plots for compartment 2 stiffer than compartment 1 using

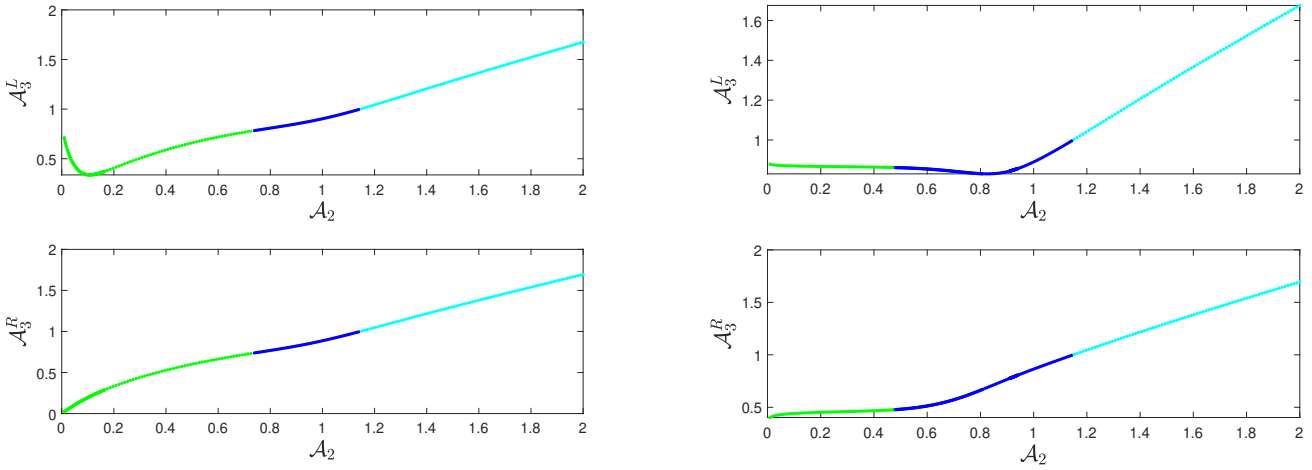

(a) **(b)**

Figure 3.37: Comparison between using general tube law and expanding tube law for case where $\mathcal{U}_1 = 0$, $\mathcal{U}_2 = 0.6$, $\mathcal{A}_1 = 1$ and $k = 0.9$ with corresponding values of $\mathcal{A}_2$, $\mathcal{A}_3^L$, $\mathcal{A}_3^R$, respectively. Figure 3.37(a) shows general tube law while, Figure 3.37(b) shows the expanding tube law.

the general tube law (Figure 3.38a) and the expanding tube law (Figure 3.38b) spanning $\mathcal{A}_2$ and $\mathcal{U}_2$ for ($\mathcal{A}_1 = 1$, $\mathcal{U}_1 = 0$) and $k = 1.1$. For the general tube law the classical solutions fill the domain of our parameter space with a small tongue of resonant solution (purple and orange) confined to low $\mathcal{A}_2$ spanning all $\mathcal{U}_2$ (Figure 3.38a). This is compared to similar parameter space plot using the expanding tube law (see Figure 3.38b) where the region of resonant solution is greatly expanded. So, using the general tube law does not eliminate resonance but restrict it to a smaller region across the parameter space.

Figure 3.39(a) illustrates parameter space plots where compartment 2 is less stiff than compartment 1 (*i.e.* $k = 0.9$) using same plots as Figure 3.38(a). In this case, neither the general tube law nor the expanding tube law exhibit resonant solutions and the plots are qualitatively similar.

Figure 3.40 and 3.41 are analogous to Figures 3.38 and 3.39, except that they are plotted in terms of the far-field profiles of compartment 1 ($\mathcal{A}_1$,$\mathcal{U}_1$) holding ($\mathcal{A}_2$,$\mathcal{U}_2$). The results are also analogous, although there is a reversal of the influence of vessel stiffness. For compartment 1 chosen less stiff than compartment 2 (*i.e.* $k = 1.1$ Figure 3.40 there no resonant solutions with either choice of tube law, and the plots are qualitatively similar (see Figure 3.41). Conversely, with compartment 2 chosen less stiff than compartment 1 ($k = 0.9$, Figure 3.41) we see that the wide tongue of resonant solution evident with the expanding tube law (Figure 3.41b) is suppressed to much smaller cross-sectional area with the general tube law (Figure 3.41a). The colour scheme are the same with those of Section 3.9.

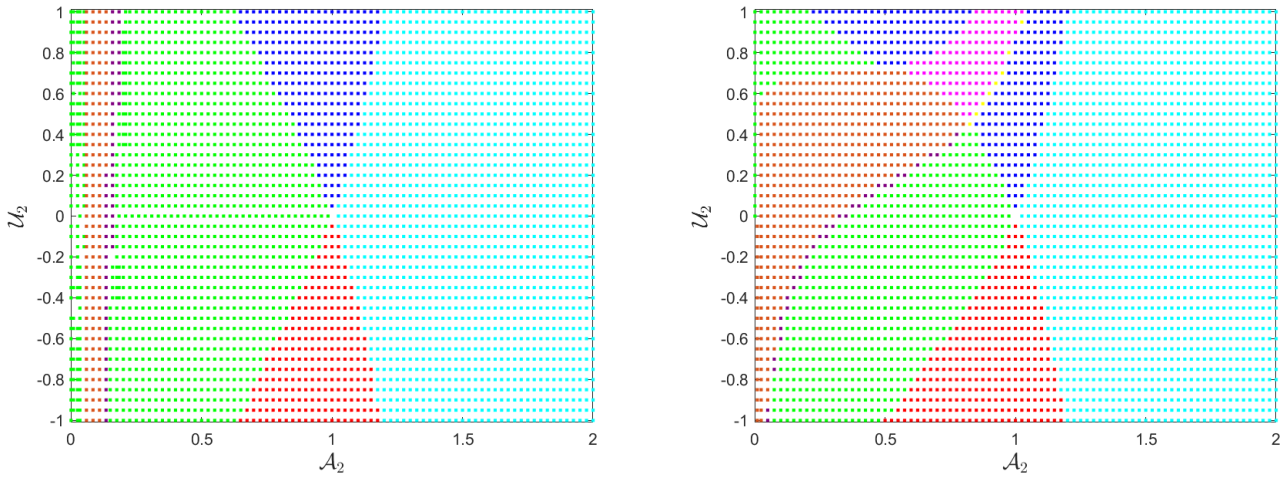

(a) **(b)**

Figure 3.38: Overview of parameter space for vessel with discontinuous material properties using the general and expanding tube law showing regions of classical and resonant solutions with $\mathcal{A}_1 = 1, \mathcal{U}_1 = 0$, $-1 \leq \mathcal{U}_2 \leq 1$, $0 \leq \mathcal{A}_2 \leq 2$ and $k = 1.1$. Figure 3.38(a) illustrates parameter space for general tube law while figure 3.38(b) illustrates parameter space for expanding tube law.

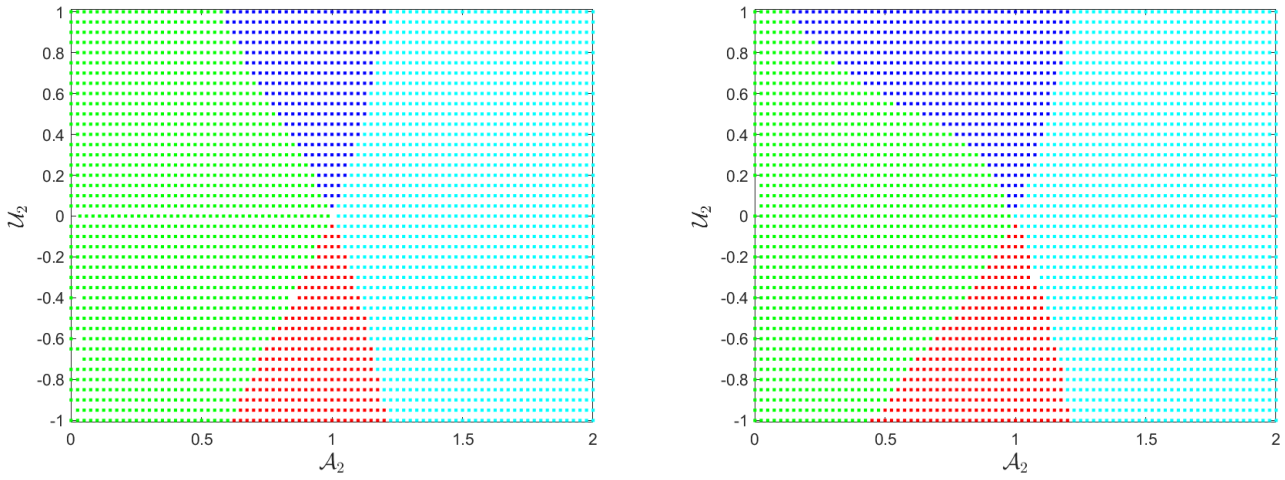

(a) **(b)**

Figure 3.39: Overview of parameter space for vessel with discontinuous material properties using the general and expanding tube law showing regions of classical solutions only with $\mathcal{A}_1 = 1, \mathcal{U}_1 = 0$, $-1 \leq \mathcal{U}_2 \leq 1$, $0 \leq \mathcal{A}_2 \leq 2$ and $k = 0.9$. Figure 3.39(a) illustrates parameter space for general tube law while figure 3.39(b) illustrates parameter space for expanding tube law.

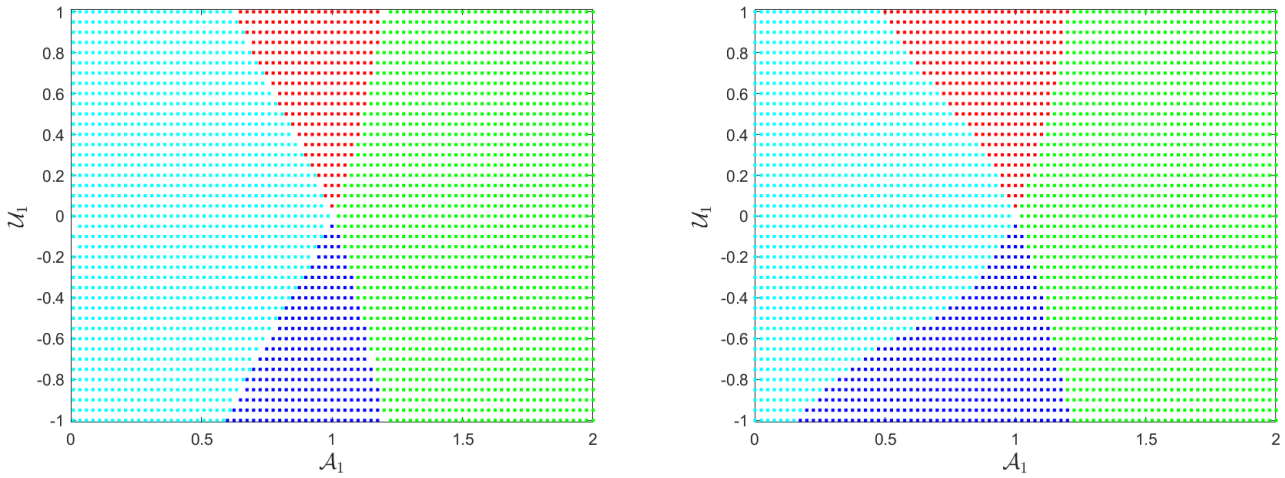

(a) **(b)**

Figure 3.40: Overview of parameter space for vessel with discontinuous material properties using the general and expanding tube law showing regions of classical solutions only with $\mathcal{A}_2 = 1, \mathcal{U}_2 = 0$, $-1 \leq \mathcal{U}_1 \leq 1$, $0 \leq \mathcal{A}_1 \leq 2$ and $k = 1.1$. Figure 3.40(a) illustrates parameter space for general tube law while figure 3.40(b) illustrates parameter space for expanding tube law.

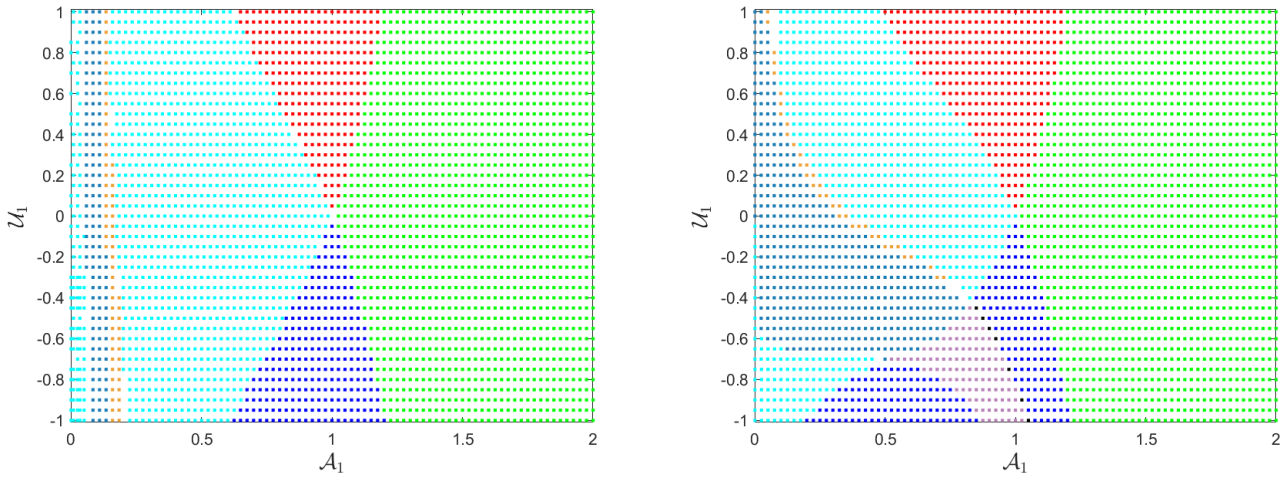

(a) **(b)**

Figure 3.41: Overview of parameter space for vessel with discontinuous material properties using the general and expanding tube law showing regions of classical and resonant solutions with $\mathcal{A}_2 = 1, \mathcal{U}_2 = 0$, $-1 \leq \mathcal{U}_1 \leq 1$, $0 \leq \mathcal{A}_1 \leq 2$ and $k = 0.9$. Figure 3.41(a) illustrates parameter space for general tube law while figure 3.41(b) illustrates parameter space for expanding tube law.

3.14 Summary and conclusion

In this chapter we have constructed the solution of the Riemann problem in a flexible-walled blood vessel with a sharp discontinuity in material properties as a mathematical model for blood flow into the retina via the optic nerve. In particular, we examined flow when the system exhibits a discontinuity in elastic stiffness between compartments and, similar to Chapter 2, we identified the four classical flow structures that can emerge in response to an abrupt discontinuity in initial conditions, each with an additional stationary wave across the point of discontinuity in elastic stiffness. However, we also showed existence of several new resonant states which form when a left or right rarefaction intersects with this stationary wave. We then proceeded to explore these possible resonances (as introduced by Han et al. [89]), showing that these filled the gaps in the parameter space left by the classical solutions. In particular, we found that (for the cases tested) there is always a unique solution across the parameter space. Interestingly, for the cases tested we only identified resonant cases in some of our parameter sweeps, with the others entirely described by the classical solutions.

Predictions are coincident between the expanding tube law and the general tube law, although resonant solutions are only evident for severely collapsed profiles using the general tube law. A consistent picture emerges as we vary the jump in stiffness across the discontinuity. When we vary the far-field properties of compartment 2 with undisturbed flow in compartment 1, resonance is only evident when compartment 1 is less stiff than compartment 2. The opposite is true when varying the properties of compartment 1 *i.e.* to see resonance, the compartment where we vary the properties must be stiffer than the other compartment (where flow is undisturbed). However, a more extensive parameter sweep is necessary to examine how this conclusion changes if the flow in the compartment with fixed properties is different to baseline (*e.g.* Figure 2.20 in Chapter 2).

The results from this chapter significantly extend preliminary work by Toro and Siviglia [105] and Han et al. [89]. In particular, we now illustrate how the resonant states first described by Han et al. [89] are connected to the classical solutions, showing that the region of Configuration C and configuration D resonance do not lead directly into a supercritical state. Furthermore, we show that the solution of the Riemann problem is unique which is in contrast with the cases of multiple solution noted by Toro and Siviglia [105]. The only case of multiple solutions maybe possible in the supercritical regime but not in the subcritical regime as claimed.

CHAPTER 4

A blood vessel with a symmetric junction

In Chapter 2 we considered a Riemann problem associated with blood flow along a single blood vessel with uniform material properties, while in Chapter 3 we extended this work to consider a Riemann problem associated with blood flow in a vessel with a sudden change in material properties (coincident with the point of discontinuity in initial conditions), with a particular emphasis on a change in vessel stiffness. Now we extend these ideas to consider a Riemann problem in a blood vessel with a junction. Here we restrict attention to a symmetric problem with a parent vessel branching into two identical daughter vessels. We find that the discontinuity associated with division of mass at the junction is sufficient to allow resonance (with all vessels identical), which is further enhanced by also allowing a change in material properties of the constituent vessels.

4.1 Model setup

In this chapter, we consider blood flow along parent vessel which bifurcates into two daughter vessels. We denote the parent vessel with the subscript p and the daughter vessels with the subscripts $d1$ and $d2$. However, in what follows we assume the daughter vessels are always identical and so we use a single subscript d. These parent and daughter vessels are of the lengths L_p^* and L_d^* with baseline cross-sectional areas $\bar{A}_p^*$ and $\bar{A}_d^*$, respectively.

In this chapter the term vessel will be used in describing the constituents of the network, while, (as before) we use the term region to describe the different pieces of the Riemann problem. The two vessels are joined together at the junction which we denote as $x^* = 0$.

Following Chapter 2 and 3, we assume that the flow in each of the vessels is homogeneous and inviscid. The density of the blood assumed constant in both vessels, denoted as ρ^*. However, in general the vessel walls are assumed to be of different stiffness, denoted as k_p^* and k_d^*, respectively. We denote the (uniform) external pressure applied to the two vessels as $\bar{p}_{ep}^*$ and $\bar{p}_{ed}^*$, respectively. We assume that the vessels exhibit a steady baseline pressure distribution denoted as p_p^* and p_d^*, respectively.

The model equations in each vessel are almost identical to those presented in Section 2.1 and Section

3.1 but with different notations given below as

$$p_j^* = \bar{p}_{ej}^* + k_j^* f\left(A_j^*/\bar{A}_j^*\right), \quad (j = p, d). \tag{4.1}$$

4.1.1 Non dimensionalization and final governing equations

In this chapter, we non-dimensionalize the governing equations with respect to the properties of the parent vessel. In particular we non-dimensionalize all lengths on the square root of the baseline cross sectional area in the parent vessel, $(\bar{A}_p^*)^{\frac{1}{2}}$, velocities on $\mathbf{u}^* = \left(\frac{k_p^*}{\rho^*}\right)^{\frac{1}{2}}$, time on $T^* = \left(\frac{\rho^* \bar{A}_p^*}{k_p^*}\right)^{\frac{1}{2}}$ and pressures on the stiffness in the parent vessel according to $p_p^* = k_p^* p_p + \bar{p}_p^*$, $p_d^* = k_p^* p_d + \bar{p}_p^*$, where $\bar{p}_p^*$ is the baseline pressure at the inlet of the parent vessel. The dimensionless variables and parameters are denoted with the same symbol as that of their dimensional counterpart without the asterisks.

The dimensionless tube law in each vessel takes the form

$$p_p = \bar{p}_{ep} + f(A_p), \tag{4.2}$$

$$p_d = \bar{p}_{ed} + kf\left(A_d/\bar{A}_d\right), \tag{4.3}$$

where the dimensionless parameters take the form

$$k = \frac{k_d^*}{k_p^*}, \quad \bar{p}_{ep} = \frac{\bar{p}_{ep}^* - \bar{p}_p^*}{k_p^*}, \quad \bar{p}_{ed} = \frac{\bar{p}_{ed}^* - \bar{p}_p^*}{k_p^*}. \tag{4.4}$$

The corresponding dimensionless vessel lengths and baseline cross-sectional areas take the form

$$L_p = \frac{L_p^*}{\sqrt{\bar{A}_p^*}}, \quad L_d = \frac{L_d^*}{\sqrt{\bar{A}_p^*}}, \quad \bar{A}_d = \frac{\bar{A}_d^*}{\bar{A}_p^*}. \tag{4.5}$$

Here, we reduce the full governing equations of the system by assuming axis-symmetry and taking a long-wavelength deformations (as in Chapters 2 and 3), this makes it consistent to reduce the junction to a single point (*i.e.* $x = 0$). The dimensionless conservation of mass and momentum equations for this problem become

$$\frac{\partial A_j}{\partial t} + \frac{\partial}{\partial x}(A_j u_j) = 0, \tag{4.6}$$

$$\frac{\partial}{\partial t}(A_j u_j) + \frac{\partial}{\partial x}(A_j u_j^2) + A_j \frac{\partial p_j}{\partial x} = 0, \quad (j = p, d), \tag{4.7}$$

analogous to (2.29),(2.30) in Chapter 2 and (3.9),(3.10) in Chapter 3.

These equations (4.6) and (4.7) are again subject to dimensionless (expanding) tube laws given in equations (4.2) and (4.3) where f characterises the expanding tube law for both parent and daughter vessels such that

$$f(s) = \left(s^m - 1\right), \tag{4.8}$$

where $m > 0$ is an exponent. We consider the more general tube law which resists collapse in Section 4.10.

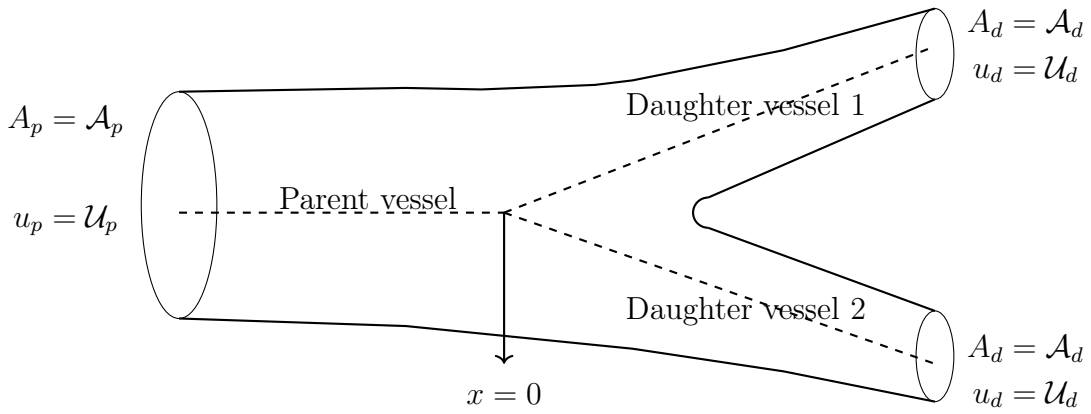

Figure 4.1: Set-up of the mathematical model.

4.1.2 Boundary conditions between vessels

The material properties between parent and daughter vessels are typically discontinuous and so we again impose continuity of flux (with equal division into the daughter vessels) and continuity of total pressure across the junction point ($x = 0$) [51, 81, 105]. Also since we have a symmetric junction, we introduce a mass splitting factor r_j such that in the parent vessel $r_p = 1$ while in the daughter vessel we have $r_d = 2$ (as the flow rate is half what it was at the parent vessel). So, we have our conditions as

$$r_p A_p u_p = r_d A_d u_d, \quad (x = 0), \tag{4.9}$$

$$\bar{p}_{ep} + (A_p^m - 1) + 1/2u_p^2 = \bar{p}_{ed} + k\left(\left(\frac{A_d}{\bar{A}_d}\right)^m - 1\right) + 1/2u_d^2, \quad (x = 0). \tag{4.10}$$

4.2 Nonlinear flow structure

We now consider a Riemann problem centered around the junction as illustrated in Figure 4.1, where the mid lines of the parent and daughter vessels intersect at a single point denoted as $x = 0$. We impose a spatially uniform (but discontinuous) initial condition across both the parent and daughter vessels. Across the parent vessel we impose $A_p = \mathcal{A}_p$, $u_p = \mathcal{U}_p$ and $c_p = \mathcal{C}_p$ such that from (4.2) the fluid pressure becomes

$$p_p = \bar{p}_{ep} + \left(\mathcal{A}_p^m - 1\right). \tag{4.11}$$

Also, across daughter vessel we impose $A_d = \mathcal{A}_d$, $u_d = \mathcal{U}_d$ and $c_d = \mathcal{C}_d$ such that from (4.3) we have

$$p_d = \bar{p}_{ed} + k\left(\left(\frac{\mathcal{A}_d}{\bar{A}_d}\right)^m - 1\right). \tag{4.12}$$

4.2.1 Riemann invariants

We follow a similar method as Section 3.2.1 to compute the Riemann invariants of the flow in the parent vessel, where we find

$$R_p = u_p \pm \frac{2}{\sqrt{m}}(A_p^{m/2} - 1), \quad \text{constant on} \quad \frac{dx}{dt} = u_p \pm \sqrt{m}A_p^{m/2} = u_p \pm c_p. \tag{4.13}$$

Similarly, the daughter vessels, we derive the Riemann invariants

$$R_d = u_d \pm \frac{2\sqrt{k}}{\sqrt{m}}\left(\left(\frac{A_d}{\bar{A}_d}\right)^{m/2} - 1\right), \quad \text{constant on} \quad \frac{dx}{dt} = u_d \pm \left(\frac{A_d}{\bar{A}_d}\right)^{m/2} = u_d \pm c_d. \tag{4.14}$$

The flow structure is similar to earlier chapters, and the system will remain in its initial state far from the junction at $x = 0$ (*i.e.* $A_p \to \mathcal{A}_p, u_p \to \mathcal{U}_p, c_p \to \mathcal{C}_p$ for $x \leq (\mathcal{U}_p - \mathcal{C}_p)t$ and $A_d \to \mathcal{A}_d, u_d \to \mathcal{U}_d, c_d \to \mathcal{C}_d$ for $x \geq (\mathcal{U}_d + \mathcal{C}_d)t$). Adjacent to the ambient region the flow will either exhibit a rarefaction wave or a shock wave (as discussed in Chapters 2 and 3). In the intermediate region between the shock(s)/rarefaction(s) the flow will generally be uniform. However, the division of mass from the parent into the two daughters and the discontinuity in material/environmental properties creates additional difficulties. Firstly, we cannot assume continuity of all variables across $x = 0$ as in Chapter 2. Instead we must specify boundary conditions (4.9) and (4.10). We also have two uniform regions around the junction, denoted as region 3 in the (parent vessel) and region 3 in the (daughter vessel), such that $A_p = \mathcal{A}_3^P$, $u_p = \mathcal{U}_3^P$ for $x < 0$ and $A_d = \mathcal{A}_3^D$, $u_d = \mathcal{U}_3^D$ for $x > 0$.

4.2.2 Parent rarefaction

We now consider a rarefaction in the parent vessel adjacent to the far-field region. This is qualitatively similar to what we have in Chapters 2 and 3 but with just a change in notation. So, following the derivations in Section 2.6.1 and 3.3.1 we have the profiles for cross-sectional area, flow velocity and wave speed as

$$A_r^P = \left(\frac{\sqrt{m}}{(m+2)}\left(\left(\mathcal{U}_p - \frac{x}{t}\right) + \frac{2\mathcal{C}_p}{m}\right)\right)^{2/m}, \quad \text{where} \quad \mathcal{C}_p = \sqrt{m}\mathcal{A}_p^{m/2}, \tag{4.15}$$

$$u_r^P = \frac{m\mathcal{U}_p}{m+2} + \frac{2\mathcal{C}_p}{m+2} + \frac{2x}{(m+2)t}, \tag{4.16}$$

$$c_r^P = \frac{m}{m+2}\left(\left(\mathcal{U}_p - \frac{x}{t}\right) + \frac{2\mathcal{C}_p}{m}\right). \tag{4.17}$$

From (4.16), if we let $A_r^P = \mathcal{A}_3^P$, $u_r^P = \mathcal{U}_3^P$ and $c_r^P = \mathcal{C}_3^P$ on $x = x_{rp}$ which is the edge of the rarefaction adjacent to region 3. We therefore have

$$x_{rp} = \left(\mathcal{U}_3^P - \mathcal{C}_3^P\right)t. \tag{4.18}$$

Substituting (4.18) into (4.29), we have at the edge of the rarefaction region adjacent to region 3

$$\mathcal{U}_3^P = \mathcal{U}_p + \frac{2}{\sqrt{m}}\left(\mathcal{A}_p^{m/2} - (\mathcal{A}_3^P)^{m/2}\right), \tag{4.19}$$

a nonlinear constraint which relates $\mathcal{U}_3^P$ and $\mathcal{A}_3^P$ to the initial conditions in the parent vessel.

We note that for the rarefaction in the parent vessel to remain in the parent vessel and be a physical solution, we need

$$(\mathcal{U}_3^P - \mathcal{C}_3^P) < 0 \quad \text{and} \quad (\mathcal{U}_3^P - \mathcal{C}_3^P) > (\mathcal{U}_p - \mathcal{C}_p). \tag{4.20}$$

4.2.3 Daughter rarefaction

For a rarefaction in the daughter vessel, we apply same method as in Section 3.3.2 of Chapter 3 but with change in notation such that the cross-sectional area, velocity and wavespeed profile in the daughter vessel are given as

$$A_r^D = \bar{A}_d\left(\frac{\sqrt{m}}{\sqrt{k}(m+2)}\left(\left(\frac{x}{t} - \mathcal{U}_d\right) + \frac{2\mathcal{C}_d}{m}\right)\right)^{2/m}, \quad \text{where} \quad \mathcal{C}_d = \sqrt{km}\left(\frac{\mathcal{A}_d}{\bar{A}_d}\right)^{m/2}, \tag{4.21}$$

$$u_r^D = \frac{m\mathcal{U}_d}{m+2} - \frac{2\mathcal{C}_d}{m+2} + \frac{2x}{(m+2)t}, \tag{4.22}$$

$$c_r^D = \frac{m}{m+2}\left(\left(\frac{x}{t} - \mathcal{U}_d\right) + \frac{2\mathcal{C}_d}{m}\right). \tag{4.23}$$

From (4.22), if we let $A_r^D = \mathcal{A}_3^D$, $u_r^D = \mathcal{U}_3^D$ and $c_r^D = \mathcal{C}_3^D$ on $x = x_{rd}$ which is the edge of the rarefaction adjacent to region 3. From (4.22), we have

$$x_{rd} = \left(\mathcal{U}_3^D + \mathcal{C}_3^D\right)t. \tag{4.24}$$

Substituting (4.24) into (4.21), we have at the edge of the rarefaction region adjacent to region 3

$$\mathcal{U}_3^D = \mathcal{U}_d + 2\sqrt{\frac{k}{m\bar{A}_d{}^m}}\left(\left(\mathcal{A}_3^D\right)^{m/2} - \mathcal{A}_d^{m/2}\right), \tag{4.25}$$

a nonlinear constraint which relates $\mathcal{U}_3^D$ and $\mathcal{A}_3^D$ to the initial conditions in the daughter vessel.

We note that for the rarefaction in the parent vessel to remain on the right hand side of the domain and be a physical solution, we need

$$(\mathcal{U}_3^D + \mathcal{C}_3^D) > 0, \quad \text{and} \quad (\mathcal{U}_3^D + \mathcal{C}_3^D) < (\mathcal{U}_d + \mathcal{C}_d). \tag{4.26}$$

4.2.4 Parent shock

For a shock in the parent vessel we follow steps similar to Section 3.3.3 and ensure conservation of mass and momentum across the shock such that the shock speed can be written as

$$\dot{s}_p = \frac{\mathcal{A}_3^P\mathcal{U}_3^P - \mathcal{A}_p\mathcal{U}_p}{\mathcal{A}_3^P - \mathcal{A}_p} = \frac{\mathcal{A}_3^P(\mathcal{U}_3^P)^2 - \mathcal{A}_p\mathcal{U}_p^2 + \frac{m}{m+1}\left((\mathcal{A}_3^P)^{m+1} - \mathcal{A}_p^{m+1}\right)}{\mathcal{A}_3^P\mathcal{U}_3^P - \mathcal{A}_p\mathcal{U}_p}. \tag{4.27}$$

We now solve (4.27) for $\mathcal{U}_3^P$ to determine the velocity immediately to the left of the junction as

$$\mathcal{U}_3^P = \mathcal{U}_p \pm \sqrt{\frac{m\left((\mathcal{A}_3^P)^{m+1} - \mathcal{A}_p^{m+1}\right)(\mathcal{A}_3^P - \mathcal{A}_p)}{(m+1)\mathcal{A}_p\mathcal{A}_3^P}}, \tag{4.28}$$

a nonlinear constraint which relates $\mathcal{U}_3^P$ and $\mathcal{A}_3^P$ to the initial conditions.

Note that from equation (4.28) there is possibility of two solutions. For the shock in the parent vessel to be physical we must also check against the Lax entropy conditions [116]

$$(\mathcal{U}_3^P - \mathcal{C}_3^P) < \dot{s}_p < (\mathcal{U}_p - \mathcal{C}_p). \tag{4.29}$$

4.2.5 Daughter shock

For a shock in the daughter vessel we consider similar steps to Section 3.3.4, while imposing conservation of mass and momentum across the shock front, we have the shock speed as

$$\dot{s}_d = \frac{\mathcal{A}_d\mathcal{U}_d - \mathcal{A}_3^D\mathcal{U}_3^D}{\mathcal{A}_3^D - \mathcal{A}_d} = \frac{\mathcal{A}_d\mathcal{U}_d^2 - \mathcal{A}_3^D(\mathcal{U}_3^D)^2 + \frac{km}{\bar{A}_d^m(m+1)}\left((\mathcal{A}_d)^{m+1} - (\mathcal{A}_3^D)^{m+1}\right)}{\mathcal{A}_d\mathcal{U}_d - \mathcal{A}_3^D\mathcal{U}_d^2}. \tag{4.30}$$

We now solve (4.30) for $\mathcal{U}_3^D$ to determine the velocity immediately to the right of the junction or just inside the parent vessel as

$$\mathcal{U}_3^D = \mathcal{U}_d \pm \sqrt{\frac{km\left(\mathcal{A}_d^{m+1} - (\mathcal{A}_3^D)^{m+1}\right)(\mathcal{A}_d - \mathcal{A}_3^D)}{(m+1)\bar{A}_d^m\mathcal{A}_d\mathcal{A}_3^D}}, \tag{4.31}$$

a nonlinear constraint which relates $\mathcal{U}_3^D$ and $\mathcal{A}_3^D$ to the initial conditions.

Note that for the shock in the daughter vessel to be physical we must also check against the Lax entropy conditions [116]

$$(\mathcal{U}_d + \mathcal{C}_d) < \dot{s}_d < (\mathcal{U}_3^D + \mathcal{C}_3^D). \tag{4.32}$$

4.2.6 Boundary conditions

Having determined the flow structure in our Riemann problem, we now rewrite the the continuity conditions (4.9) and (4.10) at $x = 0$ in the updated notation as

$$r_p \mathcal{U}_3^P \mathcal{A}_3^P = r_d \mathcal{U}_3^D \mathcal{A}_3^D, \tag{4.33}$$

$$\bar{p}_{ep} + \left((\mathcal{A}_3^P)^m - 1\right) + \frac{1}{2}(\mathcal{U}_3^P)^2 = \bar{p}_{ed} + k\left(\left(\frac{\mathcal{A}_3^D}{\bar{A}_d}\right)^m - 1\right) + \frac{1}{2}(\mathcal{U}_3^D)^2. \tag{4.34}$$

4.3 Numerical method

Similar to Chapters 2 and 3, we apply Newton's method to solve for the four classical flow structures (*i.e.* parent rarefaction, daughter shock (PRDS), parent shock, daughter rarefaction (PSDR), parent shock, daughter shock (PSDS), parent rarefaction, daughter rarefaction (PRDR)) by determining the values of $\mathcal{A}_p^P$ and $\mathcal{A}_d^D$ as a function of the far-field conditions. In each case again, across the junction we assume continuity of flux (4.33) and continuity of total pressure (4.34). For PRDS we use equations (4.19) and (4.31), for PSDR we use (4.28) and (4.19), for PSDS we use (4.28) and (4.31) while for PRDR we use (4.19) and (4.19). In our Newton's method we choose a variety of initial conditions and iterate until the solution converges to one of the possible solutions which also satisfies the physicality conditions ((4.20) and (4.26) for rarefactions and (4.29) and (4.32) conditions for shocks).

4.4 Simple connection across the junction: no resonance

We now consider the analogue of the four classical cases presented in Chapter 2 while accounting for a division of mass across the junction. We consider in turn PRDS (see Section 4.4.1), PSDR (see Section 4.4.2), PSDS (see Section 4.4.3) and PRDR (see Section 4.4.4). We represent PRDS solution with a green dashed line, PSDR solution with a cyan dashed line, PSDS solution with a red dashed line and PRDR solution with a blue dashed line always applying the physicality conditions (4.20), (4.26) for rarefactions and (4.29), (4.32) for shocks.

4.4.1 Parent rarefaction, daughter shock

Figure 4.2 illustrates a parent rarefaction, daughter shock (PRDS) solution across a blood vessel junction with no change in material or environmental properties. The flow profiles in Figure 4.2 are computed using far-field conditions $\mathcal{A}_p = 1.6$, $\mathcal{A}_d = 1.2$, $\mathcal{U}_p = 0$, $\mathcal{U}_d = 0.5$, $k = 1$ while $p_{ep} = p_{ed} = 0$, $\bar{A}_d = 1$. Using our Newton's method we now compute $\mathcal{A}_3^P = 1.322$, $\mathcal{A}_3^D = 1.366$, $\mathcal{U}_3^P = 4.079$ and $\mathcal{U}_3^D = 1.973$. Using the above far-field conditions there is a slight expansion in cross-sectional area from the parent to the daughter vessels (see Figure 4.2a), but the a large reduction in flow speed (see Figure 4.2b), respectively. Figure 4.2(d), on the other hand, illustrates continuity of flux across the junction and we can see a direct half split of flux across the two daughter vessels.

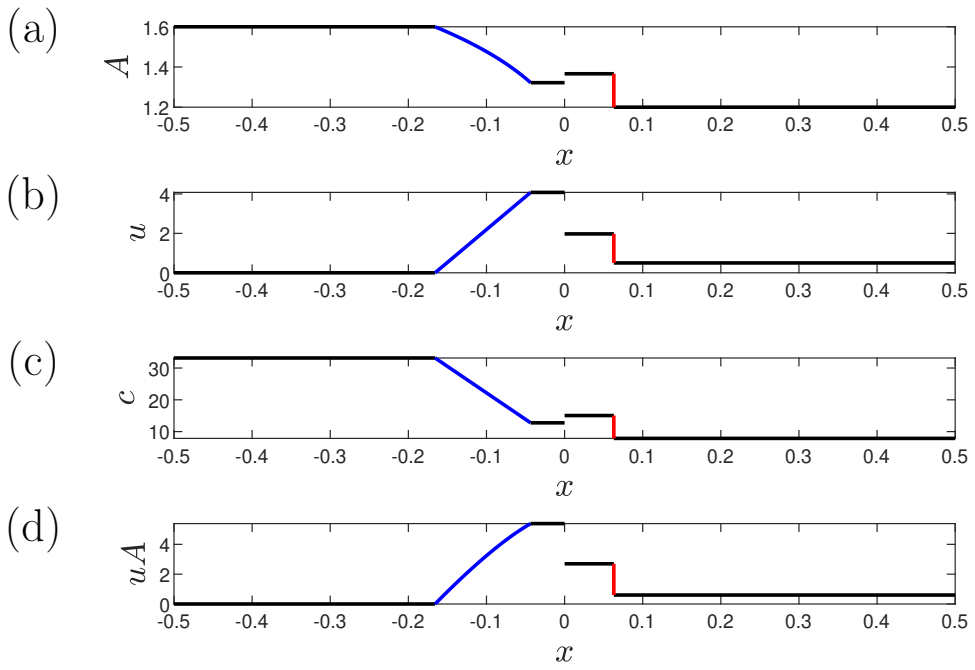

Figure 4.2: Parent rarefaction, daughter shock with discontinuity at $x = 0$. Figure 4.2(a) displays profile of cross-sectional area, Figure 4.2(b), displays profile of flow speed, Figure 4.2(c) displays profile of the wave speed and Figure 4.2(d) Parent rarefaction, daughter shock showing continuity of flux at $x = 0$. We choose $\mathcal{A}_p = 1.6$, $\mathcal{A}_d = 1.2$, $\mathcal{U}_p = 0$, $\mathcal{U}_d = 0.5$, $k = 1.0$ and using Newton's method we compute $\mathcal{A}_3^P = 1.322$, $\mathcal{A}_3^D = 1.366$, $\mathcal{U}_3^P = 4.079$ and $\mathcal{U}_3^D = 1.973$ at $t = 0.005$.

4.4.2 Parent shock, daughter rarefaction

In Figure 4.3, we consider a parent shock wave and a daughter rarefaction fan (PSDR) solution across a blood vessel junction with no change in material properties. An illustration of this flow structure is reproduced using the far-field conditions in Figure 4.3 with $\mathcal{A}_p = 1.0$, $\mathcal{A}_d = 1.45$, $\mathcal{U}_p = 0$, $\mathcal{U}_d = 0.35$, $k = 1.0$, $\bar{A}_d = 1$ and applying the Newton method we have that $\mathcal{A}_3^P = 1.319$, $\mathcal{A}_3^D = 1.333$, $\mathcal{U}_3^P = -2.107$ and $\mathcal{U}_3^D = -1.043$. Figure 4.3(a) using the above far-field conditions shows a slight decrease in cross-sectional area from daughter to parent vessel leading to a resultant large decrease in the flow speed across the junction from daughter to parent vessels (see Figure 4.3b).

4.4.3 Parent shock, daughter shock

Figure 4.4 illustrates a parent shock and daughter shock (PSDS) solution across a blood vessel junction with no jump in material or environmental properties. An example of this class of wave profile is computed using far-field conditions $\mathcal{A}_p = 1.0$, $\mathcal{A}_d = 0.9$, $\mathcal{U}_p = 0$, $\mathcal{U}_d = -0.5$, $\bar{A}_d = 1$ and $k = 1.0$ using Newtons method we compute $\mathcal{A}_3^P = 1.044$, $\mathcal{A}_3^D = 1.044$, $\mathcal{U}_3^P = -0.151$ and $\mathcal{U}_3^D = -0.075$. Using the above far-field conditions we see from Figure 4.4(a) a slight decrease in cross-sectional area from

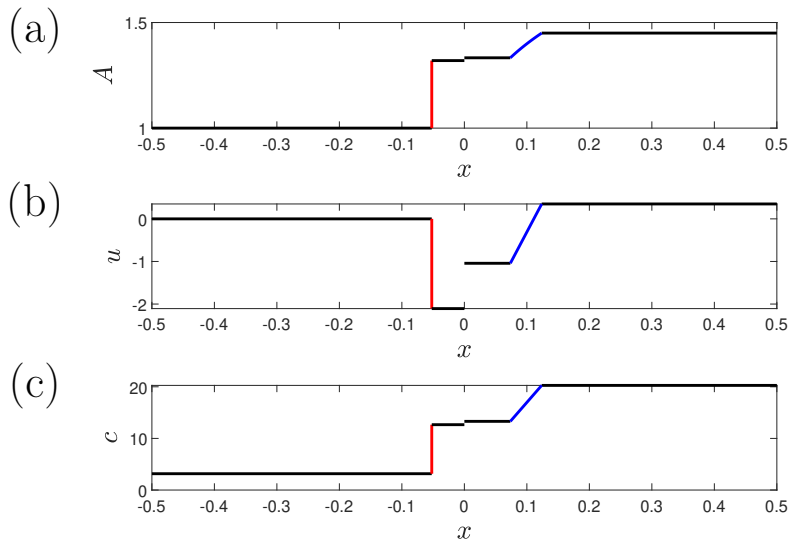

Figure 4.3: Parent shock, daughter rarefaction with discontinuity at $x = 0$. Figure 4.3(a) displays profile of cross-sectional area; Figure 4.3(b) displays profile of flow speed and Figure 4.3(c) displays profile of the wave speed. We choose $\mathcal{A}_p = 1.0$, $\mathcal{A}_d = 1.45$, $\mathcal{U}_p = 0$, $\mathcal{U}_d = 0.35$, $k = 1.0$ and using Newton's method we compute $\mathcal{A}_3^P = 1.319$, $\mathcal{A}_3^D = 1.333$, $\mathcal{U}_3^P = -2.107$ and $\mathcal{U}_3^D = -1.043$ at $t = 0.006$.

daughter to parent vessel with a large decrease in the flow speed across the junction from daughter to parent vessels (see Figure 4.4b).

4.4.4 Parent rarefaction, daughter rarefaction

In Figure 4.5, we consider a rarefaction wave in the parent vessel and rarefactions wave in the daughter vessels (PRDR) with no jump in material or environmental properties. We show an example of such behaviour using the far-field conditions $\mathcal{A}_p = 1.1$, $\mathcal{A}_d = 1.05$, $\mathcal{U}_p = 0$, $\mathcal{U}_d = 0.5$, $k = 1.0$ where using Newtons method we compute $\mathcal{A}_3^P = 1.040$, $\mathcal{A}_3^D = 0.933$, $\mathcal{U}_3^P = 0.250$, $\mathcal{U}_3^D = 0.140$. Typical profiles are shown in Figure 4.5, where we have reduction in area with less reduction in flow speed across the junction from parent to daughter vessels.

Note that in all four cases considered in Section 4.4 the cross-sectional area remained almost identical across the junction, with the division of mass accommodated by an approximate halving of the flow speed.

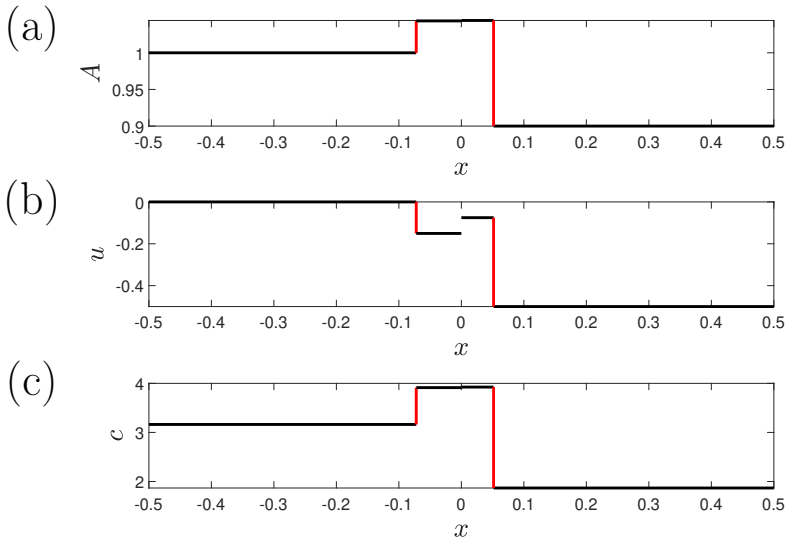

Figure 4.4: Parent shock, daughter shock with discontinuity at $x = 0$. Figure 4.4(a) displays profile of cross-sectional area; Figure 4.4(b) displays profile of flow speed and Figure 4.4(c) displays profile of the wave speed. We choose $\mathcal{A}_p = 1.0$, $\mathcal{A}_d = 0.9$, $\mathcal{U}_p = 0$, $\mathcal{U}_d = -0.5$, $\bar{A}_d = 1$ and $k = 1.0$ using Newton's method we compute $\mathcal{A}_3^P = 1.044$, $\mathcal{A}_3^D = 1.044$, $\mathcal{U}_3^P = -0.151$ and $\mathcal{U}_3^D = -0.075$ at $t = 0.009$.

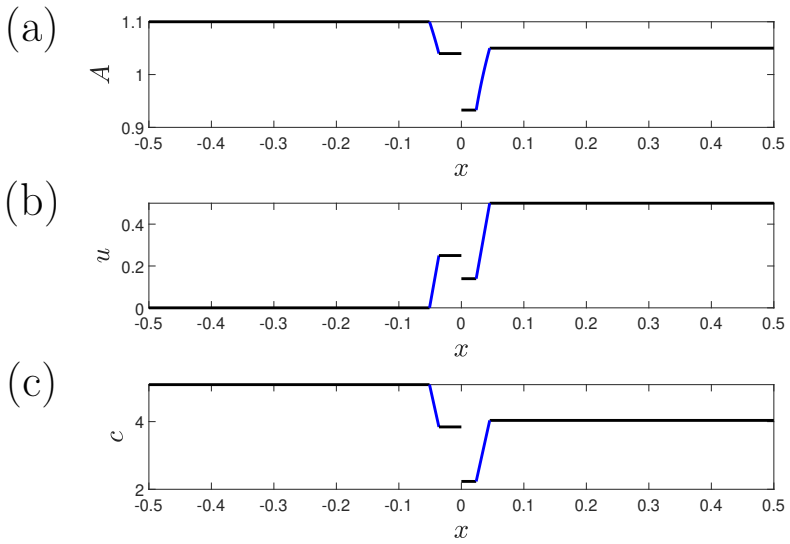

Figure 4.5: Parent rarefaction, daughter rarefaction with discontinuity at $x = 0$. Figure 4.5(a) displays profile of cross-sectional area; Figure 4.5(b) displays profile of flow speed and Figure 4.5(c) displays profile of the wave speed. We choose $\mathcal{A}_p = 1.1$, $\mathcal{A}_d = 1.05$, $\mathcal{U}_p = 0$, $\mathcal{U}_d = 0.5$, $k = 1.0$ and using Newton's method we compute $\mathcal{A}_3^P = 1.040$, $\mathcal{A}_3^D = 0.933$, $\mathcal{U}_3^P = 0.250$, $\mathcal{U}_3^D = 0.140$ at $t = 0.01$.

4.5 Small amplitude waves

In this section we consider small amplitude perturbations to analytically derive a reduced form of wave splitting across a blood vessel junction. In this case, similar to Section 3.6 of Chapter 3, it is necessary to set $\bar{A}_d = 1$, $\bar{p}_{ep} = \bar{p}_{ed} = 0$ for consistency. We consider equations (4.6) and (4.7) and linearise the variables according to

$$A_p = 1 + \epsilon\hat{A}_p, \quad A_d = 1 + \epsilon\hat{A}_d, \quad u_p = \bar{u}_p + \epsilon\hat{u}_p, \quad u_d = \bar{u}_d + \epsilon\hat{u}_d, \quad p_p = \epsilon\hat{p}_p, \quad p_d = \epsilon\hat{p}_d, \tag{4.35}$$

where $\epsilon \ll 1$ is the perturbation amplitude and $\bar{u}_p$, $\bar{u}_d$ are some constant velocities which we choose depending on boundary conditions. Furthermore, we express the Riemann problem boundary conditions as

$$\mathcal{A}_p = 1 + \epsilon\hat{\mathcal{A}}_p, \quad \mathcal{A}_d = 1 + \epsilon\hat{\mathcal{A}}_d, \quad \mathcal{U}_p = \bar{u}_p + \epsilon\hat{\mathcal{U}}_p, \quad \mathcal{U}_d = \bar{u}_d + \epsilon\hat{\mathcal{U}}_d. \tag{4.36}$$

Note, however that in this linearised problem $\hat{\mathcal{A}}_p$ and $\hat{\mathcal{U}}_p$ are coupled together by the equations, as are $\hat{\mathcal{A}}_d$ and $\hat{\mathcal{U}}_d$ (ie. they cannot be chosen independently).

We consider only terms of $O(\epsilon)$, where we have for the parent vessel

$$\frac{\partial\hat{A}_p}{\partial t} + \bar{u}_p\frac{\partial\hat{A}_p}{\partial x} + \frac{\partial\hat{u}_p}{\partial x} = 0, \tag{4.37}$$

$$\frac{\partial\hat{u}_p}{\partial t} + \bar{u}_p\frac{\partial\hat{u}_p}{\partial x} = -\frac{\partial\hat{p}_p}{\partial x}, \tag{4.38}$$

$$\hat{p}_p = \hat{A}_p f'(1). \tag{4.39}$$

We further differentiate (4.37) with respect to t, and substitute (4.38) to have

$$\frac{\partial^2\hat{A}_p}{\partial t^2} = \frac{\partial^2}{\partial x^2}(\bar{u}_p^2\hat{A}_p + 2\bar{u}_p\hat{u}_p) + \frac{\partial^2\hat{p}_p}{\partial x^2}. \tag{4.40}$$

Similarly, for the daughter vessel, we have

$$\frac{\partial\hat{A}_d}{\partial t} + \bar{u}_d\frac{\partial\hat{A}_d}{\partial x} + \frac{\partial\hat{u}_d}{\partial x} = 0, \tag{4.41}$$

$$\frac{\partial\hat{u}_d}{\partial t} + \bar{u}_d\frac{\partial\hat{u}_d}{\partial x} = -\frac{\partial\hat{p}_d}{\partial x}, \tag{4.42}$$

$$\hat{p}_d = k\hat{A}_d f'(\bar{A}_d). \tag{4.43}$$

Again, further differentiating (4.41) with respect to t, and substituting (4.42) we have

$$\frac{\partial^2\hat{A}_d}{\partial t^2} = \frac{\partial^2}{\partial x^2}(\bar{u}_d^2\hat{A}_d + 2\bar{u}_d\hat{u}_d) + \frac{\partial^2\hat{p}_d}{\partial x^2}. \tag{4.44}$$

We write both $\hat{p}_p$ and $\hat{p}_d$ in terms of $\hat{A}_p$ and $\hat{A}_d$, respectively, such that we have

$$\frac{\partial^2 \hat{A}_p}{\partial t^2} = \frac{\partial^2}{\partial x^2}(\bar{u}_p^2 \hat{A}_p + 2\bar{u}_p \hat{u}_p) + f'(1)\frac{\partial^2 \hat{A}_p}{\partial x^2}. \tag{4.45}$$

$$\frac{\partial^2 \hat{A}_d}{\partial t^2} = \frac{\partial^2}{\partial x^2}(\bar{u}_d^2 \hat{A}_d + \bar{u}_d \hat{u}_d) + kf'(\bar{A}_d)\frac{\partial^2 \hat{A}_d}{\partial x^2}. \tag{4.46}$$

For $\bar{u}_p = \bar{u}_d = 0$ above (*i.e.* no base flow in both (4.45) and (4.46)) we have

$$\frac{\partial^2 \hat{A}_p}{\partial t^2} = f'(1)\frac{\partial^2 \hat{A}_p}{\partial x^2}, \tag{4.47}$$

$$\frac{\partial^2 \hat{A}_d}{\partial t^2} = kf'(\bar{A}_d)\frac{\partial^2 \hat{A}_d}{\partial x^2}, \tag{4.48}$$

where $\hat{c}_p = \pm\sqrt{f'(1)}$ and $\hat{c}_d = \pm\sqrt{kf'(\bar{A}_d)}$ are the linearised wavespeeds in the parent and daughter vessels, respectively.

We now proceed to solve (4.47) and (4.48), by looking for a travelling wave solution of the form $z = t \pm x/c_j$ such that for a cross-sectional area profile of amplitude $\hat{\mathcal{A}}_j$. For the parent vessel, the profiles of the incoming wave take the form

$$\hat{A}_p = \hat{\mathcal{A}}_p g_1(t - x/c_p), \tag{4.49}$$

$$\hat{p}_p = \hat{\mathcal{A}}_p f'(1) g_1(t - x/c_p), \tag{4.50}$$

$$\hat{u}_p = \hat{\mathcal{A}}_p \frac{f'(1)}{c_p} g_1(t - x/c_p), \tag{4.51}$$

where $g_1(t - x/c_p)$ is the form of the wave determined by the initial conditions.

For the reflected wave in the parent vessel, we have the amplitude given as $\hat{\mathcal{A}}_p^r$ such that the profiles are given as

$$\hat{A}_p^r = \hat{\mathcal{A}}_p^r g_2(t + x/c_p), \tag{4.52}$$

$$\hat{p}_p^r = \hat{\mathcal{A}}_p^r f'(1) g_2(t + x/c_p), \tag{4.53}$$

$$\hat{u}_p^r = -\hat{\mathcal{A}}_p^r \frac{f'(1)}{c_p} g_2(t + x/c_p), \tag{4.54}$$

where $g_2(t + x/c_p)$ is the form of the wave in the parent vessel also determined by matching at the junction. Note that once the incoming wave has reflected the total wave amplitude in the parent vessel is the sum of the incident wave $\hat{\mathcal{A}}_p$ and reflected wave $\hat{\mathcal{A}}_p^r$, given as $\hat{\mathcal{A}}_3^P$. This is the analog to $\mathcal{A}_3^P - 1$ in the full Riemann problem.

For the daughter vessel, we have from (4.48)

$$\hat{A}_d = \hat{\mathcal{A}}_d g_3(t - x/c_d), \tag{4.55}$$

$$\hat{p}_d = \hat{\mathcal{A}}_d k f'(\bar{A}_d) g_3(t - x/c_d), \tag{4.56}$$

$$\hat{u}_d = \hat{\mathcal{A}}_d \frac{kf'(\bar{A}_d)}{c_d} g_3(t - x/c_d), \tag{4.57}$$

where $g_3(t-x/c_d)$ is the form of the wave in the daughter vessel determined by matching at the junction.

We match the waves across the junction $x = 0$ by first linearizing the continuity of flux condition (4.33) and continuity of total pressure condition (4.34) and set $\bar{u}_p = \bar{u}_d = 0$, to obtain

$$\hat{u}_p = 2\hat{u}_d, \tag{4.58}$$

$$\hat{p}_p = \hat{p}_d. \tag{4.59}$$

To match at $x = 0$, we substitute (4.51), (4.54) and (4.57) into (4.58) and (4.50), (4.53) and (4.56) into (4.59) to have

$$\hat{\mathcal{A}}_p\sqrt{f'(1)}g_1(t) - \hat{\mathcal{A}}_p^r\sqrt{f'(1)}g_2(t) = 2\hat{\mathcal{A}}_3^D\sqrt{kf'(\bar{A}_d)}g_3(t), \tag{4.60}$$

$$\hat{\mathcal{A}}_p f'(1)g_1(t) + \hat{\mathcal{A}}_p^r f'(1)g_2(t) = \hat{\mathcal{A}}_3^D kf'(\bar{A}_d)g_3(t). \tag{4.61}$$

For consistency at the junction we require $g_1 = g_2 = g_3$ and solving (4.60) and (4.61) simultaneously we have

$$\hat{\mathcal{A}}_3^P = \frac{2\hat{\mathcal{A}}_p kf'(\bar{A}_d)}{kf'(\bar{A}_d) + 2\sqrt{kf'(\bar{A}_d)}\sqrt{f'(1)}}, \tag{4.62}$$

$$\hat{\mathcal{A}}_3^D = \frac{2\hat{\mathcal{A}}_p f'(1)}{kf'(\bar{A}_d) + 2\sqrt{kf'(\bar{A}_d)}\sqrt{f'(1)}}. \tag{4.63}$$

Figure 4.6 shows the relationship between this linearised solution and numerical solution of the nonlinear Riemann problem along a slice of the parameter space, tracing a bifurcation diagram using $\mathcal{A}_p$ as a bifurcation parameter holding $\mathcal{A}_d = 1$, $\mathcal{U}_p = \mathcal{U}_d = 0$. Along this slice we have a transition from LRRS solution to LSRR solution as $\mathcal{A}_p$ increases through 1 (denoted by green and cyan lines, respectively). We also have a thick black line representing the analytical solution of our linearised model, such that close to $\mathcal{A}_p = 1$ we see that the analytically predicted solutions are tangential to the numerically computed solutions.

So far we have considered the classical wave profiles which are possible for flow in a blood vessel with a junction. In what follows we observe that these four cases are insufficient to span the parameter space, and there are a number of extra (resonant) cases which arise as a result of the splitting of mass across the junction and also modified by a jump in material/environmental properties. We consider these resonant cases in Section 4.6 below.

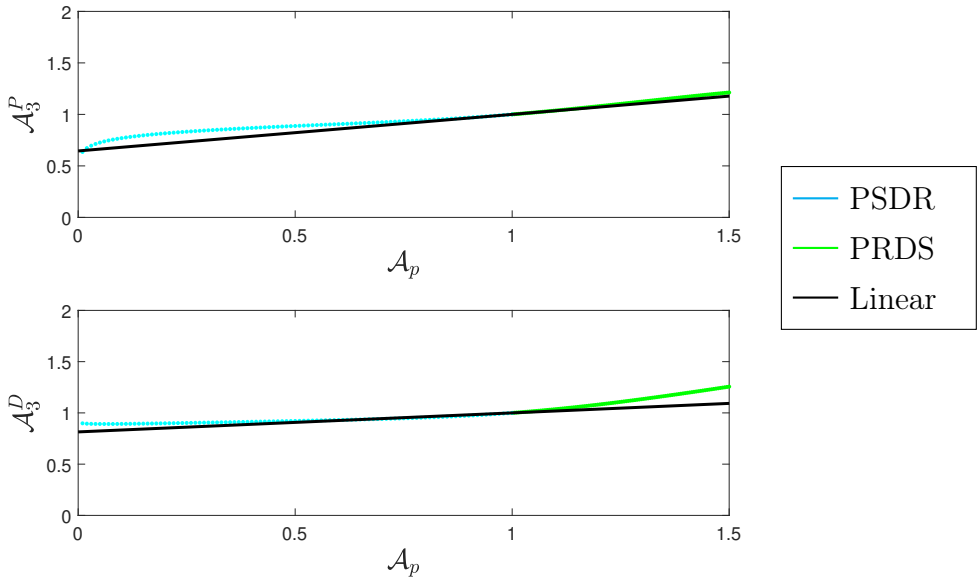

Figure 4.6: Bifurcation diagram showing comparison with Numerical and analytical solution of our wave. The numerical solution is denoted by the green and cyan lines representing PRDS and PSDR solutions, respectively. While the black thick line represent the analytical solution of our model.

4.6 Resonance

In Section 4.4, we have generalised the four standard cases of Chapter 2 to consider flow across a blood vessel junction. Here we show again that due to division of mass across the junction our four standard cases are insufficient to span the parameter space. Here, we follow a similar approach to Chapter 3 to derive new resonant configurations for the junction Riemann problem (not previously derived in other work on the junction problem [87, 88]). In designing this approach we incorporated splitting of mass across the junction and also a jump in stiffness from parent to daughter vessels. Below we plot bifurcation diagrams to illustrate these resonant solutions and finally explore the wider parameter space.

4.6.1 Riemann solution of configuration C^+

Figure 4.7 illustrates the Riemann problem for configuration C^+, which is a modified version of configuration C as used in Chapter 3. Here, we have a rarefaction in the parent vessel that becomes transcritical and resonates with the stationary wave at the junction producing three successive waves around the junction, each separated by a small distance $\epsilon \ll 1$; a supercritical stationary wave ($x = -\epsilon$), a zero speed shock ($x = 0$) and a subcritical stationary wave ($x = \epsilon$). Between these two stationary waves we have an intermediate zone, denoted as the s zone. Crucially, in this asymptotic region we allow the mass splitting parameter r_s to take an intermediate value between that of the parent ($r_p = 1$) and that of the daughter ($r_d = 2$). Furthermore, the zone also exhibits external pressure $\bar{p}_{es}$, baseline cross-sectional area $\bar{A}_s$, and stiffness k_s. So, across that intermediate zone between $x = -\epsilon$ and $x = \epsilon$, we have different parameters with subscript s, which are all things that can change from the parent to

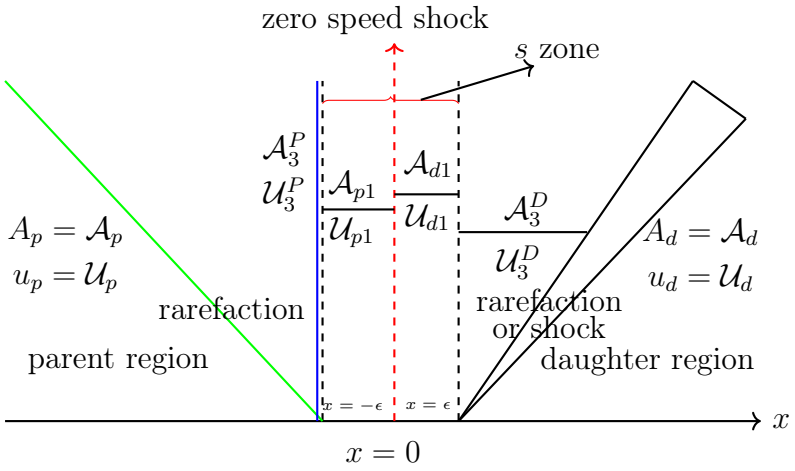

Figure 4.7: Sketch of the Riemann problem for configuration C^+

the daughter vessels. However, these intermediate quantities cannot be specified independently. As in Chapter 3, we assume they are linearly interpolated based on a single parameter s such that $0 \leq s \leq 1$ and

$$(r_s, \bar{A}_s, \bar{p}_{es}, k_s) = (r_p, \bar{A}_p, \bar{p}_{ep}, k_p) + s(r_d - r_p, \bar{A}_d - \bar{A}_p, \bar{p}_{ed} - \bar{p}_{ep}, k_d - k_p).$$

At the edge of the transcritical rarefaction in the parent vessel we employ the procedure in Section 3.7 and we have cross-sectional area, flow speed and wave speed as

$$A_r^P(x,t) = \left(\frac{\sqrt{m}\mathcal{U}_p}{(m+2)} + \frac{2\mathcal{C}_p}{\sqrt{m}(m+2)} - \frac{\sqrt{m}x}{(m+2)t} \right)^{2/m}, \tag{4.64}$$

$$u_r^P(x,t) = \frac{m\mathcal{U}_p}{m+2} + \frac{2\mathcal{C}_p}{m+2} + \frac{2x}{(m+2)t}, \tag{4.65}$$

$$c_r^P(x,t) = \frac{m\mathcal{U}_p}{m+2} + \frac{2\mathcal{C}_p}{m+2} - \frac{mx}{(m+2)t}, \tag{4.66}$$

which span all the way from $x = (\mathcal{U}_p - \mathcal{C}_p)t$ to $x = -\epsilon$. Again, at the outer edge of the supercritical stationary wave (i.e. $x = -\epsilon$), following similar method as in Section 3.7 we denote $A_r^P = \mathcal{A}_3^P$, $u_r^P = \mathcal{U}_3^P$ and $c_r^P = \mathcal{C}_3^P$, such that the profiles inner limit of the outer solution as $\epsilon \to 0$ of these profiles becomes

$$\mathcal{A}_3^P = \left(\frac{\sqrt{m}\mathcal{U}_p}{(m+2)} + \frac{2\mathcal{C}_p}{\sqrt{m}(m+2)} \right)^{2/m}, \tag{4.67}$$

$$\mathcal{U}_3^P = \mathcal{C}_3^P = \frac{m\mathcal{U}_p}{m+2} + \frac{2\mathcal{C}_p}{m+2}. \tag{4.68}$$

Now, between the inner edge of the supercritical stationary wave and the zero speed shock we let the profiles ($-\epsilon < x < 0$) be denoted as $A_p = \mathcal{A}_{p1}$, $u_p = \mathcal{U}_{p1}$ and $c_p = \mathcal{C}_{p1}$ and impose continuity of flux

and total pressure across the stationary wave, to have

$$r_p\mathcal{A}_3^P\mathcal{U}_3^P = r_s\mathcal{A}_{p1}\mathcal{U}_{p1}, \tag{4.69}$$

$$\bar{p}_{ep} + \frac{1}{2}(\mathcal{U}_3^P)^2 + ((\mathcal{A}_3^P)^m - 1) = \bar{p}_{es} + \frac{1}{2}(\mathcal{U}_{p1})^2 + k_s\left(\left(\frac{\mathcal{A}_{p1}}{\bar{A}_s}\right)^m - 1\right), \tag{4.70}$$

where we note that the properties to the right of the stationary wave (*i.e.* r_s, k_s, $\bar{p}_{es}$, $\bar{A}_s$) are to be determined.

Across the uniform region between the zero speed shock and the subcritical stationary wave (*i.e.* $0 < x < \epsilon$) we denote the profiles as $A_d = \mathcal{A}_{d1}$, $c_d = \mathcal{C}_{d1}$ and $u_d = \mathcal{U}_{d1}$, respectively. We now invoke the conservation of mass and momentum across the zero speed shock front as

$$\dot{s}_{res} = \frac{\mathcal{A}_{d1}\mathcal{U}_{d1} - \mathcal{A}_{p1}\mathcal{U}_{p1}}{\mathcal{A}_{d1} - \mathcal{A}_{p1}} = \frac{\mathcal{A}_{d1}(\mathcal{U}_{d1})^2 - \mathcal{A}_{p1}(\mathcal{U}_{p1})^2 + \frac{k_s m}{\bar{A}_s^m(m+1)}\left((\mathcal{A}_{d1})^{m+1} - (\mathcal{A}_{p1})^{m+1}\right)}{\mathcal{A}_{d1}\mathcal{U}_{d1} - \mathcal{A}_{p1}\mathcal{U}_{p1}}. \tag{4.71}$$

Simplifying, we have that

$$\mathcal{U}_{d1} = \mathcal{U}_{p1} \pm \sqrt{\frac{k_s m\left((\mathcal{A}_{d1})^{m+1} - (\mathcal{A}_{p1})^{m+1}\right)(\mathcal{A}_{d1} - \mathcal{A}_{p1})}{\mathcal{A}_{d1}\mathcal{A}_{p1}\bar{A}_s^m(m+1)}}, \tag{4.72}$$

a nonlinear equation connecting $\mathcal{A}_{d1}$ to $\mathcal{U}_{d1}$.

Between the subcritical stationary wave and the existing wave in the daughter vessel we denote $A_d = \mathcal{A}_3^D$, $u_d = \mathcal{U}_3^D$ and $c_d = \mathcal{C}_3^D$. Across this subcritical stationary wave, we impose continuity of flux and total pressure (*i.e.* conditions (4.33) and (4.34)) to have

$$r_s\mathcal{A}_{d1}\mathcal{U}_{d1} = r_d\mathcal{A}_3^D\mathcal{U}_3^D, \tag{4.73}$$

$$\bar{p}_{es} + \frac{1}{2}(\mathcal{U}_{d1})^2 + k_s\left(\left(\frac{\mathcal{A}_{d1}}{\bar{A}_s}\right)^m - 1\right) = \bar{p}_{ed} + \frac{1}{2}(\mathcal{U}_3^D)^2 + k\left(\left(\frac{\mathcal{A}_3^D}{\bar{A}_d}\right)^m - 1\right). \tag{4.74}$$

The (uniform) flow to the right of the subcritical stationary wave is then connected to the daughter region with two flow possibilities, which is either a shock or a rarefaction. First we consider if it is a shock (see Section 4.2.5) and the subsequently consider the case where it is a rarefaction (see Section 4.2.3).

For a shock in the daughter vessel, we invoke conservation of mass and momentum across the shock front at $x = s_d$ as

$$\dot{s}_d = \frac{\mathcal{A}_d\mathcal{U}_d - \mathcal{A}_3^D\mathcal{U}_3^D}{\mathcal{A}_d - \mathcal{A}_3^D}, \tag{4.75}$$

$$\dot{s}_d = \frac{\mathcal{A}_d(\mathcal{U}_d)^2 - \mathcal{A}_3^D(\mathcal{U}_3^D)^2 + \frac{m}{m+1}\left(((\mathcal{A}_d)^{m+1}) - (\mathcal{A}_3^D)^{m+1}\right)}{\mathcal{A}_d\mathcal{U}_d - \mathcal{A}_3^D\mathcal{U}_3^D}. \tag{4.76}$$

Equating equations (4.75) and (4.76) and simplifying, we have

$$\mathcal{U}_3^D = \mathcal{U}_d \pm \sqrt{\frac{km\left((\mathcal{A}_d)^{m+1} - (\mathcal{A}_3^D)^{m+1}\right)(\mathcal{A}_d - \mathcal{A}_3^D)}{\mathcal{A}_d \mathcal{A}_3^D \bar{A}_d^m (m+1)}}, \tag{4.77}$$

a nonlinear equation connecting $\mathcal{A}_3^D$ to $\mathcal{U}_3^D$.

Note that for the configuration C^+ to be a physical solution, we apply physicality conditions on the transcritical rarefaction and both shocks, and also on the parameters to be determined. For a transcritical left rarefaction with a right propagating shock, we have

$$\begin{aligned} (\mathcal{U}_3^P - \mathcal{C}_3^P) > (\mathcal{U}_p - \mathcal{C}_p), \qquad & (\mathcal{U}_{p1} - \mathcal{C}_{p1}) > (\mathcal{U}_3^P - \mathcal{C}_3^P), \\ (\mathcal{U}_d + \mathcal{C}_d) < \dot{s}_d < (\mathcal{U}_3^D + \mathcal{C}_3^D), \qquad & 0 \le s \le 1. \end{aligned} \tag{4.78}$$

Conversely, for a rarefaction in the daughter vessel adjacent to the far-field region, we have the profiles of each variable given as

$$A_r^D(x,t) = \bar{A}_d \left(\frac{\sqrt{m}}{\sqrt{k}(m+2)} \left(\left(\frac{x}{t} - \mathcal{U}_d \right) + \frac{2\mathcal{C}_d}{m} \right) \right)^{2/m}, \quad \text{where} \quad \mathcal{C}_d = \sqrt{km} \left(\frac{\mathcal{A}_d}{\bar{A}_d} \right)^{m/2}, \tag{4.79}$$

$$u_r^D(x,t) = \frac{m\mathcal{U}_d}{m+2} - \frac{2\mathcal{C}_d}{m+2} + \frac{2x}{(m+2)t}, \tag{4.80}$$

$$c_r^D(x,t) = \frac{m}{m+2} \left(\left(\frac{x}{t} - \mathcal{U}_d \right) + \frac{2\mathcal{C}_d}{m} \right). \tag{4.81}$$

At the edge of the daughter rarefaction, where $A_r^D = \mathcal{A}_3^D$, $u_r^D = \mathcal{U}_3^D$ and $c_r^D = \mathcal{C}_3^D$ such that

$$x_{rd} = (\mathcal{U}_3^D + \mathcal{C}_3^D)t. \tag{4.82}$$

Substituting (4.82) into (4.79), we have at the edge of the daughter region

$$\mathcal{U}_3^D = \mathcal{U}_d + 2\sqrt{\frac{k}{m\bar{A}_d^m}} \left((\mathcal{A}_3^D)^{m/2} - \mathcal{A}_d^{m/2} \right). \tag{4.83}$$

The physicality condition for configuration C^+ with a daughter rarefaction is given as

$$\begin{aligned} (\mathcal{U}_3^P - \mathcal{C}_3^P) > (\mathcal{U}_p - \mathcal{C}_p), \qquad & (\mathcal{U}_{p1} - \mathcal{C}_{p1}) > (\mathcal{U}_3^P - \mathcal{C}_3^P), \\ (\mathcal{U}_3^D + \mathcal{C}_3^D) < (\mathcal{U}_d + \mathcal{C}_d), \qquad & 0 \le s \le 1. \end{aligned} \tag{4.84}$$

We note that the case $s = 0$ corresponds to the properties of the intermediate region $(-\epsilon \le x \le \epsilon)$ being identical to the parent vessel, while the case $s = 1$ corresponds to the properties of the intermediate region being identical to the daughter vessels.

4.6.2 Riemann solution for configuration D^+

Figure 4.8 is an illustration of another resonant setup, analogous to configuration D of Han et. al. (2015) [89], and discussed previously in Chapter 3. This resonance arises from either PRDR or PRDS,

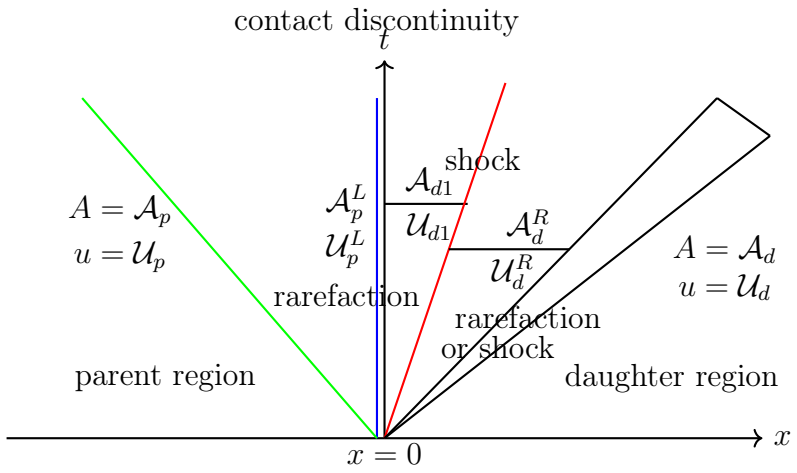

Figure 4.8: Sketch of the Riemann problem for configuration D^+

where the parent rarefaction resonates with the stationary wave and generates a new propagating shock wave in the daughter vessels, while the transcritical rarefaction in the parent vessel resonates with the stationary wave.

In this case the transcritical parent rarefaction profile is identical to configuration C^+ and given by equations (4.64), (4.65) and (4.66), respectively. At the edge of the transcritical parent rarefaction similar to configuration C^+ we let $A_r^P = \mathcal{A}_3^P$, $u_r^P = \mathcal{U}_3^P$ and $c_r^P = \mathcal{C}_3^P$ such that we have

$$\mathcal{A}_3^P = \left(\frac{\sqrt{m}\mathcal{U}_p}{(m+2)} + \frac{2\mathcal{C}_p}{\sqrt{m}(m+2)}\right)^{2/m}, \tag{4.85}$$

$$\mathcal{U}_3^P = \mathcal{C}_3^P = \frac{n\mathcal{U}_p}{m+2} + \frac{2\mathcal{C}_p}{m+2}. \tag{4.86}$$

Denoting the flow profiles in the region between the stationary wave and the newly generated propagating shock wave as $A_d = \mathcal{A}_{d1}$, $u_d = \mathcal{U}_{d1}$ and $c_d = \mathcal{C}_{d1}$, we impose the continuity of flux and continuity of total pressure over the contact discontinuity to have

$$r_p \mathcal{A}_3^P \mathcal{U}_3^P = r_d \mathcal{A}_{d1}\mathcal{U}_{d1}, \tag{4.87}$$

$$\bar{p}_{ep} + \frac{1}{2}(\mathcal{U}_3^P)^2 + \left((\mathcal{A}_3^P)^m - 1\right) = \bar{p}_{ed} + \frac{1}{2}(\mathcal{U}_{d1})^2 + k\left(\left(\frac{\mathcal{A}_{d1}}{\bar{A}_d}\right)^m - 1\right). \tag{4.88}$$

Across the resonant shock wave produced in the daughter vessels, we invoke conservation of mass and momentum across the front at $x = s_{res}(t)$ which takes the form

$$\dot{s}_{res} = \frac{\mathcal{A}_3^D\mathcal{U}_3^D - \mathcal{A}_{d1}\mathcal{U}_{d1}}{\mathcal{A}_d^s - \mathcal{A}_{d1}}, \tag{4.89}$$

$$\dot{s}_{res} = \frac{\mathcal{A}_3^D(\mathcal{U}_3^D)^2 - \mathcal{A}_{d1}(\mathcal{U}_{d1})^2 + \frac{km}{\bar{A}_d^m(m+1)}\left((\mathcal{A}_3^D)^{m+1} - (\mathcal{A}_{d1})^{m+1}\right)}{\mathcal{A}_3^D\mathcal{U}_3^D - \mathcal{A}_{d1}\mathcal{U}_{d1}}. \tag{4.90}$$

Equating equations (4.89) and (4.90) and simplifying, we have

$$\mathcal{U}_3^D = \mathcal{U}_{d1} \pm \sqrt{\frac{km\left((\mathcal{A}_3^D)^{m+1} - (\mathcal{A}_{d1})^{m+1}\right)(\mathcal{A}_3^D - \mathcal{A}_{d1})}{\mathcal{A}_3^D \mathcal{A}_{d1}(m+1)\bar{A}_d^m}}, \tag{4.91}$$

a nonlinear equation connecting $\mathcal{A}_3^D$ to $\mathcal{U}_3^D$.

The second wave in the daughter vessels can be either a shock or rarefaction, and we then apply a similar approach as in configuration C^+ and use (4.77) for a shock wave in the daughter vessels or (4.83) for a rarefaction wave in the daughter vessel. Note, for configuration D^+ to be a physical solution, we impose the following conditions if the far right wave is a shock

$$\begin{aligned} (\mathcal{U}_p - \mathcal{C}_p) < 0, \quad \mathcal{A}_p > \mathcal{A}_3^P, \qquad & (\mathcal{U}_{21} - \mathcal{C}_{21}) > 0, \\ (\mathcal{U}_3^D - \mathcal{C}_3^D) < \dot{s}_{res} < (\mathcal{U}_{21} - \mathcal{C}_{21}), \qquad & (\mathcal{U}_d + \mathcal{C}_d) < \dot{s}_d < (\mathcal{U}_3^D + \mathcal{C}_3^D). \end{aligned} \tag{4.92}$$

Conversely, if the second wave in the daughter vessels is a rarefaction we impose

$$\begin{aligned} (\mathcal{U}_p - \mathcal{C}_p) < 0, \quad \mathcal{A}_p > \mathcal{A}_3^P, \qquad & (\mathcal{U}_{21} - \mathcal{C}_{21}) > 0, \\ (\mathcal{U}_3^D - \mathcal{C}_3^D) < \dot{s}_{res} < (\mathcal{U}_{21} - \mathcal{C}_{21}), \qquad & (\mathcal{U}_3^D + \mathcal{C}_3^D) < (\mathcal{U}_d + \mathcal{C}_d), \end{aligned} \tag{4.93}$$

Note that the new shock produced in the daughter vessels as a result of the parent rarefaction resonating with the stationary wave must satisfy Lax entropy condition for a shock wave in the parent vessel, since this was produced from the resonance of the parent rarefaction.

4.7 Results of the Riemann problem with no change in material or environmental properties

We now present a summary of the predictions of the Riemann problem. We first assume no jump in material or environmental properties across the junction and so the discontinuity at the junction is driven by the division of mass across the symmetric junction.

We consider several distinct values of the flow speed in the parent and daughter vessels tracking the different flow structures while continuously varying either the cross-sectional area in the daughter vessel (see Section 4.7.1) or the cross-sectional area in the parent vessel (see Section 4.7.2). In each of the cases below we choose $\bar{p}_{ep} = \bar{p}_{ed} = 0$, $\bar{A}_d = 1$.

4.7.1 Variation of cross-sectional area in daughter vessel

Case 1

In Figure 4.9 we consider $\mathcal{U}_p = \mathcal{U}_d = 0$, $\mathcal{A}_p = 1$ with equal division of mass and no jump in material or environmental properties across the junction and construct a bifurcation diagram by varying the value of $\mathcal{A}_d$. We have that for large $\mathcal{A}_d$ the system exhibits a PSDR solution which then transitions to a PRDS solution as $\mathcal{A}_d$ decreases through 1. This is qualitatively similar to case 1 in Chapter 3. However, despite continuity of all material and environmental properties across the junction the behaviour for smaller $\mathcal{A}_d$ is more complicated. As $\mathcal{A}_d$ decreases the PRDS solution exhibits a limit

point as the parent rarefaction becomes transcritical at $\mathcal{A}_d \approx 0.582$ (see Figure 4.9a) producing a second (unphysical) branch underneath. As $\mathcal{A}_d$ decreases below the critical point, the physical branch of PRDS transitions into a configuration C^+ resonance solution with a shock in the daughter vessel, which further transitions to a configuration D^+ resonance solution with a shock in the daughter vessel (transcritical parent rarefaction, shock and daughter shock denoted as tPRSDS). We note that we have only one physical solution for all $\mathcal{A}_d$ and that division of mass across the junction is sufficient to induce resonance. To further analyse our solution, we plot the profiles of cross-sectional area, velocity and wavespeed (Figure 4.10a) and the corresponding characteristic diagram (Figure 4.10b) of PRDS just above the limit point at $\mathcal{A}_d = 0.6$ (denoted (i)) on the bifurcation diagram of Figure 4.9. Each of the three spatial profiles are discontinuous at the junction, with most of the division of flux accommodated by the jump in flow velocity. However, the rarefaction in the parent vessel extends almost all the way to the junction, also evident in the characteristics diagram (Figure 4.10b), and so the rarefaction is at the point of becoming transcritical.

Furthermore, Figure 4.11 explores the resonant region for case 1 in greater detail. Figure 4.11(a) illustrates the mass splitting factor r_s across the range of C^+ resonance and verifies that it falls in the range of $r_p = 1 \leq r_s \leq 2 = r_d$. In this case the class D^+ resonance solution persists as $\mathcal{A}_d$ decreases and the resonant shock and the daughter shock coalesce at $\mathcal{A}_d = 0$ as their speeds become identical in this limit (see Figure 4.10b). This is further illustrated in the spartial profiles of the configuration D^+ solution ($tPRSDS$) (panel (ii) and (iii)); for $\mathcal{A}_d \approx 0.3$ (see Figure 4.12a) the two shocks are far apart while for $\mathcal{A}_d \approx 0.05$ (see Figure 4.12b) the two shocks are almost coincident. Some of the features exhibited in this case are similar to the cases discussed below and so we do not be explore them again in detail.

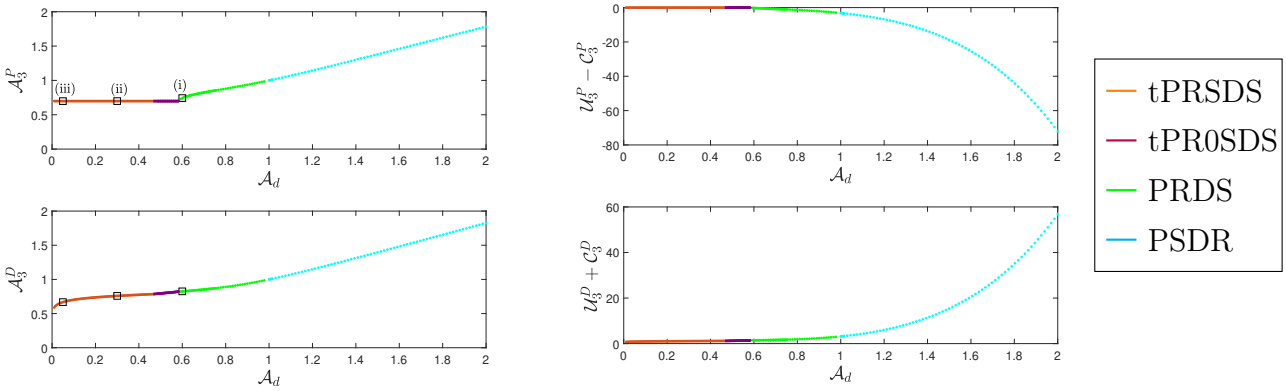

Figure 4.9: Case 1: Bifurcation diagram for case where $\mathcal{U}_p = 0$, $\mathcal{U}_d = 0$, and $\mathcal{A}_p = 1$ with corresponding values of $\mathcal{A}_d$. $\mathcal{A}_3^P$, $\mathcal{A}_3^D$, $\mathcal{U}_3^P - \mathcal{C}_3^P$ and $\mathcal{U}_3^D + \mathcal{C}_3^D$, respectively.

Case 2

In Figure 4.13 we extend case 1 to include flow sucked out of the parent vessel, setting $\mathcal{U}_p = -0.5$, $\mathcal{U}_d = 0$, $\mathcal{A}_p = 1$ with splitting of mass across the junction and construct a bifurcation diagram by varying the value of $\mathcal{A}_d$. In this case, unlike in the case where $\mathcal{U}_d = \mathcal{U}_p = 0$, we have three classical wave configurations and two resonant solutions. For large value of $\mathcal{A}_d$ the system exhibits a PSDR solution

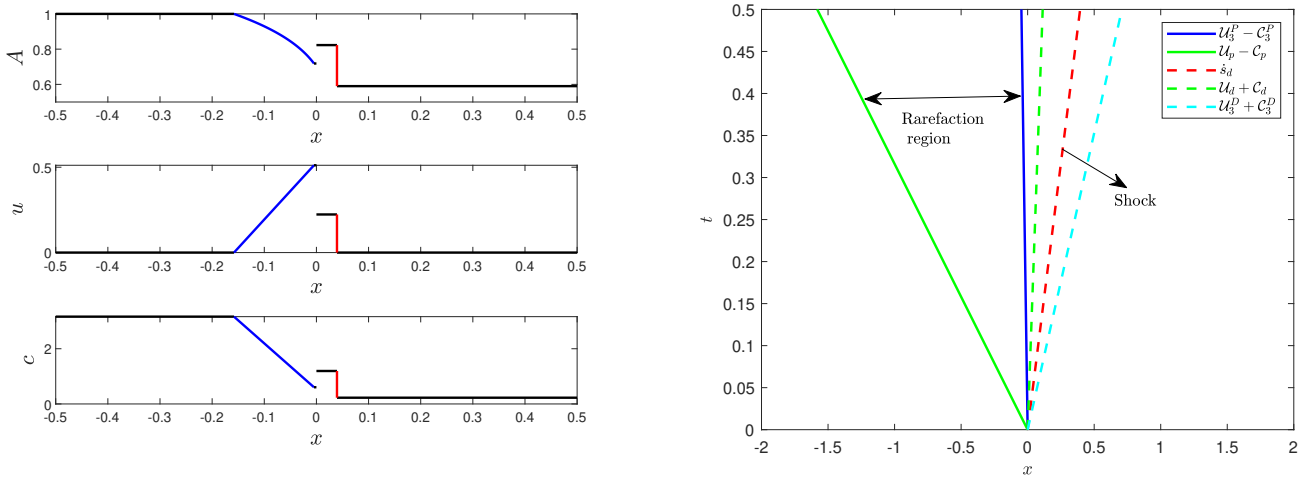

(a) **(b)**

Figure 4.10: Illustration of wave profiles and characteristics curves for PRDS for $\mathcal{U}_p = 0$, $\mathcal{U}_d = 0$, $\mathcal{A}_p = 1$ and $\mathcal{A}_d = 0.6$. Figure 4.10(a) shows the wave profile while Figure 4.10(b) illustrates the characteristic lines.

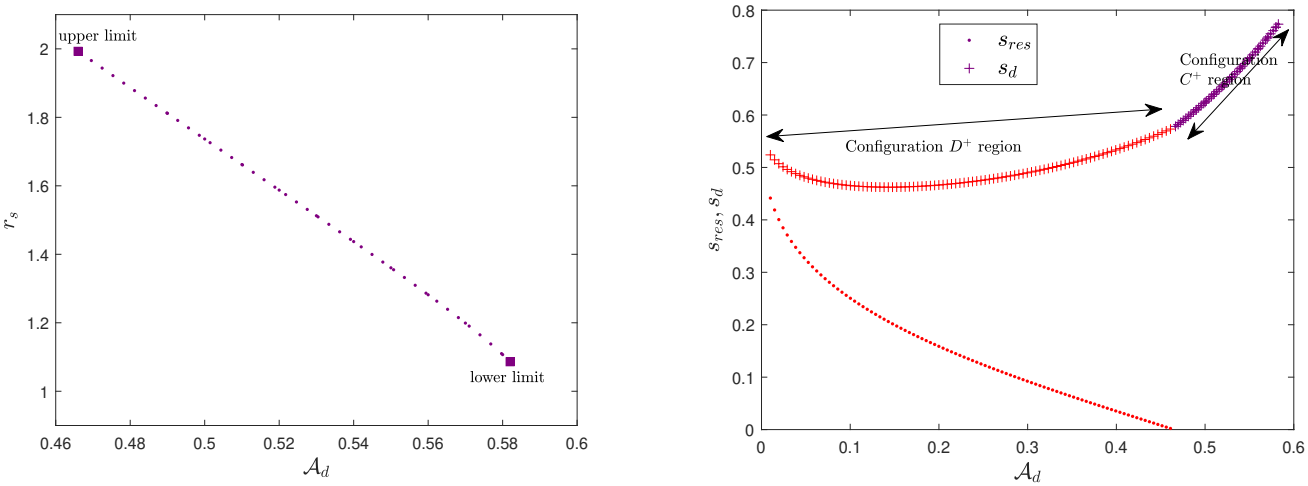

(a) **(b)**

Figure 4.11: Illustration of the range of splitting factor r_s across the configuration C solution for $\mathcal{U}_p = 0$, $\mathcal{U}_d = 0$, and $\mathcal{A}_p = 1$ and the two shock waves in the daughter vessels for configuration D solution.

which then transitions to a PRDR solution as $\mathcal{A}_d$ decreases. As $\mathcal{A}_d$ decreases further the PRDR solution then transitions to PRDS solution which then exhibits a transcritical limit point at $\mathcal{A}_d \approx 0.427$ which then connects to a second (unphysical) branch of PRDS. As $\mathcal{A}_d$ decreases further the physical branch of PRDS transitions into a configuration C^+ resonant solution (tPR0SDS) and as $\mathcal{A}_d$ decreases further

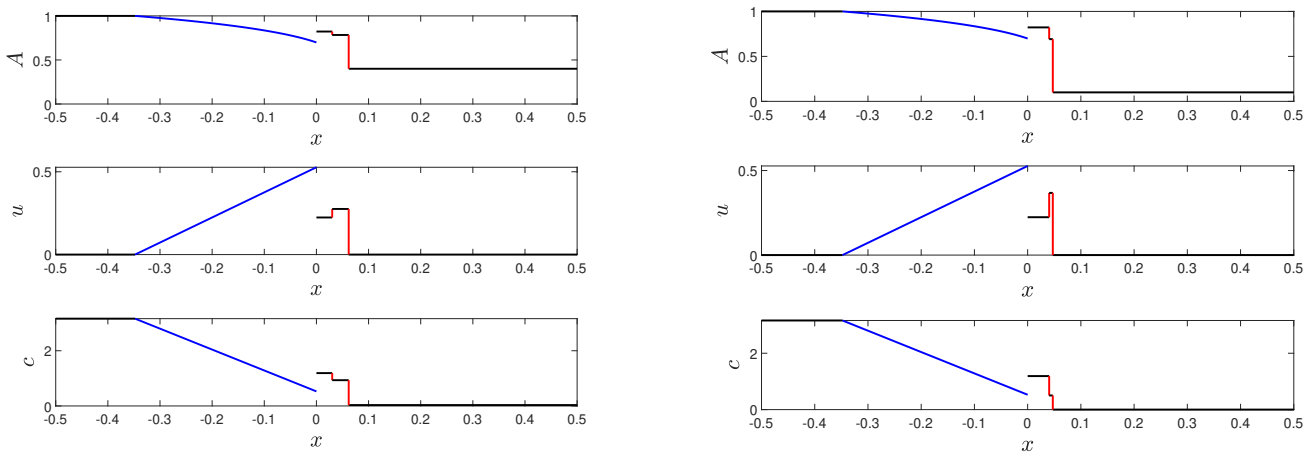

(a) **(b)**

Figure 4.12: Wave profiles of the configuration D solution with a daughter shock for $\mathcal{U}_p = 0$, $\mathcal{U}_d = 0$, and $\mathcal{A}_p = 1$. Figure 4.12(a) shows the configuration D solution for $\mathcal{A}_d = 0.3$, while Figure 4.12(b) shows the configuration D solution for $\mathcal{A}_d = 0.05$.

the configuration C^+ solution transitions to a configuration D^+ solution (tPRSDS). Here, we note that suction of flow in parent vessel introduces additional classical solution and suppresses resonance by restricting it to a smaller range of values of $\mathcal{A}_d$. Again we note that the propagating shocks in the daughter vessels remain distinct for $\mathcal{A}_d > 0$ (although they appear to approach one another as $\mathcal{A}_d \to 0$) and so the resonant solution does not subsequently become classical again for smaller $\mathcal{A}_d$.

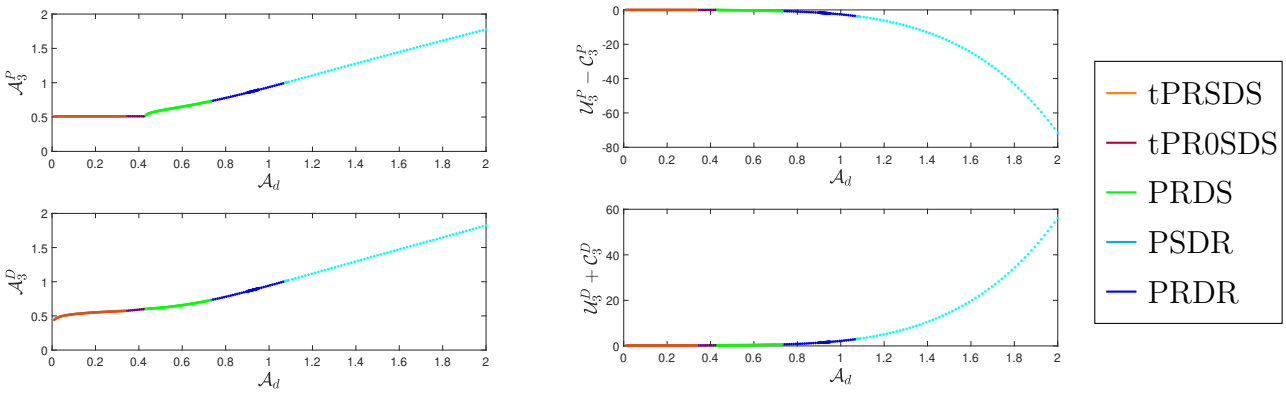

Figure 4.13: Case 2: Bifurcation diagram for case where $\mathcal{U}_p = -0.5$, $\mathcal{U}_d = 0$, and $\mathcal{A}_p = 1$ with corresponding values of $\mathcal{A}_d$, $\mathcal{A}_3^P$, $\mathcal{A}_3^D$, $\mathcal{U}_3^P - \mathcal{C}_3^P$ and $\mathcal{U}_3^D + \mathcal{C}_3^D$, respectively.

Case 3

In Figure 4.14 we consider flow injected into the parent vessel with $\mathcal{U}_p = 0.5$ $\mathcal{U}_d = 0$, $\mathcal{A}_p = 1$, with splitting of mass across the junction and construct a bifurcation diagram by varying the value of $\mathcal{A}_d$. As in cases 1 and 2 the system exhibits PSDR for large $\mathcal{A}_d$ but then transitions to PSDS as $\mathcal{A}_d$ decreases (similar to case 3 in Chapter 3). With further decrease in $\mathcal{A}_d$ the PSDS solution transitions to a PRDS solution which then exhibits a transcritical turning point at $\mathcal{A}_d \approx 0.663$. Beyond this point, the system further transitions to a configuration C^+ resonant solution (tPR0SDS) and subsequently into a configuration D^+ solution (tPRSDS). We also note that with injection of flow into the parent vessel the width of the resonant region is increased compared to cases 1 and 2.

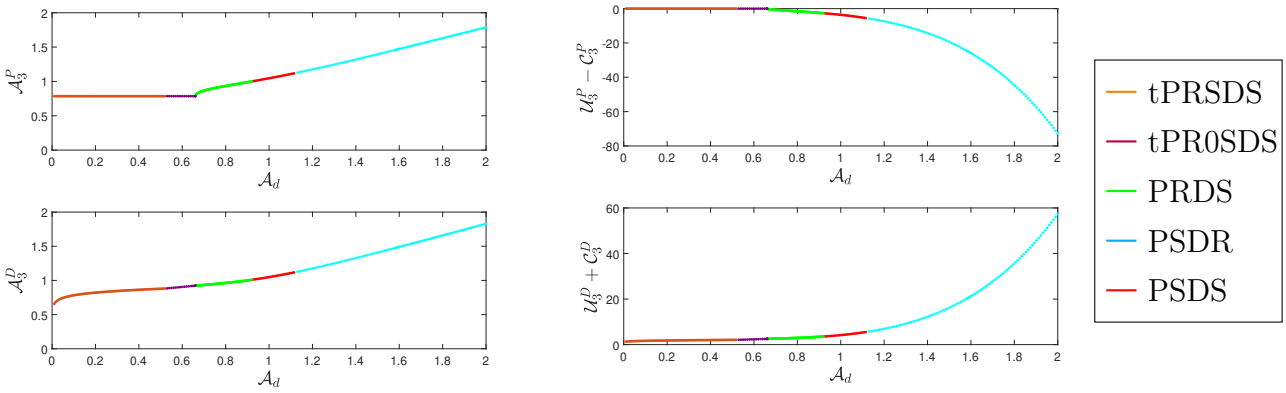

Figure 4.14: Case 3: Bifurcation diagram for case where $\mathcal{U}_p = 0.5$, $\mathcal{U}_d = 0$, and $\mathcal{A}_p = 1$ with corresponding values of $\mathcal{A}_d$, $\mathcal{A}_3^P$, $\mathcal{A}_3^D$, $\mathcal{U}_3^P - \mathcal{C}_3^P$ and $\mathcal{U}_3^D + \mathcal{C}_3^D$, respectively.

Case 4

In Figure 4.15 we consider flow injected into the daughter vessels at the distant end, setting $\mathcal{U}_p = 0$ $\mathcal{U}_d = -0.6$, $\mathcal{A}_p = 1$ and construct a bifurcation diagram by varying the value of $\mathcal{A}_d$. This system shows three classical wave solutions and two resonant solutions. For large $\mathcal{A}_d$ the system exhibits a PSDR which then transitions to a PSDS solution as $\mathcal{A}_d$ decreases. Further decrease in $\mathcal{A}_d$ sees the PSDS solution transition into a PRDS solution which then exhibits a turning point at $\mathcal{A}_d \approx 0.137$. The physical branch of PRDS solution then transitions into a configuration C^+ resonant solution (tPR0SDS) as $\mathcal{A}_d$ decreases below 0.137. With further decrease in $\mathcal{A}_d$ the configuration C^+ solution (tPR0SDS) transitions into a configuration D^+ solution (tPRSDS). Here, we note that with injection of flow out of the daughter vessel the resonance solution takes up smaller region for low $\mathcal{A}_d$ compared to case 3 suction of flow out of the daughter vessel and again the resonance persists as $\mathcal{A}_d \to 0$.

Case 5

In Figure 4.16 we consider $\mathcal{U}_p = 0$ $\mathcal{U}_d = 0.6$, $\mathcal{A}_p = 1$ and construct a bifurcation diagram by varying the value of $\mathcal{A}_d$. This case shows that for large $\mathcal{A}_d$ the system exhibits a PSDR which the transitions into a PRDR as $\mathcal{A}_d$ decreases. The PRDR solution exhibits a transcritical turning point at $\mathcal{A}_d \approx 0.993$

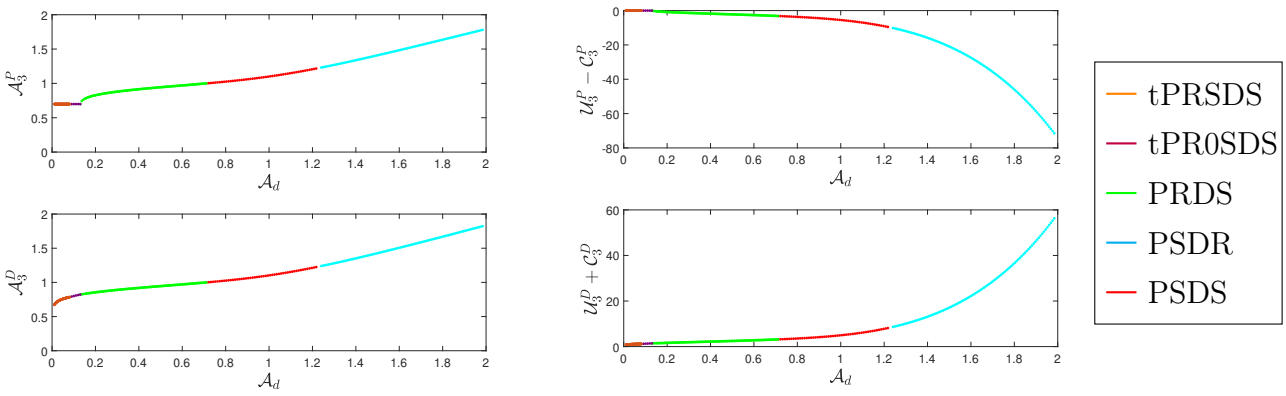

Figure 4.15: Case 4: Bifurcation diagram for case where $\mathcal{U}_p = 0$, $\mathcal{U}_d = -0.6$, and $\mathcal{A}_p = 1$ with corresponding values of $\mathcal{A}_d$, $\mathcal{A}_3^P$, $\mathcal{A}_3^D$, $\mathcal{U}_3^P - \mathcal{C}_3^P$ and $\mathcal{U}_3^D + \mathcal{C}_3^D$, respectively.

producing an unphysical branch beneath. Conversely, for low $\mathcal{A}_d$ the system exhibits a PRDS solution which further transitions into a PRDR solution as $\mathcal{A}_d$ increases. This branch of PRDR again exhibits a turning point at $\mathcal{A}_d \approx 0.533$ producing an unphysical branch. These two transcritical points leave a gap across the region $0.52 \lesssim \mathcal{A}_d \lesssim 0.99$. For larger values of $\mathcal{A}_d$, the system transitions into a configuration C^+ resonant solution (transcritical parent rarefaction, zero speed shock and daughter rarefaction denoted as tPR0SDR) and then subsequently into configuration D^+ solution (transcritical parent rarefaction, shock and daughter rarefaction denoted as tPRSDR). However, we note that the region of configuration C^+ solution is significantly shorter than cases 1 to 4 above as it transitions into classical solution.

Figure 4.17 explores in detail the resonant region in the loop between the two transcritical PRDR solutions. Figure 4.17(a) illustrates the mass splitting factor r_s, showing the upper and lower limits and verifying that it falls in the range $1 \leq r_s \leq 2$. Furthermore from Figure 4.17(b) we see that the configuration D^+ solution (tPRSDR) does not persist for all $\mathcal{A}_d$ (as in case 1-4) but transitions into a classical PRDR solution for $\mathcal{A}_d \lesssim 0.521$ (analogous to Figure 3.18 of Chapter 3). At this transition point (marked (i) in Figure 4.16) the outer edge of the rarefaction in the daughter vessel x_{rd} coalesces with the resonant shock s_{res} (*i.e.* their speed approach each other) for a finite value of $\mathcal{A}_d$, unlike in cases 1-4 when the two shocks did not entirely coalesce until the tube had zero area ($\mathcal{A}_d = 0$).

We further illustrate this coalesce by plotting the wave profile of the configuration D^+ solution (tPRSDR) for two values of $\mathcal{A}_d$ in Figure 4.18. Figure 4.18(a) is for the point marked (ii) in Figure 4.16 which is far from the coalescence point (*i.e.* $\mathcal{A}_d \approx 0.8$ where we see that the shock and the rarefaction in the daughter vessel are far from each other). Conversely, Figure 4.18(b) illustrate profiles for the point denoted (iii) in Figure 4.16 which is close to the coalescence point where the shock and the daughter rarefaction are almost merging together.

In Figure 4.19 we also compare the locations of the two edges of the almost transcritical rarefactions at the points labelled as (i) and (iv) in Figure 4.16. Figure 4.19(a) corresponds to panel (i), where we have that the PRDR solution is close to the limit point and the two edges of the daughter rarefaction are very close together while Figure 4.19(b) shows that for large $\mathcal{A}_d$ (*i.e.* panel (iv)) we have that the PRDR solution close to the limit point exhibits an almost transcritical rarefaction but the outer edge of the rarefaction in the daughter vessel are very distinct and so a new shock is born when the system

becomes resonant. Hence, these two limit points are very different. The limit point close to point (iv) transitions clearly into a resonant solution generating an additional shock wave while the limit point close to point (i) is associated with merging of the resonant shock and the daughter rarefaction. At first glance it appears strange that the system should behave in a nonlocal manner *i.e.* why interaction of two waves in the daughter vessel at some $x > 0$ is sufficient to suppress the resonance at the stationary wave ($x = 0$). This interaction is a topic of future work

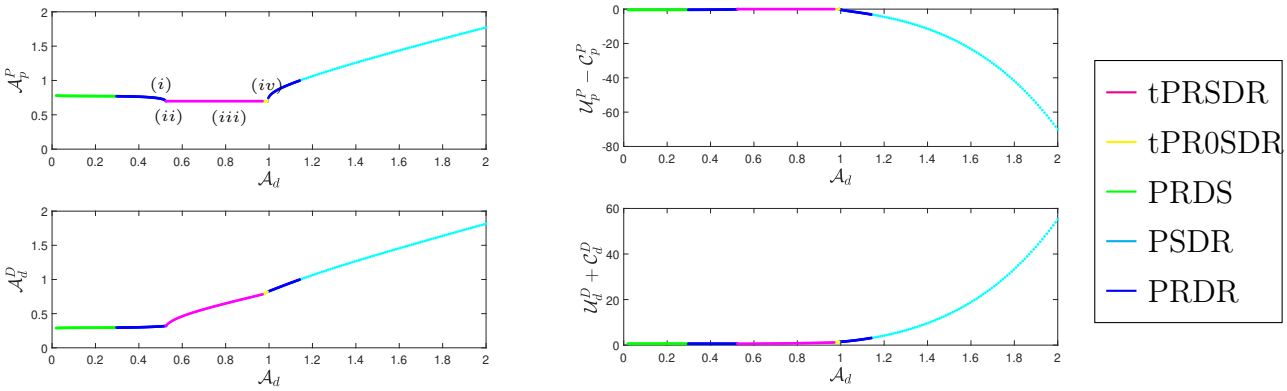

Figure 4.16: Case 5: Bifurcation diagram for case where $\mathcal{U}_p = 0$, $\mathcal{U}_d = 0.6$, and $\mathcal{A}_p = 1$ with corresponding values of $\mathcal{A}_d$, $\mathcal{A}_3^P$, $\mathcal{A}_3^D$, $\mathcal{U}_3^P - \mathcal{C}_3^P$ and $\mathcal{U}_3^D + \mathcal{C}_3^D$, respectively.

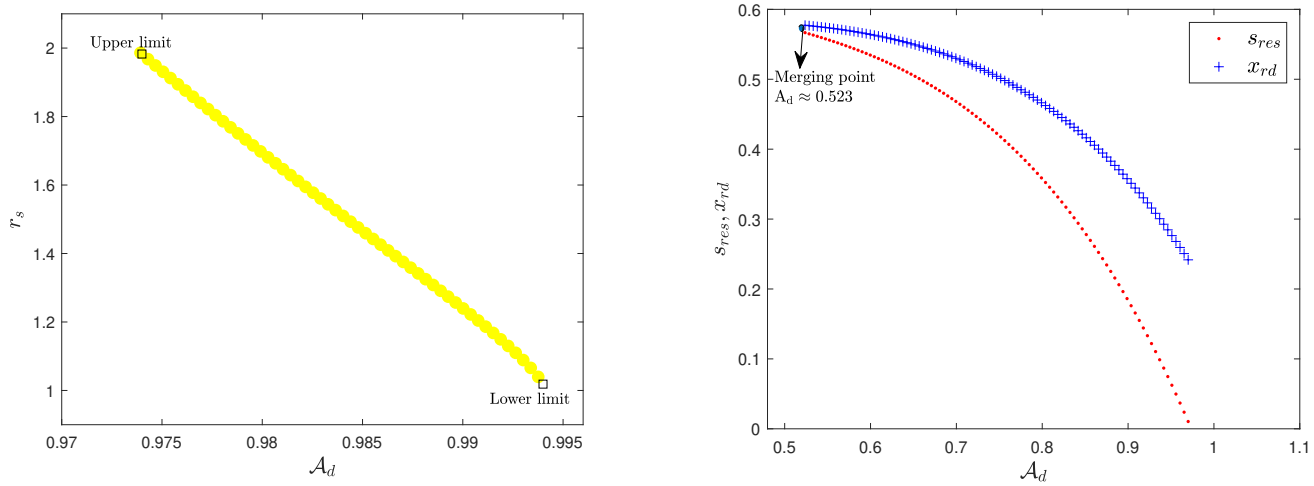

(a) **(b)**

Figure 4.17: Illustration of the splitting mass factor and the configuration D^+ solution (tPRSDR). Figure 4.17(a) is the range of the splitting of mass factor, while Figure 4.17(b) illustrates the resonant shock and the outer edge of the rarefaction in the daughter vessel.

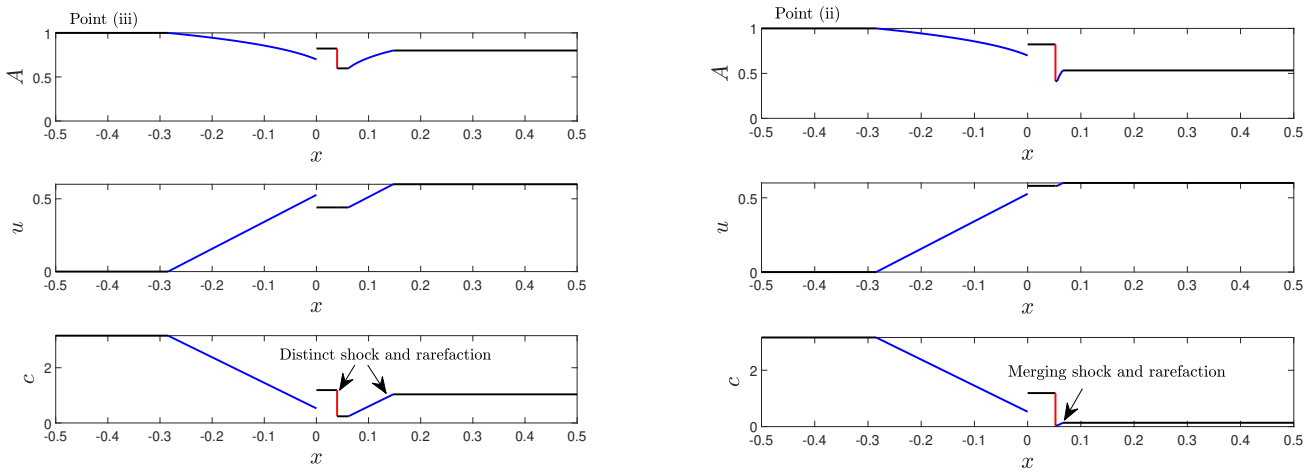

(a) **(b)**

Figure 4.18: Illustration of the splitting mass factor and the configuration D^+ solution (tPRSDR). Figure 4.18(a) illustrates the wave profile for configuration D^+ solution (tPRSDR) for $\mathcal{U}_p = 0, \mathcal{U}_d = 0.6$, $\mathcal{A}_p = 1$ and $\mathcal{A}_2 = 0.8$, while Figure 4.18(b) illustrates the wave profile for configuration D^+ solution (tPRSDR) for $\mathcal{U}_p = 0, \mathcal{U}_d = 0.6$, $\mathcal{A}_p = 1$ and $\mathcal{A}_2 = 0.533$.

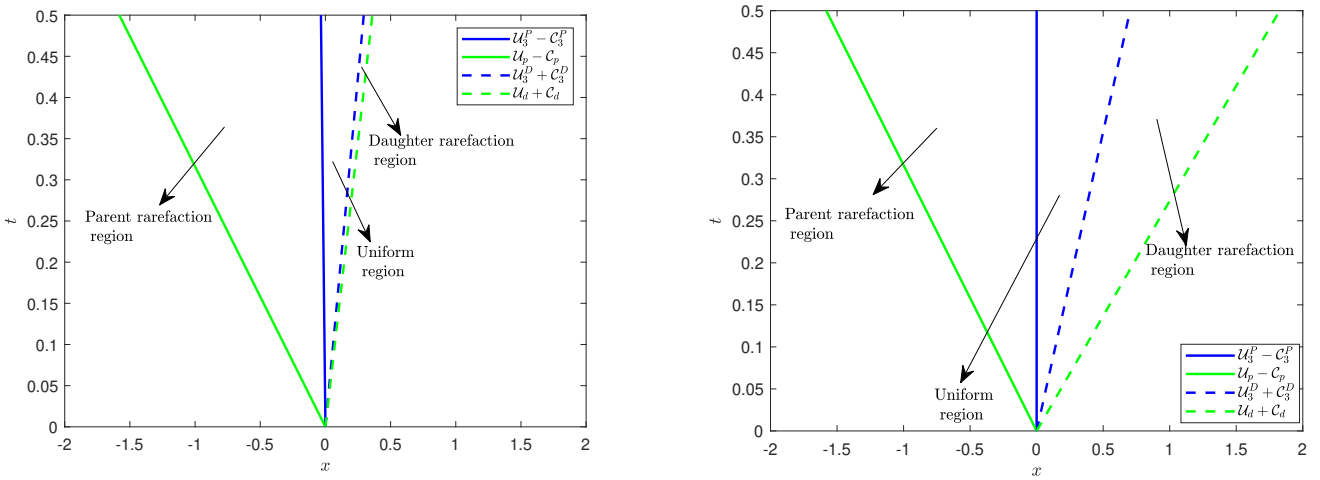

(a) **(b)**

Figure 4.19: Illustration of the PRDR solutions at both sides of the resonance solution for $\mathcal{U}_p = 0$, $\mathcal{U}_d = 0.6$, $\mathcal{A}_p = 1$. Figure 4.19(a) is the PRDR characteristics profile for $\mathcal{A}_d = 0.52$, while Figure 4.19(b) is the PRDR characteristics profile for $\mathcal{A}_d = 0.993$.

4.7.2 Variation of cross-sectional area in parent vessel

Case 6

In Figure 4.20 we consider similar setup to case 1, but here we construct a bifurcation diagram by varying the value of $\mathcal{A}_p$ for $\mathcal{U}_p = \mathcal{U}_d = 0$, and $\mathcal{A}_d = 1$. Here the system for low $\mathcal{A}_p$ exhibits a PSDR solution which then transitions to PRDS solution as $\mathcal{A}_p$ increases. The PRDS exhibits a turning point as the rarefaction in the parent vessel becomes transcritical at $\mathcal{A}_p \approx 1.707$. Beyond $\mathcal{A}_p = 1.707$ the PRDS transitions into configuration C^+ resonant solution (tPR0SDS). We note that case 6 is a mirror image of case 1.

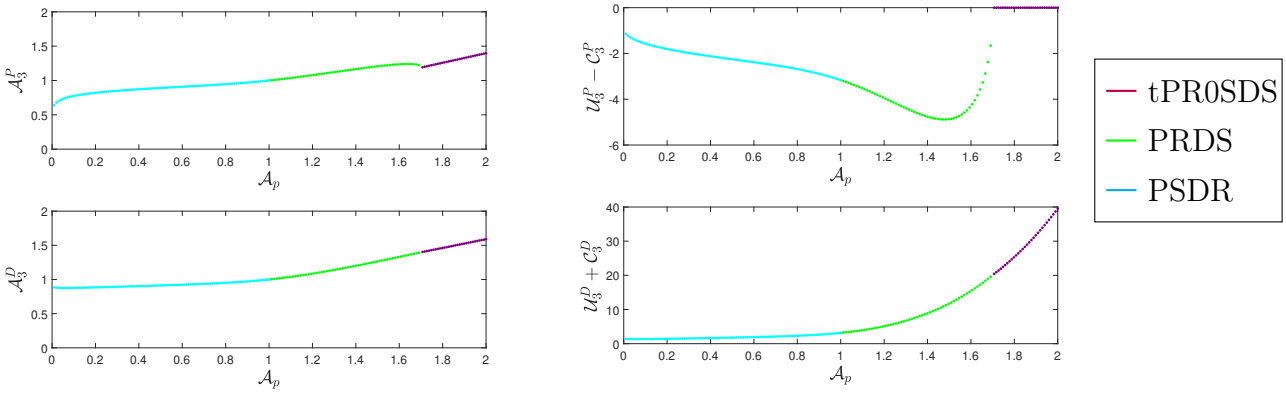

Figure 4.20: Case 6: Bifurcation diagram for case where $\mathcal{U}_p = 0$, $\mathcal{U}_d = 0$, and $\mathcal{A}_d = 1$ with corresponding values of $\mathcal{A}_p$, $\mathcal{A}_3^P$, $\mathcal{A}_3^D$, $\mathcal{U}_3^P - \mathcal{C}_3^P$ and $\mathcal{U}_3^D + \mathcal{C}_3^D$, respectively.

Cases 7, 8 and 9

In Figure 4.21 we consider three different cases and construct a bifurcation by varying the value of $\mathcal{A}_p$. Figure 4.21(a) shows a bifurcation diagram where $\mathcal{U}_d = 0, \mathcal{U}_p = -0.6$ and $\mathcal{A}_d = 1$, Figure 4.21(b) shows a bifurcation diagram where $\mathcal{U}_d = 0$, $\mathcal{U}_p = 0.6$ and $\mathcal{A}_d = 1$, and Figure 4.21(c) shows a bifurcation diagram where $\mathcal{U}_p = 0$, $\mathcal{U}_d = -0.6$ and $\mathcal{A}_d = 1$. In the three cases we have that the system exhibits a PSDR wave for low $\mathcal{A}_p$ and PRDS for large $\mathcal{A}_p$ with the PRDS wave and exhibiting a turning point and transitioning into a configuration C^+ resonant solution (tPR0SDS). What is different between the three solutions is that for flow out of the parent value we have a PRDR solutions, (see Figure 4.21a) between the PSDR and PRDS solution but for inflow into the parent vessel and outflow in the daughter vessel we have PSDS solution between the PSDR and PRDS solutions (see Figure 4.21(b) and 4.21(c)), respectively.

Case 10

In Figure 4.22 we consider $\mathcal{U}_p = 0$ $\mathcal{U}_d = 0.6$, $\mathcal{A}_d = 1$ and construct a bifurcation diagram by varying the value of $\mathcal{A}_p$. The system exhibits PSDR solution for low $\mathcal{A}_p$ which then transitions to PRDR as $\mathcal{A}_p$ increases. The PRDR exhibits a turning point at $\mathcal{A}_p \approx 1.182$ where the parent rarefaction resonates with the stationary wave. As $\mathcal{A}_p$ increases the physical solution of PRDR transitions into a configuration

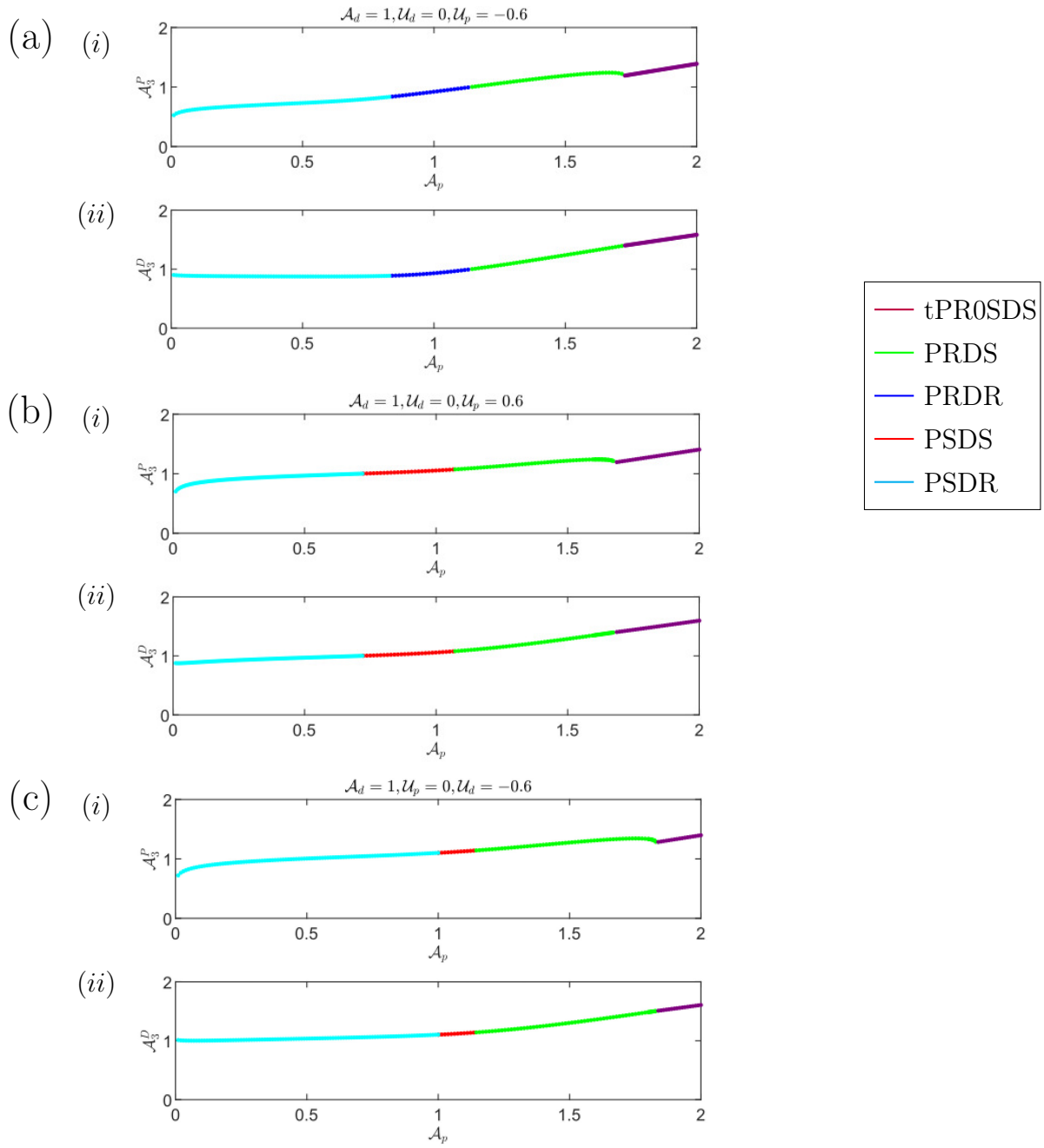

Figure 4.21: Case 7, 8, and 9: Bifurcation plot of physical solutions cases 7 to 9. Figure 4.21(a) displays the bifurcation plot for case 7 with $\mathcal{U}_p = -0.6$, $\mathcal{U}_d = 0$, $\mathcal{A}_d = 1.0$ while varying $\mathcal{A}_p$. Figure 4.21(b) displays the bifurcation plot for case 8 with $\mathcal{U}_p = 0.6$, $\mathcal{U}_d = 0$, $\mathcal{A}_d = 1.0$ while varying $\mathcal{A}_p$, and Figure 4.21(c) displays the bifurcation plot for case 9 with $\mathcal{U}_p = 0$, $\mathcal{U}_d = -0.6$, $\mathcal{A}_d = 1.0$ while varying $\mathcal{A}_p$.

C^+ solution (tPR0SDR) which persists as $\mathcal{A}_p$ increases. Note that in this case the configuration C^+

solution spans a much larger interval than all other configuration C^+ solutions shown in the cases above. We probe this further in Figure 4.23, verifying that the PRDR solution exhibits a turning point resulting from the rarefaction in the parent vessel resonating with the stationary wave at $\mathcal{A}_p \approx 1.190$ (see Figure 4.23a). To investigate why we have a larger range of configuration C^+ solution, we plot the mass splitting factor r_s in the intermediate zone as a function of $\mathcal{A}_p$ (see Figure 4.23b) and we see that the value of r_s increases very slowly with $\mathcal{A}_p$) and may even be saturating), so any transition to configuration D^+ does not occur within the range of $\mathcal{A}_p$ considered and the zero speed shock remains trapped between the stationary waves.

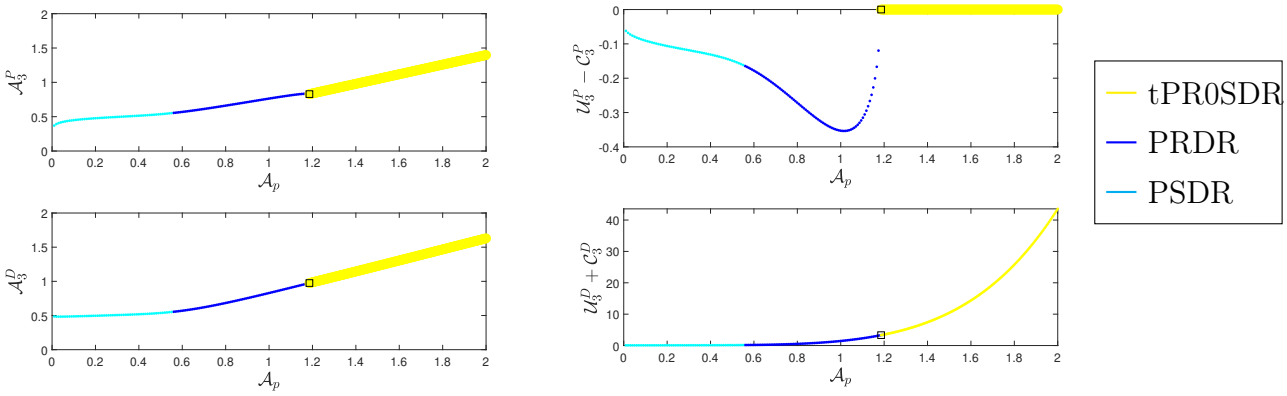

Figure 4.22: Case 10: Bifurcation diagram for case where $\mathcal{U}_p = 0$, $\mathcal{U}_d = 0.6$, $\mathcal{A}_d = 1$ and $k = 1$ with corresponding values of $\mathcal{A}_p$, $\mathcal{A}_3^P$, $\mathcal{A}_3^D$, $\mathcal{U}_3^P - \mathcal{C}_3^P$ and $\mathcal{U}_3^D + \mathcal{C}_3^D$, respectively.

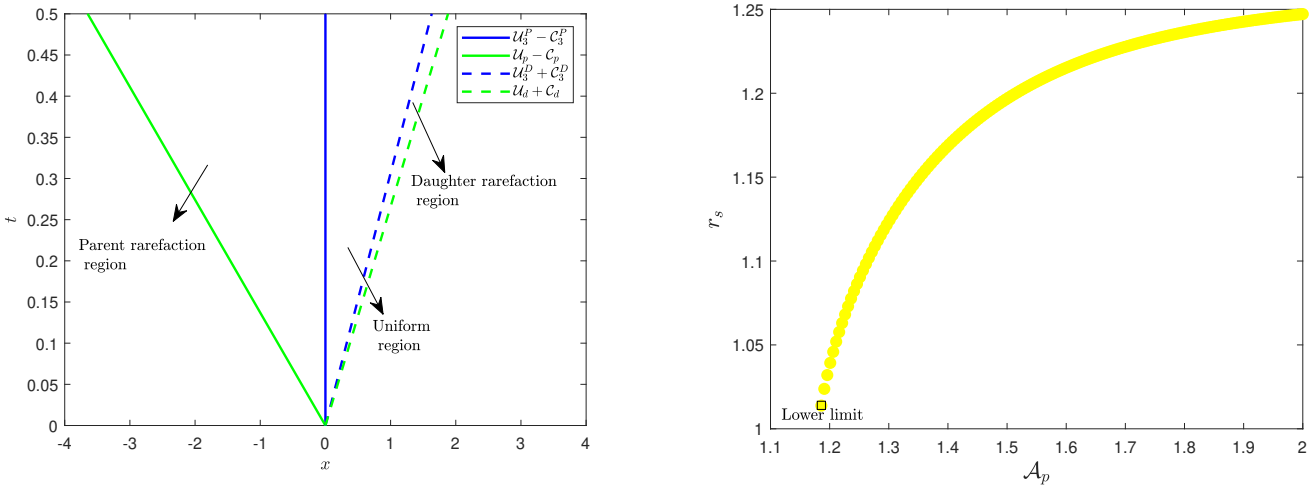

(a) **(b)**

Figure 4.23: Illustration of the profile for PRDR solution and intermediate splitting factor r_s. Figure 4.23(a) shows the profile of PRDR solution close to the transcritical point (*i.e.* $\mathcal{A}_p \approx 1.182$) while Figure 4.23(b) shows the range of the intermediate splitting factor r_s.

4.8 Overview of parameter space

We now summarise the overall behaviour of the system by producing a plot that highlights the different solutions that can occur across the parameter space. As in previous chapters, we still have that the green, blue, red and cyan points represent the classical solutions ie. PRDS, PRDR, PSDS and PSDR, respectively. The resonant solution have colours consistent with the cases above: Yellow circles represent configuration C^+ resonant solution with parent transcritical rarefaction and daughter rarefaction (tPR0SDR), purple circles denote configuration C^+ resonant solution with parent transcritical rarefaction and right shock (tPR0SDS), magenta circles denote configuration D^+ resonant solution with parent transcritical rarefaction and daughter rarefaction (tPRSDR) and orange circles denote a configuration D^+ resonant solution with parent transcritical rarefaction and daughter shock (tPRSDS).

Figure 4.24 illustrates a parameter space encompassing cases 1, 4 and 5 for the solution spanned by $\mathcal{U}_d$ and $\mathcal{A}_d$ (while fixing $\mathcal{U}_p = 0$, $\mathcal{A}_p = 1$). Here we just have splitting of mass from parent to daughter vessel with both vessels assumed of same stiffness ($k = 1$). We have the four classical solutions enveloping the four quadrants in a similar way to previous chapters. However, there is a new tongue of resonant solutions due to the division of mass across the junction. This tongue of resonant solutions spans mainly low values of $\mathcal{A}_d$ (*i.e.* when the daughter vessel is collapsed), but gradually expands to the region where the daughter area is expanded for large values of $\mathcal{U}_d$. The figure is similar to to Figure 3.27 in Chapter 3 such that as $\mathcal{A}_d$ decreases for fixed $\mathcal{U}_p$ the system always exhibits a configuration C^+ resonance for a small interval followed by a configuration D^+ resonance. Notably, the resonant region persists all the way to $\mathcal{A}_d = 0$ for almost all cases where the daughter wave is a shock as in cases $1 - 4$ (with an exception at $\mathcal{U}_d = 0.55$ where we have two shocks merging for finite $\mathcal{A}_d \lesssim 0$. which appeared for $\mathcal{A}_d \lesssim 0.025$). However, when the daughter wave is a rarefaction the resonant solution returns to classical for low $\mathcal{A}_d$ in a similar manner to case 5 above. This loss of resonance was discussed in Section 4.7.1 above. Note that at first glance it may seem strange to have a rarefaction-rarefaction solution within the supercritical region for the daughter *i.e.* top left of Figure 4.24. However, we note the similarity to Figure 2.21 in Chapter 2 where again we have a rarefaction in the supercritical region followed by a subcritical flow in region 1. However, here the parent flow is subcritical and the daughter flow is supercritical while the piece of region 3 in the parent is subcritical and the piece in the daughter vessel is supercritical. Hence, the stationary wave is along a jump from subcritical to supercritical flow. Plots of characteristics and profiles are shown in Figure 4.26.

Figure 4.25 shows a parameter space plot spanned by $\mathcal{U}_p$ and $\mathcal{A}_p$ encompassing cases 6 to 8 (while we fix $\mathcal{U}_d = 0$, $\mathcal{A}_d = 1$ and $k = 1$). Here, for low values of $\mathcal{A}_p$ the parameter space is spanned by four quadrants filled with classical solutions. However, for a highly expanded parent vessel (*i.e.* $\mathcal{A}_p > 1.5$) the PRDS solution transition into a configuration C^+ resonant solution with a daughter shock as in case 6, the solution persists for all values of $\mathcal{A}_p$ tested, but we expect it will eventually transition to configuration D^+ for large $\mathcal{A}_p$. Notably, the transition to resonance is almost perfectly independent of $\mathcal{U}_p$ (*i.e.* the transition line in Figure 4.25 is almost vertical).

These two figures show that splitting the mass across the junction drives a resonant solution, but this is more evident when the area of the daughter vessel is compressed below the baseline cross-sectional area than when the cross-sectional area of the parent vessel is expanded.

We now extend these results to also include a jump in stiffness across the junction.

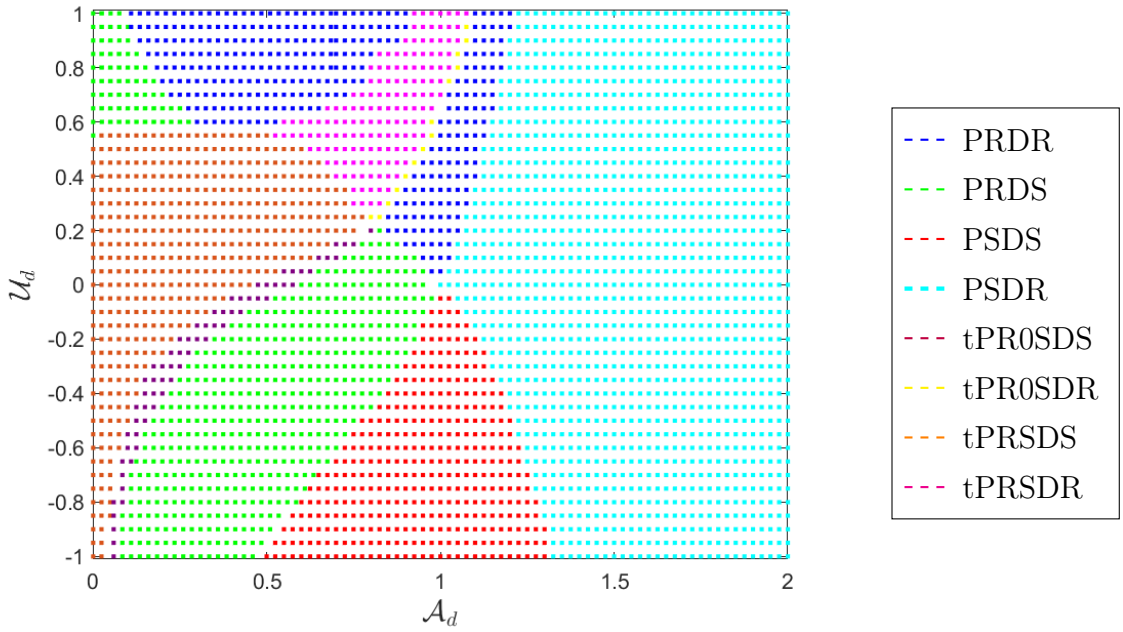

Figure 4.24: Overview of the parameter space spanned by $\mathcal{U}_d$ ($-1.0 \leq \mathcal{U}_d \leq 1.0$) and $\mathcal{A}_d$ ($0 \leq \mathcal{A}_d \leq 2.0$) with $\mathcal{U}_p = 0$, $\mathcal{A}_p = 1$, $k = 1$ and $\bar{A}_d = 1$.

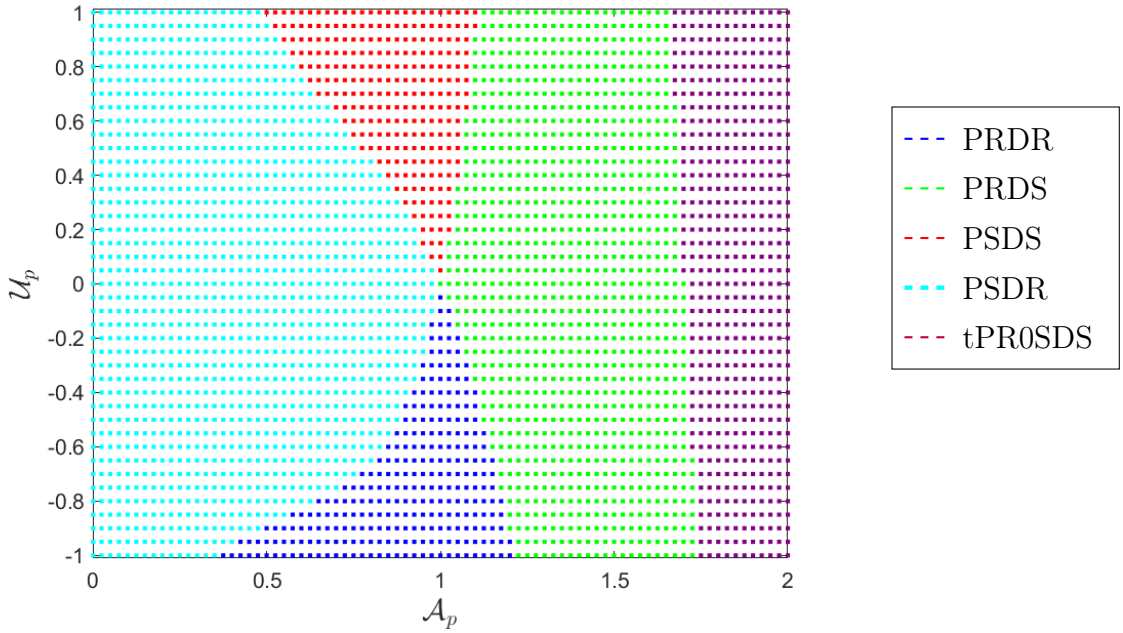

Figure 4.25: Overview of the parameter space spanned by $\mathcal{U}_p$ ($-1.0 \leq \mathcal{U}_p \leq 1.0$) and $\mathcal{A}_p$ ($0 \leq \mathcal{A}_p \leq 2.0$) with $\mathcal{U}_d = 0$, $\mathcal{A}_d = 1$, $k = 1$ and $\bar{A}_d = 1$.

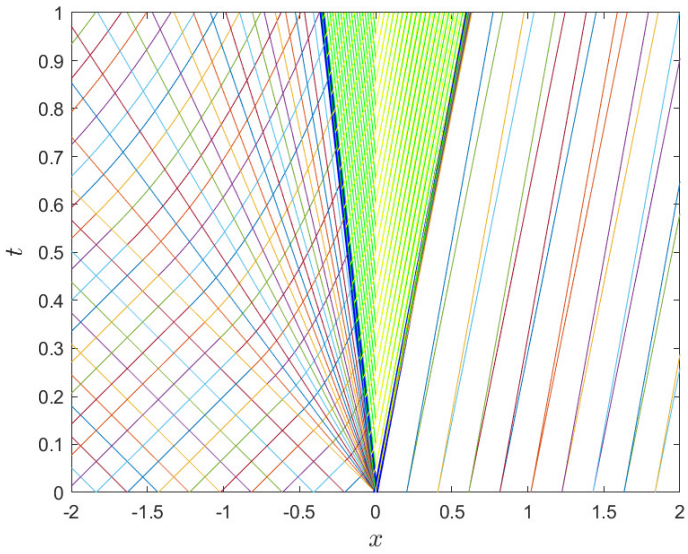

Figure 4.26: Characteristics profile for a supercritical daughter rarefaction

4.8.1 Variation of cross-sectional area in daughter vessel with jump in stiffness

We now extend our analysis to consider both splitting of mass and a jump in stiffness across the symmetric junction. We consider three representative values of the far-field flow speed in the parent vessel (i.e. $\mathcal{U}_d = 0$, $\mathcal{U}_d = -0.6$, $\mathcal{U}_d = 0.6$), tracking the different flow state while continuously varying the far-field cross-sectional area in the daughter vessel $\mathcal{A}_d$ and holding both the far-field cross-sectional area and flow speed in the parent vessel fixed (i.e. $\mathcal{A}_p = 1$, $\mathcal{U}_p = 0$). In all instances we we have that the stiffness constant k can either be greater or less than 1.

Case 11

In Figure 4.27 and 4.28 we consider $\mathcal{U}_p = \mathcal{U}_d = 0$, $\mathcal{A}_p = 1$ with both splitting of mass and jump in stiffness across the junction and construct a bifurcation by varying the value of $\mathcal{A}_d$ analogous to case 1 summarised in Figure 4.9.

In Figure 4.27 we set the daughter vessel to be more stiff than the parent vessel (setting $k = 1.1$). Following this, the bifurcation diagram exhibits two classical solutions and two resonant solutions similar to Figure 4.9. The only significant difference is that the PRDS solution exhibits a limit point at $\mathcal{A}_d \approx 0.697$ which is slightly increased compared to Figure 4.9 (with $k = 1$).

Meanwhile, in Figure 4.28 we consider the case where the parent vessel is stiffer than the daughter vessel (setting $k = 0.9$) where we also have two classical solutions and two resonant solutions but the limit point of PRDS is reduced to $\mathcal{A}_d \approx 0.232$ showing that with less stiffness in the daughter vessel the region of resonance is reduced.

Furthermore, in Figure 4.29 we have a case where the daughter vessel is far less stiff than the parent vessel *i.e.* $k = 0.8$ and it is seen that the bifurcation diagram only exhibits two classical solutions, PRDS for low $\mathcal{A}_d$ and PSDR for large $\mathcal{A}_d$ with no resonant solution. Hence, these figures indicate that

decreasing the stiffness of the daughter vessel compared to the parent vessel reduces the size of the resonant region. To show suppression of resonance with change in stiffness in Figure 4.31(b) we plot the bifurcation diagram as a function of $\mathcal{A}_d$ as k reduces from 1.1 to 0.8; it seen that the three solutions are qualitatively and quantitatively similar for $\mathcal{A}_d \geq 1$ but for low $\mathcal{A}_d$ the resonance region continues to get suppressed as k decreases until it is entirely absent.

To probe the solution from Figure 4.27 with $k = 1.1$ further, we plot the characteristics profile of the PRDS solution close to the limit point (see Figure 4.30a) which shows that the parent rarefaction is approaching transcriticality, as in other cases above. We also plot the parameters that are changing in the intermediate zone (see Figure 4.30b), namely the mass splitting factor r_s, and the stiffness k_s across the range of our configuration C^+ resonance. The figure shows complete agreement with our earlier assumption that the intermediate parameters interpolate between the two values on either side. Lastly, we also plot the speed of the two shocks present in the configuration D^+ resonant solution to show that the resonant solution persists for all $\mathcal{A}_d$, and the resonant shock and the daughter shock coalesce as $\mathcal{A}_d \to 0$ (see Figure 4.31).

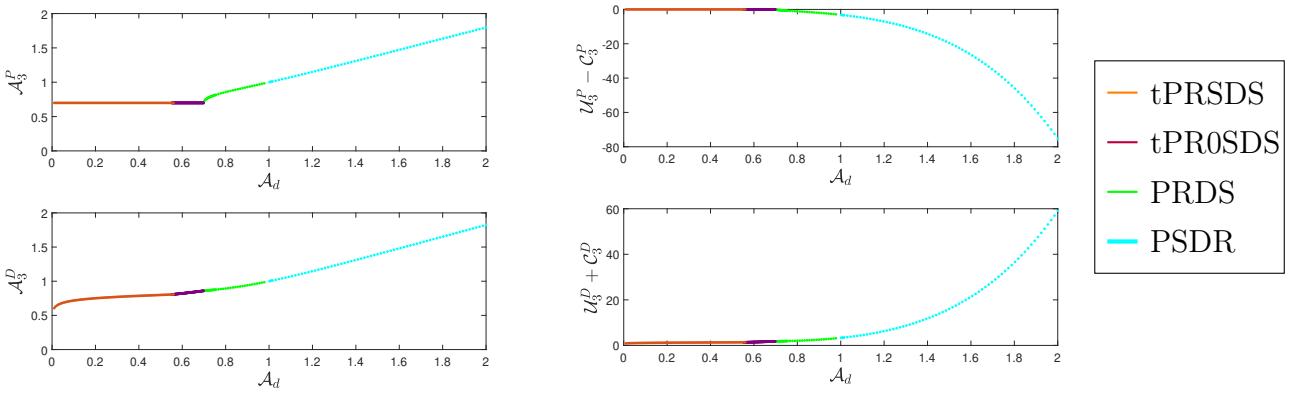

Figure 4.27: Case 11: Bifurcation diagram for case where $\mathcal{U}_p = 0$, $\mathcal{U}_d = 0$, $\mathcal{A}_p = 1$ and $k = 1.1$ with corresponding values of $\mathcal{A}_d$, $\mathcal{A}_3^P$, $\mathcal{A}_3^D$, $\mathcal{U}_3^P - \mathcal{C}_3^P$ and $\mathcal{U}_3^D + \mathcal{C}_3^D$, respectively.

Case 12

In Figure 4.32 we consider $\mathcal{U}_p = 0$ $\mathcal{U}_d = -0.6$, $\mathcal{A}_p = 1$ with splitting of mass and jump in stiffness and construct a bifurcation by varying the value of $\mathcal{A}_d$ (with three chosen values of the stiffness). This system exhibits similar behaviour with that of Figure 4.15 with the only difference been that the limit point of PRDS is shifted by the value of k showing again that an increase in stiffness in the daughter vessel promotes resonance. Also, similar to Figure 4.27, resonance can be suppressed entirely by reducing the stiffness in the daughter vessel below a critical value.

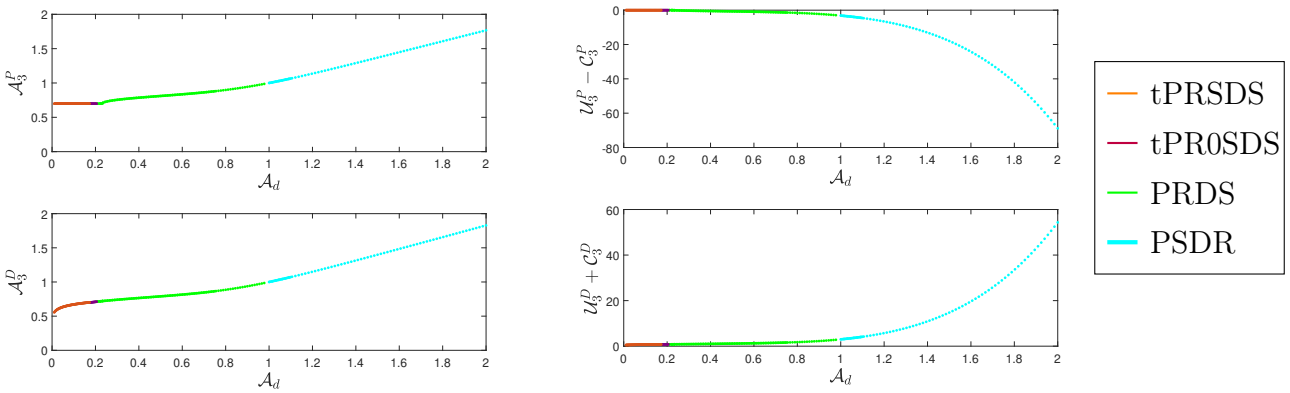

Figure 4.28: Case 11a: Bifurcation diagram for case where $\mathcal{U}_p = 0$, $\mathcal{U}_d = 0$, $\mathcal{A}_p = 1$ and $k = 0.9$ with corresponding values of $\mathcal{A}_d$, $\mathcal{A}_3^P$, $\mathcal{A}_3^D$, $\mathcal{U}_3^P - \mathcal{C}_3^P$ and $\mathcal{U}_3^D + \mathcal{C}_3^D$, respectively.

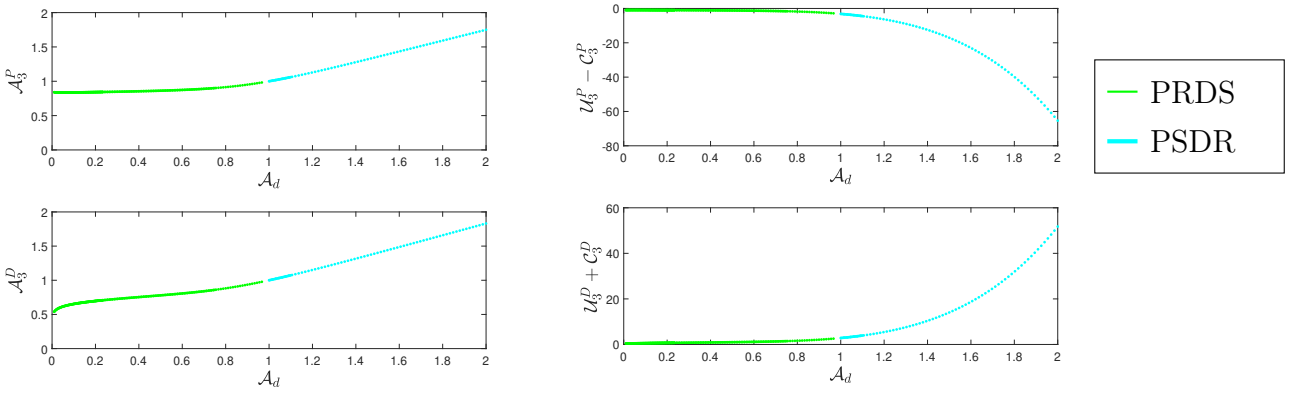

Figure 4.29: Case 11b: Bifurcation diagram for case where $\mathcal{U}_p = 0$, $\mathcal{U}_d = 0$, $\mathcal{A}_p = 1$ and $k = 0.8$ with corresponding values of $\mathcal{A}_d$, $\mathcal{A}_3^P$, $\mathcal{A}_3^D$, $\mathcal{U}_3^P - \mathcal{C}_3^P$ and $\mathcal{U}_3^D + \mathcal{C}_3^D$, respectively.

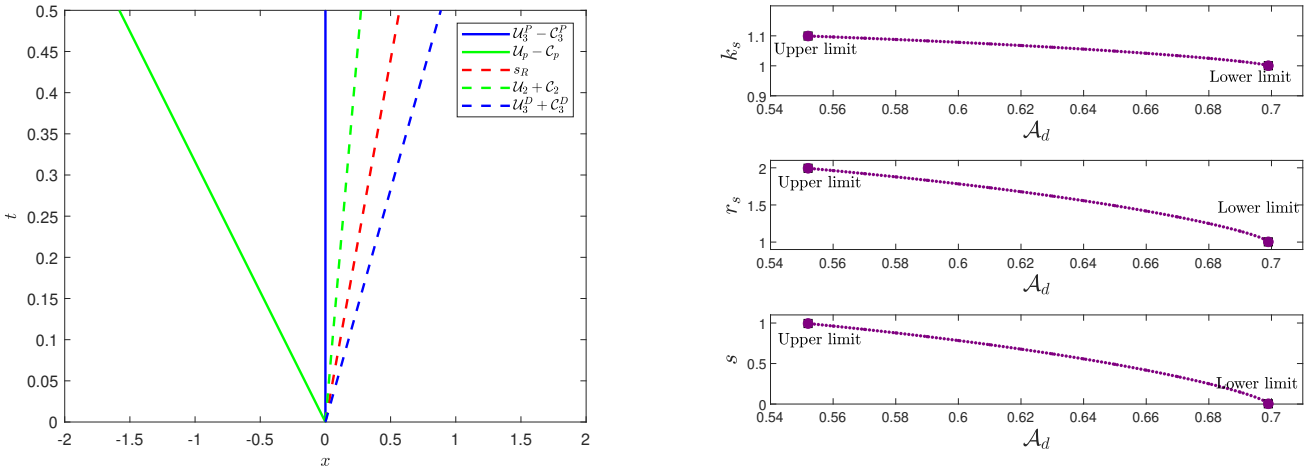

(a) **(b)**

Figure 4.30: Illustration of the transcritical rarefaction and daughter shock and the different intermediate parameters. Figure 4.30(a) shows that the resonance of the parent rarefaction with the stationary wave while Figure 4.30(b) shows the two parameters that changes from parent to daughter vessel denoted as r_s and k_s. It also shows the range from parent to daughter vessel denoted as s.

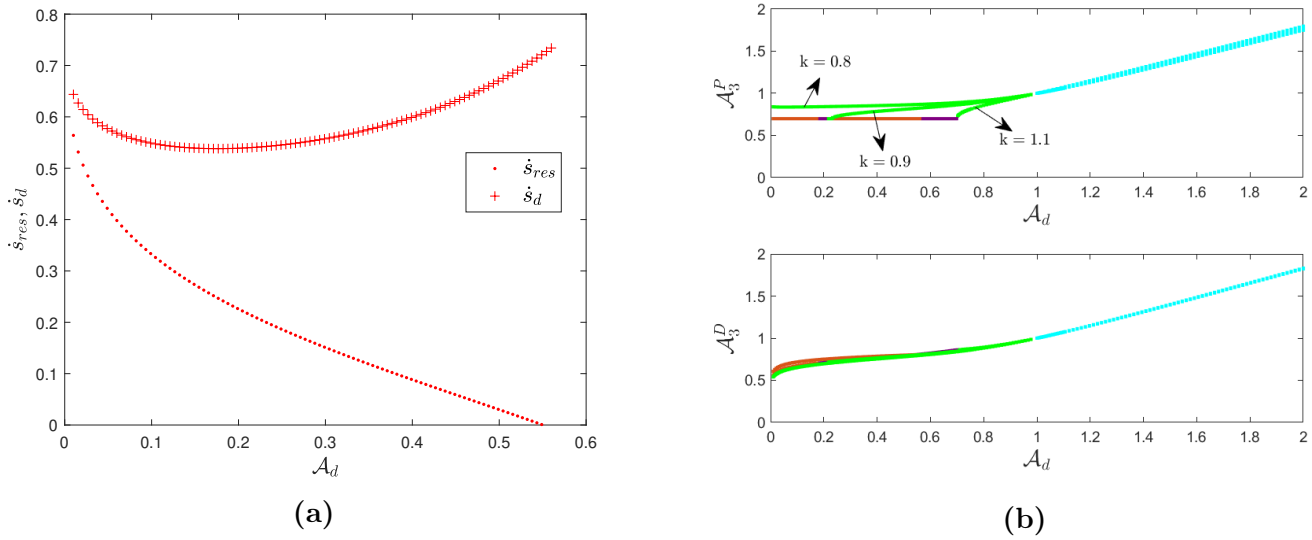

(a) **(b)**

Figure 4.31: Figure 4.31(a) illustrates the two shocks in the daughter vessel, while Figure 4.31(b) shows the bifurcation diagram for various values of k.

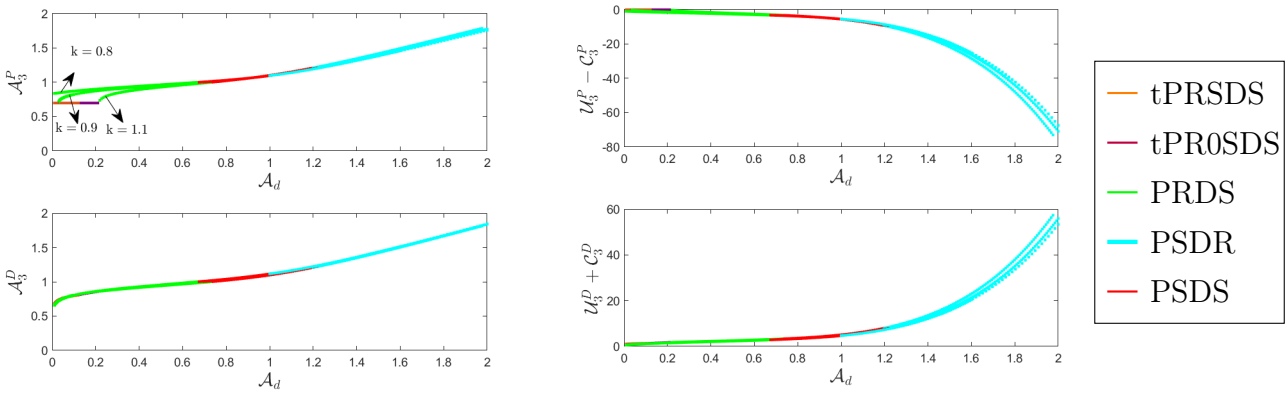

Figure 4.32: Case 12: Bifurcation diagram for case where $\mathcal{U}_p = 0$, $\mathcal{U}_d = -0.6$, $\mathcal{A}_p = 1$ and various values of k with corresponding values of $\mathcal{A}_d$, $\mathcal{A}_3^P$, $\mathcal{A}_3^D$, $\mathcal{U}_3^P - \mathcal{C}_3^P$ and $\mathcal{U}_3^D + \mathcal{C}_3^D$, respectively.

Case 13

In Figures 4.33-4.35 we consider the case where $\mathcal{U}_p = 0$ $\mathcal{U}_d = 0.6$, $\mathcal{A}_p = 1$ with splitting of mass and jump in stiffness and construct a bifurcation by varying the value of $\mathcal{A}_d$ for several values of the stiffness parameter.

Figure 4.33 shows a bifurcation diagram where we have $\mathcal{U}_d = 0.6$ for $k = 1.1$. For large $\mathcal{A}_d$ the system exhibits a PSDR which the transitions into a PRDR as $\mathcal{A}_d$ decreases. The PRDR exhibits a limit point at $\mathcal{A}_d \approx 1.011$. The physical branch of PRDR then transitions into a configuration C^+ solution (tPR0SDR) with a daughter rarefaction which then subsequently transitions into a configuration D^+ solution (tPRSDR) with a daughter rarefaction. As $\mathcal{A}_d$ further decreases the configuration D^+ solution with daughter rarefaction then transitions into another configuration D^+ solution (tPRSDS) with daughter shock which then persists as $\mathcal{A}_d \to 0$. This is different to case 5, (where $k = 1$) where the resonant cases were trapped between two PRDR solutions (see Figure 4.16).

Furthermore, Figure 4.34 shows a bifurcation diagram where we have $\mathcal{U}_d = 0.6$ but here $k = 0.9$. Again, for large $\mathcal{A}_d$ the system exhibits a PSDR solution which transitions into a PRDR solution as $\mathcal{A}_d$ decreases. The PRDR exhibits a turning point at $\mathcal{A}_d \approx 0.951$. For low $\mathcal{A}_d$ the system exhibits PRDS solution which transitions into a PRDR solution and once again exhibits another turning point at $\mathcal{A}_d \approx 0.844$, creating a gap between two PRDR solutions. This loop was completed with two resonant solutions, configuration C^+ solution (tPR0SDR) and configuration D^+ solution (tPRSDR), respectively sharing qualitative agreement with Figure 4.16, except that the resonance region is much smaller in this case; the configuration C^+ region is so narrow that it can barely be seen on the scale plotted. Lastly, in Figure 4.35 we have a case where $k = 0.8$ where again we have no resonant solution but just three classical solutions. For large $\mathcal{A}_d$ we have PSDR which then transitions to PRDR as $\mathcal{A}_d$ decreases. Further decrease of $\mathcal{A}_d$ sees the PRDR transition into a PRDS. This further strengthens our former result that resonance can be suppressed entirely with a sufficiently large decrease in stiffness from the parent to the daughter vessels.

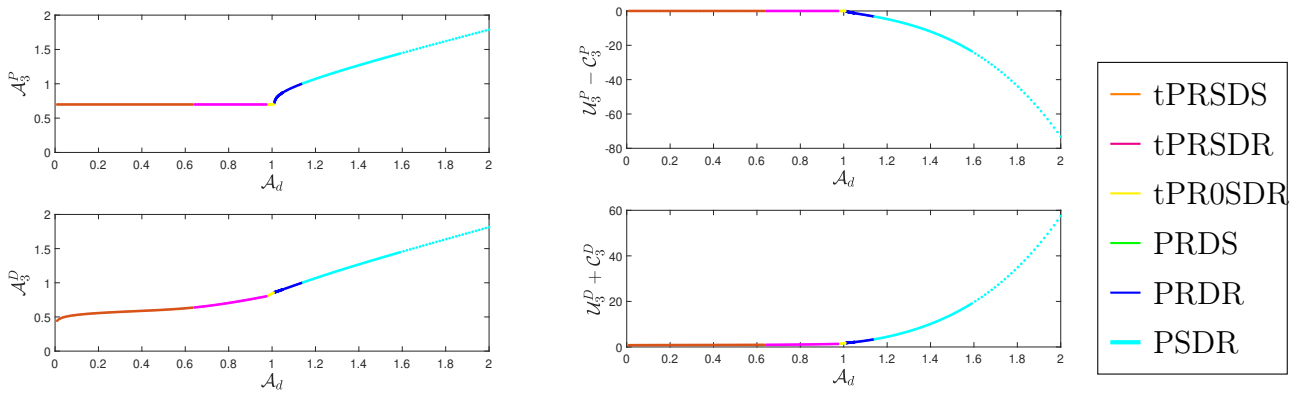

Figure 4.33: Case 13a: Bifurcation diagram for case where $\mathcal{U}_p = 0$, $\mathcal{U}_d = 0.6$, $\mathcal{A}_p = 1$ and $k = 1.1$ with corresponding values of $\mathcal{A}_d$, $\mathcal{A}_3^P$, $\mathcal{A}_3^D$, $\mathcal{U}_3^P - \mathcal{C}_3^P$ and $\mathcal{U}_3^D + \mathcal{C}_3^D$, respectively.

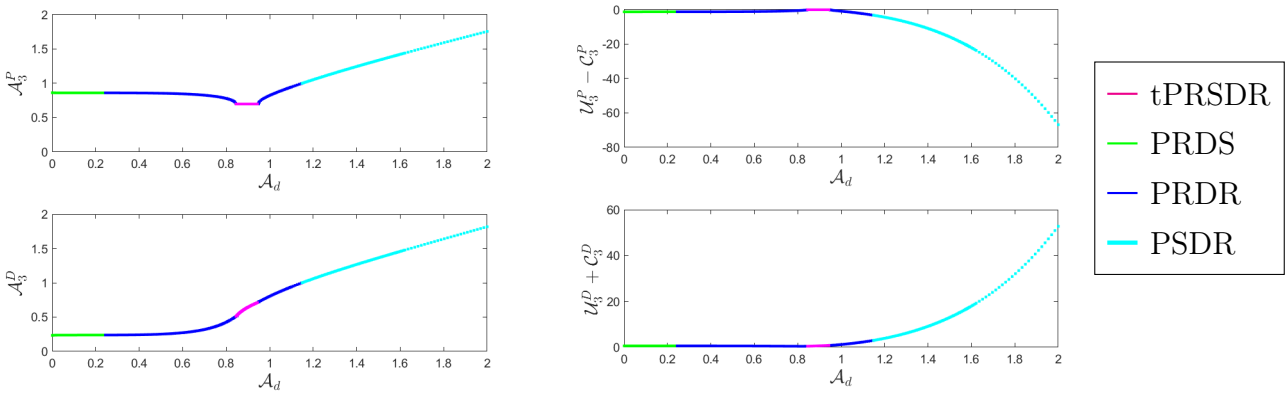

Figure 4.34: Case 13b: Bifurcation diagram for case where $\mathcal{U}_p = 0$, $\mathcal{U}_d = 0.6$, $\mathcal{A}_p = 1$ and $k = 0.9$ with corresponding values of $\mathcal{A}_d$, $\mathcal{A}_3^P$, $\mathcal{A}_3^D$, $\mathcal{U}_3^P - \mathcal{C}_3^P$ and $\mathcal{U}_3^D + \mathcal{C}_3^D$, respectively.

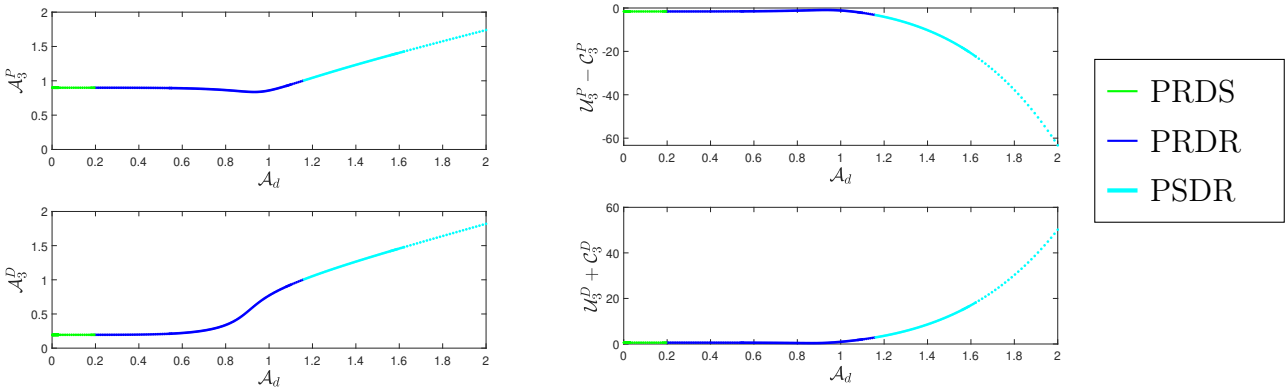

Figure 4.35: Case 13c: Bifurcation diagram for case where $\mathcal{U}_p = 0$, $\mathcal{U}_d = 0.6$, $\mathcal{A}_p = 1$ and $k = 0.8$ with corresponding values of $\mathcal{A}_d$, $\mathcal{A}_3^P$, $\mathcal{A}_3^D$, $\mathcal{U}_3^P - \mathcal{C}_3^P$ and $\mathcal{U}_3^D + \mathcal{C}_3^D$, respectively.

4.8.2 Variation of cross-sectional area in parent vessel with jump in stiffness

Here, for each case as in Section 4.8.2 we assume splitting of mass and in stiffness across the symmetric junction and construct bifurcation diagrams while varying the cross-sectional area in the parent vessel $\mathcal{A}_p$. We consider distinct values of the flow speed in the parent vessels (*i.e.* $\mathcal{U}_d = \mathcal{U}_p = 0$, $\mathcal{U}_p = -0.5$, $\mathcal{U}_p = 0.5$), tracking the different flow structures while continuously varying the cross-sectional area in the parent vessel and keeping both the cross-sectional area and flow speed in the daughter vessel fixed (*i.e.* $\mathcal{A}_d = 1$, $\mathcal{U}_d = 0$).

Case 14

In Figure 4.36 we consider $\mathcal{U}_p = \mathcal{U}_d = 0$, $\mathcal{A}_d = 1$ and construct a bifurcation by varying the value of $\mathcal{A}_p$ for both splitting of mass and jump in stiffness.

The system exhibits two classical solutions *i.e.* PSDR for low $\mathcal{A}_P$ and PRDS for large $\mathcal{A}_p$ with the

PRDS solution transitioning into a configuration C^+ solution. The only difference is that for $k = 1.1$ the limit point of PRDS solution is $\mathcal{A}_p \approx 1.727$ while for $k = 0.9$ the limit point of PRDS solution is $\mathcal{A}_p \approx 1.677$ showing that decreasing the value of k increases the resonant region for large $\mathcal{A}_p$.

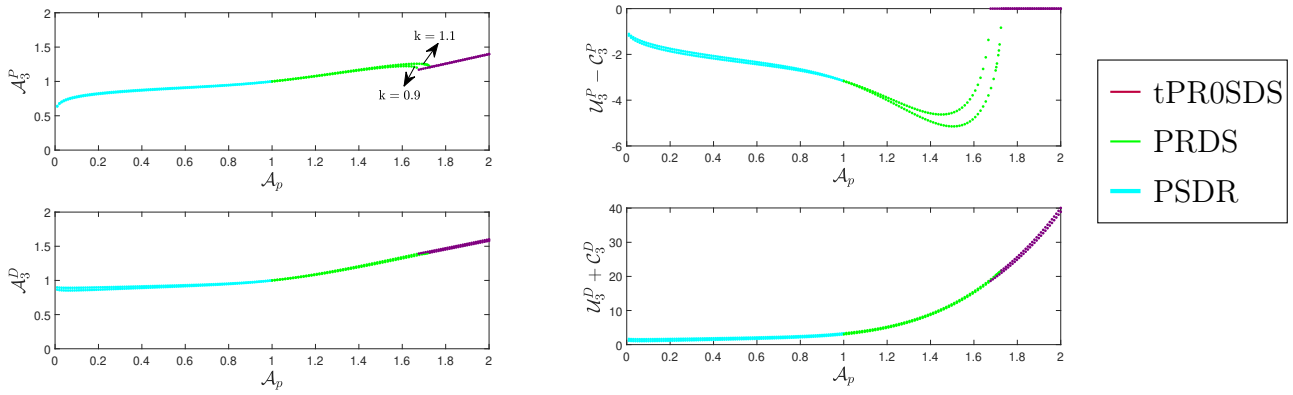

Figure 4.36: Bifurcation diagram for case where $\mathcal{U}_p = 0$, $\mathcal{U}_d = 0$, $\mathcal{A}_d = 1$ for decreasing values of k with corresponding values of $\mathcal{A}_p$, $\mathcal{A}_3^P$, $\mathcal{A}_3^D$, $\mathcal{U}_3^P - \mathcal{C}_3^P$ and $\mathcal{U}_3^D + \mathcal{C}_3^D$, respectively.

4.9 Overview of the parameter space with a jump in stiffness

We now summarise the overall behaviour of the system by producing parameter space plots that highlights the different solutions that can occur across the parameter space when also incorporating a jump in stiffness. As in Section 4.8, we use the same colours to represent the different solutions.

Figure 4.37 illustrates a parameter space spanned by the far-field conditions in the daughter vessel $\mathcal{U}_d$ and $\mathcal{A}_d$ while fixing $\mathcal{A}_p = 1$ and $\mathcal{U}_p = 0$ for daughter vessel stiffer than the parent vessel ($k = 1.1$) and splitting of mass from parent to daughter vessels encompassing cases 11, 12 and 13. As before, the four classical solutions appear in the different quadrants of our parameter space but for low values of $\mathcal{A}_d$ we have a large tongue of resonant solutions (magenta, purple, orange and yellow) which increases in size as $\mathcal{U}_2$ increases, consistent with the analysis of the bifurcation diagram in Section 4.8, we see that an increase in stiffness from parent to daughter vessel promotes resonance, enlarging the tongue compared to $k = 1$ (see Figure 4.24).

Figure 4.38 we have parameter space spanned by $\mathcal{U}_d$ and $\mathcal{A}_d$ while fixing $\mathcal{A}_p = 1$ and $\mathcal{U}_p = 0$ but here the daughter vessel is less stiff than the parent vessel (*i.e.* $k = 0.9$). The classical solutions span four quadrants in the parameter space (as in Figure 4.37) except that now we have a smaller tongue of resonant solutions for low $\mathcal{A}_d$ (purple, orange and yellow).

Again in Figure 4.39 we have parameter space spanned by $\mathcal{U}_d$ and $\mathcal{A}_d$ while fixing $\mathcal{A}_p = 1$ and $\mathcal{U}_p = 0$ but here the daughter vessel is even less stiff than the parent vessel (*i.e.* $k = 0.8$). Here contrary to Figures 4.37 and 4.38, we have that the four classical cases span the entire space with no resonant solutions. This implies that resonance can be suppressed by reducing the stiffness of the daughter vessel.

Hence, a decrease in stiffness from the parent to the daughter vessel seems to move the transition to resonance to lower cross-sectional area, which suppresses resonance when varying the far-field properties

of the daughter vessel (Figure 4.37) but promotes resonance when varying the far-field properties of the parent vessel (Figure 4.38).

We noted that for $k = 0.8$ we have no resonant solutions when the profile of the parent vessel are held at their baseline values ($\mathcal{A}_p = 1, \mathcal{U}_p = 0$). To investigate this further we varied the far-field conditions in the parent vessel and re plot the parameter space spanned by $\mathcal{U}_d$ and $\mathcal{A}_d$. Figure 4.42 shows that increasing either the cross-sectional area or flow speed in the parent vessel triggers resonance. Hence, resonance is still present in the system and is only with specific far-field condition in the parent vessel that is can be entirely suppressed.

Finally, Figure 4.40 illustrates a parameter space spanned by the far-field conditions in the parent vessel $\mathcal{U}_p$ and $\mathcal{A}_p$ while fixing $\mathcal{A}_d = 1$ and $\mathcal{U}_d = 0$ for daughter vessel stiffer than the parent vessel ($k = 1.1$) and splitting of mass from the parent to daughter vessel, encompassing case 14. We have the four classical solutions in the four quadrants with one resonant solution for large values of $\mathcal{A}_p$; thus threshold has been slightly increased compared to the case with no jump in stiffness (*i.e.* resonance has been suppressed). Furthermore, in Figure 4.41 we have the corresponding parameter space for the daughter vessel less stiff than the parent vessel, which exhibits qualitatively similar behaviour except now the region of resonant solutions is expanded compared to Figure 4.40 (the threshold for the onset of configuration C^+ has been slightly reduced).

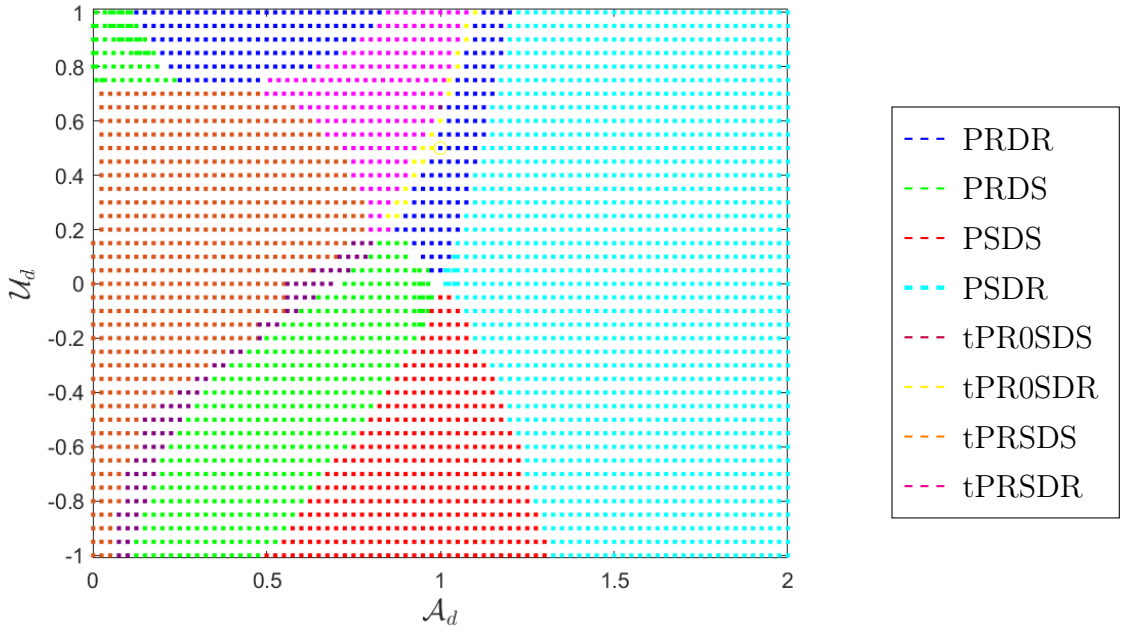

Figure 4.37: Overview of the parameter space spanned by $\mathcal{U}_d$ ($-1.0 \leq \mathcal{U}_d \leq 1.0$) and $\mathcal{A}_d$ ($0 \leq \mathcal{A}_d \leq 2.0$) with $\mathcal{U}_p = 0$, $\mathcal{A}_p = 1$, $k = 1.1$ and $\bar{A}_d = 1$.

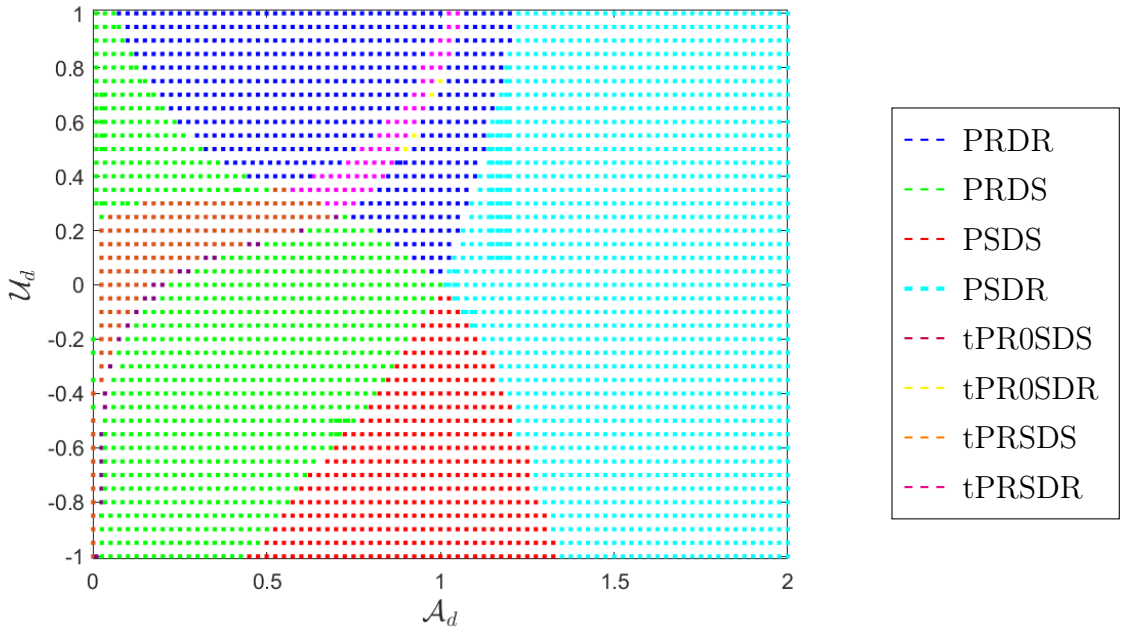

Figure 4.38: Overview of the parameter space spanned by $\mathcal{U}_d$ ($-1.0 \leq \mathcal{U}_d \leq 1.0$) and $\mathcal{A}_d$ ($0 \leq \mathcal{A}_d \leq 2.0$) with $\mathcal{U}_p = 0$, $\mathcal{A}_p = 1$, $k = 0.9$ and $\bar{A}_d = 1$.

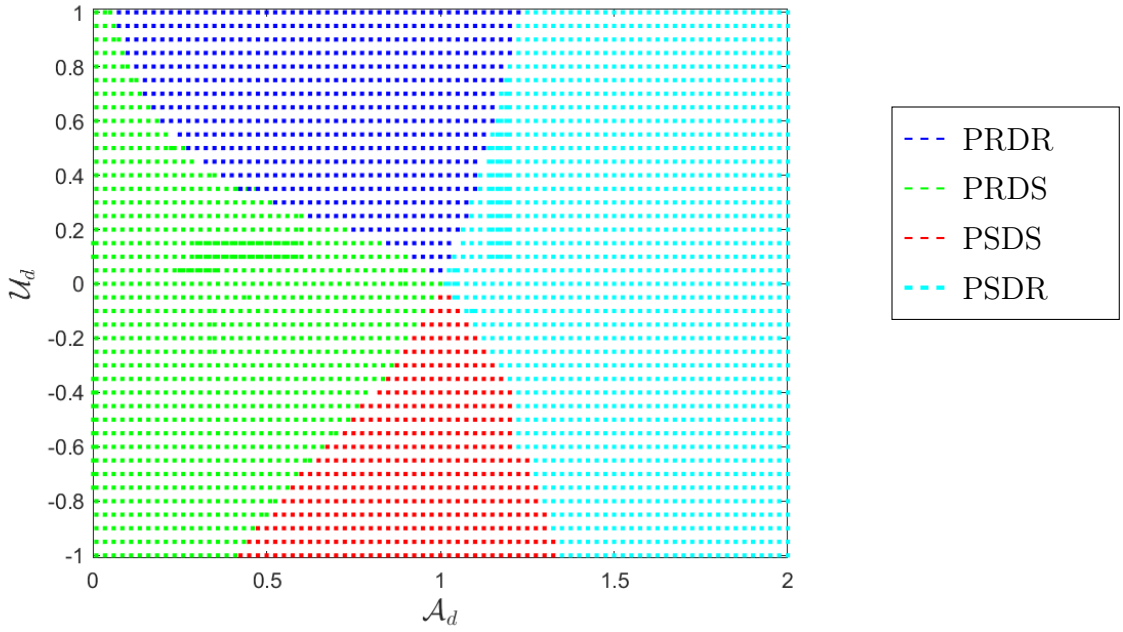

Figure 4.39: Overview of the parameter space spanned by $\mathcal{U}_d$ ($-1.0 \leq \mathcal{U}_d \leq 1.0$) and $\mathcal{A}_d$ ($0 \leq \mathcal{A}_d \leq 2.0$) with $\mathcal{U}_p = 0$, $\mathcal{A}_p = 1$, $k = 0.8$ and $\bar{A}_d = 1$.

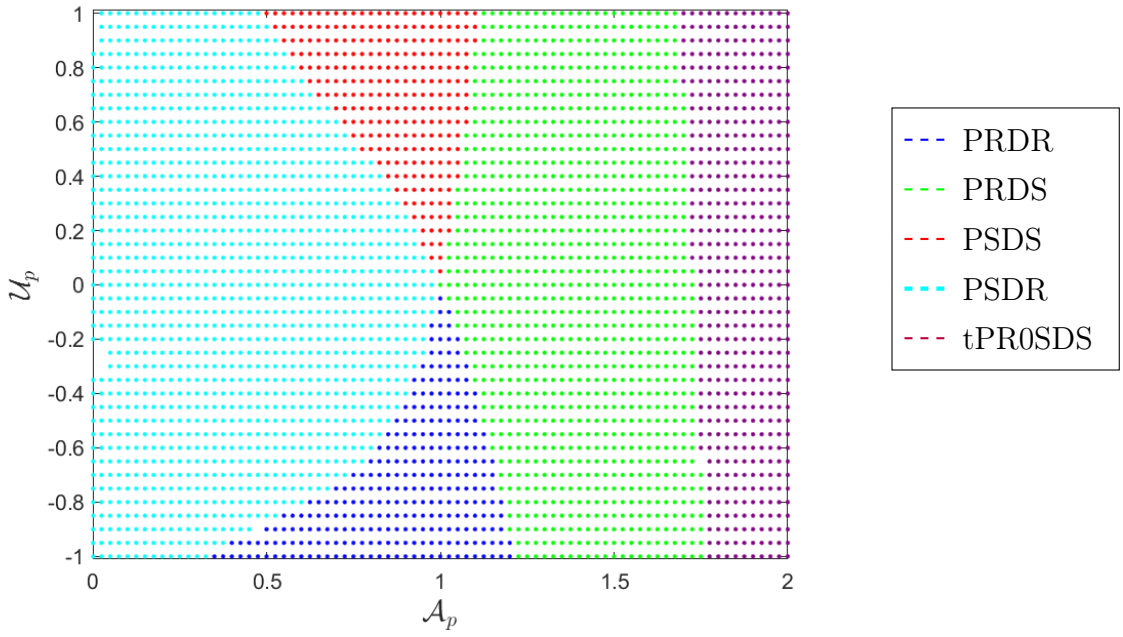

Figure 4.40: Overview of the parameter space spanned by $\mathcal{U}_p$ ($-1.0 \leq \mathcal{U}_p \leq 1.0$) and $\mathcal{A}_p$ ($0 \leq \mathcal{A}_p \leq 2.0$) with $\mathcal{U}_d = 0$, $\mathcal{A}_d = 1$, $k = 1.1$ and $\bar{A}_d = 1$.

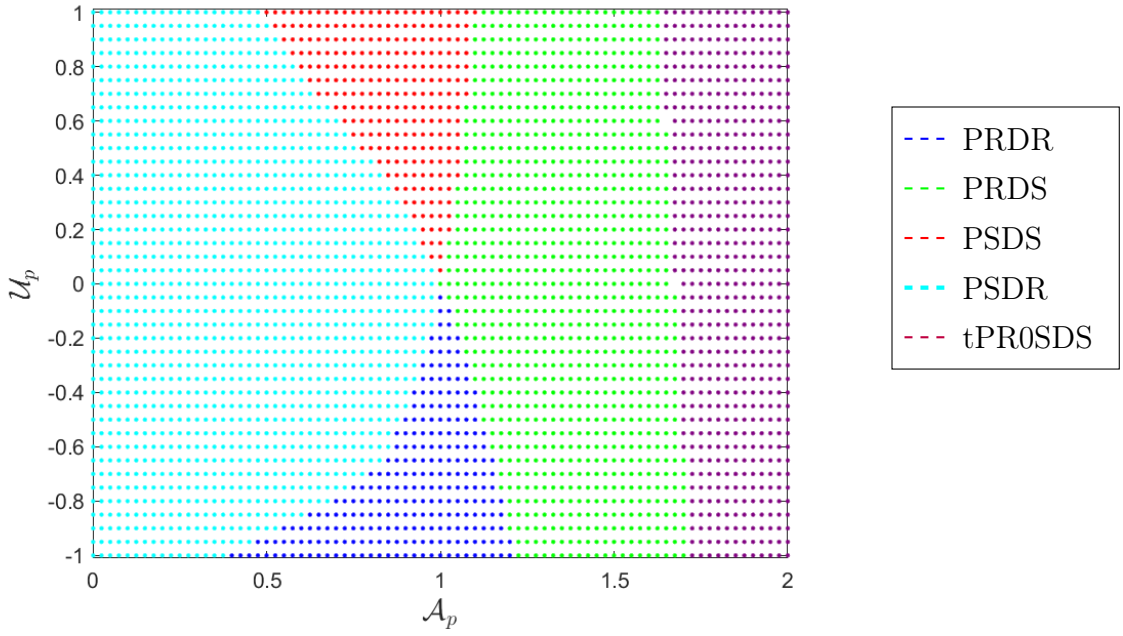

Figure 4.41: Overview of the parameter space spanned by $\mathcal{U}_p$ ($-1.0 \leq \mathcal{U}_p \leq 1.0$) and $\mathcal{A}_p$ ($0 \leq \mathcal{A}_p \leq 2.0$) with $\mathcal{U}_d = 0$, $\mathcal{A}_d = 1$, $k = 0.9$ and $\bar{A}_d = 1$.

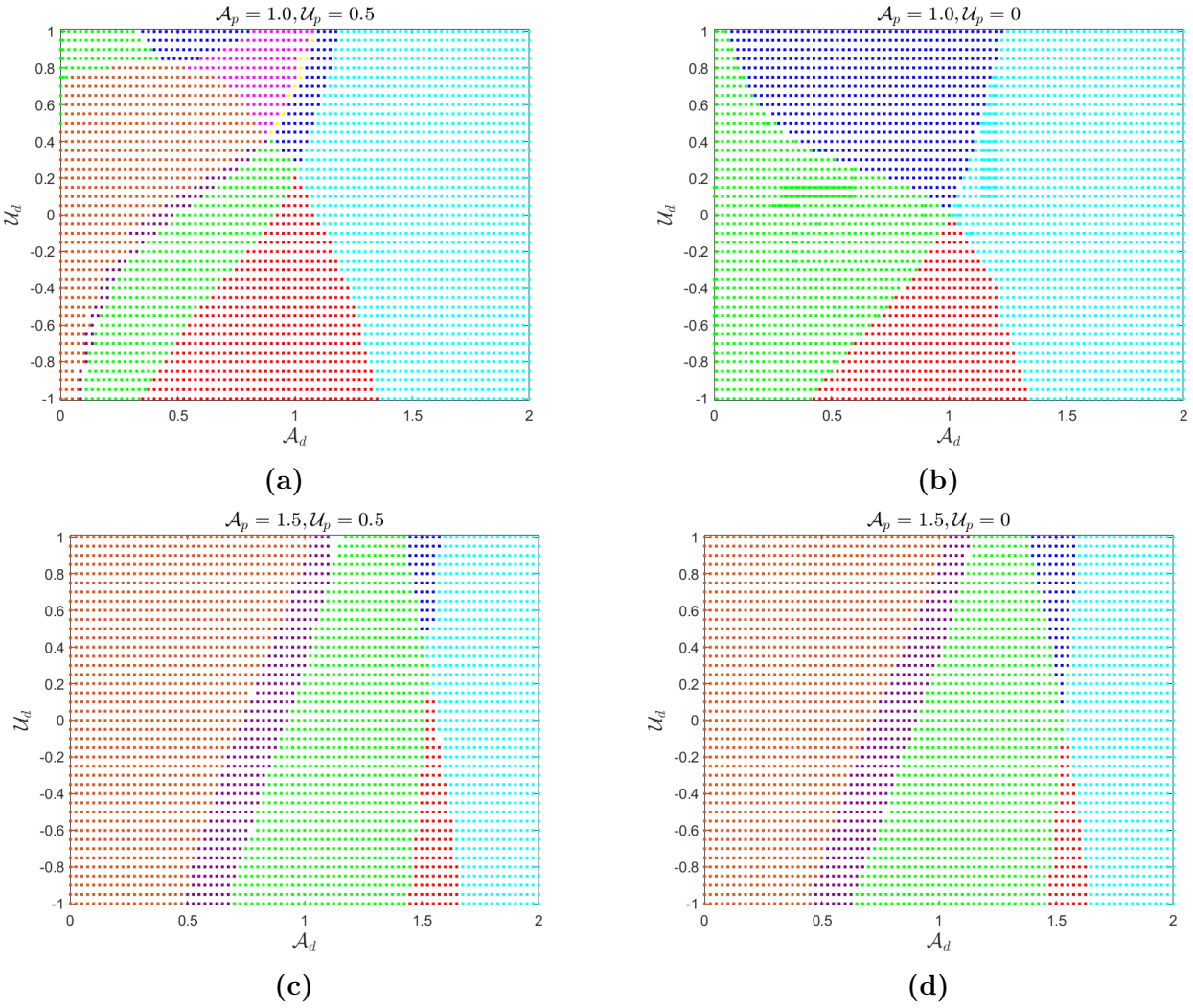

Figure 4.42: Parameter space plot of our Newton method with different initial conditions. Figure 4.42(a) for $\mathcal{U}_p = 0.5$, $\mathcal{A}_p = 1.0$, $k = 0.8$, Figure 4.42(b) for $\mathcal{U}_p = 0$, $\mathcal{A}_p = 1$, $k = 0.8$, Figure 4.42(c) for $\mathcal{U}_p = 0.5$, $\mathcal{A}_p = 1.5$, $k = 0.8$, Figure 4.42(d) for $\mathcal{U}_p = 0$, $\mathcal{A}_p = 1.5$, $k = 0.8$, respectively.

4.10 General tube law

In this section, we explore the Riemann problem in a blood vessel with a symmetric junction using the general tube law which resist both expansion and compression. The model setup is the same as used in this chapter except that in this case some integrals for the Riemann invariants cannot be done analytically, so the solution involves numerical integration. So, following Section 4.1.1 we have our dimensionless conservation of mass and momentum equations given as

$$\frac{\partial A_j}{\partial t} + \frac{\partial}{\partial x}(A_j u_j) = 0, \tag{4.94}$$

$$\frac{\partial}{\partial t}(A_j u_j) + \frac{\partial}{\partial x}(A_j u_j^2) + A_j \frac{\partial p_j}{\partial x} = 0, \quad (j = p, d), \tag{4.95}$$

These equations (4.94) and (4.95) are again subject to dimensionless general tube laws in each of the parent or daughter vessel, given as

$$p_p = \bar{p}_{ep} + f(A_p), \tag{4.96}$$

$$p_d = \bar{p}_{ed} + kf\left(\frac{A_d}{\bar{A}_d}\right), \tag{4.97}$$

where f denote the general tube laws for both parent and daughter vessels such that

$$f(s) = s^m - s^{-n}, \tag{4.98}$$

where both m and n are non-negative exponents describing the resistance to expansion and collapse of our blood vessel. In particular we choose $m = 10$ and $n = 3/2$ following Brook et. al. [44].

4.10.1 Riemann problem

We now consider a Riemann problem centered around the junction, where we impose a uniform initial condition in both the parent and daughter vessels. At the inlet of the parent vessel we impose $A_p = \mathcal{A}_p$, $u_p = \mathcal{U}_p$ such that in the parent vessel and from (4.96) the fluid pressure becomes

$$p_p = \bar{p}_{ep} + \left(\mathcal{A}_p^m - \mathcal{A}_p^{-n}\right). \tag{4.99}$$

Also, at the daughter vessel we impose $A_d = \mathcal{A}_d$, $u_d = \mathcal{U}_d$ and such from (4.97) we have

$$p_d = \bar{p}_{ed} + k\left(\left(\frac{\mathcal{A}_d}{\bar{A}_d}\right)^m - \left(\frac{A_d}{\bar{A}_d}\right)^{-n}\right). \tag{4.100}$$

4.10.2 Riemann invariants

Here we follow similar method as in Section 4.2.1, such that for the parent vessel we have

$$\begin{aligned} R_p &= u_p \pm \int_1^{A_p} \sqrt{mA^{*(m-2)} + nA^{*-(n+2)}}\, dA^*, \quad \text{constant on} \\ \frac{dx}{dt} &= u_p \pm \sqrt{mA_p^m + nA_p^{-n}} = u_p \pm c_p. \end{aligned} \tag{4.101}$$

Also, for the daughter vessel, we have

$$\begin{aligned} R_d &= u_d \pm \int_{\bar{A}_d}^{A_d} \sqrt{k\left(mA^{*(m-2)} + nA^{*-(n+2)}\right)}\, dA^*, \quad \text{constant on} \\ \frac{dx}{dt} &= u_d \pm \sqrt{k\left(m\left(\frac{A_d}{\bar{A}_d}\right)^m + n\left(\frac{A_d}{\bar{A}_d}\right)^{-n}\right)} = u_d \pm c_d. \end{aligned} \tag{4.102}$$

4.10.3 Boundary conditions between vessels

Here, we consider same conditions as in Section 4.1.2 and impose boundary conditions across the stationary wave as

$$r_p A_p u_p = r_d A_d u_d, \quad (x = 0), \tag{4.103}$$

$$\bar{p}_{ep} + (A_p^m - A_p^{-n}) + 1/2u_p^2 = \bar{p}_{ed} + k\left(\left(\frac{A_d}{\bar{A}_d}\right)^m - \left(\frac{A_d}{\bar{A}_d}\right)^{-n}\right) + 1/2u_d^2, \quad (x = 0). \tag{4.104}$$

4.10.4 Nonlinear flow structure

As in Section 4.2 the flow will exhibit either shocks or rarefactions adjacent to the ambient region and exhibit a uniform state across the intermediate region. Again due to splitting of mass and discontinuity in material properties across the junction we specify boundary conditions as in (4.103), (4.104).

4.10.5 Parent rarefaction

Following a similar method to Section 4.2.2 we have that at the edge of the rarefaction in contact with region 3 ($x = x_r$), we have that $u_r^P = \mathcal{U}_3^P$, $A_r^P = \mathcal{A}_3^P$ and $c_r^P = \mathcal{C}_3^P$ such that

$$x_r^p = \Bigg(\mathcal{U}_p + \int_1^{\mathcal{A}_p} \sqrt{mA^{*(m-2)} + nA^{*-(n+2)}}dA^* - \sqrt{m(\mathcal{A}_3^P)^m + n(\mathcal{A}_3^P)^{-n}} - \int_1^{\mathcal{A}_3^P} \sqrt{mA^{*(m-2)} + nA^{*-(n+2)}}dA^*\Bigg)t. \tag{4.105}$$

Simplifying, we have that at the edge of the rarefaction region adjacent to region 3

$$\mathcal{U}_3^P = \mathcal{U}_p + \int_1^{\mathcal{A}_p} \sqrt{mA^{*(m-2)} + nA^{*-(n+2)}}dA^* - \int_1^{\mathcal{A}_3^P} \sqrt{mA^{*(m-2)} + nA^{*-(n+2)}}dA^* \tag{4.106}$$

From above, we can apply Simpson's rule to numerically integrate for $\mathcal{U}_3^P$ for a given value of $\mathcal{A}_3^P$. Note, we use same physicality conditions (4.20) as in Section 4.2.2.

4.10.6 Daughter rarefaction

For negative characteristics entering the rarefaction region (R) from the far-field region in the daughter vessel, we have $u_r = \mathcal{U}_d$, $c_r = \mathcal{C}_d$. Here, we also follow the same method as in Section 4.2.3, such that at the edge of the rarefaction in contact with region 3 ($x = x_r^D$), we have that $u_r^D = \mathcal{U}_3^D$, $A_r^D = \mathcal{A}_3^D$ and $c_r^D = \mathcal{C}_3^D$ such that

$$x_{rd} = \Bigg(\mathcal{U}_d + \int_{\bar{A}_d}^{\mathcal{A}_3^D} \sqrt{k(mA^{*(m-2)} + nA^{*-(n+2)})}dA^* + \sqrt{k(m(\mathcal{A}_3^D)^m + n(\mathcal{A}_3^D)^{-n})} - \int_{\bar{A}_d}^{\mathcal{A}_d} \sqrt{k(mA^{*(m-2)} + nA^{*-(n+2)})}dA^*\Bigg)t. \tag{4.107}$$

Simplifying, we have that at the edge of the rarefaction region adjacent to region 3

$$\mathcal{U}_3^D = \mathcal{U}_d - \int_1^{\mathcal{A}_d} \sqrt{k(mA^{*(m-2)} + nA^{*-(n+2)})}dA^* + \int_1^{\mathcal{A}_3^D} \sqrt{k(mA^{*(m-2)} + nA^{*-(n+2)})}dA^* \quad (4.108)$$

Again, we use Simpson's rule to evaluate our integral and solve for $\mathcal{U}_3^D$ for a given $\mathcal{A}_3^D$.

4.10.7 Parent shock

For a shock wave in the parent vessel we follow a similar method as in Section 4.2.4 and write (4.94) and (4.95) in conserved form as

$$\frac{\partial A_p}{\partial t} + \frac{\partial}{\partial x}(A_p u_p) = 0, \quad (4.109)$$

$$\frac{\partial}{\partial t}(A_p u_p) + \frac{\partial}{\partial x}\left(A_p u_p^2 + \frac{m}{m+1}A_p^{m+1} - \frac{n}{n-1}A_p^{-(n-1)}\right) = 0. \quad (4.110)$$

We now have the shock speed written as (following the same method in Section 4.2.4)

$$\dot{s}_p = \frac{\mathcal{A}_3^P\mathcal{U}_3^P - \mathcal{A}_p\mathcal{U}_p}{\mathcal{A}_3^P - \mathcal{A}_p}, \quad (4.111)$$

$$\dot{s}_p = \frac{\mathcal{A}_3^P(\mathcal{U}_3^P)^2 + \frac{m}{m+1}\mathcal{A}_3^{P^{m+1}} - \frac{n}{n-1}(\mathcal{A}_3^P)^{-(n-1)} - \mathcal{A}_p\mathcal{U}_p^2 - \frac{m}{m+1}\mathcal{A}_p^{m+1} + \frac{n}{n-1}\mathcal{A}_p^{-(n-1)}}{\mathcal{A}_3^P\mathcal{U}_3^P - \mathcal{A}_p\mathcal{U}_p}. \quad (4.112)$$

We now equate (4.111) and (4.112) and simplify to compute the velocity immediately to the left of the junction as

$$\mathcal{U}_3^P = \mathcal{U}_p + \sqrt{\frac{\left(\frac{m}{m+1}\left((\mathcal{A}_3^P)^{m+1} - \mathcal{A}_p^{m+1}\right) + \frac{n}{n-1}\left(\mathcal{A}_p^{-(n-1)} - (\mathcal{A}_3^P)^{-(n-1)}\right)\right)(\mathcal{A}_3^P - \mathcal{A}_p)}{\mathcal{A}_p\mathcal{A}_3^P}}, \quad (4.113)$$

a nonlinear constraint which relates $\mathcal{U}_3^P$ and $\mathcal{A}_3^P$ to the initial conditions.

Note that we also impose the physicality conditions on parent shock (4.29) as in Section 4.2.4.

4.10.8 Daughter shock

We now consider a shock wave in the daughter vessel. Following similar method to Sections 4.2.5 and 4.10.7, the velocity immediately to the right of the junction is given by

$$\mathcal{U}_3^D = \mathcal{U}_d + \sqrt{\frac{\left(\frac{km}{(m+1)A_d{}^m}\left(\mathcal{A}_d^{m+1} - (\mathcal{A}_3^D)^{m+1}\right) + \frac{kn}{(n-1)A_d{}^n}\left((\mathcal{A}_3^D)^{-(n-1)} - \mathcal{A}_d^{-(n-1)}\right)\right)(\mathcal{A}_d - \mathcal{A}_3^D)}{\mathcal{A}_d\mathcal{A}_3^D}}, \quad (4.114)$$

a nonlinear constraint which relates $\mathcal{U}_3^D$ and $\mathcal{A}_3^D$ to the initial conditions. Again physicality conditions (4.32) as in Section 4.2.5.

4.10.9 Boundary conditions

Having determined the flow structure, we can now rewrite the the continuity conditions (4.103) and (4.104) at $x = 0$ in terms of the variables of the Riemann problem in the form

$$r_p \mathcal{U}_3^P \mathcal{A}_3^P = r_d \mathcal{U}_3^D \mathcal{A}_3^D, \tag{4.115}$$

$$\bar{p}_{ep} + \left((\mathcal{A}_3^P)^m - (\mathcal{A}_3^P)^{-n}\right) + \frac{1}{2}(\mathcal{U}_3^P)^2 = \bar{p}_{ed} + k\left(\left(\frac{\mathcal{A}_3^D}{\bar{A}_d}\right)^m - \left(\frac{\mathcal{A}_3^D}{\bar{A}_d}\right)^{-n}\right) + \frac{1}{2}(\mathcal{U}_3^D)^2. \tag{4.116}$$

4.10.10 Numerical method

Here, similar to Section 4.3 we apply a Newton iteration approach to solve for the four classical flow structures (*i.e.* parent rarefaction, daughter shock (PRDS), parent shock, daughter rarefaction (PSDR), parent shock, daughter shock (PSDS), parent rarefaction, daughter rarefaction (PRDR)). Following similar methods as above we determine the values of $\mathcal{A}_3^P$ and $\mathcal{A}_3^D$ as a function of the initial conditions. Again, we assume continuity of flux (4.115) and continuity of total pressure (4.116) across the junction

4.11 Resonance

In this section, similar to Section 4.6, we show that due to the division of mass across the junction our four standard cases are insufficient to span the parameter space. So, following a similar approach to Section 4.6, we derive new resonant configurations for the junction Riemann problem using the general tube law. As above we incorporate splitting of mass across the junction and also a jump in stiffness from parent to daughter vessels.

4.11.1 Riemann solution of configuration C^+ using general tube law

In this section, we use explore Riemann problem for configuration C^+ using the general tube law. We follow the same set up as in Section 4.6.1 and use the same notation such that the transcritical rarefaction spans all the way from $x = (\mathcal{U}_p - \mathcal{C}_p)t$ to $x = -\epsilon$. Again, on the outer edge of the supercritical stationary wave (*i.e.* $x = -\epsilon$), following similar method as in Section 4.6.1 we denote $A_r^P = \mathcal{A}_3^P$, $u_r^P = \mathcal{U}_3^P$ and $c_r^P = \mathcal{C}_3^P$, such that the profiles inner limit as $\epsilon \to 0$ becomes

$$\mathcal{U}_3^P = \mathcal{C}_3^P = \sqrt{k\,(m(\mathcal{A}_3^P)^m + n(\mathcal{A}_3^P)^{-n})}. \tag{4.117}$$

Also, as in Section 4.6.1, across the supercritical stationary wave ($x = -\epsilon$) we impose continuity of flux and total pressure, to have

$$r_p \mathcal{A}_3^P \mathcal{U}_3^P = r_s \mathcal{A}_{p1} \mathcal{U}_{p1}, \tag{4.118}$$

$$\bar{p}_{ep} + \frac{1}{2}(\mathcal{U}_3^P)^2 + ((\mathcal{A}_3^P)^m - (\mathcal{A}_3^P)^{-n}) = \bar{p}_{es} + \frac{1}{2}(\mathcal{U}_{p1})^2 + k_s\left(\left(\frac{\mathcal{A}_{p1}}{\bar{A}_s}\right)^m - \left(\frac{\mathcal{A}_{p1}}{\bar{A}_s}\right)^{-n}\right). \tag{4.119}$$

Following a similar method to before, imposing a zero speed shock at $x = 0$ gives the flow velocity as

$$\mathcal{U}_{d1} = \mathcal{U}_{p1} + \sqrt{\frac{\left(\frac{k_s m}{(m+1)\bar{A}_s{}^m}\left(\mathcal{A}_{d1}^{m+1} - (\mathcal{A}_{p1})^{m+1}\right) + \frac{k_s n}{(n-1)\bar{A}_s{}^n}\left((\mathcal{A}_{p1})^{-(n-1)} - \mathcal{A}_{d1}^{-(n-1)}\right)\right)(\mathcal{A}_{d1} - \mathcal{A}_{p1})}{\mathcal{A}_{d1}\mathcal{A}_{p1}}}, \tag{4.120}$$

a nonlinear equation connecting $\mathcal{A}_{d1}$ to $\mathcal{U}_{d1}$.

At $x = \epsilon$ we have a subcritical stationary wave where we impose continuity of flux and total pressure (*i.e.* conditions (4.115) and (4.116)) to have

$$r_s \mathcal{A}_{d1}\mathcal{U}_{d1} = r_d \mathcal{A}_3^D \mathcal{U}_3^D, \tag{4.121}$$

$$\bar{p}_{es} + \frac{1}{2}(\mathcal{U}_{d1})^2 + k_s\left(\left(\frac{\mathcal{A}_{d1}}{\bar{A}_s}\right)^m - \left(\frac{\mathcal{A}_{d1}}{\bar{A}_s}\right)^{-n}\right) = \bar{p}_{ed} + \frac{1}{2}(\mathcal{U}_3^D)^2 + k\left(\left(\frac{\mathcal{A}_3^D}{\bar{A}_d}\right)^m - \left(\frac{\mathcal{A}_3^D}{\bar{A}_d}\right)^{-n}\right) \tag{4.122}$$

Furthermore, the (uniform) flow to the right of the subcritical stationary wave is then connected to the daughter region with two flow possibilities, which is either a shock or a rarefaction.

For a shock in the daughter vessel, we have

$$\mathcal{U}_3^D = \mathcal{U}_d + \sqrt{\frac{\left(\frac{km}{(m+1)\bar{A}_d^m}\left(\mathcal{A}_d^{m+1} - (\mathcal{A}_3^D)^{m+1}\right) + \frac{kn}{(n-1)\bar{A}_d^n}\left((\mathcal{A}_3^D)^{-(n-1)} - \mathcal{A}_d^{-(n-1)}\right)\right)(\mathcal{A}_d - \mathcal{A}_3^D)}{\mathcal{A}_d\mathcal{A}_3^D}}, \tag{4.123}$$

a nonlinear equation connecting $\mathcal{A}_3^D$ to $\mathcal{U}_3^D$. Note we also apply the physicality conditions (4.78).

Conversely, for a rarefaction in the daughter vessel adjacent to the far-field region, following similar method as in Section 4.6.1, we have at the edge of the daughter region

$$\mathcal{U}_3^D = \mathcal{U}_d - \int_1^{\mathcal{A}_d} \sqrt{k(mA^{*(m-2)} + nA^{*-(n+2)})}dA^* + \int_1^{\mathcal{A}_3^D} \sqrt{k(mA^{*(m-2)} + nA^{*-(n+2)})}dA^* \tag{4.124}$$

Again, we use Simpson's rule to evaluate our integrals to solve for $\mathcal{U}_3^D$ for a given $\mathcal{A}_3^D$, and also apply physicality conditions (4.84).

4.11.2 Riemann solution for configuration D^+

Here, we extend resonant setup for configuration D of Han et. al. (2015) [89] using the general tube law ((4.99), (4.100)). The setup is analogous to that of Section 4.6.2 (see Figure 4.8) and the notation is identical. At the edge of the transcritical parent rarefaction we let $A_r^P = \mathcal{A}_3^P$, $u_r^P = \mathcal{U}_3^P$ and $c_r^P = \mathcal{C}_3^P$, where the flow speed is equal to the wave speed given as

$$\mathcal{U}_3^P = \mathcal{C}_3^P = \sqrt{k\left(m(\mathcal{A}_3^P)^m + n(\mathcal{A}_3^P)^{-n}\right)}, \tag{4.125}$$

and the cross-sectional area is to be determined from (4.125) by Newtons's method.

Following a similar method in Section 4.6.2 we impose continuity of flux and total pressure across

the contact discontinuity to have

$$r_p \mathcal{A}_3^P \mathcal{U}_3^P = r_d \mathcal{A}_{d1} \mathcal{U}_{d1}, \tag{4.126}$$

$$\bar{p}_{ep} + \frac{1}{2}(\mathcal{U}_3^P)^2 + \left((\mathcal{A}_3^P)^m - (\mathcal{A}_3^P)^{-n}\right) = \bar{p}_{ed} + \frac{1}{2}(\mathcal{U}_{d1})^2 + k\left(\left(\frac{\mathcal{A}_{d1}}{\bar{A}_d}\right)^m - \left(\frac{\mathcal{A}_{d1}}{\bar{A}_d}\right)^{-n}\right). \tag{4.127}$$

Across the resonant shock wave produced in the daughter vessels, we invoke conservation of mass and momentum across the front at $x = s_{res}(t)$ and follow same method as in Section 4.6.2 and compute the velocity of the resonant shock as

$$\mathcal{U}_3^D = \mathcal{U}_{d1} + \sqrt{\frac{\left(\frac{km}{(m+1)\bar{A}_d^m}\left((\mathcal{A}_3^D)^{m+1} - (\mathcal{A}_{d1})^{m+1}\right) + \frac{kn}{(n-1)\bar{A}_d^n}\left((\mathcal{A}_{d1})^{-(n-1)} - (\mathcal{A}_3^D)^{-(n-1)}\right)\right)(\mathcal{A}_3^D - \mathcal{A}_{d1})}{\mathcal{A}_3^D \mathcal{A}_{d1}}}, \tag{4.128}$$

a nonlinear equation connecting $\mathcal{A}_3^D$ to $\mathcal{U}_3^D$.

The second wave in the daughter vessels can be either a shock or rarefaction, and we then apply a similar approach as in configuration C^+ of Section 4.11.1 and use (4.123) for a shock wave in the daughter vessels or (4.124) for a rarefaction wave in the daughter vessel. Note, we also impose the appropriate physicality conditions for shocks ((4.29), (4.32)) and rarefactions ((4.20), (4.26)).

In what follows, we summarise the results of solutions in parameter space plots and compare them with the results from the expanding tube law.

4.12 Overview of parameter space with no jump in material properties using general tube law

In this section, we summarise the overall behaviour of our system with a nonlinear tube law by producing parameter space plots similar to Section 4.8.

Figure 4.43(a) illustrates a parameter space spanned by $\mathcal{A}_d$ and $\mathcal{U}_d$ for a case where we have just splitting of mass across the junction using the general tube law. The classical solutions fill the domain of our parameter space with a small tongue of resonant solution (purple and yellow) for small values of $\mathcal{A}_d$ (*i.e.* when the vessel is collapsed). The configuration C^+ solution with a daughter shock (purple) is confined to low $\mathcal{A}_d$ spanning all values of $\mathcal{U}_d$, while the configuration C^+ with a daughter rarefaction spans only a tiny region for low $\mathcal{A}_d$ with $\mathcal{U}_d > 0.85$. We expect configuration D^+ is present for very small $\mathcal{A}_d$ but we have not been able to compute these solutions. Comparing this to the analogous parameter space plot using the expanding tube law (see Figure 4.43b), they both exhibit the four classical cases close to the base state but the region of configuration C^+ and D^+ resonant solutions (purple, orange, magenta and yellow) is much larger. So, using the general tube law does not eliminate resonance resulting from splitting of mass across the junction, but confines it to a much smaller region of the parameter space.

In Figure 4.44(a) we have the parameter space spanned by $\mathcal{A}_p$ and $\mathcal{U}_p$ using the general tube law with just splitting of mass across the junction. Here we have that the only resonant solution is confuguration C^+ (purple), confined to large values of $\mathcal{A}_p$ (across all $\mathcal{U}_p$). Comparing to a similar case using the expanding tube law (Figure 4.44(b)) we see a strong qualitative similarity between the two although

(as expected since the tube laws are essentially identical for large cross-sectional area).

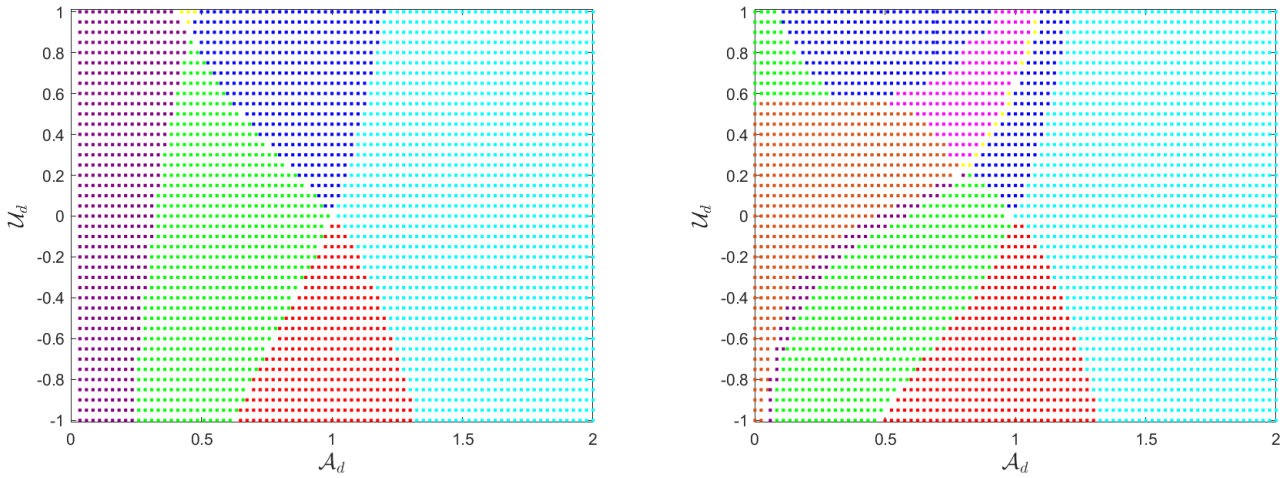

(a) **(b)**

Figure 4.43: Overview of parameter space for vessel with splitting of mass across a junction using the general and expanding tube law showing regions of classical and resonant solutions with $\mathcal{A}_p = 1$, $\mathcal{U}_p = 0$, $-1 \leq \mathcal{U}_d \leq 1$, $0 \leq \mathcal{A}_d \leq 2$ and $k = 1$. Figure 4.43(a) illustrates parameter space for general tube law while Figure 4.43(b) illustrates parameter space for expanding tube law.

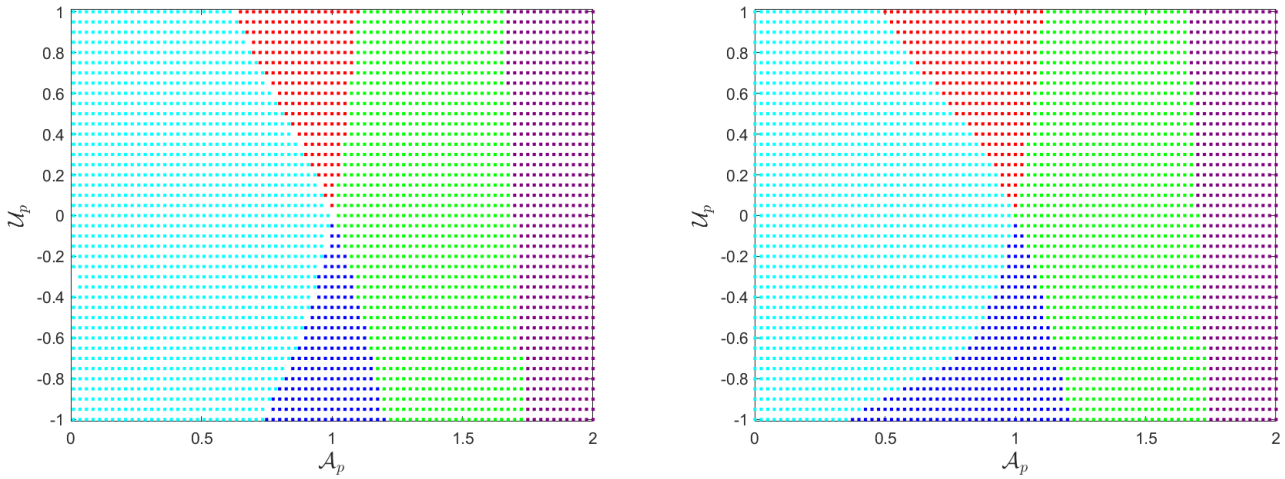

(a) **(b)**

Figure 4.44: Overview of parameter space for vessel with splitting of mass across a junction using the general and expanding tube law showing regions of classical and resonant solutions with $\mathcal{A}_d = 1$, $\mathcal{U}_d = 0$, $-1 \leq \mathcal{U}_p \leq 1$, $0 \leq \mathcal{A}_p \leq 2$ and $k = 1$. Figure 4.44(a) illustrates parameter space for general tube law while Figure 4.44(b) illustrates parameter space for expanding tube law.

4.13 Overview of parameter space with splitting of mass and jump in material properties using general tube law

In this section, we summarise the overall behaviour of our system by producing parameter space plots using the general tube law. In each case we compare with parameter space plot using the expanding tube law.

Figure 4.45 illustrates a parameter space spanned by $\mathcal{U}_d$ and $\mathcal{A}_d$ while fixing $\mathcal{A}_p = 1$ and $\mathcal{U}_p = 0$ for daughter vessel stiffer than the parent vessel ($k = 1.1$) and splitting of mass from parent to the daughter vessel. For the general tube law (Figure 4.45a) the behaviour for large $\mathcal{A}_d$ is very similar to the expanding tube law (Figure 4.45b). However, for $\mathcal{A}_d < 1$ it is evident that the region of the resonant solution is pushed to much smaller values of $\mathcal{A}_d$ *i.e* using the general tube law, which includes resistance to collapse, suppresses the region of resonant solutions. A similar feature is found in Figure 4.46 when the daughter vessels are chosen less stiff than the parent vessel ($k = 0.9$), where resonant solutions are once again suppressed to low values of $\mathcal{A}_d$.

Finally, Figures 4.47 and 4.48 illustrate parameter space plots spanned by $\mathcal{U}_p$ and $\mathcal{A}_p$ while fixing $\mathcal{A}_d = 1$ and $\mathcal{U}_d = 0$. In these cases the region of resonant solutions for large $\mathcal{A}_p$ are almost unchanged (this is not suprising as the two choices of tube law aree well in this region), while the behaviour for smaller $\mathcal{A}_p$ is slightly modified. Hence, as for the expanding tube law, an increase in stiffness of the daughter vessels (*i.e.* k increasing) reduces the region of resonant solutions.

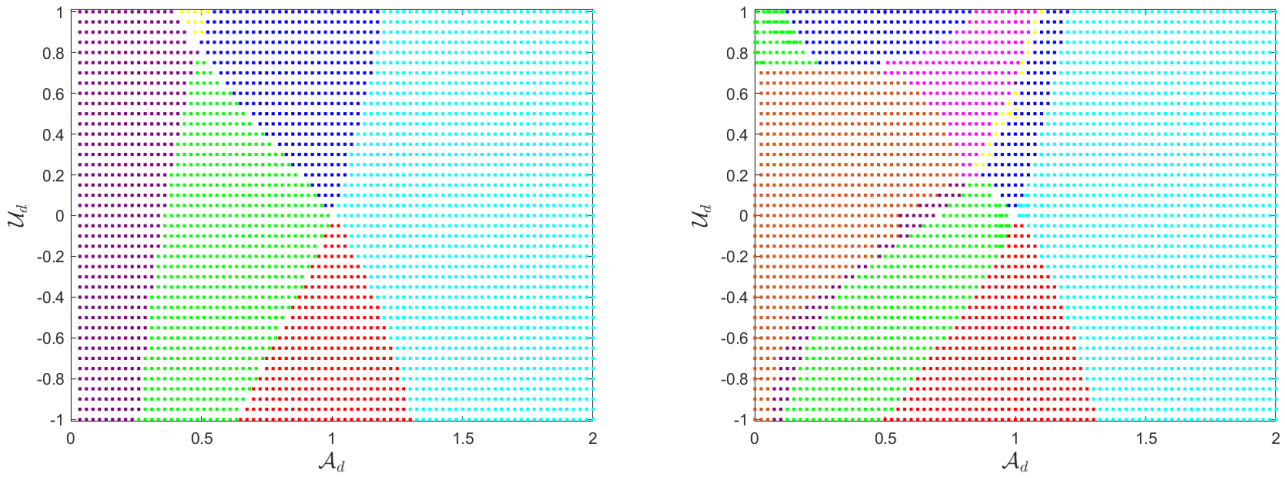

Figure 4.45: Overview of parameter space for vessel with splitting of mass across a junction using the general and expanding tube law showing regions of classical and resonant solutions with $\mathcal{A}_p = 1$, $\mathcal{U}_p = 0$, $-1 \leq \mathcal{U}_d \leq 1$, $0 \leq \mathcal{A}_d \leq 2$ and $k = 1.1$. Figure 4.45(a) illustrates parameter space for general tube law while Figure 4.45(b) illustrates parameter space for expanding tube law.

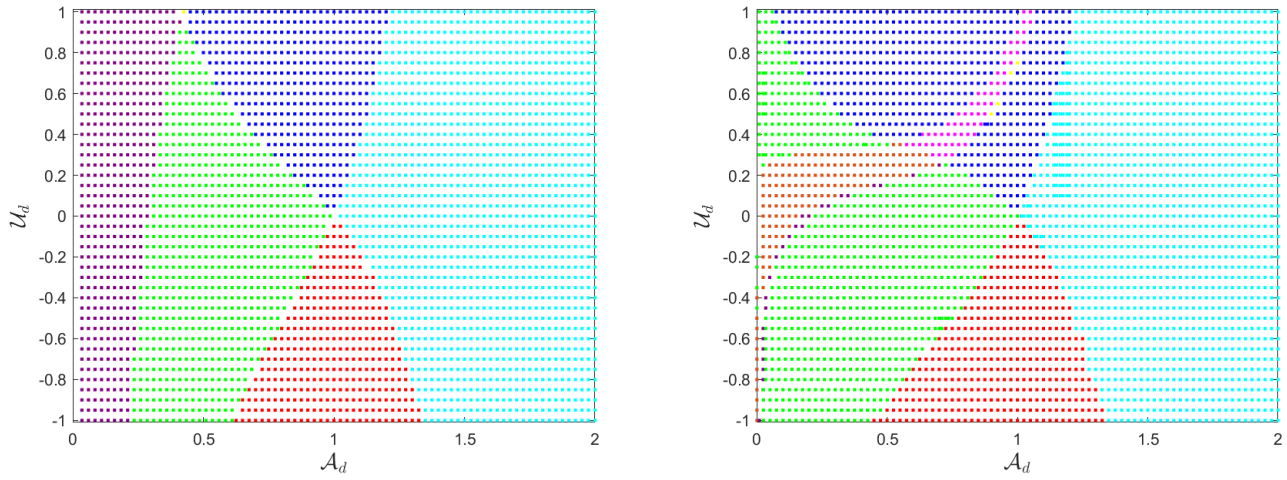

(a) **(b)**

Figure 4.46: Overview of parameter space for vessel with splitting of mass across a junction using the general and expanding tube law showing regions of classical and resonant solutions with $\mathcal{A}_p = 1$, $\mathcal{U}_p = 0$, $-1 \leq \mathcal{U}_d \leq 1$, $0 \leq \mathcal{A}_d \leq 2$ and $k = 0.9$. Figure 4.46(a) illustrates parameter space for general tube law while Figure 4.46(b) illustrates parameter space for expanding tube law.

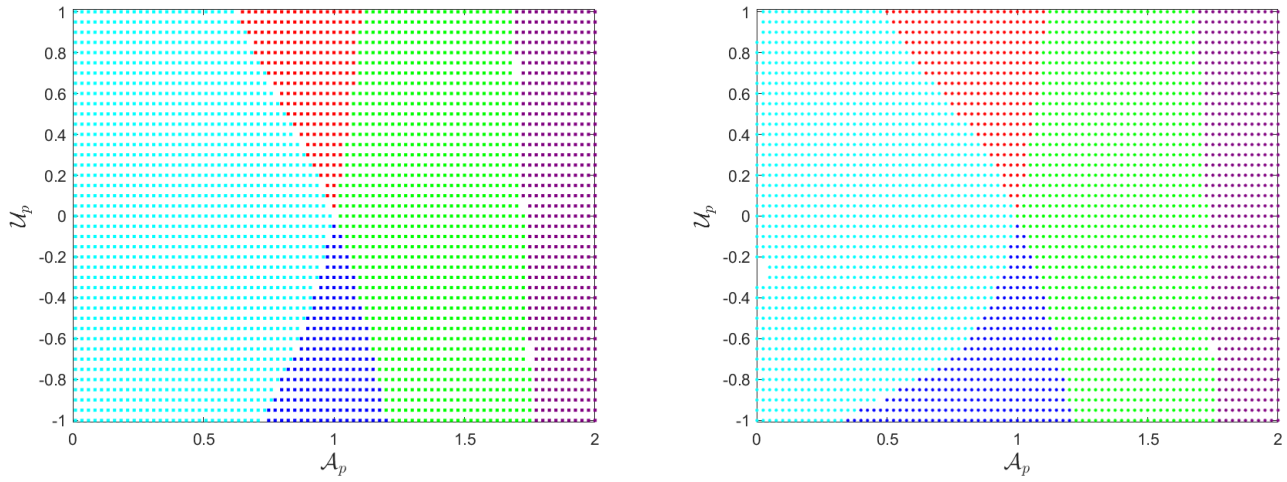

(a) **(b)**

Figure 4.47: Overview of parameter space for vessel with splitting of mass and jump in stiffness across a junction using the general and expanding tube law showing regions of classical and resonant solutions with $\mathcal{A}_d = 1$, $\mathcal{U}_d = 0$, $-1 \leq \mathcal{U}_p \leq 1$, $0 \leq \mathcal{A}_p \leq 2$ and $k = 1.1$. Figure 4.47(a) illustrates parameter space for general tube law while Figure 4.47(b) illustrates parameter space for expanding tube law.

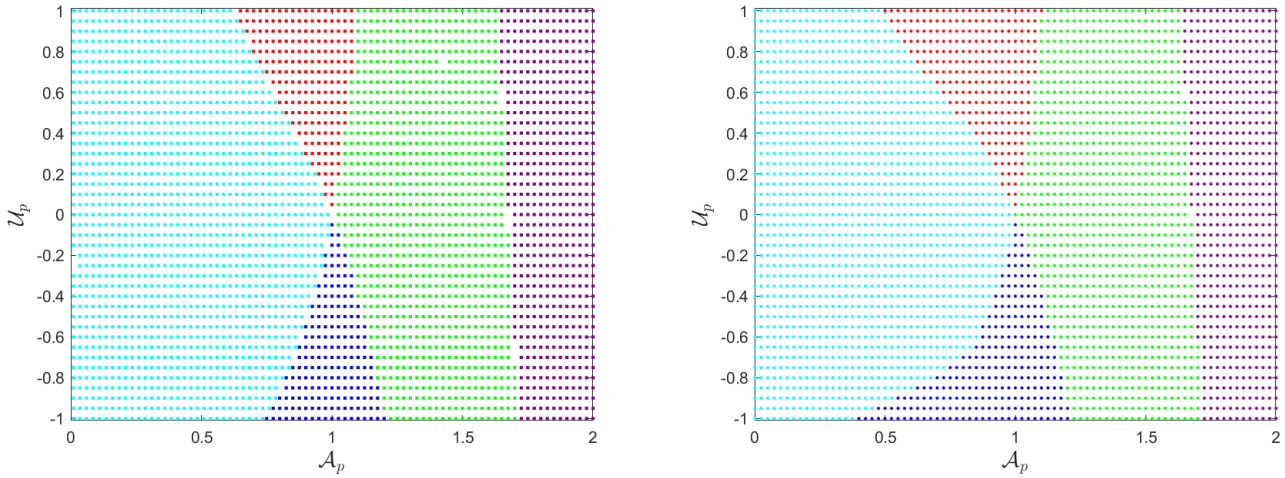

(a) **(b)**

Figure 4.48: Overview of parameter space for vessel with splitting of mass and jump in stiffness across a junction using the general and expanding tube law showing regions of classical and resonant solutions with $\mathcal{A}_d = 1, \mathcal{U}_d = 0, -1 \leq \mathcal{U}_p \leq 1, 0 \leq \mathcal{A}_p \leq 2$ and $k = 0.9$. Figure 4.48(a) illustrates parameter space for general tube law while Figure 4.48(b) illustrates parameter space for expanding tube law.

4.14 Summary

In this chapter we have constructed solutions to the Riemann problem in a blood vessel with a junction, reminiscent of blood flow in the retinal circulation. As in previous chapters, we identified the response to an instantaneous discontinuity in cross-sectional area and/or velocity applying the ideas to a symmetric junction. We identified analogs of the four classical wave configurations in a single vessel (similar to Brook et al. [44]). We described the system using bifurcation diagrams constructed as a function of the cross-sectional area of the parent or daughter vessels, while fixing other far-field parameters. These bifurcation diagrams (from our Newton's method) showed that the classical solutions were not able to span the parameter space (as in the case with a jump in material properties). We identified a series of resonant solutions which span these gaps, drawing inspiration from previous work by Han et. al. [89] and our work in Chapter 3.

For all vessels having the same material and environmental properties (so the only discontinuity is due to the division of mass from parent to daughter) the system exhibits resonance for low values of the daughter cross-sectional area in the far-field and large values of the of the parent cross-sectional area in the far-field. Both predictions are preserved when using a more general form of tube law which resists collapse.

Generalising the analysis to also include a jump in elastic stiffness across the junction, having the daughter stiffer than the parent pushes the resonant region to larger values of the parent far-field cross-sectional area (reducing the size of the resonant region with respect to the parent cross-sectional area, Figure 4.45) and larger values of the daughter far-field cross-sectional area (increasing the size of the resonant region with respect to the daughter cross-sectional area). Again these observations are independent of the form of the tube law used.

Hence, as we change the far-field properties of the flow and the relative stiffness of the vessels on either side of the bifurcation, the size and form of the resonant region shifts. We therefore expect that simulation in networks of vessels (*e.g.* to mimick the retinal circulation) in networks will also exhibit similar resonances, and the presence of additional (resonant) shocks could lead to interesting new dynamical features in the global wave propagation.

The work in this chapter provides entirely new insight into the junction Riemann problem, extending the classical subcritical analysis of Contarino et al. [87] to span the entire parameter space, capturing the resonant interaction between a rarefaction and the stationary wave at the junction. In this way it extends the analysis of Han et al. [89] to a junction problem, showing how the system merges smoothly from the subcritical state to the transcritical state. Indeed, simulations of shock propagation across flexible-walled junction (using a Godunov finite volume method with patching conditions across the junction) by collaborator Tampsin Spelman [44] have demonstrtaed a sub-transcritical transition, entirely consistent with the transition point predicted by our Riemann problem [119]. Of course, the patching conditions used in Spelman's simulation will become inacurate in the transcritical regime, and instead this method could be adopted to include our new junction Riemann problem. This is deferred to future work.

CHAPTER 5

Summary and Conclusion

In this thesis we have developed building blocks toward a full computational model for blood flow in the human retinal circulation, considering a simple model for blood flow in single complaint vessels spanning from the optic nerve into the retina, coupled together using appropriate conditions at junctions. The flow equations constructed are hyperbolic, so to solve the model we constructed a classical Riemann problem which forms part of sophisticated finite volume methods designed to capture shocks.

In Chapter 2, we presented a simple model for blood flow through a single complaint vessel mimicking blood flow in the central retinal vessels which pass along the center of the optic nerve. We constructed the classical Riemann problem, where the finite domain spans a narrow region of the vessel with uniform material properties. The Riemann problem is constructed in response to an instantaneous discontinuity in flow and tube cross-sectional area across an interface, while examining the resultant wave propagation. We introduced a new numerical scheme (based on Newton's method) to explore the entire parameter space, identifying four possible flow structures that can emerge in response to the discontinuity, similar to Brook et al. [44, 86]. We further explored the system using bifurcation diagrams constructed as a function of the far-field cross-sectional area (while fixing all other parameters). The bifurcation diagrams initially showed existence of multiple branches of solution (earlier identified by Spiller et al. [86]) but we imposed physicality and Lax entropy conditions to obtain only physical solutions and determined that the solution was always unique. We further merged these bifurcation diagrams to produce an overview of the parameter space, where we identified a region where our system shows no solution as the vessel becomes completely collapsed. We compared this outcome with solutions generated using the algorithm of Brook et al. [44] and the outcomes were both qualitatively and quantitatively similar.

In Chapter 3 we extended our model to consider blood flow in the central retinal blood vessels with an abrupt change in material properties, mimicking flow through the optic nerve into the retina via the optic disc (similar to Han et al. [89], Toro and Siviglia [105]). We again constructed a Riemann problem for this complaint vessel imposing an abrupt jump in vessel stiffness coincident with the point of initial discontinuity in the Riemann problem. We identified analogies of the four classical flow structures but with an additional stationary wave across the point of discontinuity in elastic stiffness. In a similar manner to Chapter 2 we also constructed bifurcation diagrams as a function of the far-field cross-sectional area (while keeping all other parameters constant), and we found that the classical solutions

were insufficient to cover the entire parameter space. Following further exploration of these gaps, we identified resonant states as one of either a left or right rarefaction becomes transcritical and resonates with the stationary wave (earlier identified by Han et al. [89] and Toro and Siviglia [105]). This is an extension of the work by Han et al. [89] as we showed how these different solutions fit together completing the gaps in the parameter space left by the classical solutions.

In Chapter 4 we presented a model for blood flow in branching retinal vessels. Similar to previous chapters we also constructed a Riemann problem, where in this case the finite domain spans a symmetric junction with a parent vessel branching into two daughter vessels. The Riemann problem is constructed in response to an instantaneous discontinuity associated with division of mass at the junction (and also possibly a jump in vessel stiffness). As before, we identified four classical wave configurations with an additional stationary wave at the junction. We explored the system using bifurcation diagrams constructed as a function of the far-field cross-sectional area of either the parent or daughter vessels (while fixing all other parameters). We identified that splitting of mass across the junction from parent to daughter vessels was sufficient to initiate resonance for low values of the daughter far-field cross-sectional area and large values of the parent far-field cross-sectional area, respectively. We extended our analysis to include a jump in vessel stiffness across the junction: with the daughter vessel stiffer than the parent vessel, our analysis showed that resonance spans a larger region of the parameter space and pushes the resonant region to larger values of the daughter far-field cross-sectional area. Conversely, for the daughter vessel less stiff than the parent vessel the resonance region spans a smaller region of the parameter space suppressing the resonance to low values of the daughter far-field cross-sectional area. Our junction Riemann problem is an extension of the generalised junction Riemann problem of Contarino et al. [87], but in our case we extend the existing analysis to include resonance and transcritical flow, demonstrating how resonance can produce additional shock waves in the system.

5.1 Future work

The motivation of this work was to build a full computational model for the retinal circulation geared towards predicting retinal haemorrhage. This thesis represents a first step in this direction, but our new Riemann solver must now be integrated into the full finite volume method for the entire vessel. In order to extend our results towards this final aim, first, we need to extend the model in chapter 4 to allow for asymmetric junctions [51, 66, 68, 69, 75] by changing our boundary conditions. We also need to extend our work to investigate the effect of flow viscosity in our system [44]. However, viscosity cannot be added directly into the Riemann problem (the equations must be inviscid to remain conservative). Instead, it will be incorporated into the full finite volume method by adjusting the fluxes between adjacent volumes to accent for the diffusive effects of viscosity. It remains to be seen if viscous effects suppress the resonant structures elucidated in this thesis.

Appendices

A MATLAB codes

A.1 MATLAB code for Chapter 2

```
% Sample of MATLAB code for classical solutions in chapter two
function Chapter_two

clc
clear
close all
format long
figure(1)
box on
A1=1.0;
% Row vector for A2
A2s=linspace(0.01,2,20);

n=10;
% Row vector for u2
u2s=linspace(-2,2,20);
u1=0;

% Tolerance for the function and solution value
options=optimset('TolX',1e-10,'TolFun',1e-10);

% Loop for iteration of A2 and u2: A2 is in reverse
for j=length(A2s):-1:1

    A2=A2s(j);
 out=[];
    for i=1:length(u2s)

        if i==1 && j==length(A2s)
            A3guess=0.5*(A2+A1);
        elseif i==1
            A3guess=A3out(1,j+1);
        elseif j<length(A2s)
            A3guess=A3out(i,j+1);
        end

        u2=u2s(i);
        clear flag1 flag2
%%%
```

```
    u32=u2+(2*sqrt(n))/n*(A3^(n/2)-A2^(n/2));
    c1=sqrt(n)*A1^(n/2);
    c3=sqrt(n)*A3^(n/2);
    u3=u32;
    LS=(A3*u3-A1*u1)/(A3-A1);
    if exit>0 && (u1-c1)>LS && (u3-c3)<LS && (u3+c3)<(u2+c2)
       A3guess=A3;
        disp('LSRR')
        disp(['A_3 = ' num2str(A3)]);
        disp(['u_3 = ' num2str(u32)]);
        flag1=1;
        flag2=0;
        A3out(i,j)=A3;u3out(i,j)=u31;A30=A3;
        out=[out;u31,u32,c3,A3];
    end

    [A3,f,exit]=fsolve(@LSRReqns,A3guess,options);

    u31=u1-sqrt((n*(A3^(n+1)-A1^(n+1))*(A3-A1))/((n+1)*A1*A3));
    u32=u2+(2*sqrt(n))/n*(A3^(n/2)-A2^(n/2));
    c3=sqrt(n)*A3^(n/2);
    c2=sqrt(n)*A2^(n/2);
    u3=u32;
    LS=(A3*u3-A1*u1)/(A3-A1);
    if exit>0 && (u1-c1)>LS && (u3-c3)<LS && (u3+c3)<(u2+c2)
        A3guess=A3;
        disp('LSRR')
        disp(['A_3 = ' num2str(A3)]);
        disp(['u_3 = ' num2str(u32)]);
        flag1=1;
        flag2=0;
        A3out(i,j)=A3;u3out(i,j)=u31;A30=A3;
        out=[out;u31,u32,c3,A3];
    end

%%%%%%%%%%%%%%%%%%%%%%%%%%%%%%%%%%%%%%%%%%%%%%%%%%%%%%%%%%%%%%%%%%%%%%%%%%%%
% left shock, right shock

[A3,f,exit]=fsolve(@LSRSeqn,A30,options);
        u31=u1+sqrt((n*(A3^(n+1)-A1^(n+1))*(A3-A1))/((n+1)*A1*A3));
        u32=u2+sqrt((n*(A2^(n+1)-A3^(n+1))*(A2-A3))/((n+1)*A2*A3));
        u3=u32;
        c1=sqrt(n)*A1^(n/2);
        c2=sqrt(n)*A2^(n/2);
        c3=sqrt(n)*A3^(n/2);
        RS=(A2*u2-A3*u31)/(A2-A3);
        LS=(A3*u31-A1*u1)/(A3-A1);

        if exit>0 && (u3+c3)>RS && (u2+c2)<RS  &&(u3-c3)<LS  && (u1-c1)>LS
            A30=A3;
            disp('LSRS')
            disp(['A_3 = ' num2str(A3)]);
            disp(['u_3 = ' num2str(u32)]);
            flag1=1;
            flag2=1;
            tot=tot+1;
            out=[out;u31,u32,c3,A3];
        end

        %%%%%%%%%%%%%%%%%%%%%%%%%%%%%%%%%%%%%%%%%%%%%%%%%%%%%%%%%%%%%%%%%%%%%%%%%%%%
        [A3,f,exit]=fsolve(@LSRSeqns,A30,options);
        u31=u1-sqrt((n*(A3^(n+1)-A1^(n+1))*(A3-A1))/((n+1)*A1*A3));
        u32=u2+sqrt((n*(A2^(n+1)-A3^(n+1))*(A2-A3))/((n+1)*A2*A3));
        u3=u32;
        c3=sqrt(n)*A3^(n/2);
        RS=(A2*u2-A3*u31)/(A2-A3);
        LS=(A3*u31-A1*u1)/(A3-A1);

       if exit>0 && (u3+c3)>RS && (u2+c2)<RS  &&(u3-c3)<LS  && (u1-c1)>LS
           A30=A3;
            disp('LSRS')
            disp(['A_3 = ' num2str(A3)]);
            disp(['u_3 = ' num2str(u32)]);
            flag1=1;
            flag2=1;
            tot=tot+1;
            out=[out;u31,u32,c3,A3];
       end

       %%%%%%%%%%%%%%%%%%%%%%%%%%%%%%%%%%%%%%%%%%%%%%%%%%%%%%%%%%%%%%%%%%%%%%%%%%%%
       [A3,f,exit]=fsolve(@LSRSeqnt,A30,options);
        u31=u1+sqrt((n*(A3^(n+1)-A1^(n+1))*(A3-A1))/((n+1)*A1*A3));
        u32=u2-sqrt((n*(A2^(n+1)-A3^(n+1))*(A2-A3))/((n+1)*A2*A3));
        u3=u32;
        c3=sqrt(n)*A3^(n/2);
        RS=(A2*u2-A3*u31)/(A2-A3);
        LS=(A3*u31-A1*u1)/(A3-A1);
```

```
            A30=A3;
             disp('LSRS')
             disp(['A_3 = ' num2str(A3)]);
             disp(['u_3 = ' num2str(u32)]);
             flag1=1;
             flag2=1;
             tot=tot+1;
             out=[out;u31,u32,c3,A3];
        end

         %%%%
```

```
        u32=u2-sqrt((n*(A2^(n+1)-A3^(n+1))*(A2-A3))/((n+1)*A2*A3));

        v=(u31)-(u32);
    end

    function  v=LSRReqn(A3)

        u31=u1+sqrt((n*(A3^(n+1)-A1^(n+1))*(A3-A1))/((n+1)*A1*A3));
        u32=u2+(2*sqrt(n))/n*(A3^(n/2)-A2^(n/2));

        v=(u31)-(u32);
    end

    function  v=LSRReqns(A3)

        u31=u1-sqrt((n*(A3^(n+1)-A1^(n+1))*(A3-A1))/((n+1)*A1*A3));
        u32=u2+(2*sqrt(n))/n*(A3^(n/2)-A2^(n/2));

        v=(u31)-(u32);
    end
function  v=LSRSeqn(A3)

        u31=u1+sqrt((n*(A3^(n+1)-A1^(n+1))*(A3-A1))/((n+1)*A1*A3));
        u32=u2+sqrt((n*(A2^(n+1)-A3^(n+1))*(A2-A3))/((n+1)*A2*A3));

        v=u31-u32;
    end

    function  v=LSRSeqns(A3)

        u31=u1-sqrt((n*(A3^(n+1)-A1^(n+1))*(A3-A1))/((n+1)*A1*A3));
        u32=u2+sqrt((n*(A2^(n+1)-A3^(n+1))*(A2-A3))/((n+1)*A2*A3));

        v=u31-u32;

    end

    function  v=LSRSeqnt(A3)

        u31=u1+sqrt((n*(A3^(n+1)-A1^(n+1))*(A3-A1))/((n+1)*A1*A3));
        u32=u2-sqrt((n*(A2^(n+1)-A3^(n+1))*(A2-A3))/((n+1)*A2*A3));

        v=u31-u32;

    end

    function  v=LSRSeqnu(A3)

        u31=u1-sqrt((n*(A3^(n+1)-A1^(n+1))*(A3-A1))/((n+1)*A1*A3));
        u32=u2-sqrt((n*(A2^(n+1)-A3^(n+1))*(A2-A3))/((n+1)*A2*A3));

        v=u31-u32;
```

A.2 MATLAB code for Chapter 3

```
% Sample of MATLAB code for classical and resonant solutions in chapter three
function Chapter_three

clc
clear
close all
format long
figure(1)
box on
A1=1.0;
% Row vector for A2
A2s=linspace(0.01,2,20);

n=10;
% Row vector for u2
u2s=linspace(-2,2,20);
u1=0;

% Tolerance for the function and solution value
options=optimset('TolX',1e-10,'TolFun',1e-10);

% Loop for iteration of A2 and u2: A2 is in reverse
for j=length(A2s):-1:1

    A2=A2s(j);
 out=[];
    for i=1:length(u2s)

        if i==1 && j==length(A2s)
            A3guess=0.5*(A2+A1);
        elseif i==1
            A3guess=A3out(1,j+1);
        elseif j<length(A2s)
            A3guess=A3out(i,j+1);
        end

        u2=u2s(i);
        clear flag1 flag2 flag3 flag4
        tot=0;
%%%
```

```
        u3left=u1+(2*sqrt(n)/n)*(A1^(n/2)-A3left^(n/2));

        RS=((A2*u2)-(A3right*u3right))/(A2-A3right);
        if exit>0 && A1>=A3left && A3right>=A2 && RS>0 && A3left>0 && A3right>0
            if flagphys==1 && (u3left-c3left)>(u1-c1) && (u3left-c3left)<0 && (u2+c2) < RS && (u3right+c3right) > RS
                A32=A3;
                disp('LRRS_b')
                disp(['A_3left = ' num2str(A3left)]);
                disp(['u_3left = ' num2str(u3left)]);
                flag1=0;
                flag2=1;
                tot=tot+1;
                out=[out;u3left,u3right,c3left,c3right,A3left,A3right];
            elseif flagphys==0
                disp('LRRS_b')
                disp(['A_3left = ' num2str(A3left)]);
                disp(['u_3left = ' num2str(u3left)]);
                flag1=0;
                flag2=1;
                tot=tot+1;
                out=[out;u3left,u3right,c3left,c3right,A3left,A3right];
            end
        end

%%%
```

```
        end

%%%%%%%%%%%%%%%%%%%%%%%%%%%%%%%%%%%%%%%%%%%%%%%%%%%%%%%%%%%%%%%%%%%%%%%%%%%%
% left shock, right shock

[A3,f,exit]=fsolve(@LSRStwoeqn,A30,options);
        A3left=A3(1);
        A3right=A3(2);
       c1=sqrt(n)*A1^(n/2);
        c3left=sqrt(n)*A3left^(n/2);
        c2=sqrt(k*n)*(A2/A2bar)^(n/2);
        c3right=sqrt(k*n)*(A3right/A2bar)^(n/2);
        u3left=u1+sqrt((n*(A3left^(n+1)-A1^(n+1))*(A3left-A1))/((n+1)*A1*A3left));
        u3right=u2+sqrt((k*n*(A2^(n+1)-A3right^(n+1))*(A2-A3right))/((n+1)*A2bar^n*A2*A3right));
        RS=(A2*u2-A3right*u3right)/(A2-A3right);
        LS=(A3left*u3left-A1*u1)/(A3left-A1);

        if exit>0 && LS<0 && RS>0 && A3left>0 && A3right>0
            if flagphys==1 && LS<(u1-c1) && LS>(u3left-c3left) && RS>(u2+c2) && RS<(u3right+c3right)
            disp('LSRS')
            A30=A3;
            disp(['A_3left = ' num2str(A3left)]);
            disp(['u_3left = ' num2str(u3left)]);
            flag1=1;
            flag2=1;
            tot=tot+1;
             out=[out;u3left,u3right,c3left,c3right,A3left,A3right];
            elseif flagphys==0
                disp('LSRS')
            disp(['A_3left = ' num2str(A3left)]);
            disp(['u_3left = ' num2str(u3left)]);
            flag1=1;
            flag2=1;
            tot=tot+1;
             out=[out;u3left,u3right,c3left,c3right,A3left,A3right];
            end
        end

        %%%%%%%%%%%%%%%%%%%%%%%%%%%%%%%%%%%%%%%%%%%%%%%%%%%%%%%%%%%%%%%%%%%%%%%%%%%%
        [A3,f,exit]=fsolve(@LSRStwoeqns,A30,options);
        A3left=A3(1);
        A3right=A3(2);

        c3left=sqrt(n)*A3left^(n/2);
        c3right=sqrt(k*n)*(A3right/A2bar)^(n/2);
        u3left=u1+sqrt((n*(A3left^(n+1)-A1^(n+1))*(A3left-A1))/((n+1)*A1*A3left));
        u3right=u2-sqrt((k*n*(A2^(n+1)-A3right^(n+1))*(A2-A3right))/((n+1)*A2bar^n*A2*A3right));
        RS=(A2*u2-A3right*u3right)/(A2-A3right);
        LS=(A3left*u3left-A1*u1)/(A3left-A1);

        if exit>0 && LS<0 && RS>0 && A3left>0 && A3right>0
            if flagphys==1 && LS<(u1-c1) && LS>(u3left-c3left) && RS>(u2+c2) && RS<(u3right+c3right)
                A30=A3;
            disp('LSRS')
            disp(['A_3left = ' num2str(A3left)]);
            disp(['u_3left = ' num2str(u3left)]);
            flag1=1;
            flag2=1;
            tot=tot+1;
             out=[out;u3left,u3right,c3left,c3right,A3left,A3right];
            elseif flagphys==0
                disp('LSRS')
            disp(['A_3left = ' num2str(A3left)]);
            disp(['u_3left = ' num2str(u3left)]);
            flag1=1;
            flag2=1;
            tot=tot+1;
             out=[out;u3left,u3right,c3left,c3right,A3left,A3right];
            end
        end

       %%%%%%%%%%%%%%%%%%%%%%%%%%%%%%%%%%%%%%%%%%%%%%%%%%%%%%%%%%%%%%%%%%%%%%%%%%%%
       [A3,f,exit]=fsolve(@LSRStwoeqnt,A30,options);
        A3left=A3(1);
        A3right=A3(2);

        c3left=sqrt(n)*A3left^(n/2);
        c3right=sqrt(k*n)*(A3right/A2bar)^(n/2);
        u3left=u1-sqrt((n*(A3left^(n+1)-A1^(n+1))*(A3left-A1))/((n+1)*A1*A3left));
        u3right=u2+sqrt((k*n*(A2^(n+1)-A3right^(n+1))*(A2-A3right))/((n+1)*A2bar^n*A2*A3right));
        RS=(A2*u2-A3right*u3right)/(A2-A3right);
        LS=(A3left*u3left-A1*u1)/(A3left-A1);

        if exit>0 && LS<0 && RS>0 && A3left>0 && A3right>0
            if flagphys==1 && LS<(u1-c1) && LS>(u3left-c3left) && RS>(u2+c2) && RS<(u3right+c3right)
            disp('LSRS')
            A30=A3;
```

```
            flag1=1;
            flag2=1;
            tot=tot+1;
             out=[out;u3left,u3right,c3left,c3right,A3left,A3right];
            elseif flagphys==0
                disp('LSRS')
            disp(['A_3left = ' num2str(A3left)]);
            disp(['u_3left = ' num2str(u3left)]);
            flag1=1;
            flag2=1;
            tot=tot+1;
             out=[out;u3left,u3right,c3left,c3right,A3left,A3right];
            end
        end
        %%%%
```

```
[S,f,exit]=fsolve(@LR0SRStwoeqn,A3g,options);

ks=S(1);
A12=S(2);
A21=S(3);
A22=S(4);
u12=A11*u11/A12;
c12=sqrt(ks*n)*(A12)^(n/2);

u21a=A12*u12/A21;
u21b=u12+sqrt((n*ks*(A21^(n+1)-A12^(n+1))*(A21-A12))/((n+1)*A12*A21*A2bar^n));
u21=u21a;
c21=sqrt(ks*n)*(A21/A2bar)^(n/2);
u22a=A21*u21/A22;
u22b=u2+sqrt((n*k*(A2^(n+1)-A22^(n+1))*(A2-A22))/((n+1)*A2*A22*A2bar^n));
u22=u22a;
c22=sqrt(k*n)*(A22/A2bar)^(n/2);
RS=(A2*u2-A22*u22)/(A2-A22);

if exit>0
    if flagphys==1 && u12-c12>0 && A1>A11 && u21+c21>0  && (u2+c2)<RS && (u22+c22)>RS && ks<=k && ks>=1 && A11<=A22
        A3g=S;
        disp('LR0SRS_a')
        disp(['A_3 = ' num2str(A22)]);
        disp(['u_3 = ' num2str(u22)]);
        flag1=0;
        flag2=1;
        flag3=1;
        tot=tot+1;
        out=[out;A11,u11,c11,A12,u12,c12,A21,u21,c21,A22,u22,c22,1];
    elseif flagphys==0
        A3g=S;
        disp('LR0SRS_a')
        disp(['A_3 = ' num2str(A22)]);
        disp(['u_3 = ' num2str(u22)]);
        flag1=0;
        flag2=1;
        flag3=1;
        tot=tot+1;
        out=[out;A11,u11,c11,A12,u12,c12,A21,u21,c21,A22,u22,c22,1];
    end
end
c1=sqrt(n)*A1^(n/2);

A11=(n*u1/(sqrt(n)*(n+2))+2*c1/(sqrt(n)*(n+2)))^(2/n);
u11=(n*u1)/(n+2)+(2*c1)/(n+2);
c11=(n*u1)/(n+2)+(2*c1)/(n+2);


[S,f,exit]=fsolve(@LR0SRStwoeqns,A3gs,options);

ks=S(1);
A12=S(2);
A21=S(3);
A22=S(4);
u12=A11*u11/A12;
c12=sqrt(ks*n)*(A12)^(n/2);

u21a=A12*u12/A21;
u21b=u12-sqrt((n*ks*(A21^(n+1)-A12^(n+1))*(A21-A12))/((n+1)*A12*A21*A2bar^n));
u21=u21a;
c21=sqrt(ks*n)*(A21/A2bar)^(n/2);
u22a=A21*u21/A22;
u22b=u2+sqrt((n*k*(A2^(n+1)-A22^(n+1))*(A2-A22))/((n+1)*A2*A22*A2bar^n));
u22=u22a;
c22=sqrt(k*n)*(A22/A2bar)^(n/2);

if exit>0
    if flagphys==1 && u12-c12>0 && A1>A11 && u21+c21>0  && (u2+c2)<RS && (u22+c22)>RS && ks<=k && ks>=1 && A11<=A22
        A3gs=S;
        disp('LR0SRS_b')
        disp(['A_3 = ' num2str(A22)]);
        disp(['u_3 = ' num2str(u22)]);
        flag1=0;
        flag2=1;
        flag3=1;
        tot=tot+1;
        out=[out;A11,u11,c11,A12,u12,c12,A21,u21,c21,A22,u22,c22,2];
    elseif flagphys==0
        A3gs=S;
        disp('LR0SRS_b')
        disp(['A_3 = ' num2str(A22)]);
        disp(['u_3 = ' num2str(u22)]);
        flag1=0;
        flag2=1;
        flag3=1;
        tot=tot+1;
```

```
end

c1=sqrt(n)*A1^(n/2);

A11=(n*u1/(sqrt(n)*(n+2))+2*c1/(sqrt(n)*(n+2)))^(2/n);
u11=(n*u1)/(n+2)+(2*c1)/(n+2);
c11=(n*u1)/(n+2)+(2*c1)/(n+2);
[S,f,exit]=fsolve(@LR0SRStwoeqnt,A3gt,options);

ks=S(1);
A12=S(2);
A21=S(3);
A22=S(4);
u12=A11*u11/A12;
c12=sqrt(ks*n)*(A12)^(n/2);

u21a=A12*u12/A21;
u21b=u12+sqrt((n*ks*(A21^(n+1)-A12^(n+1))*(A21-A12))/((n+1)*A12*A21*A2bar^n));
u21=u21a;
c21=sqrt(ks*n)*(A21/A2bar)^(n/2);
u22a=A21*u21/A22;
u22b=u2-sqrt((n*k*(A2^(n+1)-A22^(n+1))*(A2-A22))/((n+1)*A2*A22*A2bar^n));
u22=u22a;
c22=sqrt(k*n)*(A22/A2bar)^(n/2);

if exit>0
    if flagphys==1 && u12-c12>0 && A1>A11 && u21+c21>0  && (u2+c2)<RS && (u22+c22)>RS && ks<=k && ks>=1 && A11<=A22
        A3gt=S;
        disp('LR0SRS_c')
        disp(['A_3 = ' num2str(A22)]);
        disp(['u_3 = ' num2str(u22)]);
        flag1=0;
        flag2=1;
        flag3=1;
        tot=tot+1;
        out=[out;A11,u11,c11,A12,u12,c12,A21,u21,c21,A22,u22,c22,3];
    elseif flagphys==0
        A3gt=S;
        disp('LR0SRS_c')
        disp(['A_3 = ' num2str(A22)]);
        disp(['u_3 = ' num2str(u22)]);
        flag1=0;
        flag2=1;
        flag3=1;
        tot=tot+1;
        out=[out;A11,u11,c11,A12,u12,c12,A21,u21,c21,A22,u22,c22,3];
    end
end

c1=sqrt(n)*A1^(n/2);

A11=(n*u1/(sqrt(n)*(n+2))+2*c1/(sqrt(n)*(n+2)))^(2/n);
u11=(n*u1)/(n+2)+(2*c1)/(n+2);
c11=(n*u1)/(n+2)+(2*c1)/(n+2);
[S,f,exit]=fsolve(@LR0SRStwoeqnu,A3gu,options);

ks=S(1);
A12=S(2);
A21=S(3);
A22=S(4);
u12=A11*u11/A12;
c12=sqrt(ks*n)*(A12)^(n/2);

u21a=A12*u12/A21;
u21b=u12-sqrt((n*ks*(A21^(n+1)-A12^(n+1))*(A21-A12))/((n+1)*A12*A21*A2bar^n));
u21=u21a;
c21=sqrt(ks*n)*(A21/A2bar)^(n/2);
u22a=A21*u21/A22;
u22b=u2-sqrt((n*k*(A2^(n+1)-A22^(n+1))*(A2-A22))/((n+1)*A2*A22*A2bar^n));
u22=u22a;
c22=sqrt(k*n)*(A22/A2bar)^(n/2);
RS=(A2*u2-A22*u22)/(A2-A22);

if exit>0
    if flagphys==1 && u12-c12>0 && A1>A11 && u21+c21>0  && (u2+c2)<RS && (u22+c22)>RS && ks<=k && ks>=1 && A11<=A22
        A3gu=S;
        disp('LR0SRS_d')
        disp(['A_3 = ' num2str(A22)]);
        disp(['u_3 = ' num2str(u22)]);
        flag1=0;
        flag2=1;
        flag3=1;
        tot=tot+1;
        out=[out;A11,u11,c11,A12,u12,c12,A21,u21,c21,A22,u22,c22,4];
    elseif flagphys==0
        %A3out(i,j)=A3;u3out(i,j)=u31;A30=A3;
        A3gu=S;
```

```
            disp(['u_3 = ' num2str(u22)]);
            flag1=0;
            flag2=1;
            flag3=1;
            tot=tot+1;
            out=[out;A11,u11,c11,A12,u12,c12,A21,u21,c21,A22,u22,c22,4];
        end
    end


%%%
```

```
            tot=tot+1;
            out=[out;A11,u11,c11,A12,u12,c12,A21,u21,c21,A22,u22,c22,2];
        elseif flagphys==0
            A3gs=S;
            disp('LRSRS_a_c')
            disp(['A_3 = ' num2str(A22)]);
            disp(['u_3 = ' num2str(u22)]);
            flag1=0;
            flag2=1;
            flag3=1;
            tot=tot+1;
            out=[out;A11,u11,c11,A12,u12,c12,A21,u21,c21,A22,u22,c22,2];
        end
    end

%%%
```

```
    se1=(A2*u2-A22*u22)/(A2-A22);
    se2=(A2*u2^2+k*n/(n+1)/A2bar^n*A2^(n+1)-A22*u22^2-k*n/(n+1)/A2bar^n*A22^(n+1))/(A2*u2-A22*u22);
    [se1,se2]
   if exit>0 && sd1>0 && se1>0 && se1>sd1 && abs(sd1-sd2)<1e-4 && abs(se1-se2)<1e-4
       if flagphys==1 &&  (u22-c22) < sd1 && sd1 <(u21-c21) && A1>A12 && 0>(u1-c1) && (u2+c2)<se1 && se1<(u22+c22) && u21-c21>0
           A3gs=S;
           disp('LRSRS_b')
           disp(['A_3 = ' num2str(A22)]);
           disp(['u_3 = ' num2str(u32)]);
           flag1=0;
           flag2=1;
           flag4=1;
           tot=tot+1;
           out=[out;A12,u32,c22,A22,A21,u12,u21,c12,c21,2];
        elseif flagphys==0
           A3gs=S;
           disp('LRSRS_b')
           disp(['A_3 = ' num2str(A22)]);
           disp(['u_3 = ' num2str(u32)]);
           flag1=0;
           flag2=1;
           flag4=1;
           tot=tot+1;
           out=[out;A12,u32,c22,A22,A21,u12,u21,c12,c21,2];
       end
    end
    c1=sqrt(n)*A1^(n/2);
    c2=sqrt(k*n)*(A2/A2bar)^(n/2);
    A12=(n*u1/(sqrt(n)*(n+2))+2*c1/(sqrt(n)*(n+2)))^(2/n);
    u12=(n*u1)/(n+2)+(2*c1)/(n+2);
    c12=(n*u1)/(n+2)+(2*c1)/(n+2);

%%%%%%%%%%%%%%%%%%%%%%%%%%%%%%%%%%%%%%%%%%%%%%%%%%%%%%%%%%%%%%%%%%%%%%%%%%%%%%%
%%%%%%%%%%%%%%%%%%%%%%%%%%%%%%%%%%%%%%%%%%%%%%%%%%%%%%%%%%%%%%%%%%%%%%%%%%%%%%%

    [S,f,exit]=fsolve(@LRSRStwoeqnt,A3gt);%,options);
    A21=S(1);
    A22=S(2);
    u21=A12*u12/A21;
    c21=sqrt(k*n)*(A21/A2bar)^(n/2);
    c22=sqrt(k*n)*(A22/A2bar)^(n/2);
    u31=u21-sqrt((k*n*((A22)^(n+1)-(A21)^(n+1))*(A22-A21))/(A22*A21*(n+1)*A2bar^n));
    u32=u2+sqrt((k*n*((A2)^(n+1)-(A22)^(n+1))*(A2-A22))/(A2*A22*(n+1)*A2bar^n));

    sd1=(A22*u22-A21*u21)/(A22-A21);
    sd2=(A22*u22^2+k*n/(n+1)/A2bar^n*A22^(n+1)-A21*u21^2-k*n/(n+1)/A2bar^n*A21^(n+1))/(A22*u22-A21*u21);
    [sd1,sd2]

    se1=(A2*u2-A22*u22)/(A2-A22);
    se2=(A2*u2^2+k*n/(n+1)/A2bar^n*A2^(n+1)-A22*u22^2-k*n/(n+1)/A2bar^n*A22^(n+1))/(A2*u2-A22*u22);
    [se1,se2]

    [A2,A21,A22]
   if exit>0 && sd1>0 && se1>0 && se1>sd1 && abs(sd1-sd2)<1e-4 && abs(se1-se2)<1e-4
       if flagphys==1 && (u22-c22) < sd1 && sd1 <(u21-c21) && A1>A12 && 0>(u1-c1) && (u2+c2)<se1 && se1<(u22+c22) && u21-c21>0
           A3gt=S;
           disp('LRSRS_c')
           disp(['A_3 = ' num2str(A22)]);
           disp(['u_3 = ' num2str(u32)]);
           flag1=0;
           flag2=1;
           flag4=1;
           tot=tot+1;
           out=[out;A12,u32,c22,A22,A21,u12,u21,c12,c21,3];
        elseif flagphys==0
           A3gt=S;
           disp('LRSRS_c')
           disp(['A_3 = ' num2str(A22)]);
           disp(['u_3 = ' num2str(u32)]);
           flag1=0;
           flag2=1;
           flag4=1;
           tot=tot+1;
           out=[out;A12,u32,c22,A22,A21,u12,u21,c12,c21,3];
       end
    end
    c1=sqrt(n)*A1^(n/2);

    A12=(n*u1/(sqrt(n)*(n+2))+2*c1/(sqrt(n)*(n+2)))^(2/n);
    u12=(n*u1)/(n+2)+(2*c1)/(n+2);
    c12=(n*u1)/(n+2)+(2*c1)/(n+2);

%%%%%%%%%%%%%%%%%%%%%%%%%%%%%%%%%%%%%%%%%%%%%%%%%%%%%%%%%%%%%%%%%%%%%%%%%%%%%%%
%%%%%%%%%%%%%%%%%%%%%%%%%%%%%%%%%%%%%%%%%%%%%%%%%%%%%%%%%%%%%%%%%%%%%%%%%%%%%%%

    [S,f,exit]=fsolve(@LRSRStwoeqnu,A3gu);%,options);
```

```
    u21=A12*u12/A21;
    c21=sqrt(k*n)*(A21/A2bar)^(n/2);
    c22=sqrt(k*n)*(A22/A2bar)^(n/2);
    u31=u21-sqrt((k*n*((A22)^(n+1)-(A21)^(n+1))*(A22-A21))/(A22*A21*(n+1)*A2bar^n));
    u32=u2-sqrt((k*n*((A2)^(n+1)-(A22)^(n+1))*(A2-A22))/(A2*A22*(n+1)*A2bar^n));
    u22=u32;
    sd1=(A22*u22-A21*u21)/(A22-A21);
    sd2=(A22*u22^2+k*n/(n+1)/A2bar^n*A22^(n+1)-A21*u21^2-k*n/(n+1)/A2bar^n*A21^(n+1))/(A22*u22-A21*u21);
    [sd1,sd2]

    se1=(A2*u2-A22*u22)/(A2-A22);
    se2=(A2*u2^2+k*n/(n+1)/A2bar^n*A2^(n+1)-A22*u22^2-k*n/(n+1)/A2bar^n*A22^(n+1))/(A2*u2-A22*u22);
    [se1,se2]
   if exit>0 && sd1>0 && se1>0 && se1>sd1 && abs(sd1-sd2)<1e-4 && abs(se1-se2)<1e-4
        if flagphys==1 && (u22-c22) < sd1 && sd1 <(u21-c21) && A1>A12 && 0>(u1-c1) && (u2+c2)<se1 && se1<(u22+c22) && u21-c21>0
            A3gu=S;
            disp('LRSRS_d')
            disp(['A_3 = ' num2str(A22)]);
            disp(['u_3 = ' num2str(u32)]);
            flag1=0;
            flag2=1;
            flag4=1;
            tot=tot+1;
            out=[out;A12,u32,c22,A22,A21,u12,u21,c12,c21,4];
         elseif flagphys==0
            A3gu=S;
            disp('LRSRS_d')
            disp(['A_3 = ' num2str(A22)]);
            disp(['u_3 = ' num2str(u32)]);
            flag1=0;
            flag2=1;
            flag4=1;
            tot=tot+1;
            out=[out;A12,u32,c22,A22,A21,u12,u21,c12,c21,4];
        end
   end

%%%
```

```
    [S,f,exit]=fsolve(@LRSRRtwoeqns,A3gs);
    A21=S(1);
    A22=S(2);

    u21=A12*u12/A21;
    c21=sqrt(k*n)*(A21/A2bar)^(n/2);
    u31=u21-sqrt((k*n*((A22)^(n+1)-(A21)^(n+1))*(A22-A21))/(A22*A21*(n+1)*A2bar^n));
    u32=u2+(2*sqrt(k*n))/(n*(A2bar)^(n/2))*((A22)^(n/2)-(A2)^(n/2));

    u22=u32;
    c22=sqrt(k*n)*(A22/A2bar)^(n/2);

    sd1=(A22*u22-A21*u21)/(A22-A21);
    sd2=(A22*u22^2+k*n/(n+1)/A2bar^n*A22^(n+1)-A21*u21^2-k*n/(n+1)/A2bar^n*A21^(n+1))/(A22*u22-A21*u21);
    [sd1,sd2]
    if exit>0 && sd1>0 && abs(sd1-sd2)<1e-4 && abs(u31-u32)<1e-4
        if flagphys==1  && (((n+2)*u32)/2-n*u2/2+c2)<(u2+c2) && abs(imag(A22))==0
            A3gs=S;
            disp('LRSRR_b')
            disp(['A_3 = ' num2str(A22)]);
            disp(['u_3 = ' num2str(u32)]);
            flag1=0;
            flag2=1;
            flag4=1;
            tot=tot+1;
            out=[out;A12,u32,c22,A22,A21,u12,u21,c12,c21,2];
        elseif flagphys==0
            A3gs=S;
            disp('LRSRR_b')
            disp(['A_3 = ' num2str(A22)]);
            disp(['u_3 = ' num2str(u32)]);
            flag1=0;
            flag2=1;
            flag4=1;
            tot=tot+1;
            out=[out;A12,u32,c22,A22,A21,u12,u21,c12,c21,2];
        end
    end


        disp(['solver has converged'])

        [A1,A2,u1,u2]

        if flag1==0 && flag2==0 % left rarefaction, right rarefaction
            col='b.';
        elseif flag1==1 && flag2==1 % left shock, right shock
            col='r.';
        elseif flag1==0 && flag2==1 % left rarefaction, right shock
            col='g.';
        elseif flag1==1 && flag2==0 % left shock, right rarefaction
            col='c.';
        elseif flag1==0 && flag2==1 && flag3==1 % left rarefaction, zero speed shock, right shock
            col='m.';
        elseif flag1==0 && flag2==0 && flag3==1 % left rarefaction, zero speed shock, right rarefaction
            col='y.';
        elseif flag1==0 && flag2==1 && flag4==1 % left rarefaction, resonant shock, right shock
            col='k.';
        elseif flag1==0 && flag2==0 && flag4==1 % left rarefaction, resonant shock, right rarefaction
            col='k--.';
        end

        figure(1)
        hold on
        plot(A2,u2,col)
        xlabel('$\mathcal{A}_2$','fontsize',14,'interpreter','latex')
        ylabel('$\mathcal{U}_2$','fontsize',14,'interpreter','latex')


    end
end

% Definition of the different functions and return the values evaluated at
% the input vector AS
 function v=LRRStwoeqn(AS)
        A3left=AS(1);
        A3right=AS(2);

        u3left=u1+(2*sqrt(n)/n)*(A1^(n/2)-A3left^(n/2));
        u3right=u2+sqrt((k*n*(A2^(n+1)-A3right^(n+1))*(A2-A3right))/((n+1)*A2bar^n*A2*A3right));

        v(1,1)=u3left*A3left-u3right*A3right;
        v(2,1)=Pe1bar+(A3left^n-1)+1/2*u3left^2-Pe2bar-k*((A3right/A2bar)^n-1)-1/2*u3right^2;

    end
```

```
        A3right=AS(2);

        u3left=u1+(2*sqrt(n)/n)*(A1^(n/2)-A3left^(n/2));
        u3right=u2-sqrt((k*n*(A2^(n+1)-A3right^(n+1))*(A2-A3right))/((n+1)*A2bar^n*A2*A3right));

        v(1,1)=u3left*A3left-u3right*A3right;
        v(2,1)=Pe1bar+(A3left^n-1)+1/2*u3left^2-Pe2bar-k*((A3right/A2bar)^n-1)-1/2*u3right^2;

     end

    function v=LSRRtwoeqn(AS)
        A3left=AS(1);
        A3right=AS(2);

        u3left=u1+sqrt((n*(A3left^(n+1)-A1^(n+1))*(A3left-A1))/((n+1)*A1*A3left));
        u3right=u2+2*sqrt(k/(n*A2bar^n))*(A3right^(n/2)-A2^(n/2));

        v(1,1)=u3left*A3left-u3right*A3right;
        v(2,1)=Pe1bar+(A3left^n-1)+1/2*u3left^2-Pe2bar-k*((A3right/A2bar)^n-1)-1/2*u3right^2;

    end

    function v=LSRRtwoeqns(AS)
        A3left=AS(1);
        A3right=AS(2);

        u3left=u1-sqrt((n*(A3left^(n+1)-A1^(n+1))*(A3left-A1))/((n+1)*A1*A3left));
        u3right=u2+2*sqrt(k/(n*A2bar^n))*(A3right^(n/2)-A2^(n/2));

        v(1,1)=u3left*A3left-u3right*A3right;
        v(2,1)=Pe1bar+(A3left^n-1)+1/2*u3left^2-Pe2bar-k*((A3right/A2bar)^n-1)-1/2*u3right^2;

    end
function  v=LSRStwoeqn(AS)

        A3left=AS(1);
        A3right=AS(2);

        u3left=u1+sqrt((n*(A3left^(n+1)-A1^(n+1))*(A3left-A1))/((n+1)*A1*A3left));
        u3right=u2+sqrt((k*n*(A2^(n+1)-A3right^(n+1))*(A2-A3right))/((n+1)*A2bar^n*A2*A3right));

        v(1,1)=u3left*A3left-u3right*A3right;
        v(2,1)=Pe1bar+(A3left^n-1)+1/2*u3left^2-Pe2bar-k*((A3right/A2bar)^n-1)-1/2*u3right^2;
    end

    function  v=LSRStwoeqns(AS)

       A3left=AS(1);
        A3right=AS(2);

        u3left=u1+sqrt((n*(A3left^(n+1)-A1^(n+1))*(A3left-A1))/((n+1)*A1*A3left));
        u3right=u2-sqrt((k*n*(A2^(n+1)-A3right^(n+1))*(A2-A3right))/((n+1)*A2bar^n*A2*A3right));

        v(1,1)=u3left*A3left-u3right*A3right;
        v(2,1)=Pe1bar+(A3left^n-1)+1/2*u3left^2-Pe2bar-k*((A3right/A2bar)^n-1)-1/2*u3right^2;
    end

    function  v=LSRStwoeqnt(AS)

       A3left=AS(1);
        A3right=AS(2);

        u3left=u1-sqrt((n*(A3left^(n+1)-A1^(n+1))*(A3left-A1))/((n+1)*A1*A3left));
        u3right=u2+sqrt((k*n*(A2^(n+1)-A3right^(n+1))*(A2-A3right))/((n+1)*A2bar^n*A2*A3right));

        v(1,1)=u3left*A3left-u3right*A3right;
        v(2,1)=Pe1bar+(A3left^n-1)+1/2*u3left^2-Pe2bar-k*((A3right/A2bar)^n-1)-1/2*u3right^2;
    end

    function  v=LSRStwoeqnu(AS)

        A3left=AS(1);
        A3right=AS(2);

        u3left=u1-sqrt((n*(A3left^(n+1)-A1^(n+1))*(A3left-A1))/((n+1)*A1*A3left));
        u3right=u2-sqrt((k*n*(A2^(n+1)-A3right^(n+1))*(A2-A3right))/((n+1)*A2bar^n*A2*A3right));

        v(1,1)=u3left*A3left-u3right*A3right;
        v(2,1)=Pe1bar+(A3left^n-1)+1/2*u3left^2-Pe2bar-k*((A3right/A2bar)^n-1)-1/2*u3right^2;

    end
 function v=LRRRtwoeqns(AS)
        A3left=AS(1);
        A3right=AS(2);

        u3left=u1+(2/sqrt(n))*(A1^(n/2)-A3left^(n/2));
        u3right=u2+2*sqrt(k/(n*A2bar^n))*(A3right^(n/2)-A2^(n/2));
```

```
        v(2,1)=Pe1bar+(A3left^n-1)+1/2*u3left^2-Pe2bar-k*((A3right/A2bar)^n-1)-1/2*u3right^2;

 end
function v=LR0SRStwoeqn(S)
        ks=S(1);
        A12=S(2);
        A21=S(3);
        A22=S(4);
        u12=A11*u11/A12;
        u21a=A12*u12/A21;
        u21b=u12+sqrt((n*ks*(A21^(n+1)-A12^(n+1))*(A21-A12))/((n+1)*A12*A21*A2bar^n));
        u21=u21a;
        u22a=A21*u21/A22;
        u22b=u2+sqrt((n*k*(A2^(n+1)-A22^(n+1))*(A2-A22))/((n+1)*A2*A22*A2bar^n));
        u22=u22a;
        v(1,1)=1/2*u11^2+(A11^n-1)-1/2*u12^2-ks*(A12^n-1);
        v(2,1)=u21a-u21b;
        v(3,1)=u22a-u22b;
        v(4,1)=Pe1bar+1/2*u21^2+ks*(A21^n-1)-Pe2bar-1/2*u22^2-k*(A22^n-1);
    end
function v=LR0SRStwoeqns(S)
        ks=S(1);
        A12=S(2);
        A21=S(3);
        A22=S(4);
        u12=A11*u11/A12;
        u21a=A12*u12/A21;
        u21b=u12-sqrt((n*ks*(A21^(n+1)-A12^(n+1))*(A21-A12))/((n+1)*A12*A21*A2bar^n));
        u21=u21a;
        u22a=A21*u21/A22;
        u22b=u2+sqrt((n*k*(A2^(n+1)-A22^(n+1))*(A2-A22))/((n+1)*A2*A22*A2bar^n));
        u22=u22a;
        v(1,1)=1/2*u11^2+(A11^n-1)-1/2*u12^2-ks*(A12^n-1);
        v(2,1)=u21a-u21b;
        v(3,1)=u22a-u22b;
        v(4,1)=Pe1bar+1/2*u21^2+ks*(A21^n-1)-Pe2bar-1/2*u22^2-k*(A22^n-1);
    end

    function v=LR0SRStwoeqnt(S)
        ks=S(1);
        A12=S(2);
        A21=S(3);
        A22=S(4);
        u12=A11*u11/A12;
        u21a=A12*u12/A21;
        u21b=u12+sqrt((n*ks*(A21^(n+1)-A12^(n+1))*(A21-A12))/((n+1)*A12*A21*A2bar^n));
        u21=u21a;
        u22a=A21*u21/A22;
        u22b=u2-sqrt((n*k*(A2^(n+1)-A22^(n+1))*(A2-A22))/((n+1)*A2*A22*A2bar^n));
        u22=u22a;
        v(1,1)=1/2*u11^2+(A11^n-1)-1/2*u12^2-ks*(A12^n-1);
        v(2,1)=u21a-u21b;
        v(3,1)=u22a-u22b;
        v(4,1)=Pe1bar+1/2*u21^2+ks*(A21^n-1)-Pe2bar-1/2*u22^2-k*(A22^n-1);
    end
    function v=LR0SRStwoeqnu(S)
        ks=S(1);
        A12=S(2);
        A21=S(3);
        A22=S(4);
        u12=A11*u11/A12;
        u21a=A12*u12/A21;
        u21b=u12-sqrt((n*ks*(A21^(n+1)-A12^(n+1))*(A21-A12))/((n+1)*A12*A21*A2bar^n));
        u21=u21a;
        u22a=A21*u21/A22;
        u22b=u2-sqrt((n*k*(A2^(n+1)-A22^(n+1))*(A2-A22))/((n+1)*A2*A22*A2bar^n));
        u22=u22a;
        v(1,1)=1/2*u11^2+(A11^n-1)-1/2*u12^2-ks*(A12^n-1);
        v(2,1)=u21a-u21b;
        v(3,1)=u22a-u22b;
        v(4,1)=Pe1bar+1/2*u21^2+ks*(A21^n-1)-Pe2bar-1/2*u22^2-k*(A22^n-1);
    end
function v=LR0SRRtwoeqn(S)
        ks=S(1);
        A12=S(2);
        A21=S(3);
        A22=S(4);
        u12=A11*u11/A12;
        u21a=A12*u12/A21;
        u21b=u12+sqrt((n*ks*(A21^(n+1)-A12^(n+1))*(A21-A12))/((n+1)*A12*A21*A2bar^n));
        u21=u21a;
        u22a=A21*u21/A22;
        u22b=u2+(2*sqrt(k*n))/(n*(A2bar)^(n/2))*((A22)^(n/2)-(A2)^(n/2));
        u22=u22a;
        v(1,1)=1/2*u11^2+(A11^n-1)-1/2*u12^2-ks*(A12^n-1);
        v(2,1)=u21a-u21b;
        v(3,1)=u22a-u22b;
```

```
function v=LR0SRRtwoeqns(S)
        ks=S(1);
        A12=S(2);
        A21=S(3);
        A22=S(4);
        u12=A11*u11/A12;
        u21a=A12*u12/A21;
        u21b=u12-sqrt((n*ks*(A21^(n+1)-A12^(n+1))*(A21-A12))/((n+1)*A12*A21*A2bar^n));
        u21=u21a;
        u22a=A21*u21/A22;
        u22b=u2+(2*sqrt(k*n))/(n*(A2bar)^(n/2))*((A22)^(n/2)-(A2)^(n/2));
        u22=u22a;
        v(1,1)=1/2*u11^2+(A11^n-1)-1/2*u12^2-ks*(A12^n-1);
        v(2,1)=u21a-u21b;
        v(3,1)=u22a-u22b;
        v(4,1)=Pe1bar+1/2*u21^2+ks*(A21^n-1)-Pe2bar-1/2*u22^2-k*(A22^n-1);
end

function v=LRSRStwoeqn(S)
        A21=S(1);
        A22=S(2);
        u21=A12*u12/A21;
        u31=u21+sqrt((k*n*((A22)^(n+1)-(A21)^(n+1))*(A22-A21))/(A22*A21*(n+1)*A2bar^n));
        u32=u2+sqrt((k*n*((A2)^(n+1)-(A22)^(n+1))*(A2-A22))/(A2*A22*(n+1)*A2bar^n));

        v(1,1)=u31-u32;

        v(2,1)=(A21)^2*Pe1bar+(A21)^2*(A12^n-1)+1/2*(A21*u12)^2-(A21)^2*Pe2bar-k*(((A21)^(n+2))/(A2bar^n)-(A21)^2)-1/2*(A12*u12)^2;

    end
    function v=LRSRStwoeqns(S)
        A21=S(1);
        A22=S(2);
        u21=A12*u12/A21;
        u31=u21+sqrt((k*n*((A22)^(n+1)-(A21)^(n+1))*(A22-A21))/(A22*A21*(n+1)*A2bar^n));
        u32=u2-sqrt((k*n*((A2)^(n+1)-(A22)^(n+1))*(A2-A22))/(A2*A22*(n+1)*A2bar^n));
        v(1,1)=u31-u32;

        v(2,1)=(A21)^2*Pe1bar+(A21)^2*(A12^n-1)+1/2*(A21*u12)^2-(A21)^2*Pe2bar-k*(((A21)^(n+2))/(A2bar^n)-(A21)^2)-1/2*(A12*u12)^2;

    end

    function v=LRSRStwoeqnt(S)
        A21=S(1);
        A22=S(2);
        u21=A12*u12/A21;
        u31=u21-sqrt((k*n*((A22)^(n+1)-(A21)^(n+1))*(A22-A21))/(A22*A21*(n+1)*A2bar^n));
        u32=u2+sqrt((k*n*((A2)^(n+1)-(A22)^(n+1))*(A2-A22))/(A2*A22*(n+1)*A2bar^n));

        v(1,1)=u31-u32;

        v(2,1)=(A21)^2*Pe1bar+(A21)^2*(A12^n-1)+1/2*(A21*u12)^2-(A21)^2*Pe2bar-k*(((A21)^(n+2))/(A2bar^n)-(A21)^2)-1/2*(A12*u12)^2;
    end
    function v=LRSRStwoeqnu(S)
        A21=S(1);
        A22=S(2);
        u21=A12*u12/A21;
        u31=u21-sqrt((k*n*((A22)^(n+1)-(A21)^(n+1))*(A22-A21))/(A22*A21*(n+1)*A2bar^n));
        u32=u2-sqrt((k*n*((A2)^(n+1)-(A22)^(n+1))*(A2-A22))/(A2*A22*(n+1)*A2bar^n));

        v(1,1)=u31-u32;

        v(2,1)=(A21)^2*Pe1bar+(A21)^2*(A12^n-1)+1/2*(A21*u12)^2-(A21)^2*Pe2bar-k*(((A21)^(n+2))/(A2bar^n)-(A21)^2)-1/2*(A12*u12)^2;

    end
function v=LRSRRtwoeqn(S)
        A21=S(1);
        A22=S(2);
        u21=A12*u12/A21;
        u31=u21+sqrt((k*n*((A22)^(n+1)-(A21)^(n+1))*(A22-A21))/(A22*A21*(n+1)*A2bar^n));
        u32=u2+(2*sqrt(k*n))/(n*(A2bar)^(n/2))*((A22)^(n/2)-(A2)^(n/2));
        v(1,1)=u31-u32;
        v(2,1)=(A21)^2*Pe1bar+(A21)^2*(A12^n-1)+1/2*(A21*u12)^2-(A21)^2*Pe2bar-k*(((A21)^(n+2))/(A2bar^n)-(A21)^2)-1/2*(A12*u12)^2;
    end

    function v=LRSRRtwoeqns(S)
        A21=S(1);
        A22=S(2);
        u21=A12*u12/A21;
        u31=u21-sqrt((k*n*((A22)^(n+1)-(A21)^(n+1))*(A22-A21))/(A22*A21*(n+1)*A2bar^n));
        u32=u2+(2*sqrt(k*n))/(n*(A2bar)^(n/2))*((A22)^(n/2)-(A2)^(n/2));
        v(1,1)=u31-u32;
        v(2,1)=(A21)^2*Pe1bar+(A21)^2*(A12^n-1)+1/2*(A21*u12)^2-(A21)^2*Pe2bar-k*(((A21)^(n+2))/(A2bar^n)-(A21)^2)-1/2*(A12*u12)^2;
    end

end
```

A.3 MATLAB code for Chapter 4

```
% Sample of MATLAB code for classical and resonant solutions in chapter
% four
function Chapter_four

clc
clear
close all
format long
figure(1)
box on
A1=1.0;
% Row vector for A2
A2s=linspace(0.01,2,20);

n=10;
% Row vector for u2
u2s=linspace(-2,2,20);
u1=0;

% Tolerance for the function and solution value
options=optimset('TolX',1e-10,'TolFun',1e-10);

% Loop for iteration of A2 and u2: A2 is in reverse
for j=length(A2s):-1:1

    A2=A2s(j);
 out=[];
    for i=1:length(u2s)

        if i==1 && j==length(A2s)
            A3guess=0.5*(A2+A1);
        elseif i==1
            A3guess=A3out(1,j+1);
        elseif j<length(A2s)
            A3guess=A3out(i,j+1);
        end

        u2=u2s(i);
        clear flag1 flag2 flag3 flag4
        tot=0;
%%%
```

```
    [A3,f,exit]=fsolve(@LRRStwoeqns,A30,options);
    A3left=A3(1);
    A3right=A3(2);

    c3left=sqrt(n)*A3left^(n/2);
    c3right=sqrt(k*n)*(A3right/A2bar)^(n/2);
    u3right=u2-sqrt((k*n*(A2^(n+1)-A3right^(n+1))*(A2-A3right))/((n+1)*A2bar^n*A2*A3right));
    u3left=u1+(2*sqrt(n)/n)*(A1^(n/2)-A3left^(n/2));

    RS=((A2*u2)-(A3right*u3right))/(A2-A3right);

    xrl=(n+2)*u3left/2 -c1-n*u1/2;

     if exit>0 && RS>0  && A3left>0 && A3right>0
        if flagphys==1 &&  xrl<0 && xrl>(u1-c1) && RS>(u2+c2) && RS<(u3right+c3right)
            A30=A3;
            disp('LRRS_b')
            disp(['A_3left = ' num2str(A3left)]);
            disp(['u_3left = ' num2str(u3left)]);
            flag1=0;
            flag2=1;
            tot=tot+1;
            out=[out;u3left,u3right,c3left,c3right,A3left,A3right];
        elseif flagphys==0
            disp('LRRS_b')
            disp(['A_3left = ' num2str(A3left)]);
            disp(['u_3left = ' num2str(u3left)]);
            flag1=0;
            flag2=1;
            tot=tot+1;
            out=[out;u3left,u3right,c3left,c3right,A3left,A3right];
        end
    end

%%%
```

```
            disp(['u_3left = ' num2str(u3left)]);
            flag1=1;
            flag2=1;
            tot=tot+1;
            out=[out;u3left,u3right,c3left,c3right,A3left,A3right];
        elseif flagphys==0
            disp('LSRR')
            disp(['A_3left = ' num2str(A3left)]);
            disp(['u_3left = ' num2str(u3left)]);
            flag1=1;
            flag2=1;
            tot=tot+1;
            out=[out;u3left,u3right,c3left,c3right,A3left,A3right];
        end
    end

%%%%%%%%%%%%%%%%%%%%%%%%%%%%%%%%%%%%%%%%%%%%%%%%%%%%%%%%%%%%%%%%%%%%%%%%%%%%%%%
% left shock, right shock

[A3,f,exit]=fsolve(@LSRStwoeqn,A30,options);
    A3left=A3(1);
    A3right=A3(2);

    c3left=sqrt(n)*A3left^(n/2);
    c3right=sqrt(k*n)*(A3right/A2bar)^(n/2);
    u3left=u1+sqrt((n*(A3left^(n+1)-A1^(n+1))*(A3left-A1))/((n+1)*A1*A3left));
    u3right=u2+sqrt((k*n*(A2^(n+1)-A3right^(n+1))*(A2-A3right))/((n+1)*A2bar^n*A2*A3right));
    RS=(A2*u2-A3right*u3right)/(A2-A3right);
    LS=(A3left*u3left-A1*u1)/(A3left-A1);

    if exit>0 && LS<0 && RS>0 && A3left>0 && A3right>0
        A30=A3;
        if flagphys==1 && LS<(u1-c1) && LS>(u3left-c3left) && RS>(u2+c2) && RS<(u3right+c3right)
            disp('LSRS')
            disp(['A_3left = ' num2str(A3left)]);
            disp(['u_3left = ' num2str(u3left)]);
            flag1=1;
            flag2=1;
            tot=tot+1;
            out=[out;u3left,u3right,c3left,c3right,A3left,A3right];
        elseif flagphys==0
            disp('LSRS')
            disp(['A_3left = ' num2str(A3left)]);
            disp(['u_3left = ' num2str(u3left)]);
            flag1=1;
            flag2=1;
            tot=tot+1;
            out=[out;u3left,u3right,c3left,c3right,A3left,A3right];
        end
    end

    %%%%%%%%%%%%%%%%%%%%%%%%%%%%%%%%%%%%%%%%%%%%%%%%%%%%%%%%%%%%%%%%%%%%%%%%%%%%%%%
    [A3,f,exit]=fsolve(@LSRStwoeqns,A30,options);
    A3left=A3(1);
    A3right=A3(2);

    c3left=sqrt(n)*A3left^(n/2);
    c3right=sqrt(k*n)*(A3right/A2bar)^(n/2);
    u3left=u1+sqrt((n*(A3left^(n+1)-A1^(n+1))*(A3left-A1))/((n+1)*A1*A3left));
    u3right=u2-sqrt((k*n*(A2^(n+1)-A3right^(n+1))*(A2-A3right))/((n+1)*A2bar^n*A2*A3right));
    RS=(A2*u2-A3right*u3right)/(A2-A3right);
    LS=(A3left*u3left-A1*u1)/(A3left-A1);

    if exit>0 && LS<0 && RS>0 && A3left>0 && A3right>0
        if flagphys==1 && LS<(u1-c1) && LS>(u3left-c3left) && RS>(u2+c2) && RS<(u3right+c3right)
            disp('LSRS')
            disp(['A_3left = ' num2str(A3left)]);
            disp(['u_3left = ' num2str(u3left)]);
            flag1=1;
            flag2=1;
            tot=tot+1;
            out=[out;u3left,u3right,c3left,c3right,A3left,A3right];
        elseif flagphys==0
            disp('LSRS')
            disp(['A_3left = ' num2str(A3left)]);
            disp(['u_3left = ' num2str(u3left)]);
            flag1=1;
            flag2=1;
            tot=tot+1;
            out=[out;u3left,u3right,c3left,c3right,A3left,A3right];
        end
    end

    %%%%%%%%%%%%%%%%%%%%%%%%%%%%%%%%%%%%%%%%%%%%%%%%%%%%%%%%%%%%%%%%%%%%%%%%%%%%%%%
    [A3,f,exit]=fsolve(@LSRStwoeqns,A30,options);
```

```
    A3right=A3(2);

    c3left=sqrt(n)*A3left^(n/2);
    c3right=sqrt(k*n)*(A3right/A2bar)^(n/2);
    u3left=u1-sqrt((n*(A3left^(n+1)-A1^(n+1))*(A3left-A1))/((n+1)*A1*A3left));
    u3right=u2+sqrt((k*n*(A2^(n+1)-A3right^(n+1))*(A2-A3right))/((n+1)*A2bar^n*A2*A3right));
    RS=(A2*u2-A3right*u3right)/(A2-A3right);
    LS=(A3left*u3left-A1*u1)/(A3left-A1);

    if exit>0 && LS<0 && RS>0 && A3left>0 && A3right>0
        A30=A3;
        if flagphys==1 && LS<(u1-c1) && LS>(u3left-c3left) && RS>(u2+c2) && RS<(u3right+c3right)
            disp('LSRS')
            disp(['A_3left = ' num2str(A3left)]);
            disp(['u_3left = ' num2str(u3left)]);
            flag1=1;
            flag2=1;
            tot=tot+1;
            out=[out;u3left,u3right,c3left,c3right,A3left,A3right];
        elseif flagphys==0
            disp('LSRS')
            disp(['A_3left = ' num2str(A3left)]);
            disp(['u_3left = ' num2str(u3left)]);
            flag1=1;
            flag2=1;
            tot=tot+1;
            out=[out;u3left,u3right,c3left,c3right,A3left,A3right];
        end
    end
    %%%%%%%%%%%%%%%%%%%%%%%%%%%%%%%%%%%%%%%%%%%%%%%%%%%%%%%%%%%%%%%%%%%%%%%%%%%%%%%
    [A3,f,exit]=fsolve(@LSRStwoeqnu,A30,options);
    A3left=A3(1);
    A3right=A3(2);

    c3left=sqrt(n)*A3left^(n/2);
    c3right=sqrt(k*n)*(A3right/A2bar)^(n/2);
    u3left=u1-sqrt((n*(A3left^(n+1)-A1^(n+1))*(A3left-A1))/((n+1)*A1*A3left));
    u3right=u2-sqrt((k*n*(A2^(n+1)-A3right^(n+1))*(A2-A3right))/((n+1)*A2bar^n*A2*A3right));

    RS=(A2*u2-A3right*u3right)/(A2-A3right);
    LS=(A3left*u3left-A1*u1)/(A3left-A1);

    if exit>0 && LS<0 && RS>0 && A3left>0 && A3right>0
        if flagphys==1 && LS<(u1-c1) && LS>(u3left-c3left) && RS>(u2+c2) && RS<(u3right+c3right)
            disp('LSRS')
            disp(['A_3left = ' num2str(A3left)]);
            disp(['u_3left = ' num2str(u3left)]);
            flag1=1;
            flag2=1;
            tot=tot+1;
            out=[out;u3left,u3right,c3left,c3right,A3left,A3right];
        elseif flagphys==0
            disp('LSRS')
            disp(['A_3left = ' num2str(A3left)]);
            disp(['u_3left = ' num2str(u3left)]);
            flag1=1;
            flag2=1;
            tot=tot+1;
            out=[out;u3left,u3right,c3left,c3right,A3left,A3right];
        end
    end

%%%%%%%%%%%%%%%%%%%
```

```
            disp('LRRR')
            disp(['A_3left = ' num2str(A3left)]);
            disp(['u_3left = ' num2str(u3left)]);
            flag1=0;
            flag2=0;
            tot=tot+1;
            out=[out;u3left,u3right,c3left,c3right,A3left,A3right];
        end
    end

%%%
```

```
if exit>0
    if flagphys==1 && A11<=A22 && u12-c12>0 && u21+c21>0 && A1>A11 && (u2+c2)<RS && (u22+c22)>RS && rs<=2 && rs>=1 && ks>=1 && ks<=1.1
        A3gs=S;
        disp('JLR0SRS_b')
        disp(['A_3 = ' num2str(A22)]);
        disp(['u_3 = ' num2str(u22)]);
        flag1=0;
        flag2=1;
        flat3=0;
        tot=tot+1;
        out=[out;A11,u11,c11,A12,u12,c12,A21,u21,c21,A22,u22,c22,ks,rs,s,2];
    elseif flagphys==0
        A3gs=S;
        disp('JLR0SRS_b')
        disp(['A_3 = ' num2str(A22)]);
        disp(['u_3 = ' num2str(u22)]);
        flag1=0;
        flag2=1;
        flat3=0;
        tot=tot+1;
        out=[out;A11,u11,c11,A12,u12,c12,A21,u21,c21,A22,u22,c22,ks,rs,s,2];
    end
end

c1=sqrt(n)*A1^(n/2);

A11=(n*u1/(sqrt(n)*(n+2))+2*c1/(sqrt(n)*(n+2)))^(2/n);
u11=(n*u1)/(n+2)+(2*c1)/(n+2);
c11=(n*u1)/(n+2)+(2*c1)/(n+2);
[S,f,exit]=fsolve(@JLR0SRStwoeqnt,A3gt,options);

s=S(1);
A12=S(2);
A21=S(3);
A22=S(4);
ks=1+s*(k-1);
rs=1+s*(2-1);
u12=1/rs*A11*u11/A12;
c12=sqrt(ks*n)*(A12)^(n/2);

u21a=A12*u12/A21;
u21b=u12+sqrt((n*ks*(A21^(n+1)-A12^(n+1))*(A21-A12))/((n+1)*A12*A21*A2bar^n));
u21=u21a;
c21=sqrt(ks*n)*(A21/A2bar)^(n/2);
u22a=rs/2*A21*u21/A22;
u22b=u2-sqrt((n*k*(A2^(n+1)-A22^(n+1))*(A2-A22))/((n+1)*A2*A22*A2bar^n));
u22=u22a;
c22=sqrt(k*n)*(A22/A2bar)^(n/2);

if exit>0
    if flagphys==1 && A11<=A22 && u12-c12>0 && u21+c21>0 && A1>A11 && (u2+c2)<RS && (u22+c22)>RS && rs<=2 && rs>=1 && ks>=1 && ks<=1.1
        A3gt=S;
        disp('JLR0SRS_c')
        disp(['A_3 = ' num2str(A22)]);
        disp(['u_3 = ' num2str(u22)]);
        flag1=0;
        flag2=1;
        flat3=0;
        tot=tot+1;
        out=[out;A11,u11,c11,A12,u12,c12,A21,u21,c21,A22,u22,c22,ks,rs,s,3];
    elseif flagphys==0
        A3gt=S;
        disp('JLR0SRS_c')
        disp(['A_3 = ' num2str(A22)]);
        disp(['u_3 = ' num2str(u22)]);
        flag1=0;
        flag2=1;
        flat3=0;
        tot=tot+1;
        out=[out;A11,u11,c11,A12,u12,c12,A21,u21,c21,A22,u22,c22,ks,rs,s,3];
    end
end

c1=sqrt(n)*A1^(n/2);

A11=(n*u1/(sqrt(n)*(n+2))+2*c1/(sqrt(n)*(n+2)))^(2/n);
u11=(n*u1)/(n+2)+(2*c1)/(n+2);
c11=(n*u1)/(n+2)+(2*c1)/(n+2);
[S,f,exit]=fsolve(@JLR0SRStwoeqnu,A3gu,options);

s=S(1);
A12=S(2);
A21=S(3);
A22=S(4);
```

```
    u12=1/rs*A11*u11/A12;
    c12=sqrt(ks*n)*(A12)^(n/2);

    u21a=A12*u12/A21;
    u21b=u12-sqrt((n*ks*(A21^(n+1)-A12^(n+1))*(A21-A12))/((n+1)*A12*A21*A2bar^n));
    u21=u21a;
    c21=sqrt(ks*n)*(A21/A2bar)^(n/2);
    u22a=rs/2*A21*u21/A22;
    u22b=u2-sqrt((n*k*(A2^(n+1)-A22^(n+1))*(A2-A22))/((n+1)*A2*A22*A2bar^n));
    u22=u22a;
    c22=sqrt(k*n)*(A22/A2bar)^(n/2);
    RS=(A2*u2-A22*u22)/(A2-A22);

    if exit>0
        if flagphys==1 && A11<=A22 && u12-c12>0 && u21+c21>0 && A1>A11 && (u2+c2)<RS && (u22+c22)>RS && rs<=2 && rs>=1 && ks>=1 && ks<=1.1

            A3gu=S;
            disp('JLR0SRS_d')
            disp(['A_3 = ' num2str(A22)]);
            disp(['u_3 = ' num2str(u22)]);
            flag1=0;
            flag2=1;
            flat3=0;
            tot=tot+1;
            out=[out;A11,u11,c11,A12,u12,c12,A21,u21,c21,A22,u22,c22,ks,rs,s,4];
        elseif flagphys==0
            A3gu=S;
            disp('JLR0SRS_d')
            disp(['A_3 = ' num2str(A22)]);
            disp(['u_3 = ' num2str(u22)]);
            flag1=0;
            flag2=1;
            flat3=0;
            tot=tot+1;
            out=[out;A11,u11,c11,A12,u12,c12,A21,u21,c21,A22,u22,c22,ks,rs,s,4];
        end
    end

%%%
```

```
    end
    c1=sqrt(n)*A1^(n/2);

    A11=(n*u1/(sqrt(n)*(n+2))+2*c1/(sqrt(n)*(n+2)))^(2/n);
    u11=(n*u1)/(n+2)+(2*c1)/(n+2);
    c11=(n*u1)/(n+2)+(2*c1)/(n+2);
    [S,f,exit]=fsolve(@JLR0SRRtwoeqns,A3gs,options);%,options);
    s=S(1);
    A12=S(2);
    A21=S(3);
    A22=S(4);
    ks=1+s*(k-1);
    rs=1+s*(2-1);
    u12=1/rs*A11*u11/A12;
    c12=sqrt(ks*n)*(A12)^(n/2);

    u21a=A12*u12/A21;
    u21b=u12-sqrt((n*ks*(A21^(n+1)-A12^(n+1))*(A21-A12))/((n+1)*A12*A21*A2bar^n));
    u21=u21a;
    c21=sqrt(ks*n)*(A21/A2bar)^(n/2);
    u22a=rs/2*A21*u21/A22;
    u22b=u2+(2*sqrt(k*n))/(n*(A2bar)^(n/2))*((A22)^(n/2)-(A2)^(n/2));
    u22=u22a;
    c22=sqrt(k*n)*(A22/A2bar)^(n/2);

    if exit>0
        if flagphys==1 && (u1-c1)<0 && (u11-c11)>(u1-c1) && (u2+c2)>(u22+c22) && ks>=1 && ks<=1.1 && rs>=1 && rs<=2
            A3gs=S;
            disp('JLR0SRR_b')
            disp(['A_3 = ' num2str(A22)]);
            disp(['u_3 = ' num2str(u22)]);
            flag1=0;
            flag2=0;
            flat3=0;
            tot=tot+1;
            out=[out;A11,u11,c11,A12,u12,c12,A21,u21,c21,A22,u22,c22,2];
        elseif flagphys==0
            A3gs=S;
            disp('JLR0SRR_b')
            disp(['A_3 = ' num2str(A22)]);
            disp(['u_3 = ' num2str(u22)]);
            flag1=0;
            flag2=0;
            flat3=0;
            tot=tot+1;
            out=[out;A11,u11,c11,A12,u12,c12,A21,u21,c21,A22,u22,c22,2];
        end
    end

%%%
```

```
        A3g=S;
        disp('JLRSRS_a')
        disp(['A_3 = ' num2str(A22)]);
        disp(['u_3 = ' num2str(u32)]);
        flag1=0;
        flag2=1;
        flat4=0;
        tot=tot+1;
        out=[out;A12,u32,c22,A22,A21,u12,u21,c12,c21,1];
    end
end

c1=sqrt(n)*A1^(n/2);

A12=(n*u1/(sqrt(n)*(n+2))+2*c1/(sqrt(n)*(n+2)))^(2/n);
u12=(n*u1)/(n+2)+(2*c1)/(n+2);
c12=(n*u1)/(n+2)+(2*c1)/(n+2);

[S,f,exit]=fsolve(@JLRSRStwoeqns,A3gs);%,options);
A21=S(1);
A22=S(2);
u21=A12*u12/(2*A21);
c21=sqrt(k*n)*(A21/A2bar)^(n/2);
u31=u21+sqrt((k*n*((A22)^(n+1)-(A21)^(n+1))*(A22-A21))/(A22*A21*(n+1)*A2bar^n));
u32=u2-sqrt((k*n*((A2)^(n+1)-(A22)^(n+1))*(A2-A22))/(A2*A22*(n+1)*A2bar^n));
u22=u32;

c22=sqrt(k*n)*(A22/A2bar)^(n/2);
sd1=(A22*u22-A21*u21)/(A22-A21);
sd2=(A22*u22^2+k*n/(n+1)/A2bar^n*A22^(n+1)-A21*u21^2-k*n/(n+1)/A2bar^n*A21^(n+1))/(A22*u22-A21*u21);
[sd1,sd2]

se1=(A2*u2-A22*u22)/(A2-A22);
se2=(A2*u2^2+k*n/(n+1)/A2bar^n*A2^(n+1)-A22*u22^2-k*n/(n+1)/A2bar^n*A22^(n+1))/(A2*u2-A22*u22);
[se1,se2]
if exit>0 && abs(sd1-sd2)<1e-4 && abs(se1-se2)<1e-4
    if flagphys==1 && (u12-c12)>(u1-c1) && 0>(u1-c1) && A1>A12 && (u22+c22)<se1 && (u2+c2)<se1 && A2<A22 && (u21-c21)>sd1 && (u22-c22)<s
        A3gs=S;
        disp('JLRSRS_b')
        disp(['A_3 = ' num2str(A22)]);
        disp(['u_3 = ' num2str(u32)]);
        flag1=0;
        flag2=1;
        flat4=0;
        tot=tot+1;
        out=[out;A12,u32,c22,A22,A21,u12,u21,c12,c21,2];
    elseif flagphys==0
        A3gs=S;
        disp('JLRSRS_b')
        disp(['A_3 = ' num2str(A22)]);
        disp(['u_3 = ' num2str(u32)]);
        flag1=0;
        flag2=1;
        flat4=0;
        tot=tot+1;
        out=[out;A12,u32,c22,A22,A21,u12,u21,c12,c21,2];
    end
end
c1=sqrt(n)*A1^(n/2);
c2=sqrt(k*n)*(A2/A2bar)^(n/2);
A12=(n*u1/(sqrt(n)*(n+2))+2*c1/(sqrt(n)*(n+2)))^(2/n);
u12=(n*u1)/(n+2)+(2*c1)/(n+2);
c12=(n*u1)/(n+2)+(2*c1)/(n+2);
[S,f,exit]=fsolve(@JLRSRStwoeqnt,A3gt);%,options);
A21=S(1);
A22=S(2);
u21=A12*u12/(2*A21);
c21=sqrt(k*n)*(A21/A2bar)^(n/2);
u31=u21-sqrt((k*n*((A22)^(n+1)-(A21)^(n+1))*(A22-A21))/(A22*A21*(n+1)*A2bar^n));
u32=u2+sqrt((k*n*((A2)^(n+1)-(A22)^(n+1))*(A2-A22))/(A2*A22*(n+1)*A2bar^n));
u22=u32;

c22=sqrt(k*n)*(A22/A2bar)^(n/2);

sd1=(A22*u22-A21*u21)/(A22-A21);
sd2=(A22*u22^2+k*n/(n+1)/A2bar^n*A22^(n+1)-A21*u21^2-k*n/(n+1)/A2bar^n*A21^(n+1))/(A22*u22-A21*u21);
[sd1,sd2]

se1=(A2*u2-A22*u22)/(A2-A22);
se2=(A2*u2^2+k*n/(n+1)/A2bar^n*A2^(n+1)-A22*u22^2-k*n/(n+1)/A2bar^n*A22^(n+1))/(A2*u2-A22*u22);
[se1,se2]

[A2,A21,A22]
if exit>0 && abs(sd1-sd2)<1e-4 && abs(se1-se2)<1e-4
```

```
                disp('JLRSRS_c')
                disp(['A_3 = ' num2str(A22)]);
                disp(['u_3 = ' num2str(u32)]);
                flag1=0;
                flag2=1;
                flat4=0;
                tot=tot+1;
                out=[out;A12,u32,c22,A22,A21,u12,u21,c12,c21,3];
            elseif flagphys==0
                A3gt=S;
                disp('JLRSRS_c')
                disp(['A_3 = ' num2str(A22)]);
                disp(['u_3 = ' num2str(u32)]);
                flag1=0;
                flag2=1;
                flat4=0;
                tot=tot+1;
                out=[out;A12,u32,c22,A22,A21,u12,u21,c12,c21,3];
            end
        end
        c1=sqrt(n)*A1^(n/2);

        A12=(n*u1/(sqrt(n)*(n+2))+2*c1/(sqrt(n)*(n+2)))^(2/n);
        u12=(n*u1)/(n+2)+(2*c1)/(n+2);
        c12=(n*u1)/(n+2)+(2*c1)/(n+2);
        [S,f,exit]=fsolve(@JLRSRStwoeqnu,A3gu);%,options);
        A21=S(1);
        A22=S(2);
        u21=A12*u12/(2*A21);
        c21=sqrt(k*n)*(A21/A2bar)^(n/2);
        u31=u21-sqrt((k*n*((A22)^(n+1)-(A21)^(n+1))*(A22-A21))/(A22*A21*(n+1)*A2bar^n));
        u32=u2-sqrt((k*n*((A2)^(n+1)-(A22)^(n+1))*(A2-A22))/(A2*A22*(n+1)*A2bar^n));
        u22=u32;

        c22=sqrt(k*n)*(A22/A2bar)^(n/2);
        sd1=(A22*u22-A21*u21)/(A22-A21);
        sd2=(A22*u22^2+k*n/(n+1)/A2bar^n*A22^(n+1)-A21*u21^2-k*n/(n+1)/A2bar^n*A21^(n+1))/(A22*u22-A21*u21);
        [sd1,sd2]

        se1=(A2*u2-A22*u22)/(A2-A22);
        se2=(A2*u2^2+k*n/(n+1)/A2bar^n*A2^(n+1)-A22*u22^2-k*n/(n+1)/A2bar^n*A22^(n+1))/(A2*u2-A22*u22);
        [se1,se2]
        if exit>0 && abs(sd1-sd2)<1e-4 && abs(se1-se2)<1e-4
            if flagphys==1 && (u12-c12)>(u1-c1) && 0>(u1-c1) && A1>A12 && (u22+c22)>se1 && (u2+c2)<se1 && A2<A22 && (u21-c21)>sd1 && (u22-c22)<s
                A3gu=S;
                disp('JLRSRS_d')
                disp(['A_3 = ' num2str(A22)]);
                disp(['u_3 = ' num2str(u32)]);
                flag1=0;
                flag2=1;
                flat4=0;
                tot=tot+1;
                out=[out;A12,u32,c22,A22,A21,u12,u21,c12,c21,4];
            elseif flagphys==0
                A3gu=S;
                disp('JLRSRS_d')
                disp(['A_3 = ' num2str(A22)]);
                disp(['u_3 = ' num2str(u32)]);
                flag1=0;
                flag2=1;
                flag4=0;
                tot=tot+1;
                out=[out;A12,u32,c22,A22,A21,u12,u21,c12,c21,4];
            end
        end

%%%
```

```
(u21-c21)
if exit>0 && sd1>0 && abs(sd1-sd2)<1e-4
    if flagphys==1 && (u22-c22)<sd1 && (u21-c21)>sd1 && (u2+c2)>0 && A2>A22
        A3g=S;
        disp('JLRSRR_a')
        disp(['A_3 = ' num2str(A22)]);
        disp(['u_3 = ' num2str(u32)]);
        flag1=0;
        flag2=0;
        flag4=0;
        tot=tot+1;
        out=[out;A12,u22,c22,A22,A21,u12,u21,c12,c21,1];
    elseif flagphys==0
        A3g=S;
        disp('JLRSRR_a')
        disp(['A_3 = ' num2str(A22)]);
        disp(['u_3 = ' num2str(u32)]);
        flag1=0;
        flag2=0;
        flag4=0;
        tot=tot+1;
        out=[out;A12,u22,c22,A22,A21,u12,u21,c12,c21,1];
    end
end

c1=sqrt(n)*A1^(n/2);

A12=(n*u1/(sqrt(n)*(n+2))+2*c1/(sqrt(n)*(n+2)))^(2/n);
u12=(n*u1)/(n+2)+(2*c1)/(n+2);
c12=(n*u1)/(n+2)+(2*c1)/(n+2);

[S,f,exit]=fsolve(@JLRSRRtwoeqns,A3gs);%,options);
A21=S(1);
A22=S(2);
u31=u2+(2*sqrt(k*n))/(n*(A2bar)^(n/2))*((A22)^(n/2)-(A2)^(n/2));
u22=u31;
c22=sqrt(k*n)*(A22/A2bar)^(n/2);
u21=A12*u12/(2*A21);
c21=sqrt(k*n)*(A21/A2bar)^(n/2);
u32=u21-sqrt((k*n*((A22)^(n+1)-(A21)^(n+1))*(A22-A21))/(A22*A21*(n+1)*A2bar^n));

sd1=(A22*u22-A21*u21)/(A22-A21);
sd2=(A22*u22^2+(k*n/((n+1)/A2bar^n))*A22^(n+1)-A21*u21^2-(k*n/((n+1)/A2bar^n))*A21^(n+1))/(A22*u22-A21*u21);
[sd1,sd2]
(u22-c22)
(u21-c21)
if exit>0 && sd1>0 && abs(sd1-sd2)<1e-4
    if flagphys==1 && (u22-c22)<sd1 && (u21-c21)>sd1 && (u2+c2)>0 && A2>A22
        A3gs=S;
        disp('JLRSRR_b')
        disp(['A_3 = ' num2str(A22)]);
        disp(['u_3 = ' num2str(u32)]);
        flag1=0;
        flag2=0;
        flag4=0;
        tot=tot+1;
        out=[out;A12,u22,c22,A22,A21,u12,u21,c12,c21,2];
    elseif flagphys==0
        A3gs=S;
        disp('JLRSRR_b')
        disp(['A_3 = ' num2str(A22)]);
        disp(['u_3 = ' num2str(u32)]);
        flag1=0;
        flag2=0;
        flag4=0;
        tot=tot+1;
        out=[out;A12,u22,c22,A22,A21,u12,u21,c12,c21,2];
    end
end


    disp(['solver has converged'])

    [A1,A2,u1,u2]

    if flag1==0 && flag2==0 % left rarefaction, right rarefaction
        col='b.';
    elseif flag1==1 && flag2==1 % left shock, right shock
        col='r.';
    elseif flag1==0 && flag2==1 % left rarefaction, right shock
        col='g.';
    elseif flag1==1 && flag2==0 % left shock, right rarefaction
        col='c.';
    elseif flag1==0 && flag2==1 && flag3==0 % left rarefaction, zero speed shock, right shock
```

```
            col='y.';
        elseif flag1==0 && flag2==1 && flag4==0 % left rarefaction, resonant shock, right shock
            col='k.';
        elseif flag1==0 && flag2==0 && flag4==0 % left rarefaction, resonant shock, right rarefaction
            col='k--.';
        end

        figure(1)
        hold on
        plot(A2,u2,col)
        xlabel('$\mathcal{A}_2$','fontsize',14,'interpreter','latex')
        ylabel('$\mathcal{U}_2$','fontsize',14,'interpreter','latex')


    end
end

% Definition of the different functions and return the values evaluated at
% the input vector AS
 function v=LRRStwoeqn(AS)
        A3left=AS(1);
        A3right=AS(2);

        u3left=u1+(2*sqrt(n)/n)*(A1^(n/2)-A3left^(n/2));
        u3right=u2+sqrt((k*n*(A2^(n+1)-A3right^(n+1))*(A2-A3right))/((n+1)*A2bar^n*A2*A3right));

        v(1,1)=u3left*A3left-2*u3right*A3right;
        v(2,1)=Pe1bar+(A3left^n-1)+1/2*u3left^2-Pe2bar-k*((A3right/A2bar)^n-1)-1/2*u3right^2;

    end

    function v=LRRStwoeqns(AS)
        A3left=AS(1);
        A3right=AS(2);

        u3left=u1+(2*sqrt(n)/n)*(A1^(n/2)-A3left^(n/2));
        u3right=u2-sqrt((k*n*(A2^(n+1)-A3right^(n+1))*(A2-A3right))/((n+1)*A2bar^n*A2*A3right));

        v(1,1)=u3left*A3left-2*u3right*A3right;
        v(2,1)=Pe1bar+(A3left^n-1)+1/2*u3left^2-Pe2bar-k*((A3right/A2bar)^n-1)-1/2*u3right^2;

    end

    function  v=LSRRtwoeqn(AS)

        A3left=AS(1);
        A3right=AS(2);

        u3left=u1+sqrt((n*(A3left^(n+1)-A1^(n+1))*(A3left-A1))/((n+1)*A1*A3left));
        u3right=u2+2*sqrt(k/(n*A2bar^n))*(A3right^(n/2)-A2^(n/2));

        v(1,1)=u3left*A3left-2*u3right*A3right;
        v(2,1)=Pe1bar+(A3left^n-1)+1/2*u3left^2-Pe2bar-k*((A3right/A2bar)^n-1)-1/2*u3right^2;
    end

    function  v=LSRRtwoeqns(AS)

        A3left=AS(1);
        A3right=AS(2);

        u3left=u1-sqrt((n*(A3left^(n+1)-A1^(n+1))*(A3left-A1))/((n+1)*A1*A3left));
        u3right=u2+2*sqrt(k/(n*A2bar^n))*(A3right^(n/2)-A2^(n/2));

        v(1,1)=u3left*A3left-2*u3right*A3right;
        v(2,1)=Pe1bar+(A3left^n-1)+1/2*u3left^2-Pe2bar-k*((A3right/A2bar)^n-1)-1/2*u3right^2;
    end
function  v=LSRStwoeqn(AS)

        A3left=AS(1);
        A3right=AS(2);

        u3left=u1+sqrt((n*(A3left^(n+1)-A1^(n+1))*(A3left-A1))/((n+1)*A1*A3left));
        u3right=u2+sqrt((k*n*(A2^(n+1)-A3right^(n+1))*(A2-A3right))/((n+1)*A2bar^n*A2*A3right));

        v(1,1)=u3left*A3left-2*u3right*A3right;
        v(2,1)=Pe1bar+(A3left^n-1)+1/2*u3left^2-Pe2bar-k*((A3right/A2bar)^n-1)-1/2*u3right^2;
    end

    function  v=LSRStwoeqns(AS)

        A3left=AS(1);
        A3right=AS(2);

        u3left=u1+sqrt((n*(A3left^(n+1)-A1^(n+1))*(A3left-A1))/((n+1)*A1*A3left));
```

```
        v(1,1)=u3left*A3left-2*u3right*A3right;
        v(2,1)=Pe1bar+(A3left^n-1)+1/2*u3left^2-Pe2bar-k*((A3right/A2bar)^n-1)-1/2*u3right^2;
    end

    function  v=LSRStwoeqnt(AS)

        A3left=AS(1);
        A3right=AS(2);

        u3left=u1-sqrt((n*(A3left^(n+1)-A1^(n+1))*(A3left-A1))/((n+1)*A1*A3left));
        u3right=u2+sqrt((k*n*(A2^(n+1)-A3right^(n+1))*(A2-A3right))/((n+1)*A2bar^n*A2*A3right));

        v(1,1)=u3left*A3left-2*u3right*A3right;
        v(2,1)=Pe1bar+(A3left^n-1)+1/2*u3left^2-Pe2bar-k*((A3right/A2bar)^n-1)-1/2*u3right^2;
    end

    function  v=LSRStwoeqnu(AS)

        A3left=AS(1);
        A3right=AS(2);

        u3left=u1-sqrt((n*(A3left^(n+1)-A1^(n+1))*(A3left-A1))/((n+1)*A1*A3left));
        u3right=u2-sqrt((k*n*(A2^(n+1)-A3right^(n+1))*(A2-A3right))/((n+1)*A2bar^n*A2*A3right));

        v(1,1)=u3left*A3left-2*u3right*A3right;
        v(2,1)=Pe1bar+(A3left^n-1)+1/2*u3left^2-Pe2bar-k*((A3right/A2bar)^n-1)-1/2*u3right^2;

    end
  function v=LRRRtwoeqns(AS)
        A3left=AS(1);
        A3right=AS(2);

        u3left=u1+(2/sqrt(n))*(A1^(n/2)-A3left^(n/2));
        u3right=u2+2*sqrt(k/(n*A2bar^n))*(A3right^(n/2)-A2^(n/2));

        v(1,1)=u3left*A3left-2*u3right*A3right;
        v(2,1)=Pe1bar+(A3left^n-1)+1/2*u3left^2-Pe2bar-k*((A3right/A2bar)^n-1)-1/2*u3right^2;

    end
function v=JLR0SRStwoeqn(S)
        s=S(1);
        A12=S(2);
        A21=S(3);
        A22=S(4);
        ks=1+s*(k-1);
        rs=1+s*(2-1);
        u12=1/rs*A11*u11/A12;
        u21a=A12*u12/A21;
        u21b=u12+sqrt((n*ks*(A21^(n+1)-A12^(n+1))*(A21-A12))/((n+1)*A12*A21*A2bar^n));
        u21=u21a;
        u22a=rs/2*A21*u21/A22;
        u22b=u2+sqrt((n*k*(A2^(n+1)-A22^(n+1))*(A2-A22))/((n+1)*A2*A22*A2bar^n));
        u22=u22a;
        v(1,1)=1/2*u11^2+(A11^n-1)-1/2*u12^2-ks*(A12^n-1);
        v(2,1)=u21a-u21b;
        v(3,1)=u22a-u22b;
        v(4,1)=Pe1bar+1/2*u21^2+ks*(A21^n-1)-Pe2bar-1/2*u22^2-k*(A22^n-1);
    end
    function v=JLR0SRStwoeqns(S)
        s=S(1);
        A12=S(2);
        A21=S(3);
        A22=S(4);
       ks=1+s*(k-1);
        rs=1+s*(2-1);
        u12=1/rs*A11*u11/A12;
        u21a=A12*u12/A21;
        u21b=u12-sqrt((n*ks*(A21^(n+1)-A12^(n+1))*(A21-A12))/((n+1)*A12*A21*A2bar^n));
        u21=u21a;
        u22a=rs/2*A21*u21/A22;
        u22b=u2+sqrt((n*k*(A2^(n+1)-A22^(n+1))*(A2-A22))/((n+1)*A2*A22*A2bar^n));
        u22=u22a;
        v(1,1)=1/2*u11^2+(A11^n-1)-1/2*u12^2-ks*(A12^n-1);
        v(2,1)=u21a-u21b;
        v(3,1)=u22a-u22b;
        v(4,1)=Pe1bar+1/2*u21^2+ks*(A21^n-1)-Pe2bar-1/2*u22^2-k*(A22^n-1);
    end

    function v=JLR0SRStwoeqnt(S)
        s=S(1);
        A12=S(2);
        A21=S(3);
        A22=S(4);
        ks=1+s*(k-1);
```

```
        u21a=A12*u12/A21;
        u21b=u12+sqrt((n*ks*(A21^(n+1)-A12^(n+1))*(A21-A12))/((n+1)*A12*A21*A2bar^n));
        u21=u21a;
        u22a=rs/2*A21*u21/A22;
        u22b=u2-sqrt((n*k*(A2^(n+1)-A22^(n+1))*(A2-A22))/((n+1)*A2*A22*A2bar^n));
        u22=u22a;
        v(1,1)=1/2*u11^2+(A11^n-1)-1/2*u12^2-ks*(A12^n-1);
        v(2,1)=u21a-u21b;
        v(3,1)=u22a-u22b;
        v(4,1)=Pe1bar+1/2*u21^2+ks*(A21^n-1)-Pe2bar-1/2*u22^2-k*(A22^n-1);
    end
    function v=JLR0SRStwoeqnu(S)
        s=S(1);
        A12=S(2);
        A21=S(3);
        A22=S(4);
        ks=1+s*(k-1);
        rs=1+s*(2-1);
        u12=1/rs*A11*u11/A12;
        u21a=A12*u12/A21;
        u21b=u12-sqrt((n*ks*(A21^(n+1)-A12^(n+1))*(A21-A12))/((n+1)*A12*A21*A2bar^n));
        u21=u21a;
        u22a=rs/2*A21*u21/A22;
        u22b=u2-sqrt((n*k*(A2^(n+1)-A22^(n+1))*(A2-A22))/((n+1)*A2*A22*A2bar^n));
        u22=u22a;
        v(1,1)=1/2*u11^2+(A11^n-1)-1/2*u12^2-ks*(A12^n-1);
        v(2,1)=u21a-u21b;
        v(3,1)=u22a-u22b;
        v(4,1)=Pe1bar+1/2*u21^2+ks*(A21^n-1)-Pe2bar-1/2*u22^2-k*(A22^n-1);
    end
function v=JLR0SRRtwoeqn(S)
        s=S(1);
        A12=S(2);
        A21=S(3);
        A22=S(4);
        ks=1+s*(k-1);
        rs=1+s*(2-1);
        u12=1/rs*A11*u11/A12;
        u21a=A12*u12/A21;
        u21b=u12+sqrt((n*ks*(A21^(n+1)-A12^(n+1))*(A21-A12))/((n+1)*A12*A21*A2bar^n));
        u21=u21a;
        u22a=rs/2*A21*u21/A22;
        u22b=u2+(2*sqrt(k*n))/(n*(A2bar)^(n/2))*((A22)^(n/2)-(A2)^(n/2));
        u22=u22a;
        v(1,1)=1/2*u11^2+(A11^n-1)-1/2*u12^2-ks*(A12^n-1);
        v(2,1)=u21a-u21b;
        v(3,1)=u22a-u22b;
        v(4,1)=Pe1bar+1/2*u21^2+ks*(A21^n-1)-Pe2bar-1/2*u22^2-k*(A22^n-1);
    end
    function v=JLR0SRRtwoeqns(S)
        s=S(1);
        A12=S(2);
        A21=S(3);
        A22=S(4);
        ks=1+s*(k-1);
        rs=1+s*(2-1);
        u12=1/rs*A11*u11/A12;
        u21a=A12*u12/A21;
        u21b=u12-sqrt((n*ks*(A21^(n+1)-A12^(n+1))*(A21-A12))/((n+1)*A12*A21*A2bar^n));
        u21=u21a;
        u22a=rs/2*A21*u21/A22;
        u22b=u2+(2*sqrt(k*n))/(n*(A2bar)^(n/2))*((A22)^(n/2)-(A2)^(n/2));
        u22=u22a;
        v(1,1)=1/2*u11^2+(A11^n-1)-1/2*u12^2-ks*(A12^n-1);
        v(2,1)=u21a-u21b;
        v(3,1)=u22a-u22b;
        v(4,1)=Pe1bar+1/2*u21^2+ks*(A21^n-1)-Pe2bar-1/2*u22^2-k*(A22^n-1);
    end


 function v=JLRSRStwoeqn(S)
        A21=S(1);
        A22=S(2);
        u21=A12*u12/(2*A21);
        u31=u21+sqrt((k*n*((A22)^(n+1)-(A21)^(n+1))*(A22-A21))/(A22*A21*(n+1)*A2bar^n));
        %u31=(A21*A22*u21*(n+1)+sqrt(n*A21*A22*(A21-A22)*(n+1)*(A21*(A21/A2bar)^n-A22*(A22/A2bar)^n)))/(A21*A22*(n+1));
        u32=u2+sqrt((k*n*((A2)^(n+1)-(A22)^(n+1))*(A2-A22))/(A2*A22*(n+1)*A2bar^n));
        %u32=(A22*A2*u2*(n+1)+sqrt(n*A22*A2*(A22-A2)*(n+1)*(A22*(A22/A2bar)^n-A2*(A2/A2bar)^n)))/(A22*A2*(n+1));
        v(1,1)=u31-u32;

        v(2,1)=Pe1bar+(A12^n-1)+1/2*(u12)^2-Pe2bar-k*(((A21)/(A2bar))^n-1)-1/2*(u21)^2;

    end
    function v=JLRSRStwoeqns(S)
```

```
        u21=A12*u12/(2*A21);
        u31=u21+sqrt((k*n*((A22)^(n+1)-(A21)^(n+1))*(A22-A21))/(A22*A21*(n+1)*A2bar^n));
        u32=u2-sqrt((k*n*((A2)^(n+1)-(A22)^(n+1))*(A2-A22))/(A2*A22*(n+1)*A2bar^n));
        v(1,1)=u31-u32;

        v(2,1)=Pe1bar+(A12^n-1)+1/2*(u12)^2-Pe2bar-k*(((A21)/(A2bar))^n-1)-1/2*(u21)^2;

    end

    function v=JLRSRStwoeqnt(S)
        A21=S(1);
        A22=S(2);
        u21=A12*u12/(2*A21);
        u31=u21-sqrt((k*n*((A22)^(n+1)-(A21)^(n+1))*(A22-A21))/(A22*A21*(n+1)*A2bar^n));
        u32=u2+sqrt((k*n*((A2)^(n+1)-(A22)^(n+1))*(A2-A22))/(A2*A22*(n+1)*A2bar^n));
        v(1,1)=u31-u32;

        v(2,1)=Pe1bar+(A12^n-1)+1/2*(u12)^2-Pe2bar-k*(((A21)/(A2bar))^n-1)-1/2*(u21)^2;

    end
    function v=JLRSRStwoeqnu(S)
        A21=S(1);
        A22=S(2);
        u21=A12*u12/(2*A21);
        u31=u21-sqrt((k*n*((A22)^(n+1)-(A21)^(n+1))*(A22-A21))/(A22*A21*(n+1)*A2bar^n));
        u32=u2-sqrt((k*n*((A2)^(n+1)-(A22)^(n+1))*(A2-A22))/(A2*A22*(n+1)*A2bar^n));
        v(1,1)=u31-u32;

        v(2,1)=Pe1bar+(A12^n-1)+1/2*(u12)^2-Pe2bar-k*(((A21)/(A2bar))^n-1)-1/2*(u21)^2;

    end
function v=JLRSRRtwoeqn(S)
        A21=S(1);
        A22=S(2);
        u21=A12*u12/(2*A21);
        u31=u21+sqrt((k*n*((A22)^(n+1)-(A21)^(n+1))*(A22-A21))/(A22*A21*(n+1)*A2bar^n));
        u32=u2+(2*sqrt(k*n))/(n*(A2bar)^(n/2))*((A22)^(n/2)-(A2)^(n/2));
        v(1,1)=u31-u32;

        v(2,1)=Pe1bar+(A12^n-1)+1/2*(u12)^2-Pe2bar-k*(((A21)/(A2bar))^n-1)-1/2*(u21)^2;
    end
    function v=JLRSRRtwoeqns(S)
        A21=S(1);
        A22=S(2);
        u21=A12*u12/(2*A21);
        u31=u21-sqrt((k*n*((A22)^(n+1)-(A21)^(n+1))*(A22-A21))/(A22*A21*(n+1)*A2bar^n));
        u32=u2+(2*sqrt(k*n))/(n*(A2bar)^(n/2))*((A22)^(n/2)-(A2)^(n/2));
        v(1,1)=u31-u32;

        v(2,1)=Pe1bar+(A12^n-1)+1/2*(u12)^2-Pe2bar-k*(((A21)/(A2bar))^n-1)-1/2*(u21)^2;
```

Bibliography

[1] Forrester, J. V., Dick, A. D., McMenamin, P. G., Roberts, F., & Pearlman, E. (2016). *Anatomy of the eye and orbit.* The eye, 2.

[2] Ranchod, T. M., Goldenberg, D. T., & Trese, M. T. (2010). *The Physiological Consequences of Vitreous Composition.* Elsevier.

[3] T. Kita, Y. Hata, T. Ishibashi, (2010) *Encyclopedia of the Eye.* Academic Press, 2010, Pages 251-256,

[4] Miller, D., & Benedek, G. B. (1973). *Intraocular light scattering: theory and clinical application.* URL="https://cir.nii.ac.jp/crid/1130000796602976000"

[5] Levin, L. A., Nilsson, S. F., Ver Hoeve, J., Wu, S., Kaufman, P. L., & Alm, A. (2011). *Adler's Physiology of the Eye E-Book: Expert Consult-Online and Print.* Elsevier Health Sciences.

[6] Yoo, S. J., Ryu, S., Kim, S., Han, H. S., & Moon, C. (2017). *Reference module in neuroscience and biobehavioral psychology.* Elsevier.

[7] Pugh, D. G., & Baird, N. N. (2011). *Sheep & Goat medicine-E-book.* Elsevier Health Sciences.

[8] Miller, P. E. (2008). *The glaucomas.* Slatter's fundamentals of veterinary ophthalmology, 230.

[9] Singh, S., & Dass, R. (1960). *The central artery of the retina II. A study of its distribution and anastomoses.* The British Journal of Ophthalmology, 44(5), 280.

[10] Britannica, The Editors of Encyclopaedia. *"iris". Encyclopedia Britannica, 6 Oct. 2023,* https://www.britannica.com/science/iris-eye. Accessed 29 November 2023.

[11] Cassani, S. (2016). *Blood circulation and aqueous humor flow in the eye: multi-scale modeling and clinical applications.* Purdue University.

[12] Masland, R. H. (2012). *The neuronal organization of the retina.* Neuron, 76(2), 266-280.

[13] Kaur, C., Foulds, W. S., & Ling, E. A. (2008). *Hypoxia-ischemia and retinal ganglion cell damage.* Clinical Ophthalmology, 2(4), 879-889.

[14] Farjo, A. A., Brumm, M. V., Soong, H. K., & Hood, C. T. (2018). *Corneal anatomy, physiology, and wound healing.* Ophthalmology E-Book, 155.

[15] Singh, S., and Dass, R. (1960). *The central artery of the retina I. Origin and course.* The British journal of ophthalmology, 44(4), 193.

[16] Spelman, T. A., and Stewart, P. S. (2020). *Shock wave propagation along the central retinal blood vessels.* Proceedings of the Royal Society A, 476(2234), 20190269.

[17] Hayreh, S. S. (1963). *The central artery of the retina its role in the blood supply of the optic nerve.* The British journal of ophthalmology, 47(11), 651.

[18] Abel, R. (2014). *The Eye Care Revolution: Prevent And Reverse Common Vision Problems, Revised And Updated.* Kensington Books.

[19] Kaur, B., & Taylor, D. (1990). *Retinal haemorrhages.* Archives of disease in childhood, 65(12), 1369.

[20] Nadarasa, J., Deck, C., Meyer, F., Bourdet, N., Raul, J. S., and Willinger, R. (2018). *Development of a finite-element eye model to investigate retinal hemorrhages in shaken baby syndrome.* Biomechanics and modeling in mechanobiology, 17(2), 517-530.

[21] Richards, P. G., Bertocci, G. E., Bonshek, R. E., Giangrande, P. L., Gregson, R. M., Jaspan, T., and Wade, A. (2006). *Shaken baby syndrome.* Archives of disease in childhood, 91(3), 205-206.

[22] Tuerkheimer, D. (2014). *Flawed convictions:" shaken baby syndrome" and the inertia of injustice.* Oxford University Press.

[23] Gilkes, M. T., and Mann, T. (1967). *Fundi of battered babies.* The Lancet, 290(7513), 468-469.

[24] Binenbaum, G., Rogers, D. L., Forbes, B. J., Levin, A. V., Clark, S. A., Christian, C. W., & Avery, R. (2013). *Patterns of retinal hemorrhage associated with increased intracranial pressure in children.* Pediatrics, 132(2), e430-e434.

[25] Binenbaum, G., Chen, W., Huang, J., Ying, G. S., & Forbes, B. J. (2016). *The natural history of retinal hemorrhage in pediatric head trauma.* Journal of American Association for Pediatric Ophthalmology and Strabismus, 20(2), 131-135.

[26] Duhaime, A. C., Gennarelli, T. A., Thibault, L. E., Bruce, D. A., Margulies, S. S., and Wiser, R. (1987). *The shaken baby syndrome: a clinical, pathological, and biomechanical study.* Journal of neurosurgery, 66(3), 409-415.

[27] Gabaeff, S. C. (2011). *Challenging the pathophysiologic connection between subdural hematoma, retinal hemorrhage and shaken baby syndrome.* Western journal of emergency medicine, 12(2), 144.

[28] Gabaeff, S. C. (2013). *Investigating the possibility and probability of perinatal subdural hematoma progressing to chronic subdural hematoma, with and without complications, in neonates, and its potential relationship to the misdiagnosis of abusive head trauma.* Legal Medicine, 15(4), 177-192.

[29] Ommaya, A. K., Hirsch, A. E., Flamm, E. S., & Mahone, R. H. (1966). *Cerebral concussion in the monkey: an experimental model.* Science, 153(3732), 211-212.

[30] King, W. J., MacKay, M., & Sirnick, A. (2003). *Shaken baby syndrome in Canada: clinical characteristics and outcomes of hospital cases.* Cmaj, 168(2), 155-159.

[31] Bandak, F. A. (2005). *Shaken baby syndrome: a biomechanics analysis of injury mechanisms.* Forensic Science International, 151(1), 71-79.

[32] Gabaeff, S. C. (2016). *Exploring the controversy in child abuse pediatrics and false accusations of abuse.* Legal Medicine, 18, 90-97.

[33] Greenwald, M. J., Weiss, A., Oesterle, C. S., and Friendly, D. S. (1986). *Traumatic retinoschisis in battered babies.* Ophthalmology, 93(5), 618-625.

[34] Clarke, M. P. (2009). *Vitreoretinal traction is a major factor in causing the haemorrhagic retinopathy of abusive head injury?–No.* Eye, 23(9), 1761-1763.

[35] Massicotte, S. J., Folberg, R., Torczynski, E., Gilliland, M. G. F., and Luckenbach, M. W. (1991). *Vitreoretinal traction and perimacular retinal folds in the eyes of deliberately traumatized children.* Ophthalmology, 98(7), 1124-1127.

[36] Green, M. A., Lieberman, G., Milroy, C. M., and Parsons, M. A. (1996). *Ocular and cerebral trauma in non-accidental injury in infancy: underlying mechanisms and implications for paediatric practice.* British Journal of Ophthalmology, 80(4), 282-287.

[37] Forbes, B. J., Cox, M., and Christian, C. W. (2008). *Retinal hemorrhages in patients with epidural hematomas.* Journal of American Association for Pediatric Ophthalmology and Strabismus, 12(2), 177-180.

[38] *Wong, A. (2008). Eye movement disorders.* Oxford University Press.

[39] Emerson, M. V., Jakobs, E., and Green, W. R. (2007). *Ocular autopsy and histopathologic features of child abuse.* Ophthalmology, 114(7), 1384-1394.

[40] Pries, A. R., Reglin, B., & Secomb, T. W. (2005). *Remodeling of blood vessels: responses of diameter and wall thickness to hemodynamic and metabolic stimuli.* Hypertension, 46(4), 725-731.

[41] Han, H. C., Chesnutt, J. K., Garcia, J. R., Liu, Q., & Wen, Q. (2013). *Artery buckling: new phenotypes, models, and applications.* Annals of biomedical engineering, 41, 1399-1410.

[42] Whitham, G. B. (2011). *Linear and nonlinear waves.* John Wiley & Sons.

[43] Fusi, L., Saccomandi, G., Sequeira, A., & Toro, E. F. (2018). *Non-Newtonian Fluid Mechanics and Complex Flows:* Levico Terme, Italy 2016 (Vol. 2212). Springer.

[44] Brook, B. S., Falle, S. A. E. G., and Pedley, T. J. (1999). *Numerical solutions for unsteady gravity-driven flows in collapsible tubes: evolution and roll-wave instability of a steady state*. Journal of Fluid Mechanics, 396, 223-256.

[45] Lighthill, M. J. (1965). *Contributions to the theory of waves in non-linear dispersive systems*. IMA Journal of Applied Mathematics, 1(3), 269-306.

[46] Han, H. C. (2008). *Nonlinear buckling of blood vessels: a theoretical study.* Journal of biomechanics, 41(12), 2708-2713.

[47] Hosseini, M., & Paparisabet, M. A. (2016). *The effects of blood flow on blood vessel buckling embedded in surrounding soft tissues.* International Journal of Applied Mechanics, 8(05), 1650065.

[48] Shubov, M. A. (2006). *Exact controllability of damped coupled Euler–Bernoulli and Timoshenko beam model.* IMA Journal of Mathematical Control and Information, 23(3), 279-300.

[49] Wang, D., Luo, X., Liu, Z., & Stewart, P. S. (2023). *Flow-induced surface instabilities in a flexible-walled channel with a heavy wall.* Journal of Fluid Mechanics, 956, A1.

[50] MERCAN, K., & Civalek, Ö. (2016). *A Simple Buckling Analysis of Aorta Artery.* International Journal of Engineering and Applied Sciences, 7(4), 34-45.

[51] Pedley, T. J. (1980). *The fluid mechanics of large blood vessels*. Cambridge Monographs on Mechanics. Cambridge University Press, 1980.

[52] Taylor, M. G. (1966). *The input impedance of an assembly of randomly branching elastic tubes.* Biophysical journal, 6(1), 29-51.

[53] Avolio, A. P. (1980). *Multi-branched model of the human arterial system.* Medical and Biological Engineering and Computing, 18, 709-718.

[54] Alastruey, J., Parker, K. H., Peiró, J., & Sherwin, S. (2009). *Analysing the pattern of pulse waves in arterial networks: a time-domain study.* Journal of engineering mathematics, 64, 331-351.

[55] Womersley, J. R. (1955). *Method for the calculation of velocity, rate of flow and viscous drag in arteries when the pressure gradient is known.* The Journal of physiology, 127(3), 553.

[56] Alastruey, J., Parker, K. H., Peiró, J., and Sherwin, S. J. (2008). *Lumped parameter outflow models for 1-D blood flow simulations: effect on pulse waves and parameter estimation*. Communications in Computational Physics, 4(2), 317-336.

[57] Alastruey, J., Moore, S. M., Parker, K. H., David, T., Peiró, J., and Sherwin, S. J. (2008). *Reduced modelling of blood flow in the cerebral circulation: coupling 1-D, 0-D and cerebral auto-regulation models*. International journal for numerical methods in fluids, 56(8), 1061-1067.

[58] Alastruey, J. P. K. H., Parker, K. H., Peiró, J., Byrd, S. M., and Sherwin, S. J. (2007). *Modelling the circle of Willis to assess the effects of anatomical variations and occlusions on cerebral flows*. Journal of biomechanics, 40(8), 1794-1805.

[59] Alastruey, J., Parker, K. H., Peiró, J., and Sherwin, S. J. (2006). *Can the modified Allen's test always detect sufficient collateral flow in the hand? A computational study*. Computer methods in biomechanics and biomedical engineering, 9(6), 353-361.

[60] Smith, N. P., Pullan, A. J., and Hunter, P. J. (2002). *An anatomically based model of transient coronary blood flow in the heart*. SIAM Journal on Applied mathematics, 62(3), 990-1018.

[61] Steele, B. N., Wan, J., Ku, J. P., Hughes, T. J., & Taylor, C. A. (2003). *In vivo validation of a one-dimensional finite-element method for predicting blood flow in cardiovascular bypass grafts*. IEEE Transactions on Biomedical Engineering, 50(6), 649-656.

[62] Stergiopulos, N., Young, D. F., and Rogge, T. R. (1992). *Computer simulation of arterial flow with applications to arterial and aortic stenoses*. Journal of biomechanics, 25(12), 1477-1488.

[63] Chabannes, V., Pena, G., & Prud'Homme, C. (2013). *High-order fluid–structure interaction in 2D and 3D application to blood flow in arteries.* Journal of Computational and Applied Mathematics, 246, 1-9.

[64] Kafi, O., El Khatib, N., Tiago, J., & Sequeira, A. (2016). *Numerical simulations of a 3D fluid-structure interaction model for blood flow in an atherosclerotic artery.* Mathematical Biosciences & Engineering, 14(1), 179-193.

[65] Jin, W., & Alastruey, J. (2021). *Arterial pulse wave propagation across stenoses and aneurysms: assessment of one-dimensional simulations against three-dimensional simulations and in vitro measurements.* Journal of the Royal Society Interface, 18(177), 20200881.

[66] De Wilde, D., Trachet, B., Debusschere, N., Iannaccone, F., Swillens, A., Degroote, J., & Segers, P. (2016). *Assessment of shear stress related parameters in the carotid bifurcation using mouse-specific FSI simulations.* Journal of biomechanics, 49(11), 2135-2142.

[67] Moerman, K. M., Konduri, P., Fereidoonnezhad, B., Marquering, H., van der Lugt, A., Luraghi, G., & McGarry, P. (2022). *Development of a patient-specific cerebral vasculature fluid–structure-interaction model.* Journal of Biomechanics, 133, 110896.

[68] Olufsen, M. S., Peskin, C. S., Kim, W. Y., Pedersen, E. M., Nadim, A., and Larsen, J. (2000). *Numerical simulation and experimental validation of blood flow in arteries with structured-tree outflow conditions*. Annals of biomedical engineering, 28(11), 1281-1299.

[69] Sherwin, S. J., Franke, V., Peiró, J., & Parker, K. (2003). *One-dimensional modelling of a vascular network in space-time variables.* Journal of engineering mathematics, 47, 217-250.

[70] Abdullateef, S., Mariscal-Harana, J., & Khir, A. W. (2021). *Impact of tapering of arterial vessels on blood pressure, pulse wave velocity, and wave intensity analysis using one-dimensional computational model.* International Journal for Numerical Methods in Biomedical Engineering, 37(11), e3312.

[71] Piccioli, F., Bertaglia, G., Valiani, A., & Caleffi, V. (2022). *Modeling blood flow in networks of viscoelastic vessels with the 1-D augmented fluid–structure interaction system.* Journal of Computational Physics, 464, 111364.

[72] Müller, L. O., & Toro, E. F. (2014). *Enhanced global mathematical model for studying cerebral venous blood flow.* Journal of biomechanics, 47(13), 3361-3372.

[73] Ghigo, A. R., Lagrée, P. Y., & Fullana, J. M. (2018). *A time-dependent non-Newtonian extension of a 1D blood flow model.* Journal of Non-Newtonian Fluid Mechanics, 253, 36-49.

[74] Reymond, P., Merenda, F., Perren, F., Rufenacht, D., and Stergiopulos, N. (2009). *Validation of a one-dimensional model of the systemic arterial tree.* American Journal of Physiology-Heart and Circulatory Physiology, 297(1), H208-H222.

[75] Müller, L. O., and Toro, E. F. (2014). *A global multiscale mathematical model for the human circulation with emphasis on the venous system.* International journal for numerical methods in biomedical engineering, 30(7), 681-725.

[76] Zhang, X., Noda, S., Himeno, R., & Liu, H. (2017). *Gravitational effects on global hemodynamics in different postures: A closed-loop multiscale mathematical analysis.* Acta Mechanica Sinica, 33, 595-618.

[77] Fullana, J. M., & Zaleski, S. (2009). *A branched one-dimensional model of vessel networks.* Journal of Fluid Mechanics, 621, 183-204.

[78] Bellamoli, F., Müller, L. O., & Toro, E. F. (2018). *A numerical method for junctions in networks of shallow-water channels.* Applied Mathematics and Computation, 337, 190-213.

[79] Vignon, I. E., and Taylor, C. A. (2004). *Outflow boundary conditions for one-dimensional finite element modeling of blood flow and pressure waves in arteries.* Wave Motion, 39(4), 361-374.

[80] Marchandise, E., and Flaud, P. (2010). *Accurate modelling of unsteady flows in collapsible tubes.* Computer Methods in Biomechanics and Biomedical Engineering, 13(2), 279-290.

[81] Sherwin, S. J., Formaggia, L., Peiro, J., and Franke, V. (2003). *Computational modelling of 1D blood flow with variable mechanical properties and its application to the simulation of wave propagation in the human arterial system.* International journal for numerical methods in fluids, 43(6-7), 673-700.

[82] Olufsen, M. S., Hill, N. A., Vaughan, G. D., Sainsbury, C., and Johnson, M. (2012). *Rarefaction and blood pressure in systemic and pulmonary arteries.* Journal of fluid mechanics, 705, 280-305.

[83] Qureshi, M. U., Vaughan, G. D., Sainsbury, C., Johnson, M., Peskin, C. S., Olufsen, M. S., and Hill, N. A. (2014). *Numerical simulation of blood flow and pressure drop in the pulmonary arterial and venous circulation.* Biomechanics and modeling in mechanobiology, 13(5), 1137-1154.

[84] Noè, U., Chen, W., Filippone, M., Hill, N., and Husmeier, D. (2016, September). *Inference in a partial differential equations model of pulmonary arterial and venous blood circulation using statistical emulation.* In International Meeting on Computational Intelligence Methods for Bioinformatics and Biostatistics (pp. 184-198). Springer, Cham.

[85] Toro, E. F. (1989). *A weighted average flux method for hyperbolic conservation laws.* Proceedings of the Royal Society of London. A. Mathematical and Physical Sciences, 423(1865), 401-418.

[86] Spiller, C., Toro, E. F., Vázquez-Cendón, M. E., & Contarino, C. (2017). *On the exact solution of the Riemann problem for blood flow in human veins, including collapse.* Applied Mathematics and Computation, 303, 178-189.

[87] Contarino, C., Toro, E. F., Montecinos, G. I., Borsche, R., & Kall, J. (2016). *Junction-generalized Riemann problem for stiff hyperbolic balance laws in networks: an implicit solver and ADER schemes.* Journal of Computational Physics, 315, 409-433.

[88] Murillo, J., & García-Navarro, P. (2021). *A solution of the junction Riemann problem for 1d hyperbolic balance laws in networks including supersonic flow conditions on elastic collapsible tubes.* Symmetry, 13(9), 1658.

[89] Han, E., Warnecke, G., Toro, E. F., and Siviglia, A. (2015). *On Riemann solutions to weakly hyperbolic systems: Part 1. Modelling subcritical flows in arteries. In Technical Report NI15003–NPA*. Isaac Newton Institute for Mathematical Sciences, University of Cambridge, UK.

[90] Takahashi, T., Nagaoka, T., Yanagida, H., Saitoh, T., Kamiya, A., Hein, T., and Yoshida, A. (2009). *A mathematical model for the distribution of hemodynamic parameters in the human retinal microvascular network.* Journal of biorheology, 23(2), 77-86.

[91] Ganesan, P., He, S., and Xu, H. (2010). *Analysis of retinal circulation using an image-based network model of retinal vasculature.* Microvascular research, 80(1), 99-109.

[92] Guidoboni, G., Harris, A., Cassani, S., Arciero, J., Siesky, B., Amireskandari, A., and Park, J. (2014). *Intraocular pressure, blood pressure, and retinal blood flow autoregulation: a mathematical model to clarify their relationship and clinical relevance*. Investigative ophthalmology & visual science, 55(7), 4105-4118.

[93] Arciero, J., Harris, A., Siesky, B., Amireskandari, A., Gershuny, V., Pickrell, A., and Guidoboni, G. (2013). *Theoretical analysis of vascular regulatory mechanisms contributing to retinal blood flow autoregulation.* Investigative ophthalmology & visual science, 54(8), 5584-5593.

[94] Stewart, P. S., and Foss, A. J. (2019). *Self-excited oscillations in a collapsible channel with applications to retinal venous pulsation.* The ANZIAM Journal, 61(3), 320-348.

[95] Beck, W. A. (1935). *Aortic Regurgitation, Diagnosis and Differential Diagnosis.* Journal of the National Medical Association, 27(1), 19.

[96] Lange, R. L., Carlisle, R. P., & Hecht, H. H. (1956). *Observations on vascular sounds: The" pistol-shot" sound and the Korotkoff sound.* Circulation, 13(6), 873-883.

[97] Anliker, M., Rockwell, R. L., & Ogden, E. (1971). *Nonlinear analysis of flow pulses and shock waves in arteries: part I: derivation and properties of mathematical model.* Zeitschrift für angewandte Mathematik und Physik ZAMP, 22, 217-246.

[98] Bonshek, R., Cowley, S., Jensen, O., Pearce, P., Ravi, A., Stewart, P., and Zouache, M. (2016). *Understanding patterns of haemorrhage in the eye*. Report on the 2014 UK Maths in Medicine Study Group available from.

[99] Garhofer, G., Werkmeister, R., Dragostinoff, N., & Schmetterer, L. (2012). *Retinal blood flow in healthy young subjects.* Investigative ophthalmology & visual science, 53(2), 698-703.

[100] Suwa, N. (1971). *Morphological and morphometrical analysis of circulation in hypertention and ischemic kidney.* Urban Schwarzenberg.

[101] Love, A. E. H. (2013). *A treatise on the mathematical theory of elasticity.* Cambridge university press.

[102] Stewart, P. S., Jensen, O. E., and Foss, A. J. (2014). *A theoretical model to allow prediction of the CSF pressure from observations of the retinal venous pulse*. Investigative ophthalmology & visual science, 55(10), 6319-6323.

[103] Kur, J., Newman, E. A., & Chan-Ling, T. (2012). *Cellular and physiological mechanisms underlying blood flow regulation in the retina and choroid in health and disease.* Progress in retinal and eye research, 31(5), 377-406.

[104] Morton, K. W., & Mayers, D. F. (2005). *Numerical solution of partial differential equations: an introduction.* Cambridge university press.

[105] Toro, E. F., and Siviglia, A. (2013). *Flow in collapsible tubes with discontinuous mechanical properties: mathematical model and exact solutions*. Communications in Computational Physics, 13(2), 361-385.

[106] Acheson, D.J. (1990) *Elementary Fluid Dynamics*. Oxford Applied Mathematics and Computing Science Series, Oxford University Press.

[107] Rubinow, S. I., & Keller, J. B. (1972). *Flow of a viscous fluid through an elastic tube with applications to blood flow.* Journal of theoretical biology, 35(2), 299-313.

[108] Toro, E. F. (1992). *Riemann problems and the WAF method for solving the two-dimensional shallow water equations*. Philosophical Transactions of the Royal Society of London. Series A: Physical and Engineering Sciences, 338(1649), 43-68.

[109] Han, E., and Warnecke, G. (2014). *Exact Riemann solutions to shallow water equations*. Quarterly of Applied Mathematics, 72(3), 407-453.

[110] Kececioglu, I., Mcclurken, M. E., Kamm, R. D., & Shapiro, A. H. (1981). *Steady, supercritical flow in collapsible tubes. Part 1. Experimental observations*. Journal of Fluid Mechanics, 109, 367-389.

[111] Mcclurken, M. E., Kececioglu, I., Kamm, R. D., & Shapiro, A. H. (1981). *Steady, supercritical flow in collapsible tubes. Part 2. Theoretical studies*. Journal of Fluid Mechanics, 109, 391-415.

[112] Kamm, R. D., and Shapiro, A. H. (1979). *Unsteady flow in a collapsible tube subjected to external pressure or body forces*. Journal of Fluid Mechanics, 95(1), 1-78.

[113] Chapman, C. J. (2000). *High speed flow*. (p. 270).

[114] Whitham, G. B. (1955). *The effects of hydraulic resistance in the dam-break problem*. Proceedings of the Royal Society of London. Series A. Mathematical and Physical Sciences, 227(1170), 399-407.

[115] Sheng, W., Zhang, Q., & Zheng, Y. (2020). *The Riemann problem for a blood flow model in arteries.* Commun. Comput. Phys., 27, 227-250.

[116] Harten, A., Hyman, J. M., Lax, P. D., and Keyfitz, B. (1976). *On finite-difference approximations and entropy conditions for shocks.* Communications on pure and applied mathematics, 29(3), 297-322.

[117] Farina, A., Fusi, L., Mikelić, A., Saccomandi, G., Sequeira, A., Toro, E. F., & Toro, E. F. (2018). *Lectures on hyperbolic equations and their numerical approximation. Non-Newtonian Fluid Mechanics and Complex Flows:* Levico Terme, Italy 2016, 91-169.

[118] Taylor, C. A., Hughes, T. J., and Zarins, C. K. (1998). *Finite element modeling of blood flow in arteries.* Computer methods in applied mechanics and engineering, 158(1-2), 155-196.

[119] Spelman, Tamsin A., Ifeanyi S. Onah, David MacTaggart, and Peter S. Stewart. (2024). *Elastic jump propagation across a blood vessel junction.* arXiv preprint arXiv:2401.02785 (2024).

[120] Formaggia, L., Lamponi, D., Tuveri, M., and Veneziani, A. (2006). *Numerical modeling of 1D arterial networks coupled with a lumped parameters description of the heart.* Computer methods in biomechanics and biomedical engineering, 9(5), 273-288.

[121] Azer, K., and Peskin, C. S. (2007). *A one-dimensional model of blood flow in arteries with friction and convection based on the Womersley velocity profile.* Cardiovascular Engineering, 7(2), 51-73.

[122] Matthys, K. S., Alastruey, J., Peiró, J., Khir, A. W., Segers, P., Verdonck, P. R., & Sherwin, S. J. (2007). *Pulse wave propagation in a model human arterial network: assessment of 1-D numerical simulations against in vitro measurements.* Journal of biomechanics, 40(15), 3476-3486.

[123] Formaggia, L., Nobile, F., Quarteroni, A., & Veneziani, A. (1999). *Multiscale modelling of the circulatory system: a preliminary analysis.* Computing and visualization in science, 2, 75-83.

[124] Kolb, H. (2011). *Facts and figures concerning the human retina.*